Evaluation of Nuclear Spent Fuel Disposal in Clay-Bearing Rock - Process Model Development and Experimental Studies

(M2SF-21SN010301072)

Spent Fuel and Waste Disposition

Prepared for
U.S. Department of Energy
Spent Fuel and Waste Science and Technology

Carlos F. Jové Colón, Tuan A. Ho,
Eric N. Coker, Carlos M. Lopez,
Kristopher L. Kuhlman, Amanda C. Sanchez,
Melissa Mills, Jessica Kruichak, Ed Matteo (SNL)

Jonny Rutqvist, Yves Guglielmi,
Mengsu Hu, Tsubasa Sasaki,
Hang Deng, Pei Li, Carl I. Steefel,
Christophe Tournassat, Hao Xu,
Shaswat Babhulgaonkar,
Jens Birkholzer (LBNL)

Kirsten B. Sauer, Florie A. Caporuscio,
Marlena J. Rock (LANL)

Mavrik Zavarin, Thomas J. Wolery,
Jaddalah Zouabe, Elliot Chang,
Haruko Wainwright (LLNL)

August 20th, 2021
SAND2021-13578 R

DISCLAIMER

This information was prepared as an account of work sponsored by an agency of the U.S. Government. Neither the U.S. Government nor any agency thereof, nor any of their employees, makes any warranty, expressed or implied, or assumes any legal liability or responsibility for the accuracy, completeness, or usefulness, of any information, apparatus, product, or process disclosed, or represents that its use would not infringe privately owned rights. References herein to any specific commercial product, process, or service by trade name, trade mark, manufacturer, or otherwise, does not necessarily constitute or imply its endorsement, recommendation, or favoring by the U.S. Government or any agency thereof. The views and opinions of authors expressed herein do not necessarily state or reflect those of the U.S. Government or any agency thereof.

This is a technical report that does not take into account the contractual limitations under the Standard Contract for Disposal of Spent Nuclear Fuel and/or High-Level Radioactive Waste (Standard Contract) (10 CFR Part 961). For example, under the provisions of the Standard Contract, DOE does not consider spent nuclear fuel in multi-assembly canisters to be an acceptable waste form, absent a mutually agreed to contract amendment. To the extent discussions or recommendations in this report conflict with the provisions of the Standard Contract, the Standard Contract provisions prevail.

Sandia National Laboratories is a multimission laboratory managed and operated by National Technology & Engineering Solutions of Sandia LLC, a wholly owned subsidiary of Honeywell International Inc. for the U.S. Department of Energy's National Nuclear Security Administration under contract DE-NA0003525.

SUMMARY

The DOE R&D program under the Spent Fuel Waste Science Technology (SFWST) campaign has made key progress in modeling and experimental approaches towards the characterization of chemical and physical phenomena that could impact the long-term safety assessment of heat-generating nuclear waste disposition in deep-seated clay/shale/argillaceous rock. International collaboration activities such as heater tests, continuous field data monitoring, and *postmortem* analysis of samples recovered from these have elucidated key information regarding changes in the engineered barrier system (EBS) material exposed to years of thermal loads. Chemical and structural analyses of sampled bentonite material from such tests as well as experiments conducted on these are key to the characterization of thermal effects affecting bentonite clay barrier performance and the extent of *sacrificial zones* in the EBS during the thermal period. Thermal, hydrologic, and chemical data collected from heater tests and laboratory experiments has been used in the development, validation, and calibration of THMC simulators to model near-field coupled processes. This information leads to the development of simulation approaches (e.g., continuum and discrete) to tackle issues related to flow and transport at various scales of the host-rock, its interactions with barrier materials, and EBS design concept. Consideration of direct disposal of large capacity dual-purpose canisters (DPCs) as part of the back-end SNF waste disposition strategy has generated interest in improving our understanding of the effects of elevated temperatures on the EBS design. This is particularly important for backfilled repository concepts where temperature plays a key role in the EBS behavior and long-term performance. This report describes multiple R&D efforts on disposal in argillaceous or clay-bearing geologic media and EBS material interactions through development and application of coupled THMC process models (e.g., reactive transport), experimental studies on clay/metal/cement barrier and host-rock (argillite) material interactions, molecular dynamic (MD) simulations of water transport during clay dehydration, and advances in thermodynamic and surface complexation database development. Laboratory-scale experiments (e.g., rock leaching, packed column) provides key data for testing reactive transport modeling involving strong couplings of fluid mixing and barrier material chemical interactions. The THM modeling focuses on heater test experiments in argillite rock and gas migration in bentonite as part of international collaboration activities at underground research laboratories (URLs). In addition, field testing at an URL involves *in situ* analysis of fault slip behavior, induced seismicity, and fault permeability. Pore-scale methods have been used to describe multiphase flow and interfacial reaction phenomena. Calorimetric and solid-fluid interaction experiments on bentonite samples from heater test under ambient and elevated temperatures permit the evaluation of ion exchange, phase stability, and mineral transformation changes that could impact clay swelling. GDSA integration activities include inclusion of coupled THM processes into the GDSA and PA modeling platform.

As in previous milestone deliverables, this report is a living document structured according to various national laboratory contributions describing R&D activities applicable to clay/shale/argillite media. The COVID-19 situation impacted some efforts, particularly laboratory activities involving experimental and material characterization studies. However, even with restrictions on performing such activities, the disposal in argillite R&D activities produced key accomplishments that are described in this report.

These R&D activities are summarized as follows:

- **Disposal in Argillite R&D and International Collaborations Activities – SNL (Part I)**
  - International Collaborations:
    - FEBEX-DP:
      - Cyclical thermogravimetric analyses (TGA/DSC) under controlled relative humidity (RH) conditions and elevated temperatures (85°C and 150°C) show that bentonite overall thermal behavior is similar to some extent for previous experiments at 60°C. However, trends for extended hydration periods (>120 minutes) at high temperatures no longer follow the trend of lower hydration periods and need to be investigated further.
      - In-situ XRD analyses of FEBEX-DP bentonite at 85°C and controlled dew point (~58°C) from dry-wet-dry conditions as a function of time can resolve changes of interlayer lattice spacing within a time period of ~24 hours. This result will be compared with temporal montmorillonite dehydration behavior TGA/DSC experiments.
      - Preliminary MD simulation results indicate two key processes determining Na-MMT dehydration: first stage of water transport exhibits an advection mechanism. The second stage represents slow desorption of the last 1-2 water molecules from the Na^{+} ions leading to a diffusion mechanism. Further MD simulations K^{+} and Ca^{+2} (K-MMT and Ca-MMT, respectively) indicate that clay dehydration process (2W to 0W) depends on the cation adsorption complexes in the interlayer.
    - Reactive-Transport Modeling of Barrier Material Leaching:
      - PFLOTRAN 1D reactive-transport model implementation of the EPA 1315 monolith leaching test or marl rock generated encouraging results representing the overall trends of temporal changes in solute concentration profiles.
    - LBNL HotBENT Heated/Unheated Column Test
      - Preliminary XRD analyses (air-dried and glycolated) of post-experiment samples collected at various radial distances from the central heating element have been completed
      - Work is planned to conduct a detailed evaluation of the XRD profile data focusing on clay structural features with radial distance from the heated zone.

- **Investigation of Coupled Processes in Argillite Rock: FY21 Progress – LBNL (Part II)**
    - LBNL has begun initial work on investigating the effect of shale-creep on the long-term performance of an argillite repository. An appropriate shale-creep model has been identified based on experimental data of various shale host rock as reported in the literature.
    - LBNL scientists are participating in three DECOVALEX-2023 tasks (A, B, and C) that include coupled processes model validation against experiments and necessary model developments.
    - Launched new work related to modeling discrete fractures in argillite using machine learning for meshing of fracture morphology, and the development of networks from images of fractured rock.
    - Numerical modeling of complex fractured rock responses in argillite has been conducted using the numerical manifold method (NMM) that allows for more realistic representation of fracture geometry in the model.
    - LBNL scientists in collaboration with international scientists have achieved substantial progress in the study of fault activation and long-term sealing behavior in argillite at the Mont Terri URL.
    - Launched a new task on modeling of concrete-clay interfaces, involving model development and application using the Lattice Boltzmann method as an alternative to continuum modeling for detailed modeling of interface alteration.
    - Launched another new task on concrete-clay interfaces that involves modeling the Cement–Opalinus Clay Interaction (CI-D) experiment at the Mont Terri URL, focused on understanding reaction-induced porosity, permeability, and diffusivity changes in both the cement and Opalinus Clay rock as a result of their interaction.
    - LBNL, in collaboration with SNL, is developing new approaches for integrating coupled process models into the Geological Disposal Safety Assessment (GDSA) and Performance Assessment (PA). In FY21, a journal paper (Sasaki and Rutqvist, 2021) was published.
- **Disposal in Argillite R&D and International Collaborations (FY21) – LANL (Part III)**
    - Hydrothermal experiments (200°C and 300°C) involved Opalinus Clay (wall rock), Wyoming bentonite, Portland cement, bentonite-steel, and novel EBS additives such as apatite. Characterization studies involved SEM-EMPA XRD, and aqueous solution compositional data of hydrothermal experiments.
    - Laboratory shutdown and/or ensuing restrictions of activities due to COVID-19 slowed progress in some experimental and characterization activities. Still, progress was made in various aspects of these activities.

- New results and interpretations from our series of experiments with Opalinus Clay, Wyoming bentonite, and ordinary Portland cement (EBS-23 through EBS-28, EBS-30, EBS-31) have been obtained.
- Two 6-week experiments and two 8-week experiments (EBS-30 and EBS-31) were completed during FY21.
- Montmorillonite is stable over the experimental time period (6 weeks to 6 months) at circum-neutral pH values and low bulk system [K+]. Zeolite formation is observed in experiments at 300ºC but not at 200ºC.
- Zeolite/aluminosilicate mineral reactions buffer the solution chemistry and pH. Recrystallization of montmorillonite to illite is not observed and zeolite forming reactions are kinetically favored.
- The addition of uncured ordinary Portland cement powder results in precursor montmorillonite dissolution and the formation of abundant feldspar, zeolite, CSH, and amorphous phases.
- Significant montmorillonite alteration occurs in the experiments with uncured OPC powder, including recrystallization to illite and loss of swelling capacity.
- Inclusion of cured OPC cement chip results in different geochemical and mineralogical effects in comparison to OPC powder.
- Mineralization at the steel-bentonite interface varies with system bulk chemistry. Fe is transferred to the bentonite buffer in the form of Fe-rich phyllosilicate phases at circum-neutral pH.
- In a cementitious, high-pH environment, Fe-rich aluminosilicate phases at the steel-bentonite interface are not observed; zeolite and CSH minerals are observed attached to the steel surface.
- Preliminary results suggest that apatite was unreactive in the bentonite.
- Launched experiments using welded steel and polished stainless steel samples with Wyoming bentonite at 300ºC, 150 bars for 6 weeks.

- **Development of the SUPCRTNE Thermodynamic Database Engine – LLNL (Part IV)**
  - Revisions of H2OI95 (1.2) code implementation of the equation-of-state (EoS) model for H_2O based on IAPWS-95 EoS model are nearly completed.
  - Current focus is the development of SUPCRTNE which is the connection of the codes SUPCRT v. 1.0 with H2OI95. SUPCRTNE will then contain the latest IAPWS-sanctioned models for water properties.

- **Non-Electrostatic Surface Complexation Database for GDSA – LLNL (Part V)**
    - Development and updates of a digitized LLNL Surface Complexation Ion Exchange (SCIE) sorption database.
    - Application of data Mining / data driven approaches to surface complexation model (SCM) database development. The objective is to apply this database development approach capturing radionuclide sorption to iron oxides, carbonates, and quartz. This is developed through an integrated data fitting workflow for retrieval and estimations of SCM parameters for use in reactive transport models.
    - As previously reported, the sorption database development approach will leverage fitting strategies to a surface complexation model (SCM) coupled to optimization software while exploiting applications of machine learning and data science techniques.

Overall Status and Future Perspectives in Disposal in Argillite R&D:

- **Experimental and thermodynamic modeling studies of barrier material interactions**
    - **Goal**: Conduct experimental and thermodynamic modeling investigations of barrier material interactions from ambient conditions up to elevated pressures and temperatures. Study degradation mechanisms of clay, cement, and metal barriers with implications to in-package chemistry and spent fuel degradation. This may also involve coupling the spent fuel degradation model (source term) with reactive transport modeling of the EBS. Developments of thermodynamic databases to be used as input feeds to coupled-process models and (geo)chemical reactive transport simulators. Development of thermodynamic parameter data for UO_2 corrosion products using first principles calculations and electrochemical model development activities has been moved to the waste form testing, modeling, and performance.
    - **Status & Accomplishments**: Progress on experimental and thermodynamic modeling activities:
        - A comprehensive suite of experiments focused on hydrothermal interactions of bentonite clay, steel materials, and argillaceous wall rock. This also involves and mechanistic characterization of steel corrosion in the presence of engineered barrier solids (e.g., bentonite, steel cement) and host rock material.
        - Extensive characterization studies (compositional, structural, geochemical) of run products integrated with thermodynamic modeling to

evaluate the occurrence secondary mineralization and clay phase stability at elevated pressures and temperatures.

- Characterization studies of bentonite samples and argillaceous rock from international repository programs (FEBEX-DP, HotBENT, Mont Terri) achieved through international collaborations.
- Thermodynamic database development for the re-analysis of thermodynamic properties of aqueous, solids, and gas species. Representation of SFWST campaign within the NEA-TDB project. Revisiting and testing the equation of state (EoS) for H_2O based on the IAPWS-95 formulation and computer code implementation. Sorption database development using data science approaches. Sorption modeling strategies using the PHREEQC-PEST code coupling for data fitting with various surface complexation models.
- 1D-3D reactive transport modeling under non-isothermal conditions using the PFLOTRAN THC simulator. The focus is on multiphase multicomponent description of barrier interactions under non-isothermal conditions using HPC platforms.

- **Perpespectives**: Future outlooks in experimental and thermodynamic modeling studies:

  - Expand experimental work towards interactions between bentonite clay, cementitious materials, steel material, and argillaceous host rock. Investigate these interactions at various temperatures and pressures to evaluate the alteration mineralogy at the interfaces of these barrier materials.
  - Conduct thermal analysis (TGA/DSC) and XRD/XRF characterization on (hydro)thermally-treated treated FEBEX-DP bentonite samples to study hydration/dehydration properties and swelling behavior. Expand MD studies on the mechanisms of water dynamics in swelling clays and compare results with the aforementioned analyses. These studies will improve our understanding of the chemical behavior of bentonite under partially saturated conditions at elevated temperatures.
  - Continue expansion of thermodynamic database development towards testing and applications to geochemical and reactive transport modeling at elevated pressures and temperatures. Experimental work provides information on these activities. Addition of machine learning (ML) approaches to the PHREEQC-PEST fitting modeling strategy for sorption

database development. Evaluate novel data-driven strategies to sorption database development.

- PFLOTRAN simulator for 3D non-isothermal reactive transport (THC) modeling of bentonite barrier – fluid interactions under variably saturated conditions. Emphasis will be given to evaluate initial saturation and RH conditions in non-isothermal simulations. Expand analysis and validation of reactive transport simulations capturing interactions of cementitious barrier material with fluids. Extend this modeling approach to DPC disposal scenarios with high thermal loads.
- Thermodynamic modeling to describe barrier material interactions focusing on interactions between cementitious and other barrier materials. Expand these evaluations towards the effect on clay phase transformation and the role of zeolite formation, particularly in the presence of cementitious phases at elevated temperatures.

- **Coupled-process model development for simulation of near-field thermal, chemical, mechanical, and transport (THMC) interactions.**
  - **Goal**: Development, testing, and validation of coupled-process models for simulation of near-field thermal, chemical, mechanical, and transport (THMC) interactions in the evaluation of barrier material performance. Programmatic engagements and collaborations with international R&D activities (e.g., URL heater tests) in repository sciences.
  - **Status & Accomplishments**: Progress on THMC model development, implementation, and validation:
    - TOUGH-FLAC THM simulator with applications to disposal in argillite R&D. Simulation of bentonite swelling behavior using the BBM (Barcelona Basic Model) and BExM (Barcelona Expansive Model) constitutive model implementations.
    - Application of a TOUGH-FLAC shale / clay rock constitutive model that captures rock anisotropic properties of elasticity, strength, thermal conductivity, permeability, and thermal expansion. This includes shale creep behavior and assessment of long-term argillite repository performance.
    - Development of TOUGH-FLAC models to simulate permeability and damage behavior in the EDZ.
    - TOUGH-RBSN simulator for coupled fracturing processes and gas migration.

- International collaborations (Mont Terri, DECOVALEX-2023): (FE Experiment – Mont Terri; COx Clay Stone – Bure, France; Closure Test Drift (CTD) experiment, Mizunami site, Japan).
- Development of numerical modeling approaches of complex fractured rocks. Modeling degradation of cement-clay interfaces using the Lattice Boltzmann method and continuum approaches.
- Fault activation monitoring using the SIMFIP tool and assessment of gathered data.

- **Perspectives**: Future outlooks in THMC model development:
  - Continue engagements with international collaborations activities involving heater tests design and process model and validation.
  - Utilize recovered samples from heater tests and sensor data for sample characterization and evaluation of EBS material behavior.
  - Expand development of continuum and discrete modeling approaches to evaluate transport phenomena at different scales.
  - Reactive transport modeling under isothermal and non-isothermal conditions focusing on barrier material interactions (clay, steel, cement).
  - Continue development of new approaches to link coupled process models into GDSA and PA.
  - Application of the SIMFIP tool for long-term *in situ* monitoring of fault movement, effects of fluid pressure, and leakage.
  - Continue development of coupled hydromechanical numerical model to analyze fault displacement, fluid pressure, and injection flowrate data.
  - Model testing and development for large-scale gas driven fracturing using 3D models. Looking forward to leverage high-performance computing (HPC) resources.
  - Development of coupled chemical-mechanical model at the microscale.
  - Characterization of microbial-abiotic processes in EBS and host rocks.
  - Development of a predictive computational model of radionuclide retention in bentonites.

Near-Term Thrust Topics (Next 1- to 2-year period)

a) Elucidation of the coupled thermal, hydrologic, mechanical, and chemical (THMC) processes affecting repository performance and

b) Development of multi-fidelity approaches for integration of process models into the GDSA framework

These thrust topics are current focus areas in the disposal in argillite work package, which are planned to continue out over the next five years as well. Continuing work includes expanding the applicability of coupled process models to elevated temperatures and integration of DPC-relevant information related to thermal management and impact on repository design concepts. Longer-term thrusts include the development of reduced order models and/or simplified model outputs for complex argillite process models.

Longer-Term Thrust Topics (Next 3- to 5-year period)

a) Simplifying the representations of THMC processes occurring from within the EBS

b) International collaborations with inputs on field testing and process understanding

Partnerships with current international programs will be nurtured and expanded in the coming years to create a collaboration bridge gaining advanced knowledge of nuclear waste disposal research from URL activities worldwide. Emphasis will be given to THM and HM modeling activities for heater test experiments at international URL's and other relevant activities (e.g., DECOVALEX2023). Specific examples of these are the heater tests at the Honorobe URL site in Japan and HotBENT at the Grimsel test site in Switzerland. The Grimsel site has provided a large suite of barrier material samples (bentonite, cement, rock) for characterization and experimental studies of fluid-bentonite interactions. These activities will continue during the next five years. Additional international collaborations include continued modeling of heater test experiments at Mont Terri. Participation in the OECD-NEA thermodynamic database (TDB) project, particularly in the review of the ancillary thermodynamic data volume which already started, and other TDB-related activities planned to take place within the next two years.

These near- and longer-term thrust topics are excerpts from the deliverable report M2SF-21SN010304054 “SFWST Disposal Research R&D 5-Year Plan – FY2021 Update” by Sassani et al. (2021)

Revision 5
01/15/2018

APPENDIX E

NTRD DOCUMENT COVER SHEET[1]

Name/Title of Deliverable/Milestone/Revision No. Evaluation of Nuclear Spent Fuel Disposal in Clay-Bearing Rock - Process Model Development and Experimental Studies M2SF-21SN010301072 / Rev.0

Work Package Title and Number SF-21SN01030107 Argillite Disposal R&D - ~~SNL~~

Work Package WBS Number 1.08.01.03.01

Responsible Work Package Manager Carlos F. Jove Colon
(Name/Signature)

Date Submitted

Quality Rigor Level for Deliverable/Milestone[2]	☐ QRL-1 ☐ Nuclear Data	☐ QRL-2	☒ QRL-3	☐ QRL-4 Lab QA Program[3]

This deliverable was prepared in accordance with Sandia National Laboratory
(Participant/National Laboratory Name)

QA program which meets the requirements of
☐ DOE Order 414.1 ☐ NQA-1 ☐ Other

This Deliverable was subjected to:

☒ Technical Review ☐ Peer Review

Technical Review (TR)
Review Documentation Provided
☐ Signed TR Report or,
☐ Signed TR Concurrence Sheet or,
☒ Signature of TR Reviewer(s) below

Peer Review (PR)
Review Documentation Provided
☐ Signed PR Report or,
☐ Signed PR Concurrence Sheet or,
☐ Signature of PR Reviewer(s) below

Name and Signature of Reviewers
Yifeng Wang (SNL)

NOTE 1: *Appendix E should be filled out and submitted with the deliverable. Or, if the PICS:NE system permits, completely enter all applicable information in the PICS:NE Deliverable Form. The requirement is to ensure that all applicable information is entered either in the PICS:NE system or by using the NTRD Document Cover Sheet.*

- *In some cases there may be a milestone where an item is being fabricated, maintenance is being performed on a facility, or a document is being issued through a formal document control process where it specifically calls out a formal review of the document. In these cases, documentation (e.g., inspection report, maintenance request, work planning package documentation or the documented review of the issued document through the document control process) of the completion of the activity, along with the Document Cover Sheet, is sufficient to demonstrate achieving the milestone.*

NOTE 2: *If QRL 1, 2, or 3 is not assigned, then the QRL 4 box must be checked, and the work is understood to be performed using laboratory QA requirements. This includes any deliverable developed in conformance with the respective National Laboratory / Participant, DOE or NNSA-approved QA Program.*

NOTE 3: *If the lab has an NQA-1 program and the work to be conducted requires an NQA-1 program, then the QRL-1 box must be checked in the work Package and on the Appendix E cover sheet and the work must be performed in accordance with the Lab's NQA-1 program. The QRL-4 box should not be checked.*

AKNOWLEDGEMENTS

The authors acknowledge our gratitude to Yifeng Wang (SNL), Ed Matteo (SNL), Philippe Weck (SNL), Charles R. Bryan (SNL), Chris Camphouse (SNL), Geoff Freeze (SNL), Emily Stein (SNL), Prasad Nair (DOE NE), and Tim Gunter (DOE NE) for their helpful discussions and contributions on various topics covered in this report. Dr. Mark A. Rodriguez (SNL) and his staff conducted the *in situ* XRD analyses on FEBEX-DP bentonite samples presented in this report. We also express our gratitude to Drs. Chen Gruber and Dr. David Kosson of Vanderbilt University for sharing their marl leaching test data and other technical information along with helpful suggestions. Dr. Liange Zheng and Sharon Borglin of LBNL kindly provided the MX-80 bentonite samples and supporting technical information of the HotBENT column experiments. This work was supported by the Spent Fuel and Waste Disposition (SFWD) office through the Department of Energy's (DOE-NE) Spent Fuel and Waste Science and Technology (SFWST) program.

TABLE OF CONTENTS

SUMMARY iv

AKNOWLEDGEMENTS xiv

TABLE OF CONTENTS xv

REVISION HISTORY xxxi

ACRONYMS xxxii

Disposal in Argillite R&D and International Collaborations Activities – SNL (Part I)

1. Introduction 1

2. International Collaboration Activities 2

   2.1 FEBEX-DP 4

      2.1.1 Thermal (TGA/DSC) Analyses 7

3. Transport-mechanical-chemical coupling effect during clay dehydration controlled by coordination number of interlayer ions: an MD simulation approach 14

   3.1 MD Simulation Methodology 16

   3.2 Discussion and Results 17

   3.3 Conclusions 25

4. 1D Reactive-Transport Modeling of Sedimentary Rock Leaching Experiments 26

   4.1 Introduction 26

      4.1.1 Marl Rock Properties 26

      4.1.2 Monolith leaching test (EPA Method 1315) 27

   4.2 1D PFLOTRAN Reactive Transport Simulations 28

   4.3 Preliminary Results and Discussion 30

5. HotBENT Heated Column Experiment: Preliminary XRD Analysis of Post-Experiment Bentonite Samples 33

   5.1 Preliminary XRD Analyses of Post-Experiment Bentonite Samples 34

6. Conclusions 37

7. FY22 Work 38

8. References 39

Investigation of Coupled Processes in Argillite Rock: FY21 Progress – LBNL (Part II)

1. Introduction 46
2. Modeling Shale Creep for the Long-Term Repository Performance 51
2.1 Introduction 51
2.2 Method 52
2.2.1 Norton-Bailey Law 53
2.2.2 Laboratory Test Results 54
2.3 Preliminary Results 56
2.3.1 Axial Strain versus Time 56
2.3.2 Log(time) versus Creep Compliance 60
2.3.3 Log(time) vs. Log(creep compliance) 63
2.4 Summary and Future Plans 67
3. FE Experiment at the Mont Terri Site (DECOVALEX-2023) 67
3.1 Description and Status of the Mont Terri FE experiment 67
3.2 TOUGH-FLAC Model of the Mont Terri FE Experiment 69
3.3 Simulation Results 72
3.4 Future work on the FE Experiment Modeling 75
4. Modeling of Thermal and Gas and Fracturing at Bure in COx Claystone (DECOVALEX-2023) .. 76
4.1 Setup of Thermal Pressurization Laboratory Experiments on COx Claystone 76
4.2 Experimental and Simulation Results for Reference Parameters 77
4.3 Future work on DECOVALEX-2023 Task A 81
5. Modeling of Gas Migration in Clay (DECOVALEX-2023) 82
5.1 Gas Migration in Clay 82
5.2 LBNL Model Approaches for Gas Migration 83
5.3 Modeling 1D gas migration 83
5.4 Blind prediction of new gas migration experiment 92
6. Machine Learning of Fracture Morphology and Mesh Optimization 94
6.1 Introduction 94
6.2 Approach 95
6.2.1 Machine Learning and Numerical Modeling 95
6.2.2 Convolutional Neural Network for Image Recognition 98
6.2.3 U-Net CNN for Image Segmentation 99

6.2.4 Neural Style Transfer 100
6.3 Examples and Results 102
6.3.1 Machine Learning of Fracture Morphology from Rock Images 102
6.3.2 Mesh generation for rough fractures using NST 103
6.3.3 Mesh generation for discrete fractures using NST 105
6.4 Summary and Perspectives 105

7. Modeling of Discrete Fractures in Argillite Rocks Based on the Numerical Maniford Method 106
7.1 Introduction 106
7.2 Numerical Manifold Method 107
7.3 Modeling Fracture Dynamics Based on NMM 109
7.3.1 Mathematical description of Dynamic Contacts of Fractures 109
7.3.2 Geometric Representation of Discrete Fractures in NMM 110
7.3.3 Numerical Implementation in NMM 112
7.4 Examples and Results 113
7.4.1 Modeling a Discrete Fracture Network 113
7.4.2 Excavation and Heating in Discrete Fractured Bedded Argillite Rock 116

8. Short- to Long-Term Hydromechanical Response of Faults and EDZ in Argillite Host Rock 120
8.1 Introduction 120
8.2 Fault architecture and reactivation behavior in shale revealed by distributed fiber optic strain sensing 121
8.2.1 Distributed Fiber Optic network setting across the Mont Terri Main Fault 122
8.2.2 DSS Methods and processing 125
8.2.3 Results – Distribution of deformation induced by the remote gallery excavation 128
8.2.4 Discussion 133
8.2.5 Conclusions 138
8.3 Imaging the three-dimensional scale of seismic and aseismic rupture 139
8.3.1 Modelling the effects of fractures interactions on leakage and induced seismicity during a clay fault zone activation 139
8.3.3 Continuous active-source seismic monitoring of the loss of integrity induced by water pressurization of the main fault at Mont Terri, Switzerland 145
8.4 Work Summary and Perspectives 151

9. Interfacial Alteration and Impacts on Radionuclides Transport 153
9.1 Introduction 153
9.2 Methods 153

9.2.1 Phase-Field Lattice Boltzmann Method (PF-LBM) ... 153
9.2.2 Lattice Boltzmann Method (LBM) for transport process under multiphase flow condition ... 156
9.2.3 Lattice Boltzmann Method (LBM) for reactions ... 157
9.2.4 Coupling framework of the multiphase flow-reactive transport LBM ... 158
9.3 Model Verification and Preliminary Results ... 159
9.3.1 Simulation setup ... 159
9.3.2 Results ... 160
9.4 Benchmark test ... 162
9.5 Summary and Future Work ... 163
10. Modeling of Cl-D Experiment at Mont Terri ... 164
10.1 Model Changes ... 164
10.1.1 Multi-porosity ... 164
10.1.2 Ionic strength and water activity ... 166
10.1.3 Status of Model Changes ... 166
10.1.4 Extension to 3D ... 166
10.1.5 Future Work for Model Development ... 167
10.2 Preliminary 2D calculations ... 167
10.3 Discussion ... 171
10.4 Future Work on Cl-D Experiment at Mont Terri ... 172
10.5 Summary ... 172
11. LINKING TO GEOLOGIC DISPOSAL SAFETY ASSESSMENT (GDSA) ... 172
12. SUMMARY OF FY21 PROGRESS AND FUTURE WORK ... 173
13 Acknowledgements ... 175
14 References ... 176

Argillite R&D and International Collaborations – LANL (FY21) (Part III)

1. Introduction ... 190
1.1 Argillite Disposal R&D ... 190
1.2 Background ... 192
1.2.1 Wyoming Bentonite in EBS Applications ... 192
1.2.2 Opalinus Clay ... 193
1.2.3 Hydrothermal Interaction of Wyoming Bentonite and Opalinus Clay ... 194

1.2.4 Previous Research in Bentonite-Portland Cement Interaction 194
1.2.5 Steel Canister-Clay Interface Zone Alteration in an Argillite-Hosted Repository . 196
1.2.6 Steel Corrosion in a Cement Environment 198
1.2.7 Designer EBS Additives 198

2 Methods 200

3 Results 202
3.1 Starting Material Characteristics 202
3.2 Aqueous Geochemistry (EBS-23 to EBS-28) 204
3.3 XRF Results 208
3.4 QXRD Results 209
3.5 Clay Mineral XRD 210
3.6 Cement Chip XRD Analyses 213
3.7 Electron Microprobe Analyses 213
3.8 Wyoming Bentonite + Durango Apatite: EBS-29 216
3.9 Steel-Bentonite Interface Mineralization 220
3.9.1 Experiment with Wyoming Bentonite and Opalinus Clay 220
3.9.2 Experiments with Portland Cement 222
3.9.3 Chemical Gradient across the Steel Surface 223
3.9.4 Steel Precipitation Thickness of Alteration Phases 225

4 Discussion 226
4.1 Portland Cement Effects 226
4.1.1 Aqueous Geochemistry 226
4.1.2 Silica Saturation 226
4.1.3 pH 227
4.2 Clay Alteration 228
4.3 Zeolite and CSH-Mineral Formation 228
4.5 Steel Corrosion and Interface Mineral Precipitation 230
4.5.1 Steel Corrosion in the Argillite Environment 231
4.5.2 Corrosion in the Cement Environment 233
4.5.3 Steel Corrosion Summary 235
4.6 Conclusions 235

5 Argillite International Collaborations 236
5.1 Horonobe URL Research 236

5.1.1 Background 236
5.1.2 Summary of FY20 Horonobe Report 237
5.1.3 FY21 LANL Experiments 237

6 Steel corrosion experiments – FY21 238
6.1 Background 238
6.2 Methods 240
6.2.1 Starting Material 240
6.2.2 Current Status 242

7. Acknowledgements 243

8. References 243

Development of the SUPCRTNE Thermodynamic Database Engine – LLNL (Part IV)

1. Introduction 254

2. Background 254

3. Earlier Work Under the UFD and SFWST Campaigns 255

4. Updating SUPCRT92 in Support of the Spent Fuel and Waste Science and Technology Program. 256
4.1. General Approach 256
4.2. H2OI95 v. 1.0: Software for Dealing with the IAPWS-95 Model (FY19) 258
4.3. H2OI95 v. 1.1: Calculation of Additional Water Properties (FY20) 259
4.4 SUPCRTNE v 1.0 and H2OI95 v. 1.2 (FY21) 261

6. Acknowledgements 262

7. References 262

Non-Electrostatic Surface Complexation Database for GDSA (LLNL) (Part V)

1. Introduction 267

2. Digitized LLNL Surface Complexation Ion Exchange (SCIE) sorption database updates 268

3. A Data Mining/Data Driven Approach to Surface Complexation Model Database Development for Reactive Transport Modeling 268
3.1 Marerials and Methods 271
3.2 Results and Discussion 275
3.3 Implications 283

4. A Data-Driven Surface Complexation Database for Reactive Transport Modeling: Radionuclide Sorption to Iron Oxides, Carbonates, and Quartz 284

5. Planned FY22 Efforts 286

7. Acknowledgments 286

8. References 286

Appendix A 292

Appendix B 295

TABLE OF FIGURES

Disposal in Argillite R&D and International Collaborations Activities – SNL (Part I)

Figure 1. Schematic layout of the FEBEX "in-situ" field test after the first partial dismantling showing the configuration of heater #2 at the GTS URL 6

Figure 2. Schematic configuration of sampling zones (indicated by vertical light blue bars) for the FEBEX-DP project. 6

Figure 3. Schematic diagram of sampling locations for the FEBEX-DP dismantling of section 49. 7

Figure 4. TGA, DTA, and DSC curves as a function of time for water adsorption/desorption cycles at 60°C for the <2 µm bentonite sample. 10

Figure 5. TGA and DSC curves as a function of time for water adsorption/desorption cycles at 60°C for the <75 µm bentonite sample 11

Figure 6. DSC curves as a function of time for the <2 µm bentonite sample for the dehydration steps at 85°C and 150°C. 12

Figure 7. *In situ* XRD spectra collected at temperatures of 85°C and 150°C, and at a dew point of ~58°C. 13

Figure 8. *In situ* XRD 001 d-spacing data for clay hydration/dehydration states collected at temperatures of 85°C and a dew point of ~58°C. 14

Figure 9. Simulation system used to study the dehydration process of Na-MMT 16

Figure 10. Mass loss (i.e., number of water molecules lost) as a function of simulation time 18

Figure 11. Simulation snapshots demonstrate water transport pathway through an MMT interlayer during the dehydration process 19

Figure 12. Coordination number of Na^+ ions and d-spacing as a function of time for first 5 ns and 50 ns simulations. 20

Figure 13. Mass loss, d-spacing, and water coordination number of Na^+ ion during the dehydration of 1W hydrated MMT at 30° and 60° C. 21

Figure 14. d-spacing and heat flow and mass as a function of time at 60 °C 22

Figure 15. Water coordination number of interlayer Na^+, K^+, and Ca^{2+} ions as a function of hydration time 23

Figure 16. Ion adsorption complexes in interlayers at 2W hydration state. 24

Figure 17. d-spacing change as a function of time during the dehydration process of Na-MMT, K-MMT, and Ca-MMT. 25

Figure 18. Bulk rock sample; epoxy-mounted sample used for 1315, and experimental set up for the 1315 test. 28

Figure 19. Mesh discretization of the solid and leaching solution domains along with dimensions of the rectangular domain. 29

Figure 20. Temporal change of pH and total Ca^{++} concentration in leachate solutions for the 1315 leaching experiment 31

Figure 21. Temporal change of total dissolved Si concentration 31

Figure 22. Temporal change of Na and K concentration 32

Figure 23. Schematic diagram of the entire experimental column setup including flow control, sensors, and cartridge heater at the column center axis. 33
Figure 24. CT scan image showing the column cross section delineating the sampling radial zones. 34
Figure 25. XRD stacked spectra of bentonite sampled in region R3 (closer to the heater) for both heated (V1) and unheated (V2) column experiments....35
Figure 26. XRD stacked spectra of bentonite sampled in region R2 (midpoint) for both heated (V1) and unheated (V2) column experiments....36
Figure 27. XRD stacked spectra of bentonite sampled in region R1 (outer) for both heated (V1) and unheated (V2) column experiments....36

Investigation of Coupled Processes in Argillite Rock: FY21 Progress – LBNL (Part II)

Figure 1-1. Schematic illustration of coupled THM processes driven by heat released from the waste package. 48
Figure 1-2. Schematic of coupled THM responses in a repository in the near field and at the repository scale caused by heating, thermal pressurization and potential gas generation. 48
Figure 1-3. TOUGH-FLAC (left) and TOUGH-RBSN models developed for coupled THM process analysis. 50
Figure 1-4. Fault activation modeling approach using TOUGH-FLAC. 50
Figure 2-1. A cubic (brick) element in FLAC3D. 53
Figure 2-2. Laboratory creep test results on shale samples. 55
Figure 2-3. Effects of parameters on axial strain behavior vs. time of the Norton-Bailey model. 59
Figure 2-4. Effects of parameters on the log(time) vs. creep compliance behavior of Norton-Bailey model. 63
Figure 2-5. Effects of parameters on the log(time) vs. log(creep compliance) behavior of Norton-Bailey model. 66
Figure 3-1. Plan view of FE experiment setup and borehole layout. 68
Figure 3-2. Heat power applied to H1, H2 and H3 during heater start-up at the Mont Terri FE experiment. 69
Figure 3-3. TOUGH-FLAC 2D numerical grid of the FE experiment for DECOVALEX-2023 benchmarking. 70
Figure 3-4. TOUGH-FLAC 3D numerical grid of the FE experiment 71
Figure 3-5. 2D model simulation result of anisotropic evolution of temperature and fluid pressure at monitoring points O1 to O6 located in the Opalinus Clay. 73
Figure 3-6. 2D model simulation result of anisotropic distribution of temperature and pressure after 5 years. 73
Figure 3-7. Comparison of water properties defined in DECOVALEX-2023 task definition with temperature dependent water properties as assumed in the TOUGH2 code 74
Figure 3-8. 3D model simulation results of heater temperatures. 75
Figure 3-9. 3D model simulation result of anisotropic evolution of temperature and fluid pressure in monitoring points O1 to O6 located in the Opalinus Clay. 75
Figure 4-1. Conceptual model of the thermal-fracturing experiments that were conducted by Braun (2019). 78

Figure 4-2. Experimental and numerically simulated temperature evolution applied during the thermal extension tests (Experimental results from Braun, 2019) 79
Figure 4-3. Experimental and numerically simulated pressure evolution during the thermal extension tests (Experimental results from Braun, 2019) 79
Figure 4-4. Experimental and numerically simulated (a) radial and (b) axial total stress evolution during the thermal extension tests (Experimental results from Braun, 2019) 80
Figure 4-5. Experimental and numerically simulated (a) axial strain and (b) effective stress evolution during the thermal extension tests (Experimental results from Braun, 2019) 81
Figure 5-1. Conceptual models of gas flow (Harrington, 2016) 82
Figure 5-2. Conceptual model for dilatant gas flow through aggregate boundaries considered in a continuum model simulations using TOUGH-FLAC. 84
Figure 5-3. 3D TOUGH-FLAC model of cylindrical sample. 85
Figure 5-4. The concept of effective gas entry pressure used for the evaluation of the initial pressure response. 88
Figure 5-5. Relation between min effective stress and permeability used in numerical modeling. 89
Figure 5-6. 3D TOUGH-FLAC model of cylindrical sample and the results of simulations of pressure. 90
Figure 5-7. Simulated and measured gas flow rate out of the sample. 90
Figure 5-8. Simulated and measured total radial stress at load cells 1, 2 and 3. 91
Figure 5-9. Simulated and measured total axial stress at injection and back ends of the sample. 91
Figure 5-10. Setup and model of the gas migration experiment 92
Figure 5-11. Modeling results of (a) pressure and (b) flow rate evolution during the gas injection test. 93
Figure 5-12. Modeling results of pore pressure and radial stress at 48 hours when there is a partial gas breakthrough at the injector that first occurred at about 40 days. 94
Figure 6-1. Schematic of machine learning. 96
Figure 6-2. CNN for recognizing rock matrix and fractures. 99
Figure 6-3. A simplified end-to-end CNN U-Net for Image Segmentation. 100
Figure 6-4. Neural style transfer model for mesh generation from a rock image. 101
Figure 6-5. Inference for an RGB input image based on Prediction on grayscale model with provided ground truth. 102
Figure 6-6. NST generated mesh for rough fractures: coarser and denser meshes. 103
Figure 6-7. NST generated mesh for rough fractures with denser meshes and thicker mesh lines. 104
Figure 6-8. Evolution of cost functions with iterations using thin-line and thick-line mesh styles. 104
Figure 6-9. NST generated mesh for discrete fractures. 105
Figure 7-1. NMM mathematical and physical meshes 107
Figure 7-2. Flexible choice of local approximation functions 108
Figure 7-3. Relating NMM to other numerical methods 108
Figure 7-4. Mechanical states of each segment of a fracture in networks: open, bonded and sliding. 109

Figure 7-5. NMM mesh generated for fractured porous rock with 20, 60, and 150 fractures 111
Figure 7-6. Geometric representation of an element with one intersection by two fractures. 111
Figure 7-7. Geometric representation of open, bonded and sliding contact states for elements divided by intersecting fractures.....112
Figure 7-8. A discrete fracture network: original image and the generated mesh. 113
Figure 7-9. Calculated pore pressure (given in MPa), effective horizontal and vertical stresses and shear stress (given in Pa) at Steps 3, 50, 200 and 500.....115
Figure 7-10. EDZ near a tunnel in bedded argillite rock: geometry, and NMM mesh. 116
Figure 7-11. NMM results of geometry and displacements at steps 500, 1000 and 2000. 117
Figure 7-12. NMM results of maximum and minimum principal stresses and shear stress at steps 500, 1000 and 2000. 118
Figure 7-13. Modeling domain with a bentonite buffer in bedded argillite rock: geometry, and NMM mesh. 118
Figure 7-14. NMM results of maximum and minimum principal stresses and shear stress at steps 500, 1000 and 2000. 119
Figure 8-1. (A) 3D perspective of the FS-B/CS-D project showing all boreholes colored by use. Boreholes D1 & D2 (blue color) are injection and pressure monitoring boreholes.....123
Figure 8-2. (A) Absolute frequency along the length of the fiber during gallery excavation. 127
Figure 8-3. On and off-fault strains 129
Figure 8-4. Main Fault displacement throughout the excavation for all boreholes 131
Figure 8-5. Deformation before the excavation breakthrough (May 26) and after (June 1; bottom row). 132
Figure 8-6. Fault response to gallery excavation 133
Figure 8-7. Schematic representations of the Main Fault and the canonical fault zone model showing the relationship between fault core/gouge, principal slip surfaces, and the ‘fault damage’ zone.....136
Figure 8-8. Fractures identified in optical televiewer logs in BCS-D4, D5, and D6 137
Figure 8-9. 3D view of the different model geometries, including a single fault, and three faults.....142
Figure 8-10. Spatial distribution of fault slip and seismicity at the end of injection for the single fault model and the fault network model. 143
Figure 8-11. Number of earthquakes per unit rock volume as function of distance from injection for the model with a single fault and three faults 144
Figure 8-12. Continuous Active-Source Seismic Monitoring (CASSM) geometry surrounding the main fault of Mont Terri. 146
Figure 8-13. An example of a source-gather for shot 5 (located in B4) at the beginning of November 10th, 2020. Receiver numbers 1-22 and 23-44 correspond to boreholes B3 and B4.....147
Figure 8-14. (A) a δt plot for a single source-receiver pair (5/35) between the dates of November 10th and November 21st (prior to injections).....148
Figure 8-15. Variations of p-waves time delay related to injection pressure and fault movements (November 2020 FS-B fault activation experiment). 149

Figure 8-16. Percent change (%δ) in RMS amplitude, and percent change in centroid frequency for source-receiver pair 5/35 with injection pressure. 150
Figure 8-17. A source-gather δt map for shot 5. 151
Figure 9-1. Main calculation procedure of phase-field LBM at each time step 156
Figure 9-2. Schematic illustration of an interface node. 157
Figure 9-3. Workflow of the coupled multiphase flow-reactive transport LBM solver 158
Figure 9-4. The initial condition of saturation (fluid distribution, 1 for the wetting fluid, 0 for the non-wetting fluid) and the initial chemical concentration. 160
Figure 9-5. Initial conditions of the saturation (fluid distribution) and chemical concentration in a capillary tube. 160
Figure 9-6. The change of spurious current magnitude with time and the saturation profile and the chemical concentration profiles across the center of the domain along the x-axis at the last time step 161
Figure 9-7. Saturation (fluid distribution) and chemical concentration at $\boldsymbol{t*=0.4}$ for different density ratios 161
Figure 9-8. Breakthrough curves from the center of the capillary tube for the density ratios 162
Figure 9-9. Porosity change predicted for the concrete-bentonite interface (x<0 concrete, and x>0 bentonite) with a linear and non-linear diffusivity-porosity relationship. 163
Figure 10-1. Schematic illustration of Cl-D field experiment at Mont Terri. 167
Figure 10-2. Schematic illustration of fluid circulation, sampling, and tracer dosing system in the Cl-D experiment at Mont Terri. 168
Figure 10-3. Initial conditions 2D simulation of system with a borehole or fracture on the left of the simulation domain, and a horizontal interface between OPA (Opalinus Clay) and concrete materials (OPC) on the right of the simulation domain. 170
Figure 10-4. Early time behavior (1 day to 10 days). 171
Figure 10-5. Diffusion-reaction simulation results from 100 to 1000 days. 171
Figure 11-1. Schematic of links between near-field coupled THM processes modeling to repository-scale GDSA and PA models. 173

Argillite R&D and International Collaborations – LANL (FY21) (Part III)

Figure 1. Schematic of a generic engineered barrier system concept in argillite host rock. Bentonite blocks surround a waste canister emplaced in a horizontal tunnel lined with cement. 191
Figure 2. Calculated temperatures for various burnup levels of spent nuclear fuel 37-PWR at the repository drift wall (wall) and waste package surface (WP) in a backfilled sedimentary rock-hosted repository. 191
Figure 4. pH (measured at 25ºC) throughout each cement EBS experiment. 205
Figure 6. Sodium, potassium, and calcium concentrations in the cement EBS experiments. 207
Figure 7. Concentrations of chloride and sulfate ions in solution in the cement EBS experiments. 208

Figure 8. QXRD pattern of the bulk post-reaction products from the cement experiments 210
Figure 9. XRD patterns of the oriented and ethylene glycol saturated < 2 µm clay fraction from the clay groundmass of the cement experiments, compared to unheated Wyoming bentonite from the OPC experiments.....212
Figure 10. XRD results from the oriented and ethylene glycol saturated clay fraction of Opalinus Clay fragments extracted from each cement experiment and unreacted Opalinus Clay. 212
Figure 11. XRD pattern on the unreacted and reacted cement chip from EBS-30 and -31. 213
Figure 12. BSE images of thin sections from EBS-23, EBS-24, EBS-25, and EBS-26 showing the petrographic context of authigenic zeolite and CSH minerals (tobermorite) 214
Figure 13. Electron microprobe analyses of zeolite and CSH minerals from EBS-23 through EBS-26 215
Figure 14. Analcime compositions divided by petrographic context within EBS-23 through EBS-26.....215
Figure 15. pH at 25ºC throughout the duration of experiment EBS-29 216
Figure 16. Cation concentrations throughout the duration of experiment EBS-29.....217
Figure 17. Phosphate concentrations throughout the duration of experiment EBS-29 217
Figure 19. Silica concentrations throughout the duration of experiment EBS-29. 218
Figure 18. Anion concentrations throughout the duration of experiment EBS-29 218
Figure 20. XRD results from the oriented clay fraction of heated bentonite from EBS-29 and unreacted Wyoming bentonite. 219
Figure 21. XRD of the apatite crystals that reacted with synthetic Opalinus Clay groundwater in a sealed gold capsule in EBS-29. 220
Figure 22. Secondary electron SEM images of the 304SS surface from EBS-19. 221
Figure 23. Secondary electron SEM images of the LCS surface from EBS-18.....221
Figure 24. Secondary electron SEM images of the 316SS surface from EBS-15 and EBS-20 222
Figure 25. Energy dispersive X-ray spectroscopy (EDS) chemical results collected along a line perpendicular to the steel surface in EBS-15 and EBS-25. 224
Figure 26. Comparison of zeolite compositions color-coded by experiment components. 230
Figure 27. Backscattered electron SEM images showing layered mineral growth that the stainless-steel surface.....231
Figure 28. A stylized representation of phyllosilicate mineral growth at the steel interface. 233
Figure 29. Cross-sectional view of the steel coupon surface from EBS-24, EBS-25, and EBS-26.....234
Figure 30. Simplified depiction on the full-scale EBS experiment at the Horonobe URL (JAEA, 2021). 237
Figure 31. Examples of the welded, polished, and reground (600 grit) coupons used in the STL experiments.....242
Figure 32. Original welded steel sample with cut lines 242

Non-Electrostatic Surface Complexation Database for GDSA (LLNL) (Part V)

Figure 1. Cumulative number of publications referencing the topics of “sorption” and “adsorption” based on the compiled data available in the Web of Science. 269

Figure 2. Workflow describing the process from literature data digitization, incorporation into the LLNL SCIE database, unit conversion and data unification, data filtration, data formatting, the SCM reaction constant fitting. 272

Figure 3. Sorption figures contained in the RES^{3}T references for U(VI) sorption to quartz. 277

Figure 5. Comparison of R values for 17 sets of RES^{3}T reaction constants prior to and after global optimization using PEST/PHREEQC. R value range from 0.6 to 0.9. 280

Figure 6. Comparison of U(VI)-quartz data fits of Kckd96_2 (R=0.84) that includes >Si(w)-O-UO_2(OH) and >Si(s)-O-UO_2(OH) surface complexes to Dk01_4 (R=0.89) that includes >Si(w)-O-UO_2(OH), >Si(s)-O-UO_2(OH), and >Si(w)-O-$UO_2CO_3^-$ surface complexes. 280

Figure 7. Comparison of quality of global fit as a function of surface complexation reactions included in 4 models of U(VI) sorption to quartz. 282

Appendices

Figure B-1. EBS-29 SEM images of post-reaction products WY bentonite....296

Figure B-2. EBS-29 SEM images of post-reaction products of apatite from WY bentonite. 297

Figure B-3. EBS-29 SEM images of post-reaction products from apatite-only capsules....298

Figure B-4. EBS-30 SEM images of post-reaction products from OPC and WY bentonite. 299

Figure B-5. EBS-30 SEM images of post-reaction cement chip surface. 300

Figure B-6. EBS-30 SEM images of post-reaction products from the 316SS surface....301

Figure B-7. EBS-31 SEM images of post-reaction cement surface. 302

Figure B-8. EBS-31 SEM images of the WY bentonite and Opalinus Clay....303

Figure B-9. EBS-31 SEM images of the post-reaction 304SS surface. 304

LIST OF TABLES

Disposal in Argillite R&D and International Collaborations Activities – SNL (Part I)

Table 1. Mineral volume fractions based on XRD data. 27

Table 2. Marl monolith properties 29

Investigation of Coupled Processes in Argillite Rock: FY21 Progress – LBNL (Part II)

Table 2-1. Model parameters used to verify the Norton-Bailey model. 56

Table 3-1. Parameters used in modeling of the Mont Terri FE experiment defined in the DECOVALEX-2023 Task Description (Thatcher and Graupner, 2020) 71

Table 4-1. Initial stress, fluid pressure and temperature for the three laboratory experiments on thermal fracturing modeled in the DECOVALEX-2023 Task A. 77

Table 4-2. Reference parameters used in modeling of the thermal fracturing experiments based on years of site investigations at the MHM URL and laboratory experiments on shale from the MHM URL..... 78

Table 5-1. Material parameters for TOUGH-FLAC modeling of Stage 1 experiment. 86

Table 6-1. Theoretical comparison between numerical modeling and machine learning. 97

Table 7-1. Computation Parameters..... 114

Table 7-2. Computation Parameters..... 116

Table 9-1. Fluid properties used in the tests 159

Table 9-2. Fluid properties used in the tests 160

Table 10-1. Initial conditions for three zones, including fracture (higher porosity zone), concrete (OPC), and Opalinus Clay (OPA). 169

Table 10-2. Self-diffusion coefficients for chemical species considered in simulations. Molecular diffusion is calculated using the Nernst-Planck equation (see Steefel et al, 2015). 169

Table 10-3. Tortuosity values for various zones in simulation, including the high porosity fracture zone, the Opalinus Clay (OPA), and the concrete (OPC). 170

Argillite R&D and International Collaborations – LANL (FY21) (Part III)

Table 1. Initial components and reaction conditions for EBS experiments in the presence of Opalinus Clay 201

Table 2. Initial components and reaction conditions for the capsules included in the EBS-29 with Durango apatite..... 202

Table 3: Brine compositions for synthetic Opalinus Clay solution modelled after data reported from the Mont Terri site (Pearson et al., 2002) used in the Opalinus Clay experiments and the composition of the Stripa synthetic solution used in the apatite experiment (after Frape et al., 2003)..... 203

Table 4. Glycolated smectite (GS) peak positions for the <2 µm clay fraction separated from the Opalinus Clay–Wyoming bentonite experiments (EBS-23 to -28). 211

Table 5. Ethylene glycol saturated smectite (GS) peak positions for the clay fraction extracted from the Wyoming bentonite-Apatite experiment 219

Table 6. Phyllosilicate (Fe-saponite/chlorite)/zeolite (analcime) thickness and growth rates. 226

Table 7: Average synthetic groundwater composition developed to mimic Wakkanai Formation groundwater at depths greater than 300 meters 238

Table 8: Initial components and reaction conditions for STL experiments. Initial components and reaction conditions for STL experiments 240

Non-Electrostatic Surface Complexation Database for GDSA (LLNL) (Part V)

Table 1. Fitting results using RES^{3}T surface complexation models. 275

Table 2. Surface complexation reaction constants based on a 3-reaction fit using non-electrostatic and diffuse layer, 1-Site, and 2-Site models. 283

Table 3. Summary of *preliminary* 1-site NEM reaction constants fit to date as part of the database development effort. 285

REVISION HISTORY

Rev0	Draft	August 20, 2021

ACRONYMS

1D, 1-D	One Dimensional
2D, 2-D	Two Dimensional
3D, 3-D	Three Dimensional
ANDRA	Agence Nationale pour la Gestion Des Déchets Radioactifs (France)
ABM	Alternative Buffer Materials
ANL	Argonne National Laboratory
BBM	Barcelona Basic Model
BGR	Bundesanstalt für Geowissenschaften und Rohstoffe (Germany)
BGS	British Geological Survey
BExM	Barcelona Expansive Model
BSE	Back-Scattered Electron
BSEI	Back-Scattered Electron Image
CDM	Continuum Damage Mechanics
CEC	Cation Exchange Capacity
CFD	Computational Fluid Dynamics
CFRT	Colloid-Facilitated Radionuclide Transport
CIEMAT	Centro de Investigaciones Energéticas, Medioambientales y Tecnológicas (Spain)
CMPM	Canadian Mixed Potential Model
CNN	Convolutional Neural Networks
CNSC	Canadian Nuclear Safety Commission
COx	Callovo-Oxfordian
CT	Computerized Tomography
CTD	Closure Test Drift
DDL	Diffuse Double Layer
DECOVALEX	DEvelopment of COupled Models and their VALidation against EXperiments
DFN	Discrete Fracture Network
DOE	Department of Energy
DOE-NE	Department of Energy, Office of Nuclear Energy
DPC	Dual-Purpose Canister
DRZ	Disturbed Rock Zone
DSC	Differential Scanning Calorimetry

DSEF	Disposal Systems Evaluation Framework
EBS	Engineered Barrier System
EDS, EDX	Energy dispersive X-ray spectroscopy
EDZ	Excavated Disturbed Zone
ESS-DIVE	Environmental Systems Science Data Infrastructure for a Virtual Ecosystem
EMP(A), EMPA	Electron Microprobe (Analysis)
ENRESA	Empresa Nacional de Residuos Radioactivos SA
EoS or EOS	Equation of State
FBG	Fiber Bragg Gratings
FCRD	Fuel Cycle Research and Development
FCT	Fuel Cycle Technologies
FCM	Fracture Continuum Model
FIB	Focused Ion Beam
FMDM or FMD	Fuel Matrix Degradation Model
FE	Full-Scale Emplacement Experiment
FEBEX	Full-scale Engineered Barriers Experiment
FEBEX-DP	Full-scale Engineered Barriers Experiment-Dismantling Project
FEP	Features, Events, and Processes
FTG	Flow Topology Graph
FY	Fiscal Year
GDSA	Geologic Disposal Safety Assessment
GDSA-PA	Geologic Disposal Safety Assessment – Performance Assessment
GREET	Groundwater REcovery Experiment in Tunnel
GTS	Grimsel Test Site
GW	Gigawatt
GWd	Gigawatt days
GWd/MT	Gigawatt (thermal) - days per Metric Ton
HC or H-C	Hydrological and Chemical
HE-E	Half-Scale Heater Test (Mont Terri)
HFO	Hydrous Ferric Oxide
HLW	High-Level nuclear Waste
HM	Hydro Mechanical

HPC	High Performance Computing
HZDR	Helmholtz Zentrum Dresden Rossendorf
IAEA	International Atomic Energy Association
IC	Ion Chromatography
IPC	In-Package Chemistry
IRSN	Institut de Radioprotection et de Sûreté Nucléaire
I-S	Illite-Smectite
JAEA	Japan Atomic Energy Agency
JNC	Japan Nuclear Cycle Development Institute
KAERI	Korea Atomic Energy Research Institute
LANL	Los Alamos National Laboratory
LASGIT	Large Scale Gas Injection Test
LBM	Lattive Boltzmann Method
LBNL	Lawrence Berkeley National Laboratory
LC	Loading Collapse
LCS	Low Carbon Steel
LT	Local Thickness
LLNL	Lawrence Livermore National Laboratory
MC	Mechanical-Chemical
ML	Machine Learning
MT	Metric Ton
MTHM	Metric Tons Heavy Metal
Micro XR CT	Micro X-ray Computer Tomography
MUSIC	Multi-Site Complexation
NAGRA	National Cooperative for the Disposal of Radioactive Waste
NBS	Natural Barrier System
NE	DOE-Nuclear Energy
NEA	Nuclear Energy Agency
NEM	Non-electrostatic Model
NIST	National Institute of Standard and Technology
NMM	Numerical Manifold Method
NS	Natural (Barrier) System

NST	Neural Style Transfer
NW	Nuclear Waste
OECD	Organization for Economic Co-operation and Development
OoR	Out of Reactor
OPC	Ordinary Portland Cement
P	Pressure
PA	Performance Assessment
PNNL	Pacific Northwest National Laboratory
PWR	Pressurized Water Reactor
QXRD	Quantitative X-ray Diffraction
R&D	Research and Development
RBSN	Rigid-Body-Spring Network
ReLU	Rectified Linear Unit
REV	Representative Elementary Volume
RH	Relative Humidity
SBR	Subsurface Biogeochemical Research
SCIE	Surface Complexation Ion Exchange
SCM	Surface complexation model
SEM	Scanning Electron Microscopy
SFWST	The Spent Fuel Waste Science and Technology
SIMFIP	Step-Rate Injection Method for Fracture *In-situ* Properties
SIT	Specific Interaction Theory
SNF	Spent Nuclear Fuel
SNL	Sandia National Laboratories
SS	Stainless Steel
T	Temperature
TGA	Thermogravimetric Analysis
t	time
TC	Thermal and Chemical
TDB	Thermodynamic Database
TEM	Transmission Electron Microscopy
TGA	Thermo-Gravimetric Analysis

TH	Thermal and Hydrological
THM	Thermal-Hydrological-Mechanical
THMC	Thermal-Hydrological-Mechanical-Chemical
TM	Thermal-Mechanical
UFD	Used Fuel Disposition
UFDC	Used Fuel Disposition Campaign
UOX	Uranium Oxide Fuel
UPC	Universitat Politècnica de Catalunya
URL	Underground Research Laboratory
VOF	Volume of Fluid
WP	Waste Package
XRD	X-ray Diffraction
XRF	X-ray Fluorescence

Disposal in Argillite R&D and International Collaborations Activities – SNL (Part I

1. Introduction

The DOE R&D program under the Spent Fuel Waste Science Technology (SFWST) campaign has made key progress to the advancement of modeling and experimental approaches towards the characterization of chemical and physical phenomena in the engineered and natural barriers that could impact the long-term safety assessment of nuclear waste disposition in deep clay/shale/argillaceous rock. Clay mineral transformations (e.g., smectite-illite) and interactions with other barrier materials (metal, cement, wall rock) at elevated temperatures can impact bentonite swelling and change the phase assemblage in the clay barrier. Direct disposal of dual-purpose canisters (DPCs) it is being considered as a feasible, less costly, and safer alternative to re-packaging. The capacity of DPCs can be up to 32-PWR SNF assemblies which leads to high thermal loads and hence high temperatures in the near-field EBS and host rock. Such high temperature conditions during the thermal period can impact the long-term bentonite barrier performance.

International collaboration activities such as heater tests, particularly *postmortem* sample recovery and analysis, have provided key information on the changes to engineered system (EBS) material exposed to extended periods of thermal loads. Chemical and structural analyses of bentonite material from such tests has been important to the characterization of these thermal effects on clay composition, thermal properties, sorption, and swelling. These are crucial to the evaluation of *sacrificial zones* in the EBS during the thermal period. The extent of these *sacrificial zones* appears to depend on temperature with distance from the waste package surface which can influence bentonite barrier performance and the EBS design concept. This is particularly important to the consideration of DPCs where temperatures in excess of ~200°C at the waste canister surface are expected. The following sections discuss the compositional, structural characterization, and thermal analyses under controlled relative humidity (RH) conditions on bentonite recovered from the heater test. In addition, molecular dynamics (MD) simulations on montmorillonite have been performed to complement the thermal analyses experiments and understand the dynamics of swelling clay dehydration and mechanisms for water transport. The hydration/dehydration dynamics of smectite swelling in bentonite is important to barrier performance and exert strong influence on its mechanical behavior.

The application of 3D reactive transport modeling using PFLOTRAN of cement liner interactions in a flooded drift experiment at an URL facility in Japan shows the importance of coupled fluid mixing and fluid/solid reactions on water chemistry. Also, a 3D reacting transport modeling problem for a single waste package under non-isothermal heating during the thermal period is being investigated. This problem evaluates the TH effects of multiphase transport and, intial saturation and relative humidity (RH) conditions in the EBS and host rock domains. This work has been expanded to conduct THC simulations (full saturation) under thermal loads of 21- and 37-PWR SNF assemblies in the waste package. The thermal load of a 21-PWR SNF assemblies has been considered in the Geologic Disposal Safety Assessment (GDSA) in the argillite reference case study.

One of the long-standing objectives of this campaign is the development of state-of-the-art simulation capabilities for high fidelity representation of key process models and integration with the GDSA. This process model development makes use of high performance computing (HPC) to build a high-fidelity performance assessment (PA) computational platform to support the safety case. A preliminary assessment of shale groundwater chemistry selection for the GDSA

argillite reference case has been conducted as part of this GDSA integration with the disposal in argillite work package. The results of this initial assessment will be documented in this report.

Some of the key items in support of the safety assessment for disposal in the argillite work package covered in this report are:

- International collaboration activities with long-standing repository science programs (e.g, Underground Research Laboratory – URL experiments). These include experimental and modeling studies on barrier material interactions. Preliminary assessment of groundwater chemistry in shale formations as part of the GDSA integration in the development of the disposal in argillite reference case.

- Experimental studies on hydrothermal interactions involving natural and engineered barrier materials (clay, steel, cement, argillite).

- Coupled Thermal-Hydrological-Mechanical-Chemical (THMC) simulations, modeling approaches to gas migration, fault movement monitoring and leakage, abiotic-biotic processes in barrier materials, and GDSA integration.

2. International Collaboration Activities

This part of the report describes updates to ongoing international collaboration activities pertaining the FEBEX-DP and DECOVALEX Task C projects. Descriptions of these underground research laboratory (URL) activities are given in Jové Colón et al. (2018a) but will repeated here for completeness. The 2018 status of work conducted at Sandia National Laboratories (SNL) on these two activities has been described in Jové Colón et al. (2018a) and were summarized along with other international collaboration activities in Birkholzer et al. (2018).

This interim report is an update of ongoing experimental and modeling work on bentonite material described in Jové Colón et al. (2019, 2020) from past international collaboration activities. As noted in Jové Colón et al. (2020), work on international repository science activities such as FEBEX-DP and DECOVALEX19 is either no longer continuing by the international partners. Nevertheless, research activities on the collected sample materials and field data are still ongoing. Descriptions of these underground research laboratory (URL) R&D activities are described elsewhere (Birkholzer et al. 2019; Jové Colón et al. 2020) but will be explained here when needed. The current reports recent reactive-transport modeling on the leaching of sedimentary rock.

Bentonite material obtained from the FEBEX-DP dismantling phase of heater #2 (see Figure 1; Section II) is still used in current calorimetric studies to investigate hydration/dehydration phenomena of this material at elevated temperatures. The FEBEX-DP phase was performed during 2015 involving the careful retrieval of (FEBEX) bentonite barrier material samples from the remaining sections of the FEBEX "*in situ* test" at the Grimsel test site (GTS) URL, Switzerland, after 18+ years of heating (García-Siñeriz et al., 2016; Martinez et al., 2016). The disassembling activity involved sampling of the barrier bentonite, steel liner, sensors, embedded metallic components (e.g., metal coupons), and near-field sections with tracer components.

Samples collected in section 49 experienced the hottest zones given its location close to the center of the (cylindrical) heater longitudinal axis. Jové Colón et al. (2019, 2020) describes the FEBEX-DP bentonite XRF compositional data along with XRD analyses, volumetric adsorption/desorption, and thermogravimetric analysis (TGA/DSC) with controlled hydration/dehydration cycles on bentonite samples collected as a function of distance from the gallery center or heater surface. Some of these experimental investigations are still ongoing for calorimetric and structural measurements conducted under variable temperature and relative humidity (RH) conditions. Information from calorimetric analyses (TGA/DSC) along with of recently obtained *in situ* XRD measurements on samples collected from the FEBEX-DP dismantling phase has been used with molecular dynamics (MD) simulation studies to evaluate montmorillonite hydration/dehydration behavior.

Jové Colón et al. (2020) describes results of the reactive transport modeling conducted as part of DECOVALEX-2019 Task C activity which involves collaboration with the GREET (Groundwater REcovery Experiment in Tunnel) at the Mizunami URL, Japan. Some of the goals of GREET were to conduct a facility-scale geochemical characterization study of short- and long-term effects of tunnel excavation activities, impacts on groundwater flow and transport, and influences on groundwater chemistry under ambient tunnel conditions (Iwatsuki et al., 2015). The hydrological and hydrochemical data obtained from these URL activities is then used in the development and evaluation of HC models to support post-closure safety and performance assessments of the repository environment. Jové Colón et al. (2019, 2020) and Birkholzer et al. (2019) describes 3D reactive transport (HC) modeling of the closure test drift (CTD) using the PFLOTRAN simulation tool focusing on shotcrete – ground water interactions of the cement liner in the water-filled tunnel. The collected field hydrological and hydrochemical monitoring data as a function of time is used to evaluate barrier material interactions effects on the flooded CTD water chemistry using a coupled-process model with heterogeneous permeability fields of the host rock surrounding the CTD. Jové Colón et al. (2020) provides the most recent results of the 3D reactive transport (HC) modeling of the CTD emphasizing on the importance of the shotcrete liner thickness (or transport length scale) in the leaching process and related transport plus chemical reaction parameters to obtain the closest representation of the temporal changes in measured solute concentrations. This reactive transport simulation study greatly benefited from previous modeling efforts of idealized cement – clay rock interactions (Matteo et al. 2019). Given the importance of barrier material leaching on the chemistry of interacting aqueous phase solutions in the near- and far-field environments, an R&D collaboration as part of the international activities involves the 1D reactive transport modeling of leaching rock material under controlled laboratory conditions. This work is done in collaborations with the Engineered Barrier System (EBS) work package and involves the work of Dr. David Kosson's group at Vanderbilt University. Their work involves quantification of mass transport through laboratory leaching tests of well-characterized rock and cement samples. Solute concentrations from the leaching experiments are then used to evaluation evaluate parameters in both geochemical modeling of solution-mineral equilibria and reactive-transport simulations. A key aspect of this work is the comprehensive description of mass transport along interfaces for a system characterized for predominantly diffusive gradients. In this report, the current focus on modeling the leaching behavior of a marl rock monolith from sedimentary formations in the northern Negev, Israel (Matteo et al. 2020). The leaching test was conducted using the EPA method 1315

(U.S. EPA, 2017) to quantify mass transfer rates under saturated conditions. Details of these and other leaching tests on cement and monolith rock samples are described by Matteo et al. (2020).

The main goals of this report update for each of the international activities are:

- FEBEX-DP:
  - Provide additional thermal analysis (DSC) data with controlled hydration/dehydration cycles on FEBEX-DP bentonite samples at temperatures of 85°C and 150°C. Only data for the dehydration steps is given in this report. In addition, present data of *in situ* XRD analyses under controlled dew point of ~58°C at a temperature of 85°C. Bentonite hydration/dehydration state controls swelling and shrinkage phenomena in bentonite.
  - Describe molecular dynamics (MD) simulation of Na-Montmorillonite (Na-MMT) dehydration focusing on water transport at the smectite interlayer. This modeling effort was motivated by the TGA/DSC, water adsorption isotherm experiments, and more recently *in situ* XRD analyses on FEBEX-DP bentonite samples to evaluate mechanism of water transport at the molecular level.
- PFLOTRAN Simulation of Marl Leaching:
  - Describe 1D reactive-transport simulations with PFLOTRAN on a marl rock monolith. Mineralogic characterization, rock properties, and solute concentration vs. time data from leaching experiment were used to constrain transport and mineral dissolution rate parameters in the reactive-transport model.
- HotBent Heated Column Experiment:
  - Provide preliminary XRD data on treated bentonite material collected after shutdown of the laboratory-scale HotBent heated column experiment. This is part of the large scale HotBent heater test field experiment at the Grimsel site.

2.1 FEBEX-DP

This section of the report describes international collaboration activities pertaining to FEBEX-DP, marl rock leaching, and HotBENT heated column test. Although work on the FEBEX-DP international repository science activities is no longer continuing by the international partners, investigations on the collected data and samples is still ongoing. Descriptions of these underground research laboratory (URL) R&D activities are given in Jové Colón et al. (2018; 2019) but will repeated here for completeness. The 2019 status of work conducted at Sandia National Laboratories (SNL) on these two activities is summarized along with other international collaboration activities in Birkholzer et al. (2019).

The post-closure period will experience high thermal loads that can drive fluid transport and barrier alteration in a variably saturated near-field environment. A a result enhanced interaction with fluids can induce phase transformation phenomena, and other potential mineralogical changes in bentonite. Jové Colón et al. (2016) describes the 2D-3D characterization of microcracks in bentonite in a FEBEX-DP shotcrete-bentonite overcore stressing the importance of desiccation/shrinkage processes in bentonite and the nature of pores/voids in shotcrete. Engineered barrier alteration has been assessed by reactive-transport models and geochemical modeling of mineral dissolution and precipitation (Marty et al., 2015; Wilson et al., 2015; Xie et al., 2015). An example is Fe-bentonite interactions which leading to mineral phase changes that

could impact swelling capacity in bentonite through alteration to a non-swelling Fe-bearing phase. Also, cation exchange in the bentonite clay could also be impacted through temperature-induced drying and wetting causing variations in the cation exchange capacity (CEC) (Muurinen, 2011). Cation exchange experiments reported by Villar et al. (2017) show that FEBEX-DP bentonite samples collected from sections closest to the heater exhibit higher concentrations of Mg and Ca and low concentrations of exchangeable Na. Further, aqueous extracts for bentonite samples collected in sections close to the heater exhibited higher aqueous concentrations of Mg, Ca, Na, and Cl relative to those sampled farther away from the heater (Villar et al., 2017). These changes in the observed aqueous concentration from these tests suggest that bentonites close to the heater were affected by thermal loads therefore inducing changes in the smectite clay phase and potentially their subsequent interactions with fluids. Figure 3 shows the radial locations of samples collected in Section 49 considered in this study. Section III describes further TGA/DSC analyses to FEBEX-DP bentonite samples at elevated temperatures under controlled moisture conditions. Motivated by the thermal studies, MD simulations of montmorillonite dehydration under certain conditions were conducted to describe this process at the molecular scale. These studies are discussed in Section IV.

FEBEX bentonite is composed of ~93% smectite with 2% quartz, 3% plagioclase, and about 2% cristobalite plus minor accessory phases such as calcite and K-feldspar (Huertas et al., 2000; Missana and García-Gutiérrez, 2007). The extent of the corroded region from the heater steel mesh support surface into the bentonite is rather limited which might explain the relatively low level of Fe alteration into the bentonite, particularly in the hotter zones of the heater.

The XRD data reported in Jové Colón et al. (2018) has been evaluated and compared between samples close to and far from the heater surface and that for unheated FEBEX bentonite. As described in Jové Colón et al. (2018), a salient feature revealed by XRF compositional analyses is the increase in Mg content with decreasing distance from the heater or towards the heater surface (~50 cm from the gallery center). An explanation for the Mg enrichment close to the heater surface is still under investigation. Potential mechanisms to be considered are (1) enhanced cation exchange of Mg from pore solution into smectite and (2) enhancement of Mg content already in smectite through removal of other readily exchangeable cations such as Na^+.

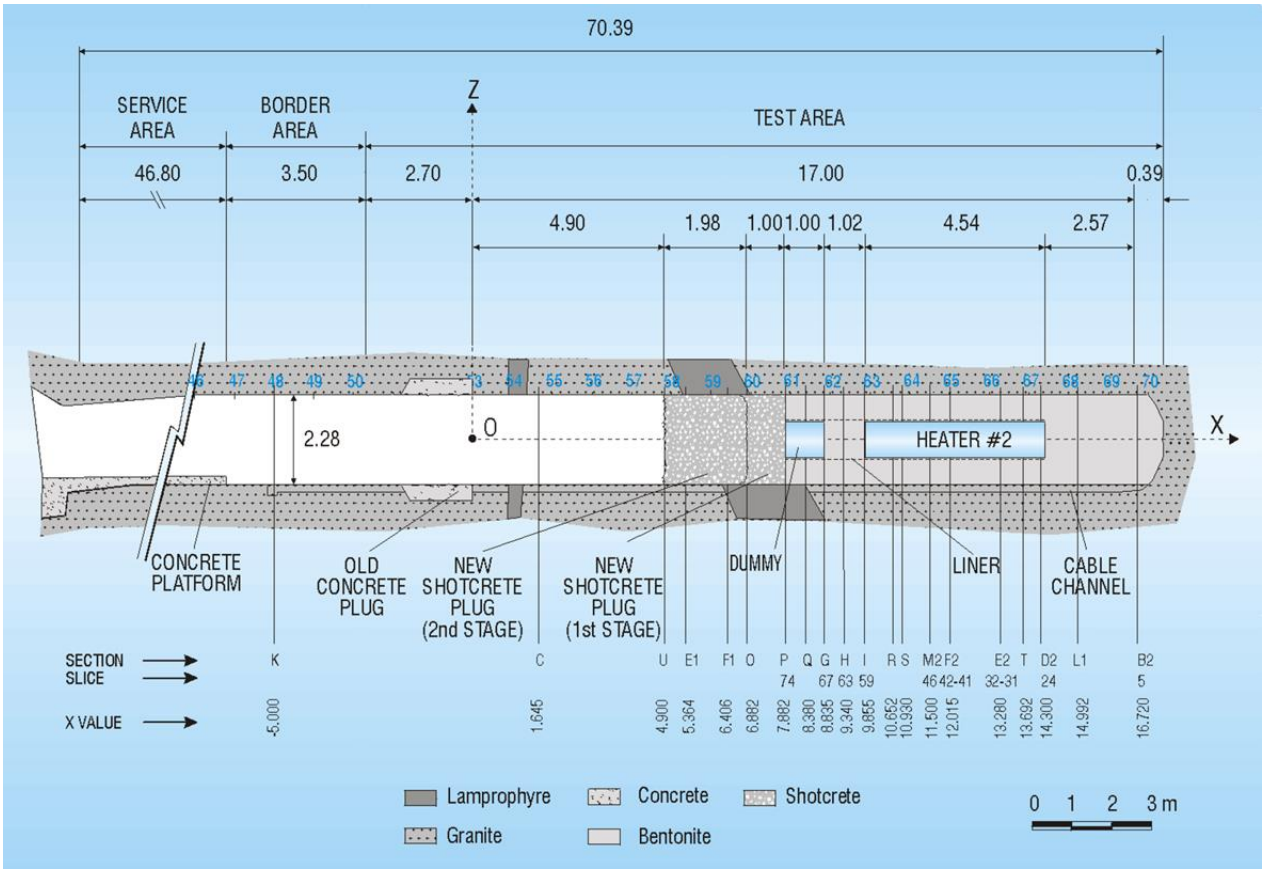

Figure 1. Schematic layout of the FEBEX "in-situ" field test after the first partial dismantling showing the configuration of heater #2 at the GTS URL (García-Siñeriz et al., 2016).

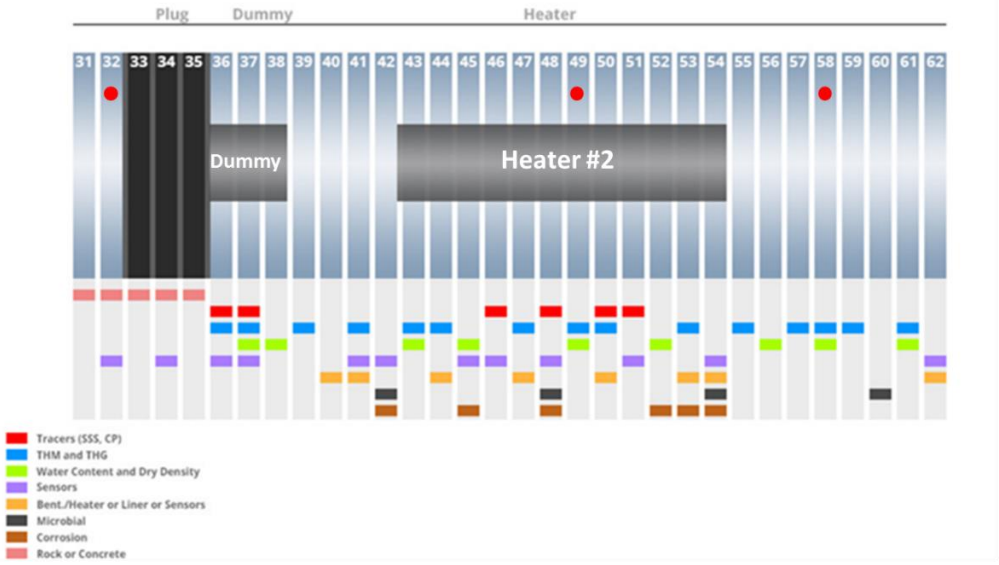

Figure 2. Schematic configuration of sampling zones (indicated by vertical light blue bars) for the FEBEX-DP project. Filled red circles indicate zones for samples obtained by Sandia National Laboratories (SNL). Source: FEBEX-DP website (members area): http://www.grimsel.com/gts-phase-vi/febex-dp/febex-dp-introduction.

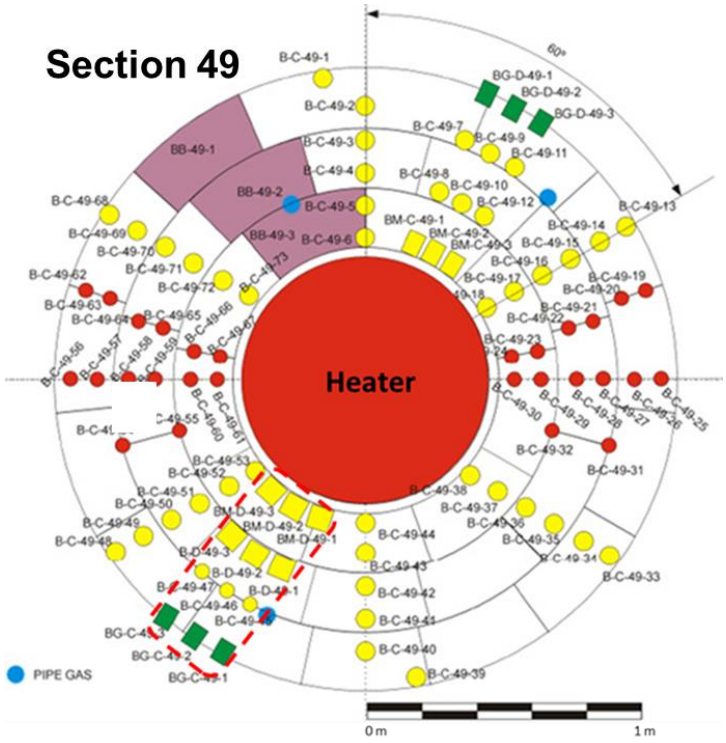

Figure 3. Schematic diagram of sampling locations for the FEBEX-DP dismantling of section 49. See Figure 2 for section location relative to the heater zone. The red-dashed line delineates the locations of samples analyzed with XRD and XRF (diagram source: FEBEX-DP website (members area): http://www.grimsel.com/gts-phase-vi/febex-dp/febex-dp-introduction).

2.1.1 Thermal (TGA/DSC) Analyses

Water adsorption/desorption behavior in expansive clay is key to this material swelling phenomena but also to water transport during hydration/dehydration processes. Thermal loads in deep geological nuclear waste repositories control RH conditions in the disposal galleries where bentonite is used as backfill barrier material. Therefore, chemo-mechanical responses and mechanisms of bentonite hydration/dehydration to changes in RH and temperature are crucial to the EBS performance. Cyclical TGA/DSC analyses under controlled RH and temperature provides important information on the kinetics of expansive clay hydration/dehydration and also provides insights on the hysteretic behavior of this process.

It should be noted that the COVID-19 situation impacted some of the laboratory activities due to laboratory shutdowns or restricted access with limited personnel under very strict working conditions. Still, some of the planned TGS/DSC experiments and *in situ* XRD analyses were conducted to temperatures of 85°C (TGA/DSC and *in situ* XRD) and 150°C (TGA/DSC only). This section of the report focuses on providing the data obtained so far but the evaluation of these results is still ongoing. It should also be noted that the *in situ* XRD setup is no longer operational. However, there are plans to continue this activity on bentonite when a functional XRD equipment becomes available.

Jové Colón et al. (2019, 2020) provides TGA/DSC analysis and water adsorption/desorption data for bentonite samples close and far from the heater surface. contained in Appendix A of Jové Colón et al. (2020). These analyses were conducted Section 49 bentonite samples using a Netzsch STA 449 F3 Jupiter with MHG humidity generator. The analyzed samples are the unheated FEBEX bentonite, BG-C-49-1, BG-C-49-3, B-C-49-7, B-C-49-8, B-C-49-11, B-C-49-12, BM-D-49-3, BM-D-49-1,2,3. Thermal analysis (thermogravimetric analysis, TGA, and Differential Scanning Calorimetry, DSC) was conducted using an STA 449 F3 Jupiter (Netzsch, Germany) with MHG humidity generator (ProUmid, Germany). The bentonite sample (ca. 20 mg) was placed in a platinum crucible and loaded into the thermal analyzer. Since the hydration state of the material as-received was not defined, it was subjected to a drying process prior to humidity cycling. Under a constant flow of dry nitrogen (200 ml/min) the specimen was heated to 150°C at 10°C/min and held for 30 minutes, then cooled to 85°C and held for about 60 minutes to ensure a consistent (dry) starting point for analysis. Bentonite hydration was carried out under a flow of 200 ml/min humid nitrogen (dewpoint 58°C); and dehydration occurred under a 200 ml/min flow of dry nitrogen. After each hydration-dehydration cycle at 85 C, the specimen was dried by heating to 150°C under 200 ml/min dry N2 and holding for 30-60 minutes before cooling to 85°C and beginning the next cycle. For the tests at a hydration-dehydration temperature of 150°C, the procedure was the same as described above, but omitting the additional drying steps between each cycle.

For the cyclical TGA/DSC analyses under controlled RH and a temperature of 60°C, bentonite samples were initially exposed to dry N_2 heated (10°C/min) to 100°C holding this temperature for 30 minutes. Still under dry N_2, the temperature was increased (10°C/min) to 150°C for another 30 minutes. Subsequently, the temperature was decreased to 60°C for 60 minutes to the expose the bentonite to a succession of dry and humid cycles (60 % RH in the generator; 50% RH close to the sample) by flowing water-wet and dry N_2 atmospheres to hydrate and dehydrate the samples. Cyclical hydration/dehydration provides key information about the adsorption/desorption rates of water, quantity of water adsorbed, and energetics of hydration/dehydration reaction. Villar et al. (2017) performed TGA/DSC on FEBEX-DP bentonite from other sampled sections. Overall, the TGA/DSC profile up to high temperatures of Villar et al. (2017) and that obtained for bulk FEBEX bentonites from Section 49 are generally similar as shown in Jové Colón et al. (2018). To the knowledge of the authors, with exception of the results reported in Jové Colón et al. (2019, 2020), no cyclical hydration/dehydration TGA/DSC study on bentonite has been conducted under controlled RH and temperature conditions. The advantage of this approach is that allows for accurate kinetic studies of water adsorption/desorption cycles for given interval durations at constant RH under controlled isothermal conditions. It also allows for characterizing the effects of thermal treatment on bentonite water adsorption/desorption.

Figure 4a (taken from Jové Colón et al., 2020) shows a representative temporal TGA/DSC profile of water adsorption/desorption cycles at 60°C as a function of time (minutes) for the less than 2 µm sample. The green line in Figure 4a this graph depicts the mass of the sample as it responds to changing RH during water adsorption/desorption cycles. Panels b and c of Figure 4 depict the desorption steps only, represented by TGA and differential TGA (or DTA) in panel b, and DSC in panel c. Notice that the x-axes in these panels refers to dehydration time. The data in these plots show that the dehydration behavior is clearly a function of the duration of hydration that precedes it. Short duration hydration steps (i.e., less than two hours; curves A-D in Figure

4) result in a dehydration process that is almost complete relative to the "dry" baseline of these cycles within a time span of approximately 45 minutes after switching back to dry gas. This is represented by a single dehydration peak in both DTA and DSC plots. As the duration of the hydration step increases beyond two hours (curves E-G in Figure 4), however, the subsequent dehydration takes a more complex form, with a changing slope in the TGA curve and clearly shown as negative peaks in the DTA plots. Note that these show up as endotherms in the DSC plots and do not begin at the onset of the bentonite dehydration, but some time thereafter.

Notice that the DTA and DSC traces are essentially mirror images of each other, since any loss of mass of the sample (DTA) is accompanied by a heat flow signal that is proportional (DSC). Figure 5 present similar data as in Figure 4 for the <75 µm bentonite samples at 60°C but for the dehydration steps only. Similar behavior for these two larger grain sizes was observed when compared to the 2 µm sample.

Figures 4 and 5 show a trend with increasing hydration time periods, in particular with regards to endothermic peaks in the DSC thermograms (Figs. 4c and 5b). For FY21, we planned to conduct thermal analyses at higher temperatures to further study this behavior under such conditions. Figure 6 shows DSC thermograms at 85°C and 150°C (Figs. 6a and 6b, respectively) at a dew point of ~58°C. TGA data (not shown) was also obtained as part of these thermal analyses. The trend observed in the DSC thermograms in Figure 6 are somewhat similar to those at 60°C up to a hydration time period of 120 minutes. However, at hydration time periods of 120 minutes or more the trend in the endothermic peaks is no longer defined by the data. There are other features in the endothermic peaks that need further evaluation and those efforts are ongoing.

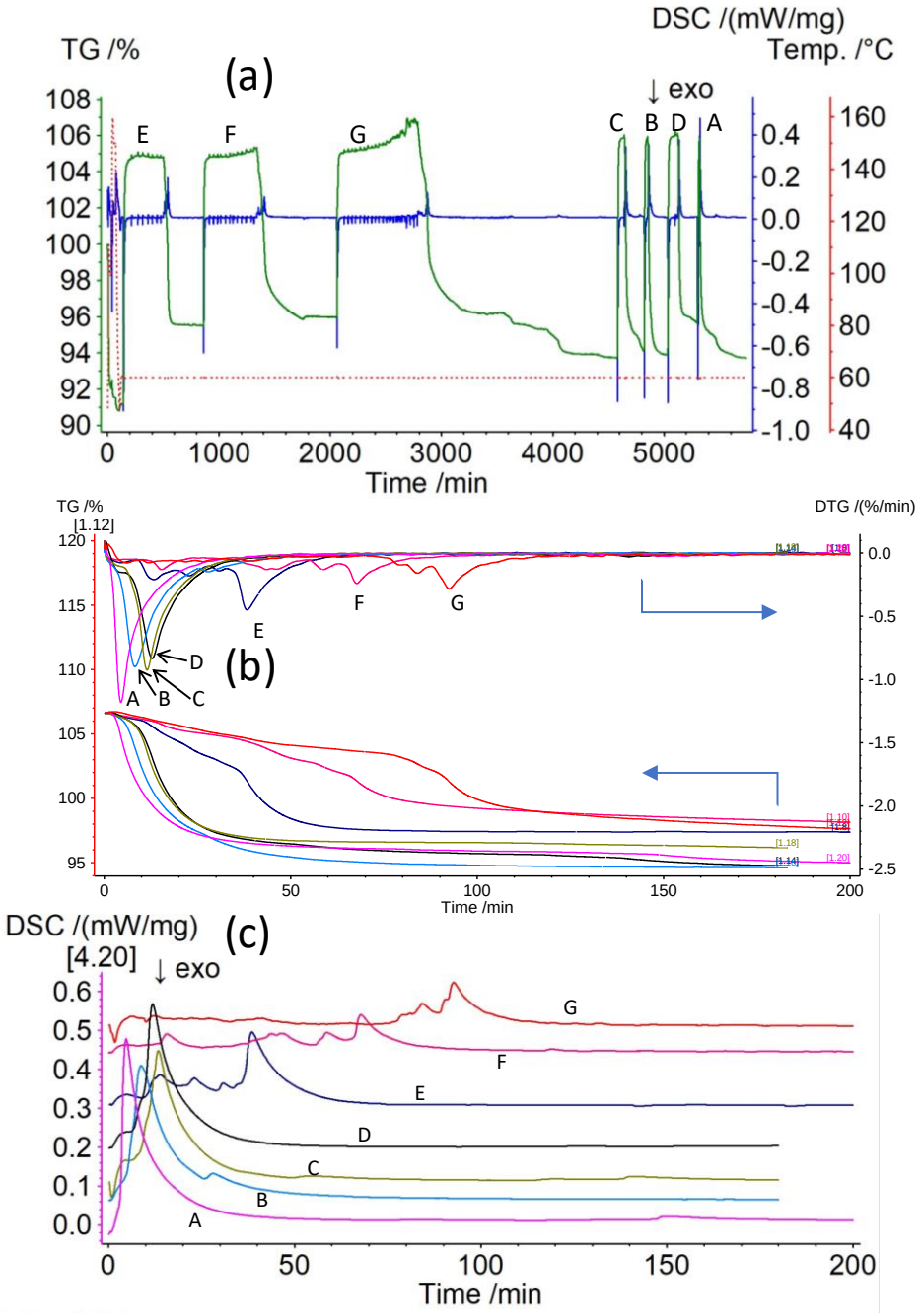

Figure 4. TGA, DTA, and DSC curves as a function of time for water adsorption/desorption cycles at 60°C for the <2 µm bentonite sample. (a) The green curve represents the thermogravimetric analysis (left y-axis). The blue curve stands for the DSC analysis (right y-axis). The red dotted line signifies the temperature (2nd right y-axis). The period of hydration was varied for each cycle, as depicted by the curve labels; A = 15 min, B = 30 min, C = 1 hour, D = 1.5 hours, E = 6 hours, F = 8 hours, and G = 12 hours. (b) TGA (lower) and DTA (upper) curves for the dehydration steps only, plotted against dehydration time. Curve labels identical to panel (a). (c) DSC measurements as a function of elapsed time for the dehydration steps; curves have been offset arbitrarily on the y-axis for clarity. (Jové Colón et al., 2020)by t_0 in graph (a) at each hydration/dehydration cycle. Curves for 180 minutes hydration (B) cycles overlap and are not differentiated within the time scale of the diagram.

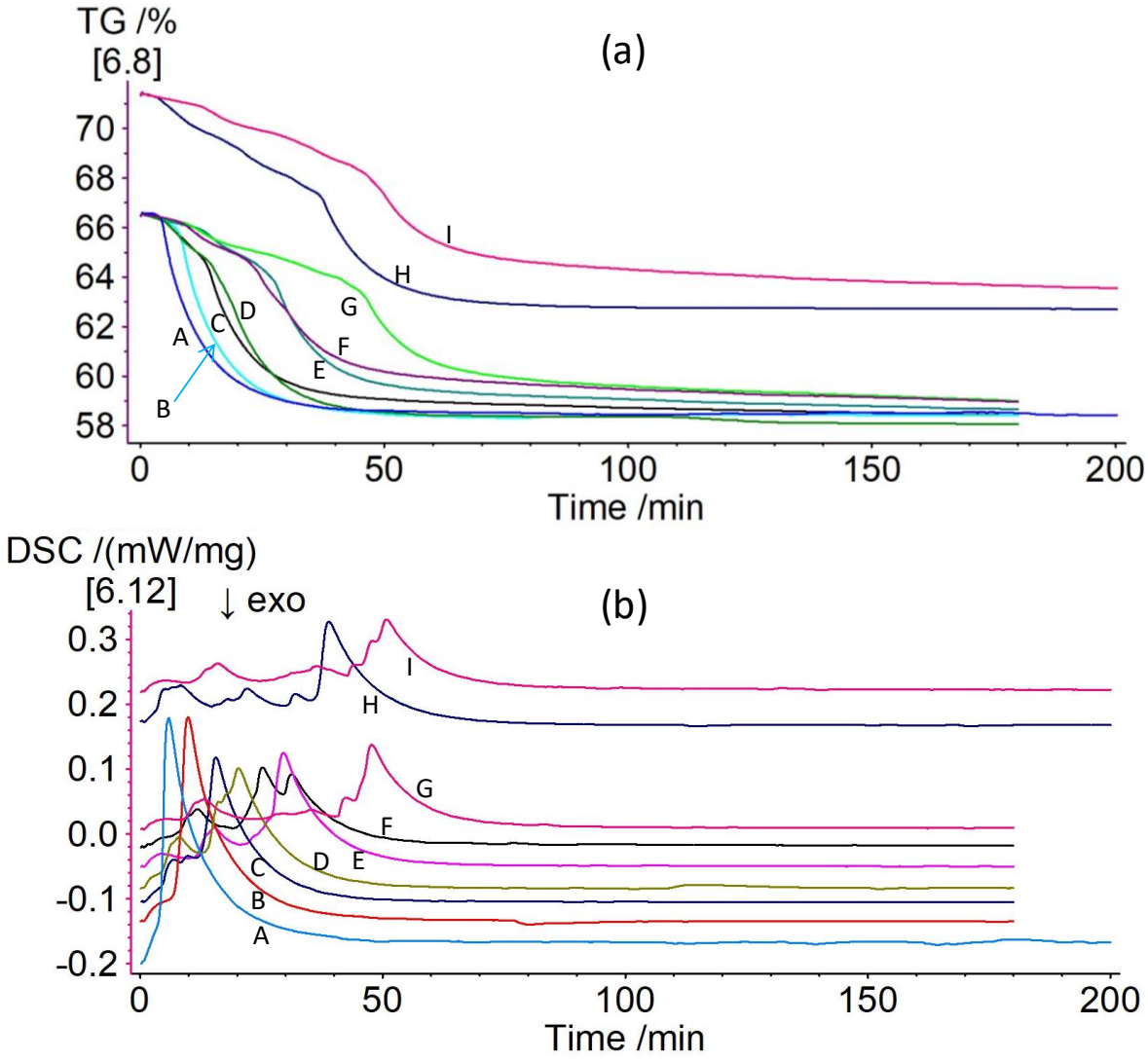

Figure 5. TGA and DSC curves as a function of time for water adsorption/desorption cycles at 60°C for the <75 µm bentonite sample. (a) TGA curves for the dehydration steps only, plotted against dehydration time. The period of hydration was varied for each cycle, as depicted by the curve labels; A = 15 min, B = 30 min, C = 1 hour, D = 1.5 hours, E = 2 hours, F = 3 hours, G = 4 hours, H = 6 hours, and I = 8 hours. (b) DSC measurements as a function of elapsed time for the dehydration steps; curves have been offset arbitrarily on the y-axis for clarity. Curve labels identical to panel (a).

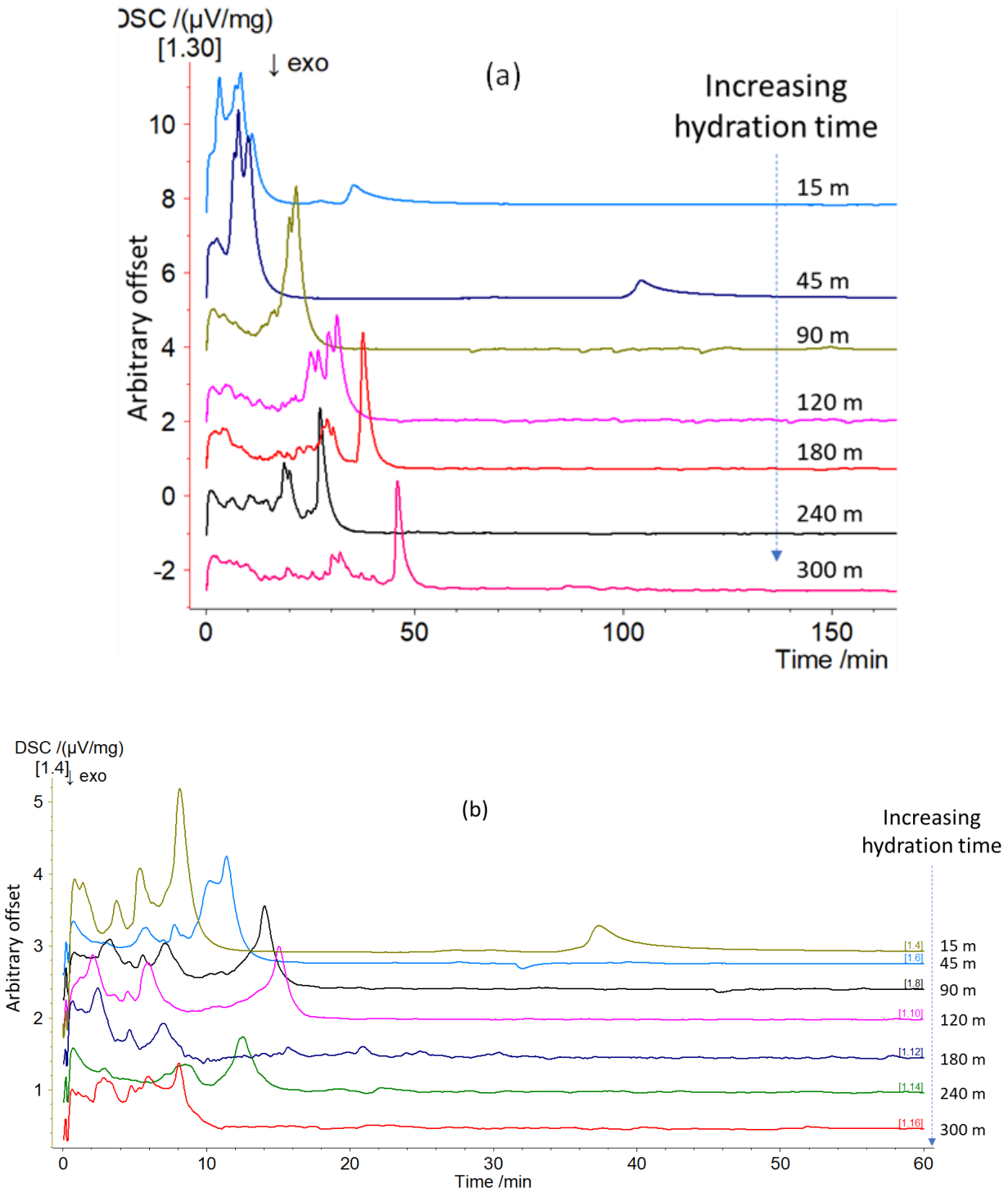

Figure 6. DSC curves as a function of time for the <2 µm bentonite sample for the dehydration steps at (a) 85°C and (b) 150°C. The moisture environment was set to a dew point of ~58°C at both temperatures. The period of hydration was varied for each cycle, as depicted by the curve labels from 15 to 300 minutes. The curves have been offset arbitrarily on the y-axis for clarity.

In situ XRD analyses were conducted at 85°C at a dew point of ~58°C. A few spectra was collected at 150°C under dry He conditions during heating. This analysis was performed using a Scintag Pad-X diffractometer equipped with a Buehler heated reaction chamber, and home-built gas and vapor delivery system. A specimen of bentonite powder was sprinkled onto a silicon wafer to make a flat bed of powder < 1 mm thick. This was placed in the reaction chamber within the diffractometer and a constant flow of helium gas (100 ml/min) was flowed through the reaction chamber. The reaction chamber was then heated to 85°C and held at that temperature for the entire experiment. In order to hydrate the sample, the helium was passed through a sparger immersed in deionized water maintained at 50 +/-5 °C. Once the hydration period (ca. 5 hours) was complete, the water sparger was bypassed. All lines between the sparger and the reaction chamber were traced with heat tape to minimize condensation of water in the lines.

Figure 7 shows the *in situ* XRD data at 85°C and 150°C (heating) illustrating the changes in the 001 peak (7-10° 2-theta) with variations in moisture conditions. Notice the broadening of the 001 peak in the periods of hydration (humid He) along with its shift towards lower 2-theta, as expected, for a more hydrated state (larger 001 d-spacing). As the system is driven towards drying conditions, the opposite is observed where the 001 peak becomes sharper, shifting towards higher 2-theta (smaller 001 d-spacing). Figure 8 depicts the variation of the 001 d-spacing with time during hydration/dehydration at a temperature of 85°C. The 001 d-spacing data looks similar to that collected at 60°C where upon switching to dry He, there is a relatively slow change before a fast and sharp drop is observed followed by a slow decaying change with continuous dehydration. This is the last set of data collected prior to equipment failure.

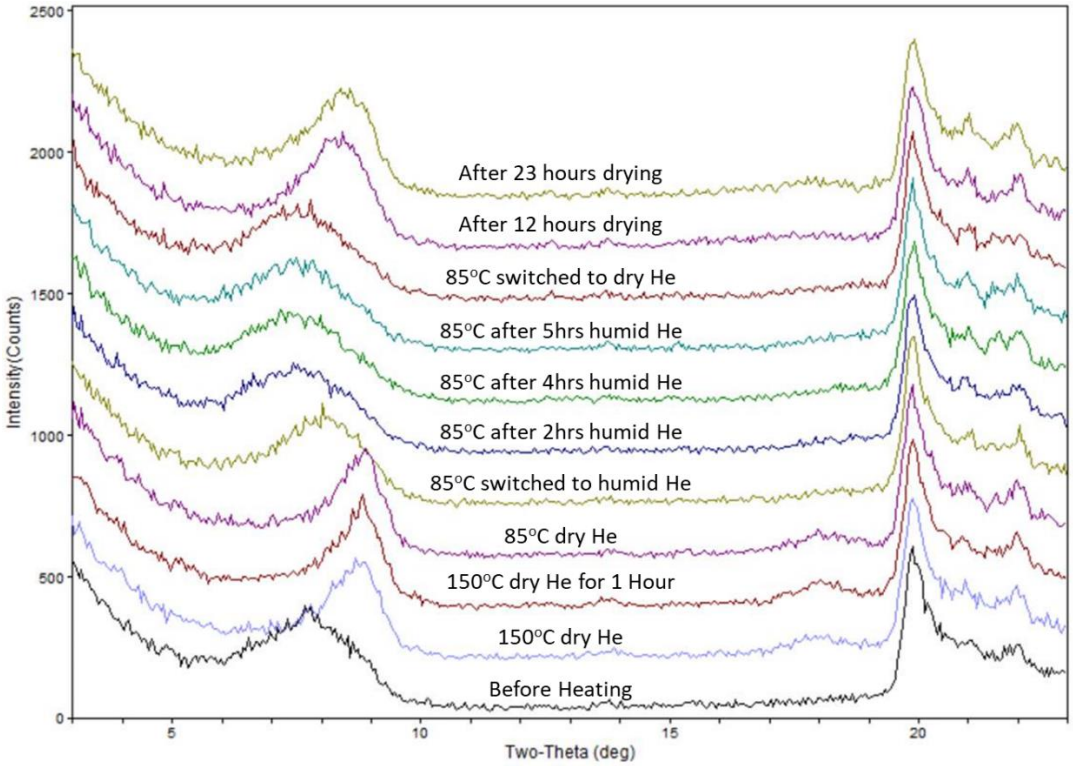

Figure 7. *In situ* XRD spectra collected at temperatures of 85°C and 150°C, and at a dew point of ~58°C. The stacked curves have been offset arbitrarily on the y-axis for clarity.

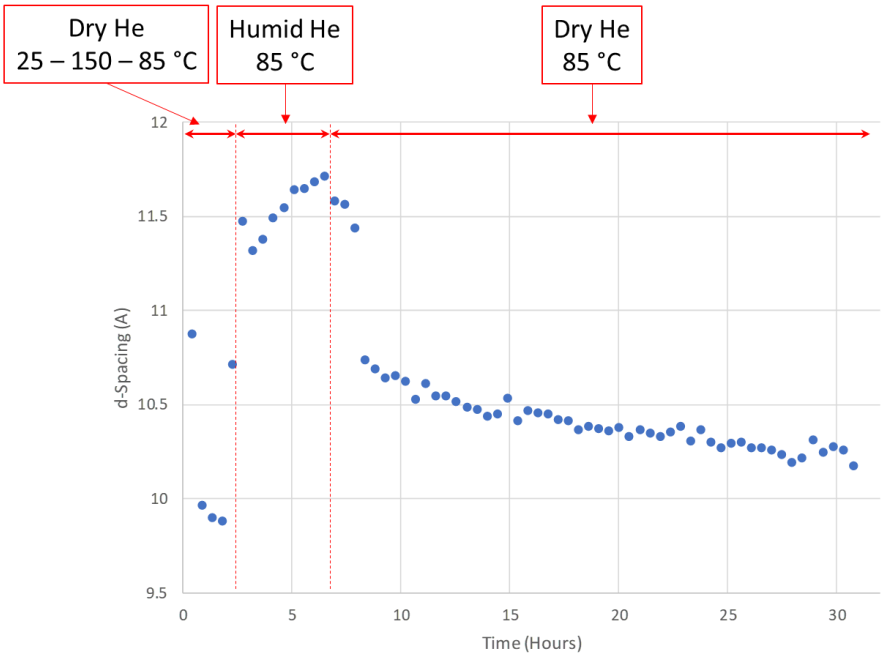

Figure 8. *In situ* XRD 001 d-spacing data for clay hydration/dehydration states collected at temperatures of 85°C and a dew point of ~58°C.

Analysis of these data is currently ongoing and is still work in progress. As before, these observations will be used with molecular dynamics (MD) simulation (Section V) to describe the mechanisms of water behavior in the smectite interlayer during evaporation. Further work is planned to conduct more cyclical TGA/DSC to further evaluate the effect of hydration time durations at higher temperatures. Similarly, there are also plans for more XRD studies under controlled RH and temperature to complement the cyclical TGA/DSC experiments when the equipment becomes available. An important aspect of these thermal studies is to assess the impact of temperature on bentonite swelling and water uptake given the anticipated high thermal loads from large canisters (e.g., dual purpose canisters or DPC's) on the surrounding bentonite barrier.

3. Transport-mechanical-chemical coupling effect during clay dehydration controlled by coordination number of interlayer ions: an MD simulation approach

Expansive clays [e.g., montmorillonite (MMT)] are phyllosilicate minerals that can adsorb a large quantity of water into interlayers resulting in very complex chemo-mechanical behavior in many environmental, geological (energy resources), and industrial systems – including the engineered barrier system (EBS) in deep-geological nuclear waste repositories (Busch et al., 2008; Gates et al., 2009; Amato, 2013; Arthur and Cole, 2014; Jové Colón et al., 2014). Understanding thermal-hydraulic-mechanical-chemical (THMC) coupling effects during clay swelling/shrinking is key to the behavior of backfill bentonite material and water transport in the near-field environment. The accuracy of a THMC model representation depends on the fundamental understanding of the link among surface charge, interlayer ion, water structure and dynamics, temperature, pressure, relative humidity (RH), d-spacing, and swelling pressure

(Teich-McGoldrick et al. 2015; Marty et al. 2020). Such understanding can be extracted from laboratory experiments investigating a d-spacing of a clay sample using X-ray diffraction (XRD) technique in a controlled RH chamber (Morodome S and Kawamura, 2009; Ferrage et al., 2010; Tamura et al., 2000; Yamada et al., 1994). A swelling curve (e.g., d-spacing vs. RH) provides a macroscopic mechanical-chemical relation that a d-spacing abruptly increases (i.e., stepwise swelling mechanism) with increasing number of water layers from zero (0W) to one (1W), two (2W) or three (3W) in an interlayer when the RH increases (Clark et al., 1937). Clays with different surface charge, charge location, and interlayer ion were intensively studied (Sun et al., 2015; Vinci et al., 2020; Liu et al., 2008) that provide relatively advanced knowledge about the macroscopic properties of expansive clays. However, experiments often probe equilibrium hydration states in an averaged manner, and have not been able to directly capture the microscopic features in a rapid swelling/shrinking process (Moyne and Murad, 2002).

Simulation techniques such as reactive transport modeling employ undeformed mesh in a finite element analysis that makes it difficult to simulate the deformation of materials and barely provide microscopic insights into the properties of a clay system. In contrast, inherent to its molecular description, molecular simulations provide a feasible approach to model the deformation of materials coupled with molecular behaviors of simulated systems (Ho et al., 2018). Unfortunately, most molecular dynamics simulations studying clay hydration/dehydration focus on structural and dynamics properties of water/ion in the clay interlayers at a certain hydration state (Holmboe et al., 2014; Ngouana et al., 2014; Rotenberg et al., 2007; Greathouse et al., 2016; Chang et al., 1995; Morrow et al., 2013). The deformation of materials from one hydration state to another, coupling with chemical alteration and water transport in the interlayer remains not well understood (Ho et al. 2019a; Whittaker et al., 2019).

Furthermore, our knowledge regarding the thermodynamic state (e.g., gas, liquid, ice-like) and transport mechanism of water molecules in the clay interlayers and its effect on swelling/shrinking is unfulfilled, compared with the knowledge acquired for other layered materials such as graphene and graphene oxide. For example, in graphene oxide interlayers, water transport is superfast in hydrophobic (graphene) regions and hindered in hydrophilic oxidized regions (Nair et al., 2012). A montmorillonite surface can have hydrophobic sites associating with siloxane groups, and hydrophilic sites associating with metal substitution in the octahedral and/or tetrahedral sheets. The abundance of these sites depends on the number of metal substitutions (i.e., surface charge density). The effect of these sites on water transport and deformation of clay has not yet been unveiled. In addition, in graphene interlayers water can flow fast due to the slip boundary condition, and such fast water flow can be modeled using a modified Hagen-Poiseuille (HP) equation, meaning that water is a Newtonian liquid (i.e., viscosity remains constant regardless of the flow rate) (Radha et al, 2016). In general, viscosity of a nano-confined fluid is different from that of bulk fluid (Ho et al. 2019b; Chen et al., 2008; Neek-Amal et al., 2016; Ye et al., 2011; Babu et al., 2011; Ortiz-Young et al. 2013). Our previous work suggested that water in the 2W state might be a Newtonian fluid with a viscosity ~3-5 times higher than bulk viscosity, and that water can flow fast in the interlayer due to a large suction pressure (~800 MPa) induced by evaporation (Ho et al., 2020). Our previous work also suggested that water transport in the early stage of the dehydration of clay can be a HP flow, followed by a slow diffusion process. Neither simulations nor experiments have been able to explore the correlation between the flow regime change with the modification of the hydration structure and chemistry of interlayer ions. We here combine molecular dynamics (MD)

simulations, thermogravimetric analysis (TGA), differential scanning calorimetry (DSC), and XRD experiments to probe the atomic resolution dynamics of the dehydration process. Our result provides a molecular picture of the coupling nature of water transport mechanism and pathway, and the collapse of clay hydrated structure.

3.1 MD Simulation Methodology

Figure 9 represents a MD simulations system we used to study the water transport mechanism in the interlayer and structural transformation of hydrated Na-MMT during the dehydration process. The Na-MMT particle, with 10 interlayers in total, has 2 edges facing the vacuum. The method to build the Na-MMT particle can be found in our previous work (Ho et al., 2019a). Briefly, from a pyrophyllite structure we create a pyrophyllite particle with edges and then substitute octahedral Al atoms by Mg atoms to obtain Mg:Al ratio of 0.75:3.25. Na^+ ions are added to the interlayers to balance the negative charges, a result of metal substitution. Water molecules are also added to obtain the 1W or 2W hydration state. The 1W or 2W hydrated Na-MMT particle is first equilibrated in an NPT (constant number of particles, pressure (coupled in the x direction), and temperature) simulation, followed by a dehydration simulation. During the dehydration simulations water molecules that move to the vacuum space (i.e., between the dash line and boundary of the simulation box) are removed at a constant rate of 5 molecules per picosecond (i.e., 5 w/ps) (Ho et al., 2016). In other words, as dehydration progresses, water molecules move from the center of the particle to the edge and are removed. Note that the removal rate used in MD is much higher than the evaporation rate at a free surface. For example, at 20% RH, 24.3°C, and 1.5 m/s of air velocity, the evaporation rate from a vessel of diameter 9.3 cm is ~1 $mg/min.cm^2$ (Hisatake et al., 1993), corresponding to 5.19×10^{-7} w/ps for our simulated system. Because of the limited computational resource and the small MD system size, the removal rate simulated is a reasonable choice.

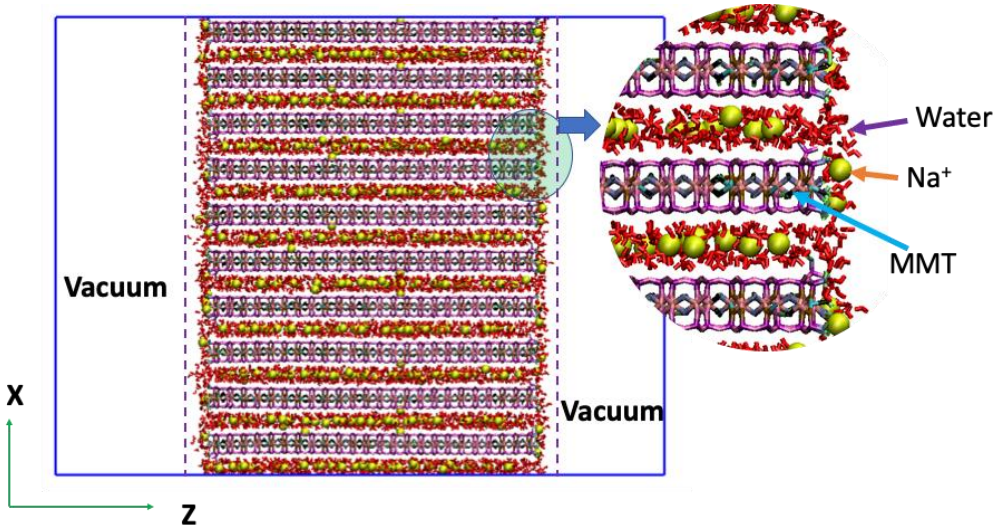

Figure 9. Simulation system used to study the dehydration process of Na-MMT. The simulation box size is 150 × 31.06 × 200 $Å^3$. When applying periodic boundary conditions for all directions, the Na-MMT particle becomes infinite in the x and y directions and finite in the z direction.

There are two processes determining the dehydration: water transport through the interlayer, and water removal (i.e., evaporation) from the edge. If the maximum possible water transport rate is

equal to or higher than the evaporation rate then the number of water molecules removed from the system equals the evaporation rate. If the maximum water transport rate is smaller than the evaporation rate then the number of water molecules removed depends on the water transport rate. During the dehydration simulation, the simulation box can shrink in the x direction under the influence of 1 atm pressure. This unique simulation setup allows us to simultaneously study the water transport, the collapse of the clay particle, and chemical changes in the interlayer. This simulation system is analogous to our experimental setup: a stream of dry N_2 at atmospheric pressure was passed over the hydrated sample for dehydration. The sample was hydrated at 60°C and 50% RH. The mass evolution, heat change, and d-spacing of the sample are monitored in-situ as a function of time using TGA/DSC, and XRD techniques. These methods are described in the previous section.

The Na-MMT particle is simulated by the ClayFF force field (Cygan et al., 2004) with additional Si-O-H and Al-O-H angle terms describing edge hydroxyl groups (Pouvreau et al., 2017; 2019). CLAYFF force field is parameterized with the flexible SPC water model (Teleman et al., 1987) and the Smith and Dang (1994) Na^+ ions model. The pairwise Lennard-Jones (LJ) potential energy is expressed as:

$V_{LJ} = 4\varepsilon\left[\left(\frac{\sigma}{r}\right)^{12} - \left(\frac{\sigma}{r}\right)^{6}\right]$, where r is the distance between two atoms, ε and σ are the depth of the potential energy well and the distance at which the LJ potential is zero, respectively. LJ interactions among atoms are calculated using the Lorentz-Berthelot mixing rules $\varepsilon_{ij} = \sqrt{\varepsilon_{ii}\varepsilon_{jj}}$ and $\sigma_{ij} = (\sigma_{ii} + \sigma_{jj})/2$. Short range interactions are calculated using a cut-off distance of 10 Å. Long range electrostatic interactions are calculated using the particle-particle-particle-mesh (PPPM) solver (Hockney and Eastwood, 1988). The simulations are conducted at 300 K or 330 K using the Nose-Hoover thermostat (Nosé et al., 1984; Martyna et al., 1994). The LAMMPS package (Plimpton, 1995) is used for all molecular dynamics (MD) simulations with a timestep of 1.0 fs.

3.2 Discussion and Results

In Figure 10 we report the mass loss (i.e., number of water molecules removed from the simulation system) as a function of simulation time during the dehydration simulation. We observe a two-stage dehydration process. At the beginning of the simulation (point A in the top left panel of Figure 10), there are two hydration layers in an interlayer (snapshot A). As the dehydration progresses, the mass loss linearly increases from point A to point B (first stage). The snapshot B indicates that at point B, there is one hydration layer in an interlayer (1W). The linear relationship is an indication that water movement through the nanochannel is faster than the water removal rate imposed, and can be modeled as advection flow (Ho et al. 2020). Further dehydration increases the mass loss nonlinearly (second stage). The nonlinear correlation indicates that the water transport rate through the interlayer is smaller than the evaporation rate, suggesting a diffusion mechanism for water transport in the second stage of the dehydration process (Ho et al. 2020). At point C, there are few water molecules in an interlayer (snapshot C).

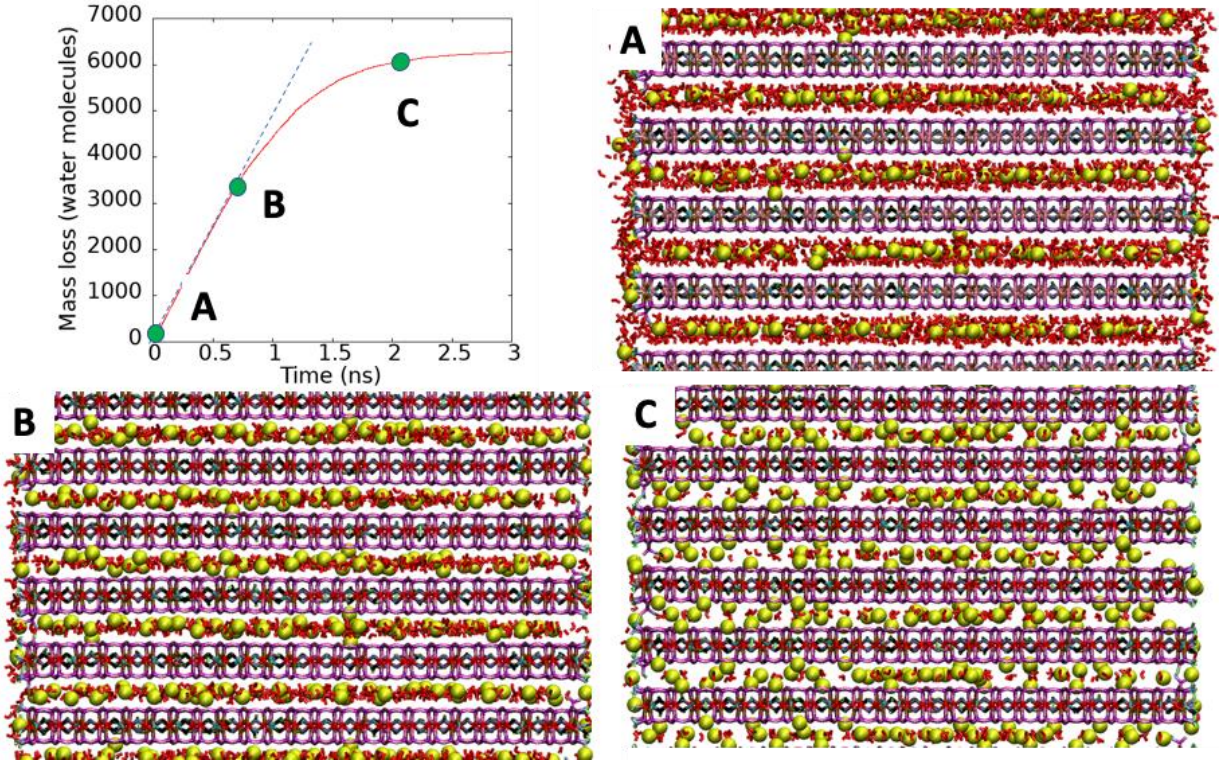

Figure 10. Mass loss (i.e., number of water molecules lost) as a function of simulation time (top left panel). Snapshots labeled A, B, and C are the configurations for the points A, B, and C marked in the top left panel, respectively. These snapshots represent the structural transformation of the Na-MMT particle during the dehydration process. The red line in the top left panel demonstrates the linear correlation between mass loss and time. The temperature is 30ºC.

In Figure 11 we report the simulation snapshots obtained from the dehydration simulations as a function of time to discuss the water transport pathway through the interlayer. At a specific time shown in Figure 11, we report the side and top views of the interlayer. From the top view snapshots, we observed that Na^+ ions (yellow spheres) tend to accumulate near the Mg atoms. Upon the dehydration, water (red) molecules that do not coordinate with Na^+ ions evacuate first, resulting in vacuum sites inside the interlayer (see snapshots at 0.3 ns and beyond). In other words, the hydrophobic sites evacuate first, and the hydrophilic sites evacuate latter. The results in Figure 11 also suggest that in the 1W hydration state (i.e., at 0.7 ns), water molecules distribution in the interlayer is not uniform (e.g., there are vacant and occupied sites). Therefore, the transition from 2W to 0W states does not necessarily go through the fully hydrated 1W hydration state (i.e., water molecules uniformly distributes in the interlayer). The water distribution in the interlayer (e.g., such as at 0.7 ns) will depend on surface charge and charge location. For high surface charge (i.e., high number of metal substitutions) and uniform charge distribution, water molecules might uniformly distribute in the interlayer. In our simulation the Mg:Al ratio of 0.75:3.25 leads to many vacant sites observed in the 1W hydration state at 0.7ns in Figure 3.

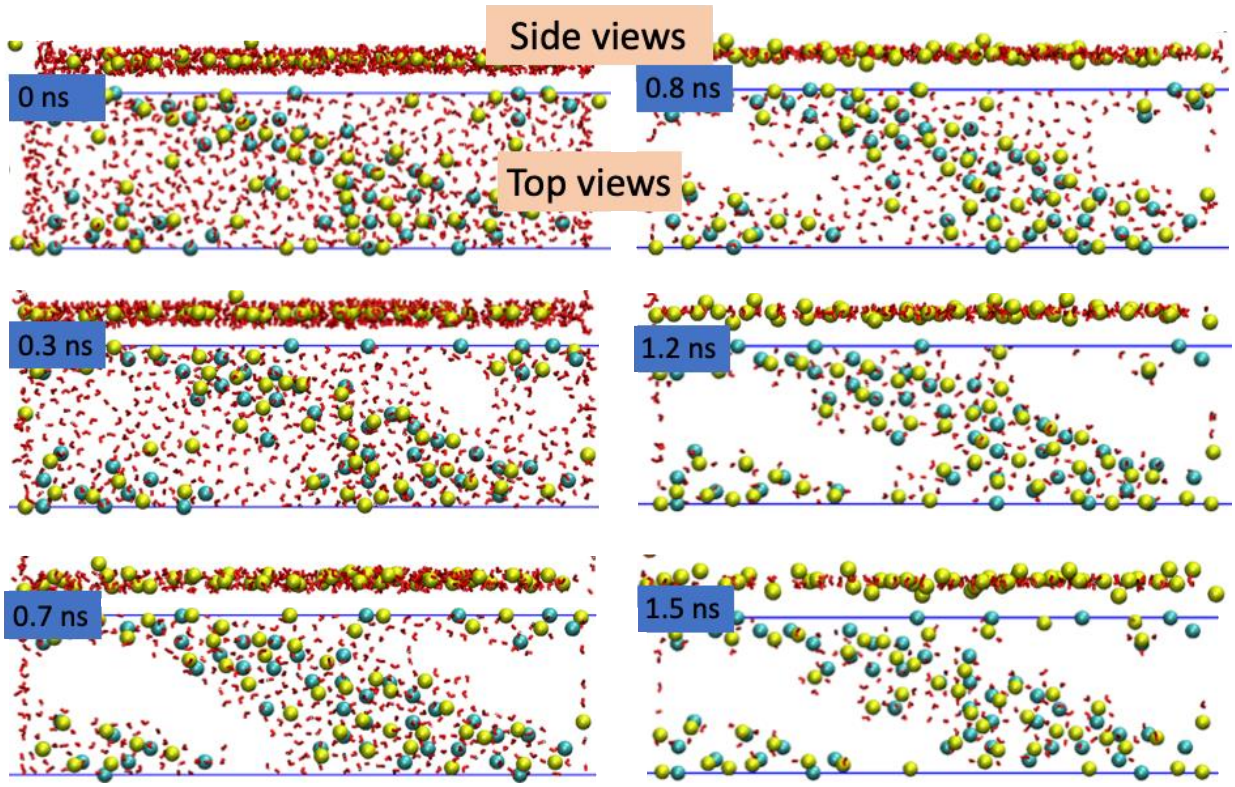

Figure 11. Simulation snapshots demonstrate water transport pathway through an MMT interlayer during the dehydration process. At a specific time, side and top views of the interlayer are reported. Cyan spheres are for Mg atoms of the MMT layer. See Figure 1 for other color codes.

In Figure 12A we report the d-spacing and water coordination number of Na^+ ions as a function of the dehydration time (coordination number is the number of water molecules that are within 3 Å from Na^+ ions). The results indicate that at the beginning of the dehydration process the coordination number insignificantly decreases (green line, Figure 12). This observation supports the result discussed in Figure 11 that water molecules near the hydrophobic sites that do not coordinate with Na^+ ions evacuate first. The subsequent steep decrease in the coordination number of Na^+ atoms is an indication for the fast removal of water molecules belonging to the Na^+ hydration shell. The steep decrease in the coordination number leads to a steep decrease in the d-spacing (red line). In other words, the collapse of the interlayer spacing from 2W to 1W (d-spacing ~12 Å) structure associates with the fast water removal of about 3 to 4 water molecules from the Na^+ hydration shell. Because of the steep decrease in coordination number, it is challenging to conclude if this short time period belongs to the first or second stage of the dehydration process. After this steep decrease, the coordination number and d-spacing slowly decrease as the dehydration process continues (Figure 12B). This result indicates that the removal of the last 1-2 water molecules associated with the Na^+ ion is very slow. The decrease of d-spacing from 11.5 Å to that of 0W state is also very slow (Figure 12B).

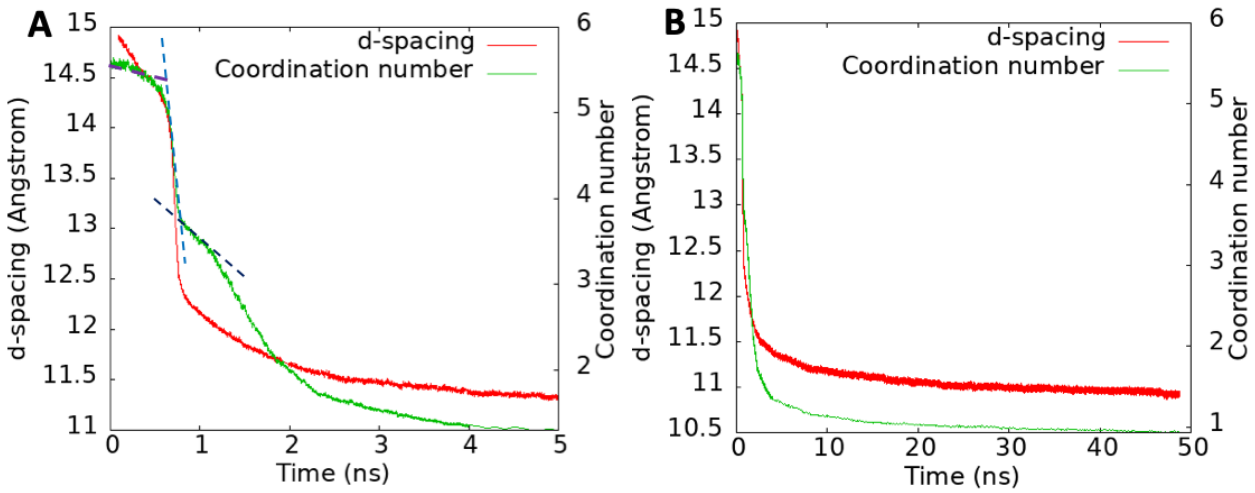

Figure 12. Coordination number of Na^+ ions and d-spacing as a function of time for first 5 ns (A) and 50 ns (B) simulations. The dashed lines in panel A demonstrate the changes in the coordination number of Na^+ ions during the dehydration process.

In Figure 13 A, B, and C we report the mass loss, d-spacing, and water coordination number of Na^+ ions during the dehydration process at 30°C and 60°C for 1W hydration state (see, snapshot in Figure 13D). Note that water molecules uniformly distribute in the interlayer in Figure 13D, unlike the water molecules distribution in 1W state shown Figure 11 (both have the same d-spacing). We observe the same phenomenon described in Figure 11 that the dehydration is a two-stage process (linear and non-linear mass loss. Because the number of water molecules available in the interlayer at 1W state is less than that in the 2W state the linear relation between mass loss and time (Figure 13A) is observed for a very short time period (i.e., first 0.2 ns), and d-spacing and coordination number steeply decreases to around 11.5 Å and 1.5, respectively. The removal of the last 1-2 water molecules from the Na^+ ions is very slow. Similar to the dehydration process of 2W hydration state (Figure 11), water molecules near hydrophobic sites evacuate first and leave hydrophobic sites unoccupied (e.g., snapshot at 0.5 ns in Figure 13E). When the dehydration simulation is carried out at 60°C, we observe that the mass loss, coordination number, and d-spacing are the same with those at 30°C at the beginning of the dehydration process. The temperature seems to impact the diffusion stage, confirmed by the smaller d-spacing (Figure 13B) and coordination number (Figure 13C) at a later time in the dehydration process (e.g., at 2ns) for 60° C, compared to those at 30° C. The water diffusion and desorption are faster than those at 30°C leading to a higher mass loss in the late hydration process.

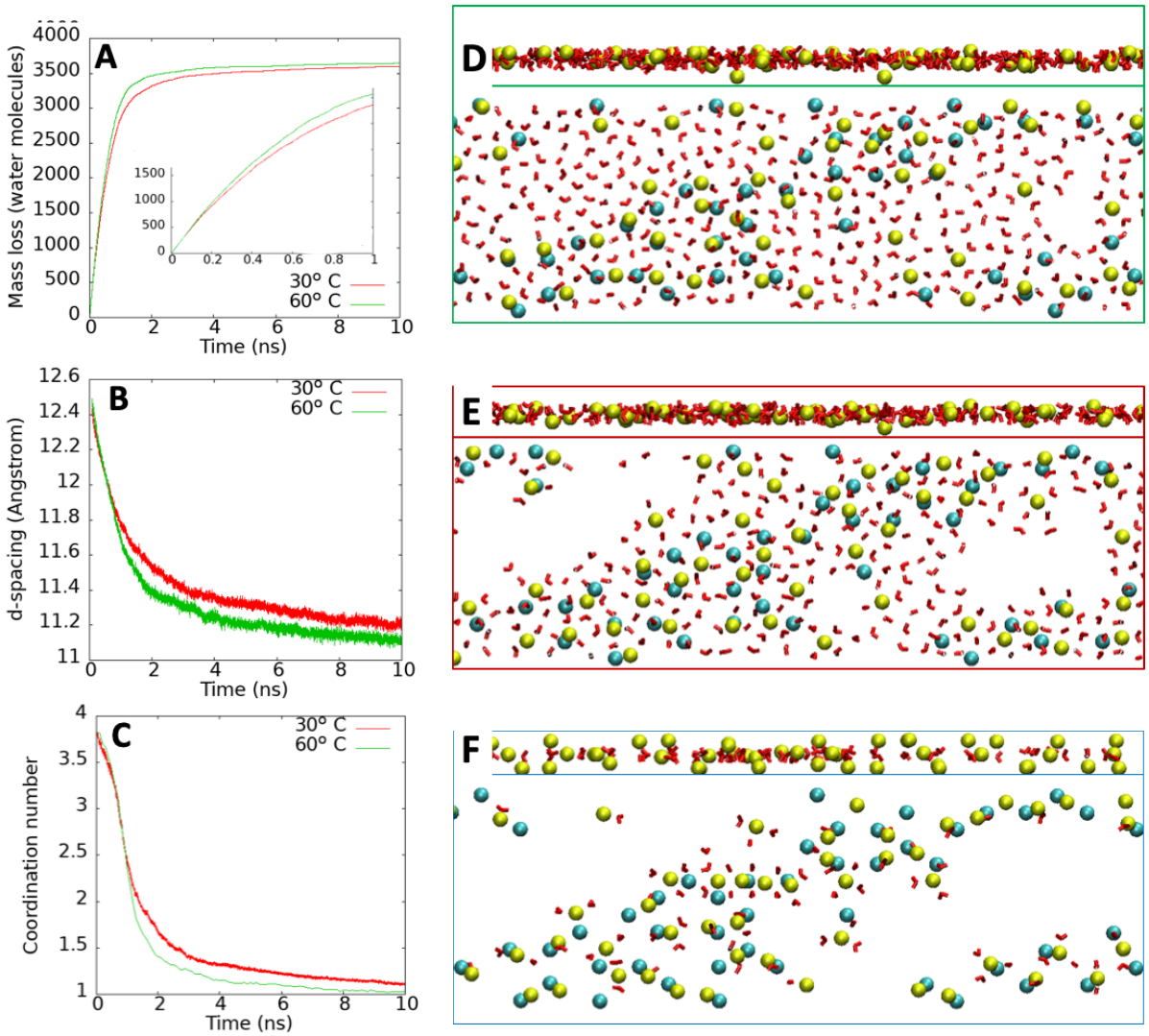

Figure 13. Mass loss (A), d-spacing (B), and water coordination number of Na^+ ion (C) during the dehydration of 1W hydrated MMT at 30° and 60° C. Side and top views of the interlayers during the dehydration of 1W MMT at 0 (D), 0.5 (E), and 3 (F) ns at 30° C. See Figs. 9 and 10 for color codes

In Figure 14 we present the experimental data for the heat flow, mass, and d-spacing as a function of dehydration time. Similar results obtained from thermogravimetric analysis were documented previously (Ho et al., 2020). At the beginning of the dehydration process there is 1 hydration layer (1W hydration state, ~12-12.5 Å d-spacing as shown in Figure 14A). On the time scale of Figure 14A we observe that the d-spacing decreases quickly to ~11 Å, and then more slowly after that. Even though there are huge differences between temporal and spatial scales in MD with those in experiment, the behavior of the d-spacing is consistent with two-stage process observed in the MD simulation (see Figure 13B). The sample mass decreases relatively rapidly at the beginning and more slowly afterward (Figure 14B), which is also supported by our simulation result (Figure 13A). There is a large endothermic peak in the DSC about 1.5h into dehydration (accompanied by an increasing rate of mass loss in the TGA), that is associated with the steep decrease in the coordination number of the interlayer ions (or fast desorption of water

from the Na^+ ion hydration shell), which is also supported by our MD result observed in Figure 13C.

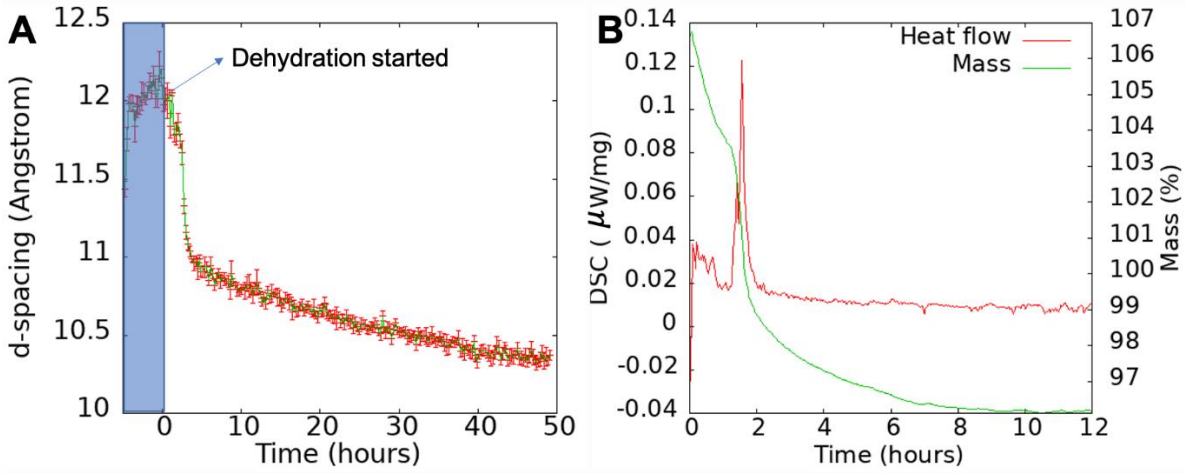

Figure 14. d-spacing (A) and heat flow and mass (B) as a function of time at 60 ºC. The sample was hydrated at 50% RH (60 ºC) for several hours. At the beginning of the dehydration process the RH was reduced to 0%. More details can be found in the method and our previous paper (Ho et al., 2020).

Further MD simulations were conducted in the remaining of FY21 to evaluate and compare water transport mechanism and structural transformation for hydrated Na-MMT, K-MMT, and Ca-MMT during the dehydration process. The results of these MD simulations are described as follows. The MD simulation methodology is very similar to that described previously in Section 3.1. The MD simulation box (150 x 31.06 x 200 Å3) contains a MMT particle with 10 interlayers, each accommodates 2 hydration layers (2W). Na^+, K^+, or Ca^{2+} ions are introduced to each interlayer to balance the structural charge. The MMT particle has 2 edges facing the vacuum. When applying periodic boundary conditions for all directions, the particle become infinite in x and y directions and finite (~110 Å) in z direction.

In Figure 15 we compare the coordination number of Na^+, K^+, and Ca^{2+} ions in the interlayers. At the beginning of the dehydration simulation, there are two hydration layers (2W hydration state) and the averaged coordination number of Na^+, K^+, and Ca^{2+} ions are 5.5, 3.2, and 8, respectively. Note that in a bulk system, averaged coordination number of Na^+, K^+, and Ca^{2+} ions are 5.8, 7.1, and 7.9, respectively.[10] The coordination number of Na^+ and Ca^{2+} ions in the 2W hydration state is similar to that of a bulk system (5.5 vs 5.8 for Na^+, and 8 vs. 7.9 for Ca^{2+}), and the coordination number of K^+ ion in 2W hydration state is much smaller (3.2 vs. 7.1) than that in a bullk system. We observe that in an interlayer, most Na^+ and Ca^{2+} ions concentrated in the center of the pore (Figure 16), i.e., they exist as the outer sphere complexes. In contrast, the majority of K^+ ions adsorb on the surface as the inner sphere complexes (Figure 16). Therefore, the adsorption complexes of ions (outer sphere vs. inner sphere) determines the difference between the water coordination number of ions in an interlayer and that of ions in the bulk.

The adsorption complex of ions depends on the hydration energy. The lower hydration energy (more negative) the more difficult for ions to strip water molecules to adsorb as inner sphere complexes. Experimental data indicate that Na^+ ions adsorb as outer sphere complexes, while K^+ ions adsorb as inner sphere complexes (Lee et al., 2012). Our MD result reproduces (Figure 16)

very well these adsorption behaviors. Ca^{2+} ions with the lowest hydration energy (most negative) among ions considered here form outer sphere complexes (Figure 16), which agrees with previous report (Sposito et al., 1999).

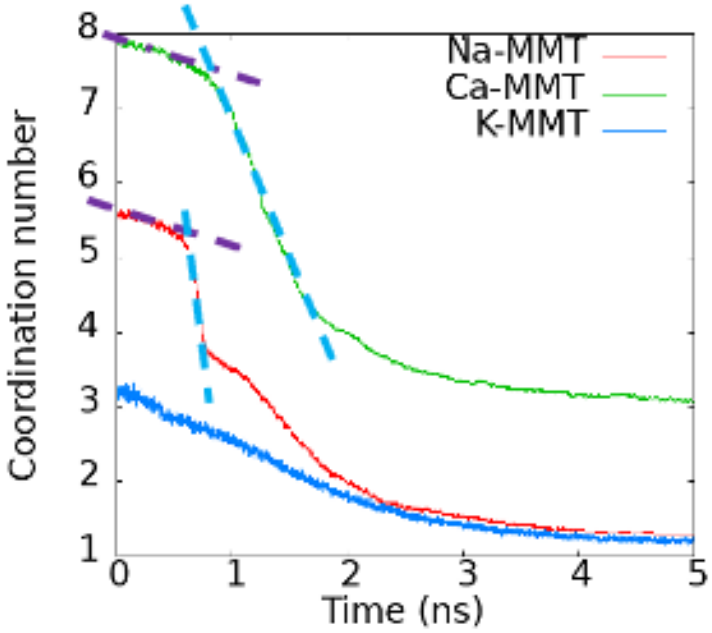

Figure 15. Water coordination number of interlayer Na^+, K^+, and Ca^{2+} ions as a function of hydration time. The dash purple and cyan lines demonstrate different stage in the variation of the coordination number as a function of time.

During the dehydration process, the decrease of the coordination number of outer sphere ions (Na^+ and Ca^{2+}) seems to follow the same trend and is different with the decrease of the coordination number of inner sphere ions (K^+). In a previous study we observed that at the beginning of the dehydration process the coordination number of Na^+ ions does not change significantly (dash purple portion of the red line, Figure 15). We observe the same conclusion for Ca^{2+} (dash purple portion of the green line, Figure 15) in this report. The reason is that at the beginning of the dehydration process the majority of water molecules associating with the hydrophobic sites are removed first during the dehydration process. A steep decrease (dash cyan line in Figure 15) in the coordination number of outer sphere ions is an indication for the fast removal of several water molecules belonging to the hydration shell. As the dehydration continues progressing, the coordination number of outer sphere ions gradually reduces.

For K-MMT, there are not many water molecules bouncing to the K^+ ions as compared to Na^+ and Ca^{2+}. Therefore, we did not observe a steep decrease in the coordination number as we observed for Na-MMT and Ca-MMT. Instead, we observed a gradual decrease in the coordination number. At the beginning of the dehydration, the rate of decrease in coordination number Na^+ K^+, and Ca^{2+} ions are the same (i.e., the slopes of the green, red, and blue lines in Figure 15 are the same at the beginning of the dehydration). For K^+ and Na^+, even though the coordination number at a specific time at the beginning of the dehydration (e.g., first 2ns) is significantly different, the coordination number for K^+ and Na^+ ions are the same at the late stage of the dehydration process. At the 2W hydration state the coordination number depends on the

adsorption complexes and when the number of water molecules reduce significantly during dehydration process (e.g., to 1W state), all ions adsorp as inner sphere complexes, leading to the same coordination number of monovalent cations.

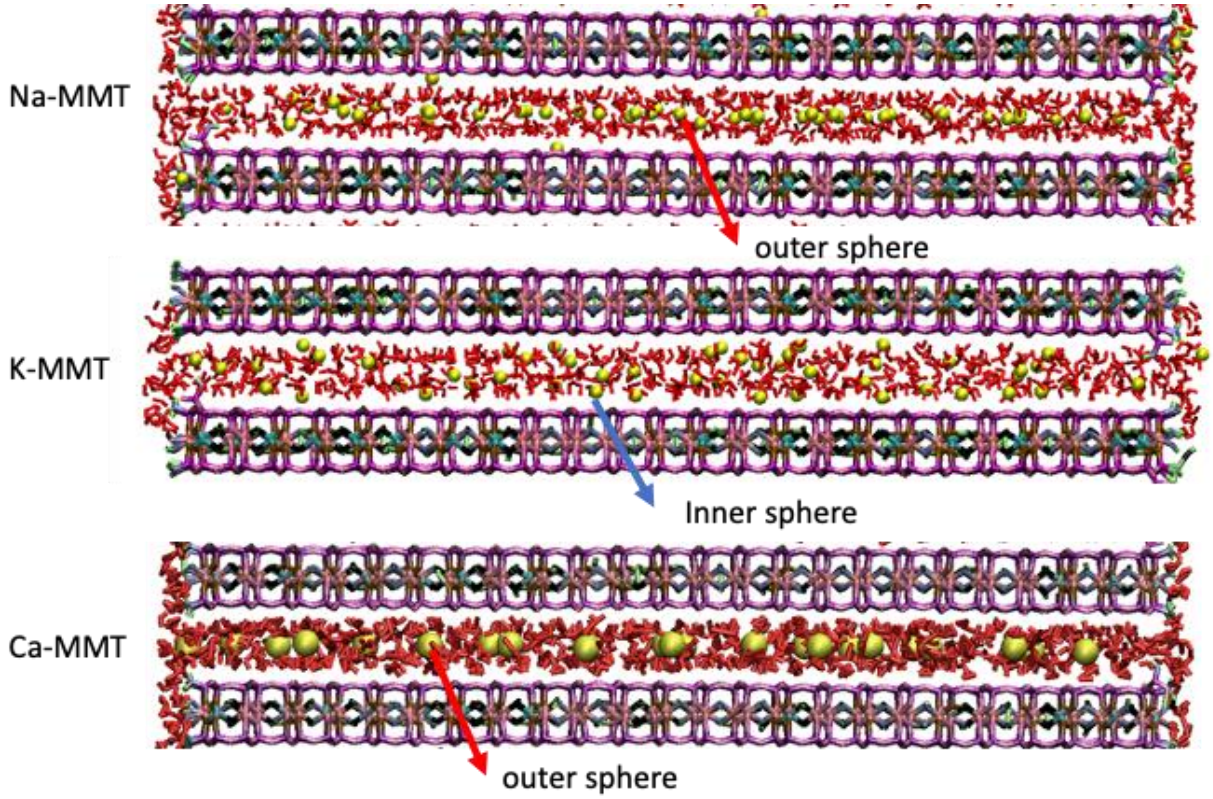

Figure 16. Ion adsorption complexes in interlayers at 2W hydration state.

The coordination chemistry of ions (inner sphere vs. outer sphere) remarkably affects the mechanical properties of smectite during the dehydration process (i.e., chemo-mechanical effect). The results in Figure 17 indicate that higher abundance of water molecules in the hydration shell leads to a slower decrease in d-spacing during the dehydration process. In an interlayer, the coordination number of cations depends on the adsorption complexes and decreases in the order of $Ca^{2+} > Na^{+} > K^{+}$. The rate of d-spacing change decreases as follows $K^{+} > Na^{+} > Ca^{2+}$. The d-spacing for K^{+} decreases steeply at the beginning of the dehydration, while for Na^{+} and Ca^{2+} a steep decease only observe when losing water in the hydration shell.

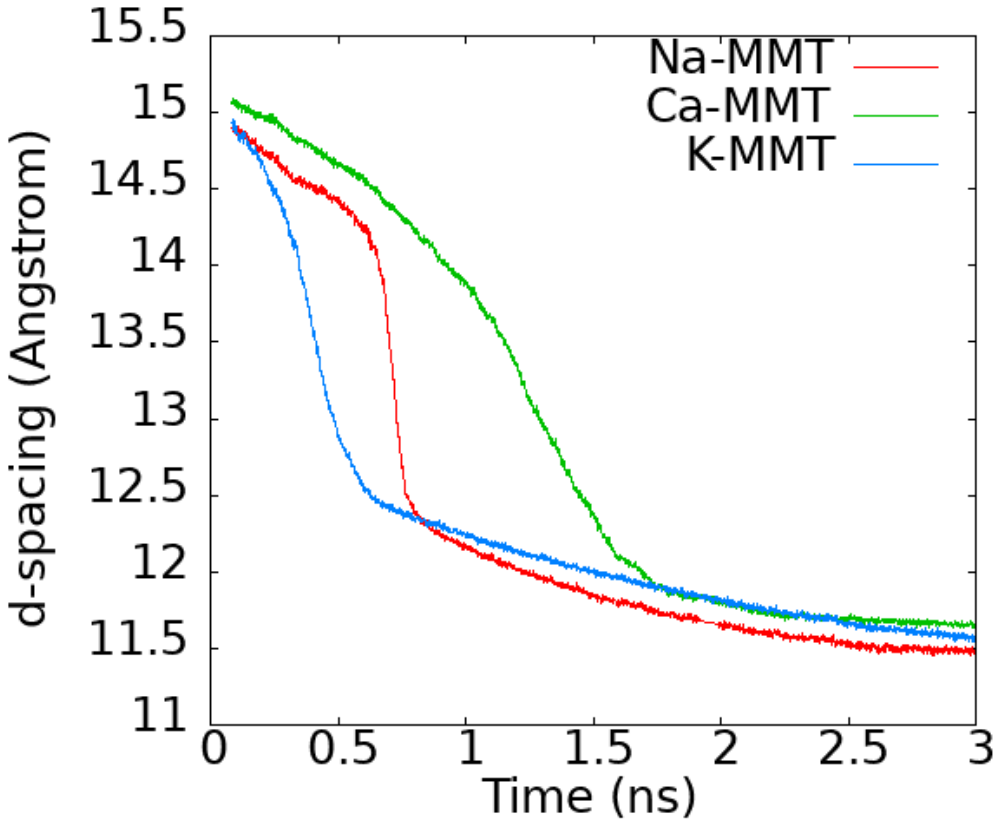

Figure 17. d-spacing change as a function of time during the dehydration process of Na-MMT, K-MMT, and Ca-MMT.

3.3 Conclusions

Using molecular dynamics simulations, we demonstrate that clay dehydration is a two-stage process. In the first stage, water transport exhibits an advection mechanism as mass loss is linear with time. The first stage is associated with the evacuation of water molecules from the hydrophobic sites and also with the fast removal of the first few water molecules from the Na^+ ion hydration shell. The second stage represents the slow desorption of the last 1-2 water molecules from the Na^+ ions. Movement of water molecules through the interlayer in the second stage follows a diffusion mechanism. These conclusions are supported by our results obtained from TGA/DSC calorimetry, and in-situ XRD measurements.

By extending the MD simulation to other cations in addition to Na^+, we demonstrate that the clay dehydration process from 2W to 0W depends on the cation adsorption complexes in the interlayer. For the 2W hydration state, most Na^+ and Ca^{2+} ions exist as the outer sphere complexes, and most K^+ ions adsorb on surfaces as the inner sphere complexes. As a result, the water coordination numbers of Na^+ and Ca^{2+} ions at 2W state are similar to those in bulk system, while the coordination number of K^+ is much smaller than that in the bulk. The coordination number of ions affects the mechanical change of the montmorillonite during the dehydration process. The higher abundance of water molecules in the hydration shell leads to a slower decrease in d-spacing.

4. 1D Reactive-Transport Modeling of Sedimentary Rock Leaching Experiments

4.1 Introduction

Matteo et al. (2019) described 1D PFLOTRAN reactive-transport simulations for the idealized case of cement-clay interactions with emphasis on the clay rock / cement interface. The role of barrier interfaces in seal performance and interactions with other barrier materials is crucial to the barrier isolation function in deep geological nuclear waste repositories (Berner et al., 2013; Gaboreau et al., 2012; Kosakowski and Berner, 2013; Soler, 2012; Soler and Mader, 2010). The effects of porosity enhancement and reduction (i.e., clogging) due to mineral dissolution/precipitation have been the focus in various reactive-transport modeling efforts including benchmark test cases for computer code inter-comparisons efforts (Marty et al., 2015; Xie et al., 2015). The main purpose behind these computational reactive-transport modeling efforts lies in the complex coupling of geochemical interactions (kinetic vs. transport controlled) for the most part involving reactive diffusion phenomena in porous media (Marty et al., 2015). The extent to which these models capture relevant physico-chemical processes with enough realism and adequacy still needs to be examined and reconciled with the limited amount of available field and experimental laboratory data.

Leaching behavior of barrier materials whether engineered or natural provides key chemical and structural characterization data of (geo)chemical interactions at interfaces. Such data is useful in the evaluation and testing of reactive-transport models such as described in Matteo et al. (2019) for cement-clayrock interactions and those described for DECOVALEX19 Task C on the GREET experiment (Jové Colón et al. 2020) where kinetic rate (e.g., solid dissolution), transport length scale, and diffusion parameters can have an effect on representing the temporal change in measured solute concentrations. In this work, a 1D PFLOTRAN reactive-transport simulation will be conducted to simulate leaching of a marl rock from the carbonate Ghareb and Nezer Formations in the northern Negev, Israel (Klein-BenDavid et al., 2019). The controlled leaching experiment of a carbonate-rich sedimentary rock with minor clay offers the opportunity of using leaching data to test this type of simulation in the presence of complex carbonate equilibria. When combined with cement at an interface, marl interactions can play a key role on cement carbonation under alkaline conditions.

4.1.1 Marl Rock Properties

The marl samples were obtained from the Yamin Plateau, northern Negev desert, in Israel specifically from the carbonate-rich Mount Scopus Group. This formation group are of Upper Cretaceous to early Paleocene age. The bulk mineralogy of the marl samples have been estimated by X-Ray diffraction (XRD) – see Table 1. The volume fractions were determined from mineral densities and the porosity of the marl sample (32%).

Table 1. Mineral volume fractions based on XRD data.

Mineral	Volume Fraction	Fraction (XRD)
Calcite	0.643	0.95
Quartz(alpha)	7.004E-03	0.01
Kaolinite	0.0212	0.03
Halite	7.537E-04	<0.01*
Sylvite	2.70E-05	<0.01*
Total	0.672	1

* Estimated, not measured by XRD. Halite and sylvite volume fractions were determine from fitting solute concentrations vs. time profiles from the PFLOTRAN 1D reactive-transport simulation. These estimates were used as a source of Na and K in the marl pore solution to account for small amounts of salt in the pores.

4.1.2 Monolith leaching test (EPA Method 1315)

Matteo et al. (2020) describes the EPA method 1315 used in the rock monolith leaching test. The description will be duplicated here for completeness. The EPA Method 1315 is a mass transfer rate, tank leaching test (U.S. EPA, 2017). The test consists of continuous leaching of water-saturated monolithic material with periodic renewal of the eluent at predetermined intervals. The concentration of constituent in each interval eluate is used to calculate the interval mass flux across the exposed surface area (mg m^{-2} sec^{-1}) and the cumulative mass release (mg m^{-2}) to the eluate. The marl leaching tests were conducted at Vanderbilt University. After each eluant exchange, the eluate is analyzed for pH, conductivity, Eh, elemental analysis by ICP-MS (EPA Method 6020B) and inductively coupled plasma optical emission spectroscopy (ICP-OES; EPA Method 6010D), dissolved organic carbon (DOC), and other parameters of interest. DOC was analyzed using Shimadzu TOC-V CPH/CPN (Shimadzu Scientific Instruments, Inc., Columbia, MD) by catalytic oxidation/non-dispersive infrared detection (NDIR) following EPA Method 9060A.

Test samples for Method 1315 were prepared by cutting approximately 2.5-cm cubes from the larger rock specimens utilizing a rock saw with a diamond blade. The 2.5-cm cubes were then cast in epoxy utilizing 5-cm by 10-cm tubes for molds and epoxy resin and hardener (Figure 18). After the samples were set, they were demolded and polished. Samples were polished using 140 grit paper for coarse polishing to expose the surface of the sample and 240 grit paper for finer polishing. Samples were then exposed under 100% relative humidity at 30°C in an environmental chamber for approximately three weeks to achieve water saturation through capillary condensation of water vapor. Samples were weighed approximately every 48 hours until constant weight indicated that saturation was achieved (approximately 2 weeks). Figure 18a show the hand rock specimens and the epoxy mounted samples along with the experimental leaching tank apparatus.

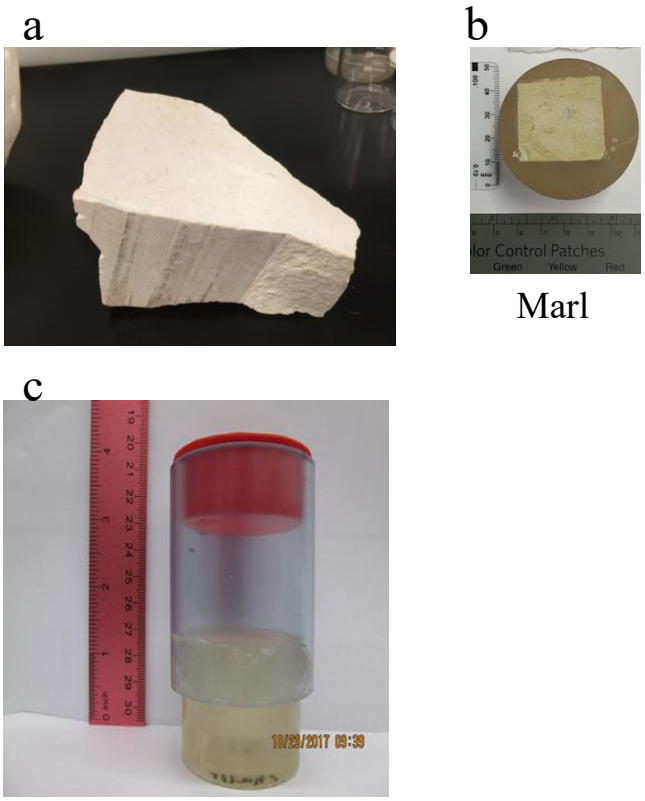

Figure 18. (a) Bulk rock sample; (b) epoxy-mounted sample used for 1315, and (c) experimental set up for the 1315 test.

4.2 1D PFLOTRAN Reactive Transport Simulations

The PFLOTRAN simulator (https://www.pflotran.org) is an open source, state-of-the-art massively parallel computer code to perform calculations for subsurface single- and multi-phase flow and reactive transport under (non)isothermal conditions. The code is designed for use on massively parallel or high performance computing (HPC) platforms where efficient scalability becomes important for large coupled process problems. Lichtner et al. (2013) provides details on PFLOTRAN simulation capabilities, reactive-transport formulations, and geochemical treatment of mineral-fluid interactions. The THERMODDEM thermodynamic database (Blanc et al., 2012; Blanc et al., 2006) was used in the simulations.

The structured mesh discretization is defined by a rectangular geometry with dimensions consistent with those of the marl sample in the leaching experiments (Figure 19). The solid monolith meshed domain is composed of 43 cells (bottom) and a single cell (top) for the leaching bath solution. The surrounding epoxy mount is considered to be inert and thus is not part of the meshed domain. No flow boundary conditions are imposed on the faces of the rectangular domain. Small pressure perturbations in the leaching solution upper “box” are allowed for some “mixing”.

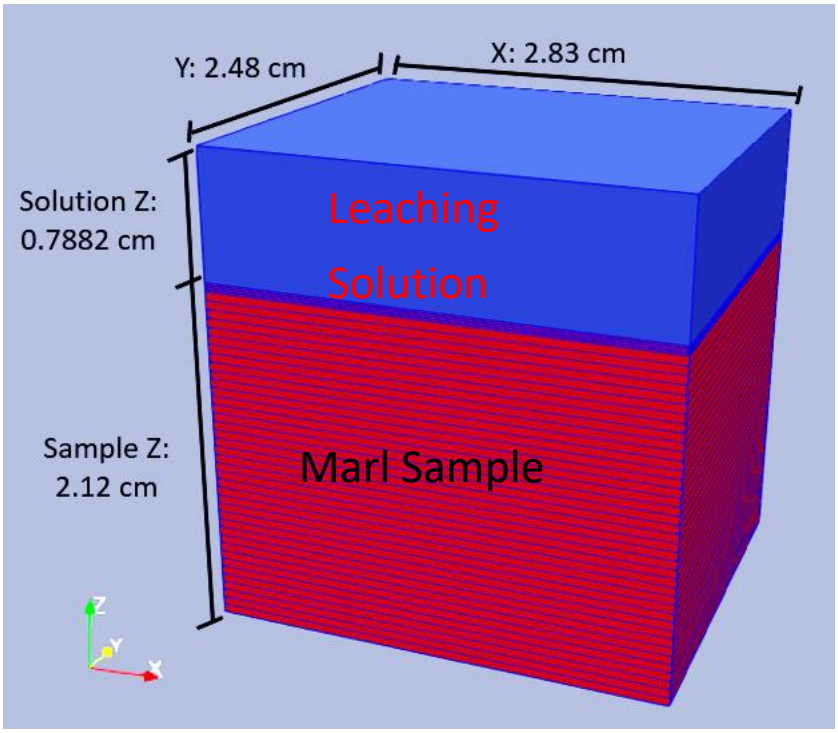

Figure 19. Mesh discretization of the solid (lower) and leaching solution (upper) domains along with dimensions of the rectangular domain. The marl sample meshed domain is composed of 43 cells and a single cell for the leaching solution.

As mentioned earlier, the porosity of the marl is 32%, with a permeability of 1×10^{-16} m^2, and unit tortuosity (Table 2). The 1D diffusion problem is isothermal at 25ºC with a diffusion coefficient of 2.5E-10 m^2/s. The diffusion coefficient was adjusted to fit the Na and K solute concentration vs. time profiles. Updates to permeability and porosity at each time step as a result of chemical interactions were considered in the simulations.

Table 2. Marl monolith properties

Parameter	Value
Porosity	0.32
Tortuosity	1
Rock Density	1947 kg/m^3 *
Permeability (Isotropic)	1.0E-16 m^2

* Derived from sample mass and dimensions.

The mineral reactive surface areas (RSAs) were set to unity except for calcite and sylvite. The former has a value of 1000 m^2/m^3 rock whereas the latter has a value of 0.1 m^2/m^3 rock. The reason for the large RSA value for calcite is to scale up its dissolution as an attempt to evaluate peak Ca concentrations early in the experiments. A transition state theory (TST) rate law implemented in PFLOTRAN was adopted for calcite dissolution using a rate constant value of 1.778E-05 mol/m^2 s. The TST model is with Ca^{++} as the prefactor species and whose activity term in the equation has unity exponent. The TST model was also used for kaolinite with a far from equilibrium dissolution rate constant of 1.12E-14 mol/m^2 s where H^+ is the prefactor species and the activity term has an exponent of 0.1. Far from equilibrium dissolution rate constants for quartz (alpha), halite, and sylvite are constrained to 5.0E-14 mol/m^2 s, 2.5E-03 mol/m^2 s, and 2.5E-02 mol/m^2 s, respectively.

The initial marl pore solution chemistry is taken as very dilute in all its components where the Ca^{++} concentration is 3.2E-05 M, constrained to match initial concentrations in the leachate solution. HCO_3^- concentration is constrained by charge balancing with initial pH 7. The dilute pore solution reacts rapidly in the initial steps of the simulation. The leaching solution or eluent chemistries at each renewal interval were obtained from Drs. Chen Gruber and David Kosson at Vanderbilt University. Blank solutions for these experiments (solutions reacting with epoxy mount without monolith sample) show excess silica that originated from the sealant use to hold the mold cast. As described previously, these eluent solutions are periodically renewed in the experiment. This excess silica concentration was corrected in the input leaching solutions. The chemistry of leaching solutions for each replenishments in the tank bath cell at the corresponding times are specified in the PFLOTRAN input deck.

4.3 Preliminary Results and Discussion

Figure 20 shows the change in pH and Ca^{++} concentration with time for the 1315 leaching experiment and the PFFLOTRAN 1D reactive-transport simulation. The overall pH trend is represented by the model except for deviations in the initial and final stages of the experiment. The initial drop in pH illustrated by the experimental data cannot be represented by the model. Similarly, the rapid initial increase and peak Ca^{++} concentration from the experiment is not described by the simulation. However, there is good agreement in predicted pH at later times (from ~950 to ~2700 hours). In an analogous manner, the predicted Ca^{++} concentrations are good agreement with the experimental data. The overall discrepancies in the pH and Ca^{++} concentration trends at these later times are considered reasonable given the nature of the experiment where multiple leachate solution batches (from periodic eluent renewals) are sampled at various times.

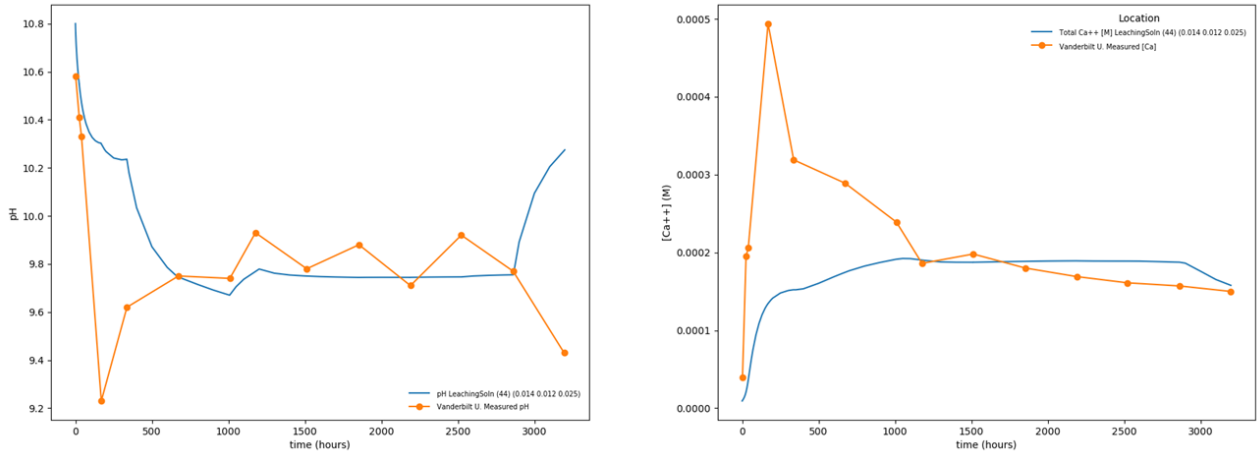

Figure 20. Temporal change of pH (left panel) and total Ca^{++} concentration (right panel) in leachate solutions for the 1315 leaching experiment. The light blue solid line stands for the 1D PFLOTRAN simulation and the connected filled orange circles represents the experimental results.

Figure 21 shows the change in total dissolved Si concentration with time depicting an overall trend in good agreement with the experimental data. It should be noted that dissolved Si concentration in the leaching solution needed to be corrected because of contamination with sealant. Similar to pH and Ca^{++} concentration trends, the initial rapid increase and peak Si concentrations are not predicted by the model. Still, there is good agreement in the overall trend and the experimental data at later times.

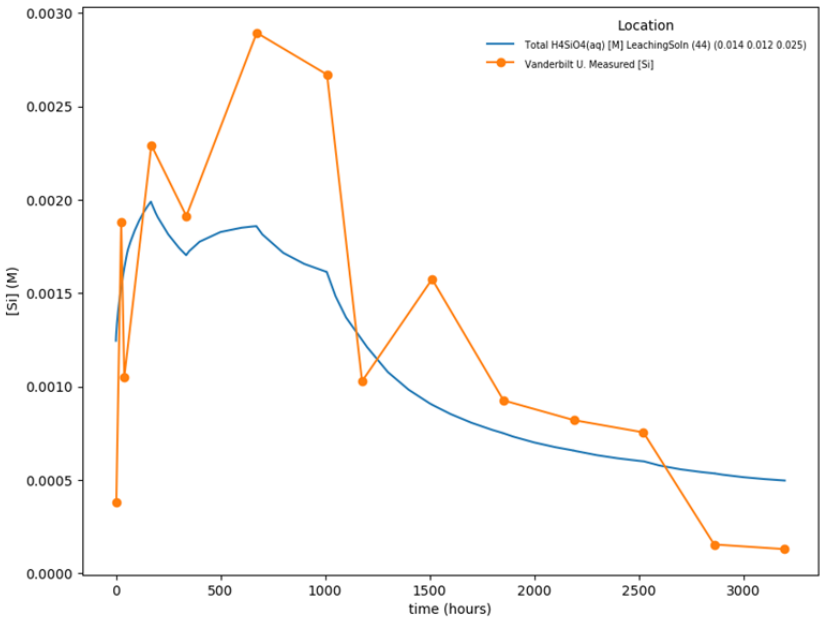

Figure 21. Temporal change of total dissolved Si concentration. The initial Si concentration in the input leaching solutions needed to be corrected due to contamination from the experimental setup.

Figure 22 shows the change in total dissolved Na and K concentrations with time where simulation results are excellent agreement with the experimental data. These Na and K concentration vs. time profiles were used to constrain the diffusion constant adopted in the model. The origin of Na and K in the marl is attributed to minor amounts of salt represent in the model by halite (NaCl) and sylvite (KCl). It is inferred that evaporative conditions in the formation of the marl rock could cause salt precipitation in the pores. Given the similarity in the overall trends of these two curves to that of the Ca^{++} concentration profile at initial times may suggest the rapid dissolution of potential Ca-bearing salt. However, no Ca-bearing salt was identified in the XRD analysis or in the marl rock mineralogy. Another potential reason for having rapid initial increases and peak solute concentrations is the fast dissolution of fine material on the surface as a result of polishing.

This study is still work in progress where more parameter sensitivities need to be evaluated. The current results show that the PFLOTRAN 1D reactive-transport model implementation of the EPA 1315 monolith leaching test can represent the overall trends of temporal changes of solute concentration profiles based on the major rock constituents. In addition to the evaluation of parameter sensitivities, other work includes effects of meshing discretization and evaluation of $pCO_2(g)$ on carbonate interactions. Testing the implementation of this 1D reactive-transport simulation approach is planned for cement-rock leaching scenarios.

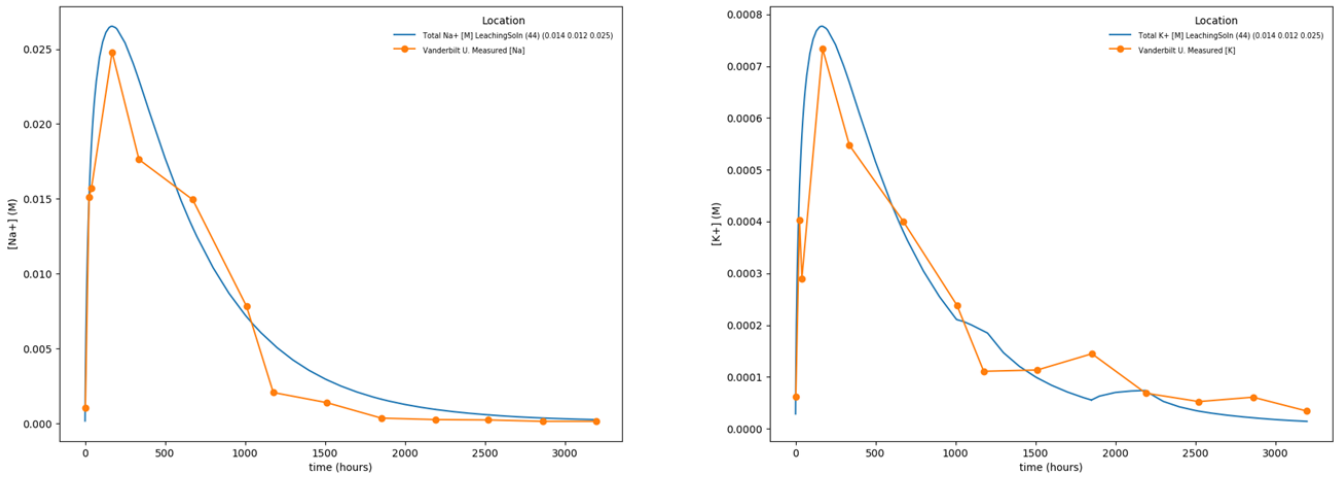

Figure 22. Temporal change of Na (left panel) and K concentration (right panel). Notice the very good agreement between model prediction and experimental data.

5. HotBENT Heated Column Experiment: Preliminary XRD Analysis of Post-Experiment Bentonite Samples

The HotBENT heated/unheated tests on packed on MX-80 bentonite columns is a laboratory-scale experiment conducted at LBNL in support of the HotBENT field-scale heater test at the Grimsel Test Site (GTS), Switzerland. The objectives of the HotBENT heater test are to study long-term THMC behavior of bentonite backfill behavior at elevated temperatures of 200°C. The laboratory-scale experiment permits the use of monitoring and characterization methods that would otherwise be either difficult to deploy, implement, or operate at the field scale. The main goals of this laboratory-scale hear column experiments are to improve our knowledge of bentonite THMC behavior at elevated temperatures under controlled hydration conditions, perform comparisons between laboratory- and field-scale experimental heater test results, and develop an experimentation platform to conduct bentonite barrier studies at high temperatures (Zheng et al., 2020). Details of the experimental setup and operations for both heated and unheated columns are given by Zheng et al. (2020).

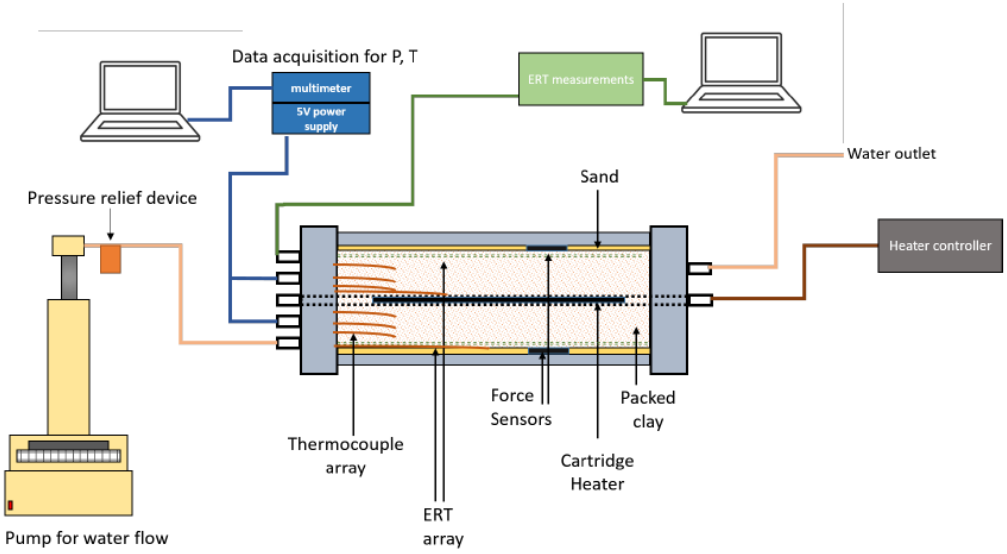

Figure 23. Schematic diagram of the entire experimental column setup including flow control, sensors, and cartridge heater at the column center axis. The sand layer between the clay and vessel wall is used to hydrate the bentonite by continuous brine flow. The inner diameter (ID) of the column is 6.5 inches, outer diameter (OD) is 7.5 inches, and the height is 18 inches (Zheng et al., 2020).

The columns experiments (Figure 23) were conducted at a temperature of 200°C with continuous sensor monitoring for 255 days. After the experiment shutdown, samples were collected from different radial regions of the column for subsequent chemical analysis and moisture content (Figure 24). The next section will provide preliminary XRD data of post-experiment bentonite samples.

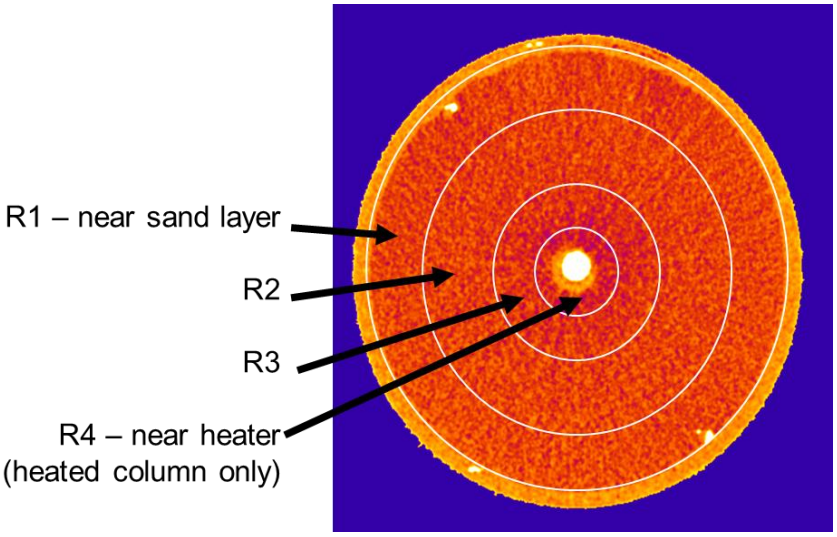

Figure 24. CT scan image showing the column cross section delineating the sampling radial zones. The outer orange color rim is the sand layer (Figure courtesy of Liange Zheng and Sharon Borglin – LBNL).

5.1 Preliminary XRD Analyses of Post-Experiment Bentonite Samples

SNL obtained samples for regions R1, R2, and R3 (Figure 24) for both heated and unheated columns from sieved size fractions of <38 microns. These samples were prepared for oriented air-dried (AD) and ethylene glycol (EG) saturated samples. Sample preparation consisted first of crushing the clay using a mortar and pestle into small particle sizes to achieve a "powder like" consistency. The samples were subsequently sieved to < 75 μm and < 38 μm particle size. The < 38 μm particles were used to make XRD mounts. XRD analysis of air-dried clay sample consisted of adding ~0.1 g of clay to a 5 mL scintillation vial. 2 mL of a 70-30% water-ethanol mixture was added to the scintillation vial to have a mass/liquid ratio of 0.05. The ethanol was added to the samples to decrease the cracking behavior of the oriented clay samples upon drying. The suspended clay was hand shaken vigorously until clay was sufficiently suspended and sonicated with a benchtop microtip sonicator for approximately 1 minute. Then using a 1000 μL micropipette the slurry was pipetted in a circular motion onto the zero-background silicon wafer. The oriented mount was placed on the countertop at ambient conditions, parafilmed and allowed to air-dry completely (overnight). After the sample had completely dried, the wafer was placed in the Bruker D2-Phaser sample holder to perform the XRD analysis. After completion of XRD analysis of the dried samples, this bentonite material was then placed into a desiccator over a pool of ethylene glycol. The desiccator was then placed in the oven heated at 60°C overnight to ensure glycol saturation of the bentonite samples. The following day the sample was removed from the desiccator and the XRD analysis was conducted immediately to ensure the bentonite remained glycol saturated. The powder diffraction data was collected using a Bruker D2 Phaser benchtop diffractometer with a CuKα (1.54 Å) X-ray wavelength. The analysis was conducted in a 2-theta range of 3 -70° with 0.5 s time per step. This resulted in XRD runs that were ~23.5 minutes in duration. Silicon wafers were chosen as the sample holders for the oriented clay mounts as it provides very low background interference and were optimal for making oriented clay slurry mounts. A desiccator was adapted into a glycolation chamber for the purposes of the

project by filling the desiccator with ethylene glycol, then heating the entire desiccator at 60℃ - the sample was placed on a petri dish above the layer of ethylene glycol at the bottom of the desiccator. The heat caused the ethylene glycol to vaporize and create a glycol vapor saturated environment within the desiccator.

These XRD analyses were conducted very recently and any evaluation of the data is very preliminary. Figure 25 shows stacked XRD spectra of bentonite sampled in region R3 (closer to the heater) for both heated (V1) and unheated (V2) column experiments. As expected, there is a close correspondence of montmorillonite peaks with PDF cards for the EG samples. Other strong peaks such as those for quartz are also identified. The appearance of a 10 Angstrom peak at 2-theta of ~9 degrees in both heated/unheated EG samples may be indicative of potential interstratified illite in the clay but this needs much further evaluation of the XRD spectra. The study of Gomez-Espina and Villar (2016) suggested the presence of interstratified illite in heated column experiments using MX-80 bentonite. Other features in the XRD spectra are peak broadening at 2-theta 6-9-10 degrees in the AD samples with increasing distance from the column center axis (regions R1 and R2) as observed in Figures 26 and 27. The regions R1 and R2 are closer to the sand layer which are expected to be more hydrated in the heated (V1) column. Such peak broadening of the 2-theta range of 6-9-10 degrees has been observed from *in situ* XRD measurements under controlled temperature and moisture conditions. Again, more work is needed to evaluate the structural data to assess the changes in bentonite hydration/dehydration under variable temperature and moisture conditions.

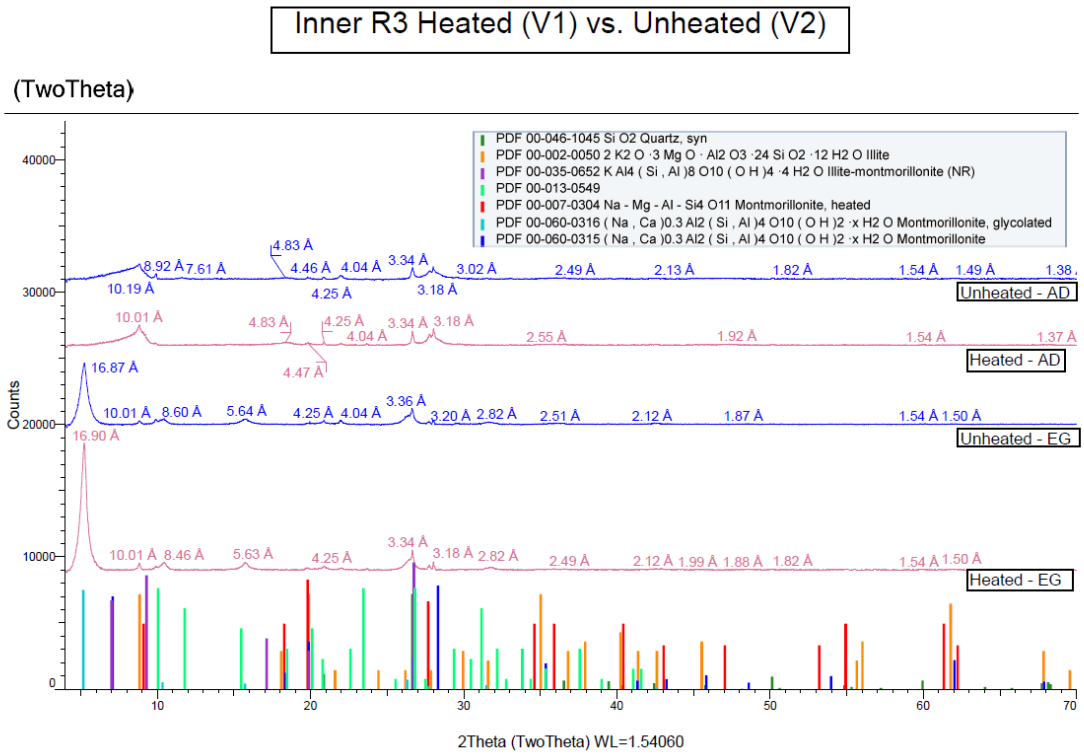

Figure 25. XRD stacked spectra of bentonite sampled in region R3 (closer to the heater) for both heated (V1) and unheated (V2) column experiments. AD stands for air-dried and EG denotes ethylene glycol saturated samples. Vertical axis scale are arbitrary counts. Vertical bars correspond to XRD peak positions from the PDF card database.

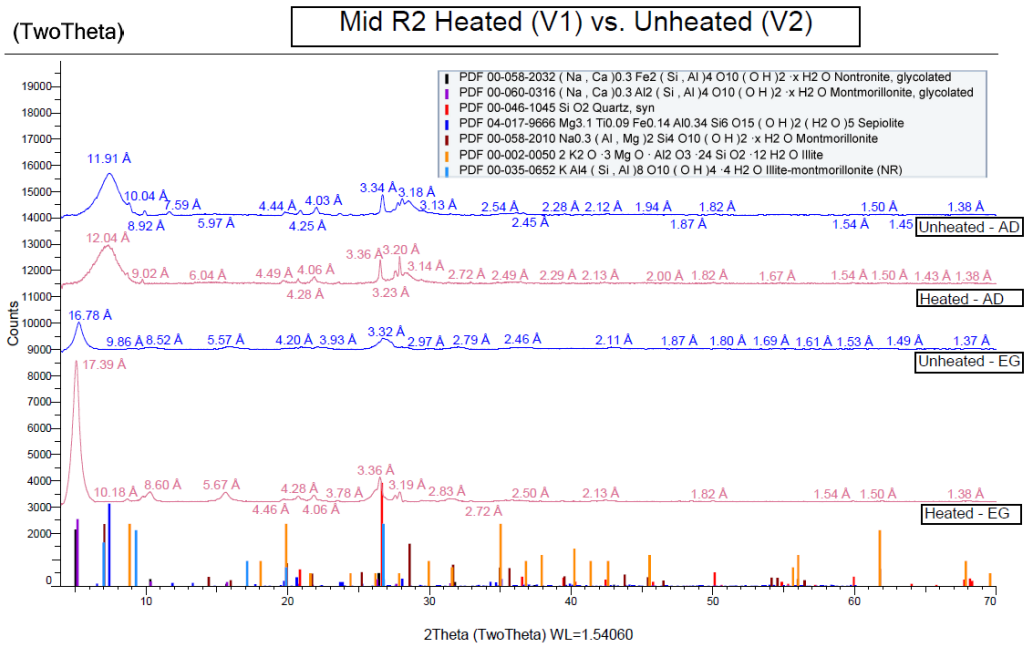

Figure 26. XRD stacked spectra of bentonite sampled in region R2 (midpoint) for both heated (V1) and unheated (V2) column experiments. AD stands for air-dried and EG denotes ethylene glycol saturated samples. Vertical axis scale are arbitrary counts. Vertical bars correspond to XRD peak positions from the PDF card database.

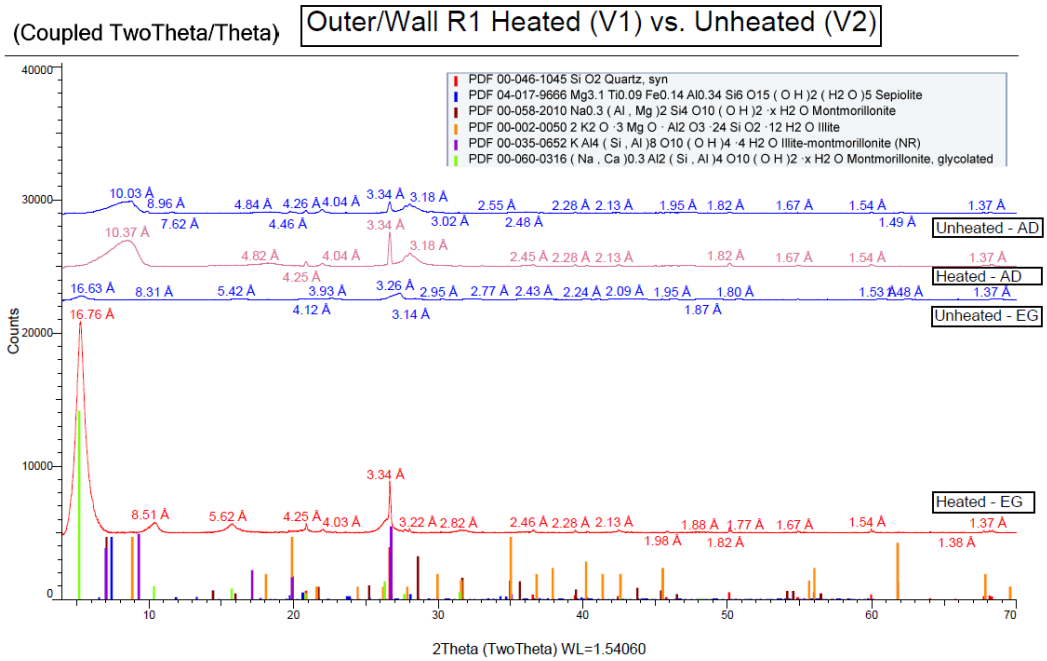

Figure 27. XRD stacked spectra of bentonite sampled in region R1 (outer) for both heated (V1) and unheated (V2) column experiments. AD stands for air-dried and EG denotes ethylene glycol saturated samples. Vertical axis scale are arbitrary counts. Vertical bars correspond to XRD peak positions from the PDF card database.

6. Conclusions

- **FEBEX-DP:**
  - Results from continuing cyclical TGA/DSC thermal analyses under controlled RH (hydration/dehydration) at elevated temperatures (85°C and 150°C) for FEBEX-DP Section 49 samples have been obtained.
  - The overall thermal behavior is similar to some extent for previous experiments at 60°C. However, trends for extended hydration periods (>120 minutes) at high temperatures no longer follow the trend of lower hydration periods and need to be investigated further. Still, the cyclical thermal analysis indicates that the dehydration behavior is a function of the duration of hydration that precedes it.
  - Molecular dynamics (MD) simulations demonstrate that clay dehydration is a two-stage process. The first stage of water transport exhibits an advection mechanism as mass loss is linear with time. The first stage is associated with the evacuation of water molecules from the hydrophobic sites. The second stage represents slow desorption of the last 1-2 water molecules from the Na^+ ions leading to a diffusion mechanism. These conclusions are supported by our results obtained from TGA/DSC calorimetry, and in-situ XRD experiments on FEDEX-DP bentonite samples. This MD work was extended to K^+ and Ca^{+2} to demonstrate that the clay dehydration process (2W to 0W) depends on the cation adsorption complexes in the interlayer.
- **Reactive-Transport Modeling of Barrier Material Leaching**
  - The PFLOTRAN 1D reactive-transport model implementation of the EPA 1315 monolith leaching test or marl rock generated encouraging results representing the overall trends of temporal changes in solute concentration profiles based on the major rock mineral components.
  - In addition to the evaluation of parameter sensitivities, future work include will include the effects of meshing discretization at the interface, evaluation of $pCO_2(g)$ on carbonate interactions, and further testing of the 1D simulation approach rock-cement leaching.
- **LBNL HotBENT Heated/Unheated Column Test: Preliminary XRD Analyses of Post-Experiment Samples**
  - Preliminary XRD analyses (AD and EG) were conducted on post-experiments samples collected at various radial distances from the central heating element. These analyses include samples from heated and unheated columns. Work is planned for additional XRD analyses and evaluation of the data.
  - The XRD spectra shows close correspondence to the montmorillonite peaks, as expected, for AD and EG samples. Although there are some commonalities in the XRD spectra for samples from both heated and unheated columns, there are also some differences such as peak broadening in samples radially farther from the column central axis.

7. FY22 Work

Planned work on **FEBEX-DP** samples for FY22 (and the remainder of FY21):

- The focus for the remainder of FY21 is to evaluate the collected data at high temperatures (85°C and 150°C), focusing on the trend loss in the temporal DSC data with increasing clay hydration periods.
- Continue cyclical thermal analyses conducted at higher temperatures and controlled moisture conditions to evaluate the effect on hydration/dehydration profiles. There are also plans to continue the *in situ* XRD analyses under controlled moisture and temperature conditions as soon as the equipment setup becomes available. There are also plan into extending thermal analyses into other types of bentonite clay material.
- Expand MD simulations on dehydration phenomena at the clay interlayer.
    - Expand the work on montmorillonite dehydration in the presence of Mg^{++} and other cations plus continuing the current work on Na^{+}, K^{+}, and Ca^{++}
    - Evaluate the effects of surface charge density on montmorillonite dehydration and water transport
    - Exploratory studies of H_2(gas) adsorption and transport/mobility in the interlayer of clay (wet, or dry) through MD simulations
    - Thermodynamic analysis of clay hydration and dehydration from MD simulations

Planned work on international collaborations work for FY22 (and the remainder of FY21):

- Continue (1D) PFLOTRAN reactive-transport modeling of leaching of rock (monolith) and cement experiments. This activity is done in concert with the EBS work package. This offers an unique opportunity of exploiting existing leaching data on barrier phases to test existing simulation approaches for hydro-chemical (HC) couplings.
- LBNL HotBENT Heated/Unheated Column Experiments
    - Continue XRD analyses of both column experiments and evaluation of collected data
    - Plans to conduct X-ray fluorescence (XRF) compositional analysis of collected samples.
    - Explore the possibility of conducting TH and THC PFLOTRAN simulations of the LBNL column experiment as part of the SKB TF. The limitation of the PFLOTRAN simulator is the lack of mechanical modeling capability.
- Explore the application of PFLOTRAN to DECOVALEX2023 Task D (Honorobe URL) for the S1-3 bentonite infiltration and maybe the S1-1 bentonite swelling pressure test. The latter will be assessed from clay hydration properties but these are not considered by the Task D teams.

8. References

Amato, I. (2013) Green cement: concrete solutions. Nature news 494, 300.

Arthur, M.A. and Cole, D.R. (2014) Unconventional hydrocarbon resources: prospects and problems. Elements 10, 257-264.

Babu, J.S. and Sathian, S.P. (2011) The role of activation energy and reduced viscosity on the enhancement of water flow through carbon nanotubes. The Journal of chemical physics 134, 194509.

Berner, U., Kulik, D.A. and Kosakowski, G. (2013) Geochemical impact of a low-pH cement liner on the near field of a repository for spent fuel and high-level radioactive waste. Physics and Chemistry of the Earth, Parts A/B/C 64, 46-56.

Birkholzer, J., Faybishenko, B., Ajo-Franklin, J., Borglin, S., Dobson, P., Gilbert, B., Guglielmi, Y., Fox, P.M., Kim, K., Nico, P., Rutqvist, J., Sonnenthal, E., Xu, H., Wu, Y., Zheng, L., Caporuscio, F.A., Reimus, P., Viswanathan, H., Jove-Colon, C.F., Wang, Y., Kuhlman, K., Matteo, E., McMahon, K. and Zavarin, M. (2019) International Collaboration Activities in Different Geologic Environments, Spent Fuel Waste Science and Technology (SFWST) Deliverable M2SF-19LB010307012 (LBNL-2001239). Lawrence Berkeley National Laboratories (LBNL), Berkeley, CA USA, 356 pp..

Blanc, P., Lassin, A., Piantone, P., Azaroual, M., Jacquemet, N., Fabbri, A. and Gaucher, A., (2012) Thermoddem: A geochemical database focused on low temperature water/rock interactions and waste materials. Applied Geochemistry, 27: 2107-2116.

Blanc, P., Piantone, P., Lassin, A. and Burnol, A., (2006) Thermochimie: Sélection de constantes thermodynamiques pour les éléments majeurs, le plomb et le cadmium, Rapport final BRGM/RP-54902-FR BRGM, France, pp. 1-157.

Busch, A., Alles, S., Gensterblum, Y., Prinz, D., Dewhurst, D.N., Raven, M.D., Stanjek, H. and Krooss, B.M. (2008) Carbon dioxide storage potential of shales. Int J Greenh Gas Con 2, 297-308.

Chang, F.-R.C., Skipper, N. and Sposito, G. (1995) Computer simulation of interlayer molecular structure in sodium montmorillonite hydrates. Langmuir 11, 2734-2741.

Chen, X., Cao, G., Han, A., Punyamurtula, V.K., Liu, L., Culligan, P.J., Kim, T. and Qiao, Y. (2008) Nanoscale fluid transport: size and rate effects. Nano letters 8, 2988-2992.

Cheshire, M.C., Caporuscio, F.A., Jové Colón, C.F., and Norskog, K.E. (2018). "Fe-saponite growth on low-carbon and stainless steel in hydrothermal-bentonite experiments." Journal of Nuclear Materials 511: 353-366.

Clark, G., Grim, R. and Bradley, W. (1937) A study of the behavior of montmorillonite upon wetting. Zeitschrift für Kristallographie-Crystalline Materials 97, 216-222.

Cygan, R.T., Liang, J.-J. and Kalinichev, A.G. (2004) Molecular models of hydroxide, oxyhydroxide, and clay phases and the development of a general force field. The Journal of Physical Chemistry B 108, 1255-1266.

Ferrage, E., Lanson, B., Michot, L.J. and Robert, J.-L. (2010) Hydration properties and interlayer organization of water and ions in synthetic Na-smectite with tetrahedral layer charge. Part 1.

Results from X-ray diffraction profile modeling. The Journal of Physical Chemistry C 114, 4515-4526.

Gaboreau, S., Lerouge, C., Dewonck, S., Linard, Y., Bourbon, X., Fialips, C.I., Mazurier, A., Pret, D., Borschneck, D., Montouillout, V., Gaucher, E.C. and Claret, F. (2012) In-Situ Interaction of Cement Paste and Shotcrete with Claystones in a Deep Disposal Context. Am J Sci 312, 314-356.

García-Siñeriz, J.L., Abós, H., Martínez, V., De la Rosa, C., Mäder, U. and Kober, F., 2016. FEBEX DP: Dismantling of heater 2 at the FEBEX "in situ" test: Description of operations - Arbeitsbericht NAB 16-11, National Cooperative for the Disposal of Radioactive Waste (NAGRA), Wettingen, Switzerland.

Gates, W.P., Bouazza, A. and Churchman, G.J. (2009) Bentonite clay keeps pollutants at bay. Elements 5, 105-110.

Gómez-Espina, R. and Villar, M. (2016) Time evolution of MX-80 bentonite geochemistry under thermo-hydraulic gradients. Clay Miner 51, 145-160.

Greathouse, J.A., Cygan, R.T., Fredrich, J.T. and Jerauld, G.R. (2016) Molecular dynamics simulation of diffusion and electrical conductivity in montmorillonite interlayers. The Journal of Physical Chemistry C 120, 1640-1649.

Grim, R.E., 1968. Clay mineralogy. International series in the earth and planetary sciences. McGraw-Hill, New York.

Ho, T.A., Criscenti, L.J. and Wang, Y. (2016) Nanostructural control of methane release in kerogen and its implications to wellbore production decline. Scientific reports 6, 1-9.

Ho, T.A., Wang, Y. and Criscenti, L.J. (2018) Chemo-mechanical coupling in kerogen gas adsorption/desorption. Phys Chem Chem Phys 20, 12390-12395.

Ho, T.A., Criscenti, L.J. and Greathouse, J.A. (2019a) Revealing transition states during the hydration of clay minerals. The journal of physical chemistry letters 10, 3704-3709.

Ho, T.A. and Wang, Y. (2019b) Enhancement of oil flow in shale nanopores by manipulating friction and viscosity. Phys Chem Chem Phys 21, 12777-12786.

Ho, T.A., Wang, Y., Jové Colón, C.F. and Coker, E.N. (2020) Fast Advective Water Flow Through Nanochannels in Clay Interlayers: Implications for Moisture Transport in Soils and Unconventional Oil/Gas Production. ACS Applied Nano Materials 3, 11897-11905.

Hockney, R. and Eastwood, J. (1988) Computer Simulation Using Particles Taylor & Francis. Inc., USA.

Holmboe, M. and Bourg, I.C. (2014) Molecular dynamics simulations of water and sodium diffusion in smectite interlayer nanopores as a function of pore size and temperature. The Journal of Physical Chemistry C 118, 1001-1013.

Huertas, F., Fuentes-Cantillana, J.L., Jullien, F., Rivas, P., Linares, J., Fariña, P., Ghoreychi, M., Jockwer, N., Kickmaier, W., Martínez, M.A., Samper, J., Alonso, E. and Elorza, F.J., (2000) Full-scale engineered barriers experiment for a deep geological repository for high-level radioactive waste in crystalline host rock (FEBEX project): Final report. EUR 19147, European Commission, Brussels.

Jové Colón, C.F., Weck, P.F., Sassani, D.C., Zheng, L., Rutqvist, J., Steefel, C.I., Kim, K., Nakagawa, S., Houseworth, J., Birkholzer, J., Caporuscio, F.A., Cheshire, M., Rearick, M.S., McCarney, M.K., Zavarin, M., Benedicto-Cordoba, A., Kersting, A.B., Sutton, M., Jerden, J.L., Frey, K.E., Copple, J.M. and Ebert, W.L. (2014) Evaluation of Used Fuel Disposition in Clay-Bearing Rock (FCRD-UFD-2014-000056). Sandia National Laboratories, SAND2014-18303 R, Albuquerque, New Mexico, 434 pp.

Jové Colón, C.F., Payne, C., Coker, E., Boisvert, L., Sanchez, A., Knight, A. and Hadgu, T. (2019) Argillite Disposal R&D International Collaborations interim report - 2019 (SAND2019-6731 R), Prepared for U.S. Department of Energy (DOE) Spent Fuel Waste Science and Technology (SFWST). Sandia National Laboratories, Albuquerque, New Mexico, 51 pp.

Jové Colón, C.F., C. Payne, and A. Knight, 2018. International Collaboration Activities on Disposal in Argilllite R&D: Progress Report, in Spent Fuel Waste Science and Technology Deliverable M4SF18SN010301092 (SAND2018-9718 R), Sandia National Laboratories: Albuquerque, New Mexico USA. p. 51.

Jové Colón, C.F., Hammond, G.E., Kuhlman, K., Zheng, L., Kim, K., Xu, H., Rutqvist, J., Caporuscio, F.A., Norskog, K.E., Maner, J., Palaich, S., Cheshire, M., Zavarin, M., Wolery, T.J., Atkins-Duffin, C., Jerden, J.L., Copple, J.M., Cruse, T. and Ebert, W.L., 2016. Evaluation of Used Fuel Disposition in Clay-Bearing Rock (FCRD-UFD-2016-000074), Sandia National Laboratories, Albuquerque, NM. SAND2016-10311 R.

Kosakowski, G. and Berner, U. (2013) The evolution of clay rock/cement interfaces in a cementitious repository for low- and intermediate level radioactive waste. Phys Chem Earth 64, 65-86. Hisatake, K., Tanaka, S. and Aizawa, Y. (1993) Evaporation rate of water in a vessel. J Appl Phys 73, 7395-7401.

Klein-BenDavid, O., Harlavan, Y., Levkov, I., Teutsch, N., Brown, K., Gruber, C. and Ganor, J. (2019) Interaction between spent fuel components and carbonate rocks. Science of The Total Environment 689, 469-480.

Lee, S. S.; Fenter, P.; Nagy, K. L.; Sturchio, N. C. (2012) Monovalent Ion Adsorption at the Muscovite (001)–Solution Interface: Relationships among Ion Coverage and Speciation, Interfacial Water Structure, and Substrate Relaxation. Langmuir, 28 (23), 8637-8650.

Lichtner, P.C., (2016) Kinetic rate laws invariant to scaling the mineral formula unit. American Journal of Science, 316(5): p. 437-469.

Lichtner, P. C., et al. (2019). PFLOTRAN user manual: A massively parallel reactive flow and transport model for describing surface and subsurface processes. http://documentation.pflotran.org

Liu, X., Lu, X., Wang, R. and Zhou, H. (2008) Effects of layer-charge distribution on the thermodynamic and microscopic properties of Cs-smectite. Geochim Cosmochim Acta, 72, 1837-1847.

Matteo, E.N., Dewers, T.A., Jove Colon, C.F., Hadgu, T., Gruber, C., Steen, M., Brown, K., Delapp, R., Brown, L. and Kosson, D. (2019) FY19 Progress of EBS International Collaborations. Sandia National Laboratories; M4SF-19SN010308082; SAND2019-10787 R, Albuquerque, NM USA, p. 38 pp.

Matteo, E., Dewers, T., Gomez, S., Hadgu, T., Zheng, L., Lammers, L.N., Fox, P., Chang, C., Xu, H., Borglin, S., Whittaker, M.L., Chou, C., Tournassat, C., Subramanian, N., Wu, Y., Nico, P., Gilbert, B., Kneafsey, T., Caporuscio, F.A., Sauer, K.B., Rock, M.J., Kalintsev, A., Migdissov, A., Alcorn, S., Buck, E.C., Yu, X.-Y., Yao, J., Son, J., Reichers, S.L., Klein-BenDavid, O., Bar-Nes, G., Meeussen, J.C.L., Gruber, C., Steen, M., Brown, K.G., Delapp, R., Taylor, A., Ayers, J. and Kosson, D.S. (2020) Evaluation of Engineered Barrier Systems FY20 Report. Sandia National Laboratories; M2SF-20SN010308042; SAND2020-11452 R, Albuquerque, NM USA.

Martinez, V., Abós, H. and García-Siñeriz, J.L., (2016) FEBEXe: Final Sensor Data Report (FEBEX "in situ" Experiment) - Arbeitsbericht NAB 16-19, National Cooperative for the Disposal of Radioactive Waste (NAGRA), Wettingen, Switzerland.

Marty, N.C., Bildstein, O., Blanc, P., Claret, F., Cochepin, B., Gaucher, E.C., Jacques, D., Lartigue, J.-E., Liu, S. and Mayer, K.U. (2015) Benchmarks for multicomponent reactive transport across a cement/clay interface. Computat Geosci, 1-19.

Marty, N.C., Grangeon, S., Lassin, A., Madé, B., Blanc, P. and Lanson, B. (2020) A quantitative and mechanistic model for the coupling between chemistry and clay hydration. Geochim Cosmochim Ac 283, 124-135.

Martyna, G.J., Tobias, D.J. and Klein, M.L. (1994) Constant pressure molecular dynamics algorithms. The Journal of chemical physics 101, 4177-4189.

McKay, J. (1992) Clay Separation. LSIS Technical Memorandum #92-1. University of Western Ohio.

Missana, T. and García-Gutiérrez, M. (2007). Sorption of bivalent ions (Ca (II), Sr (II) and Co (II)) onto FEBEX bentonite. Physics and Chemistry of the Earth, Parts A/B/C, 32(8): 559-567.

Montes-H, G., J. Duplay, L. Martinez, Y. Geraud, and B. Rousset-Tournier (2003) Influence of interlayer cations on the water sorption and swelling–shrinkage of MX80 bentonite. Applied Clay Science, 23(5-6): p. 309-321.

Morodome, S. and Kawamura, K. (2009) Swelling behavior of Na-and Ca-montmorillonite up to 150 C by in situ X-ray diffraction experiments. Clay Clay Miner 57, 150-160.

Morrow, C.P., Yazaydin, A.O.z.r., Krishnan, M., Bowers, G.M., Kalinichev, A.G. and Kirkpatrick, R.J. (2013) Structure, energetics, and dynamics of smectite clay interlayer hydration: Molecular dynamics and metadynamics investigation of Na-hectorite. The Journal of Physical Chemistry C 117, 5172-5187.

Moyne, C. and Murad, M.A. (2002) Electro-chemo-mechanical couplings in swelling clays derived from a micro/macro-homogenization procedure. Int J Solids Struct 39, 6159-6190.

Muurinen, A. (2011) Measurements on Cation Exchange Capacity of Bentonite in the Long-Term Test of Buffer Material (LOT), Working Report 2011-10. POSIVA, Eurajoki, Finland, pp. 30.

Nair, R., Wu, H., Jayaram, P., Grigorieva, I. and Geim, A. (2012) Unimpeded permeation of water through helium-leak–tight graphene-based membranes. Science 335, 442-444.

Neek-Amal, M., Peeters, F.M., Grigorieva, I.V. and Geim, A.K. (2016) Commensurability effects in viscosity of nanoconfined water. ACS nano 10, 3685-3692.

Ngouana W, B.F. and Kalinichev, A.G. (2014) Structural arrangements of isomorphic substitutions in smectites: Molecular simulation of the swelling properties, interlayer structure, and dynamics of hydrated Cs–montmorillonite revisited with new clay models. The Journal of Physical Chemistry C 118, 12758-12773.

Nosé, S. (1984) A molecular dynamics method for simulations in the canonical ensemble. Molecular physics 52, 255-268.

Ortiz-Young, D., Chiu, H.-C., Kim, S., Voïtchovsky, K. and Riedo, E. (2013) The interplay between apparent viscosity and wettability in nanoconfined water. Nature communications 4, 1-6.

Plimpton, S. (1995). "Fast Parallel Algorithms for Short-Range Molecular Dynamics." J Comp Phys 117: 1-19.

Pouvreau, M., Greathouse, J.A., Cygan, R.T. and Kalinichev, A.G. (2017) Structure of hydrated gibbsite and brucite edge surfaces: DFT results and further development of the clayFF classical force field with metal–O–H angle bending terms. The Journal of Physical Chemistry C 121, 14757-14771.

Pouvreau, M., Greathouse, J.A., Cygan, R.T. and Kalinichev, A.G. (2019) Structure of hydrated kaolinite edge surfaces: DFT results and further development of the ClayFF classical force field with metal–O–H angle bending terms. The Journal of Physical Chemistry C 123, 11628-11638.

Radha, B., Esfandiar, A., Wang, F., Rooney, A., Gopinadhan, K., Keerthi, A., Mishchenko, A., Janardanan, A., Blake, P. and Fumagalli, L. (2016) Molecular transport through capillaries made with atomic-scale precision. Nature 538, 222-225.

Rotenberg, B., Marry, V., Vuilleumier, R., Malikova, N., Simon, C. and Turq, P. (2007) Water and ions in clays: Unraveling the interlayer/micropore exchange using molecular dynamics. Geochim Cosmochim Acta, 71, 5089-5101.

Smith, D.E. and Dang, L.X. (1994) Computer simulations of NaCl association in polarizable water. The Journal of Chemical Physics 100, 3757-3766.

Soler, J.M. (2012) High-pH plume from low-alkali-cement fracture grouting: Reactive transport modeling and comparison with pH monitoring at ONKALO (Finland). Appl Geochem 27, 2096-2106.

Soler, J.M. and Mader, U.K. (2010) Cement-rock interaction: Infiltration of a high-pH solution into a fractured granite core. Geologica Acta 8, 221-233.

Sposito, G.; Skipper, N. T.; Sutton, R.; Park, S.-h.; Soper, A. K.; Greathouse, J. A. (1999) Surface geochemistry of the clay minerals. Proceedings of the National Academy of Sciences, 96 (7), 3358-3364.

Sun, L., Hirvi, J.T., Schatz, T., Kasa, S. and Pakkanen, T.A. (2015) Estimation of montmorillonite swelling pressure: A molecular dynamics approach. The Journal of Physical Chemistry C 119, 19863-19868.

Tamura, K., Yamada, H. and Nakazawa, H. (2000) Stepwise hydration of high-quality synthetic smectite with various cations. Clay Clay Miner 48, 400-404.

Teich-McGoldrick, S.L., Greathouse, J.A., Jové-Colón, C.F. and Cygan, R.T. (2015) Swelling Properties of Montmorillonite and Beidellite Clay Minerals from Molecular Simulation:

Comparison of Temperature, Interlayer Cation, and Charge Location Effects. The Journal of Physical Chemistry C, 119(36): 20880-20891.

Teleman, O., Jönsson, B. and Engström, S. (1987) A molecular dynamics simulation of a water model with intramolecular degrees of freedom. Molecular Physics 60, 193-203.

U.S. EPA (2017) SW-846 Test Method 1315: Mass Transfer Rates of Constituents in Monolithic or Compacted Granular Materials Using a Semi-Dynamic Tank Leaching Procedure, Washington, D.C.

Villar, M.V., Fernandez, A.M., Romero, E., Dueck, A., Cuevas, J., Plotze, M., Kaufhold, S., Dohrmann, R., Iglesias, R.J., Sakaki, T., Voltolini, M., Zheng, L., Kawamoto, K. and Kober, F. (2017) FEBEX-DP Post-mortem THM/THG Analysis Report, NAGRA Arbeitsbericht NAB 16-17. NAGRA, Wettingen, Switzerland, pp. 187 pp.

Vinci, Doriana, Baptiste Dazas, Eric Ferrage, Martine Lanson, Valérie Magnin, Nathaniel Findling, and Bruno Lanson (2020) "Influence of layer charge on hydration properties of synthetic octahedrally-charged Na-saturated trioctahedral swelling phyllosilicates." Applied Clay Science 184: 105404.

Wang, Y., T. Hadgu, E. A. Kalinina, J. Jerden, V. K. Gattu, W. Ebert, H. Viswanathan, J. Hyman, S. Karra, N., Knapp, N. Makedonska, P. Reimus, K. Telfeyan, P. M. Fox, P. S. Nico, M. Zavarin, E. Balboni, and C. Atkins-Duffin: Evaluation of Spent Fuel Disposition in Crystalline Rocks: FY17 Progress Report, Spent Fuel and waste Disposition, SFWD-SFWST-2017-000007, September, 2017.

Wilson, J.C., Benbow, S., Sasamoto, H., Savage, D. and Watson, C. (2015) Thermodynamic and fully-coupled reactive transport models of a steel-bentonite interface. Applied Geochemistry.

Xie, M.L., Mayer, K.U., Claret, F., Alt-Epping, P., Jacques, D., Steefel, C., Chiaberge, C. and Simunek, J. (2015) Implementation and evaluation of permeability-porosity and tortuosity-porosity relationships linked to mineral dissolution-precipitation. Computat Geosci 19, 655-671.

Yamada, H., Nakazawa, H., Hashizume, H., Shimomura, S. and Watanabe, T. (1994) Hydration behavior of Na-smectite crystals synthesized at high pressure and high temperature. Clay Clay Miner 42, 77-80.

Ye, H., Zhang, H., Zhang, Z. and Zheng, Y. (2011) Size and temperature effects on the viscosity of water inside carbon nanotubes. Nanoscale research letters 6, 1-5.

Investigation of Coupled Processes in Argillite Rock: FY21 Progress – LBNL (Part II)

1. Introduction

Shale and argillite geological formations have been considered as potential host rocks for geological disposal of high-level radioactive waste (HLW) throughout the world because of their low permeability, low diffusion coefficient, high retention capacity for radionuclides, and capability to self-seal fractures. Low permeability of shale and argillite is well-known in the hydrogeology community, because these rocks usually serve as aquitards that limit groundwater movement, and in petroleum industry, because they act as caprocks limiting the rise of buoyant petroleum fluids. While fractures can occur in argillite and shale, these formations often demonstrate the tendency to self-seal fractures, reducing the effects of fractures on bulk permeability. Other favorable characteristics of argillite/shale are the strong sorptive behavior for many radionuclides, reducing conditions because of the lack of oxygen transport from the surface, and chemical buffering the effects of materials that could be introduced during repository construction and operation.

The focus of research within the Spent Fuel and Waste Science and Technology (SFWST), formerly called Used Fuel Disposition (UFD), Campaign is on repository-induced interactions of the host rock and an engineered barrier system (EBS) bentonite, which may affect the potential repository safety characteristics. The research is focused on investigations of thermal-hydrological-mechanical-chemical (THMC) processes that occur because of repository construction and waste emplacement. Some of the key questions addressed in this report include investigations of the formation of an excavation damaged zone (EDZ) near tunnels and the evolution of near field coupled thermo-hydro-mechanical (THM) processes after the waste emplacement.

Within the SFWST program, LBNL's work on argillite disposal research & development (R&D) started in 2010 by leveraging on previous experience on coupled THM processes modeling within domestic and international nuclear waste programs (Rutqvist et al., 2001; 2002; 2011). Much of this work has been dedicated to the development and validation of coupled THM simulators for modeling of near-field coupled processes. From a safety assessment perspective, near-field coupled processes are relatively short-lived, but could give rise to permanent changes, such as the formation of a thermally altered or a damaged zone around excavations, which could provide a pathway for transport of radionuclides if released from a waste package (Figure 1-1). For a repository hosted in clay-rock, the mechanical evolution and swelling of the protective buffer surrounding the waste package (often bentonite) are imperative to its functions, such as to provide long-term mechanical support to seal the EDZ. At the same time, the mechanical evolution of the buffer is governed by complex coupled interactions of temperature and hydraulics, micro- and macro-structures of bentonite and the host rock. Currently, more advanced constitutive mechanical models are being applied, which, however, require a large number of input parameters to describe processes at different field scales. It is important to test and validate the models at a relevant field scale, in addition to verification and validation against independent analytical and numerical solutions and laboratory experiments.

Figure 1-2 illustrates a schematic of occurrence of coupled THM processes at the repository scale, such as activation of faults or fractures, creation of new fractures due to thermal stress, and thermal pressurization. Thermal pressurization is a process of pressure increase due to thermal expansion of pore-fluids being trapped because of low permeability of a porous argillite host rock. Another potential cause of near field coupled THM processes is gas generation within the waste package,

as well as seismic motion from a distant earthquake. The potential implication for repository performance related to the activation of faults includes creation of (permeable) flow paths, induced seismicity and a potential shear load on a waste canister.

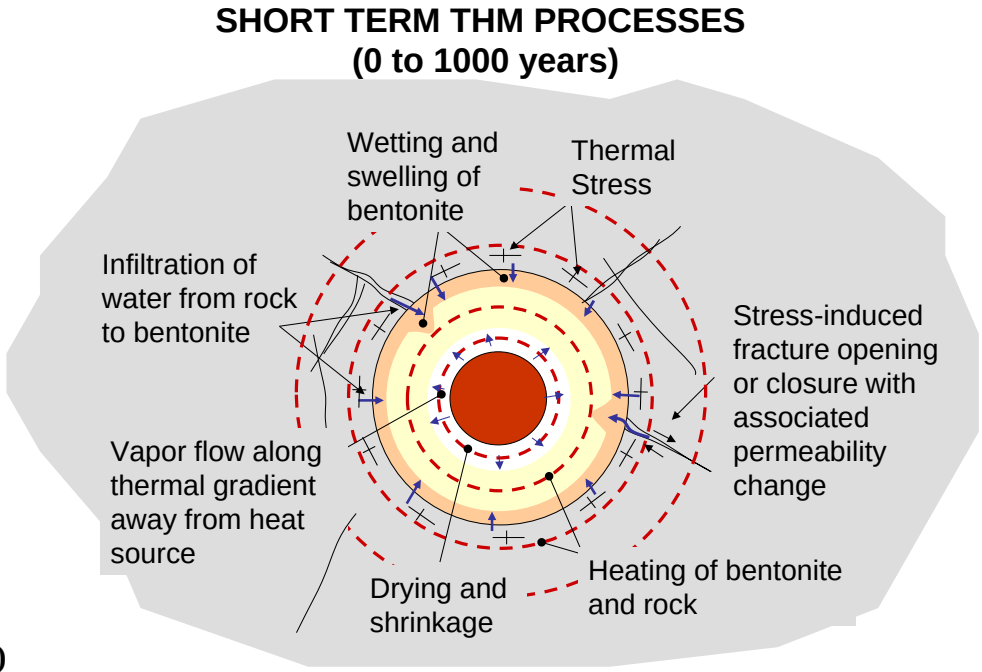

(a)

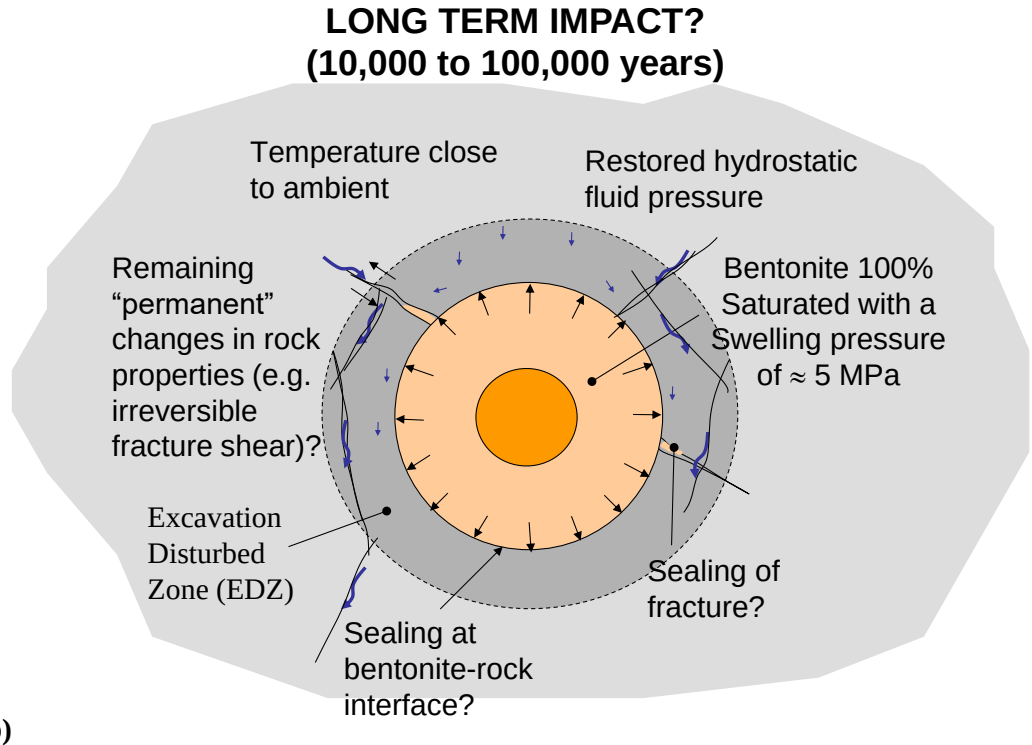

(b)

Figure 1-1. Schematic illustration of coupled THM processes driven by heat released from the waste package: (a) short-term THM processes, and (b) long-term impact of early time coupled THM processes.

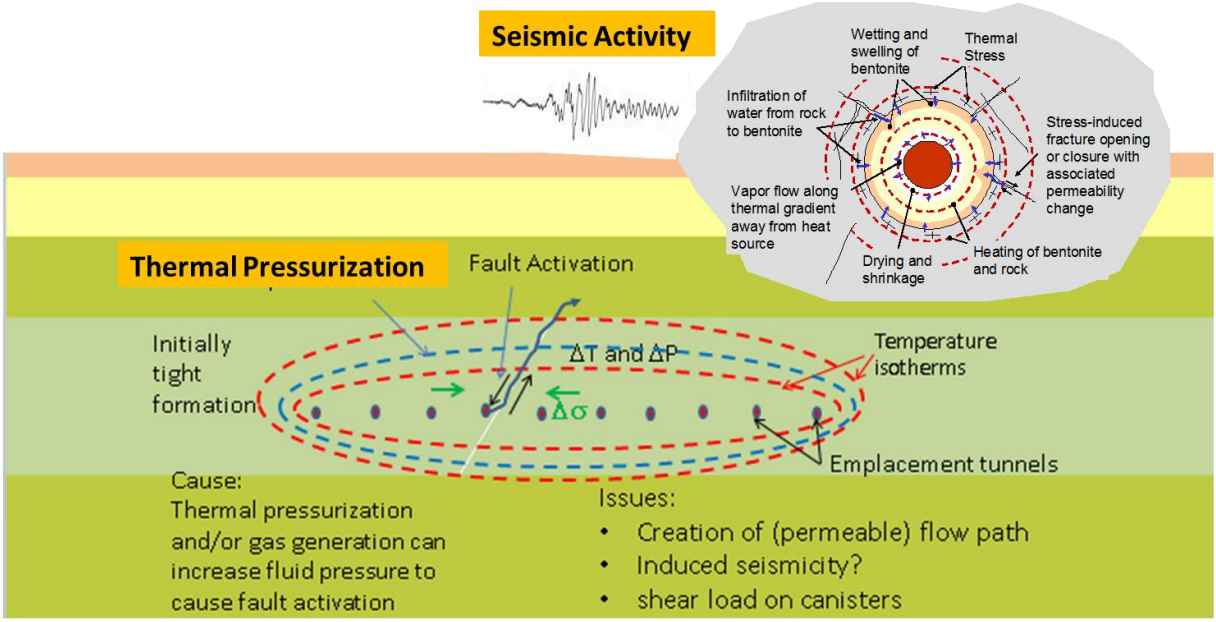

Figure 1-2. Schematic of coupled THM responses in a repository in the near field (upper right) and at the repository scale caused by heating, thermal pressurization and potential gas generation.

LBNL is developing and applying complementary coupled simulation approaches to model THM processes (Figure 1-3). TOUGH-FLAC, based on linking LBNL's TOUGH2 multiphase fluid flow simulator with the FLAC3D geomechanics code, provides an efficient continuum modeling approach with state-of-the-art constitutive models for bentonite and host rock (Rutqvist et al., 2002; Rutqvist 2011; 2017). For rigorous modeling of the THM behavior of bentonite-based (swelling) buffer and backfill materials, the BBM (Barcelona Basic Model) and BExM (Barcelona Expansive Model) have been incorporated into TOUGH-FLAC (Rutqvist et al., 2011; 2014b; Vilarrasa et al., 2016). Constitutive models to describe anisotropic THM behavior of shale rock have also been adapted. This model development has been accompanied by extensive testing, verification and validation, including participation within international collaborative projects, such as DECOVALEX. In FY2021, journal papers stemming from the previous DECOVALEX-2019 project were published. These papers are related to upscaling of THM properties, using model simulations, from a laboratory scale sample up to a full repository scale (Xu et al., 2020; 2021). In FY2021, development work has been continued on improving the calculation speeds using the newest version of TOUGH (TOUGH3) and a newest version of FLAC3D (V6 and V7), with linking through Python scripts, which were first presented in Rinaldi et al. (2018). Migrating to FLAC3D V7 also requires re-implementation and testing of BBM and BExM. Moreover, in FY2021 we added new creep modeling capabilities, including implementation of constitutive creep models for the assessment of long-term creep deformations.

Discrete fracture models, which are complementary to the continuum TOUGH-FLAC models, are also developed and applied within LBNL's Argillite repository work scope. This includes

TOUGH-RBSN simulator, based on linking the TOUGH2 simulator with the Rigid-Body-Spring Network (RBSN) model, which enables for explicit modeling of discrete fractures and a fracturing process (Asahina et al. 2014; Kim et al., 2017; 2020; 2021). The TOUGH-RBSN is most suitable for detailed analysis of fracturing in laboratory samples, as well as within the EDZ. Another most recent addition to this model development and applications is modeling of discrete fractured-porous media based on the Numerical Manifold Method (NMM) (Hu et al., 2020a). This model has been applied for the analysis of fractured, granular and porous media at difference scales--from the micro-scale to macro-scale. The NMM is complementary to TOUGH-FLAC in that it can represent complex fracture networks more accurately and can be used to study underlying mechanics to understand the macroscopic behavior. The TOUGH-FLAC enables modeling of the evolution of the EBS, EDZ, and surrounding host rock at a larger scale. TOUGH-FLAC with appropriate constitutive models is also used to calculate the evolution of permeability and transport properties in the EDZ, which can then be used as input to future safety assessment models and the Geologic Disposal Safety Analysis (GDSA).

In addition, the ongoing work is focused on modeling of the fault activation. This includes, for example, development of capabilities for modeling of fault slip, induced seismicity, and associated changes in fault permeability. Figure 1-4 presents one such model, involving the TOUGH-FLAC simulator, with a discrete representation of a fault plane, a slip weakening fault rupture model, and with the potential for modeling seismic wave propagation as available in the FLAC3D code. This model can also be applied for modeling of activation and creation of new flow paths resulting from the over pressure due to gas generation or thermal pressurization, as illustrated in Figure 1-2. In addition, 3DEC, a code based on the distinct element method, is applied for modeling fault activation and fractured rock coupled processes.

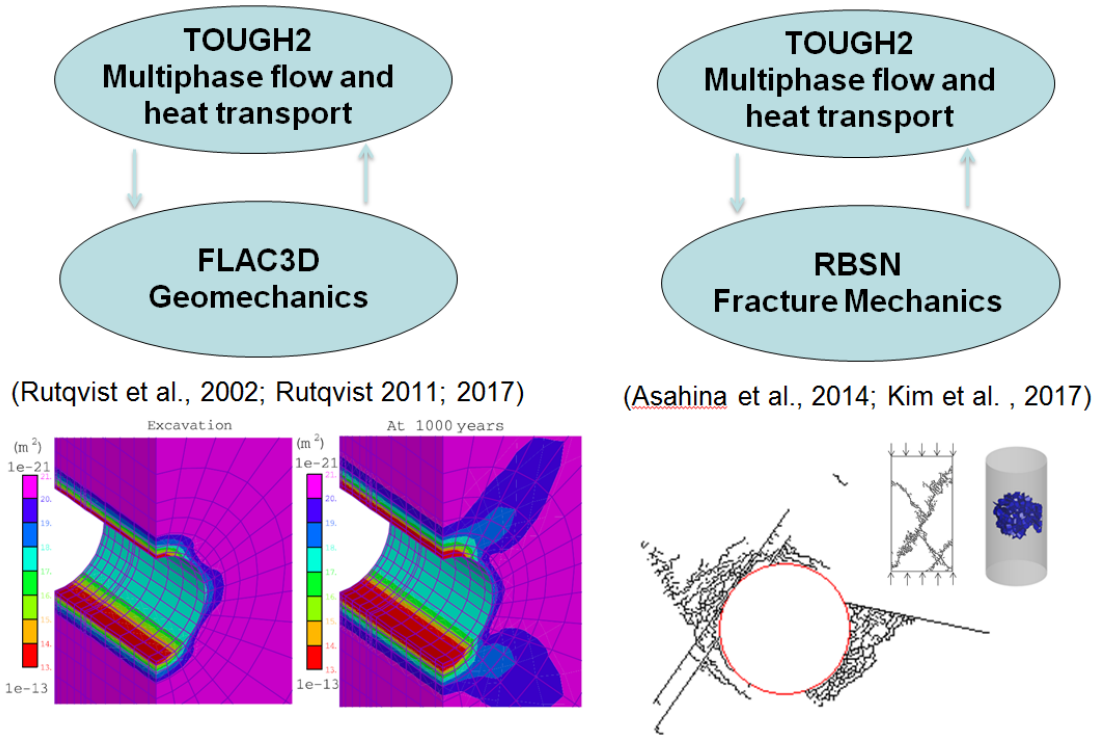

Figure 1-3. TOUGH-FLAC (left) and TOUGH-RBSN (right) models developed for coupled THM process analysis.

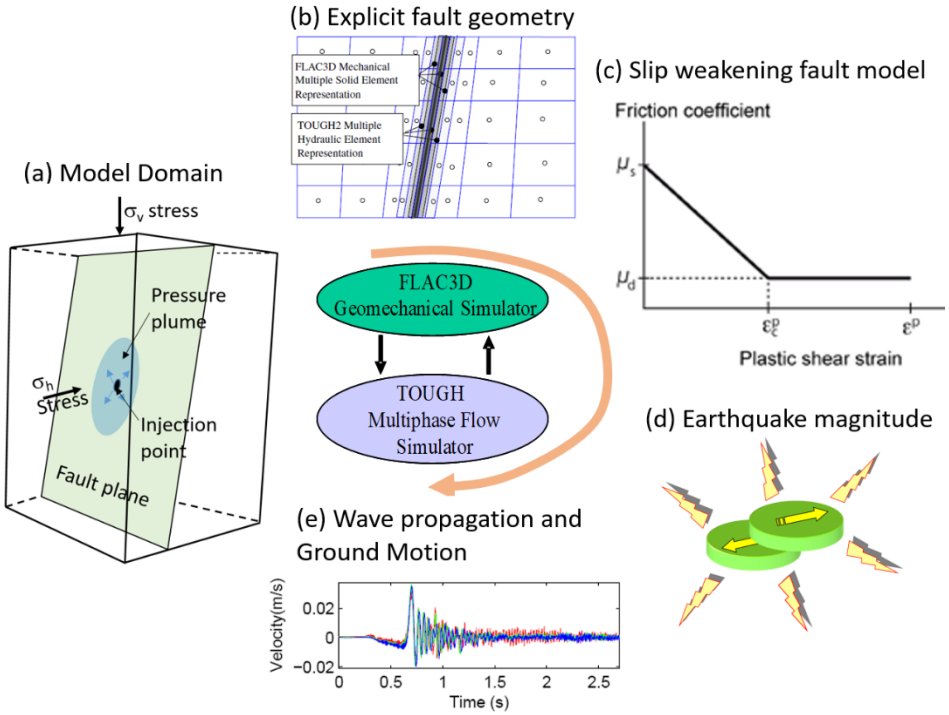

Figure 1-4. Fault activation modeling approach using TOUGH-FLAC (Rutqvist and Rinaldi, 2019).

This section of the report describes LBNL R&D activities. These activities address key Features, Events, and Processes (FEPs), which have been ranked in importance from medium to high, as listed in Table 7 of the Used Fuel Disposition Campaign Disposal Research and Development Roadmap (FCR&D-USED-2011-000065 REV 1) (Nutt, 2012). Specifically, they address FEP 2.2.01, Excavation Disturbed Zone, for clay/shale, by investigating how coupled processes affect EDZ evolution; FEP 2.2.05, Flow and Transport Pathways; and FEP 2.2.08, Hydrologic Processes, and FEP 2.2.07, Mechanical Processes, as well as FEP 2.2.12, Gas Sources and Effects.

The activities documented in this report also address a number of research topics identified in the R&D Plan for Used Fuel Disposition Campaign (UFDC) Natural System Evaluation and Tool Development (Wang, 2011), including Topics S3, Disposal System Modeling – Natural System; P1, Development of Discrete Fracture Network (DFN) Model; P14, Technical Basis for Thermal Loading Limits; and P15, Modeling of Disturbed Rock Zone (DRZ) Evolution (Clay Repository).

Sections 2 present the status of a creep model implementation and testing for clay rock in the TOUGH-FLAC code coupling. When implemented and tested, the model will be applied for modeling the impact of creep deformation in the long-term THM evolution around a repository in argillite rock. Sections 3 and 4 present results related to Task A and Task C of a new DECOVALEX-2023 project, namely the Mont Terri FE (Full-scale Emplacement) Experiment conducted at the Mont Terri Laboratory, Switzerland, modeling tasks related thermal and gas fracturing at the *in situ* heater experiments at the Meuse/Haute-Marne (MHM) URL in Bure, France. Section 5 presents LBNL's activities focused on modeling gas migration in bentonite related to Task B of the international DECOVALEX project. Section 6 presents new applications of machine learning of fracture morphology and mesh optimization. Section 7 presents new development and applications related to modeling of fractured argillite around a heated tunnel. Section 8 presents new field test results and modeling related to controlled fault activation experiments at the Mont Terri Laboratory. Related to geochemistry, Section 9 presents development of a model using Phase-Field Lattice Boltzmann Method (PF-LBM) for application to interfaces (such as cement-bentonite interfaces), and Section 10 present new modeling of the Cement–Opalinus Clay Interaction (CI) Experiment at the Mont Terri Laboratory. Finally, in Section 11 (authored by Jonny Rutqvist), we present current status on the integration of coupled THM processes models into the Geologic Disposal Safety Assessment (GDSA) and Performance Assessment (PA), and in Section 12, we provide a summary of the FY21 work as presented in this milestone report.

2. Modeling Shale Creep for the Long-Term Repository Performance

2.1 Introduction

Safety assessment of geological nuclear waste repositories is imperative to identify risks associated with storing radionuclides in subsurface formations for a long period of time. This could predict potential leakage of radionuclides and countermeasures could be devised and incorporated into repository design in advance.

Rock creep results in time-dependent strain accumulation/stress relaxation, which could affect the safety of geological nuclear waste repositories. Potential pathways for radionuclides are

fractures generated in the rock around the repositories, whose occurrence depends mainly on the stress development due to heat flux from the nuclear waste package. As the heating effect continues for hundreds of thousands of years, the stress development and deformations in the rock are long-term phenomena, which renders rock creep relevant in the safety assessment.

The primary objective of this study are: (i) to implement a creep law in the constitutive model to simulate the creep deformation of shale, (ii) to calibrate the developed creep model against laboratory test results of shale creep, and (iii) to implement the calibrated creep model in a thermo-hydromechanically (TMH)-coupled simulation of geological nuclear waste repositories.

The end goal of this study is to investigate the effect of creep deformation of the rock on the permeability change in the formation. By comparing modelling results between cases with and without rock creep, the effect of the long-term time-dependent rock deformation on the generation of leakage pathways (rock fractures) can be evaluated quantitatively.

In the following sections, a preliminary study addressing the objective (i) is presented. First, an appropriate creep law for shale is identified as the Norton-Bailey law based on laboratory test results in the literature. Second, FLAC3D, which is a finite difference code to simulate rock/soil behavior, is used to implement the Norton-Bailey law to simulate the laboratory test of shale creep. The validity of implementing the Norton-Bailey law for shale and a way forward to satisfy the objective (i) are then discussed.

2.2 Method

FLAC3D was used to run verification simulation for the Norton-Bailey creep model. One cubic element was generated in FLAC3D, and Young's modulus of 20 GPa and Poisson's ratio of 0.3 are assigned. The volumetric stress of -10 MPa (negative stress values indicate compression) and the deviatoric stress of 0 MPa (i.e., $\sigma_{xx} = \sigma_{yy} = \sigma_{zz} = -10$ MPa, $\tau_{xy} = \tau_{yz} = \tau_{xz} = 0$ MPa) were assigned to the element as the initial condition.

To shear the element, the pressure normal to the top boundary was increased to -20 MPa (i.e., $\sigma_{zz} = -20$ MPa) while the normal displacement at the bottom boundary was fixed and the pressure normal to the side boundaries was maintained at -10 MPa (i.e., $\sigma_{xx} = \sigma_{yy} = -10$ MPa). The differential stress of 10 MPa (i.e., $\sigma_{zz} - \sigma_{xx} = -10$ MPa) was maintained for two weeks' time to assess the creep behavior of Norton-Bailey model.

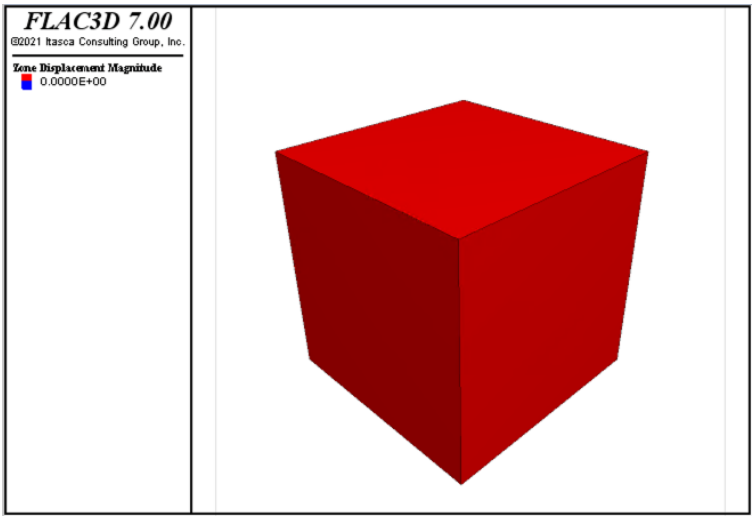

Figure 2-1. A cubic (brick) element in FLAC3D.

2.2.1 Norton-Bailey Law

Norton-Bailey law is a deviatoric creep law, which can be used to model both the primary and secondary creeps together. It is formulated as follows:

$$\dot{\epsilon}_{cr} = F_{cr} m \left(\frac{\epsilon_{cr,e} + \epsilon_{shift}}{t_{ref} F_{cr}} \right)^{\frac{m-1}{m}} n_D$$

where

$$F_{cr} = A \left(\frac{\sigma_e}{\sigma_{ref}} \right)^n$$

$$n_D = \frac{3}{2} \frac{\sigma_{ij}^d}{\sigma_e}$$

$$\epsilon_{cr,e} = \int \dot{\epsilon}_{cr,e} dt = \int \sqrt{\frac{2}{3} \dot{\epsilon}_{cr} : \dot{\epsilon}_{cr}} dt$$

where $\dot{\epsilon}_{cr}$ is creep strain rate tensor, m is time-hardening exponent, ϵ_{shift} is effective creep strain shift, $\epsilon_{cr,e}$ is effective creep strain, $\dot{\epsilon}_{cr,e}$ is effective creep strain rate, σ_{ij}^d is deviatoric stress tensor, σ_e is von Mises effective stress, A is a coefficient, n is a hardening parameter, σ_{ref} is a reference stress, t_{ref} is a reference time.

2.2.2 Laboratory Test Results

Figure 2-2 shows laboratory test results on the creep behavior of shale samples. In this laboratory test, cylindrical shale samples were first applied with a confining pressure of ~ -10 MPa (in compression) and then sheared by applying differential stress (i.e., difference between axial stress and confining stress). The change in axial strain was measured for as long as two weeks to assess the creep behavior of the shale samples.

Figure 2-2a shows axial strain vs. time plots, which indicate a gradual increase in the axial strain with time. Figure 2-2b shows log(time) vs. creep compliance, which is defined as the accumulated axial strain divided by the differential stress. This figure indicates that the power law would be appropriate to model the creep behavior of the shale samples, which is the reason why the Norton-Bailey model is investigated in this study. Figure 2-2c shows log(time) vs. log (creep compliance) graphs, which are approximated by linear curves on the bi-logarithmic plot.

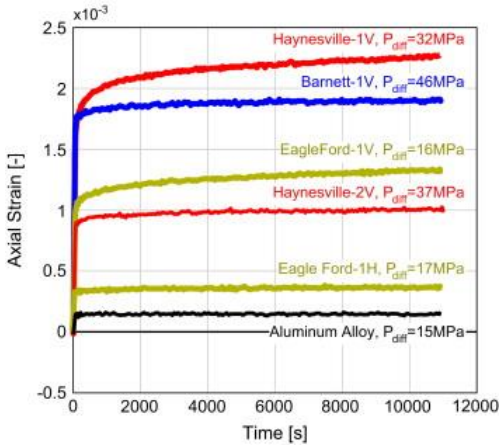

(a)

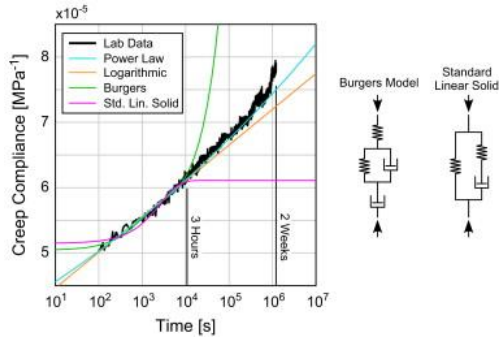

(b)

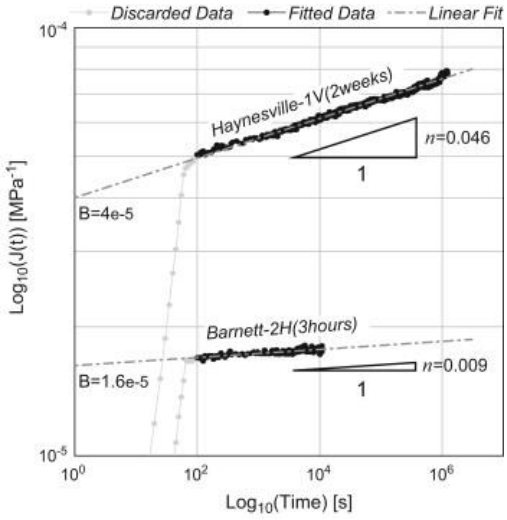

(c)

Figure 2-2. Laboratory creep test results on shale samples: (a) time vs. strain; (b) log(time) vs. creep compliance; (c) log(time) vs. log(creep compliance) (after Sone & Zoback (2014).

In order to qualitatively match the abovementioned laboratory test results, parameters of the Norton-Bailey model are changed (Table 2-1). Results of changes of axial strain and creep compliance with time are presented in the following section.

Table 2-1. Model parameters used to verify the Norton-Bailey model.

	Base	**Low_1**	**Low_2**	**Upp_1**	**Upp_2**
A (s^{-1})	$1.0 \cdot 10^{-6}$	$1.0 \cdot 10^{-7}$	$1.0 \cdot 10^{-8}$	$2.0 \cdot 10^{-6}$	$4.0 \cdot 10^{-6}$
n (-)	0.01	0.001	0.0001	0.2	0.4
m (-)	0.5	0.3	0.1	0.55	0.6
ϵ_{shift} (με)	1.0	0.01	0.0001	100	10000
σ_{ref} (MPa)	1.0	0.01	0.0001	100	10000
t_{ref} (s)	1.0	0.1	0.01	5.0	10.0

2.3 Preliminary Results

2.3.1 Axial Strain versus Time

Figure 2-3 shows the effect of changing the parameter values listed in Table 2-1 in the time-axial strain domain. Calculations show that increasing parameter values of A, n, m, and t_{ref} increases the axial (creep) strain, whereas the other parameters, ϵ_{shift} and σ_{ref} are inversely correlated with the creep strain.

The effect of σ_{ref} is found to be extremely minor compared to the other parameters, as changing σ_{ref} by plus or minus four orders of magnitudes from the base value of 1.0 MPa did not change the creep strain by more than ±5%. The same trend was computed for the parameter ϵ_{shift} as long as the change was within two orders of magnitudes from the base value (1.0 με). Also, decreasing the parameter value of n below the base value of 0.01 did not affect the creep strain (only increasing it affected the result).

Comparing the computed results with the laboratory test result (Figure 2-2a) shows that the axial strain level at two weeks' time in both cases approximately ranges between 0.05% and 0.25%, which indicates a good agreement between the modeling and laboratory test results. In the following sections, these numerical plots are converted into log(time)-creep compliance and log(time)-log(creep compliance) plots to compare more closely against the laboratory test results.

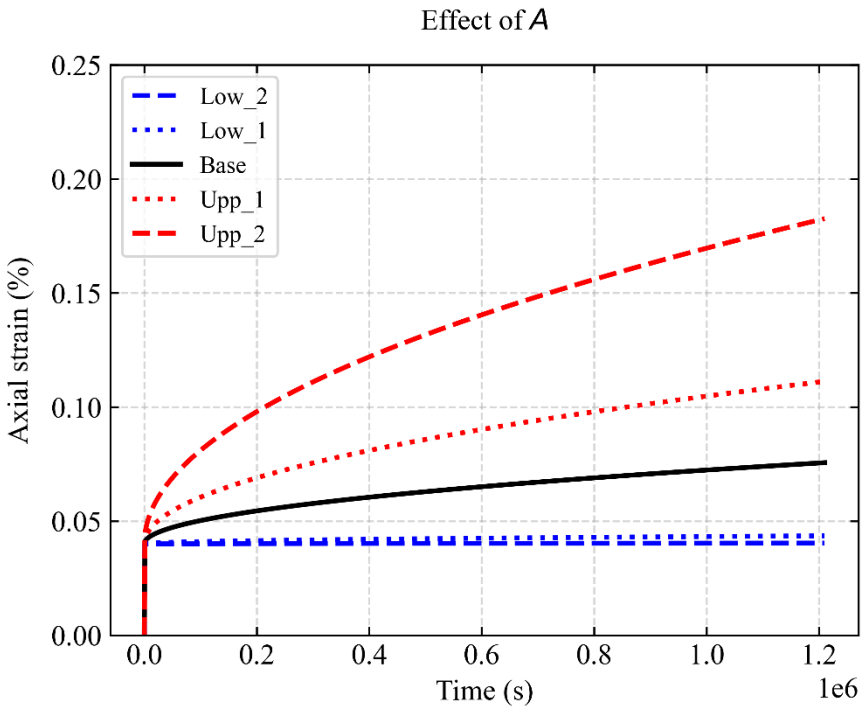
Effect of A
Low_2
Low_1
Base
Upp_1
Upp_2
Axial strain (%)
0.25
0.20
0.15
0.10
0.05
0.00
0.0
0.2
0.4
0.6
0.8
1.0
1.2
Time (s)
1e6

(a)

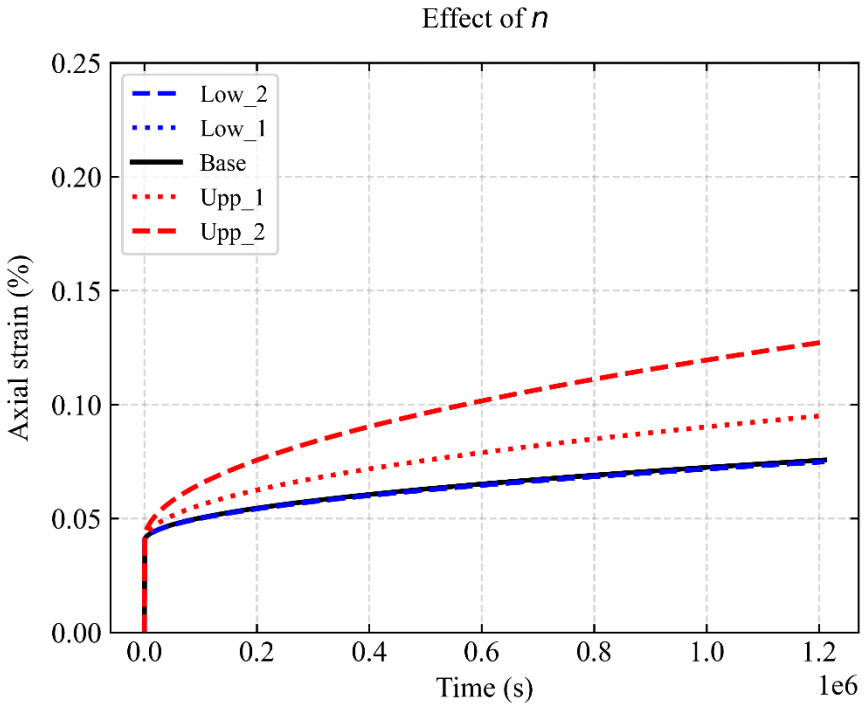
Effect of n
Low_2
Low_1
Base
Upp_1
Upp_2
Axial strain (%)
0.25
0.20
0.15
0.10
0.05
0.00
0.0
0.2
0.4
0.6
0.8
1.0
1.2
Time (s)
1e6

(b)

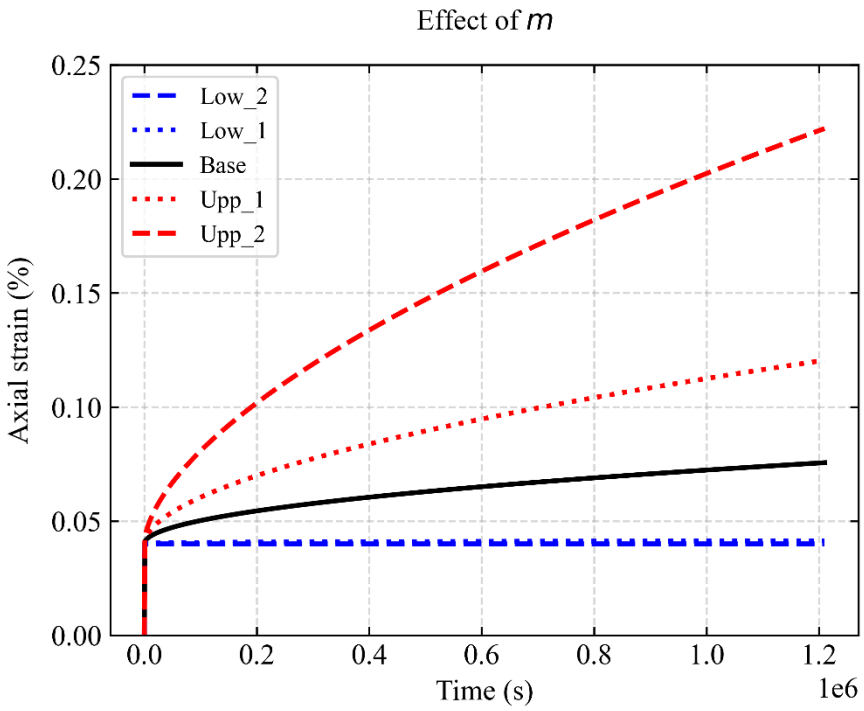
Effect of m
Low_2
Low_1
Base
Upp_1
Upp_2
Axial strain (%)
0.25
0.20
0.15
0.10
0.05
0.00
0.0
0.2
0.4
0.6
0.8
1.0
1.2
Time (s)
1e6

(c)

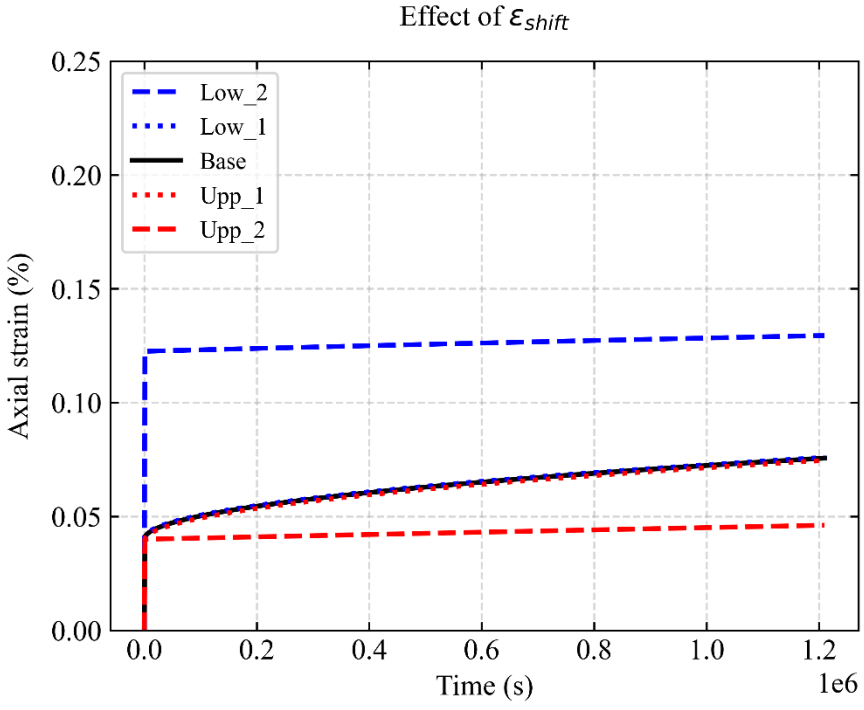
Effect of ε_{shift}
Low_2
Low_1
Base
Upp_1
Upp_2
Axial strain (%)
0.25
0.20
0.15
0.10
0.05
0.00
0.0
0.2
0.4
0.6
0.8
1.0
1.2
Time (s)
1e6

(d)

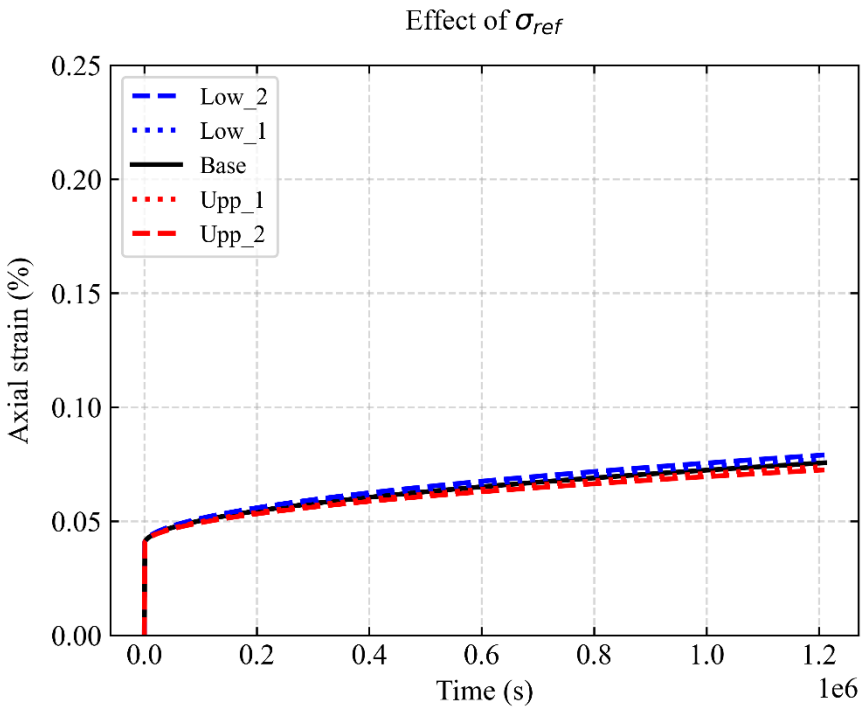

(e)

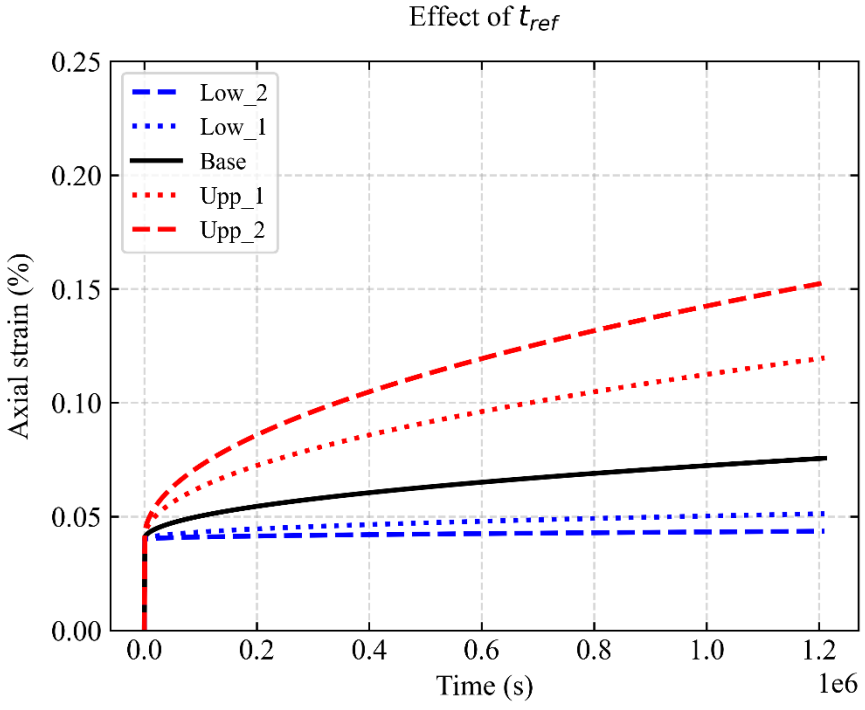

(f)

Figure 2-3. Effects of parameters on axial strain behavior vs. time of the Norton-Bailey model: (a) $\boldsymbol{A}$; (b) $\boldsymbol{n}$; (c) $\boldsymbol{m}$; (d) $\boldsymbol{\epsilon_{shift}}$; (e) $\boldsymbol{\sigma_{ref}}$; (f) $\boldsymbol{t_{ref}}$.

2.3.2 Log(time) versus Creep Compliance

Figure 2-4 shows log(time) vs. creep compliance plots of the simulation results. Creep compliance is defined as accumulated axial strain divided by the differential stress (i.e., 10 MPa). Regardless of the parameter values, it is found that the log(time) vs. creep compliance plots are concave up, with increasing trends that are in agreement with the experimental results (Figure 2-2b), although the increase in slope with log(time) is much less pronounced (i.e., close to linear) in the laboratory test result. Possible causes of the discrepancy could be either errors in laboratory measurements or modeling implementation. These will be investigated in a future study.

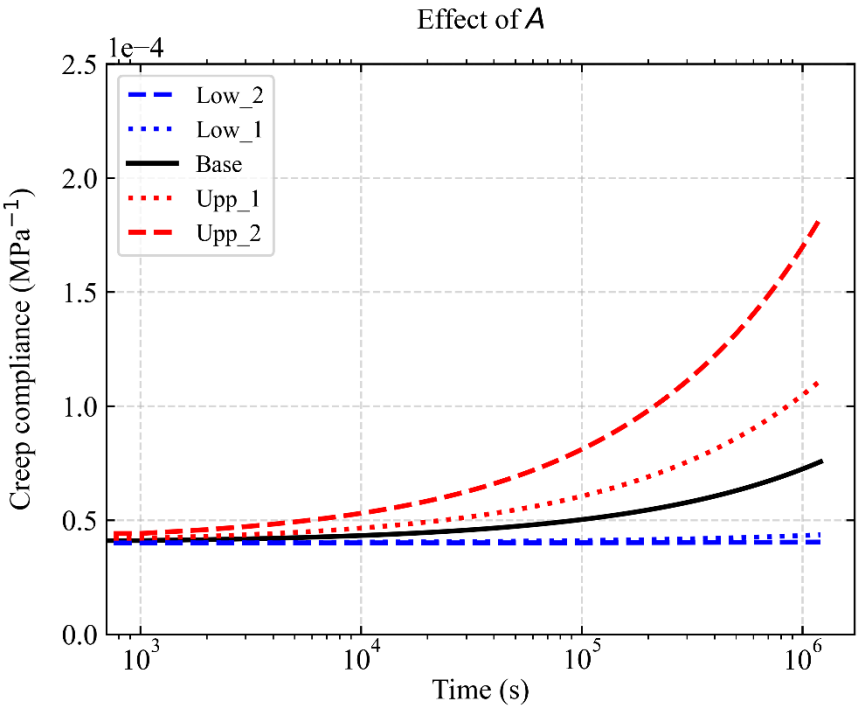

(a)

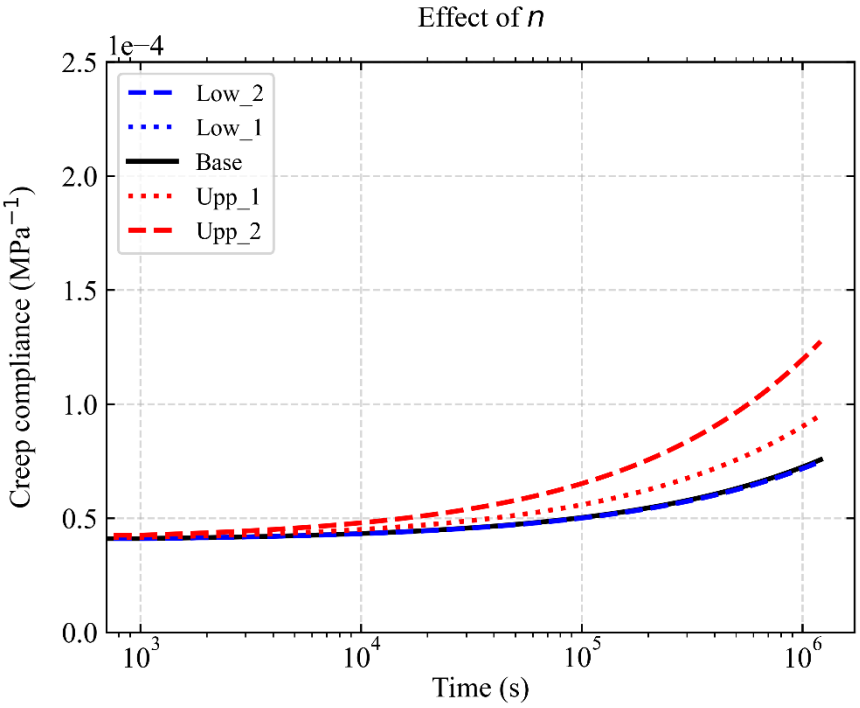
Effect of n
1e−4
2.5
2.0
1.5
1.0
0.5
0.0
Creep compliance (MPa^{-1})
Low_2
Low_1
Base
Upp_1
Upp_2
10^3
10^4
10^5
10^6
Time (s)

(b)

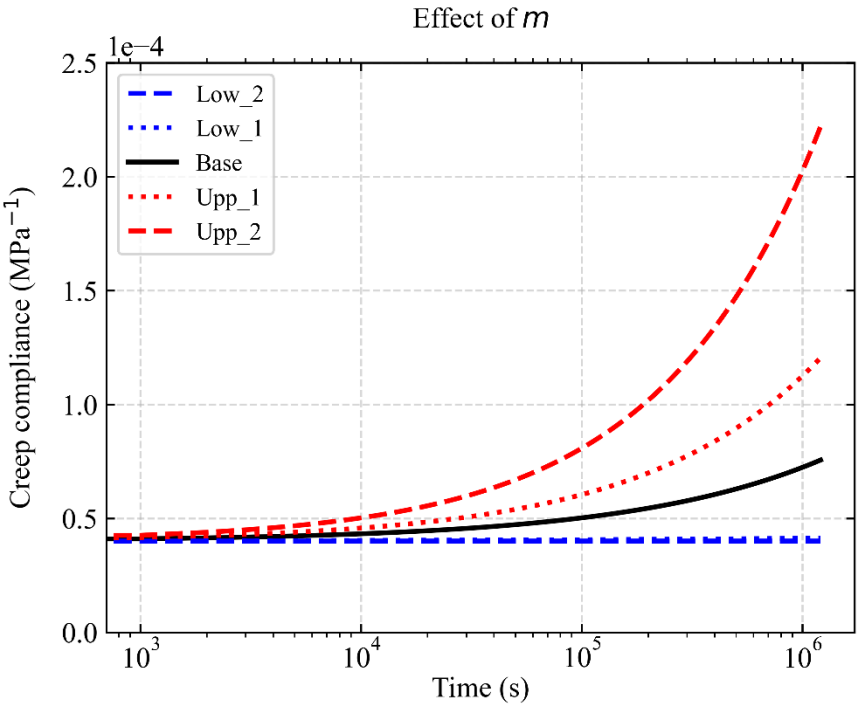
Effect of m
1e−4
2.5
2.0
1.5
1.0
0.5
0.0
Creep compliance (MPa^{-1})
Low_2
Low_1
Base
Upp_1
Upp_2
10^3
10^4
10^5
10^6
Time (s)

(c)

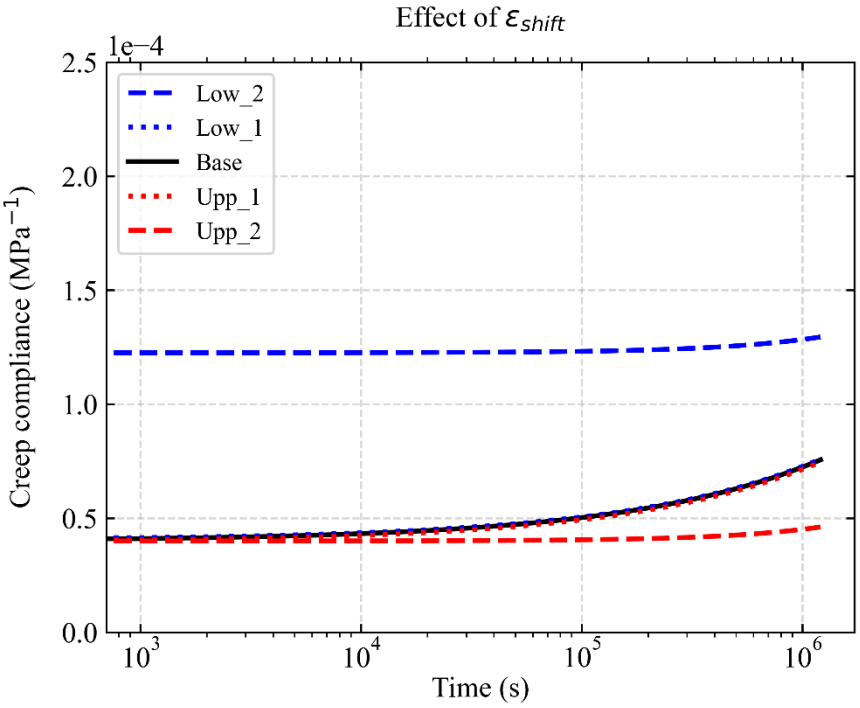
Effect of ε_{shift}
1e−4
2.5
2.0
1.5
1.0
0.5
0.0
Creep compliance (MPa^{-1})
Low_2
Low_1
Base
Upp_1
Upp_2
10^3
10^4
10^5
10^6
Time (s)

(d)

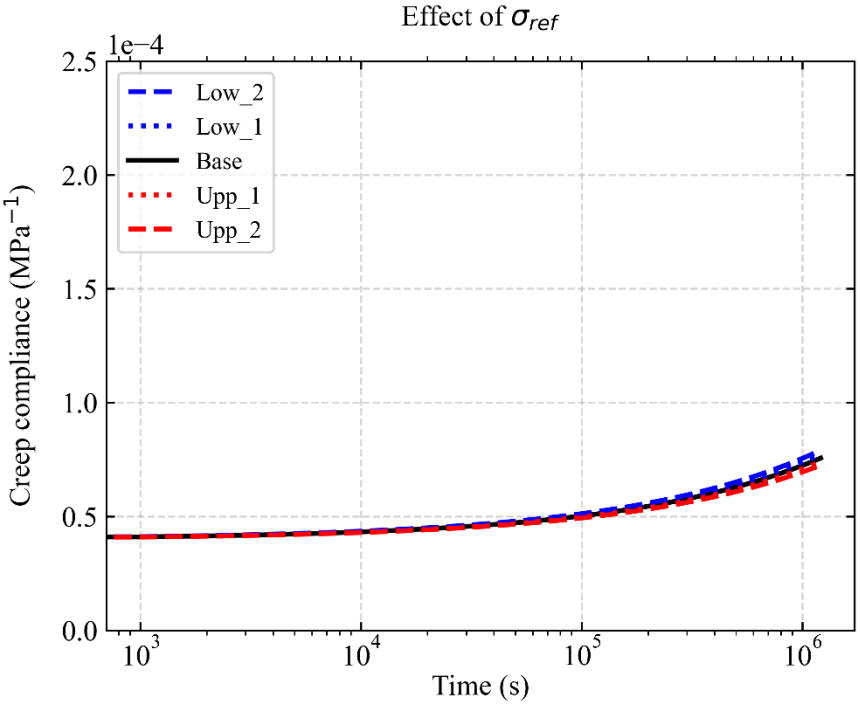
Effect of σ_{ref}
1e−4
2.5
2.0
1.5
1.0
0.5
0.0
Creep compliance (MPa^{-1})
Low_2
Low_1
Base
Upp_1
Upp_2
10^3
10^4
10^5
10^6
Time (s)

(e)

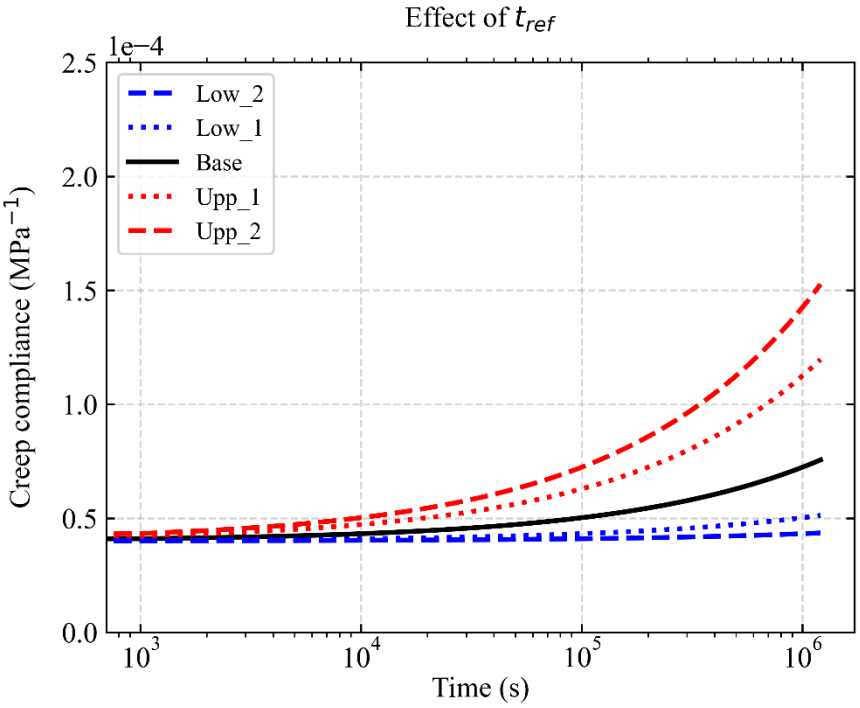

(f)

Figure 2-4. Effects of parameters on the log(time) vs. creep compliance behavior of Norton-Bailey model: (a) $\boldsymbol{A}$; (b) $\boldsymbol{n}$; (c) $\boldsymbol{m}$; (d) $\boldsymbol{\epsilon_{shift}}$; (e) $\boldsymbol{\sigma_{ref}}$; (f) $\boldsymbol{t_{ref}}$.

2.3.3 Log(time) vs. Log(creep compliance)

Figure 2-5 shows log(time) vs. log(creep compliance) plots of the simulation results. It is found that the log-log plots are still slightly concaved up, with increasing trends, whereas the experimental result (Figure 2-2) is linear on the bi-log plot. The discrepancy will be addressed from viewpoints of both numerical and experimental errors in a future study.

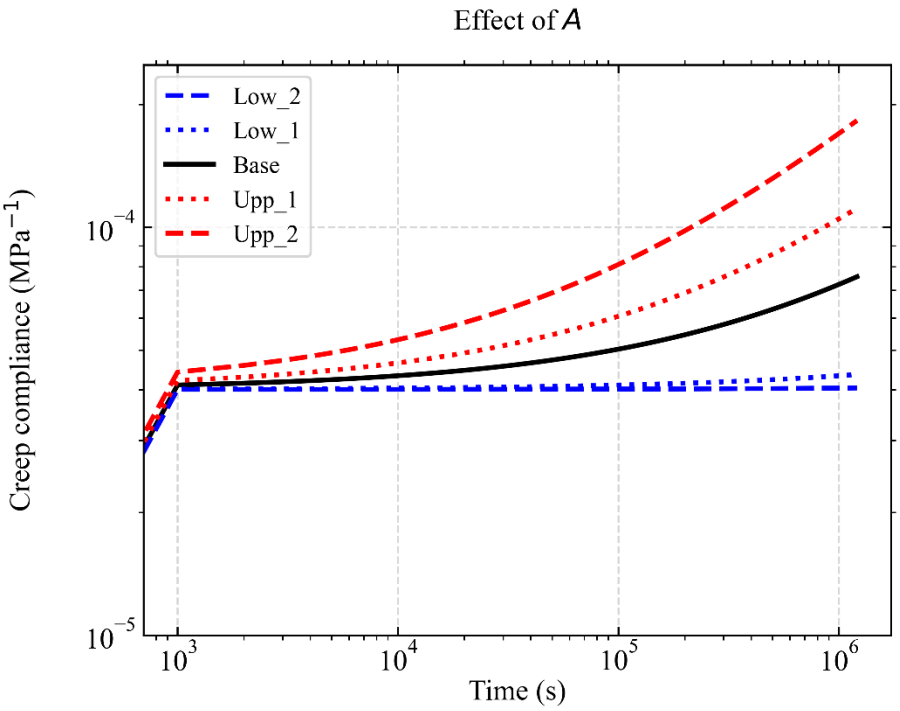
Effect of A
Low_2
Low_1
Base
Upp_1
Upp_2
Creep compliance (MPa^{-1})
10^{-4}
10^{-5}
10^{3}
10^{4}
10^{5}
10^{6}
Time (s)

(a)

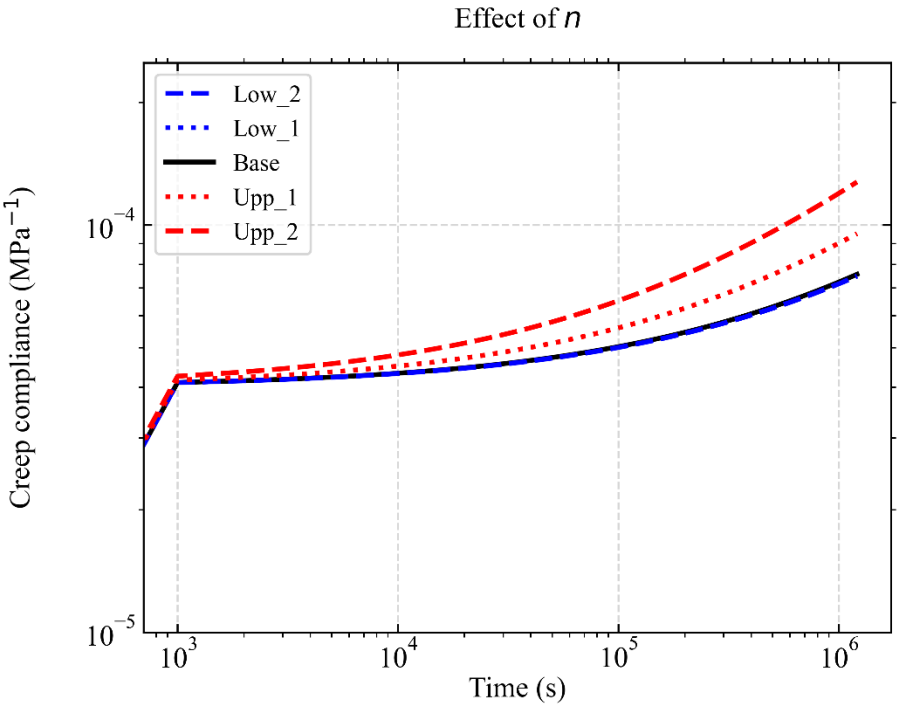
Effect of n
Low_2
Low_1
Base
Upp_1
Upp_2
Creep compliance (MPa^{-1})
10^{-4}
10^{-5}
10^{3}
10^{4}
10^{5}
10^{6}
Time (s)

(b)

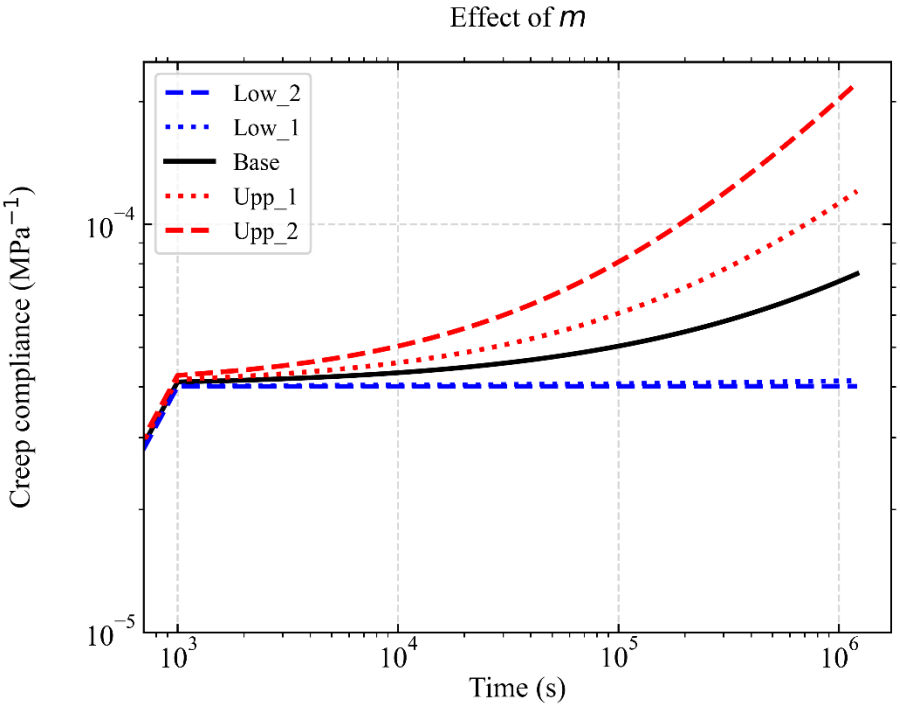
Effect of m
Low_2
Low_1
Base
Upp_1
Upp_2
Creep compliance (MPa^{-1})
10^{-4}
10^{-5}
10^{3}
10^{4}
10^{5}
10^{6}
Time (s)

(c)

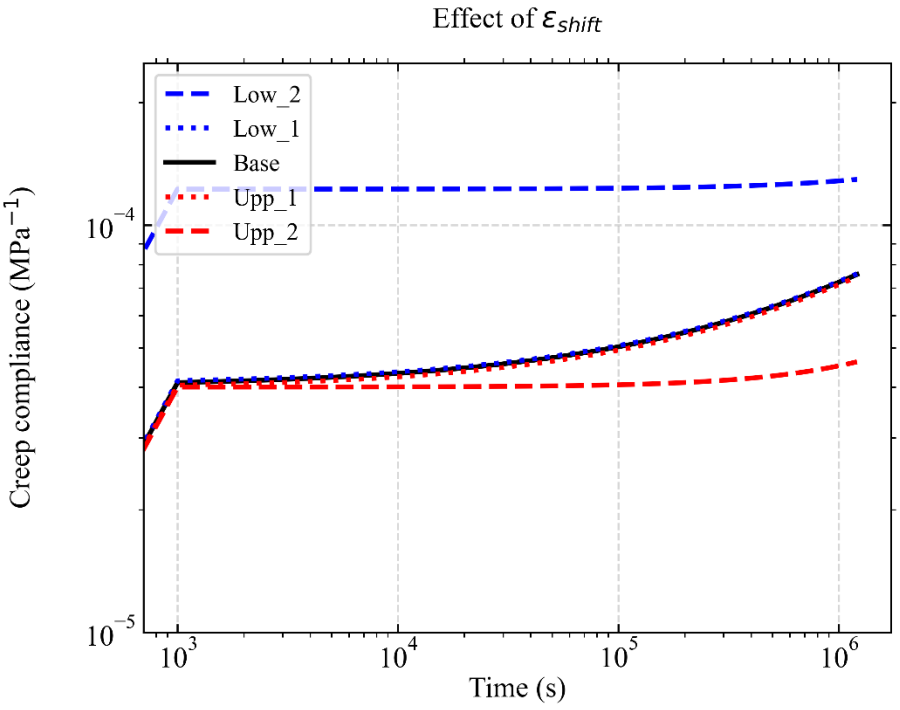
Effect of ε_{shift}
Low_2
Low_1
Base
Upp_1
Upp_2
Creep compliance (MPa^{-1})
10^{-4}
10^{-5}
10^{3}
10^{4}
10^{5}
10^{6}
Time (s)

(d)

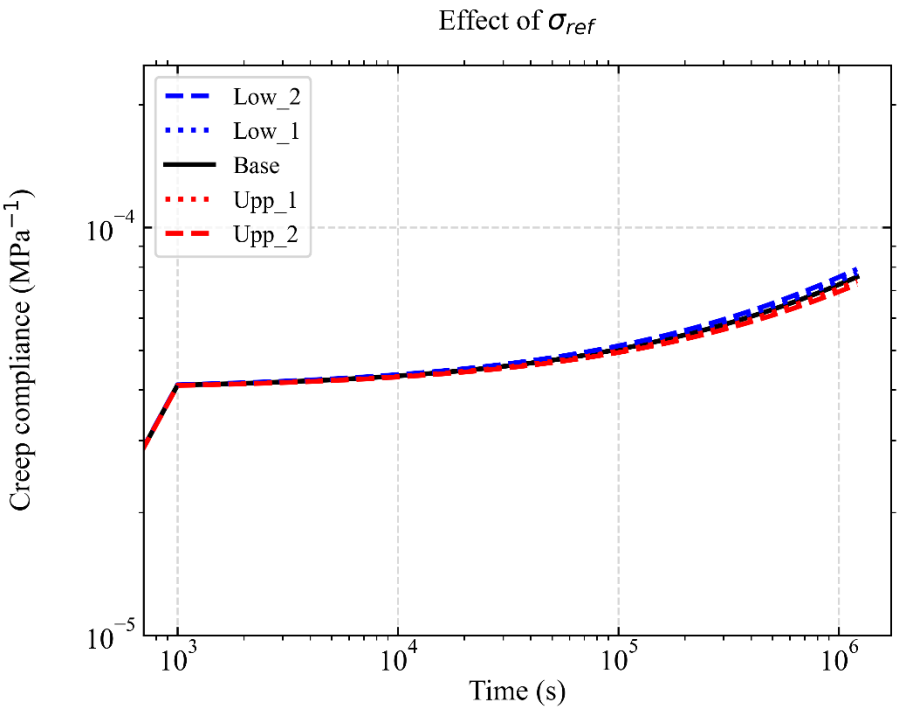

(e)

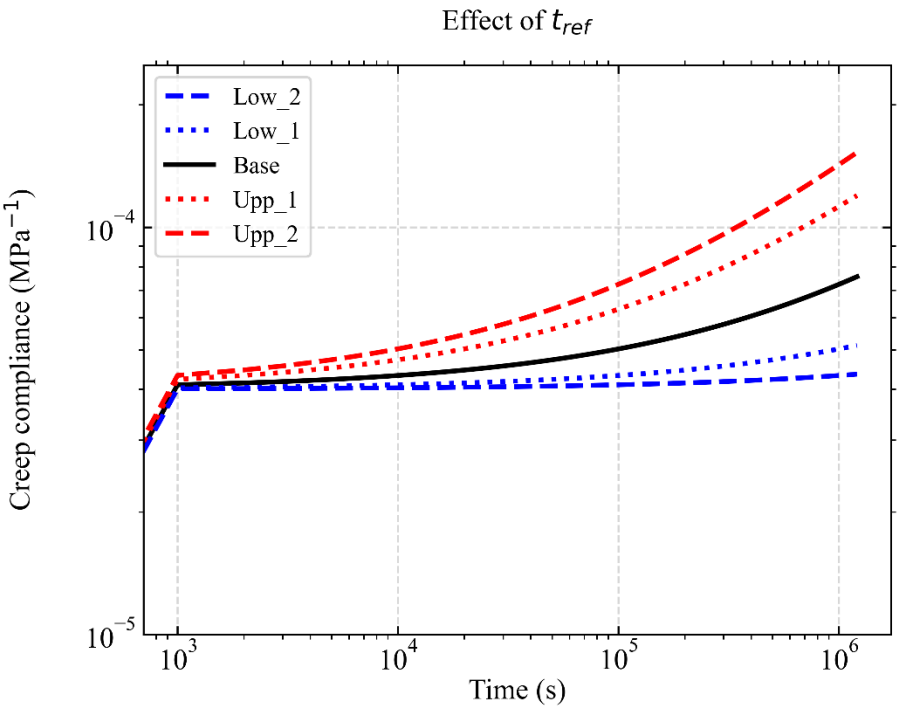

(f)

Figure 2-5. Effects of parameters on the log(time) vs. log(creep compliance) behavior of Norton-Bailey model: (a) $\boldsymbol{A}$; (b) $\boldsymbol{n}$; (c) $\boldsymbol{m}$; (d) $\boldsymbol{\epsilon_{shift}}$; (e) $\boldsymbol{\sigma_{ref}}$; (f) $\boldsymbol{t_{ref}}$.

2.4 Summary and Future Plans

In this study, the Norton-Bailey law is implemented in order to simulate in FLAC3D the creep behavior of shale samples. A parametric study is carried out to evaluate the effect of model parameters and to qualitatively match the simulation results with the laboratory test results. It is shown that the numerical results are in a reasonable agreement with the laboratory test results. A remaining challenge is to assess the discrepancy in the log(time)-log(creep compliance) plots where the numerical results show a concave up curve, with increasing trends while the experimental results show linear trends.

In a future study, possible causes of the discrepancy will be addressed by assessing errors in both numerical implementation and laboratory measurements. An improved and calibrated creep model will then be implemented in a THM-coupled simulation of geological nuclear waste repositories, in order to assess the effect of rock creep on the long-term safety assessment of nuclear waste repositories.

3. FE Experiment at the Mont Terri Site (DECOVALEX-2023)

In this section, we present the current status of LBNL's modeling of the FE Experiment at Mont Terri and updated results of TOUGH-FLAC. Because the FE Experiment at Mont Terri is now a task of the ongoing DECOVALEX-2023 project, this section, written by Jonny Rutqvist, is focused on new model development and results associated with the DECOVALEX-2023 project.

3.1 Description and Status of the Mont Terri FE experiment

The Mont Terri FE experiment has been conducted by NAGRA, Switzerland, as an ultimate test for the performance assessment of geologic disposal in Opalinus Clay, with focus on both the EBS components and the host-rock behavior. It is one of the largest and longest-duration heater tests worldwide, with focus on both the EBS components and the host-rock behavior. The FE experiment is being conducted in the side tunnel at Mont Terri, excavated along the claystone bedding planes, extending 50 m in length and about 2.8 m in diameter (Figure 3-1). Heating from emplaced waste is simulated by three heat-producing canisters of 1500 W maximum power each. Temperature is expected to exceed 100°C, with a target temperature of 125 to 135°C at the inner part of the buffer. A sophisticated monitoring program has been implemented, including dense instrumentation of the bentonite buffer and host rock, and extensive geophysical monitoring.

The experiment provides data needed for the validation of THM coupling effects and processes taking place in the host rock, such as the emplacement tunnel temperature, saturation, and swelling pressure. The Mont Terri field scale experiment is used to achieve realistic temperature, saturation, and stress gradients. It will also be possible to test backfilling technology with granular bentonite, as well as lining technology with shotcrete, anchors, and steel ribs. Processes examined in the test cover many aspects of a repository evolution, such as criteria of desaturation of the EDZ during tunnel excavation and operation (including ventilation for about one year), as well as reconsolidation of the EDZ, resaturation, thermal stresses, and thermal pore-pressure increase after backfilling and heating (heating and a monitoring period for >10 years).

In 2011, a niche in front of the FE tunnel was constructed, following by a first phase of instrumentation of the rock mass surrounding the tunnel, using boreholes drilled from the niche.

The FE tunnel was excavated by a road-header in 2012, following by instrumentation. The tunnel was kept open for a one-year ventilation period. This followed by emplacing the heaters, bentonite buffer, and a concrete plug, after which the heating was gradually turned on during the fall of 2014 and early 2015, with applying the full heat power of 1350 W at all three heaters (H1, H2, H3), starting on February 18, 2015 (Figure 3-2). The heating is expected to go on for at least 15 years, with continuous monitoring of THM processes in both the bentonite buffer and a surrounding rock. After over 5 years of heating, temperature at the heaters is approaching 130°C, and a relative humidity near the heaters in granular bentonite buffer stays low at around 10 to 20%. Some wetting is also taking place at other parts of the buffer, at some locations reaching full saturation. No substantial swelling stress has yet been developed in the granular bentonite at this stage of the project.

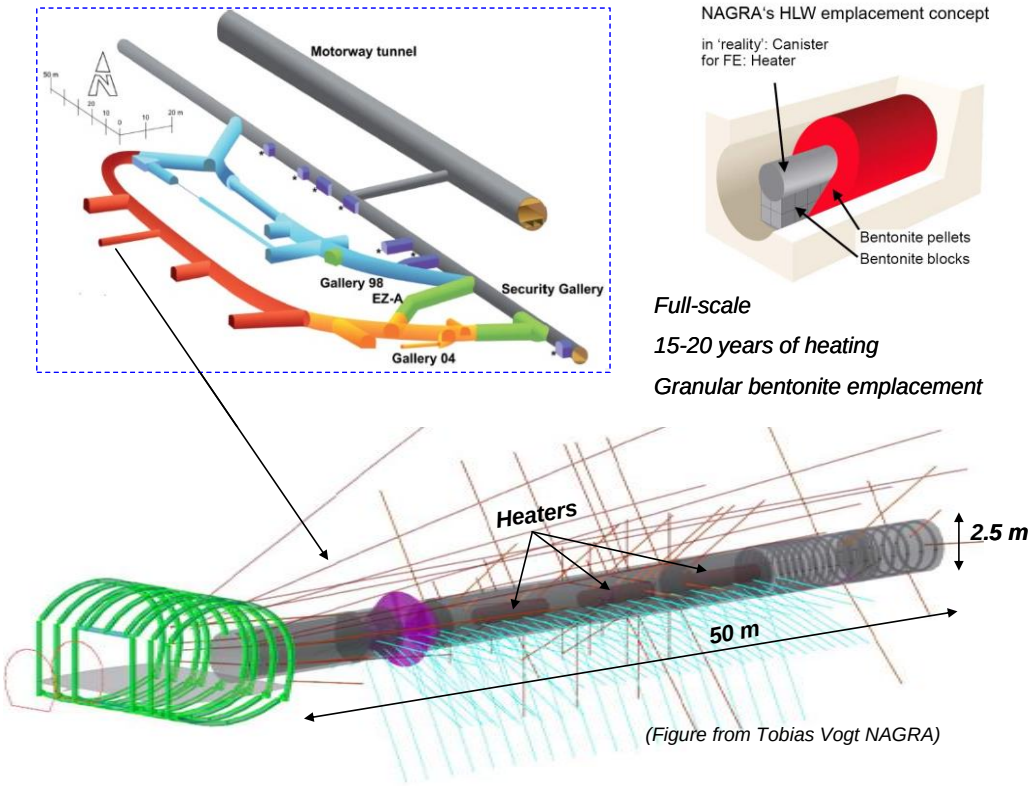

Figure 3-1. Plan view of FE experiment setup and borehole layout.

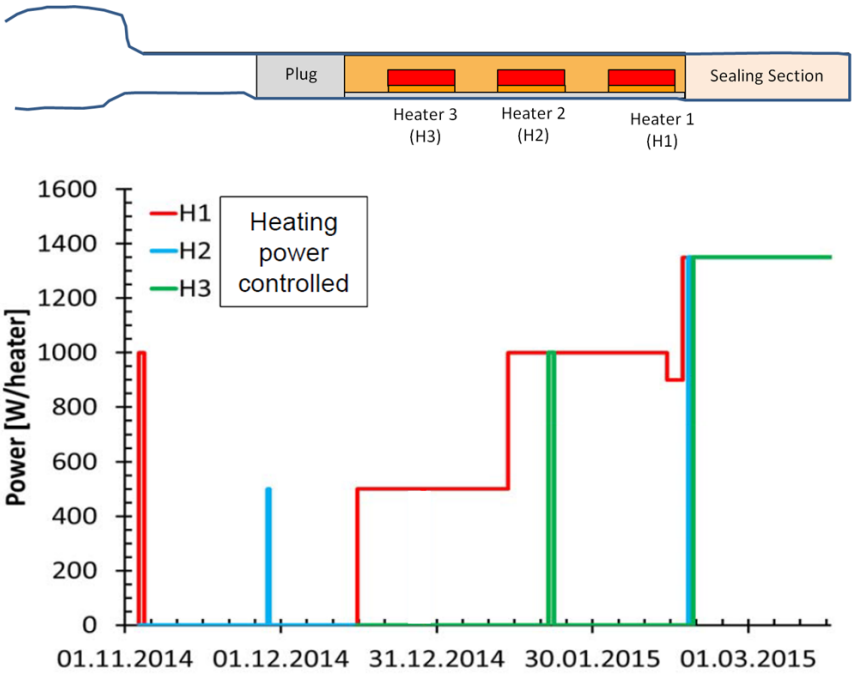

Figure 3-2. Heat power applied to H1, H2 and H3 during heater start-up at the Mont Terri FE experiment.

3.2 TOUGH-FLAC Model of the Mont Terri FE Experiment

For the FE experiment modeling, we have developed a conceptual model and a modeling approach based on the previous milestone reports (Houseworth et al., 2013; Zheng et al., 2014, 2015, 2016; 2017). In FY18 and FY19, Rutqvist et al. (2018; 2019; 2020) continued to update the model based on a comparison with longer term field data. In FY21 the 3D model has been updated considering a dip of 34° of bedding in the area compared to the previous model that assumed a dip of 45°. In addition, a new 2D model was developed for Benchmarking within the DEOVALEX-2023 project. Here we present the new models and discuss the results that have been developed associated with the DECOVALEX-2023 project. The DECOVALEX-2023 project is at the stage of blind prediction to perform comparison to data in the future. Therefore, no field data will be presented in the current FY21 report.

Using TOUGH-FLAC, the host rock is modeled taking into account anisotropic properties considering bedding planes of the Opalinus Clay. To accurately model anisotropic thermal and hydrological behavior, we created a TOUGH2 inclined mesh. Anisotropic mechanical material behavior is simulated using available elastic anisotropic model in FLAC3D with parameters given by the DECOVALEX-2023 task. For the bentonite, we are not considering the mechanical behavior of the buffer as (a) no significant swelling stress has been developed at the experiment, and (b) the DECOVALEX-2023 project is focused on the THM processes in the host rock rather than the bentonite buffer.

Figures 3-3 and 3-4 show the numerical grids of the FE experiment developed for the DECOVALEX-2023 Task C modeling. Figure 3-3 presents a new 2D grid that was applied in the initial benchmark simulations for the DECOVALEX-2023. Figure 3-4 presents the updated 3D

TOUGH-FLAC numerical grid of the FE experiment. This model grid includes all material components used for modeling of the FE experiment, including the layered Opalinus Clay host rock, excavation disturbed zone, tunnel, three heaters, bentonite buffer, concrete liner, and a concrete plug. The following initial conditions for the model simulations were selected: 2 MPa pore-fluid pressure, 15°C temperature, and σ_x = 4.5 MPa, σ_y = 2.5 MPa, σ_z = 6.5 MPa for the host rock. Because the 2 MPa pore pressure does not represent hydrostatic conditions, the process is affected by the existing tunnel system. In our regular simulations, we first ran a simulation with an open tunnel at the atmospheric pressure for one year, creating a pressure drop and hydraulic gradient around the tunnel. Thereafter, we assumed instantaneous emplacement of the heater and the buffer to start the heating simulation. The outer boundary conditions for all the outer boundary edges of the model are fixed zero displacement and no heat of fluid transfer. Simulations indicate that these boundaries are being placed far enough from the heat source so that there is no effect of the outer boundaries.

The thermal and hydraulic material properties for modeling the FE experiment are given in Table 3-1 as defined by the DECOVALEX-2023 task description (Thatcher and Graupner, 2020). Some of these properties are slightly different from the properties applied in our previous model simulations of the FE experiment. After comparing with actual field data, some of the material properties may be calibrated to achieve a better agreement with field data. In the 2D model simulation a heat load of 293 W/m was assumed. This number was calculated as the total heat decay power for one canister (1350 W) divided by the length of the canisters (4.6 m).

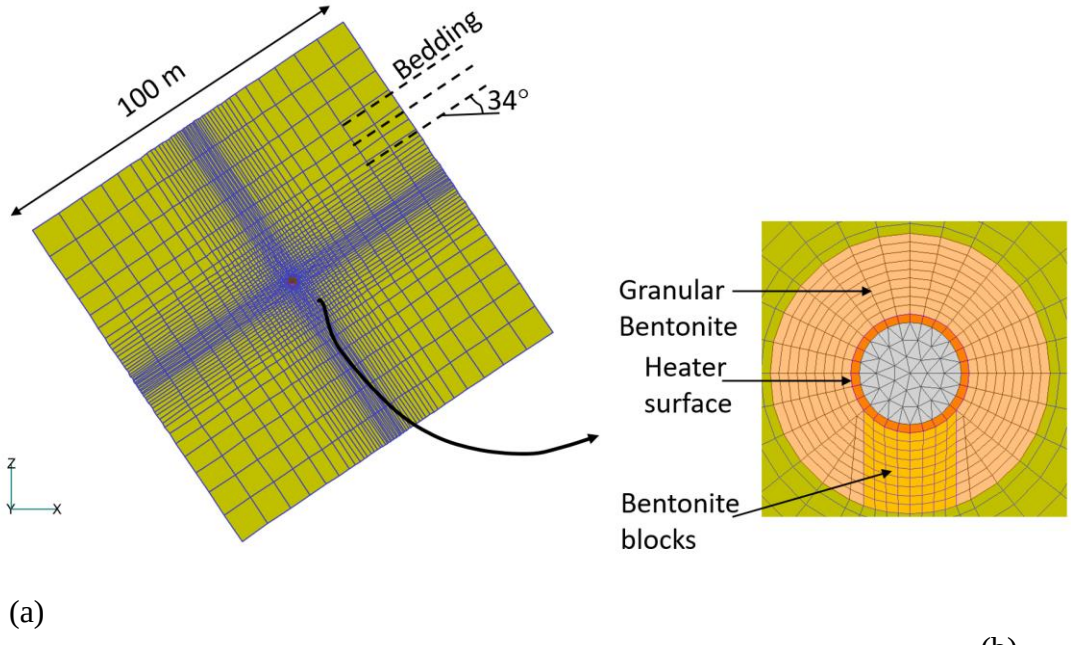

Figure 3-3. TOUGH-FLAC 2D numerical grid of the FE experiment for DECOVALEX-2023 benchmarking: (a) Entire model, and (b) Materials and gridding of the EBS.

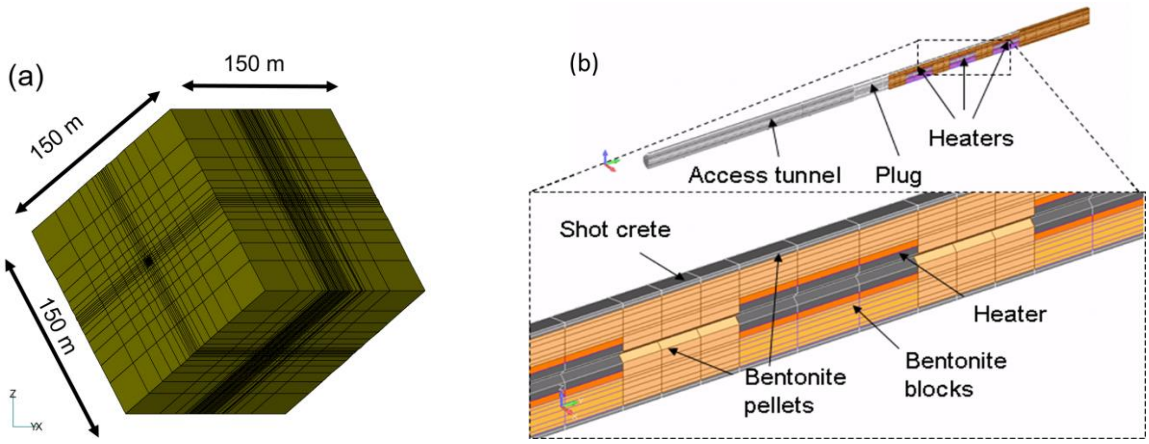

Figure 3-4. TOUGH-FLAC 3D numerical grid of the FE experiment: (a) Entire model, and (b) Materials and gridding of the EBS.

Table 3-1. Parameters used in modeling of the Mont Terri FE experiment defined in the DECOVALEX-2023 Task Description (Thatcher and Graupner, 2020)

Input parameters		Symbol	Unit	OPA [1]	GBM [3]	Bentonite blocks [4]	Concrete
Thermal parameters	Dry thermal conductivity parallel and perpendicular to bedding	$\lambda_{dry,\parallel}$	*W/mK*	2.4	0.35	0.26	0.1
		$\lambda_{dry,\perp}$	*W/mK*	1.3			
	Saturated thermal conductivity parallel and perpendicular to bedding	$\lambda_{sat,\parallel}$	*W/mK*	2.4	1.2	0.96	0.3
		$\lambda_{sat,\perp}$	*W/mK*	1.3			
	Solid specific heat capacity	c_s	J/kgK	995	800	800	750
Hydraulic parameters	Dry Bulk Density	ρ_{bulk}	*kg/m³*	2340	1490	1690	1725
	Porosity	ϕ	-	0.13	0.331	0.331	0.25
	Intrinsic permeability	$k_{i,\parallel}$	*m²*	5.0E-20	3.5E-20	1.0E-22	1.0E-19
		$k_{i,\perp}$		1.0E-20			
	Van Genuchten Entry Pressure	p_e	*MPa*	20.0	28.6	30	1
	van Genuchten n	n	-	2.5	2.0	1.67	1.49
	van Genuchten maximum water saturation	s_{max}	-	1.0	1.0	1.0	1
	van Genuchten residual water saturation	s_r	-	0.0	0.0	0.0	0.01
	Pore compressibility	c_{pore}	*1/Pa*	8.66E-10	1.05E-07	1.13E-07	1.40E-10
Mechanical parameters	Young's modulus	$E_\parallel$	*MPa*	8000	18	24	20000
		$E_\perp$		4000			
	Shear modulus	$G_\perp$	*MPa*	3500	-	-	-
	Poisson ratio	$\nu_\parallel$	-	0.35	0.35	0.2	0.15
		$\nu_\perp$		0.25			
	Linear thermal expansion	α_T	*1/K*	1.5E-05	3.0E-06	3.0E-06	1.5E-05
	Biot coefficient	α	-	1	1	1	1
Fluid parameters	Reference water density	ρ_{fluid_ref}	*kg/m³*	1000			
	Fluid compressibility	c_{fluid}	*1/Pa*	4.65E-10			
	Linear thermal expansion water	α_w	*Pa s*	4.00E-04			
	Vapour diffusivity (vapour in air)	D_v	*m²/s*	2.42E-05			

3.3 Simulation Results

The simulations for the DECOVALEX-2023 will be focused on the pressure evolution in the host rock surrounding the tunnel. Nevertheless, the evolution of coupled THM processes in the buffer could have an impact, in particular, due to the strong capillarity suction from the partially saturated bentonite. Figures 3-5 and 3-6 present the simulation results of temperature and fluid pressure for the 2D benchmarking simulation. Along the bedding both thermal conductivity and permeability are higher than across the bedding. Therefore, temperature in monitoring points O1 to O3 located along the bedding increases faster than in point O4 to O6. This faster temperature increase results in a stronger thermal pressurization early on. However, the higher permeability along the bedding also results in a faster pressure decline after the initial pressure pulse. In fact, the fluid pressure close to the tunnel is strongly impacted by the capillary suction in the bentonite which tends to draw water from the surrounding host rock. This is illustrated in Figure 3-6b, where the blue area around the tunnel is an area of very low fluid pressure. Figure 3-5b shows that the pressure in point O1 goes to near zero at 800 day, meaning that the host rock is desaturated at that location.

Model comparison with other modeling teams in the DECOVALEX-2023 project revealed a systematic difference in the results of modeling of the fluid pressure. The modeling results from the LBNL TOUGH simulations tend to result in a lower thermal pressurization compared to the benchmark solution developed in the DECOVALEX-2023 project. The reason for this difference was explained by the fact that TOUGH used the built-in temperature dependent water properties from steam tables, while in the task description, temperature-independent constant values of water properties were given. Figure 3-7 shows a comparison to the temperature dependent properties and the constant value defined in the DECOVALEX-2023 description. As shown, for the temperature range from 15 to 40°C, the thermal expansivity defined in the DECOVALEX-2023 is higher than the temperature dependent values that are used in TOUGH2. The reason for the constant thermal expansivity in the DECOVALEX-2023 was to have a simplified case for comparison and a code-to-code verification between the modeling teams. However, it appears that it will be important to have an accurate model for thermal expansivity of water for an accurate prediction of thermal pressurization around a repository tunnel.

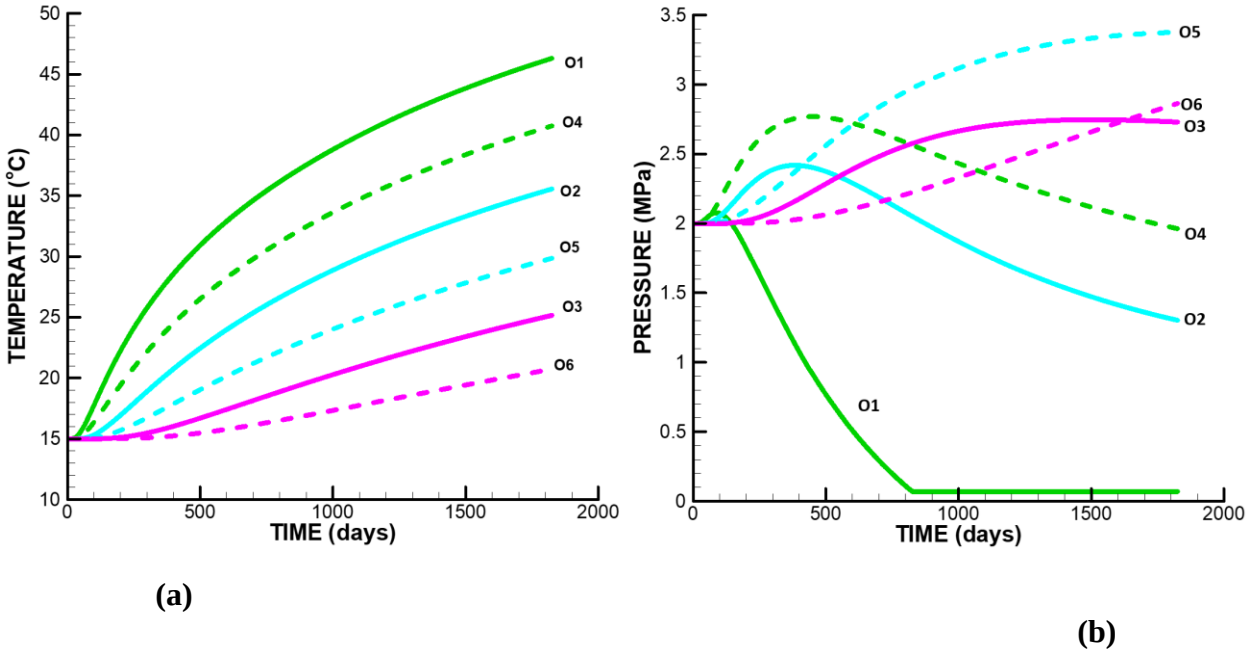

Figure 3-5. 2D model simulation result of anisotropic evolution of (a) temperature and (b) fluid pressure at monitoring points O1 to O6 located in the Opalinus Clay.

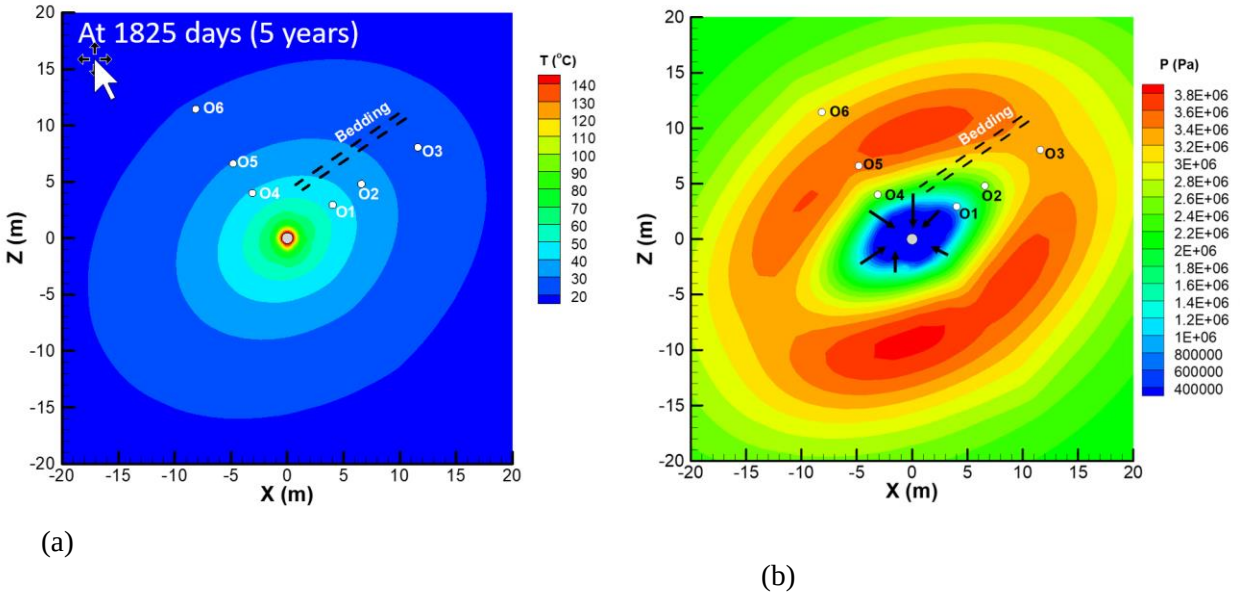

Figure 3-6. 2D model simulation result of anisotropic distribution of (a) temperature and (b) pressure after 5 years.

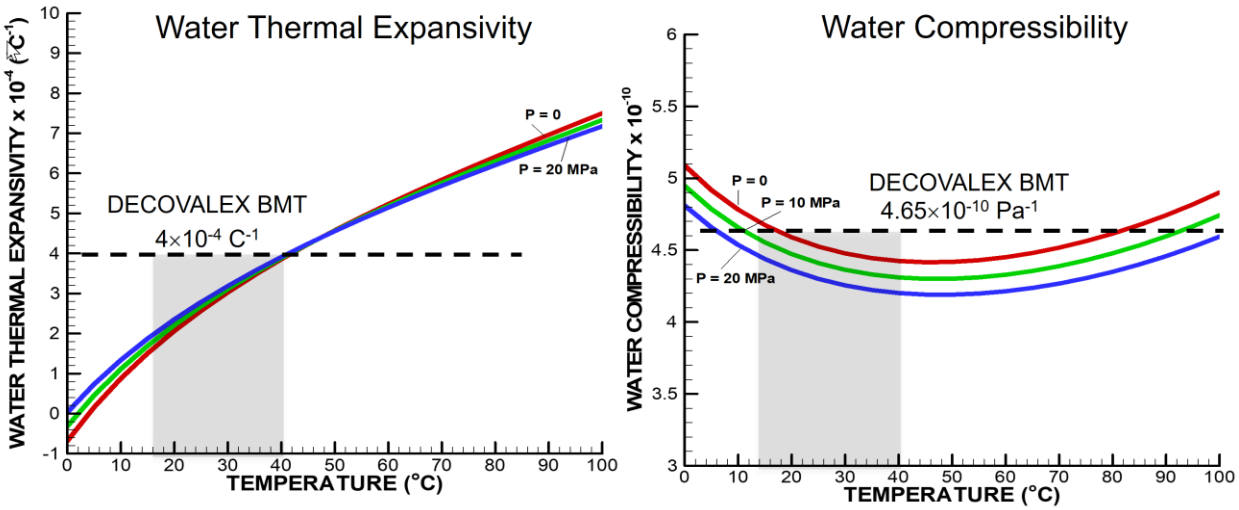

(a) (b)

Figure 3-7. Comparison of water properties defined in DECOVALEX-2023 task definition with temperature dependent water properties as assumed in the TOUGH2 code: (a) water thermal expansivity, and (b) water compressibility.

Figures 3-8 and 3-9 show selected results from the full 3D model simulations. Figure 3-8 shows that the heater temperature goes up to 130°C. Highest temperature occurs on top of the middle heater (H2) on the top, while the temperatures on top of the two outer heaters (H1 and H3) are slightly lower. Moreover, the results show that the heater temperature is slightly lower at the bottom of H2 compared to that at the top of H2. The lower temperature at the bottom can be attributed to the higher degree of saturation and a higher thermal conductivity of the bentonite blocks below the heaters. Comparison of the results depicted in Figure 3-9 for the 3D model to the results shown in Figure 3-5 for the 2D case shows that temperature increased much less for the case of 3D modeling. The lower temperature increase also results in a lower thermal pressurization in the 3D modeling compared to the previous 2D modeling. The 2D model overestimates temperature as a result of the greater heat load (293 w/m) and the lack of out of plane heat loss that is considered in a full 3D model. These results indicate that thermal pressurization is quite small.

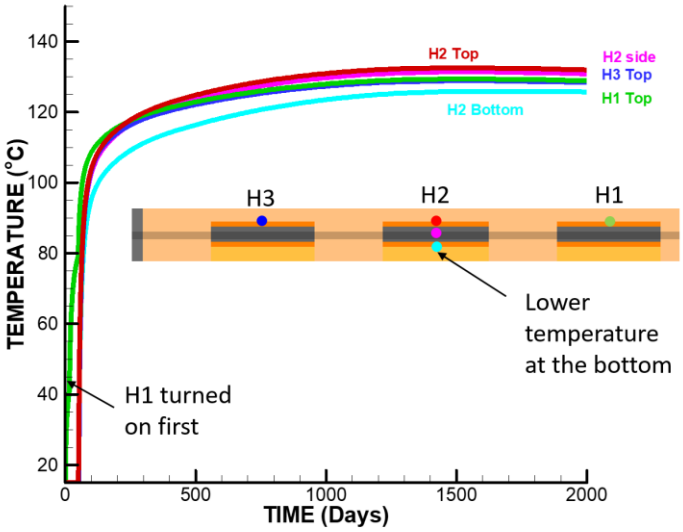

Figure 3-8. 3D model simulation results of heater temperatures.

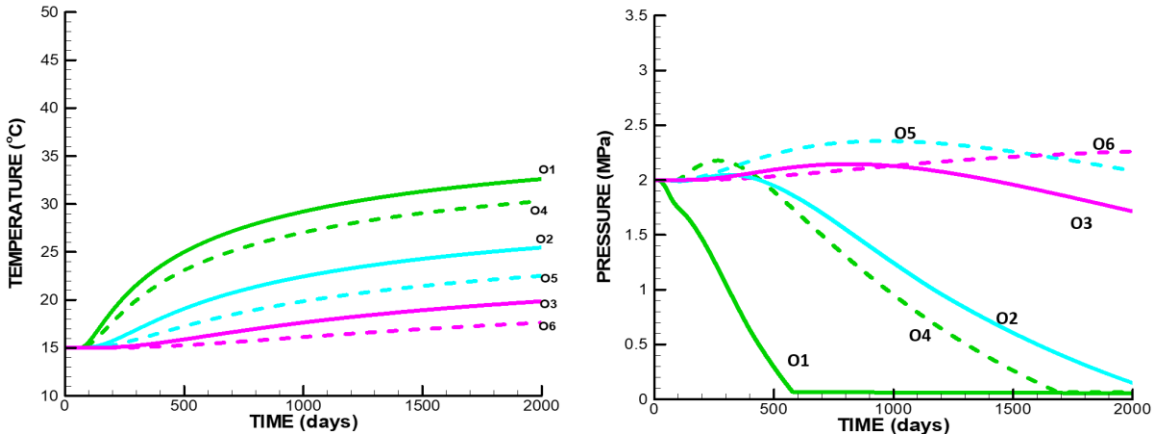

(a) (b)

Figure 3-9. 3D model simulation result of anisotropic evolution of (a) temperature and (b) fluid pressure in monitoring points O1 to O6 located in the Opalinus Clay.

3.4 Future work on the FE Experiment Modeling

We have conducted several types of modeling over the past few years, including benchmarking, heating design modeling, model predictions and interpretative modeling. Currently, we are active in the DECOVALEX-2023 project and this provides additional code-to-code verifications. The next step in the DECOVALEX-2023 will involve comparison to field data for the first 5 years of the experiment. This will also involve comparison of mechanical responses in the host rock such as strain. After this we will then resume our regular Mont Terri project simulation of the field data going beyond 5 years. This will also involve the modeling of the excavation and ventilation

phase before the heaters were turned on. Finally, the work for Mont Terri project will focus more on the evolution of the bentonite buffer and the stress in the bentonite buffer.

4. Modeling of Thermal and Gas and Fracturing at Bure in COx Claystone (DECOVALEX-2023)

In this section, we present recent TOUGH-FLAC modeling results related to thermal and gas fracturing experiments, conducted in Callovo-Oxfordian claystone (COx) at the Meuse/Haute-Marne Underground Research Laboratory (MHM URL) in Bure, France. Modeling of heater tests is conducted as part of Task A of the DECOVALEX-2023 project. The DECOVALEX-2023 Task A started in FY2021 with some benchmark modeling and modeling of laboratory experiments of thermal pressurization with fracturing. Here we present the progress in modeling of thermal pressurization experiments from Braun (2019). Modeling of gas fracturing has also started but will be completed and presented in future milestone reports. The modeling work was performed by Hao Xu and Jonny Rutqvist, who also wrote this section.

4.1 Setup of Thermal Pressurization Laboratory Experiments on COx Claystone

The first step in modeling the thermal fracturing experiment at MHM URL is modeling of the laboratory experiment to characterize a fracturing process of the COx under thermal loading. This involved modeling of a series of thermal extension tests performed on COx samples taken from the MHM URL. The laboratory samples are subjected to different thermal loads, while lateral deformations are constrained and the vertical total stress remains constant on the top of the sample.

Three samples (EXT1, EXT2, and EXT3) were collected at the MHM URL, and tested under different initial conditions to investigate the effect of the initial stress state and the initial temperature on the stress-strain behavior and the tensile strength of the COx. Figure 4-1 shows a conceptual model of the experiments which are described in detail in Braun (2019). The sample fluid pressure was measured through drainage lines connected to a geotextile, wrapped around the specimen inside a jacket. The jacket, a neoprene membrane was put over the specimen and the geotextile, providing isolation between the confining fluid and the pore fluid. An internal aluminum force sensor measured the axial total stress. Axial and radial strains were recorded through the strain gages glued on the sample at mid-height (Braun, 2019).

The samples were first loaded under different confining pressure, σ_0, and then were saturated under a fluid pressure of P= 0.1 MPa; swelling strains stabilized after about two days (Figure 4-1). After hydration, different initial conditions for each sample were set prior to heating. The confining pressure, initial stress (negative stress in compression), pore pressure and temperature are listed in Table 4-1. Pore pressure was measured The initial stress state of EXT1 is close to the anisotropic *in-situ* stress in the MHM URL (Wileveau et al., 2007). EXT2 started at a lower stress, and EXT3 started at similar radial stress as EXT1, but with a reduced axial stress. Hydraulic equilibrium was ensured by awaiting until no significant deformations could be observed.

Table 4-1. Initial stress, fluid pressure and temperature for the three laboratory experiments on thermal fracturing modeled in the DECOVALEX-2023 Task A.

Sample	σ_0	σ_{a0}	σ_{r0}	p_{w0}	T_0
	MPa	MPa	MPa	MPa	˚C
EXT1	-8	-12.6	-11.8	4.9	25
EXT2	-5	-4.8	-5.6	2.1	24
EXT3	-12	-7.2	-12.4	4.0	35

During the thermal extension test, the drainage valve was closed and the servo-control of confining pressure was switched on to maintain radial strains of zero, while the axial total stress was kept constant on the top of the sample. Heating rates were set to 10.0°C/h for EXT1 and EXT3, and to 5.0°C/h for EXT2.

4.2 Experimental and Simulation Results for Reference Parameters

Figure 4-2 shows the evolution of the applied thermal load in the experiments and in the numerical modeling. Figure 4-3, 4-4 and 4-5 present experimental and modeled evolutions of fluid pressure, total stresses, axial strain and effective stresses. The main processes occurring during the thermal extension tests can be summarized as follows: (1) An increase of pore pressure due to thermal pressurization, (2) an increase of axial extension and radial total stress due to lateral constrained deformations, and (3) an eventual failure, once the specimen reached its tensile strength. The axial total stress remained almost constant, with some variation due to the friction of the piston. The radial total stress and the pore pressure experienced a continuous increase due to heating.

The model simulation result using the reference parameters listed in Table 4-2 provides a good qualitative agreement with the experimental results, whereas quantitatively significant deviations occur. The agreement is the best for EXT1, where the pressure is accurately modeled, axial strains are fairly well modeled, while stresses show a more significant deviation. For EXT2 and 3 the pressure is not as well modeled, while the total stress is more close to the experimental results. Overall, it was not possible to obtain a good match to all three experiments with the same input material properties. A calibration of the material properties was performed and some of the disagreements between modeling and experimental results were reduced, but consistent parameter set was not obtained. One problem in the numerical simulations is the boundary conditions, such as the axial stress at the top boundary that in the experiment is not exactly constant as assumed in the modeling. Another issue with the current TOUGH-FLAC model applied to this problem is that the tensile failure process is ignored.

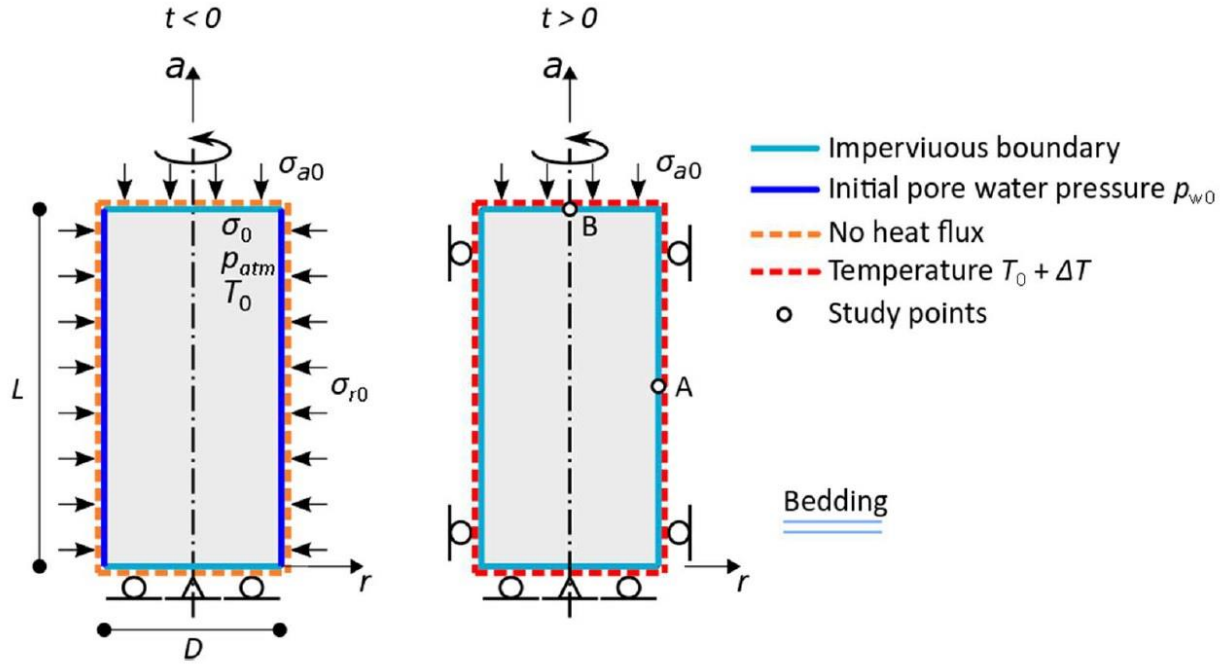

Figure 4-1. Conceptual model of the thermal-fracturing experiments that were conducted by Braun (2019).

Table 4-2. Reference parameters used in modeling of the thermal fracturing experiments based on years of site investigations at the MHM URL and laboratory experiments on shale from the MHM URL.

Parameters	Unit	Notation	Value
Young's modulus (parallel to bedding)	10^9 Pa	E_h	6.0
Young's modulus (perpendicular to bedding)	10^9 Pa	E_v	4.0
Poisson ratio (Parallel to bedding)	-	ν_{hh}	0.3
Poisson ratio (Perpendicular to bedding)	-	ν_{vh}	0.3
Shear modulus (Perpendicular to bedding)	10^9 Pa	G_{vh}	1.7
Density of solid grains	kg/m^3	ρ_s	2770
Biot coefficient	-	b	0.8
Porosity	-	ϕ	0.18
Permeability (parallel to bedding)	10^{-20} m^2	$K_{w,h}$	4.0
Permeability (perpendicular to bedding)	10^{-20} m^2	$K_{w,v}$	1.33
Equivalent thermal conductivity (parallel to bedding)	W/m/K	λ_h	1.95
Equivalent thermal conductivity (perpendicular to bedding)	W/m/K	λ_v	1.28
Heat capacity of porous medium	J/kg/K	C_p	800
Volumetric thermal expansion of solid grains	10^{-5} 1/K	β_s	4.5

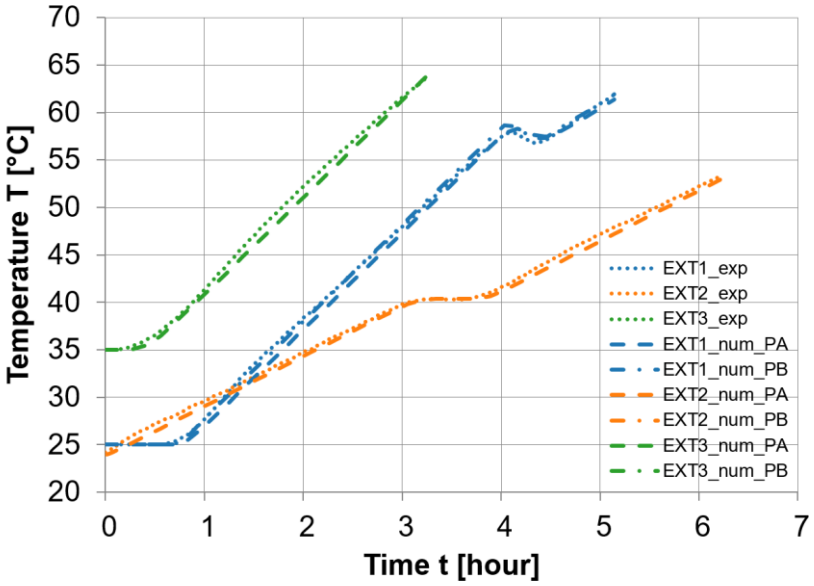

Figure 4-2. Experimental and numerically simulated temperature evolution applied during the thermal extension tests (Experimental results from Braun, 2019)

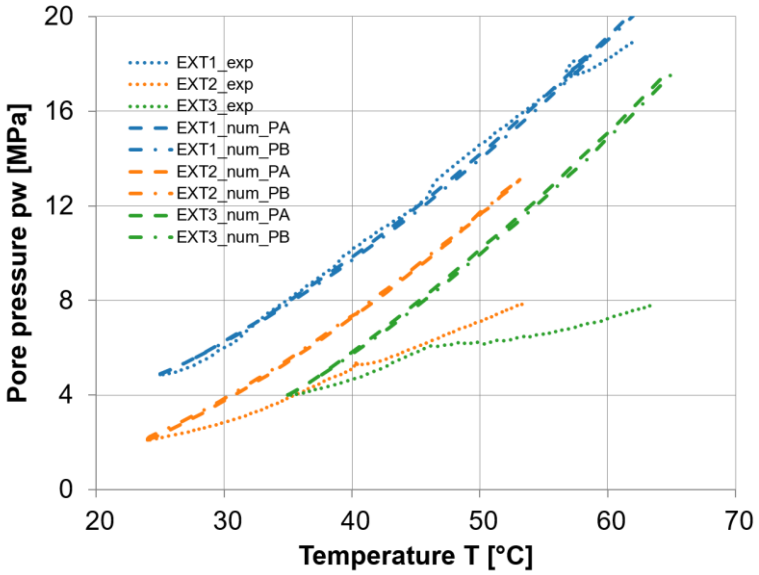

Figure 4-3. Experimental and numerically simulated pressure evolution during the thermal extension tests (Experimental results from Braun, 2019)

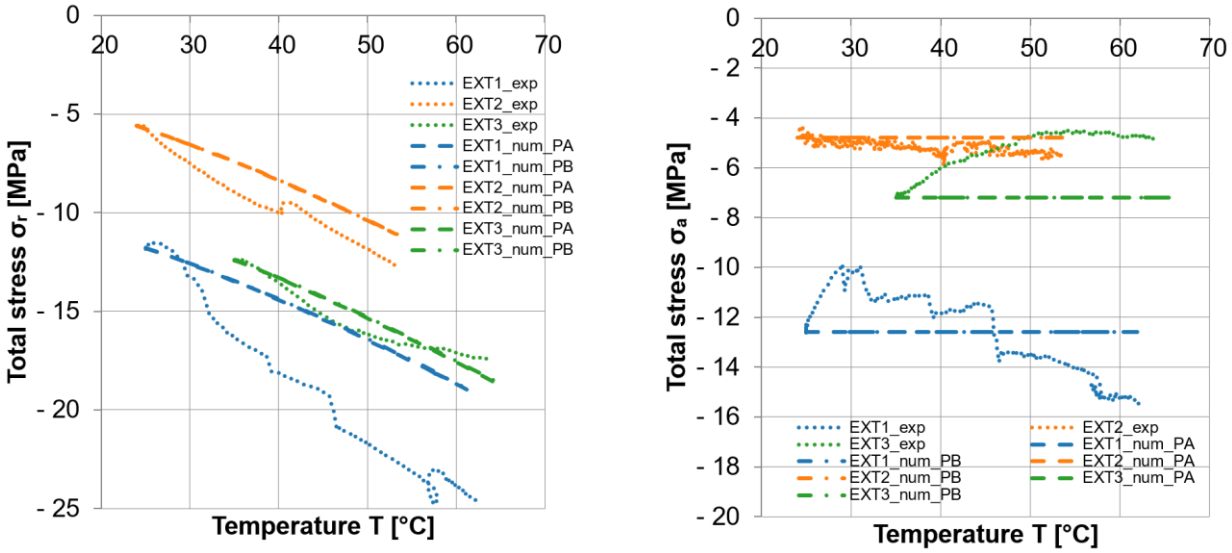

(a) (b)

Figure 4-4. Experimental and numerically simulated (a) radial and (b) axial total stress evolution during the thermal extension tests (Experimental results from Braun, 2019)

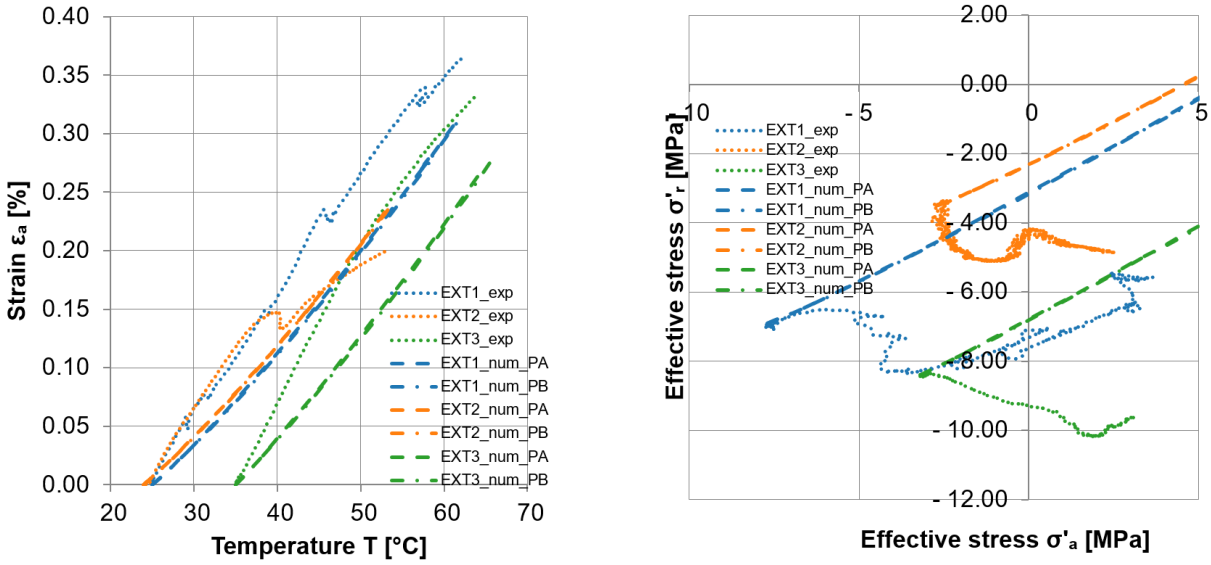

(a) **(b)**

Figure 4-5. Experimental and numerically simulated (a) axial strain and (b) effective stress evolution during the thermal extension tests (Experimental results from Braun, 2019)

4.3 Future work on DECOVALEX-2023 Task A

The next steps in FY2021 will be to complete the modeling of the thermal pressurization laboratory tests considering tensile failure by applying the FLAC3D ubiquitous joint model. Meanwhile the modeling benchmark tests related to gas fracturing, which has just started, will be completed for comparison to the results of other modeling teams within DEOCVALEX-2023 Task A. The goal is to use similar constitutive models for both the thermal and gas fracturing experiments. The heating of the *in situ* experiment will also be modeled before the next DECOVALEX-2023 workshop.

5. Modeling of Gas Migration in Clay (DECOVALEX-2023)

In this section we present the results of LBNL's activities aimed at modeling gas migration in clay related to Task B of the DECOVALEX-2023 project. The Task B of the DECOVALEX-2023 can be considered as a continuation of a similar task of the previous DECOVALEX-2019 Task A. Task B of DECOVALEX-2023 is led by scientists from the British Geological Survey (BGS). The BGS has also performed laboratory gas migration experiment that are modeled in this task. In FY21, LBNL conducted new simulations for a blind prediction of a gas migration experiment that is yet to be performed. Meanwhile, LBNL's DECOVALEX-2019 work on gas migration have been published in a journal paper (Kim et al., 2021) as well as in joint paper with other participants of DECOVALEX-2019 Task A (Tamayo-Mas, 2021).

5.1 Gas Migration in Clay

Four primary phenomenological models describing gas flow, shown in Figure 5-1, can be defined as following: (1) gas movement by diffusion and/or solution within interstitial fluids along prevailing hydraulic gradients; (2) gas flow in the original porosity of the fabric, commonly referred to as viscocapillary (or two-phase) flow; (3) gas flow along localized dilatant pathways, which may or may not interact with the continuum stress field; and (4) gas fracturing of the rock similar to that performed during hydrocarbon stimulation exercises (Harrington, 2016).

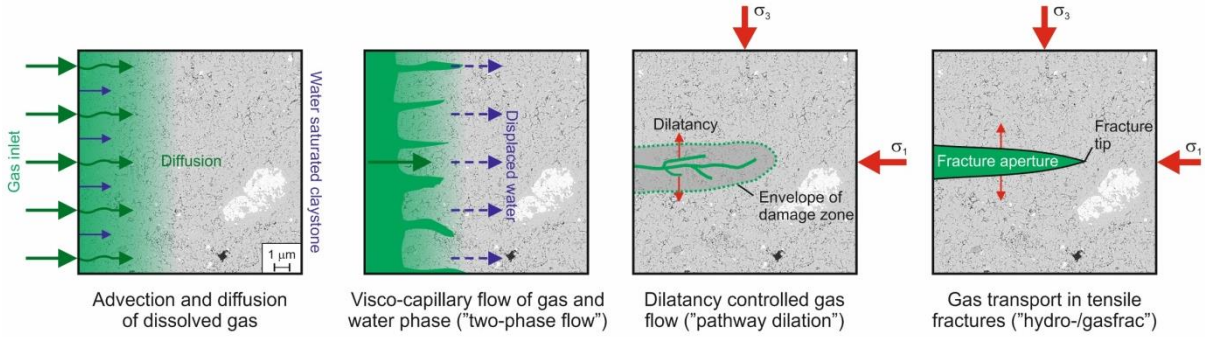

Figure 5-1. Conceptual models of gas flow (Harrington, 2016)

Studies on gas migration in clays (Horseman et al., 1999; 2004; Harrington and Horseman, 1999) indicate that classic concepts of porous medium two-phase flow are inappropriate and continuum approaches to modeling gas flow may be questionable, depending on the scale of the processes and resolution of the numerical model. However, the details of the dilatant mechanisms controlling gas entry, flow and pathway sealing are unclear. As such, development of new and novel numerical representations for the quantitative treatment of gas in clay-based repository systems is therefore required (Harrington, 2016).

5.2 LBNL Model Approaches for Gas Migration

LBNL explored two complementary approaches for modeling gas migration associated with DECOVALEX-2019 Task A:

1) Continuum modeling approach using TOUGH-FLAC simulator (Rutqvist et al., 2011), and

2) Discrete fracture modeling approach using TOUGH-RBSN simulator (Kim et al., 2017).

The continuum approach is based on current developments and applications of TOUGH-FLAC for the modeling of long-term THM performance of nuclear waste repositories in clay host rocks. The TOUGH2 code and other continuum models have been used in the past to model gas migration in clay considering heterogeneous clay properties with pressure dependent permeability, but without considering geomechanical coupling (e.g., Senger and Marschall, 2008; Senger et al., 2014). The discrete fracture modeling approach is based on the TOUGH-RBSN simulator, in which the opening of grain boundaries for dilatant gas migration is modeled explicitly using a fracture mechanics approach. The TOUGH-RBSN provided the only discrete fracture model applied to gas migration in DECOVALEX-2019 (Kim et al., 2021; Tamayo-Mas et al., 2021).

For DECOVALEX-2023 we will focus on the development of the heterogeneous continuum approach. We will develop the double structure approach for gas migration, involving the interaction between micro- and macro-porosity of the clay.

5.3 Modeling 1D gas migration

Here we present the results of modeling of the 1D gas migration experiment that is part of DECOVALEX-2023 Task B as an initial case for model development and calibration of model parameters. The modeling is conducted with the continuum model approach having the following basic approach and material models

1) Multiphase (gas and liquid) flow;

2) A linear poro-elastic model;

3) A linear moisture swelling model; and

4) A gas permeability model related to minimum effective compressive stress.

The linear poro-elastic model is based on the assumption of a linear elastic response, based on an effective stress law, and responding to the maximum phase pore pressure (either gas pressure for partially saturated media or liquid pressure for fully saturated media. The model is given by

$$\sigma' = \sigma - P^{\emptyset} \tag{5.1}$$

where

$$P^{\emptyset} = Max(P^{l}, P^{g}) \tag{5.2}$$

where P^{ϕ} is the pore pressure, and P^{l} *and* P^{g} are liquid and gas phase pressures, respectively.

The linear moisture swelling model implies a swelling strain as a function of liquid saturation, leading to a swelling stress, according to

$$\Delta\sigma_{sw} = 3K\Delta\varepsilon_{sw} = 3K\Delta S_l\beta_{sw} \tag{5.3}$$

where S_l is liquid saturation, and β_{sw} is the moisture swelling coefficient. These models have been used in the past for simplified modeling of bentonite behavior and are described in Rutqvist et al. (2011). The applied gas permeability model considers a fracture-like behavior of permeability for dilatant flow paths (Figure 5-2). In this model, permeability is a non-linear function of the effective minimum compressive stress.

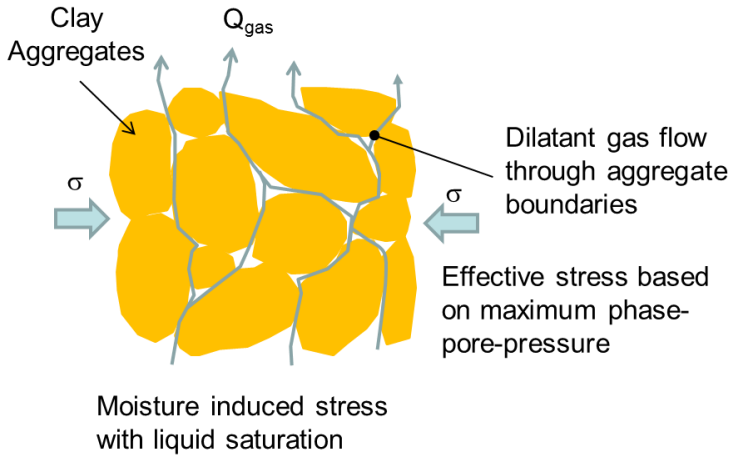

Figure 5-2. Conceptual model for dilatant gas flow through aggregate boundaries considered in a continuum model simulations using TOUGH-FLAC.

A full 3D model has been developed to model heterogeneous material properties. However, modeling simulations conducted to date have been done assuming homogeneous properties of the MX-80. The test geometry in this case is a 3D model as shown in Figure 5-3. The sample dimensions are 120 mm long and 60 mm diameter. We included additional elements on the top and bottom in the TOUGH2 fluid flow domain to simulate the injection and back-pressure filters.

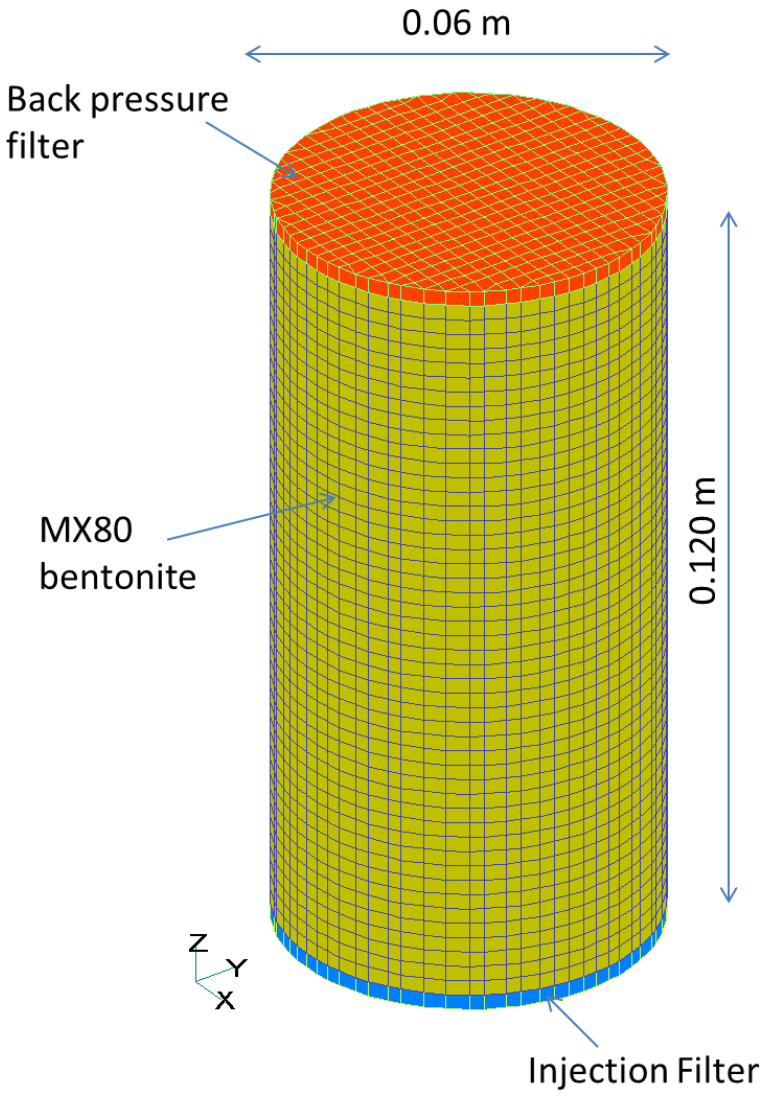

Figure 5-3. 3D TOUGH-FLAC model of cylindrical sample.

Initial conditions of 1 MPa fluid pressure and fully water saturated sample were used for modeling. In the current modeling, the injection pressure was controlled at the injection boundary elements at full gas saturation, with variable pressure ranging according to measured data. A back pressure of 1 MPa was maintained in the elements simulating the back pressure filter. The simulation starts at 20 days assuming a fully saturated sample, the initial axial stress of 9.5 MPa and the radial initial stress of 6.5 MPa. In simulations, the sample was assumed to be mechanically confined.

Sensitivity studies were conducted to perform matching the simulation and experimental results. Finally, some material properties were fixed, while others were used for final matching of simulation results. Table 5-1 lists the basic and specific material parameters that will be

explained. The parameters marked in bold in Table 5-1 were calibrated. Other parameters were fixed, including those denoted as basic reference values, which are typical for MX-80 bentonite and given by the DECOVALEX-2019 task Lead.

Table 5-1. Material parameters for TOUGH-FLAC modeling of Stage 1 experiment.

	Meaning	Symbol [units]	Value
Basic reference values	Young's modulus	E [MPa]	307
	Poisson's ratio	ν [-]	0.4
	Porosity	ϕ_0 [-]	0.44
	Intrinsic permeability	k_0 [m^2]	3.4×10^{-21}
HM coupling parameters	Pore compressibility[1]	c_p [Pa^{-1}]	4.44×10^{-9}
	Biot's coefficient	α_p [-]	1
	Swelling coefficient	$\boldsymbol{\beta_{sw}}$ **[-]**	**0.02**
	Max aperture for stress-k	**bho [m]**	$\mathbf{29x10^{-6}}$
	Reference stress for stress-k	$\boldsymbol{\sigma_{n,ref}}$ **[MPa]**	**0.2**
van Genuchten capillary pressure model	Capillary pressure parameter	P_0 [MPa]	18
	Residual liquid saturation	S_{lr} [-]	0.01
	Shape factor	λ [-]	0.45
Corey relative permeability	Residual liquid saturation	S_{lr} [-]	0.1
	Residual gas saturation	$\boldsymbol{S_{gr}}$ **[-]**	**0.11**
	Enhancement factor for k_{rg}	$\boldsymbol{m_g}$ **[-]**	**375**

Based on the results of matching the stress evolution from experimental and modeling data, it is required to consider both the poro-elastic stress changes and the moisture swelling effect. During gas injection, the poro-elastic stress change will tend to increase the compressive stress, because the sample is confined mechanically. The poro-elastic stress increase is roughly proportional to the pressure changes, which far exceeds the observed stress changes. However, considering the effect of bentonite swelling, or in the case of shrinkage due to reduced water saturation as gas is injected, some of the poro-elastic stress changes will be offset and the observed stress evolution can be matched reasonable well. In simulations the Young's modulus was fixed at 307 MPa, which is a reasonable approximation for saturated or near saturated bentonite, taking into account the dry density and a confining stress. To match the observed stress magnitude a moisture

swelling parameter of β_{sw} = 0.02 was determined through sensitivity analysis. Poisson's ratio was set to 0.4.

The van Genuchten (1980) capillary pressure model is used to define the water retention curve given by

$$P_c(S) = P_0\left([S^*]^{-1/\lambda} - 1\right)^{1-\lambda} \tag{5.4}$$

with $S^* = (S - S_{lr})/(1 - S_{lr})$. The following capillary pressure parameters are adopted for bentonite (Senger and Marschall, 2008): the van-Genuchten capillary pressure parameter P_0=18 MPa, shape factor λ=0.45, and residual liquid saturation S_{lr}=0.01.

The relative permeability-saturation relationships of liquid and gaseous phases are parameterized using Corey's model as

$$\begin{aligned} k_{rl}(S) &= \hat{S}^4 \\ k_{rg}(S) &= m_g\left(1 - \hat{S}\right)^2\left(1 - \hat{S}^2\right) \end{aligned} \tag{5.5}$$

where $\hat{S} = (S - S_{lr})/\left(1 - S_{lr} - S_{gr}\right)$, and m_g is a multiplying factor for the enhanced gas permeability (Corey, 1954). The residual saturations S_{lr} and S_{gr} are provided to limit the mobility of the respective phase, i.e., both liquid and gaseous phases mobility can vary only in the range of $S = \left[S_{lr}, 1 - S_{gr}\right]$.

For matching the abrupt gas breakthrough occurred at a gas pressure of about 10 MPa in the gas injection chamber, the concept of an effective gas entry pressure, P_{ge}, was applied according to Senger and Marschall (2008). The concept is illustrated in Figure 5-4, where a residual gas saturation of S_{gr} = 0.11, which is a parameter of the gas relative permeability function) corresponds to the effective gas entry pressure P_{ge} = 10 MPa.

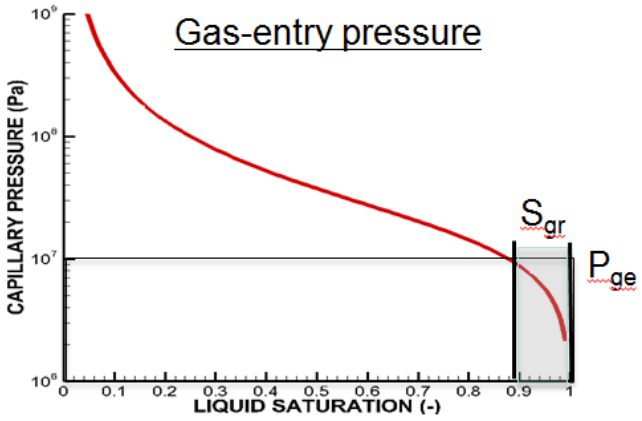

Figure 5-4. The concept of effective gas entry pressure used for the evaluation of the initial pressure response.

In the current simulations, the intrinsic permeability was set to a fixed value of $k = 3.4\times10^{-21}$ m^2 based on other independent laboratory tests as described in Tamayo-Mas et al. (2021). The gas entry pressure was necessary to prevent any gas migration and pressure changes to occur in the sample until about 60 days, when abrupt increases of sample pressure occurred. The gas permeability can increase more strongly with the gas saturation as well as a result of changes in effective stress. A relation between permeability and effective minimum compressive stress is shown in Figure 5-5 and simulates a fracture flow like behavior in each continuum element. First the permeability of an element is calculated as

$$k_{FC} = k_{matrix} + k_{fracture} = k_{matrix} + \frac{b_h^3}{12d} \tag{5.6}$$

where d is the element size and b_h is hydraulic conducting fracture aperture is calculated as

$$b_h = \frac{b_{h0}}{1+9\left(\frac{\sigma_n - p}{\sigma_{n,ref}}\right)} \tag{5.7}$$

where b_{h0} is a residual permeability maintained even at very high stress, σ_n is the stress normal to fracture plane, p = pore pressure, and $\sigma_{n,\,ref}$ is a reference stress. In this modeling, σ_n is assumed to be equal to the least compressive principal stress, and $\sigma_n - P$ would be the least compressive effective principal stress. The two parameters, bh0 = 2.9×10^{-6} m, and $\sigma_{n,ref} = 0.2\times10^6$ Pa were determined by trial simulations to obtain the best possible match with experimental data.

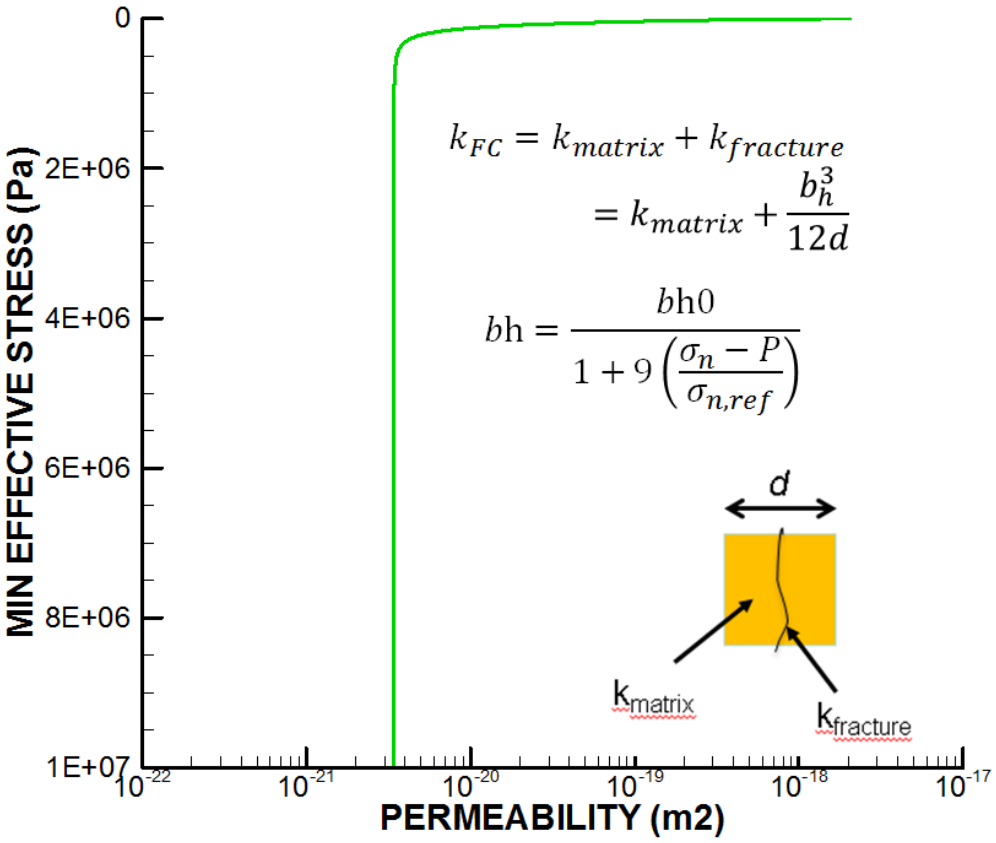

Figure 5-5. Relation between min effective stress and permeability used in numerical modeling.

The simulation results with comparison to measured data are shown in Figures 5-6 to 5-9. The measured abrupt pressure increase within the sample after about 67 days was captured very well in the modeling (Figure 5-6). The subsequent general pressure decline is also captured, though some of the pressure fluctuations at around 80 days are not captured in the modeling.

The abrupt increase in outflow rate and the maximum magnitude is also accurately captured in the modeling (Figure 5-7). The observed subsequent complete shut-down of gas flow is not captured in the modeling, which shows a more gradual decline in gas flow rate.

The general evolution and magnitudes in radial and axial stresses are also modelled quite accurately (Figures 5-8 and 5-9). The modeling shows a bit more uniform stress compared to the data, and the stress decline toward the end is not captured in the modeling. The reason might be the assumption of linear elastic mechanical material model, while bentonite generally shows a non-linear elastic behavior. Another possible reason is that the injection pressure was controlled during the entire injection period, while modeling the actual injection rate and the injection chamber might provide a different behavior during the shut-in.

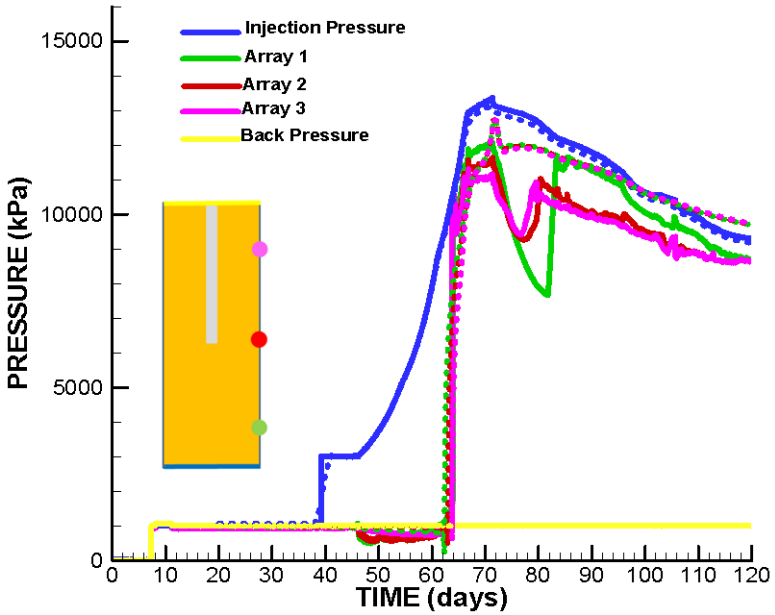

Figure 5-6. 3D TOUGH-FLAC model of cylindrical sample and the results of simulations of pressure.

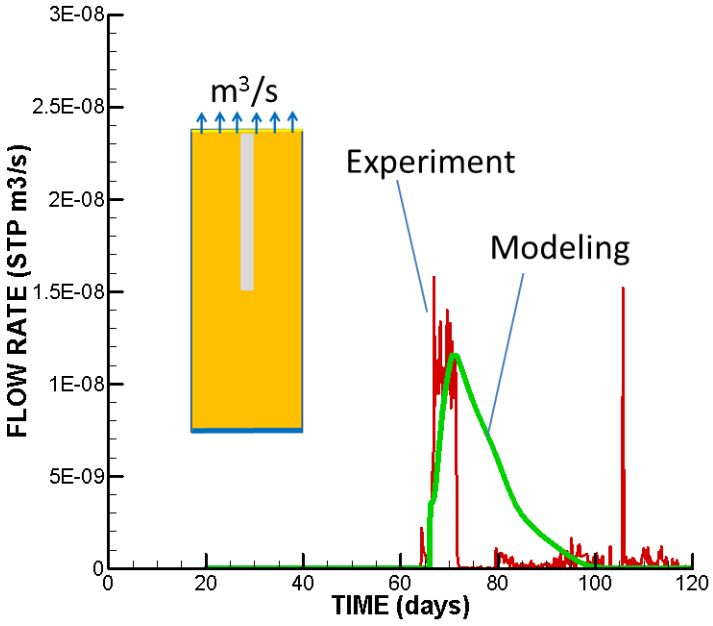

Figure 5-7. Simulated (green line) and measured (red line) gas flow rate out of the sample.

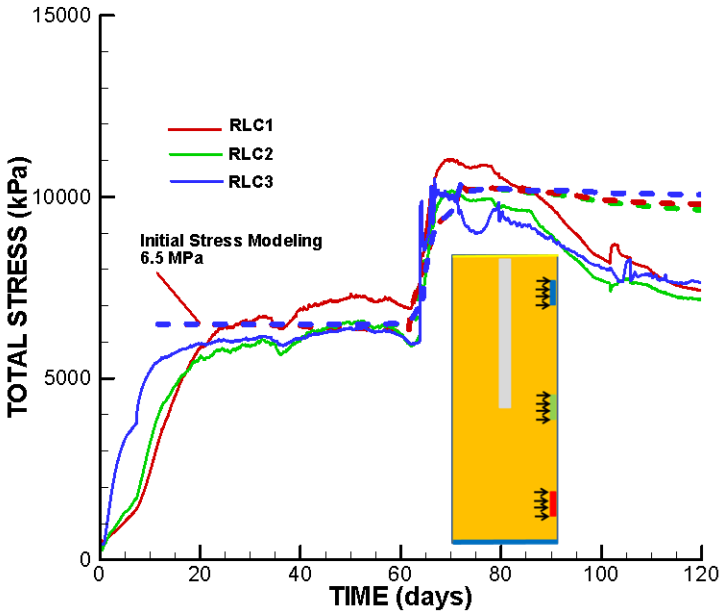

Figure 5-8. Simulated (dashed lines) and measured (solid lines) total radial stress at load cells 1, 2 and 3.

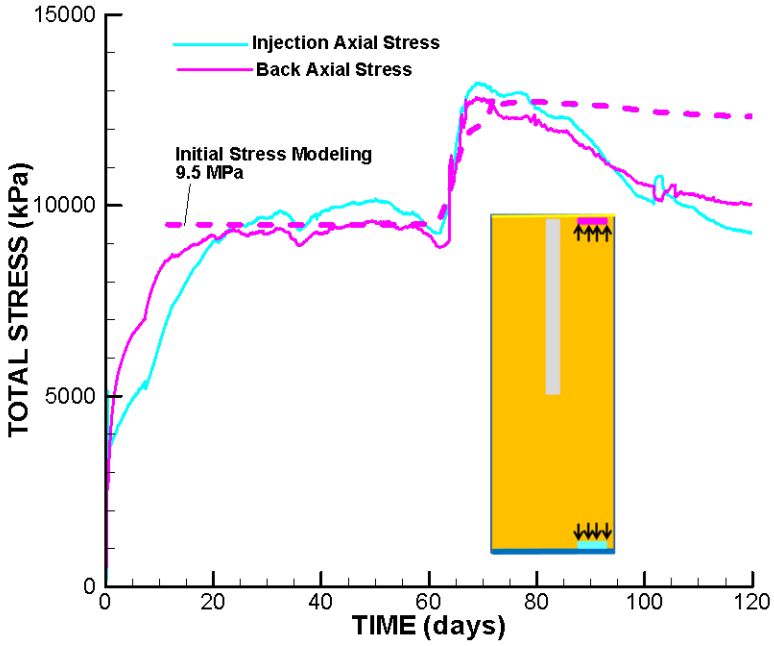

Figure 5-9. Simulated (dashed lines) and measured (solid lines) total axial stress at injection and back ends of the sample.

In summary, the homogeneous material model with simple linear poro-elastic and moisture swelling model, taking into account stress-dependent gas permeability and an effective gas entry pressure, could capture the main features of the experiment, including pressure, stress and flow evolution. The biggest deviation from the data occurred just after 70 seconds, when the experimental gas flow appears to shut-down completely.

5.4 Blind prediction of new gas migration experiment

A brand-new gas migration experiment for a bentonite sample is being conducted by the BGS. The experiment is being conducted on the same type of MX-80 bentonite as that used in the 1D flow experiments and modeling in Section 5.1. In this case gas injection is conducted from a gas injector at the center of the sample as illustrated in Figure 5.10a. Gas flow rate is measured at the outlet filter on the top of the sample. The sample size is 60 mm vertically and 60 mm in diameter. The red arrows in Figure 5.10a indicate the layout of 24 sensors used for measuring total stress. A sample was first hydrated to full saturation before commencing the gas injection. The injection rate is 180 µL/hour of helium gas into an injection chamber with a volume of 250 mL. The outflow filter is kept at a constant pressure of 1 MPa. Before applying the constant injection rate of 180 µL/hour, the gas pressure at the injector was increased to 2 MPa, while the initial fluid pressure in the sample was 1 MPa.

In this case as an initial step the modeling was conducted on a simplified axisymmetric model (Figure 5-10b) in order to investigate how to tread the boundary condition for injecting a constant volumetric rate and to measure outflow through a filter on the top of the sample. The conceptual model for gas migration and the material properties were kept exactly the same as in the previous 1D gas migration modeling. The initial total stress after waster saturation, but before gas injection, was set to 6.5 MPa.

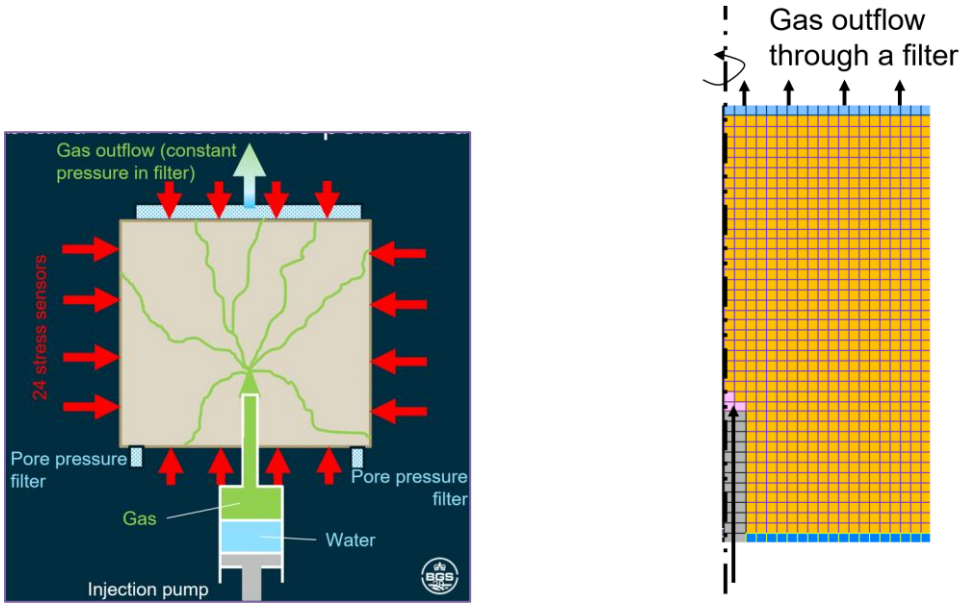

Figure 5-10. Setup and model of the gas migration experiment. (a) Conceptual model from BGS, and (b) axisymmetric numerical model for TOUGH-FLAC simulations.

Figures 5-11a,b present the simulation results of pressure and flow rate as a function of time. At a constant injection rate, the injection pressure increases gradually from the start of the injection at 22 days (Figure 5-11a). At 40 days there is some sign of limited gas breakthrough at the injector. This is indicated in Figure 11b by a slight flow increase at the injector at 40 days. This limited gas breakthrough is also shown in Figure 5-12a with a sharp propagation of gas pressure into the sample. This gas breakthrough also impacts the stress in the sample (Figure 5-12b).

After 50 days, there is a sharp increase in injection rate, and about 5 days thereafter, there is a sharp increase in outflow rate. At the same time, pressure within the sample increases sharply. The gas breakthrough occurred at an injection pressure of about 7.5 MPa. The gas injection rate peaks 6e-9 m^3/s at standard temperature and pressure (STP). The injection rate then declined especially after the injector is shut-in.

These results are preliminary and can serve as an initial model prediction of the gas injection test that has not yet been completed. More data on the actual initial stress in the sample will be released to the modelling teams of the DECOVALEX-2023. The next step in this will be to apply heterogeneous clay properties, but this will require a full 3D model. Within the DECOVALEX-2023 task, we are also planning to test the application of a dual continuum model to better capture the micro- and macro structural scales.

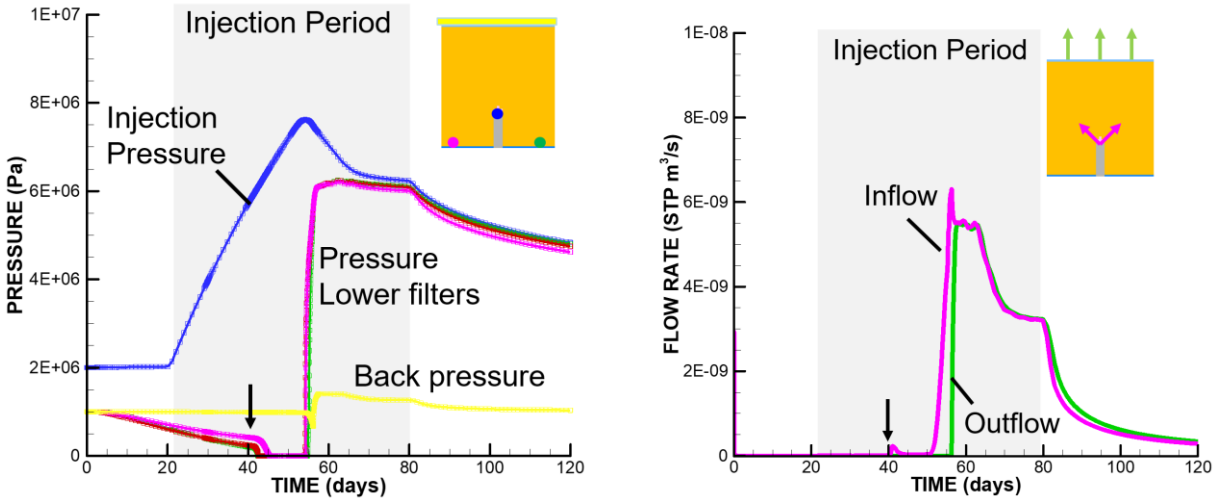

(a) (b)

Figure 5-11. Modeling results of (a) pressure and (b) flow rate evolution during the gas injection test.

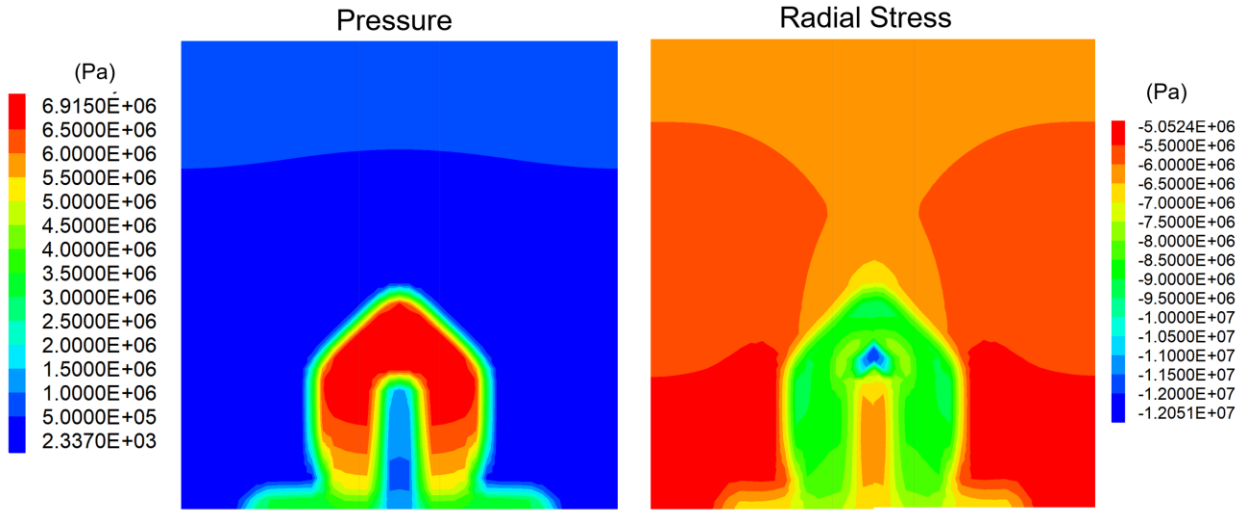

(a) (b)

Figure 5-12. Modeling results of (a) pore pressure and (b) radial stress at 48 hours when there is a partial gas breakthrough at the injector that first occurred at about 40 days.

6. Machine Learning of Fracture Morphology and Mesh Optimization

6.1 Introduction

Based on geometric features, fractures can be categorized into three different scales: discrete thin fractures, rough fractures with certain widths and with asperities (may or may not be filled with minerals), and microscale grain assemblies and asperities (Hu et al., 2017a; Hu and Rutqvist, 2020a, 2020b, 2021). At reservoir scales, fractures often appear in groups, arbitrarily oriented and intersecting with each other, thus forming a network. These fractures are usually very thin (e.g., microns to millimeters) relative to their length (meters). When a single fracture is examined more closely, it is often rough and may be filled with minerals and connected to smaller fractures in the surrounding rock. Zooming into the microscale, a single fracture becomes a rough channel with asperities made up of a number of tightly contacting mineral grains.

Recognizing the geometry of fractures and generating meshes with proper geometric representation are essential first steps in numerical modeling of fractures and rock matrix at any of these aforementioned scales and can be challenging and/or expensive. At the discrete fracture scale, arbitrarily oriented and intersected fractures may lead to a great number of unevenly sized blocks that have many sharp corners. A number of mesh generators have been developed for discrete fracture networks (e.g., the well-known dfnWorks developed by Hyman et al., 2015). However, it is challenging to consider a large number of fractures embedded in rock matrix. At the microscale, these asperities create surfaces that are not smooth. Because of the challenges associated with dynamics of contacts between a number of arbitrarily shaped blocks, only rarely can a mechanical model be applied at this scale (Hu and Rutqvist, 2020b). More widely, fluid flow, transport and/or reaction are often modeled at this scale (Al-Yaarubi et al., 2005; Zou et al., 2015; Steefel, 2019), in which case the most common meshing technique is to use rectangular elements to map the rough fracture channels.

Convolutional neural networks (CNN) model is a deep learning approach that has been widely applied to image recognition (Simonyan and Zisserman, 2015; Babhulgaonkar et al., 2020; Rabbani et al., 2020). When a CNN model is trained to recognize an image, features from the input image are extracted by an image filter (a layer), and this multiple-layer filtered information is forward propagated toward the output layer so as to form a filtered version of the image with original 'content' (e.g., geometry). By combining CNN for content presentation and 'style' presentation of texture information, Gatys et al. (2015) introduced neural style transfer (NST) to create new artworks. This was achieved by optimizing the approximation of a 'content' with texture of a 'style' and by constructing a loss function as a weighted average of the loss function of content and the loss function of style. Since its invention, NST has drawn considerable interest as a new approach for creating artwork artificially. However, this approach has not been applied in science or engineering to the authors' knowledge.

We will make full use of a CNN architecture named U-Net for image recognition and an NST model by combining digital rock fractures that represent 'content' with numerical meshes that represent 'style' to generate and optimize meshes at multiple scales. We will first introduce the U-Net for studying the morphology of a rough fracture at the core scale where fracture asperities are explicitly represented. Then, we will introduce the approaches and the structures that we used for the NST calculation. Finally, we apply the NST to generate new meshes for rough fractures with explicit asperities formed in rock, a network of fractures embedded in rock, and a sand aggregate with multiple grains.

6.2 Approach

6.2.1 Machine Learning and Numerical Modeling

Machine learning (ML) has been an increasingly popular research approach in recent years, and has been applied in disciplines ranging from social science to natural sciences, geosciences (Mital et al., 2020; Dumont et al., 2020; Karpatne et al., 2018), and engineering. The approach benefits from the flexibility and generality of using statistics and algorithms that enable computers to learn without explicitly programming the physics.

When the desired output is given, for example by measurement, synthesis, or results produced by other approaches such as numerical modeling, a general statistical distribution (linear, polynomial, logistic, gaussian, or their combination) can be learned. This is called supervised machine learning. When the desired output is not given, the machine learns the pattern of the data and finds the trend by itself. This is called unsupervised machine learning. Linear and nonlinear data distribution functions lead to continuous solutions, as desired in regression problems. In contrast, logistic regression in combination with a set of discontinuous functions may lead to a number of discontinuous numbers that determine the decision boundaries. This type of problem is categorized as a classification problem.

A typical supervised ML algorithm involves the following steps:

(1) Construct the hypothesis (a guess of the output). These possible hypotheses include the aforementioned linear, polynomial, logistic, gaussian, or a network that combines these functions (known as a neural network)

$$\mathbf{h} = g(\boldsymbol{\theta}^{\mathbf{T}}\mathbf{x}) \tag{6.1}$$

where **h** represents the hypothesis, and **x** is the matrix of the input data with a number of features and a number of examples. **θ** is the vector of weight factors that need to be determined, which function as fitting coefficients of the distribution constrained by the available datasets for a given output.

(2) Construct the cost function, which can be understood as the cost of deviation of a hypothesis from the given output

$$\mathrm{J} = \gamma[\mathrm{f}(\mathbf{h} - \mathbf{y})] \tag{6.2}$$

where the first term *f* is the function of deviation of **h** from given output **y.** For a linear regression problem, it becomes

$$f(\mathbf{h} - \mathbf{y}) = \frac{1}{2}(\mathbf{h} - \mathbf{y})^{\mathrm{T}}(\mathbf{h} - \mathbf{y}) \tag{6.3}$$

If using regularization to enhance convergence, the cost function adds

$$\mathrm{J}_{reg} = \lambda\boldsymbol{\theta}^{\mathbf{T}}\boldsymbol{\theta} \tag{6.4}$$

and the cost function becomes

$$\mathrm{J} = \gamma[\mathrm{f}(\mathbf{h} - \mathbf{y}) + \lambda\boldsymbol{\theta}^{\mathbf{T}}\boldsymbol{\theta}] \tag{6.5}$$

where λ is the penalty factor to prevent overfitting.

Based on Equation (6.2), the solution of each component of **θ** can be found by minimizing the cost function:

$$\theta_j^{k+1} = \theta_j^k - \alpha\frac{\partial \mathrm{J}}{\partial \theta_j^k} \tag{6.6}$$

where superscript *k* refers to the iteration number, the subscript *j* refers to the *j*th feature, and α is the learning rate (or step size).

(4) Repeat steps (1)-(3) until the fitting coefficient vector **θ** reaches convergence. A simplified schematic of machine learning is shown in Figure 6-1.

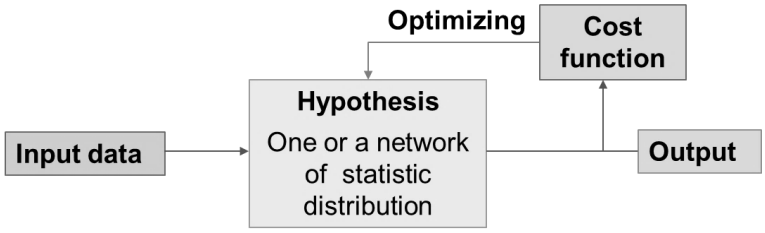

Figure 6-1. Schematic of machine learning.

Based on the features generalized above, the following similarities can be found between machine learning and numerical modeling, as listed in Table 6-1.

Table 6-1. Theoretical comparison between numerical modeling and machine learning.

Numerical modeling	Machine learning
Linear interpolation: $\varphi = \mathbf{w}^{\mathbf{T}}\boldsymbol{\varphi}$ (6.7)	Linear hypothesis: $\mathbf{h} = \boldsymbol{\theta}^{\mathbf{T}}\mathbf{x}$ (6.12)
Higher-order interpolation: $\mathbf{f} = \mathcal{A}(\mathbf{w}^{\mathbf{T}})\mathcal{L}(\boldsymbol{\varphi})$ (6.8)	Neural network: $\mathbf{h} = g(\boldsymbol{\theta}^{\mathbf{T}}\mathbf{a}), \ldots \mathbf{a} = \boldsymbol{\theta}^{\mathbf{T}}\mathbf{x}$ (6.13)
Total potential energy: $\Pi = \beta[D(f)]$ (6.9)	Cost function: $J = \gamma[f(\mathbf{h} - \mathbf{y})]$ (6.2)
Penalty method for boundary constraints: $\Pi_{bc} = \frac{1}{2}\eta(\boldsymbol{\varphi} - \overline{\boldsymbol{\varphi}})^{\mathbf{T}}(\boldsymbol{\varphi} - \overline{\boldsymbol{\varphi}})$ (6.10)	Regularization: $J_{reg} = \lambda\boldsymbol{\theta}^{\mathbf{T}}\boldsymbol{\theta}$ (6.4)
Iteration (e.g., Newton-Raphson iteration): $\varphi_j^{k+1} = \varphi_j^k - \frac{1}{k}R^k / \frac{\partial R^k}{\partial \varphi_j^k}$ (6.11)	Gradient descent: $\theta_j^{k+1} = \theta_j^k - \alpha\frac{\partial J}{\partial \theta_j^k}$ (6.6)

In Equation (6.7), $\mathbf{w}^{\mathbf{T}}$ represents the shape function, $\boldsymbol{\varphi}$ is the field variable at interpolation units, φ is the field variable. Equation (6.7) represents a typical linear interpolation that may be used in different numerical methods such as finite element, finite difference, finite volume, numerical manifold methods. Comparison between these numerical methods in terms of interpolation was made by Hu & Rutqvist (2020a). Similarity between linear interpolation in numerical modeling and linear hypothesis in ML is made explicit if Equations (6.7) and (6.12) are compared.

Equation (6.8) represents higher-order interpolation with a larger number of degrees of freedom (DOFs). These include (1) Formulation 1: increasing the number of interpolation nodes leading to high-order weight functions, and (2) Formulation 2: increasing the order of interpolation units from a constant value while keeping the same weight function (Wang et al., 2016). Comparing Equations (6.7) and (6.13), we find that if function *g* is linear, then this type of hypothesis resembles the second formulation of higher-order interpolation. Equation (6.13) will be explained in more detail in Section 2.2.

Equation (6.9) represents the total potential energy function for maintaining the balance of solid and/or momentum, and/or mass considering all types of boundary constraints (Hu et al., 2017b) for numerical modeling. Similarly, the cost function as expressed in Equation (6.2) represents the cost of deviation between a hypothesis and the given output. If the linear interpolation is based on physical laws, similarities can be further found with the expanded versions of total potential function for numerical modeling and cost function for ML.

In order to apply boundary constraints, the penalty method is often used by giving a large penalty number to penalize deviation from a certain boundary constraint. Similarity between this with the regularization term in the cost function is made explicit if Equations (6.4) and (6.10) are compared.

Finally, in order to solve the equation in numerical modeling, total potential energy is minimized to represent equilibrium. One approach to derive the solution for nonlinear equation is to use Newton iteration as expressed in Equation (6.11). Similarly, gradient descent is a common way to minimize the cost function for machine learning so that the most accurate values of $\boldsymbol{\theta}$ can be gradually learned, while the most accurate hypothesis $\mathbf{h}$ can be achieved for a given set of values $\mathbf{y}$. In this study, because we use a rather deep neural network (i.e., with many layers), the Adam

optimization algorithm as a first-order gradient-based algorithm is applied for optimization (Kingma and Ba, 2015).

To summarize, similarities between numerical modeling and ML can be found if similar interpolation structure are used. The major difference is that in ML the weighting factors **θ** need to be derived for a given **x**. In numerical modeling, **x** needs to be solved and weight factors are typically constructed by shape functions of numerical grids. If the physical meanings of **x** and **θ** are swapped**,** ML can be identical to numerical modeling in terms of constructing the hypothesis, cost function and minimizing the cost function to derive the **θ.** Because of these similarities, computer codes that were designed for ML and numerical modeling may be shared.

Whether ML or deep learning can be applied widely for physical analysis of geosciences depends on two important questions:

(1) If there is a lack of data, can machine learning perform like a numerical model?

(2) What can machine learning do to bridge the fields of experiments and numerical modeling?

The similarity between machine learning and numerical modeling derived in this section provides the theoretical demonstration that machine learning can function like a numerical model. In a recent study by Sirignano and Spiliopoulos (2018), machine learning was trained to solve partial differential equations, and thus functions like a physics solver. However, building on 60 years of experience in the development of numerical models for analyzing physics across temporal and spatial scales, numerical model supervised machine learning could be a promising pathway to integrate the advantages of both.

Between experiments and numerical modeling, there are at least two challenging steps: (1) image processing may require considerable effort when attempted using traditional approaches, and (2) determination of physical properties can be difficult. These challenges can be overcome with the help of machine learning. In addition, machine learning can be easily applied to predict statistical trends and to classify patterns. With the development of CNN, machine learning has been increasingly used in the fields of image processing, but prediction of the dynamic evolution of geometry can be challenging. Thus, ML supervised by experiments and numerical modeling may be a promising approach if there are sufficient datasets.

6.2.2 Convolutional Neural Network for Image Recognition

Deep neural networks make use of multiple layers of different types of functions to establish a highly nonlinear (or discontinuous) propagation of information from the input and output. The general hypothesis of a deep neural network can be expressed as:

$$\begin{cases} \mathbf{y} = \mathbf{a}^{[l]} = g^{[l]}\left(\boldsymbol{\theta}^{[l]^{\mathbf{T}}}\mathbf{a}^{[l-1]}\right) \\ \mathbf{a}^{[l-1]} = g^{[l-1]}(\boldsymbol{\theta}^{[l-1]^{\mathbf{T}}}\mathbf{a}^{[l-2]}) \\ \vdots \\ \mathbf{a}^{[1]} = g^{[1]}\left(\boldsymbol{\theta}^{[1]^{\mathbf{T}}}\mathbf{x}\right) \end{cases} \tag{6.14}$$

where the superscript l refers to the total number of layers of a neural network architecture. In Equation (6.14), the hypothesis may involve a number of layers of linear or nonlinear algebraic transformation functions g in different layers. If l =2 (only two layers), and if g(z)=z, this neural

network is simplified as a linear regression problem; If l =2 and if g is a sigmoid function, this neural network is simplified as a classification problem.

In most cases, however, the purpose of introducing multiple layers is to introduce additional orders for enhanced approximation, which is achieved when multiple layers are combined. These layers include an input layer, several hidden layers and an output layer. Therefore, such enhanced approximation is realized as Equation (6.14), functioning like a propagation from the bottom to the top row. With increased number of layers, the function becomes highly nonlinear. Solving $\boldsymbol{\theta}$ in each layer is challenging. Thus, back-propagation is used to solve $\boldsymbol{\theta}$ from the output layer to the input layer. Embedded in the steps of a typical ML routine, a neural network consists of a forward propagation routine to construct the hypothesis and a back-propagation routine to approximate the $\boldsymbol{\theta}$ until convergence is reached.

In the field of image recognition where images are represented by pixels, the input data are represented as a tensor, i.e., image height x image width x color depth. CNN has been widely used for processing these data and recognizing features. Different types of CNN have been developed to accommodate different types or sizes of data. Figure 6-2 shows a concept of using the CNN that consists of several layers to classify rock matrix and fractures from an image. In the CNN, different layers can be used to realize higher-order approximation and matrix transformation with multiplication of a number of different functions. These layers include convolutional, rectified linear unit (ReLU), normalized exponential (softmax), pooling, and fully connected layers. The structure of the VGG-19 network that is used in this study was introduced by Simonyan and Zisserman (2015).

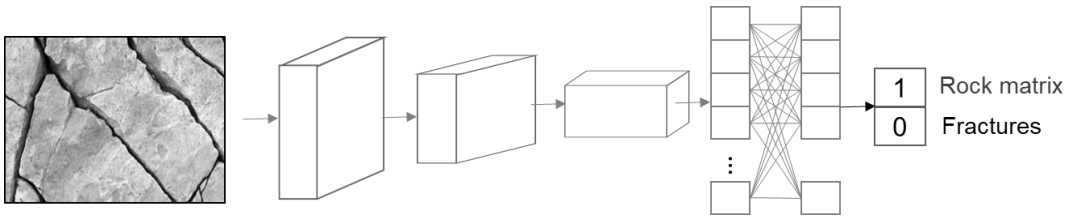

Figure 6-2. CNN for recognizing rock matrix and fractures.

6.2.3 U-Net CNN for Image Segmentation

In order to learn fracture morphology, a simplified end-to-end convolutional neural network based on U-Net architecture was used (Ronneberger et al., 2015). Image segmentation is the process of partitioning a digital image into multiple segments, a set of pixels, based on specified criteria. The granularity level provided by the image segmentation technique can help us better delineate objects of interest in the image (Blaschke et al., 2004). To get a simplified U-Net neural network for image segmentation, the number of convolutional layers and features were reduced at each layer to save memory and computation while still preserving good performance in prediction.

The simplified U-Net used for image segmentation is shown in Figure 6-3, consisting of four stages: convolution, max pooling, up-sampling and again convolution to obtain general information combining localization and contextual information necessary to predict a good segmentation map. Here an input image with a dominant rough fracture with explicit asperities is fed to a U-Net neural network that contains a contracting path to capture context on the left side and a symmetric expanding path that enables precise localization on the right (Wu et al., 2019).

In the left contracting direction, each step contains two convolutional layers followed by a ReLU activation and a max pooling operation with stride 2 (meaning the (dx, dy) for stepping over our input will be (2, 2)) and will not overlap regions for down-sampling. ReLU is a rectified linear activation function responsible for transforming the summed weighted input from the node into the activation of the node (Rezatofighi et al., 2019). The max pooling operation is used for down-sampling to reduce the size of the image for dimensionality-reduction. Every step in the right expanding path contains an up-sampling process and two convolutional layers followed by a ReLU activation. The need for an up-sampling operation is to convert a low-resolution image to a high-resolution image to recover the information lost during max pooling. The implementation of U-Net architecture is done using PyTorch, and the final output image is the predicted mask obtained using image segmentation.

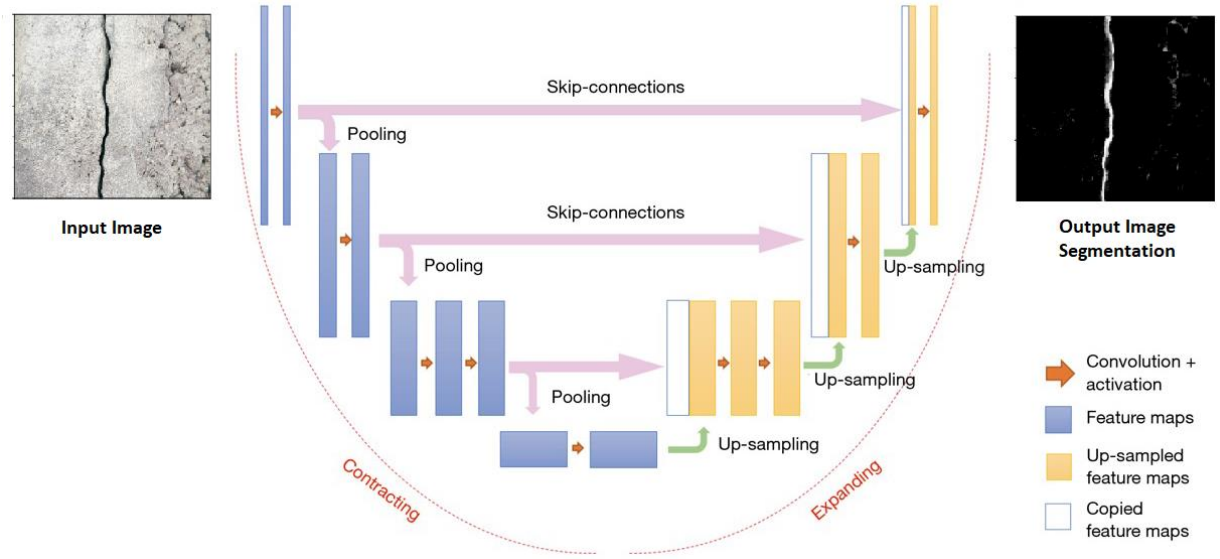

Figure 6-3. A simplified end-to-end CNN U-Net for Image Segmentation.

6.2.4 Neural Style Transfer

Based on image recognition, neural style transfer (NST) was introduced by Gatys et al. (2015) to create new artworks by combining CNN for content presentation with style presentation of texture information. Thus, the NST generates images that match the content and style of the content image and style image, respectively. This is achieved by constructing a total cost function J consisting of weighted average of the cost function associated with the content cost function and the style cost function:

$$\mathrm{J} = \alpha J_{content}(R, C) + \beta J_{style}(R, S) \tag{6.15}$$

where R, C and S represent functions associated with generated (resulted), content and style images. The weighting factors α and β are user defined.

In order to approximate the content image, the cost function of a certain selected hidden layer is:

$$J_{content}(R, C) = \frac{1}{4hwn}\Sigma(\mathbf{a}^{(C)} - \mathbf{a}^{(R)})^2 \tag{6.16}$$

where h, w and n mean height, width and the total number of channels of this hidden layer, respectively. This hidden layer therefore has a function (activation) **a** with a dimension of $h \times w \times n$.

In order to properly represent the 'style' in an image, the inner product (that projects one vector on another to represent similarity) is used to define the style matrix:

$$\mathbf{G} = \mathbf{a}\mathbf{a}^{\mathrm{T}} \tag{6.17}$$

The cost function for the style is the weighted average of cost function of each layer:

$$J_{style}(R,S) = \frac{1}{4h^2w^2n^2}\sum_{k=1}^{l}\varsigma_k \sum_{j=1}^{n(k)}\sum_{i=1}^{n(k)}(G_{ij}^{(S,k)} - G_{ij}^{(R,k)})^2 \tag{6.18}$$

where ς_k is the weighting factor of layer k, satisfying $\sum_{k=1}^{l}\varsigma_k = 1$. For simplicity, evenly distributed weighting factors among different layers can be used. With this specially constructed cost function involving both content and style images, we are able to generate new images that keeps the content of the content image and the style of the style image.

Considering that the VGG-19 model (Simonyan and Zisserman, 2015) was trained on very large image datasets, we applied the 19-layer VGG network to conduct our NST simulation for mesh generation. In this network, the shallower layers are designed to detect lower-level features such as edges and corners. The deeper layers are used to detect higher-level features such as rock, fractures, or other mineral fillings. The structure and schematics of the neural style transfer model for mesh generation are shown in Figure 6-3, in which a 19-layer VGG network is included in the middle. As shown in Figure 6-4, because this approach for generating mesh is based on machine learning the content of the rock images and learning the style of the mesh, the only data that is required for the mesh generation are the image of the content (rock image) and the image of the mesh style. The learning process is indeed an optimization process from an initial generated noisy image to the final generated image that achieves the minimized total cost, and thus has the best approximation to the content of the rock image with the mesh style. Optimization of the total cost function is done by using the Adam optimization algorithm (Kingma and Ba, 2015).

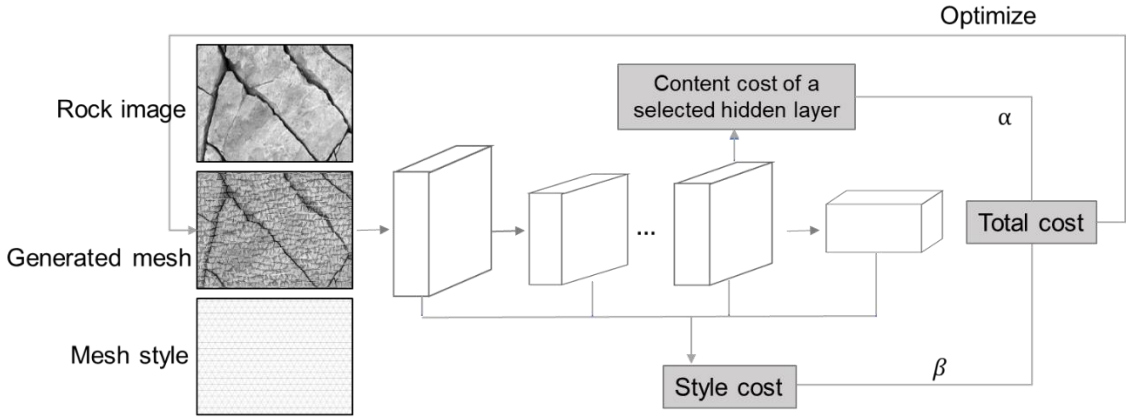

Figure 6-4. Neural style transfer model for mesh generation from a rock image.

6.3 Examples and Results

We first applied the CNN model to learn fracture morphology and recognize fractures from images. Then, we used the NST model with the 19-layer network to generate numerical meshes for various systems of interest in the geosciences. We extracted images of rock fractures at different scales to provide the contents for the examples. These included an image that contains several dominant and rough fractures, and an image that contains a network of densely intersecting discrete fractures. In order to understand how the NST works and to avoid additional complexity that is introduced by the complexity of the style, we used uniform triangles in terms of size, shape and distribution as the style images to explore this use of ML for mesh generation.

6.3.1 Machine Learning of Fracture Morphology from Rock Images

We applied the CNN model to recognize fractures from the image at the core scale. We trained the CNN model using 60 images containing different crack patterns and validated the model using other 15 images. All the images were resized to 600 × 600 pixels and fed to the neural network in batches with each batch of three images, due to GPU memory limitation. We used the Adam method (Kingma et al., 2014) to optimize the network parameters with well-suited learning rate and train the network with a predefined number of epochs, where all the 60 training images are processed at each epoch. The model was trained on RGB and grayscale images with the estimation of average loss for every 50 epochs.

As we validated the trained CNN model on the validation set, the best inference obtained for an RGB input image based on prediction on the grayscale model with provided ground truth is shown in Figure 6-5, where ground truth refers to the accuracy of the training set's classification for CNN.

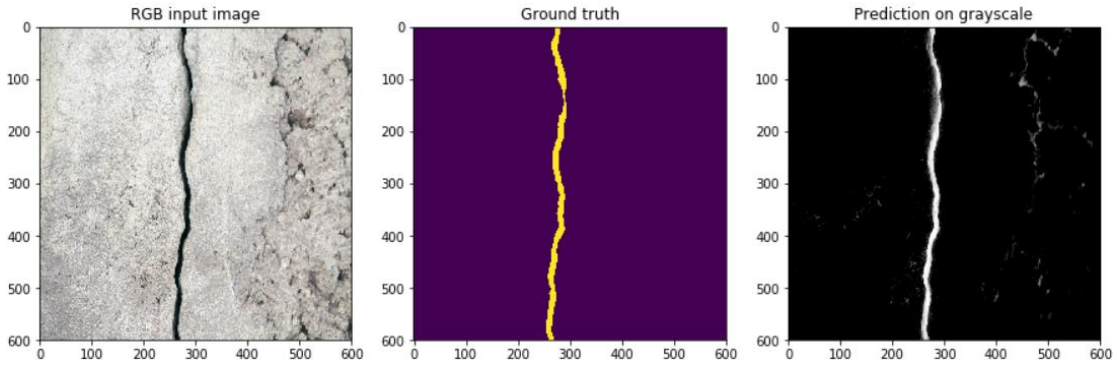

Figure 6-5. Inference for an RGB input image based on Prediction on grayscale model with provided ground truth.

To evaluate our model, we used the dice score or mean Intersection over Union (IoU) as a performance metric. The dice score or mean IoU is estimated between the model inference and the predicted mask. The IoU for a proposed set and a true set of object pixels is calculated as (Rezatofighi et al., 2019):

$$IoU = \frac{target \cap prediction}{target \cup prediction} = \frac{\quad}{\quad} \tag{6-19}$$

The dice score obtained for the prediction result in Figure 6-5 is 72.54% based on the model's inference and the predicted mask.

6.3.2 Mesh generation for rough fractures using NST

We applied the NST algorithm to generate meshes for an image of rock containing several dominant and rough fractures. We tried two different densities of triangles as the style. Figure 6-6 shows the results. As can be noted, the NST learned the boundaries of rock and fractures from the rock image and applied the triangular styles to the images that were recognized. The sizes of triangles in the generated mesh are the same as in the style image. With the size and shape of the triangles kept in the generated image, the algorithm rearranged the orientations of the triangles to accommodate the fractures and rock matrix. Comparing the generated meshes with coarse triangle style (top) and dense triangle style (bottom), we can see that the algorithm is 'smart' enough to distribute triangular grid cells along fractures even with coarse triangles.

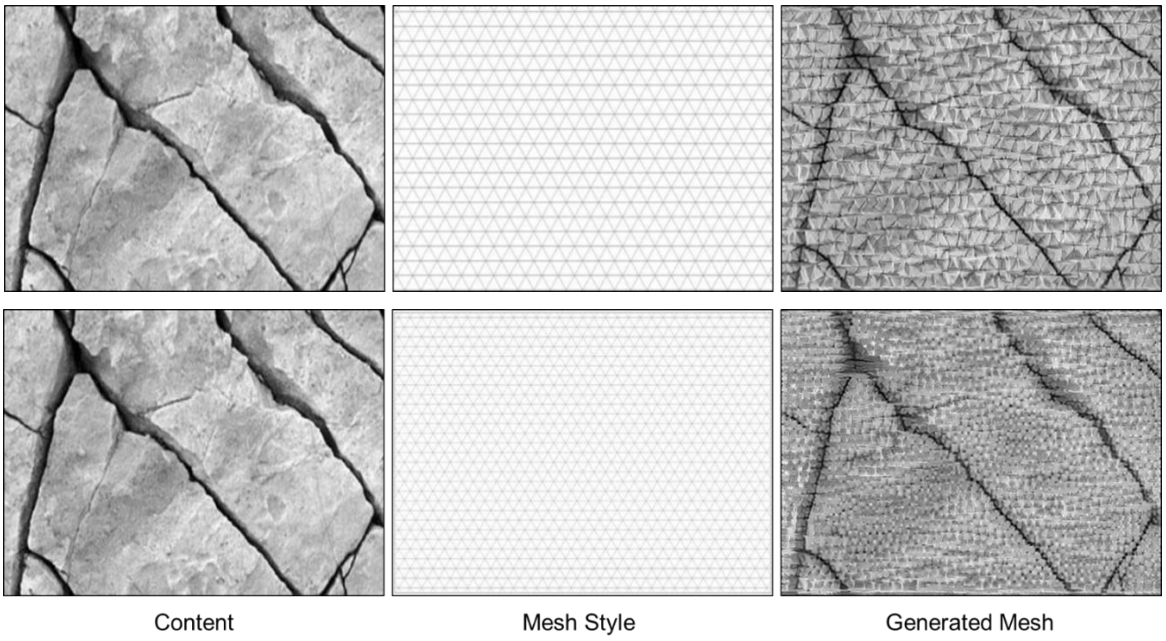

Figure 6-6. NST generated mesh for rough fractures: coarser (top) and denser (bottom) meshes.

However, the mesh that was generated using the denser meshing style was not clear, suggesting insufficient resolution of the style image. In order resolve this issue, we used a new style image with the same density of the mesh but with thicker mesh lines. The result is shown in Figure 6-6. Despite that some elements are not perfectly triangular in Figure 6-7 due to non-triangular meshes on the boundaries in the style image, we can see that the mesh that is generated with the thick-line style becomes clearer than the one that is shown in Figure 6-6.

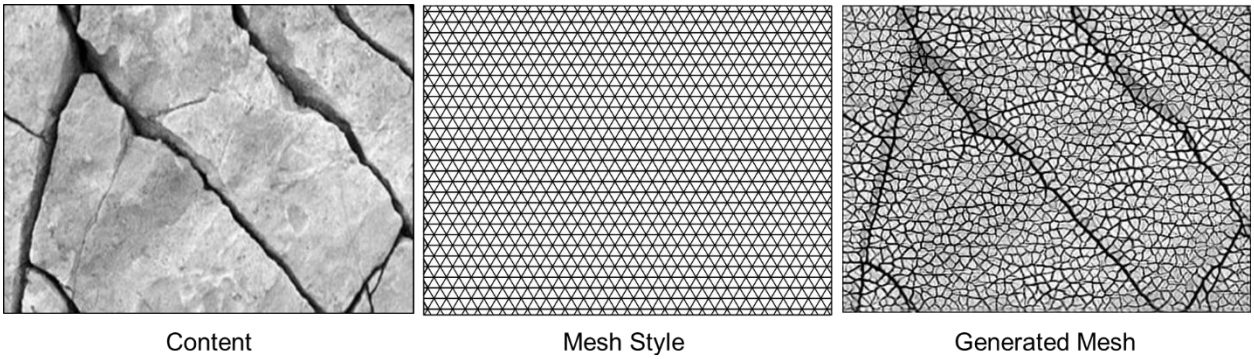

Figure 6-7. NST generated mesh for rough fractures with denser meshes and thicker mesh lines.

In order to analyze the differences caused by the thickness of the lines in the mesh style, we plot the changes of cost functions over iterations in Figure 6-8. On the left, we show the changes of total cost, content cost and style cost corresponding to the thin-line style (Figure 6-6). On the right, the changes are corresponding to the thick-line mesh style (Figure 6-7). Both images are 400 pixels by 300 pixels- such low resolution is used for only demonstrating the approach with smaller computational effort. For both cases, we used $\alpha = 10, \beta = 40$. By comparing the changes, we can see larger content and style costs for the thick-line style, leading to a higher total cost. However, with increased number of iterations, a larger decrease can be found in the thick-line style. The total cost does not reach a convergence value (a larger than zero rate) until 200 iterations for the thin-line style. However, the total cost reaches convergence after 150 iterations.

From this example we see that because the generation is automatic despite the complexity of the geometric features, this new NST technique can potentially save a great deal of effort for mesh generation and optimization by achieving a good balance between the density of the mesh and the presentation of the geometric features. From the comparison between the low-resolution thin-line and high-resolution thick-line style images, we show that it is important to provide a good balance of resolutions between the content and the style images.

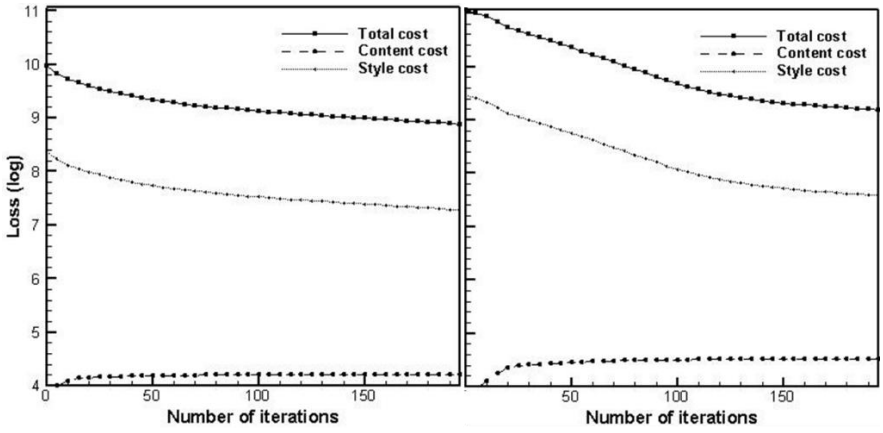

Figure 6-8. Evolution of cost functions with iterations using thin-line (left) and thick-line mesh styles (right).

6.3.3 Mesh generation for discrete fractures using NST

We applied the NST algorithm for mesh generation from a rock image with a dense intersecting fracture network (Figure 6-9). This image contains more than 100 densely intersected fractures, including a long and sinuous fracture running from the left to the bottom of the domain. We used the coarse triangles as style. It can be observed that the NST model captures all the fractures and arranged the triangles along the intersecting fractures. In particular, if we examine the long and rough fractures, we see that all the non-smooth line segments are well represented in the generated mesh.

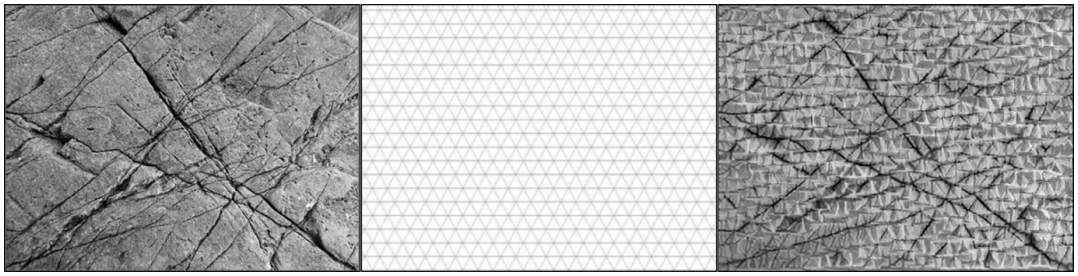

Figure 6-9. NST generated mesh for discrete fractures.

6.4 Summary and Perspectives

In this study, we explored applications of machine learning at two scales by using images and results from laboratory experiments. First, we used U-Net based convolutional neural network (CNN) for studying the morphology of a rough fracture at the core scale where fracture asperities are explicitly represented. We show a preliminary result of CNN prediction of the rough fracture. The dice score of 72.54% suggests the accuracy of the CNN model is acceptable.

Then we made use of neural style transfer (NST) by combining digital rock fractures at multiple scales that represent ‘content’ with numerical meshes that represent ‘style.’ We used a 19-layer VGG network to conduct our NST simulations, where the shallower layers are designed to detect lower-level features (such as edges, corners) and the deeper layers are used to detect higher-level features such as rock, fractures, or other mineral fillings. By optimizing the cost function to achieve approximation to represent both the content and the style, numerical meshes were generated and optimized.

We applied two different densities of triangles as style images to a rock sample with rough fractures. By using NST, we can generate a rather coarse mesh with the coarse triangle style. We also applied the NST to generate meshes for discrete fractures. Good representation of the geometric features with a rather coarse triangle style was achieved in both examples. From the comparison between the low-resolution and high-resolution style images, we show that it is important to provide a good balance of resolutions between the content and the style images. Based on the examples, we show that this new NST approach for generation mesh is automatic. This new approach can potentially make mesh generation and optimization much more efficient, with the result that a good balance between the density of the mesh and the presentation of the geometric features can be achieved. Because the mesh generation routine is automatic, the NST technique is very promising for application of simple mesh patterns (e.g., evenly sized or adaptively refined triangles, rectangles, spheres) to generate and optimize meshes for complex geometric features in the geosciences.

In FY21, the following two articles have been published:

- ✓ Babhulgaonkar S, Hu M, Luu K, Derakhshandeh Z, Rutqvist J. Machine learning of fracture morphology and growth in geological media: Preliminary study. 2nd International Conference on Coupled Processes in Fractured Geological Media: Observation, Modeling, and Application (CouFrac) 2020, Seoul, Korea. (Based on the presentation by Babhulgaonkar et al. (2020) at the 2nd International Conference on Coupled Processes in Fractured Geological Media: Observation, Modeling, and Application (CouFrac) based on the work of learning fracturing morphology by using the CNN model).

  Hu M, Rutqvist J, Steefel CI. Mesh Generation and Optimization from Digital Rock Fractures Based on Neural Style Transfer. Journal of Rock Mechanics and Geotechnical Engineering 2021. https://doi.org/10.1016/j.jrmge.2021.02.002

In FY22, we will extend this work to the following activities:

- ➢ We will apply CNN model to predict the growth of wing cracks by using experimental data;
- ➢ We will use the NST model to explore adaptive mesh refinement with non-evenly sized triangles/rectangles as styles;
- ➢ We will combine the NST model with 3D digital rock images (if available, and data from images is sufficient) to overcome the challenges associated with 3D mesh generation.

7. Modeling of Discrete Fractures in Argillite Rocks Based on the Numerical Maniford Method

7.1 Introduction

Models that explicitly account for discrete fractures can be categorized depending on the geometric representation of the fractures. For modeling mechanics of fractures, there are two types of models: *n*-dimensional solid element models (Rutqvist et al., 2009), and discontinuous interface models where fractures are modeled as interfaces between discontinuous rock blocks (Lisjak et al., 2016). The *n*-dimensional solid element models (Rutqvist et al., 2009) are appropriate for representing fractures with unignorably apertures, but when fracture apertures are much smaller than fracture lengths, the use of *n*-dimensional solid elements becomes computationally expensive. By comparison, the discontinuous mechanical interface model for discrete fractures have been proven to be promising for analyzing coupled HM processes in fractured porous media where fracture contact dynamics (dynamic changes of contact locations and contact states) can be rigorously considered (Hu et al., 2016, 2017b, 2020a).

The numerical manifold method (NMM, Shi, 1992, 1996), based on the theory of mathematical manifolds is a promising method for analyzing both continuous and discontinuous media. In the past two decades, NMM has been successfully applied to analyze mechanical processes in geologic media involving higher-order interpolation, fracture propagation, wave propagation across fractured media, slope stability, fracturing of sandstone and microscale mechanics of deformable geomaterials with dynamic contacts (Hu & Rutqvist, 2020b). For fluid flow analysis, NMM also has been successfully applied for analyzing moving interface problems such as free surface flow (Wang et al., 2014, 2016). For analyzing flow and fully coupled processes of

fractured porous media at different scales, the authors have previously developed a series of models (Hu et al. 2016, 2017a, 2017b, 2020a).

We will make use of the developed NMM for discrete fractures to analyze stability and evolution of excavation damage zone in response to excavation and heat that is generated by the nuclear waste in bedded argillite rock formation. We will first briefly introduce the fundamentals of NMM. Then we will describe the model for discrete fractures, including mathematical and geometry representation and numerical implementation. We will show an example of coupled hydro-mechanical processes in a discrete fractured rock from a real image. Then we will analyze mechanical dynamics of a tunnel and a damage zone in bedded argillite rock subjected to excavation and heating.

7.2 Numerical Manifold Method

The NMM (Shi, 1992) is based on the concept of "manifold" in topology. In NMM, independent meshes for interpolation and integration are defined separately. Based on this approach, an initially one-time generated, non-conforming mesh (not necessarily conforming with the physical boundaries) can be used and flexible local approximations can be constructed and averaged to establish global approximations for both continuous and discontinuous analysis.

In NMM, independent mathematical and physical covers are defined. A mathematical cover is a set of connected patches that cover the entire material domain. For example, we can use a quadrilateral patch, a circular patch, or a rectangular patch as a mathematical cover (such as the A, B, C in Figure 7-1). Features such as density and shape of these mathematical patches define the precision of the interpolation. The physical patches are simulated using mathematical patches divided by boundaries and discontinuities, defining the integration fields. The union of all the physical patches forms a physical cover. For example, physical patch C is the entire model domain, while physical patch B is divided from mathematical patch B by boundaries. Physical patch A (divided from mathematical patch A by boundaries) is further divided into physical patches A_1 and A_2 by the inner discontinuity. The overlapping areas by multiple physical patches are defined as elements. As a result, the model domain Ω is discretized into five elements: A_1BC (the overlap of physical patches A_1, B and C), A_1C, A_2C, BC, and C. From Figure 7-1, we can see that the shape of the mathematical patches can be arbitrary; the relative location of the mathematical patches to the model domain can also be arbitrary (only if satisfying $\Omega \subset AUBUC$), and the number of physical patches on each element can be arbitrary.

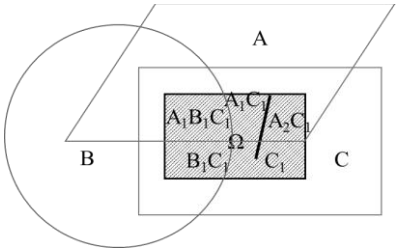

Figure 7-1. NMM mathematical and physical meshes.

On each physical patch, a local function is assigned, such as one that is constant, one that is linear, or any function that is able to capture the behavior of the solution on the patch. The weighted average of the local patch functions forms the global approximation. For example, if

using linear local functions, we can construct a global second-order approximation (Figure 7-2a, Wang et al., 2016). If using a local function with a jump of the first derivative, we can simulate a material interface crossing patches and elements (Figure 7-2b, Hu et al., 2015b). Generally, using discontinuous local functions, we can simulate fractures (Figure 7-2c, Hu et al., 2016, 2017b). With this dual-mesh concept, the NMM is capable of simulating both continuum and discontinuum with accurate geometric representation and flexible numerical approximation. With the advantages of dual-mesh concept, NMM also has been successfully applied to analyzing moving interface problems such as free surface flow (Wang et al., 2014, 2016).

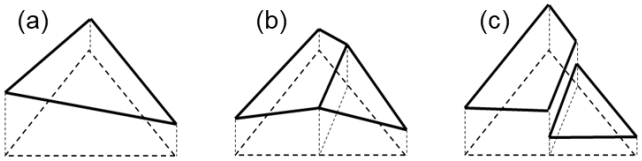

Figure 7-2. Flexible choice of local approximation functions: (a) linear function (Wang et al., 2016), (b) a jump junction for a weak discontinuity (Hu et al., 2015b), (c) a discontinuous function for a fracture (Hu et al., 2016, 2017b).

NMM, with the concept of global approximation can be related to other numerical methods as shown in Figure 7-3. Using a bilinear weight function on rectangles with a constant local function, NMM simplifies to the finite element method. Using a piecewise linear weight function in each direction with a constant local function, NMM simplifies to the finite volume method (Hu and Rutqvist, 2020c). Using a constant weight function with a constant local function, NMM simplifies to the discrete element method. Using a constant weight function with a linear patch function (resulting in a notable difference from DEM with constant patch function), NMM simplifies to the DDA. Here we do not attempt to compare all aspects of numerical methods including (1) interpolation/approximation, (2) construction of global equilibrium (transforming differential to integral equations), (3) approaches of integration, and (4) solving of linear or nonlinear global equations. We only compare aspect (1), i.e., approximation/interpolation as it defines fundamentals of a numerical method. Overall, the NMM provides a flexible and general approach to include continuous and discontinuous methods in a unified form.

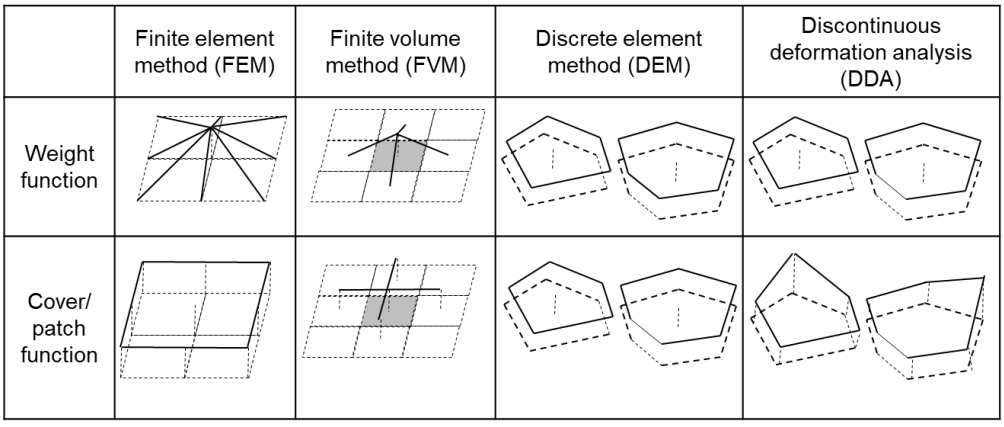

Figure 7-3. Relating NMM to other numerical methods.

In this study, constant patch functions and linear weight functions composed of shape functions of math triangular meshes are used to approximate temperature, fluid pressure and displacements, which are generally expressed as follows:

$$\varphi = \mathbf{w}^{\mathbf{T}}\boldsymbol{\varphi}_{\mathbf{pc}} \tag{7.1}$$

where φ, $\mathbf{w}$ and $\boldsymbol{\varphi}_{\mathbf{pc}}$ are field variables (such as hydraulic head or fluid pressure and displacements), weight function and physical patch functions.

7.3 Modeling Fracture Dynamics Based on NMM

7.3.1 Mathematical description of Dynamic Contacts of Fractures

The mechanical state of a fracture is quite complicated. A fracture may have several segments and each of the segment could be open, bonded, or sliding, as shown in Figure 7-4. The contact state is impacted by fluid flow and mechanical deformation, and may be dynamically changing. For the mechanics, these three states have different boundary constraints.

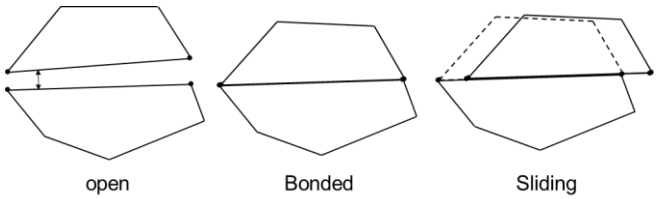

Figure 7-4. Mechanical states of each segment of a fracture in networks: open, bonded and sliding.

When the segment of a fracture is open, we consider that it has linear constitutive behavior, described as:

$$\delta\boldsymbol{\sigma}'_{\boldsymbol{f}} = \mathbf{k}_{\boldsymbol{f}}\left[\!\left[\mathbf{u}_{\boldsymbol{f}}\right]\!\right] \tag{7.2}$$

where $\boldsymbol{\sigma}'_{\boldsymbol{f}}$ denotes a tensor of effective stress in both normal and tangential directions of a segment of a fracture, $\mathbf{k}_{\boldsymbol{f}}$ is the stiffness tensor of the segment, and $\left[\!\left[\mathbf{u}_{\boldsymbol{f}}\right]\!\right]$ is the jump of displacements in both normal and tangential directions of the fracture segment.

When a segment of a fracture is bonded, the distance between the two sides of the segment should be zero, satisfying

$$\mathbf{d}_{\boldsymbol{f}} = \mathbf{0} \tag{7.3}$$

where $\mathbf{d}_{\boldsymbol{f}}$ is the vector of distance, including the normal distance $\mathrm{d}_{f,n}$ between the two surfaces of the fracture segment**,** and relative distance $\mathrm{d}_{f,s}$ along the two surfaces. $\mathbf{d}_{\boldsymbol{f}}$ is calculated by accounting for original distances, and the relative displacements of the two surfaces while they are moving and deforming.

When a segment of a fracture is sliding, Coulomb's law of friction is satisfied in the tangential direction, while the normal distance between the two surfaces of the fracture segment should be zero

$$F_f = F_n'\tan\varphi\,\mathrm{sgn}\left(\mathrm{d}_{f,s}\right) \cap \mathrm{d}_{f,n} = 0 \tag{7.4}$$

So far, we have described two interfaces (i.e., a fracture segment as a contact pair) in open, bonded and sliding contact states. In dynamic conditions, these contact states may be changed as follows. If two interfaces were separated, but become bonded later, constraints in Equation (7.3) should be added. If a fracture segment was open, but then it is in sliding state, constraints in Equation (7.4) should be added.

If two interfaces were bonded but open later, we need to consider one condition: in order to break the bonds, the effective force in the direction normal to the contacting face $\boldsymbol{F_n'}$ needs to be larger than the force associated with the tensile strength $\boldsymbol{T}$. This criterion for separating two contacting faces in the direction normal to their contact face can be expressed as

$$\boldsymbol{F_n' > T} \tag{7.5}$$

If Equation (7.5) is satisfied, the two contact faces are no longer in contact, therefore the constraints in Equation (7.3) should be removed.

If two interfaces were bonded but transfer to a sliding state, we need to consider one condition: in order to initiate sliding, the force in the direction of contacting face $\boldsymbol{F_s}$ needs to be larger than the shear strength $\boldsymbol{S}$. The shear strength usually consists of frictional force (satisfying Coulomb's law of friction) and cohesive force $\boldsymbol{F_{cohe}}$. This criterial for shearing two bonded faces in the direction along their contact faces can be expressed as

$$\boldsymbol{F_s > S = F_n'}\tan\varphi' + \boldsymbol{F_{cohe}} \tag{7.6}$$

where φ' is the internal friction angle. If Equation (7.6) is satisfied, the two faces are transferred from bonded to sliding state. Comparing Equations (7.3) and (7.4) we find that the constraint in the direction normal to contacting face should be retained, while in the sliding direction, the constraint needs to be changed.

If two interfaces slide on each other but then become separated, constraints in Equation (7.4) should be removed. If they become bonded, the constraints should be modified in the direction of the contacting face so that no relative shear displacement will occur.

Thus, using Equations (7.2)-(7.6), we are able to describe the three different contact states of two contact faces, dynamic changes of these contact states, and criteria that need to be satisfied for changes of the contact states- i.e., the threshold of tensile or shear failure along interfaces.

7.3.2 Geometric Representation of Discrete Fractures in NMM

In order to explicitly simulate discrete fractures, we need to geometrically represent both fractures and rock matrix. In NMM, we use a triangular mathematical mesh to overlap the entire simulation domain. Once the mathematical mesh is generated, we can use the same tree-cutting algorithm (Shi, 1992; Hu et al., 2017b) to generate the physical covers and elements, divided by fractures and boundaries, considering locations of triangle edges. Figure 7-5 shows different meshes for fractured porous rock domains with 20, 60 and 150 fractures. The triangular mathematical meshes are independent of the fracture geometry. Indeed, fractures and boundaries divide mathematical meshes into arbitrarily shaped physical covers and elements. By using two coincided lines to represent a fracture, all fractures are accounted for in the calculation, including isolated fractures that do not intersect with other fractures but where their interaction with the

rock matrix cannot be ignored. It is also interesting to note that with the tree cutting algorithm we are readily able to model cases of fluid flow in porous media with sealed fractures.

Corresponding to the mechanical states of fractures described by Equations (7.2)-(7.4), each fracture is discretized into several line segments and these segments may have different contact states. Thus, it is possible to consider complicated behavior such as shear dilation or uneven opening of a fracture. And the density of fracture discretization is consistent with the global meshing density (shown in Figure 7-5), which can be selected flexibly.

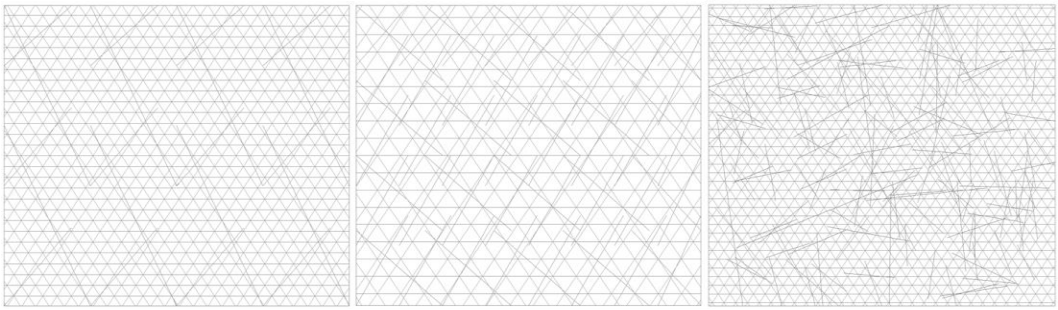

Figure 7-5. NMM mesh generated for fractured porous rock with (a) 20, (b) 60, and (c) 150 fractures

An important issue for calculation of discrete fractures is how to simulate intersections of fractures. Figure 7-6 demonstrates a geometric representation of two intersecting fractures, which also intersect with a triangular mathematical mesh. Figure 7-6 illustrates that two intersecting fractures divide the triangle into four different parts (A, B, C, D). Then modeling of fluid flow and contact states (satisfying constraints described by Equations (7.2)-(7.4)) will be performed taking into account four pairs of parallel interfaces (interfaces between A and B, C and D, B and C, and A and D) to account for the opening, bonded and sliding states of the surfaces of each fracture.

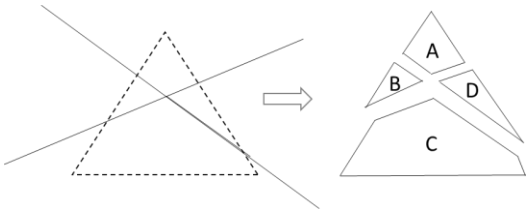

Figure 7-6. Geometric representation of an element with one intersection by two fractures.

Fractures in open and bonded states or alteration between these two states are easier to simulate because this does not require changes of contact pairs. A concept of a zero-dimensional fracture model was proposed by Hu et al. (2016), and can be used to simulate discrete fracture networks. Zero-dimensional fracture model assumes that a fracture is approximated by two surfaces being initially parallel, but these surfaces may become non-parallel after deformation and motion, or opening of the fracture caused by fluid pressure. This capability is included in the algorithm.

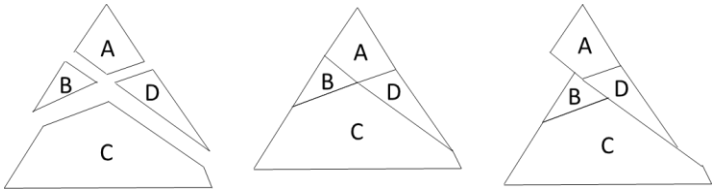

Figure 7-7. Geometric representation of open, bonded and sliding contact states for elements divided by intersecting fractures.

A significant challenge for modeling coupled processes in fracture networks is to simulate shearing along fractures, as this leads to dynamic changes of contacts between different elements. As shown in Figure 7-7, when the four blocks A, B, C, D in contact (when the fractures are completely bonded), the contact pairs are A and B, B and C, C and D, and A and D. But when sliding (slip) occurs at one of the fractures, the contact pairs become A and B, B and C, B and D, C and D, D and A. By using a rigorous contact algorithm that updates contact pairs each time step, sliding along fractures can be rigorously and explicitly represented.

The zero-dimensional fracture model is distinct from zero-thickness models, as the zero-dimensional model considers the thickness of a fracture and its change under deformation. With no need to introduce additional DOFs for fractures, such an approach is very flexible to model existing and initiated fractures as well as shearing and re-opening of fractures.

7.3.3 Numerical Implementation in NMM

For calculation of the contact between two fracture surfaces, there are different potential energy terms associated with different contact states described in Equations (7.2)-(7.4).

When a fracture segment is open, the linear fracture constitutive behavior described as Equation (7.2) is represented by its corresponding strain energy

$$\Pi_{f,open} = \int \boldsymbol{\sigma}_{\boldsymbol{f}}' \, d\varepsilon_f \, d\Omega = \frac{1}{2} \int \left[\!\left[\mathbf{u}_{\boldsymbol{f}}\right]\!\right]^{\mathrm{T}} \mathbf{k}_{\boldsymbol{f}} \left[\!\left[\mathbf{u}_{\boldsymbol{f}}\right]\!\right] ds \tag{7.7}$$

When a segment of a fracture is bonded, the continuity of relative distance described as Equation (7.3) is enforced by using the penalty method

$$\Pi_{f,closed} = \frac{1}{2} \mathbf{d}_{\boldsymbol{f}}^{\mathbf{T}} \mathbf{g}_{\boldsymbol{f}} \mathbf{d}_{\boldsymbol{f}} \tag{7.8}$$

where $\mathbf{g}_{\boldsymbol{f}}$ represents the stiffness of penalty springs in normal and tangential directions.

When the two surfaces of a fracture segment are sliding, the continuity of displacement in the normal direction should be satisfied and this is realized with normal component of Equation (7.8). In the tangential direction, potential energy associated with sliding state for the two surfaces corresponding to Equation (7.4) is

$$\boldsymbol{\Pi}_{f,sliding} = g_{f,n} d_{f,n} \mathrm{sgn}\left(\mathrm{d}_{f,s}\right) \tan\varphi \, \mathbf{d}_{f,s} \tag{7.9}$$

where the vector signs of $\boldsymbol{\Pi}_{f,sliding}$ and $\mathbf{d}_{f,s}$ represent the two sides of one fracture segment that may have different shearing displacements. By accounting for this together with geometric representation as shown in Figure 7-7, sliding (slip) along fracture surfaces can be accurately simulated.

With the above formulae, we are able to consider open, bonded and frictional sliding states of each segment of a fracture. Dynamic transformation of contact states can be computed by adjusting contact constraints. In some cases, we also need to detect whether such changes from one contact state to another would happen before switching to the other contact state.

Within each time step, iterations may be carried out several times and pre-assumed contact states may be adjusted until the enforced contacts reach convergence. In a dynamic process, contact pairs may change all the time and for the same contact pairs, these three states may transfer dynamically. Thus, within each time step before reaching the next time step and after the equilibrium equations are solved with enforcement of contact constraints corresponding to the pre-assumed contact states, contact states are re-evaluated to examine if they are consistent with the previously assumed contact states (Hu and Rutqvist, 2020b). If they are consistent for each contact pair, the calculation proceeds to the next time step. If they are not consistent, the contact states will be adjusted based on criteria described by Equations (7.5)-(7.6) and the calculation is looped back to re-solve the equilibrium equations until such consistency is reached. Such iterations may be carried out several times within each time step so as to ensure convergence for contact state.

7.4 Examples and Results

In this section, we describe the application of the NMM model for discrete fractures to analyze two different examples. We first apply the model to analyze coupled hydro-mechanical processes in a discrete fractured rock from a real image. Then we will analyze mechanical dynamics of a tunnel and a damage zone in bedded argillite rocks subjected to excavation and heating.

7.4.1 Modeling a Discrete Fracture Network

We extracted a network of discrete thin fractures from an outcrop image (Figure 7-8a), and then conducted modeling for analyzing coupled hydro-mechanical processes in this system. The geometric representation and the mesh that we constructed are shown in Figure 7-8b. This domain contains 126 thin fractures, and a number of them are well connected to form a major non-planar fracture running through the domain from the left boundary to the bottom boundary. We set the domain size as 10m × 8m but this could be arbitrary as fractures exist at several scales.

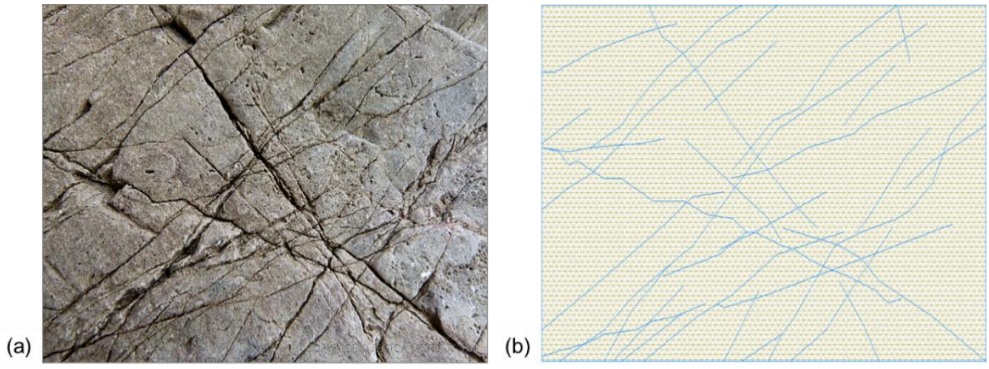

Figure 7-8. A discrete fracture network: (a) original image and (b) the generated mesh.

Table 7-1. Computation Parameters.

Materials	Parameter	Value
Fluid	Mass density, ρ_f	1000kg/m^3
	Dynamic viscosity, μ_f	1×10^{-3}Ns/m^2
Rock Matrix	Young's modulus	4GPa
	Poisson's ratio	0.3
	Permeability	1×10^{-11} m/s
	Biot-Willis coefficient, α	1
	Biot's modulus, M	∞
	Mass density	2300kg/m^3
Fractures	Shear stiffness	4,000 Pa/m
	Normal stiffness	10^4 Pa/m
	Factor, f	1
	Residual hydraulic aperture, b_{hr}	0.35μm
	Friction angle	0°

Initially, the effective stress is 10 MPa in the horizontal direction and 5MPa in the vertical direction, and the fluid pressure is 1.5 MPa. All boundaries are fixed mechanically in both directions. A constant injection pressure of 2 MPa is applied on the left boundary, while the pressure on the right boundary is kept constant at 1.5 MPa. The other boundaries are no-flux boundaries. The time step that we used for the calculation is 20μs. The purpose of this simulation is to investigate fluid flow and mechanics changes within a network of densely populated discrete thin fractures. Table 7-1 provides material parameters used for simulations. Low values of fracture stiffness and shear strength are used in the model to induce complex shear activation response with significant stress redistribution and HM changes.

The calculated fluid pressure is shown in Figure 7-9 (top row). As can be seen, from the beginning (Step 3), a gradient is generated in the domain from the left to the right. At Step 50, the fluid flows preferentially along the major fracture paths where intersections are denser in the horizontal direction. At Step 200, the fluid pressure begins to dissipate, indicating that opening of some fractures occur. At Step 500, the pressure increases in a preferential direction, especially along the long non-planar fracture formed with a number of fracture segments. This distribution at Step 500 can be correlated with the stress distribution shown below the pore pressure distribution in Figure 7-9.

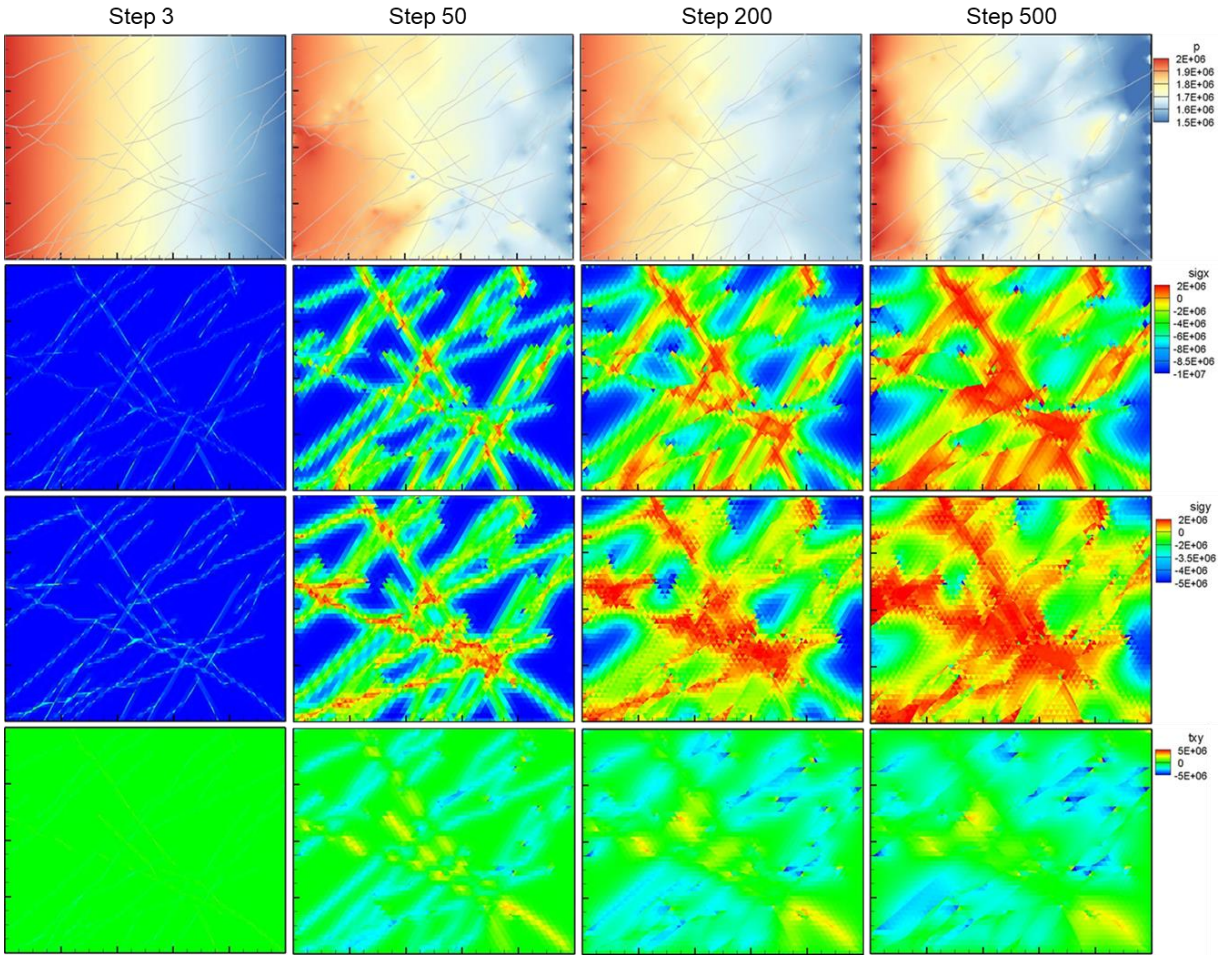

Figure 7-9. From top to bottom: calculated pore pressure (given in MPa), effective horizontal and vertical stresses and shear stress (given in Pa) at Steps 3, 50, 200 and 500.

In terms of mechanical changes, Figure 7-9 illustrates that at Step 3 the effective and shear stresses in the domain are quite uniform except for localized areas near the discrete fractures. At this point, shear stress has not accumulated yet. At step 50, a significant stress redistribution has taken place as a result of shear and normal displacement in fractures. This fracture deformation was triggered by an initial shear stress and zero fracture shear strength, which induce shear activation. The fracture deformation along with fixed outer boundaries tends to relax stresses within the model, especially in areas of several intersecting fractures. The stress relaxation and redistribution increase with further steps, and shear stress develops in adjacent fractures undergoing shear, especially apparent around shallowly dipping fractures. The stress relaxes to such a degree that effective stress becomes tensile in the matrix between intersecting fractures especially near the center for the model. If we compare the pore pressure distribution with the shear stress distribution, we find similar patterns of distribution, suggesting that shearing occurs with increased permeability.

7.4.2 Excavation and Heating in Discrete Fractured Bedded Argillite Rock

We applied the NMM model to preliminarily analyze excavation and heating in bedded argillite rock where the discrete fractures are considered at the tunnel, and simulated a localized 5m×3m domain. The tunnel is located in the center of the domain, with a diameter of 2.5 m. The beddings (yellow) and fractures (grey) are shown in Figure 7-10. The NMM mesh that is generated for calculation is shown in Figure 7-10b. The in-situ stress in the domain is 3 MPa horizontally and 5 MPa vertically. 5 MPa of loading is applied on both top and bottom surfaces, whereas the left and right boundaries are fixed.

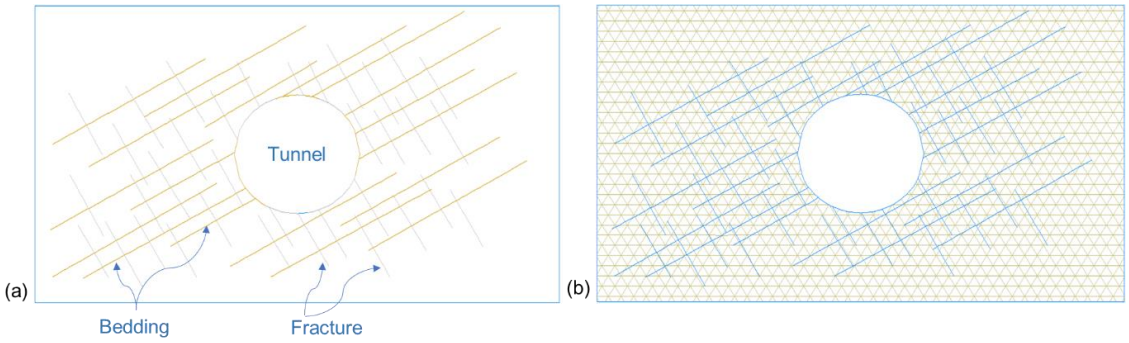

Figure 7-10. EDZ near a tunnel in bedded argillite rock: (a) geometry, and (b) NMM mesh.

We consider the fractures that are not cemented, i.e., the cohesion and tensile strength are both zero, while the friction angle is 30°. And we consider the beddings are interfaces with 3 MPa cohesion and 0.5 MPa tensile strength. Other computation parameters are listed in Table 7-2. In the first case, we focus on the stability analysis of the excavation damage zone (EDZ), and the bentonite buffer and canister are not considered. The tunnel walls are not supported, thereby free to move.

Table 7-2. Computation Parameters.

Materials	**Parameter**	**Value**
Rock Matrix	Young's modulus	10GPa
	Poisson's ratio	0.3
Fractures	Friction angle	30°
Beddings	Friction angle	40°
	Cohesion	3MPa
	Tensile Strength	0.5Mpa
Canister	Young's modulus	50GPa
	Poisson's ratio	0.3
Bentonite buffer	Young's modulus	50MPa
	Poisson's ratio	0.3

The results of simulations of the first case are shown in Figure 7-10. The time step is 10 μs in this fully dynamic simulation of the excavation response. The results of 500, 1000 and 2000 steps are shown in Figure 7-11, which represents times up to 0.02 seconds at 2000 steps. Within a short term, we are able to see what happens right after the tunnel is excavated. As expected, because the tunnel surfaces are free to move, this problem becomes a large-displacement problem. As shown in Figure 7-10, some blocks on the upper right and lower left areas start to move after the shear stress exceeds the shear strength along the beddings. Meanwhile, the blocks on the lower right have the tendency to move, but due to confinement, they do not have notable displacements compared with those in upper right and lower left regions.

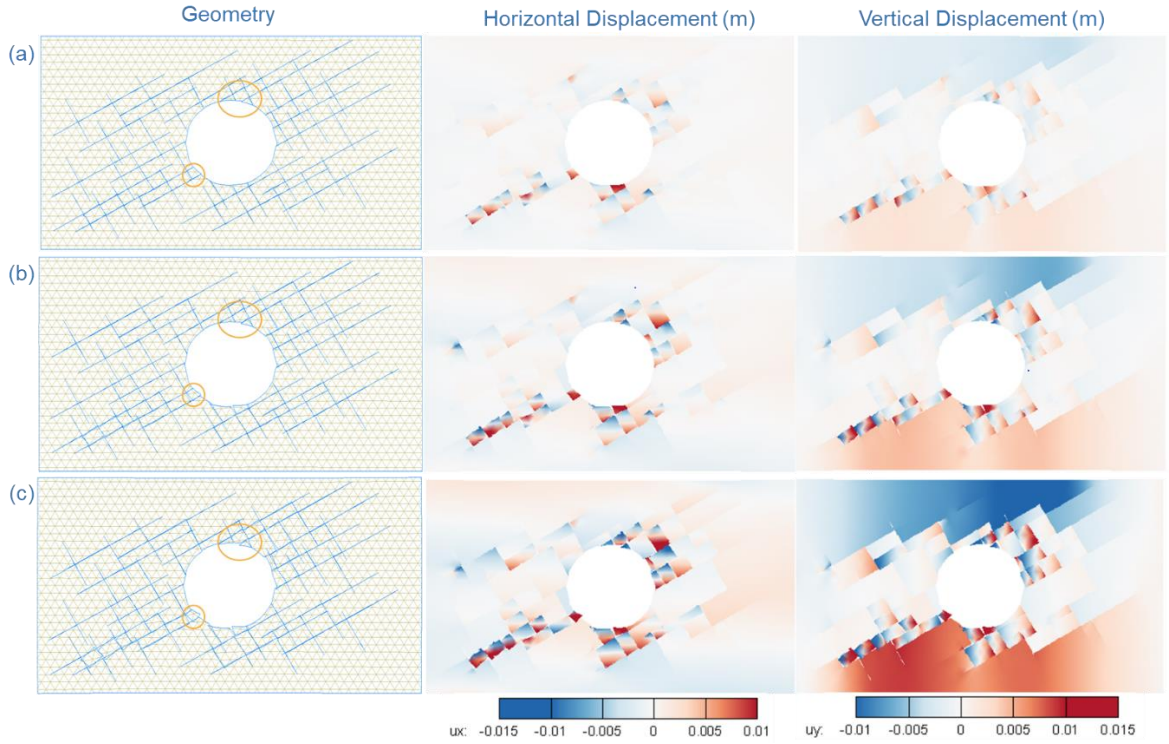

Figure 7-11. NMM results of geometry and displacements at steps (a) 500, (b) 1000 and (c) 2000.

The stress (shown in Figure 7-12) appears to have similar pattern as the displacements, i.e., the upper left and lower right have dominant stress changes. In particular, shear stress is high in these areas along beddings while maximum tensile stress becomes quite high at the fractures adjacent to the shearing zones. If the simulation is continued without the tunnel support, blocks on the tunnel wall will gradually move to the tunnel center until equilibrium is reached. This scenario is just to demonstrate the modeling capabilities of capturing both large displacements and high stress in a complex bedded argillite rock (Figure 7-13). The analysis could be extended by considering a layer of shotcrete on the tunnel wall to simulate support that could be used to provide guidance for reinforcing the tunnel.

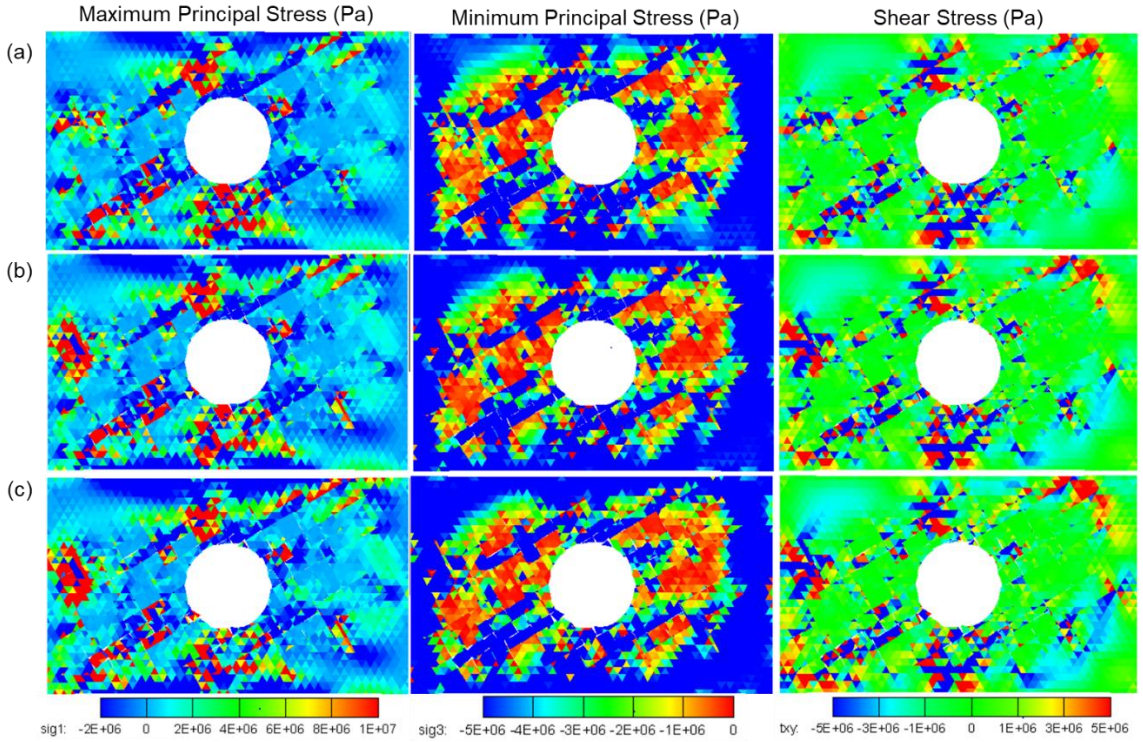

Figure 7-12. NMM results of maximum and minimum principal stresses and shear stress at steps (a) 500, (b) 1000 and (c) 2000.

In the second case, we considered a bentonite buffer emplaced in the tunnel with a simulated nuclear waste canister placed in the center of the bentonite buffer (Figure 7-13). The diameter of the canister is 1.0 m and the rest of the tunnel is filled with bentonite. We assumed a swelling stress of 3 MPa in the bentonite buffer. This 3 MPa swelling stress is translated into support stress of 3 MPa normal to the tunnel walls. At the same time, we assumed that the canister generates heat in the buffer and host rock, leading to a thermal stress. The parameters of the bentonite buffer and the canister are shown in Table 7-2. We keep the other geometric and physical settings same as in the first case, and ran a rather short-term analysis to see early-time responses.

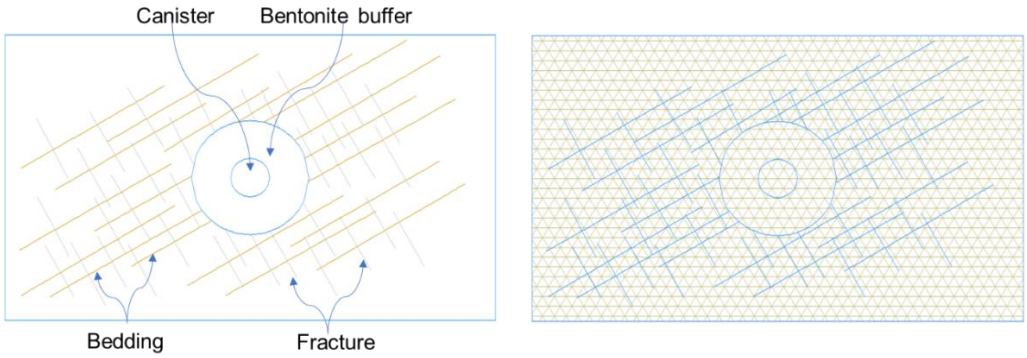

Figure 7-13. Modeling domain with a bentonite buffer in bedded argillite rock: (a) geometry, and (b) NMM mesh.

The stress evolution is shown in Figure 7-14. In general, there is an overall increase in compressive stress compared to that of the excavation case. The host rock stress increases because of thermal stress that can develop between the fixed model boundaries at the left and right boundaries. The system is more confined as the tunnel is filled with bentonite with a swelling stress of 3 MPa. Still, due to the heterogeneity of the complex fracture network, there are locations where high tensile stress develops, such as at the bottom-left region along fractures, which is consistent with the shear stress distribution. Though no fractures became opened (due to confinement), they may eventually be opened. Compared with the first case, no large displacements occurred.

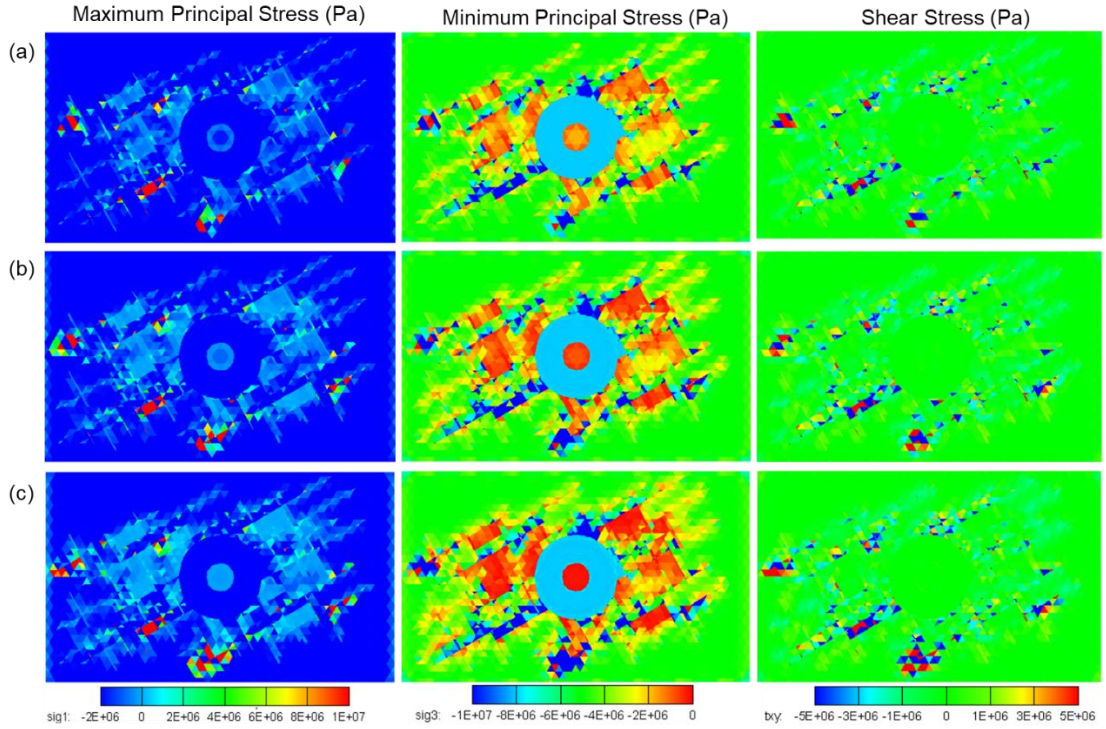

Figure 7-14. NMM results of maximum and minimum principal stresses and shear stress at steps (a) 500, (b) 1000 and (c) 2000.

7.5 Summary and Perspectives

We demonstrated the complexities inherent in processes occurring in discrete interacting fractures, which may not be captured using a simplified continuum model. We made use of the developed NMM for discrete fractures and conducted analysis of discrete fracture dynamics as results of (1) coupled HM processes in a fractured rock mass, and (2) excavation and heating around a simulated nuclear waste tunnel in fractured and bedded argillite. The key points and research activities can be summarized as follows:

- ✓ Shearing can be dominating in discrete fracture dynamics and therefore significantly impact the evolution of permeability and pore pressure in the networks;
- ✓ Our model can provide theoretical guidance for tunnel support after excavation with identification of movement of blocks on the tunnel wall;

- ✓ We conducted early-term preliminary analysis of heating induced stress changes in the bedded argillite rock where a soft bentonite buffer is placed in the center. We show the complexity in the mechanical response captured with the discrete fracture model.

In FY22, we will extend this work to the following activities:

- ➢ We will conduct more thorough analyses of the thermal-mechanical changes of the bedded argillite rock by using finer meshes to analyze long-term stress and fracture networks responses;
- ➢ We will introduce criteria of fracturing to investigate not only opening and shearing of existing (pre-defined) fractures but also new fracture growth induced by thermal stress.

8. Short- to Long-Term Hydromechanical Response of Faults and EDZ in Argillite Host Rock

In this section we report the results of the Mont Terri fault activation experiments that are of cross-cut interest related to several DOE program offices as well as international consortia. The section is written by Yves Guglielmi, and included work with main collaborators: C.Hopp, F.Cappa, J.Ajo-Franklin, P.Cook, F.Soom and M.Robertson, who are all affiliates of the LBNL.

8.1 Introduction

Repository-induced effects such as creation of an Excavation Damage Zone (EDZ), gas generation and thermally-induced pore pressure perturbations, may result in the reactivation of pre-existing features (fractures, faults or bedding planes) within the host rock and consequent permeability increase. Understanding such reactivation due to pressure and stress changes, the possible formation of permeable pathways, and their potential long-term sealing is critical in assessing the performance of radioactive waste repositories in shale formations. In 2015, a fault activation experiment was conducted by injecting high-pressure synthetic pore water in a fault zone intersecting the Opalinus Clay formation at 300 m depth in the Mont Terri URL (Switzerland). In 2018, a new experiment started with the permanent installation of a new sensor to monitor long term coupled fault pore pressure and three-dimensional displacements.

The key concluding points from these experiments are:

- Complex opening and slip was measured on the fault at fluid activation pressures close to the normal stress applied on the fault,
- High transmissivity flow paths developed at least temporarily and “local” (~meters) to the injection under high pressure injection, and their development was conditioned by rupture propagation within the fault zone,
- Fault reactivation and leakage produced mainly aseismic movements and a limited number of small magnitude seismic events,
- When injection pressures dropped, an instantaneous mechanical closing of the fault is observed. Nevertheless, a residual hydraulic permeability is measured. Since 2015, the

pressure in the ruptured patch slowly increased but did not fully recover, remaining ~0.45 MPa below its initial value. This may highlight slow sealing of the activated fault patch.

In 2019, significant pore pressure changes coupled to fault displacements were triggered by ongoing excavation work for a new Mont Terri gallery ~40 to 50 m away from the fault, at distances significantly farther than a few tunnel diameters. In November 2020, a new fluid injection experiment was conducted with a much larger monitoring array than the 2015 experiment, including time lapse seismic imaging of fault leakage and movements.

In Section 8.2, we display a more complete analysis of the remote fault activation induced by the excavation of a new Mont Terri gallery in 2018, using data from the extensive array of distributed fiber optic strain monitoring deployed in several boreholes crosscutting the Main Fault. We discuss how localize the strains are on the fault zone and off the fault zone, highlighting the effect of the fault architecture on the distributed deformations. We show that because the Main Fault and more typically shale faults display an architecture with a limited fractured damage zone, there is no stain gradient developing from the high deforming core towards the intact rock. Indeed, peaks in shear strain localize at the top and bottom sharp interfaces between the fault core and the intact rock.

In Section 8.3, we first show continued numerical analyses of the FS experiment. Here we explore the link between the fault zone complexity, the size of the leakage volume and the induced seismicity. We highlight that a complex fault zone where multiple fractures are activated produces a small amount of seismicity and local channeling. This is related to fractures stress interactions, seismicity being aligned at these fractures intersections. Second, we show the preliminary results of the time-lapse seismic imaging conducted during the FS-B experiment. Although this is still in the processing of the data, first results confirm that changes in p-waves' velocities are measurable, and correlated to changes in effective stress and deformations induced during and after the injection. These changes confirm that the leakage volume is local within the fault zone. Instantaneous changes relate to fracture opening while delayed changes might highlight some irreversible shear damage following activation. In Section 8.4, we detail the key conclusions from this year's current work and work perspectives.

8.2 Fault architecture and reactivation behavior in shale revealed by distributed fiber optic strain sensing

In May and June of 2019, prior to the actual fault activations planned in the CS-D and FS-B experiments at Mont Terri, the exhaustive multi-parameter monitoring network captured significant pore pressure changes coupled to fault displacements triggered by ongoing excavation work for a new Mont Terri gallery. This unexpected hydromechanical response of a fault ~40 to 50 m away from an excavation, thus at distances significantly farther than a few tunnel diameters, is of crucial importance in assessing the long-term loss of faulted host rock integrity. Here we present a synthesis of measurements from a suite of six boreholes intersecting the fault. Each borehole is instrumented with a loop of single-mode fiber optic cable, grouted behind casing. The boreholes also contain separate strain (extensometer) and displacement (SIMFIP) sensors, co-

located with the Distributed Optical Fiber System (DOFS), which allowed us to validate our Distributed Brillouin Strain Sensing (DSS) measurements. We compared the sensitivity of the multi-borehole fiber array to the movement occurring within the Main Fault Zone in response to the stress perturbation triggered by the remote gallery excavation. Using independent measurements of the same displacement from co-located or proximal sensors with respect to the fibers, we will discuss the consistency between sensors, exploring if a grouted fiber-behind-casing installation achieves the same performance as of established methods (e.g., extensometers) with greater ease of installation and much higher spatial resolution. We discuss how a grouted fiber-behind-casing installation complements established methods and what the fiber reveals about the structure of a clay-hosted fault zone. Finally, we use the fiber measurements to infer the factors controlling which planes are activated by remote stress transfer from the gallery excavation front.

8.2.1 Distributed Fiber Optic network setting across the Mont Terri Main Fault

The Mont Terri Rock Laboratory, operated by the Swiss Geological Survey, is located on one limb of a fault-bend anticline within a low-permeability claystone unit known as the Opalinus clay (Bossart et al., 2017; Hostettler et al., 2017). The Opalinus clay is a potential target formation for Switzerland's nuclear waste repositories (Bossart et al., 2017). The galleries of the MTRL are intersected by a kilometer-scale thrust fault zone, the so-called Main Fault (Jaeggi et al., 2017), which offers researchers the opportunity to investigate the effect of fault activation on the leakage potential of a self-sealing clay unit (Guglielmi et al., 2017, 2020; Zappone et al., 2020). The Mont Terri Main Fault consists of a thrust zone, 1 to 3 m in width, bounded by two major fault planes characterized by a strike of N066^o to N075^o and a dip of 45^o to 65^{o}SE (Figure 8-1). The CS-D and FS-B projects, directed by ETH Zürich and Lawrence Berkeley National Lab (LBNL), respectively, are focused on understanding how a minor fault reactivation can affect the integrity of a clay unit considered an analogue host rock or caprock. A 70-m x 70-m x 70-m volume, crosscut by the Main Fault, is instrumented with 23 boreholes hosting various systems recording pressure and flow rate into multiple injection intervals, active and passive-source seismicity, and geomechanical strain/displacement/tilt. Figure 8-1 shows all boreholes drilled by CS-D/FS-B. Here we focus on the CS-D boreholes (colored in the foreground of Figure 8-1). The FS-B boreholes are shown in gray in the background.

In this study, we focus on instruments deployed in seven boreholes that have been drilled through the Main Fault zone (BCS-D1–7; Figure 8-1). BCS-D1 and BCS-D2 are injection and fluid-monitoring boreholes, respectively, and are equipped with multi-level straddle-packer assemblies to enable the isolation of several depth intervals. Boreholes BCS-D3, D4, D5, and D6 are cased with PVC and house the electromagnetic and seismic monitoring systems (Zappone et al., 2020). Finally, BCS-D7 contains the SIMFIP instrument (Guglielmi et al., 2013), explained in greater detail below. The depth of the Main Fault zone intersection with each borehole, as verified by image logging and core, varies from 11 to 28 m below the gallery floor. The thickness of the fault zone varies between 1 and 3 meters and is characterized by a laterally heterogeneous mix of fault gouge, C'-type shear bands, scaly clay, and meso- and micro-scale folds (Nussbaum et al., 2011). Here 'scaly clay' refers to a mass of unaltered, Opalinus microlithons, separated by slickensides, and is pervasive throughout the Main Fault (Jaeggi et al.,

2017). Fault planes within the Main Fault zone are mostly oriented subparallel to the fault zone itself, but also include a set of fractures normal to it (Wenning et al., 2020). In addition, a series of ENE-striking, bedding-parallel fractures, with similar strike but shallower dip than the Main Fault, are intersected by the CS-D boreholes (Zappone et al., 2020). Bedding in the Opalinus is oriented subparallel to the Main Fault, striking N055°, and dipping SE046°, roughly 15° shallower than the Main Fault.

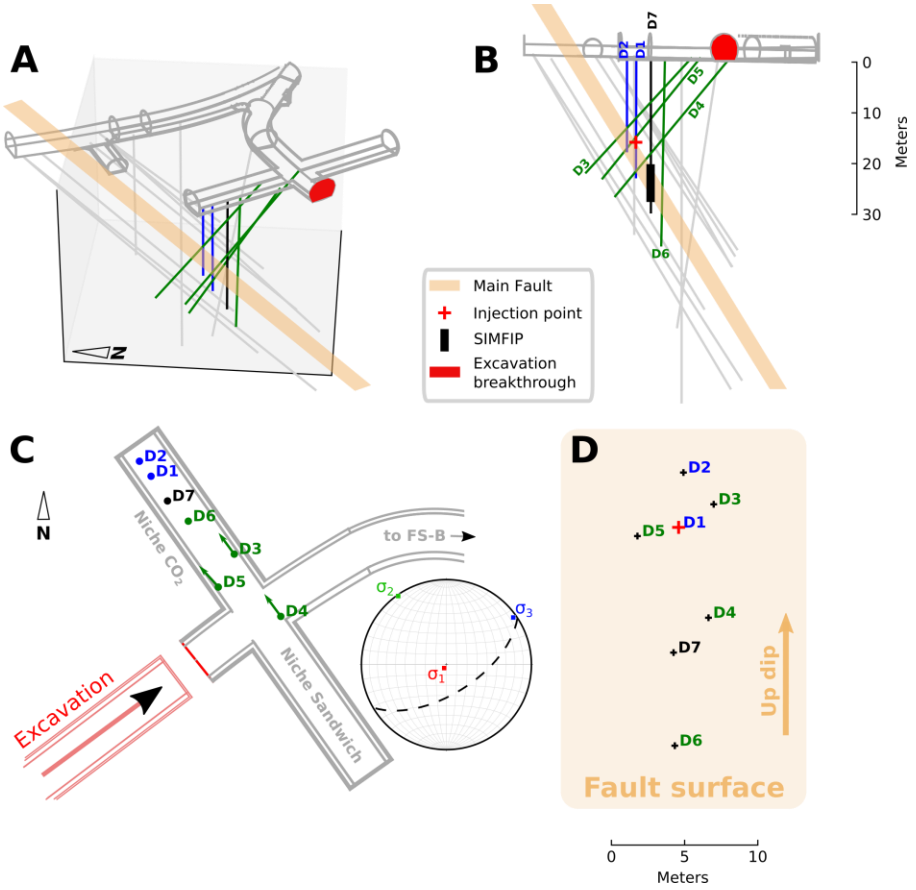

Figure 8-1. (A) 3D perspective of the FS-B/CS-D project showing all boreholes colored by use. Boreholes D1 & D2 (blue color) are injection and pressure monitoring boreholes. Boreholes shown in green contain monitoring systems, and Borehole D7 (showin in black) contains the SIMFIP displacement sensor. Light gray symbols in the background indicate the FS-B boreholes. All boreholes are instrumented with distributed fiber optic sensors except D7. (B) Cross-section along Niche CO2 with the injection point in D1 indicated by a red cross. (C) A map view of the borehole collar locations in Niche CO2 and lower hemisphere stereonet projection of the principal stress axes estimated by Guglielmi et al. (2020). Dotted line shows the approximate orientation of the Main Fault (D) Intersection points for each well with the top of the Main Fault

Boreholes BCS-D1 through D6 contain a single 3.2 mm-diameter loop of BRUsensTM strain sensing cable that itself comprises a single optical fiber hermetically sealed and strain-locked within a metal tube and an outer nylon sheath. These cables are designed to measure strains of up

to 1% (10000 µE). In BCS-D1 and D2 (blue color, Figure 8-1), the fiber optic cable (BRUSens 3.2 mm V4 metallic) is anchored by a compression ferrule at the top of each injection interval (with four and six intervals in D1 and D2, respectively). However, these boreholes were not drilled at the time of the excavation and so are omitted from the data analysis. In boreholes BCS-D3, D4, D5, and D6, the fiber (BRUSens 3.2 mm V9 grip) is cemented behind the PVC casing using a grout mix of 81.9 L water, 4.9 kg bentonite, and 50.1 kg cement (green boreholes, Figure 8-1). This provides continuous measurements along the entire length of each borehole. In these cases, the nylon cable jacket is textured to provide optimized strain coupling between the fiber and the grout so that, in theory, only the grout strain is being measured, with the assumption made that the grout is coupled to the host rock. Each of these boreholes also includes a single resin 'plug' to mitigate against fluid traveling along the cemented annulus (Figure 8-2B). These plugs are 0.5–2 m thick sections where the resin replaces the grout in the annulus between the borehole wall and the PVC casing. Borehole diameter ranges from 101 to 146 mm, with consistent PVC casing diameter of 80 mm. The fiber loops in each borehole are connected into a multi-borehole circuit and interrogated by an Omnisens DITEST temperature and strain unit, using the Brillouin Optical Time Domain Analysis technique (Horiguchi & Tateda, 1989). A chain of 12 potentiometers is cemented behind casing alongside the fiber-optic loop in borehole BCS-D5 (Zappone et al., 2020; Rinaldi et al., 2020). Each potentiometer is connected to the adjacent units by a PVC tube and measures borehole axial displacement relative to the neighboring units with a maximum displacement of 100 mm. This chain of potentiometers provides a co-located measurement of displacement with respect to the optical fibers, allowing us to directly verify the measurements made with the DSS system. In borehole BCS-D7, a combined three-dimensional-displacement, pressure, and fluid electrical conductivity probe, the SIMFIP (Guglielmi et al., 2013), is clamped above and below the Main Fault. The clamps are 6.3 meters apart allowing the SIMFIP to measure the relative displacement across the entire Main Fault zone. The instrument uses six fiber-Bragg gratings attached to a bespoke aluminum cage to resolve the full 3D displacement field with micrometer precision. The SIMFIP is alone in BCS-D7, and therefore is not co-located with any portion of the fiber optic loop. Understanding this limitation, here we use its three-dimensional fault displacement measurement in comparison to the DSS data.

Excavation of Gallery 18 began on March 14, 2018, and lasted for more than one year. During much of this time, the excavation front was far from the Main Fault monitoring zone, which, itself, was completed in May 2018. The installation of the CS-D systems occurred between August and December 2018. During the first half of 2019, the final stages of excavation occurred as indicated in Figure 8-1. Excavation passed along the strike of the Main Fault at a constant 23 m distance from the upper fault zone interface. Breakthrough occurred adjacent to the CS-D experiment on May 27, 2019 (red faces in Figure 8-1). Prior to the breakthrough, movement was not detected by the DSS monitoring system until May 22, 2019, when the excavation front was

26 m from the SIMFIP. We therefore focus on the period between May 22 and June 3, 2019, when deformation was observed.

8.2.2 DSS Methods and processing

When a laser pulse is sent along an optical fiber, some amount of that light is scattered backwards by its interaction with changes in the refractive index of the fiber. There are three components of this backscattered light relevant to DOFS: one is elastic (Rayleigh) and two are inelastic (Raman and Brillouin). We are concerned here with the Brillouin component, which arises from an incident photon's interaction with crystal lattice vibrations that holds some of the optical fiber's heat. As the interaction is inelastic, the backscattered light is frequency shifted by some amount that linearly depends on the temperature and strain in the fiber (Horiguchi and Tateda, 1989) as:

$$\Delta V_B = \frac{\partial V_B}{\partial E} \times \Delta E + \frac{\partial V_B}{\partial T} \times \Delta T \tag{8.1}$$

where ΔV_B is the change in Brillouin frequency shift for given changes in strain, ΔE, and temperature, ΔT. $\frac{\partial V_B}{\partial E}$ and $\frac{\partial V_B}{\partial T}$ are the strain and temperature change coefficients, respectively, which for this work are 500 MHz/% and 1.0 MHz/^{o}C. Using Equation (8.1), the DITEST interrogator determines the combined temperature and strain contribution to the measured Brillouin frequency shift. Each measure is related to a given point along the fiber by recording the launch and arrival time of the probe pulse with respect to the speed of light. Because the light pulse from the interrogator has a finite length, measurements are averaged over the corresponding length of fiber. This is referred to as the spatial resolution (or often the 'gauge length'). The Brillouin frequency shift for one gauge length is reported as a single measurement at a point along the fiber that we call a 'channel.' The spatial sampling and spatial resolution were 0.26 and 0.5-to-1.0 meters, respectively, for each of the periods of our study. Notice that the channel spacing is less than the spatial resolution. Therefore, the DSS measurement is a sliding window with a width equal to the spatial resolution, slid along the fiber in increments defined by the spatial sampling. Because the Brillouin frequency shift is sensitive to both temperature and strain changes, a number of methods are employed to deconvolve their contributions. Often, an independent measurement of temperature (for example from a Raman scattering system) is used to remove the temperature contribution from the Brillouin measurements. Alternatively, a "strain free" cable is sometimes decoupled from the system of interest and can be co-located with a coupled cable and connected in series. In our case we had access to neither, but we make the assumption that the temperature change within our testbed is negligible with respect to the changes in Brillouin shifts being measured (Madjdabadi et al., 2014, 2016; Hartog, 2017).

As mentioned above, for any given distributed strain measurement, its distance along the fiber is accurately known from the two-way travel time in relation to the speed of light. Translating this distance into a borehole coordinate requires a process of 'mapping,' whereby the distances along-fiber are matched to the known locations of the features we want to measure (in this case boreholes BCS-D1–D6). We decide to map distance to location by observing a single Brillouin frequency shift measurement along the entire fiber length (i.e., one time sample; Figure 8-2A). Because the fiber is installed as a loop in each borehole, we expect there to be symmetry in the

measurements about the bottom of the boreholes. In other words, the downgoing and upgoing legs of the fiber in a given borehole should measure roughly the same strain. For the case of our experiment, the BRUsens cable is grouted into the boreholes (or attached to the casing above the packers in D1 and D2), while the sections of fiber between boreholes are standard patch cables lying in a cable tray along the gallery wall. The difference in fiber coating and installation produces an obvious difference in the Brillouin frequency measurement that allows us to map the along fiber distances corresponding to the entry and exit points for each borehole. In Figure 8-2A, the entry and exit points for each borehole are indicated by dotted lines, with the bottom shown as a single solid line. The mapped along-fiber lengths agree with field measurements of the cable lengths set in the gallery. By manually selecting the point of greatest symmetry for each borehole and accounting for their known drilled depths, we isolate the slice corresponding to each borehole. The process of borehole mapping should, in theory, result in two parallel sections (legs) of fiber in each borehole; one downgoing and one upgoing. Assuming that each is measuring approximately the same strain field, the measurements should be equal between up and down-going fiber for a given depth.

Figure 8-2B shows both the down- and upgoing fiber leg in each borehole on June 3, 2019, following the breakthrough of the excavation on May 27, 2019. The symmetry in measurements between fiber legs is visually apparent. The depths at which measurements are not symmetric typically coincide with depths where the fiber is expected to be poorly coupled to the rock mass, for example at the borehole collar or at the depths where grout is replaced by the resin plugs (beige bands, Figure 8-2B). But while the symmetry of the measurements between down and upgoing legs is evident, the absolute value measured at a given depth on either leg can vary significantly. This is likely a result of heterogeneous coupling of the fiber to grout and the grout to the rock mass. This could be the result of changes in the distribution of grout (e.g., air pockets) or to the effect of other equipment installed in the borehole. For example, in BCS-D5 the chain potentiometer might affect the strain measured on the fiber closest to it, but have less effect on the opposing leg. Also, for the inclined, grouted boreholes, the stress state may vary along the borehole circumference. In this case, fiber legs on opposing sides of the borehole could measure different responses to stress perturbation, even for the same depth in the borehole.

Figure 8-2C shows the difference between down- and upgoing fiber measurements for all measurement times and channels, colored by borehole. The statistics for the distributions shown in Figure 8-2C are reported in Figure8-2D. The fact that the distributions are nearly zero-mean signifies that there is no systematic preference for higher or lower values measured by one leg with respect to the other. The standard deviations of the curves in Figure 8-2D, however, range from 4.83 to 28.39 μE. This means that the measured strain at a given depth in a borehole might vary by tens of microstrains depending on which leg is selected, significantly increasing the uncertainty in the measured strain.

Finally, we quantify the measurement noise following Madjdabadi et al. (2016). For each channel in a borehole, we calculated 3 standard deviations for a reference time period (with no

expected strain signal). We then average this value over all channels in the sensor, resulting in a single noise value per borehole (Figure 8-2E). The noise levels range from 11.44 to 20.95 µE, meaning that each segment of the fiber cannot confidently resolve strains of less than these values.

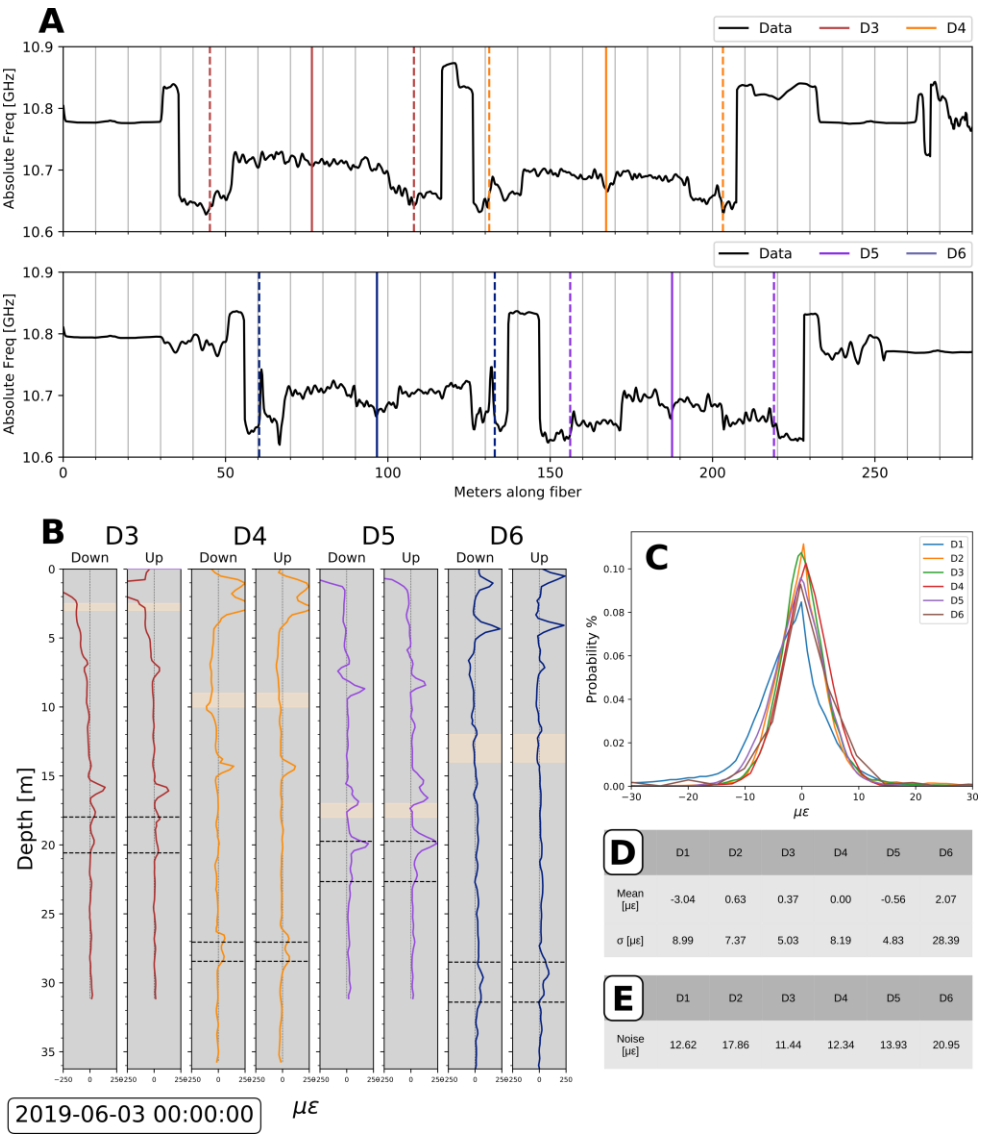

Figure 8-2. (A) Absolute frequency along the length of the fiber during gallery excavation. The two panels correspond to two separate fiber optic loops, each with two boreholes. Boreholes D1 and D2 were added after excavation was completed. (B) Distributed strains on the down and up- going leg of each on 3 June 2019, following the breakthrough of the excavation front on 27 May 2019. The depth to the Main Fault is marked with dotted lines, resin plugs are shown in beige. (C) Kernel density estimates for the difference between the up-going and down-going legs of fiber in each borehole. (D) Statistics describing the difference between down and up-going fibers for each borehole. (E) Average 3-standard-deviation noise for each borehole.

Two final artifacts are then removed from the data. The first artifact is an ambiguity in the exact position of each channel. The ambiguity arises because the channel location is reported at the center of the light pulse (for our tests either 0.5 or 1.0-m long). But the strain could be concentrated at any point (or points) inside the pulse. We follow Madjdabadi et al. (2016) and apply a realignment step detailed in the supplements. The second artifact is a series of systematic shifts in the measured strain for all points in the fiber. These apparently correlate with shifts in the gain of the signal returned to the interrogator, although the two values should not be related. We undertook a process of removing these shifts for times where the gain also shifted.

8.2.3 Results – Distribution of deformation induced by the remote gallery excavation

8.2.3.1 Correlation of DSS strains with geological features observed in boreholes

Main result is that strains localize in the EDZ on a number of discrete fractures outside the fault zone and at the fault zone boundaries. The deformations in the EDZ are up to one order of magnitude larger than in deeper zones. Figure 8-3B shows the measured strains in the upper 7 m of each borehole. Boreholes D3 and D5 show contractions of >800 and 600 µE, respectively. In contrast, D4 and D6 each show two smaller magnitude peaks of extensional strain, each 200 µE. The discrete spikes in the strain shown in Figure 8-3B show that deformation is probably concentrated on preexisting fractures intersecting the gallery and niches. The EDZ around the CS-D niche where our boreholes are located was already stable by the time of the Gallery 18 breakthrough detailed in this work. We are therefore observing the response of a stable, preexisting EDZ as it merges with the new, unstable EDZ surrounding the approaching gallery excavation. The strains shown in Figure 8-3B are the result of complicated interactions between a new gallery and the preexisting galleries and niches. A complicated modeling exercise will be required to shed more light on the patterns shown in Figure 8-3B. At depths >7 m deeper than the EDZ, strain is localized on several distinct features visible (Figure 8-3A, colored arrows). In boreholes D3, D4, and D5, off-Main Fault deformations are >100 µE, comparable to and exceeding the strain measured within the Main Fault zone. Approximately 18% of the off-Main Fault fractures identified in core logs correspond to the features indicated by arrows in Figure 1-3A. Geological interpretation of the core classifies the deepest non-fault feature in BCS-D3 (16 m depth) as an interval of scaly clay layers. Optical televiewer (OTV) images for D3 were too poor for accurate data analysis. The single shallow feature in D4, as identified in OTV logs, corresponds to a single fracture striking N052°, dipping SE69°. The 15–16-m depth interval in BCS-D5 is classified as a distinct fault zone, four meters above the Main Fault (strike N014–060°, dip 20–70°SE). The 8-meter anomaly in D5 corresponds to a series of features classified as either ‘bedding’ or ‘fracture planes’ in the core (strikes N053–082°, dips 54–74°SE). Unfortunately, due to the 1-m spatial resolution, DSS anomalies cannot be assigned to any single feature where fracture density is >1 / meter (Figure 8-3).

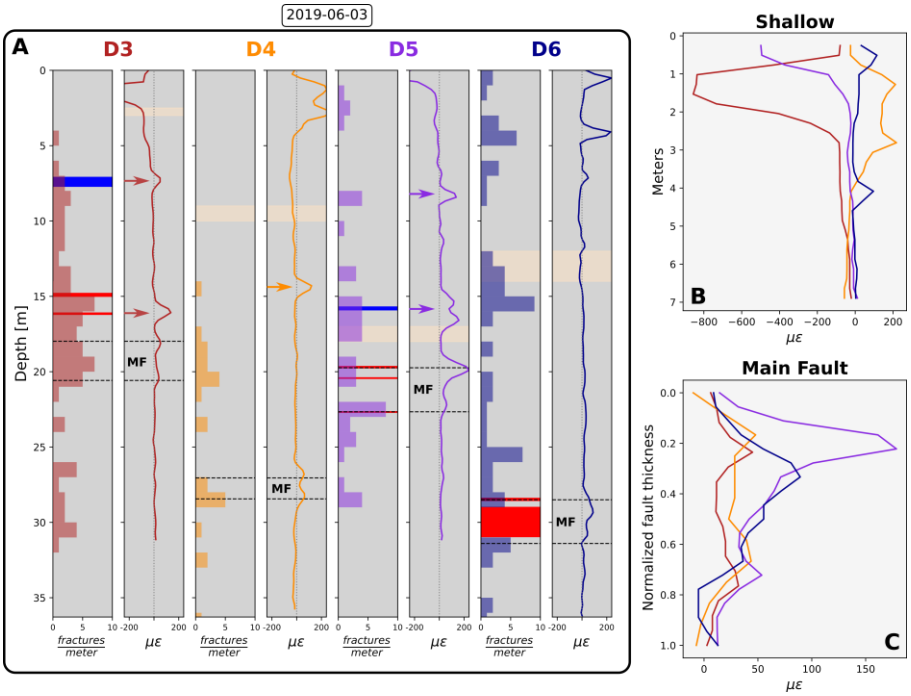

Figure 8-3. On and off-fault strains: (A) Measured strain and fracture density estimated from core. Solid red lines indicates depths of scaly clay identified during core characterization, blue indicates a fracture zone (when not also identified with scaly clay). D4 was drilled with destructive methods so we report fracture density from optical televiewer logs. Resin plugs are in beige, fault top and bottom are indicated by horizontal dotted lines. Arrows show above-fault features recorded on both the up and down-going fibers. (B) Strains for the upper 7 m of each borehole. (C) Strains within the fault zone for each borehole. Depths are normalized to the fault zone thickness in each borehole.

Figure 8.3C shows the strains measured within the Main Fault zone for all boreholes. Because the thickness of the fault zone varies significantly between holes, we normalize the depths in order to better compare the distribution of strain within the fault zone. In all boreholes, strain localizes on the uppermost interface of the fault zone. In D5, 240 µE accumulates on this surface, with lesser magnitudes in the other boreholes. Strain also localizes on the lower interface of the fault zone, with relatively little strain measured within the fault zone itself. This suggests that the interfaces between fault zone and intact rock serve as multiple principal shear zones. Core analysis indicates up to 1cm of black or gray fault gouge at the top and bottom of the fault zone (Wenning et al., 2020). Compared to the other boreholes, strain in D6 (particularly on the upgoing fiber) appears more distributed over the entire fault zone. D6 is vertical and therefore oblique to the Main Fault. The fiber axis in D6 is therefore more closely aligned with the fault interface than in D3, D4, or D5, meaning it may better capture small amounts of shear distributed within the entire fault zone. Slip on the upper Main Fault interface, being closer to the excavation, probably relieves some of the stress that otherwise would have been transmitted to the lower interface, thereby producing an apparent gradient, with higher strain concentrated on the upper interface.

8.2.3.2 Temporal evolution of DSS strains

Figure 8-4A summarizes the Main Fault deformation with time as observed by DSS in Boreholes D3, D4, D5, and D6 and by the SIMFIP in D7. The DSS data are integrated across the Main Fault zone to better compare to the SIMFIP, which is measuring relative displacement across the entire zone. We rotate the SIMFIP displacement tensor into Main Fault coordinates and show displacement as shear parallel to the fault and as opening normal to the fault. These data reveal two distinct modes of Main Fault activation: predominant shear deformation before the excavation breakthrough (Figure 8-4; green line), followed by predominant opening-mode deformation after the breakthrough. This change in behavior reflects the changing orientation of fault loading from the excavation. When the excavation front is still at a distance from our sensors, the loading vector is oblique to the fault and results on mostly shear slip. At breakthrough, the force of the overburden removal is approximately normal to the fault, resulting in mostly fault opening. Figure 8-4B shows the evolution of displacement on the features above the Main Fault (indicated by arrows in Figure 8-3A). The pattern shown is similar to that of the Main Fault zone, with similar amounts of displacement occurring for each excavation pulse. The features in D5, being closer to the source of stress perturbation, show larger displacements, on average, than those of the other boreholes. From the perspective of the DSS fibers, the change in the mode of fault movement cannot be discriminated because the fiber measurement is sensitive only to changes along the fiber axis. Nevertheless, the fiber system is obviously sensitive to shear on the Main Fault (see D5, in purple, during the shear-mode period in the Figure 8-4A).

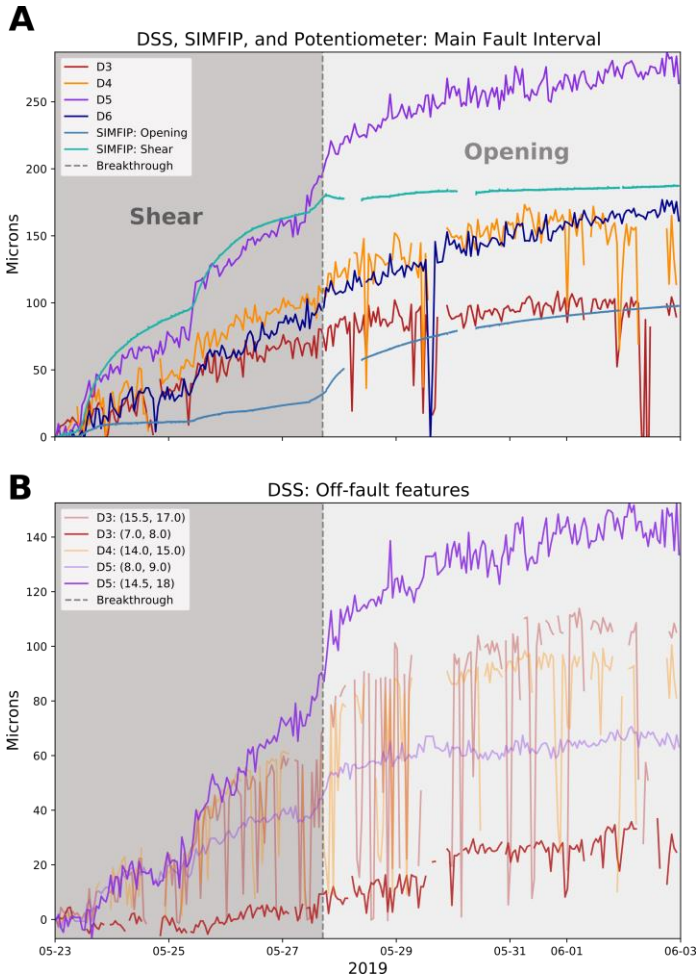

Figure 8-4. (A) Main Fault displacement throughout the excavation for all boreholes. DSS mea-surements have been integrated over the Main Fault depth interval, as identified by core and log- ging. The displacements measured by the SIMFIP have been decomposed into two components: one parallel to the Main Fault (green) and one normal to the fault (blue). (B) Displacement for each of the anomalies indicated with and arrow in Figure 8-3A. The legend indicates the depth range over which strain was integrated for each. The time of the breakthrough is identified with a vertical dotted line.

8.2.3.3 DSS strain evolution compared to the orientation of the excavation front

Figure 8-5 shows the observed deformations in 3-dimensions. Figure 8-5A shows results for May 26, 2019, before the breakthrough, while Figure 8-5B shows observations from June 1, 2019, just after breakthrough. The polygons on the left show the distribution of displacement on a plane parallel to the fault. For each hour, we performed a linear interpolation between the integrated DSS measurements in each borehole and the vector sum of the SIMFIP displacements (all of which are shown in Figure 8-4). While the spatial extent of the boreholes is fairly limited, there is a clear negative gradient in fault zone displacement from left to right (SW to NE) and top to bottom (shallower to deeper). This is consistent with the orientation of the excavation front, approximately indicated by the red arrow, which is closest to the Main Fault intersection with D5 and therefore induces the largest strain perturbation at that point. The black arrow is the projection of the SIMFIP displacement onto the fault plane for the preceding hour. This

displacement represents an oblique reverse sense of shear across the fault zone, pointing in the direction of greatest strain perturbation, in good agreement with the deformation gradient. Once breakthrough occurs, little shear occurs.

We also plot the DSS data in cross section, superimposed on the trajectories of the boreholes (Figure 8-5; right hand column). The SIMFIP displacement vector (in the plane of the cross section) is again shown as a black arrow. The Main Fault interfaces, defined by their logged depths, are figured in dotted gray. We also overlay the approximate orientation of the bedding of the Opalinus in green dotted lines. The depths of the figured bedding planes shown are approximate, and we have figured the ones that best fit with peaks in DSS strain. The peaks in the strain curves are not present at all boreholes suggesting local reactivation of these bedding planes. Note that, in comparison, strain on the Main Fault (whose orientation and depth are well constrained) is observed in all boreholes.

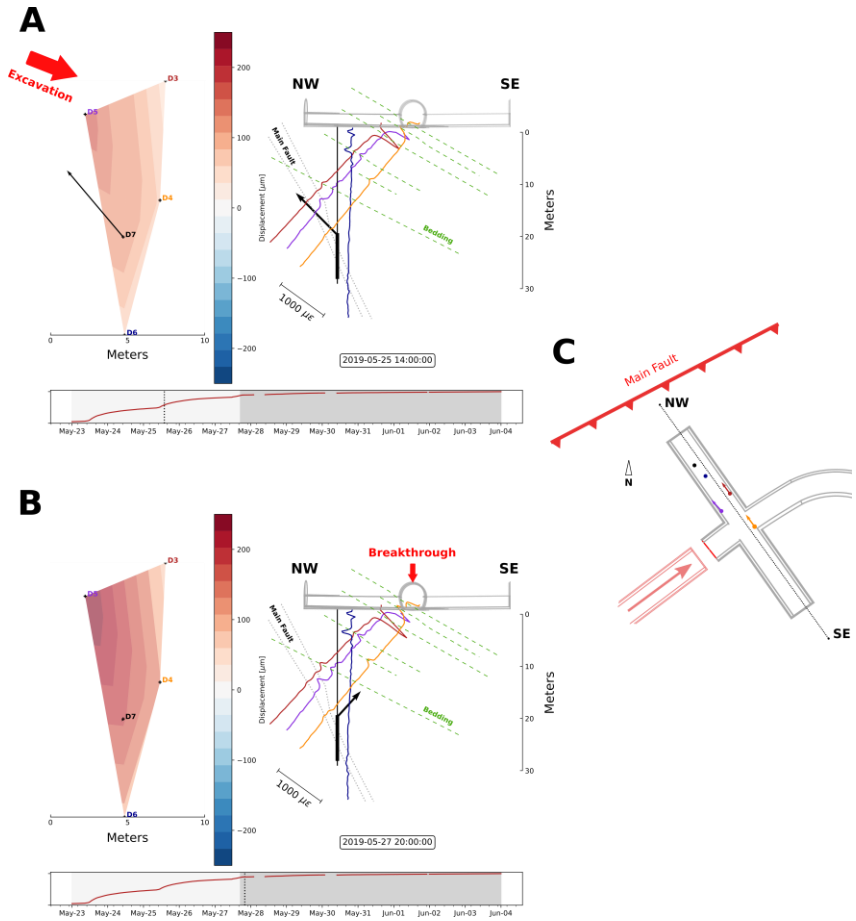

Figure 8-5. (A) Deformation before the excavation breakthrough (May 26) and (B) after (June 1; bottom row). The left column shows displacement along the fault plane, linearly interpolated between boreholes. The right column shows a cross-section along Niche CS-D with the strain curves in Figure 1-3 projected onto the boreholes. Borehole D7 is shown in gray with the SIMFIP indicated by the black box. The direction of SIMFIP displacement (magnitude not to scale) is shown as a black arrow, projected onto the fault plane and the cross-section in the left and right columns, respectively. (C) Layout of Niche CO2 showing the excavated gallery, Main Fault, and boreholes.

8.2.4 Discussion

8.2.4.1 Comparison of DSS measurements to other instruments

In Figure 8-6A, we show both the chain potentiometer (red) and DSS measurements (purple) in BCS-D5 on 3 June 2019 following the excavation breakthrough. The fracture density as estimated from analysis of drill core is shown in black. The potentiometer string has a variable spatial resolution defined by the spacing of the anchor points between individual elements. The spacing between elements is smallest across the Main Fault interval (0.5 m). Two other elements of roughly 8 m in length are placed above the fault. At the depth of the Main Fault interval, the chain potentiometer and fiber optic measurements both clearly show that most of the movement within the fault interval is concentrated at the uppermost interface, where displacements of 282 µm and 210 µm are measured, respectively. A smaller magnitude peak is also observed at the bottom fault interface, respectively of 80 and 67 μm on the potentiometer and DSS. Above the fault, the DSS retains its 1 m spatial resolution, whereas the potentiometer averages displacements over two 8 m intervals (from 11–19 m and 2–11 m). Two other large deformations are measured by the DSS: one just above the resin plug (16–17 m) and one at 8 m depth. The chain potentiometer, on the other hand, measures no displacement over its shallow intervals due to its lack of spatial resolution.

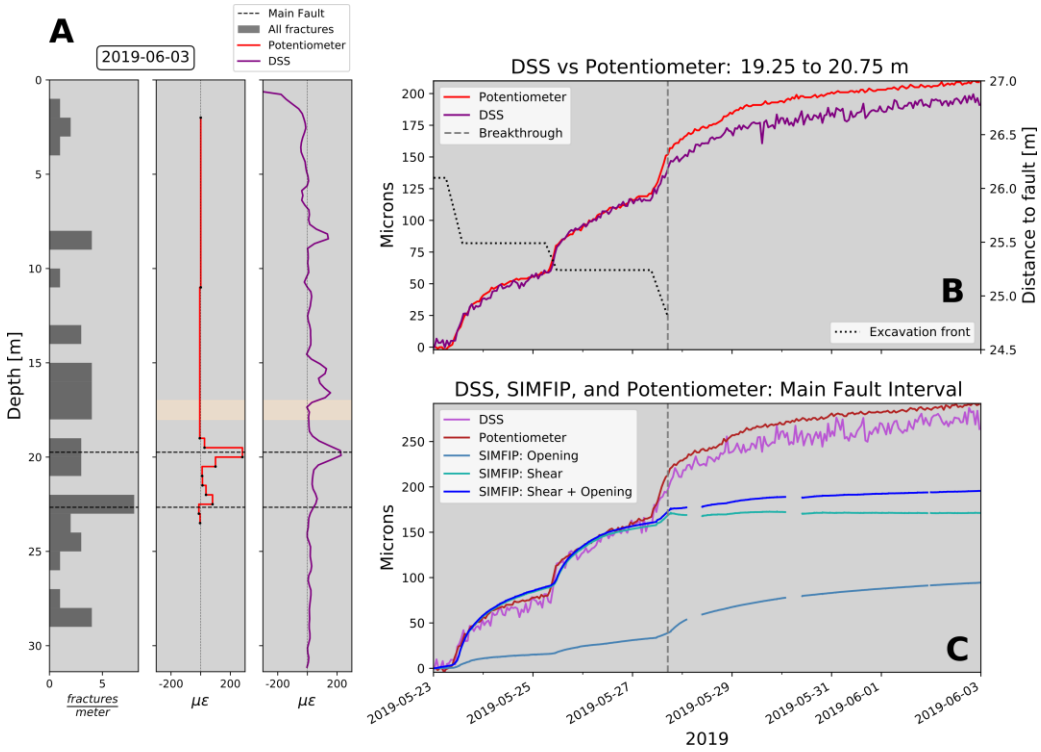

Figure 8-6. Fault response to gallery excavation: (A) Comparison between fracture density, potentiometer extensional strain and DSS strain six days after the breakthrough of Gallery 18 at Niche CO2. (B) Time series comparison between DSS and potentiometer integrated between 19.25 and 20.75 m depth in D5. The dotted line shows the distance of the excavation front to the top of the fault at BCS-D5. The dashed line is the time of the breakthrough. (C) Potentiometer, DSS, and SIMFIP measurements over the fault zone. SIMFIP total shear is light green, and borehole- parallel displacement is gray-blue. The dark blue curve shows the synthetic DSS measurement modeled from SIMFIP data.

Figure 8-6B shows a time series comparison between the DSS and the potentiometer in BCS-D5. We integrated over the three potentiometer's elements at 19.75, 20.25, and 20.75 m depths and did the same for the DSS across this depth interval to produce the displacement traces shown. The match between the two instruments is excellent, with a normalized cross correlation coefficient of 0.996, when combined with the match shown in Figure 8-6A, and indicates that the strain magnitudes measured by the DSS system are accurate (if we accept the industry standard potentiometer as a ground-truth). This shows that the DSS can accurately quantify the strain field, thereby complementing results from previous studies where DSS could be used only in a qualitative manner (Krietsch et al., 2018; Valley et al., 2012).

We also investigated the ability of the DSS system to detect shear displacement. Fiber optics are only able to measure changes along the axis of the fibers themselves (i.e., lengthening or shortening). In our case this means we can best resolve deformation of the rock mass, which is oriented parallel to the axis of the boreholes. Obviously, the deformation field is not perfectly aligned with our fibers because it is typically localized on fractures and faults that will intersect our boreholes at oblique angles. This means that much of the movement we would like to measure will be oblique to the fiber optic sensor. The nature of DSS measurements in shear has been tested in the laboratory (e.g., Madjdabadi et al., 2016), but only for a fiber anchored between two points, not grouted over tens of meters. The SIMFIP instrument installed in BCS-D7 provides us a unique opportunity to estimate the amount of shear applied to the DSS fiber in BCS-D5. We first make the assumption that the displacement measured across the Main Fault at BCS-D7 can be used as a proxy for displacement at BCS-D5, although the distance between the boreholes is roughly seven meters along the fault interface and the fault interface dips more steeply in D5 than in D7. We rotate the SIMFIP displacement tensor into the borehole coordinates of BCS-D5, such that one component is parallel to the borehole axis and the other two are perpendicular. We then compute the total displacement perpendicular to the borehole (i.e., total shear). We add the borehole-parallel and borehole-normal components of the rotated SIMFIP tensor (vector summation) to give the blue curve shown in Figure 8-6C. To directly compare this synthetic with the actual DSS and potentiometer measurements, we integrate both across the fault interval. The DSS and potentiometer curves in Figure 8-6C, still in excellent agreement when integrated across the fault, closely match the blue SIMFIP curve for the first two excavation pulses. This corresponds to the period of shear-mode deformation of the Main Fault. This tells us that the distributed DSS and potentiometer measurements are sensitive to more than simply borehole-parallel displacements, instead measuring the correct magnitude of applied shear as well. Interestingly, for the final period of excavation, when the SIMFIP measured mostly normal-mode opening, the potentiometer and DSS measure much larger displacements.

We suggest two potential causes of this discrepancy:

1. The fault slips differently at D5 than that at D7, and we cannot simply assume that the SIMFIP measurements accurately reflect movement even a few meters away. Indeed, the surface of the Main Fault is actually quite complex. For example, the upper fault interface at D5 strikes N244° and dips 81°NW (possibly overturned) while in D7 it is more consistent with the overall Main Fault trend (strike N037°, dip 64°SE; Zappone et al., 2020). The opposing dips at the two boreholes may lead to completely different slip mechanisms in

response to the gallery excavation, perhaps with shear continuing at D5 where none occurs at D7.

2. The distributed nature of the potentiometer and DSS allow them to measure different phenomena than the SIMFIP, which only senses between two points. The onset of opening mode deformation indicates a significant change in the stress state acting on the fault and may be activating fractures within the fault zone that were not active during the shear stage, or changing their mode of deformation.

8.2.4.2 What controls features reactivation tens of meters away from the excavation front?

Effect of the Main Fault architecture

The DSS measurements indicate that the two Main Fault zone interfaces accommodate most of the fault slip related to the gallery excavation, with no single, central slip surface. This is particularly evident in the inclined boreholes D3, D4, and D5 (Figure 8-3c). In all cases, strain decays quickly away from the fault interfaces, suggesting a lack of damage zone, as is clearly shown, for example, in core samples and optical logs (Jaeggi et al., 2017; Jeanne et al., 2017; Amann et al., 2018). This pattern of slip on the bounding interfaces, as opposed to a "central" slip surface, may be the result of the high compliance of the fault zone relative to the host rock (Jeanne et al., 2017). During the gallery excavation, for example, unloading would lead to 'bulging' of the fault zone and slip at the interfaces. Given that there is no damage zone, no gradient of deformation from the principal slip zone towards the intact host rock is observed.

This might highlight a typical mechanical behavior of shale faults. Indeed, fault zones are commonly conceptualized as a fault core, where the majority of the slip concentrates, and a surrounding damage zone that accommodates progressively less slip with distance from the core (Caine et al., 1996; Shipton and Cowie, 2003, Figure 8-7). The Main Fault, however, has an altogether different architecture, with a thick, heterogeneous layer bounded by two weak interfaces. These interfaces comprise a layer of fault gouge and scaly clay that abut undisturbed Opalinus Clay host rock (Jaeggi et al., 2017; Nussbaum et al., 2011; Amann et al., 2018, Figure 8-7). Between the two bounding planes, the fault is a complex mixture of scaly clay fabric and secondary fractures (also filled with scaly clay). In addition, SIMFIP measurements from a previous experiment at the MTRL indicate that the fault zone has a Young's modulus 2–5 times less than the host rock (Jeanne et al., 2017). This evidence suggests that the Main Fault can be treated as a thick layer with weak boundaries and no surrounding damage zone.

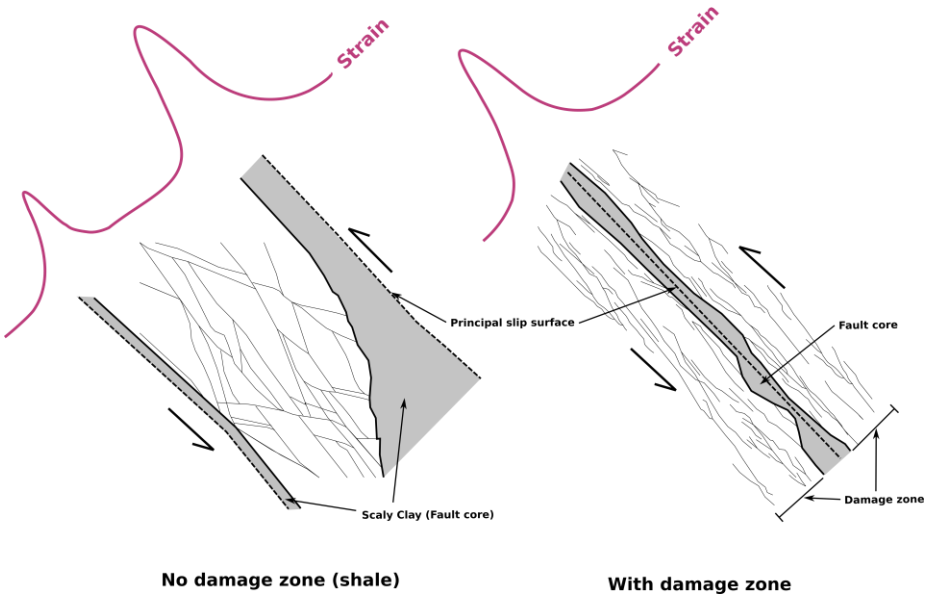

Figure 8-7. Schematic representations of the Main Fault (left; adapted from Jaeggi et al., 2017) and the canonical fault zone model (right; adapted from Shipton and Cowie, 2003) showing the relationship between fault core/gouge, principal slip surfaces, and the 'fault damage' zone. Theoretical DSS measurements are shown in purple for slip on either type of fault.

A number of secondary fracture sets exist within the Main Fault (Wenning et al., 2020) that might contribute to deviations from this 'two-peaked' pattern (for example, the strain measured in the fault zone at D6; Figure 8-3C. In addition, the interaction of the bedding-parallel fracture set (cross sections; Figure 8-7) with the Main Fault is not well understood. Given that the bedding-parallel fractures represent a later stage of deformation, they may cross cut the Main Fault itself (Nussbaum et al., 2011). If this is the case, these secondary fractures may actually be accommodating significant deformation in the rock mass, including in the Main Fault interval. However, as shown by the projection of the SIMFIP vector onto the Figure 8-7b cross section, the opening-mode deformation of the Main Fault is more normal to the steeper-dipping Main Fault interfaces than the shallower, bedding-parallel fractures, suggesting that the Main Fault interface itself is activated during opening.

Effects of stress versus intrinsic mechanical properties to explain why some off-fault features locally reacted rather than others.

In many cases, the strain that accumulated on secondary (i.e., non-Main Fault) fractures exceeded that of the Main Fault interfaces. For example, the 16-m anomaly in D3 displays nearly twice the displacement of the top or bottom interfaces of the Main Fault. In addition, the anomalies in D4 and D5 display similar deformation magnitudes to the Main Fault zone. Although a number of these secondary structures were activated, the vast majority of those identified in logs were not. For a given fracture, activation is controlled by its orientation in the local stress state and its intrinsic properties (e.g., cohesion, coefficient of friction, Handin, 1969; Freed, 2005), but identifying which will activate for given stress perturbation is difficult.

To investigate what distinguished the active fractures from the non-active ones, we separated all OTV-picked fractures into three groups: those inside the fault zone, active fractures outside the

fault zone, and inactive fractures outside the fault zone. Figure 8-8 shows each plane identified in the BCS-D4, D5, and D6 optical televiewer logs colored by slip tendency (increasing from blue to red) when subjected to the stress field determined by Guglielmi et al. (2020) for the MTRL. As detailed by Wenning et al. (2020), the Main Fault zone includes a variety of fracture sets of varying orientations, including fault-zone parallel fractures and WNW-dipping fractures, which are the most prone to slip of any of the identified features (red features, Figure 8-8A). As we mentioned above, however, slip localized on the upper and lower fault zone interfaces, which are further from failure in the in-situ stress conditions (dashed black lines and adjacent green lines, Figure 8-8).

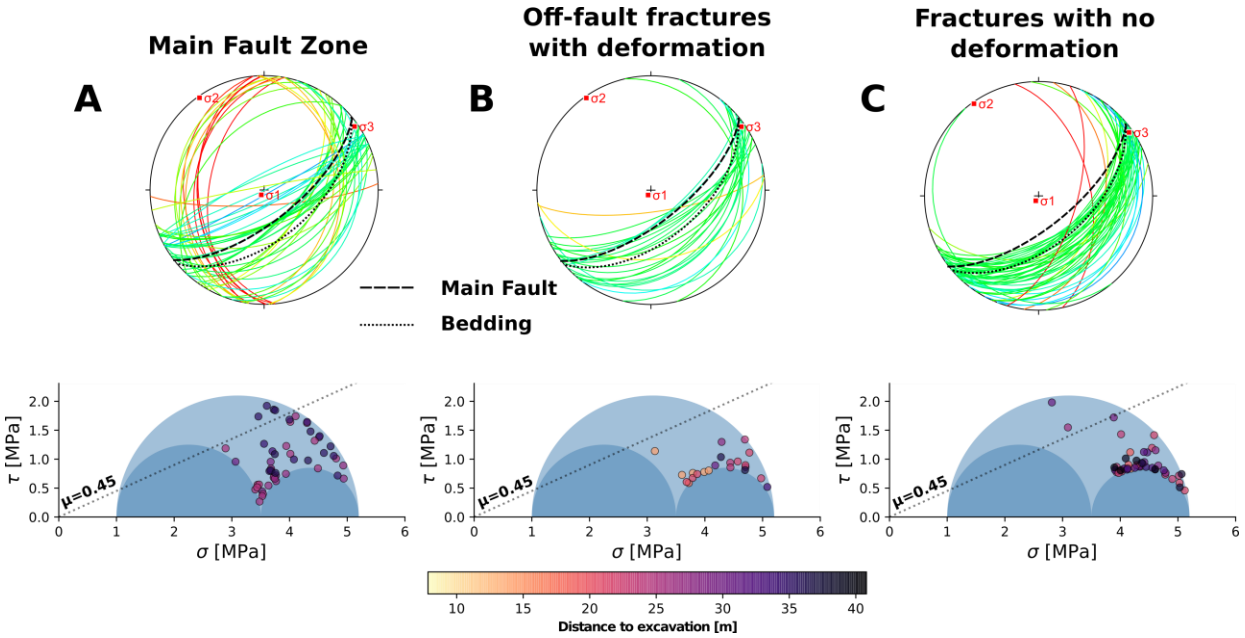

Figure 8-8. Fractures identified in optical televiewer logs in BCS-D4, D5, and D6: (A) Within the Main Fault zone, (B) outside of the Main Fault but displaying deformation on DSS, (C) All other fractures. The upper plots are lower hemisphere projections of poles and planes, colored by slip tendency in the local stress regime estimated by Guglielmi et al. (2020) (blue=low, red=high tendency). Dotted line shows the orientation of bedding at the MTRL, the dashed line shows the approximate orientation of the Main Fault. The lower row plots show the state of stress on each fracture relative to a Mohr Coulomb failure envelope for cohesionless fractures. Following Orellana et al. (2018), a peak coefficient of friction of μ=0.45 is used. The color of each dot corresponds to the distance from the feature to the excavation front (light=closer, dark=farther).

The off-fault fractures predominantly strike NE, with dips ranging from ~10–70° (Figure 8-8B-C). In a static stress state, the features that displayed a DSS signal are no more likely to slip than those which showed no deformation, making it difficult to discern in advance, solely from OTV logs, which features would be most likely to slip. These sets of features also span the orientation of both bedding and the Main Fault zone, meaning we cannot confidently state whether one or the other is hosting the deformation that is being measured. This is partially an effect of the DSS spatial resolution. Resolution prevents us from assigning strain to single features located within the 1-m gauge length of a DSS peak and may obscure subtle variations between slipping and non-slipping features. Because the induced stress perturbation decreases with distance from the excavation, we

color each feature in the lower row of Figure 8-8 by its distance from the breakthrough point. The features in column B, associated with strain signals outside the fault zone, are closer to the excavation front (on average, shown by their lighter color) than either the Main Fault itself, or the features displaying no strain. This suggests that, for features outside the weak fault zone, the distance to the stress perturbation has a weak control on whether they activate. The failure criterion used in Figure 8-8 assumes cohesionless fractures with a coefficient of friction of 0.45, taken as a representative value from Opalinus core testing performed by Orellana et al. (2018). Nearly all of the activated structures fall well below the failure criterion, suggesting that either the stress perturbation from the excavation was on the order of multiple MPa, or that the activated fractures are actually intrinsically weaker than our simple analysis suggests, or (likely) both. Careful characterization of the core indicates that most of the activated structures are associated with either (1) a lens of scaly clay, consisting of shear-realigned grains or (2) highly fractured zones where core was either lost or fragmented (red and blue solid lines in Figure 8-3A, respectively). The production of scaly clay is a product of shear, and produces a zone of weakness onto which further slip will tend to accumulate (Laurich et al., 2018). It is therefore possible that the fractured zones also contained small amounts of scaly clay that was not recovered during coring and therefore not classified as such. In any case, the correlation between DSS anomalies and the depth of known lenses of scaly clay (Figure 8-3A) suggests that the presence of scaly clay is the main controlling factor on fracture weakness, and, therefore, these features most likely able to activate under remote loading. At the MTRL, scaly clay may have developed on both bedding parallel secondary faults and on the Main Fault-parallel structures, despite their somewhat distinct orientations. This makes both sets of features susceptible to reactivation, and candidates for fluid flow within the Opalinus Clay.

8.2.5 Conclusions

We presented measurements from seven boreholes intersecting a fault zone in clay rock at the Mont Terri Rock Laboratory in Switzerland. Our dataset encompasses a period of new gallery excavation that remotely triggered slip along the fault. One chain potentiometer and one high-resolution 3D displacement sensor, installed alongside the fibers, allowed us to corroborate the magnitudes of the strain measurements made via DSS with independent systems.

During the excavation, located about 30 m away from our instrumented boreholes, strains ranging from 50–240 μE were measured mainly at the top and bottom of the fault zone at each of our boreholes, well above the maximum 3σ noise level of 20 μE. We showed that the DSS measurement has a significant sensitivity to shear strain in a grouted borehole and thus can be used as a proxy to estimate fault slip. The complex mechanical response of the gallery excavation damage zone was also captured on the DSS. Outside the EDZ, the DSS measurements show that deformation in the rock mass localized on several discrete fractures identified in core and logs. No strain gradient was observed from the excavation front showing the strongly anisotropic response of the shale formation. Within the Main Fault, deformation concentrated on the upper and lower fault zone interfaces, with relatively little deformation occurring inside the fault zone. Core samples revealed zones of fault gouge on these interfaces, indicating past episodes of slip and present-day mechanical weakness. The DSS measurements thus support a fault model consisting of a single, thick fault zone with no surrounding damage zone. Slip occurs at both interfaces between the fault zone and the undisturbed host rock, possibly due to bulk deformation of the

relatively compliant fault zone geology. Since there is no fault damage zone, there is no strain gradient developing from the main slip zone. This is in contrast to the canonical fault model for harder rocks where most slip occurs on a central fault core while a strain gradient extends away from the core within the surrounding fault damage zone. Outside the fault zone, deformation concentrated at depths associated with lenses of scaly clay or highly-fractured intervals (as indicated in core samples), likely on bedding-parallel fractures. Most fractures identified in OTV logs were not reactivated, despite nearly all having a similar orientation versus the ambient stress. Therefore, we conclude that fracture reactivation during the excavation was controlled by the intrinsic properties of the fractures, likely the presence or absence of scaly clay and fault gouge resulting in a low-cohesion, low-friction surface. Identifying these signs of past slip and weakness in the drilling core could be a means of forecasting which structures are primed for activation during future experiments.

Previous grouted DSS measurements have only proven to be of qualitative use. In contrast to these previous studies, we show how a grouted network of fiber optic cables can complement other monitoring systems to quantify the subsurface strain field. While additional case studies like ours are necessary to expand the existing understanding of these fiber optic measurements, they should prove useful in monitoring rock mass movements in many energy and geotechnical applications. Taking our network of boreholes intersecting a fault as an example, similar systems at Mont Terri and in other settings could be valuable in constraining the 2- and 3-D strain field near faults and fractures and can therefore help fill in our understanding of the spectrum of slip behavior that eventually culminates in induced seismicity.

8.3 Imaging the three-dimensional scale of seismic and aseismic rupture

8.3.1 Modelling the effects of fractures interactions on leakage and induced seismicity during a clay fault zone activation

We developed models to mimic the decametric-scale in-situ experiments of fault activation caused by fluid injection at 340 m depth in the low permeability shales ($k \sim 1 \times 10^{-18}$ m^2) within the Mont Terri Underground Research Laboratory (Switzerland) (Guglielmi et al., 2020a). The activated fault zone is called the Main Fault, and is described in the previous section. A first experiment called FS was conducted in 2015, with a reduced seismic monitoring array that did not allow an accurate localization of the induced seismic events. We recently conducted a new experiment called FS-B in November 2020, this time with an extensive seismic array. These experiments allowed the observation of fluid flow and rupture growth along multiple secondary fault branches within the fault zone. Both experiments mainly produced aseismic fault deformation and a small number of low-magnitude earthquakes of roughly -4 to -2. In addition, induced events seem to be localized outside the fault pressurized patch. Thus, field experiments show that the physics of fault reactivation by injection of fluid are complex, and that there are multiple controlling factors, not just the mineralogy of the fault zone which is typically the dominant factor at the laboratory scale. The orientation of displacement vectors measured *in situ* show a large variability that is related to interactions between multiple second order fractures in the fault core rather than slip on a well-defined plane (Guglielmi et al., 2020a). Here we explore how the fault zone internal complexity can influence the aseismic fault movement.

8.3.1.1 Model setting

We model a fluid injection and seismicity in a fault network using the 3D Distinct Element Code (3DEC) (Itasca Consulting Group, 2016). The code allows us to resolve, in one model, the interaction between fluid flow with two-way hydromechanical coupling, aseismic slip and seismic rupture in a system of discrete faults intersecting impervious elastic rocks. The location and magnitude of seismic events are estimated from the seismic slip and the ruptured area (see Wynants-Morel et al., 2020 for further information on the numerical method). The earthquake rupture model falls into the class of "inherently discrete models" (Rice, 1993).

The model uses the cubic law to describe the coupling between fluid flow, pressure and the hydraulic aperture change given by

$$\vec{Q} = -\frac{b_h^3 \cdot w}{12\mu_f}\vec{\nabla P} \tag{8.2}$$

where $\vec{Q}$ is the flow rate vector (m^3/s), $\vec{\nabla P}$ is the fluid pressure gradient (Pa/m), μ_f is the viscosity of fluid (Pa.s), w is the fault width (m), and b_h is the hydraulic aperture (m), which can vary both as a function of the change in effective normal stress ($\Delta\sigma_n'$, total normal stress minus fluid pressure), and dilation caused by shear slip. Then, the hydraulic aperture is linked to the permeability (k in m^2) as follows

$$b_h = b_{ho} + \frac{\Delta\sigma_n'}{k_n} + \Delta u_s \cdot \tan\psi, \text{ and } k = \frac{b_h^2}{12} \tag{8.3}$$

where b_{ho} (m) is the initial aperture at zero normal stress, k_n is the fault stiffness (Pa/m), Δu_s (m) is the shear slip increment, and ψ is the dilation angle (°).

Fault slip initiates based on the Mohr-Coulomb failure criterion ($\tau = \mu \cdot \sigma_n'$, where τ is the shear stress at which slip initiates, σ_n' is the effective normal stress) (Jaeger et al., 1979). The evolution of fault friction during sliding is calculated with the rate-and-state friction law (Dieterich, 1979; Marone, 1998):

$$\mu(v,\theta) = \mu_0 + a\, ln\left(\frac{v}{v_0}\right) + b\, ln\left(\frac{v_0\theta}{D_c}\right), \text{ with } \frac{d\theta}{dt} = 1 - \frac{v\theta}{d_c} \tag{8.4}$$

where μ_o is the friction coefficient at a reference slip velocity (v_o), the parameters a and b are rate-and-state constants, and d_c is the critical slip distance over which friction decreases.

To model both aseismic and seismic slip along the faults, we use an adaptive time stepping scheme with a time step around 1 second during inter-seismic periods and a reduced time step comprised between 10^{-6} and 10^{-3} second during the co-seismic ruptures. To detect a seismic

event, the transition from aseismic to seismic slip is defined when the slip velocity on cell along the fault reaches a threshold of seismic slip velocity (Wynants-Morel et al., 2020) defined by the rock elastic properties and the fault frictional properties. For each seismic slip, the code detects the origin and arrest time, and the hypocenter is identified as the first cell whose slip velocity exceeds of 0.1 mm/s. The event size is then quantified by the seismic moment (M_o) and the moment magnitude (M_w)

$$M_o = AG\bar{\delta}, \text{ and } M_w = \frac{2}{3}\log(M_o) - 6 \quad (8.5)$$

where G is the rock shear modulus and $\bar{\delta}$ is the average seismic slip (m) on the ruptured area (A in m^2).

The internal structure of the fault zone, its physical properties and the geology of the host rock were extensively characterized in previous works (Nussbaum et al., 2011; Nussbaum et al., 2017; Orellana et al., 2018a; Orellana et al., 2018b; Orellana et al., 2019). These data were used to set-up the models developed in this study. We compare a model (40 m × 40 m × 40 m) with a single planar fault and a model with three interconnected faults (Figure. 8-9a-b). Each fault segment has initial uniform hydromechanical properties, representing a conductive, rate-weakening fault (b_{ho} = 20 microns; μ_o = 0.6, (a-b) = -0.002, and d_c = 10 microns). The remote principal stress (σ_z = 5.3 MPa, σ_x = 3.8 MPa, σ_y = 4.7 MPa) and fluid pressure (P_o = 0.5 MPa) applied at the model boundaries and resolved on the fault planes are constant. These values of stress were estimated in-situ at the depth of experiments (Guglielmi et al., 2020a).

After the initialization of the background stress and fluid pressure conditions, a fluid injection is modeled as a point source in the fault. The fluid pressure is increased step by step from 0.5 MPa to 5.4 MPa (Figure 8-9c). The total time of injection is 650 seconds. In the model, fluid flow occurs in the activated parts in shear failure of the fault plane, and prevent flow from occurring in the remaining elastic parts, consistently with previous observations of fault activation in shales (Guglielmi et al., 2015; Guglielmi et al., 2020a). We tested the sensitivity of the calculated seismicity to different levels of fault criticality by including a deviatoric component (σ_{xy} = 0.1 to 1.5 MPa) to change the shear stress without modifying the normal stress among the tests.

8.3.1.2 Model Results

Through our models, results show that a local fluid injection can produce different fluid pressure distribution according to the number of faults and the initial stress conditions (Figures 8-9d-g). High-fluid pressures are distributed over a larger patch on a single fault, while they are more concentrated around the injection in the case of a fault network. An initial high stress state favors a larger diffusion of fluid pressure along the faults than an initial low stress state.

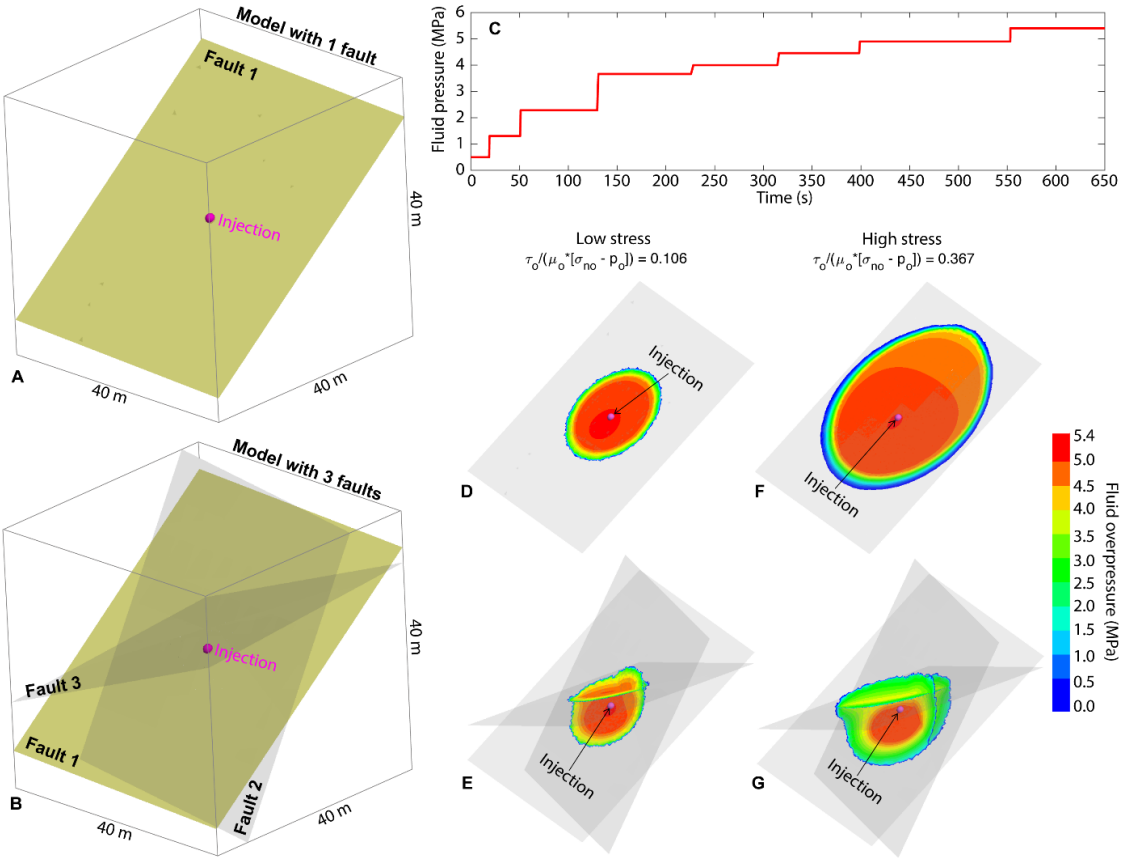

Figure 8-9. 3D view of the different model geometries, including (A) a single fault, and (B) three faults. The yellow fault, labeled "Fault 1", is the fault where the fluid injection is applied (magenta dot). (C) Fluid pressure history applied at the injection point. (D-E) Spatial distribution of the fluid overpressure at the end of injection (650 s) for low and high background stress ratios.

The fluid injection also induces significant aseismic slip near the injection that then contributes to trigger micro-seismicity within a fault volume, especially on the secondary structures and fault intersections at a distance from injection in the main fault plane (Figure 8-10). Figure 8-10 also shows that the location of seismic events is influenced by the number of faults and the initial stress. The seismic events are aligned along the intersection between the faults, and the moment magnitude (M_w) of seismic events are comprised between -4 and -1 depending on the initial stress state (Figure 8-11).

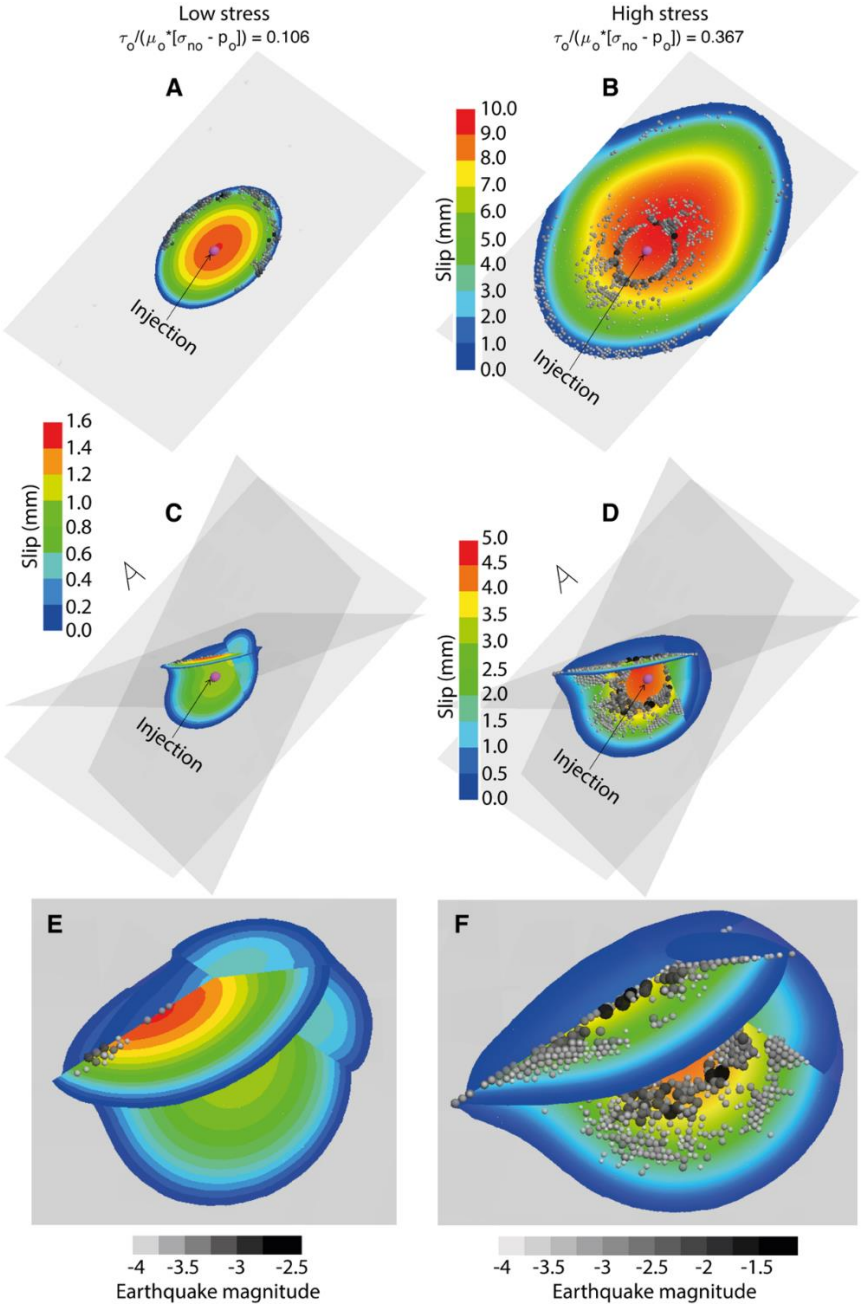

Figure 8-10. Spatial distribution of fault slip and seismicity at the end of injection for the (A-B) single fault model and (C-D) the fault network model. (E-F) Close-up view of the fault network model with a different viewing angle (upper view). Results are presented for two ratios of initial shear stress versus strength (background stress ratio): low (left panels) and high (right panels). The diameter of the spheres is associated with the size of events.

Figure 8-11 also indicates that the seismicity is triggered at distance from injection (about 3 m for a single fault model, and about 2 m for a fault network model), and that the pressure and shear stress fronts affect a zone of about 10-20 m for the fault network model and of about 10-33 m for the single fault model at the end of the simulation.

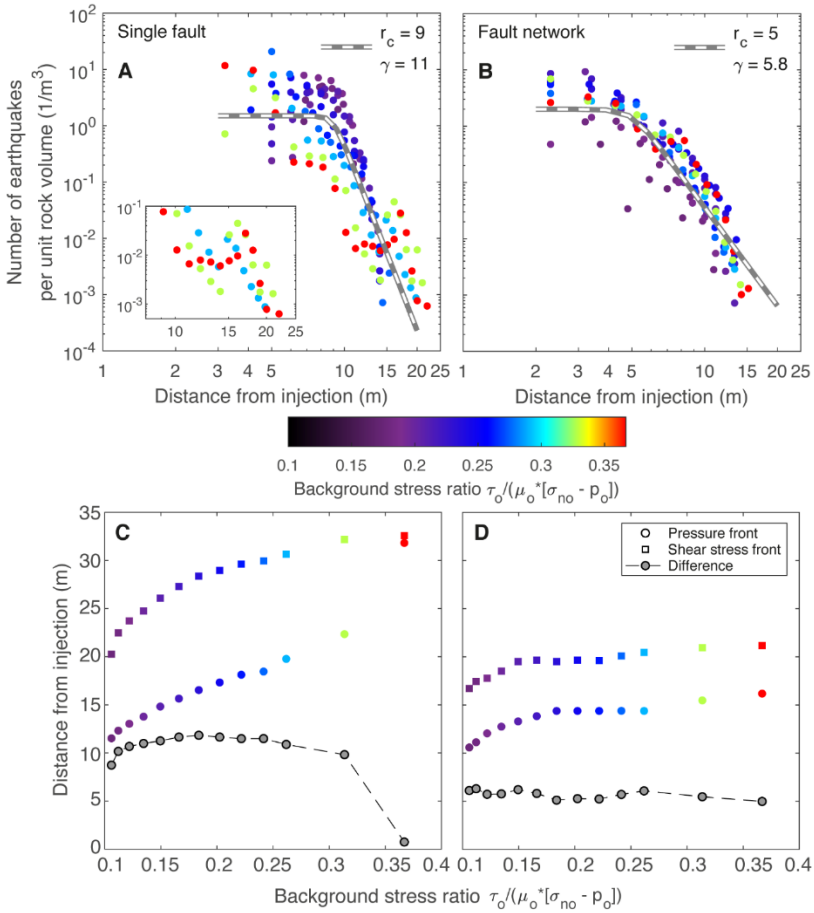

Figure 8-11. Number of earthquakes per unit rock volume as function of distance from injection for the model with (A) a single fault and (B) three faults. Position of the fronts of fluid pressure and shear stress at the end of injection for the model with (C) a single fault and (D) three faults. The difference between the shear and pressure fronts is ploted with the gray dot and the dashed line.

8.3.1.3 Conclusion

A variety of physical mechanisms has been proposed to explain aseismic and seismic slip activation within fault zones pressurized with fluids. Our 3D modeling study emphasizes that the architecture of the fault zone, the initial state of stress, and the fault permeability evolution have an important effect on the fluid pressure diffusion, the growth of aseismic slip and the triggering and distribution of seismicity during fluid injection. Our results highlight that secondary features interaction within the fault zone and the competition between fluid pressurization and stress transfer associated both to pressurization and co-seismic rupture are viable mechanisms affecting induced seismic events in low permeability host rock. The mechanism can drive the fault network to multiple seismic ruptures together or separately at each individual fault segment. The resulting induced seismic sequence exhibits a heterogeneous distribution in space and complex spatial-temporal characteristics. During fluid injection, the size and timing of pressurization and associated stress perturbation may vary significantly between faults zones. Thus, further studies of fault stability with controlled fluid injection experiments are needed and may provide

important new insights into the physical processes controlling the interplay between the fault network, frictional properties, stress perturbation and permeability evolution for assessing what factors determine if fault rupture is seismic or aseismic during hydraulic stimulation. This preliminary approach will be extended to the analyses of the seismicity induced during the FS-B experiment which is in process, but is already providing more accurately localized events compared to the FS experiment.

8.3.3 Continuous active-source seismic monitoring of the loss of integrity induced by water pressurization of the main fault at Mont Terri, Switzerland

8.3.3.1 FS-B Experiment

The FS-B experiment aims at imaging long-term fluid flow as well as permeability and stress variations through a ruptured minor fault to assess the performance of radioactive waste repositories in shale formations. The first FS-B fault stimulation experiment took place on November 21st, 2020. We injected at 40.4 m depth below the Mont Terri galleries, in a 1 m long interval set across the top of the Main Fault zone (Figure 8-12). We conducted six injections at constant flowrates of 2 l/min (injection 1), 6 l/min (injection 2), 9.8 l/min (injection 3), 9.94 l/min (injection 4), 9.55 l/min (injection 5) and 10 l/min (injection 6). The five first injections were 10 minutes long. Injection 6 was 20 minutes long. The injection interval was shut-in between the injection periods. Fault hydraulically opened when injection pressure was between 5 and 6 MPa. After a cumulated injected volume of 178 liters, a hydraulic connection occurred with boreholes set in gallery 2008, intersecting the fault 15–18 m away along strike from the injection point. No clear hydraulic connection was observed in boreholes intersecting the fault in the CS-D niche, 8 to 10 m up-dip from the injection point. These first results show an apparent heterogeneity in the fault leakage that preferentially initiated parallel to the fault strike where leakage was measured to be about 26% of the injected flowrate. Borehole displacements and deformations were observed on many points. They range in the order of 60 to 130 10^{-6} m. Ten times smaller signals were observed in the non-hydraulically connected CS-D zone showing that this zone was deformed during the stimulation, but clearly not hydraulically connected.

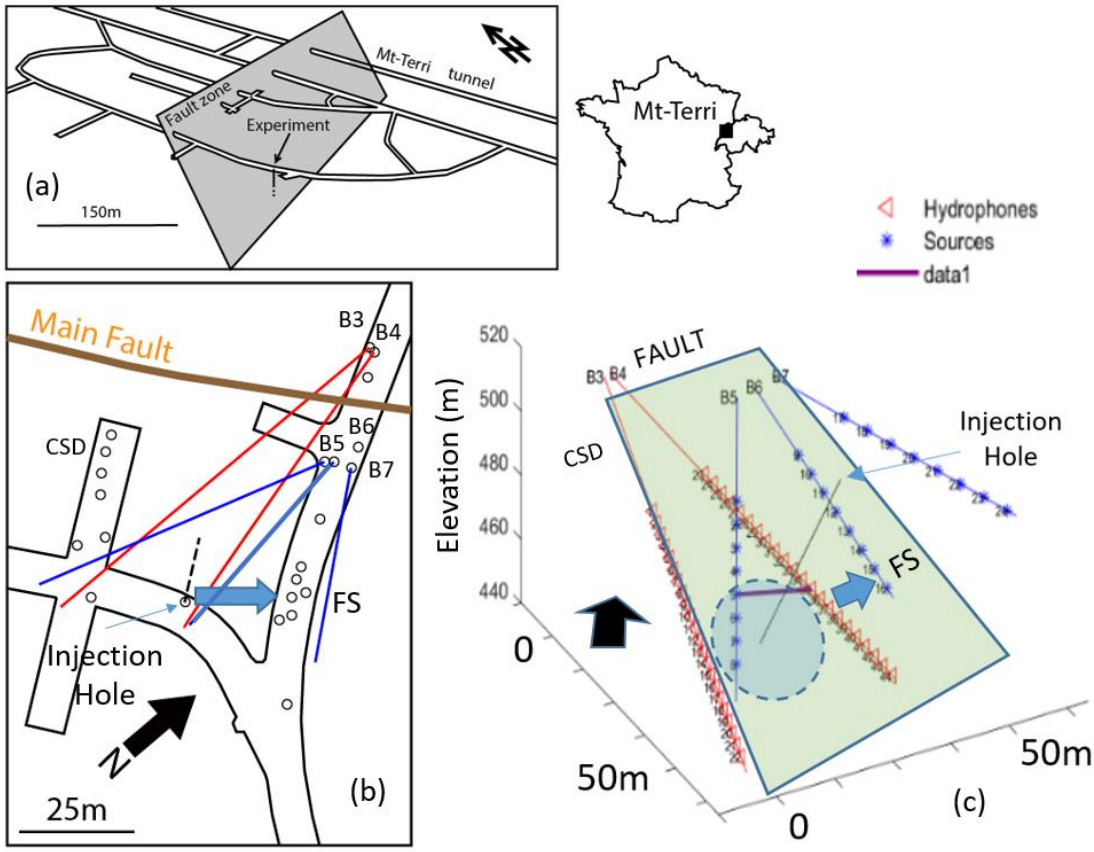

Figure 8-12. Continuous Active-Source Seismic Monitoring (CASSM) geometry surrounding the main fault of Mont Terri. (a) Experiment location in the Mont Terri underground laboratory. (b) Map view of the FS-B experiment (circles indicate vertical boreholes crosscutting the fault). Colored lines are the inclined boreholes instrumented with CASSM. Blue arrow shows the hydraulic connection that occurred between injector and monitor during the experiment. (c) Three-dimensional view of the CASSM setting (fault is simplified as the green plane). The receiver boreholes, B3 and B4, are in the footwall and the source boreholes, B5, B6, and B7, are in the hanging wall. The injection borehole is inclined, making a 30-40° angle with the fault plane.

8.3.3.2 Continuous active-source seismic monitoring (CASSAM) geometry and acquisition

The CASSM technology (Daley et al., 2007-2011; Silver et al., 2007; Marchesini et al., 2017) is used to monitor a volume of 70x70x70 m^3, crosscut by the Mont Terri Main Fault (Figure 8-12). The volume is instrumented with 23 boreholes, creating a unique fault-testing field laboratory, permanently monitored by a large array of instruments including DAS-DTS-DSS fibers, pressure and 3D fault displacement sensors, tiltmeters, passive acoustic and seismic sensors. The CASSM system includes five dedicated monitoring wells (Figure 8-12b-c). Three boreholes have a total of 24 piezoelectric seismic sources (8 each); the other two boreholes have 44 hydrophones in two arrays (22 each). The receiver boreholes (B3 and B4) are in the foot wall of the fault, while the source boreholes (B5, B6, and B6) are in the hanging wall. During CASSM acquisition, each source is activated 16 times, while all 44 hydrophones are recording at 48 kHz and stacking to increase signal to noise ratio (SNR). The acquisition process cycles through all sources to

generate a single CASSM epoch. An example of a source-gather is shown in Figure 8-13A. The time to complete each full sequence is about 8 minutes, the temporal resolution of this system.

The CASSM data shown below is from November 10th to 23rd, 2020 (~2700 epochs).

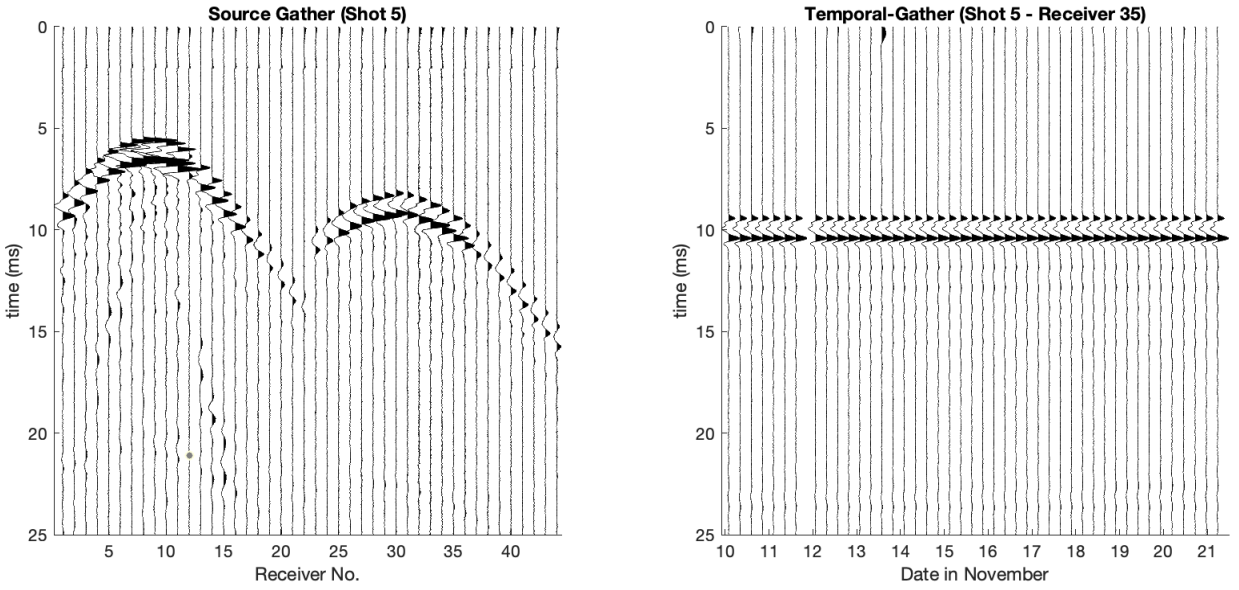

Figure 8-13. (A) An example of a source-gather for shot 5 (located in B4) at the beginning of November 10th, 2020. Receiver numbers 1-22 and 23-44 correspond to boreholes B3 and B4. (B) An example of a temporal-gather prior to injections for shot 5 and receiver 35.

The system ran continuously without issue, providing information about background noise prior to the injections. We are interested in velocity change rather than absolute velocity hence differences in travel time along fixed ray paths are the primary measurable. Temporal gathers allow us to observe changes in waveforms as a function of calendar time for a single source-receiver pair (Figure 8-13B). Differences in arrival time (δt) are often too small (~10s of μs) to be observed by visual inspection. To measure these small changes in arrival time, we follow the processing flow of Silver et al. (2007). We window the data to 3 ms intervals around the first arrival and interpolate the data from 48 kHz to 480 MHz. Traces were then cross-correlated with the first trace on November 10th, 2020, to estimate subsequent delays due to the fault manipulation experiment. To test the precision of the CASSM system, we followed this workflow to obtain δt for epochs between November 10th and November 21st (Figure 8-14), before any injections occurred. From this data, we can see that the CASSM system is stable; the standard deviation of delay times is 895 ns, close to previous estimates using a similar system (i.e., Silver et al., 2007).

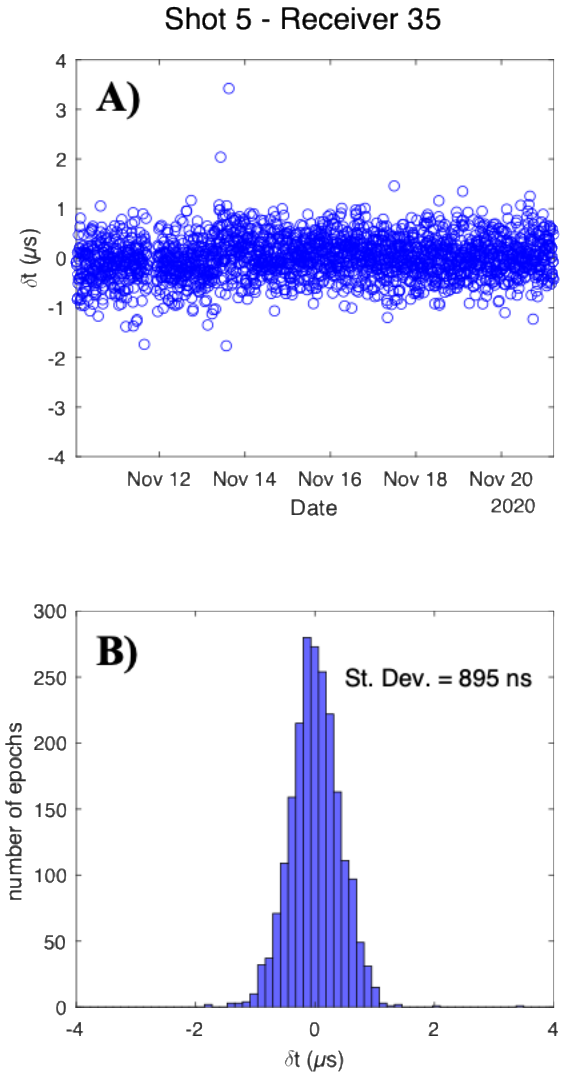

Figure 8-14. (A) a δt plot for a single source-receiver pair (5/35) between the dates of November 10th and November 21st (prior to injections). (B) The corresponding histogram, showing the stability of the CASSM system. The delay time standard deviation is 895 ns.

8.3.3.3 Preliminary results and discussion

Differences in travel time (δt) were calculated for all source receiver pairs. An example of a δt curve for a source-receiver pair is shown in Figure 8-15. Also plotted is the injection pressure during the experiment. From this curve, injections 2 through 6 are observed with δt values ranging from 8 to 15 μs. The first injection was not detected by any source-receiver pair, likely due to the small injection volume. Travel time variations almost instantaneously follow the injection pressure variations, decreasing when pressure increases and increasing when the injection is shut-in. After the last injection, the delays do not return to background noise, suggesting that a long-term change in the fault has occurred.

We interpret the "instantaneous" variations in delay time with injection pressure as related to mechanical opening and closing of compliant fractures within the fault zone. A decrease in P-wave velocity (increase in delay time) as a function of injection pressure is consistent with laboratory data showing similar reductions as a function of decreased normal stress (e.g. Pyrak-Nolte et al 1990). Likewise, similar signatures are observed during hydraulic fracturing operations, albeit at lower accuracies in the context of time-lapse VSP studies (e.g., Binder et al. 2018, 2020). The apparent long-term change in travel times match the irreversible fault deformations recorded on the strain monitoring array. It might relate to fault zone shear-induced damage or to delayed leakage of the injected fluid volume in this low permeability clay fault environment.

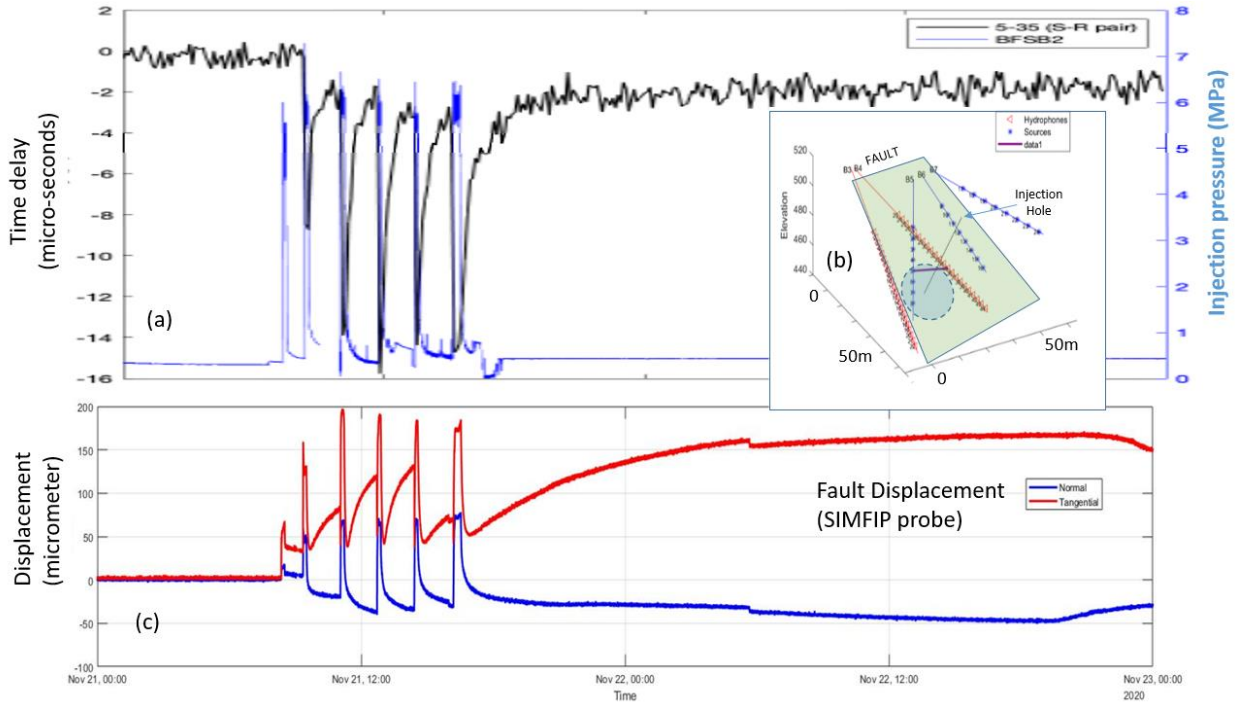

Figure 8-15. Variations of p-waves time delay related to injection pressure and fault movements (November 2020 FS-B fault activation experiment). (a) p-waves time delay (black) and injection pressure (blue); (b) Location of the seismic ray path considered in figure a (blue dashed circle figures the pressurized fault zone); (c) Fault tangential (red) and opening (blue) displacement measured at the injection borehole.

In addition to the δt response, we calculated the percent change in RMS amplitude and centroid frequency during the same period for the source-receiver pair, 5 and 35, respectively (Figure 8-16). Change in RMS amplitude were measured during the last four brine injections, while changes in centroid frequency occurred during the last five brine injections. While the amplitude and centroid estimates have higher noise levels than our phase delay measurements, they are consistent and suggest that P-wave attenuation is increasing as a function of injection pressure.

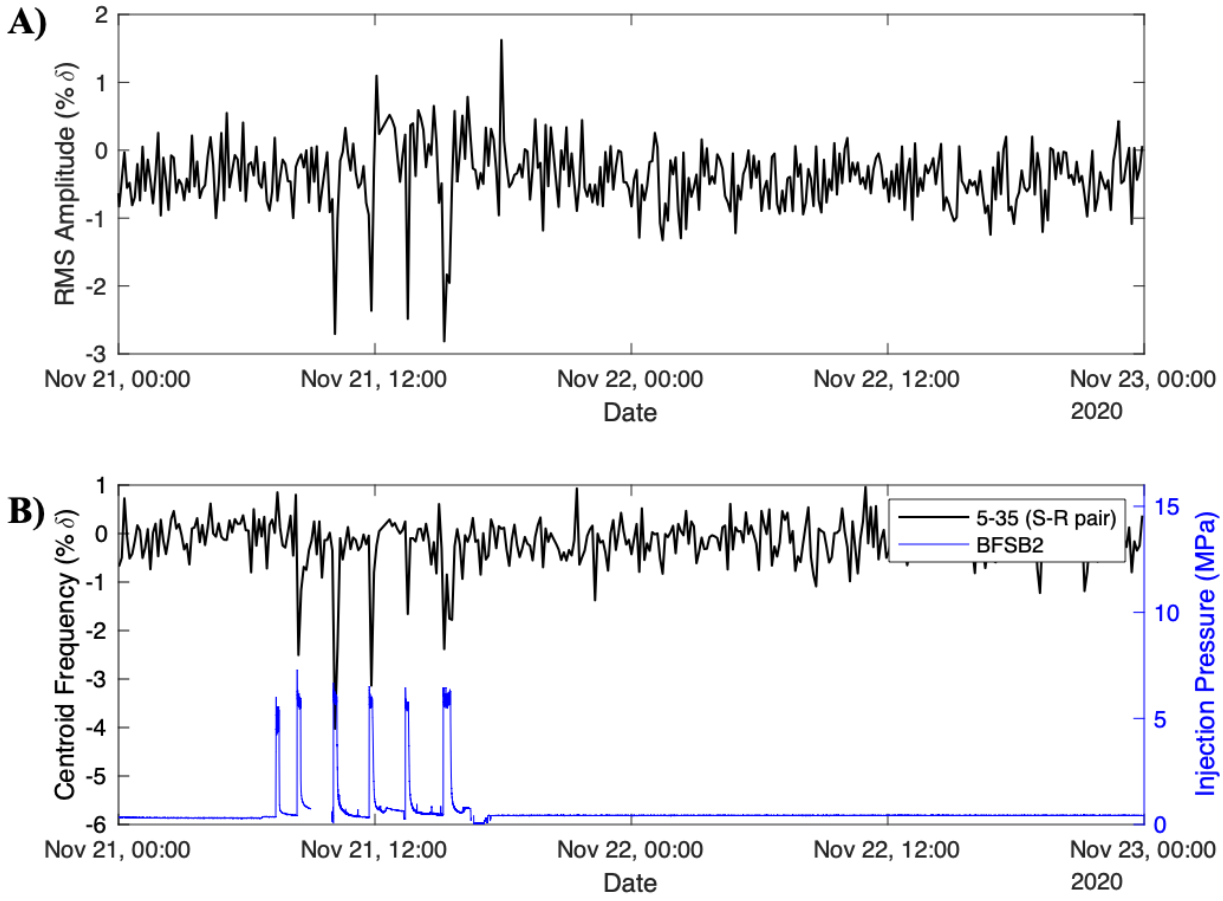

Figure 8-16. (A) Percent change (%δ) in RMS amplitude, and (B) percent change in centroid frequency for source-receiver pair 5/35 with injection pressure (blue).

Figure 8-17 shows δt curves for all receivers for shot 5. That is, the *y*-axis represents receivers 1 through 44, the *x*-axis are the dates between November 20th and 23rd, and the color represents the δt. The horizontal blue lines in the map represent source-receiver pairs that exceed the standard deviation set by the standard deviation of all source-receiver pairs. We observe that only a small number of receivers detect the injections (i.e., receivers 32-36 in Figure 8-13). These receivers had ray-paths that travelled close to the injection point, suggesting that the activated fault patch is small compared to the entire CASSM array aperture. This is consistent with pressure observations that show a localized hydraulic leakage within the activated fault zone (Figures 8-12 b-c).

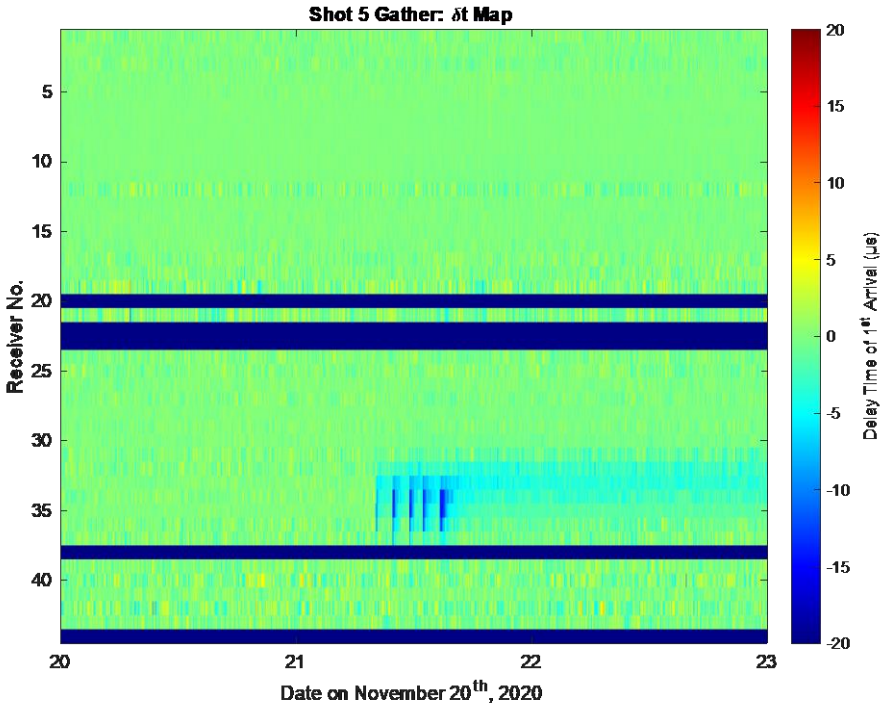

Figure 8-17. A source-gather δt map for shot 5. Horizontal dark blue lines are rejected source-receiver pairs due to poor SNR.

8.3.3.4 Conclusions

The CASSM approach was used to detect injections of brine into the Mont Terri Main Fault and the subsequent reactivation. They were detected by small changes in P-wave travel time (i.e., 8 to 15 μs) as well as amplitude reductions and a decrease in first arrival centroid frequency. A small number of receivers were able to detect the injections suggesting that the fault activated patch was localized. Further tomographic imaging will be conducted to determine the size of this patch and the temporal dynamics of fault healing.

8.4 Work Summary and Perspectives

The architecture of fault zones affecting argillite layers indicates activation mechanisms characterized by a high strain localization at the fault zone "boundaries." This is because these faults apparently display a reduced fracture damage zone, and a thick highly deformable and heterogeneous core "layer" with abrupt contact with the surrounding intact rock. The result is that deformation and leakage may be "contained" within the "layer," with the possibility for preferential slip at the layer's interface. Second order fracture interactions within the fault zone and the fact that leakage relates to rupture favor local stress concentrations at fractures' intersection. This may reduce the possibility for a large stress change at rupture, limit the number and magnitude of seismic events, favor aseismic movements and local fluid channeling, and potentially slow the potential post activation sealing processes (because of high dilation eventually occurring at fracture intersections).

The perspectives of work until the end of FY21 are the following:

- We will continue processing data from the new experiment in Mont Terri (FS-B) using the time-lapse p-waves tomographic images to explore the intricate relationships between aseismic flow paths and seismic volumes within a thick fault zone. When the first images are processed, we will analyze these velocity images using a 3DEC fully coupled hydromechanical model in terms of leakage and ruptured areas. In addition, we will extend the numerical models to explore the effects of different fault zone complexity on induced seismicity, and we will eventually compare to measured seismic events and strains (DSS, DAS and SIMFIP) from the experiment.
- In parallel, LBNL will be involved in the thermo-hydrofracture *in situ* testing at ANDRA (France). A first experiment is scheduled at the Bure Underground Laboratory in Fall 2021. ANDRA experiment setting consists of 10 Boreholes about 20 m long, drilled horizontal and parallel to the maximum horizontal stress of ~17 MPa. The minimum horizontal and the vertical stresses are considered close to each other of ~12 MPa. The initial pore pressure is 4.7 MPa. Heater devices will be set in the boreholes over a 10 m length. The rock will be "fast" heated to 90°C by the 8 peripheral horizontal boreholes and the two "central" ones. While heating, pore pressure, temperature and induced seismicity will be monitored from outside the heated volume. Repeated active seismic source monitoring will also be conducted to image the HF propagation. Heating phase will last about one month, and it will be followed by a characterization phase of the hydrofracture, through a horizontal borehole drilled in the center of the heated volume. Given the state of stresses, the experiment should eventually produce a near horizontal hydrofracture which extent should "theoretically" be constrained by the heating design, respectively of a maximum 3 m width and a 10m length. Many uncertainties are associated to this experiment about the fracturing occurrence, mode and dimensions. During the cooling period, LBNL will use a SIMFIP probe to characterize the eventual damage and thermal-hydrofracture generated during the heating phase.

9. Interfacial Alteration and Impacts on Radionuclides Transport

9.1 Introduction

Interfaces where materials of distinct chemical and physical properties meet are regions where chemical gradients are largest. The resulting chemical reactions within mm-cm of the interfaces can largely change the transport properties of the materials. In nuclear waste disposal systems, complex geochemical alterations have been reported at the interfaces of cannister-clay/bentonite [*Kaufhold et al.*, 2018; *Pignatelli et al.*, 2014], concrete-argillite or clays in general [*Bartier et al.*, 2013; *Bernard et al.*, 2020; *Mader et al.*, 2017], bentonite-argillite [*Zheng et al.*, 2017], concrete-bentonite [*Alonso et al.*, 2017; *Fernandez et al.*, 2017; *Gaboreau et al.*, 2020; *Huertas et al.*, 2009], and concrete-bitumen [*Bertron et al.*, 2014]. For instance, in presence of concrete, the leachate is alkaline and can perturb the engineered barrier or the host rocks. In the concrete, the dissolution of portlandite can result in porosity increase [*Bartier et al.*, 2013]. In the bentonite, mineral dissolution can be triggered, which buffers the pH change. Furthermore, precipitation of secondary mineral phases including Mg silicates [*Fernandez et al.*, 2018] and illitization [*Bartier et al.*, 2013] can occur, which may reduce the porosity at the interface. The porosity will affect the diffusive transport of the radionuclides, and it has also been reported that the interfaces can serve as preferential pathways for gas migration and thus the changes at the interface can impact gas migration in the nuclear waste disposal system [*Liu et al.*, 2016].

However, current continuum scale reactive transport models often do not describe accurately the drastic changes in mineral phases in the vicinity of the interface and the resulting changes in pore structure and thus the diffusivity and permeability. To address this research gap, the overarching goal of this task is to use pore-scale multiphase reactive transport model to simulate the alteration within mm of the interface, where the alteration is most intense. This modeling effort will focus on the development of the conceptual model, development of the reaction networks, and analyzing the alteration at the concrete/bentonite, a region where chemical reaction occurs with two phase flow in the bentonite side and single phase flow in the concrete, and at the concrete/argillite, where chemical reactions occur under saturated condition. For this purpose, two modeling approaches will be leveraged. One is a finite volume method based on the pore-scale model that couples CrunchTope and OpenFOAM. However, given the high computational cost, it will be challenging to simulate the domain size needed in our investigation. This approach will therefore largely serve as benchmark purpose for small scale simulations in comparison with the Lattice Boltzmann Method (LBM). The LBM-based multiphase reactive transport model, which is more computationally efficient especially in the CPU-GPU hybrid computation environment [Ye et al. 2015; Riesinger et al. 2017; Fakhari et al. 2017], is being developed in our task. This section reports the progress of the Lattice Boltzmann code and test simulation results for verification. In addition, a geochemical benchmark test has been developed for future pore-scale modeling, and the continuum scale modeling results are presented here.

9.2 Methods

9.2.1 Phase-Field Lattice Boltzmann Method (PF-LBM)

Phase-field lattice Boltzmann method (PF-LBM) is derived from the conservative phase-field theory, and is capable of considering high density and viscosity ratios at the same time with

relatively high computational efficiency, compared to several other popular multicomponent multiphase lattice Boltzmann methods, such as Shan-Chen LBM, color-gradient LBM. Given the properties of the fluids involved in the nuclear waste storage systems, PF-LBM is adopted here.

A series of equations were solved to track the interface and calculate the hydrodynamic parameters (e.g., velocity and pressure fields). One key governing equation is the phase-field equation (Chiu and Lin, 2011])

$$\frac{\partial \phi}{\partial t} + \nabla \cdot \phi \boldsymbol{u} = \nabla \cdot M \left[\left(\nabla \phi - \frac{\nabla \phi}{|\nabla \phi|} \frac{[1-4(\phi-\phi_0)^2]}{\xi} \right) \right] \tag{9.1}$$

where ϕ is the phase field value; M is the mobility; ϕ_0 is the average value of two extreme values, i.e., ϕ_L of the low-density fluid and ϕ_H of the high-density fluid; ξ is the interfacial thickness; and $\boldsymbol{u}$ is the velocity, and is solved by the continuity and momentum equations for incompressible multiphase flow, as given by equations (9.2) and (9.3), respectively.

$$\frac{\partial \rho}{\partial t} + \nabla \cdot \rho \boldsymbol{u} = 0 \tag{9.2}$$

$$\rho \left(\frac{\partial \boldsymbol{u}}{\partial t} + \boldsymbol{u} \cdot \nabla \boldsymbol{u} \right) = -\nabla p + \nabla \cdot (\mu [\nabla \boldsymbol{u} + (\nabla \boldsymbol{u})^T]) + \boldsymbol{F}_s + \boldsymbol{F}_b \tag{9.3}$$

where ρ and μ are the local fluid density and viscosity, respectively; p is the macroscopic pressure; $\boldsymbol{F}_s$ is the surface tension force; $\boldsymbol{F}_b$ is the body force. The surface tension force $\boldsymbol{F}_s$ is given by (Fakhari et al. 2017; Fakhari et al. 2018)

$$\boldsymbol{F}_s = \eta_\phi \nabla \phi \tag{9.4}$$

where

$$\eta_\phi = 4\beta(\phi - \phi_L)(\phi - \phi_H)(\phi - \phi_0) - \kappa \nabla^2 \phi \tag{9.5}$$

η_ϕ is the chemical potential for binary fluids, β and κ are coefficients related to the surface tension and the interface thickness.

To solve the interface-tracking equation (9.1), the lattice Boltzmann equation below (9.6) is implemented to update the binary fluids distribution using the D2Q9 scheme (Fakhari and Bolster. 2017; D. Fakhari et al. 2018)

$$h_i(\boldsymbol{x} + \boldsymbol{e_i}\Delta t, t + \Delta t) = h_i(\boldsymbol{x}, t) - \frac{h_i(\boldsymbol{x},t) - \bar{h}_i^{eq}(\boldsymbol{x},t)}{\tau_\phi + \frac{1}{2}} + F_i^\phi(\boldsymbol{x}, t) \tag{9.6}$$

The forcing term for the surface tension force is given by

$$F_i^\phi(\boldsymbol{x}, t) = \Delta t \frac{[1-4(\phi-\phi_0)^2]}{\xi} w_i \cdot \frac{\nabla \phi}{|\nabla \phi|} \tag{9.7}$$

where h_i is the phase-field distribution function; τ_ϕ is the phase-field relaxation time; $\boldsymbol{e_i}$ mesoscopic velocity set in D2Q9 scheme ($i = 0, \cdots, 8$); w_i is the weight coefficient on each direction of D2Q9 scheme, $\bar{h}_i^{eq}$ is the phase-field equilibrium function and calculated by

$$\bar{h}_i^{eq} = h_i^{eq} - \frac{1}{2} F_i^\phi \tag{9.8}$$

where $h_i^{eq} = \phi\Gamma_i = \phi w_i \left(1 + \frac{\boldsymbol{e_i}\cdot\boldsymbol{u}}{c_s^2} + \frac{(\boldsymbol{e_i}\cdot\boldsymbol{u})^2}{2c_s^4} - \frac{\boldsymbol{u}\cdot\boldsymbol{u}}{2c_s^2}\right)$, c_s is the speed of sound in the system, and $c_s = 1/\sqrt{3}$ in the simulations. To update the phase/fluid distribution, the distribution functions on each lattice are summed

$$\phi = \sum_i h_i \tag{9.9}$$

Then the local density of each lattice is updated by

$$\rho = \rho_L + (\phi - \phi_L)(\rho_H - \rho_L) \tag{9.10}$$

where ρ_H and ρ_L are the density of the high- and low-density fluid, respectively.

To recover the hydrodynamic properties (e.g., pressure, velocity) in Equation (9.3), the following lattice Boltzmann equation is solved (Fakhari et al. 2017; Fakhari et al. 2018)

$$g_i(\boldsymbol{x} + \boldsymbol{e_i}\Delta t, t + \Delta t) = g_i(\boldsymbol{x}, t) + \Omega_i(\boldsymbol{x}, t) + \boldsymbol{F}_{si}(\boldsymbol{x}, t) \tag{9.11}$$

where g_i is the hydrodynamic distribution function, $\boldsymbol{F}_{si}$ is the forcing term for the surface tension force

$$\boldsymbol{F}_{si}(\boldsymbol{x}, t) = \left[(\Gamma_i - w_i)(\rho_H - \rho_L)c_s^2 + \Gamma_i\eta_\phi\right](\boldsymbol{e}_i - \boldsymbol{u}) \cdot \nabla\phi \tag{9.12}$$

For the collision term Ω_i, we use the multiple-relaxation time (MRT) collision operator to improve the numerical stability (Fakhari and Bolster. 2017, Fakhari et al. 2017)

$$\Omega_i(\boldsymbol{x}, t) = -\mathbf{M}^{-1}\hat{\mathbf{S}}\mathbf{M}\left(g_i - \bar{g}_i^{eq}\right) \tag{9.13}$$

where $\mathbf{M}$ is an orthogonal matrix for transforming the distribution functions from physical space into moment space, $\hat{\mathbf{S}}$ is a diagonal relaxation matrix and is

$$\hat{\mathbf{S}} = diag(1, 1, 1, 1, 1, 1, 1, s_v, s_v) \tag{9.14}$$

and

$$s_v = \frac{1}{\tau + 1/2} \tag{9.15}$$

where τ is the relaxation time and computed via

$$\tau = \frac{\mu}{\rho c_s^2} \tag{9.16}$$

The local viscosity μ is updated using a linear interpolation

$$\mu = \mu_L + (\phi - \phi_L)(\mu_H - \mu_L) \tag{9.17}$$

where μ_L and μ_H are the viscosities of the light and heavy fluid, respectively. The modified equilibrium function $\bar{g}_i^{eq}$ is

$$\bar{g}_i^{eq} = g_i^{eq} - \frac{1}{2}F_i \tag{9.18}$$

in which

$$g_i^{eq} = pw_i + \rho c_s^2(\Gamma_i - w_i) \tag{9.19}$$

After solving eqn(11), the hydrodynamic pressure (p) and velocity are calculated by (Fakhari and Bolster. 2017; D. Fakhari et al. 2018)

$$\boldsymbol{u} = \frac{1}{\rho c_s^2}\sum_i g_i \boldsymbol{e}_i + \frac{\Delta t}{2\rho}(\boldsymbol{F}_s + \boldsymbol{F}_b) \tag{9.20}$$

$$p = \sum_i g_i + \frac{\Delta t}{2}(\rho_H - \rho_L)c_s^2 \boldsymbol{u}\cdot\nabla\phi \tag{9.21}$$

Figure 9-1 shows the main calculation procedure at each time step

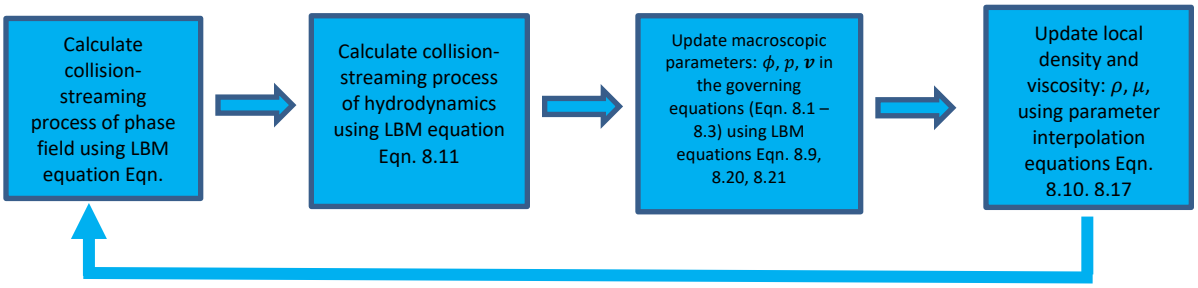

Figure 9-1. Main calculation procedure of phase-field LBM at each time step

9.2.2 Lattice Boltzmann Method (LBM) for transport process under multiphase flow condition

The advection-diffusion equation for single phase flow can be recovered from the LBM evolution equation and equilibrium distribution function. Recently, a unified approach for modeling chemicals in multiphase flow system has been developed to include the interface effect, and the evolution equation for chemical m using the D2Q5 scheme is (Riaud et al. 2014; Zhao et al. 2015; Fu et al. 2018)

$$f_{j,m}(\boldsymbol{x}+\boldsymbol{e_j}\Delta t, t+\Delta t) = f_{j,m}(\boldsymbol{x},t) + \left(-\frac{1}{\tau_j}\right)\left[f_{j,m}(\boldsymbol{x},t) - f_{j,m}^{eq}(\boldsymbol{x},t)\right] + \beta_{j,m}W(x_r)f_{j,m}^{eq(0)}\cos\theta \tag{9.22}$$

where $\boldsymbol{e_j}$ is mesoscopic velocity set in D2Q5 scheme ($j = 0,\cdots,4$), the function $W(x_r)$ indicates whether chemicals can be transported in a fluid ($W(x_r) = 0$ for wetting fluid in which transport is allowed; $W(x_r) = -1$ for non-wetting fluid and the chemicals are pushed back into the wetting fluid), $\beta_{j,m}$ is an empirical parameter to tune the interface profile while keeping the same topology, $f_{j,m}^{eq(0)} = w_j C_m$, and θ is the angle between the normal vector of the interface $\mathbf{n}$ and the lattice direction of the flow system $\boldsymbol{e_i}$, which is the mesoscopic velocity set in D2Q9 scheme, $\cos\theta = \frac{\boldsymbol{e_i}\cdot\mathbf{n}(\boldsymbol{x},t)}{|\boldsymbol{e_i}||\mathbf{n}(\boldsymbol{x},t)|}$. The equilibrium distribution $f_{j,m}^{eq}$ is calculated by:

$$f_{j,m}^{eq}(\boldsymbol{x},t) = w_j C_m(\boldsymbol{x},t)\left(1. + \frac{1}{c_s^2}\boldsymbol{e_j}\cdot\boldsymbol{u}\right) \tag{9.23}$$

where C_m is the local concentration of mth chemical; w_j is the weight coefficient on each direction of D2Q5 scheme.

At the end of each time step, the distribution function is computed and used to update the local concentration of the chemical:

$$C_m(\boldsymbol{x},t) = \sum_j f_{j,m}(\boldsymbol{x},t) \tag{9.24}$$

9.2.3 Lattice Boltzmann Method (LBM) for reactions

The reaction solver is an LBM implementation based on TOUGTHREACT, and all the units are converted to the dimensionless lattice units. The details of conversion between physical units and lattice units can be found in Krüger et al. (2017) and Chen et al. (2014). Homogeneous reactions in the bulk fluid and heterogeneous reactions at mineral interfaces are included in the reaction solver. To reduce the computational cost, the total concentration (Ψ_j) of primary species j is tracked and the calculation of its distribution function ($G_{\alpha j}, \alpha$ represents the mesoscopic velocity set direction in D2Q5 scheme) follows the same principle as Eqn. 9.22. For the homogeneous reactions in the bulk fluid, the total concentration of jth primary species has relationship with the jth primary species and ith secondary species

$$\Psi_j = \sum_\alpha G_{\alpha j} = C_j + \sum_{i=1}^{N_R} v_{ji} C_i \tag{9.25}$$

Where Ψ_j is the total concentration of the jth primary species, N_R is the number of secondary species, C_j is the concentration of jth primary spices, C_i is the concentration of ith secondary species, v_{ji} is the stoichiometric coefficient. Assuming the homogeneous reactions reach equilibrium instantaneously, the concentration of the ith secondary species is calculated as follows

$$C_i = (\gamma_i)^{-1} K_i \sum_{j=1}^{N_C} (\gamma_j C_j)^{v_{ji}} \tag{9.26}$$

where N_c is the number of the primary species, K_i is the equilibrium constant of the ith homogeneous reaction and γ_i is the activity of the ith secondary species, which is the product of this particular homogenous reaction.

For the heterogeneous reactions at the mineral interfaces, mineral reactions are represented via a boundary condition for Ψ_j (Kang et al. 2006)

$$D \frac{\partial \Psi_j}{\partial n} = -\sum_{m=1}^{N_m} v_{jm} k_m (1 - K_m Q_m) \tag{9.27}$$

Where k_m and K_m are the reaction rate and equilibrium constant of mth mineral reactions, respectively, and the ion activity product Q_m is defined as

$$Q_m = \prod_{j=1}^{N_C} (\gamma_j C_j)^{v_{jm}} \tag{9.28}$$

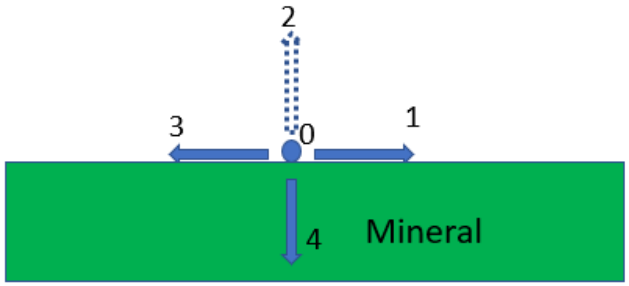

Figure 9-2. Schematic illustration of an interface node.

Figure 9-2 is a schematic plot for an interface node. After each streaming process, G_{2j} is an unknown distribution function in the direction 2 and the concentration of jth primary (C_j) spices needs to be updated as a result of the mineral reactions. By applying the approaches proposed by He et al. (1998) and Kang et al. (2002, 2003), the relationship below is obtained

$$2G_{4j} = \frac{\Psi_j}{2} - \frac{1}{c}\sum_{m=1}^{N_m} v_{jm}k_m(1 - K_m Q_m) \tag{9.29}$$

With Equations (9.25) and (9.26), this equation is solved numerically to update C_j. Then unknown G_{2j} can be calculated

$$G_{2j} = G_{2j}^{eq} + G_{4j}^{eq} - G_{4j} \tag{9.30}$$

9.2.4 Coupling framework of the multiphase flow-reactive transport LBM

Figure 9-3 shows the workflow of the coupled multiphase flow-reactive transport LBM, in which the three LBM solvers described above are coupled together in a sequential manner.

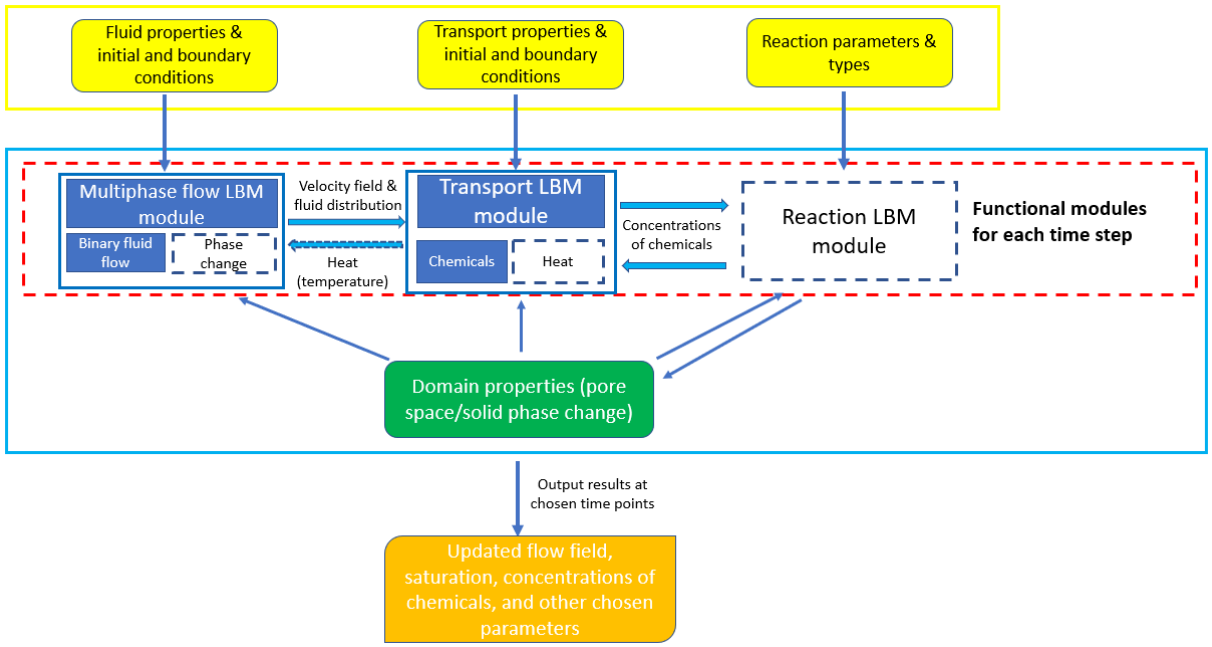

Figure 9-3. Workflow of the coupled multiphase flow-reactive transport LBM solver. The yellow rectangular illustrates the initialization of the corresponding LBM module. The blue rectangular highlights the LBM modules called at each time step and the update of pore-scale information. The blue dash-line rectangular represents modules/capabilities currently being developed or can be added in the future, highlighting the flexibility of the framework.

After the initialization mentioned above, at each time step, the multiphase flow solver calculates the flow field and fluid distribution first. Then this information is used by the transport solver, which considers the interface effect, to update the chemical concentrations in pore space. The updated concentrations are passed to the reaction LBM solver. The concentrations of the

chemicals are updated based on the geochemical reactions, and the pore geometry is also updated for computing fluid flow and transport in the next time step.

Currently, the fully coupled LBM solver is still under the development to integrate and test the integration between the reaction LBM solver and the flow and transport solvers.

9.3 Model Verification and Preliminary Results

Two sets of tests were performed to verify the coupled multiphase flow-transport LBM solver. The first test involves a static wetting fluid bubble with a conservative tracer surrounded by the non-wetting fluid. This test is to verify that the interface effect stops the chemical from diffusing through the interface when the fluids are immiscible to each other. The second set of tests consider the transport process under multiphase flow condition in a capillary tube, to verify that the solver is able to solve advection-diffusion process under multiphase flow condition correctly. Several different density ratios were tested.

9.3.1 Simulation setup

To test the capability of the solver in simulating fluid properties that can be encountered in natural and engineering systems, three sets of the density and viscosity ratios were used in the simulations, as summarized in Table 9-1, in dimensionless lattice units. All the system uses the same dynamic viscosity ratio, $M = {\mu_w}/{\mu_{nw}} = 50$, as in the water-air system. The diffusion coefficient of the non-reactive chemical is $0.03lu^2/t$.

Table 9-1. Fluid properties used in the tests

Properties	System 1 (lattice unit/physical unit)	System 21 (lattice unit/physical unit)	System 31 (lattice unit/physical unit)
Density (wetting fluid)	**1.0 /1000 $kg \cdot m^{-3}$**	**1.0 /1000 $kg \cdot m^{-3}$**	**1.0 /1000 $kg \cdot m^{-3}$**
Kinematic viscosity (wetting phase)	**0.1671.78e-6m^2/s**	**0.1671.78e-6m^2/s**	**0.167/1.78e-6m^2/s**
Density (non-wetting fluid)	**0.1//100 $kg \cdot m^{-3}$**	**0.01/10 $kg \cdot m^{-3}$**	**0.001/1 $kg \cdot m^{-3}$**
Kinematic viscosity (non-wetting fluid)	**0.0334/3.56e-7m^2/s**	**0.334/3.56e-6m^2/s**	**3.34/3.56e-5m^2/s**
Surface tension	**0.04/0.07N/s**	**0.04/0.07N/s**	**0.04/0.07N/s**

The initial conditions of the saturation (fluid distribution) and chemical concentration are shown in Figure 9-4. Since the phase-field LBM is a diffuse interface method, the fluids and chemical concentration interfaces are not sharp. The thickness of the interface is limited to 4 lattices, as a tradeoff between interface sharpness and numerical stability.

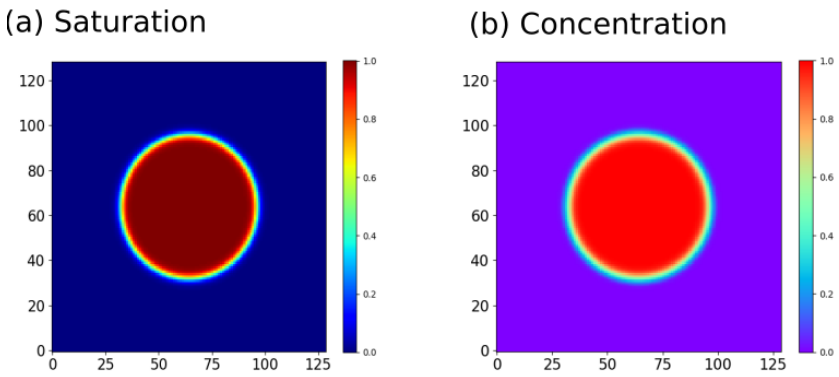

Figure 9-4. (a) the initial condition of saturation (fluid distribution, 1 for the wetting fluid, 0 for the non-wetting fluid); (b) the initial chemical concentration.

For the tests of the transport process in the capillary tube, the dimension of the capillary tube is 200×20 lattices and each lattice is 2 microns in physical unit. The contact angle on the wall of tube is 20°. The boundary conditions of the flow, fluid phase (wetting fluid), and chemical concentration at the inlet and outlet are summarized in Table 9-2 and illustrated in Figure 9-5. A flow velocity $v_{in} = 0.01 lu/t$ was used at the inlet for all the simulations.

Table 9-2. Fluid properties used in the tests

Boundary condition	Flow	Phase (wetting fluid)	Chemical concentration
Inlet	**Constant velocity**	**Constant value**	**Constant value**
Outlet	**Zero-gradient**	**Zero-gradient**	**Zero-gradient**

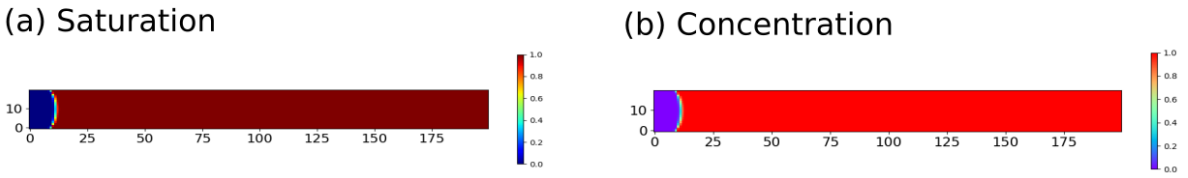

Figure 9-5. Initial conditions of the saturation (fluid distribution) and chemical concentration in a capillary tube.

9.3.2 Results

Figure 9-6 shows the results from the static bubble tests with different fluid density ratios. Figure 9-6(a) presents the change of spurious current magnitude with time. Spurious current is an unphysical velocity around the interface, and it can cause numerical instability when it is too high. Its magnitude in all three tests is small ($\sim 10^{-5}$), confirming that the phase-field LBM is able to simulate properly the high density – high viscosity ratio conditions. Figure 9-6(b) presents the profiles of fluid saturation and chemical concentration across the domain center in

the x-axis direction. The two profiles are well aligned, showing no chemical diffusion through the interface of two immiscible fluids.

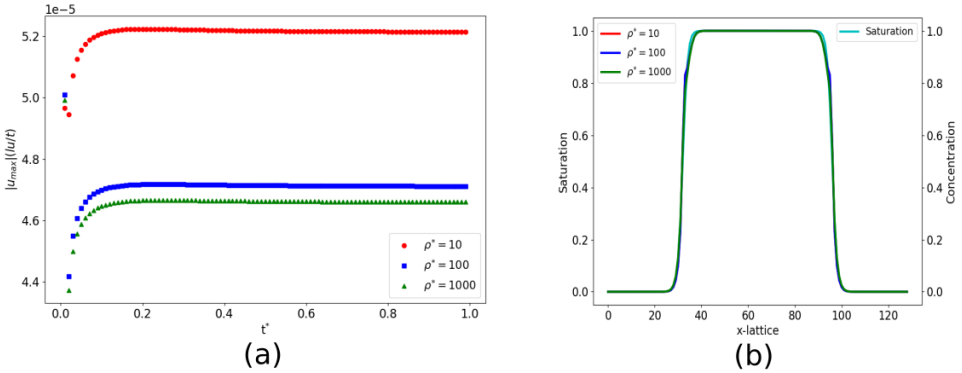

Figure 9-6. (a) the change of spurious current magnitude with time; (b) the saturation profile and the chemical concentration profiles across the center of the domain along the x-axis at the last time step

Figures 9-7 and 9-8 are the results from the tests of the drainage and transport process in a capillary tube. As the static droplet test, non-reactive chemical only exists in wetting fluid. At the chosen time point, the saturation (fluid distribution) and chemical concentration show the same patterns (Figure 9-5), confirming that the interface effect works properly in the flow condition. The density ratios did not affect the flow patterns and thus the distribution of the solute, as the flow behavior is more sensitive to the dynamic viscosity ratio.

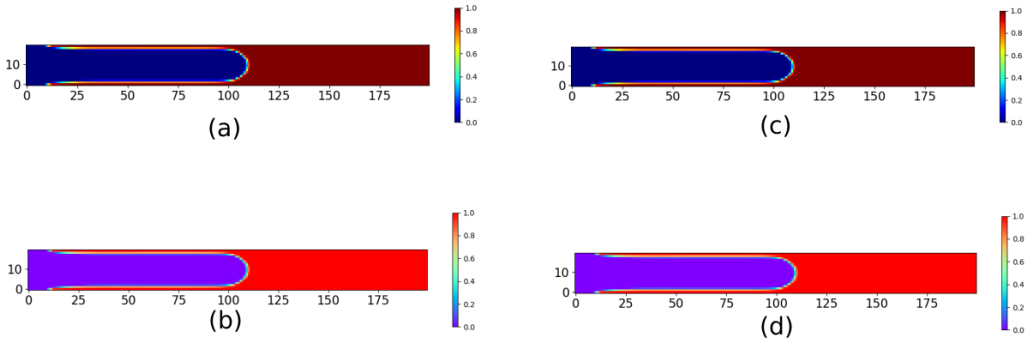

Figure 9-7. Saturation (fluid distribution) and chemical concentration at $\boldsymbol{t^* = 0.4}$ for different density ratios. (a) and (b) are saturation (fluid distribution) and chemical concentration in 2D for $\boldsymbol{\rho^* = 10}$; (c) and (d)) are saturation (fluid distribution) and chemical concentration in 2D for $\boldsymbol{\rho^* = 100}$.

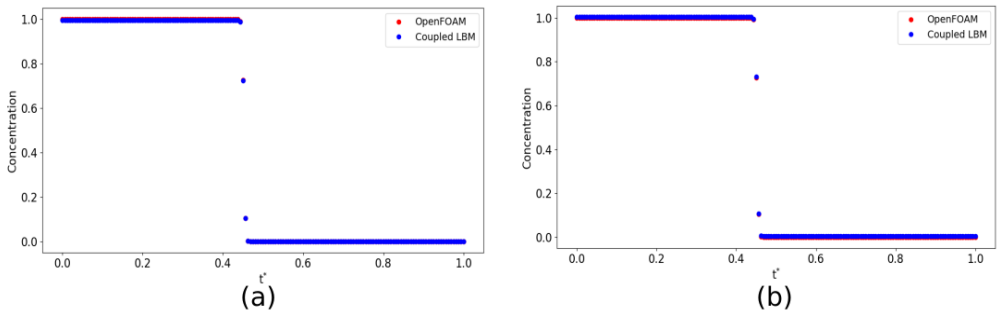

Figure 9-8. Breakthrough curves from the center of the capillary tube for the density ratios: (a) $\boldsymbol{\rho^* = 10}$, (b) $\boldsymbol{\rho^* = 100}$.

To further benchmark the results, comparative simulations were performed using the open source software CrunchFoam-v1812. Figure 9-6 shows the comparison of the breakthrough curves plotted from the two solvers. Good agreement is observed for both density ratios, confirming that the coupled LBM solver is able to simulate transport under the multiphase flow within the range of fluid property parameters tested in these simulations. Further code development is undergoing to improve numerical stability and expanding the capability to simulate even higher density ratio (e.g., $\rho_w/\rho_{nw} = 1000$).

9.4 Benchmark test

For the benchmark test, a bentonite-concrete interface region was simulated following geochemical conditions reported for the FEBEX *in situ* test (Turrero and Cloet, 2017). While the benchmark problem was for a concrete-bentonite interface, the contrast in key characteristics is similar to the concrete-argillite interface. Furthermore, given the experimental data availability for the benchmark problem, it provides a useful test case for demonstrating the importance of capturing pore-scale alteration and thus local transport properties and for model verification. Here, two comparative simulations were considered, one assumes that the effective diffusivity changes linearly with local porosity, whereas the second case assumes a non-linear dependence of diffusivity on porosity with an exponent of 2. It was evident that the evolution of the porosity over time depends on the relationship between transport properties and porosity change caused by mineral reactions (Figure 9-9). A nonlinear diffusivity-porosity relationship results in more porosity change in a wider region close to the interface. Previous studies have shown that the relationship between diffusivity and porosity is largely dependent on pore-scale chemical processes (Deng et al., 2021). Therefore, it is critical to investigate the interface alteration at pore scale in order to accurately capture the system evolution.

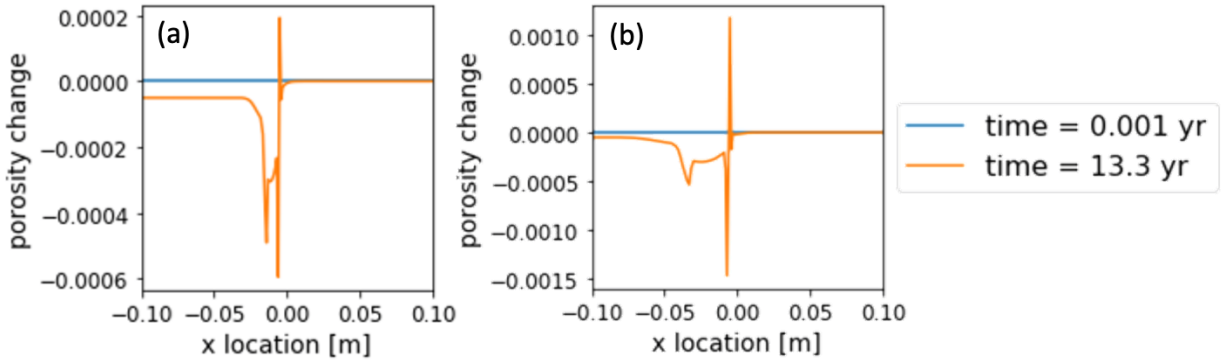

Figure 9-9. Porosity change predicted for the concrete-bentonite interface (x<0 concrete, and x>0 bentonite) with a linear (a) and non-linear (b) diffusivity-porosity relationship.

9.5 Summary and Future Work

We performed a set of continuum-scale benchmark modeling tests that showed the impact of transport-porosity relationship on the dynamic alteration in the interfacial regions, which highlighted the need of accurately capturing local transport properties. As such, a pore-scale perspective is required to better predict interface alteration. In this study, a fully coupled multiphase flow-reactive transport Lattice Boltzmann model framework is being developed for pore-scale modeling investigations. LBM was chosen because of its computational efficiency and the need of covering a computational domain with sizes of mm-cm in modeling the interfacial alteration. The two-phase flow phase-field LBM solver and the transport solver were developed and verified using a static bubble test and a capillary drainage test. The preliminary results showed that the current solver is capable of solving transport under multiphase flow conditions when the fluid density and viscosity ratios are in a certain range. These two solvers are currently being coupled with the reaction module. Our future work will include

(a) Verification of the fully coupled LBM using literature examples, and

(b) Simulations based on the geochemical benchmark problem with increasing complexity to simulate

physical and chemical processes at the interfacial area of argillite host rock, concrete and bentonite.

10. Modeling of Cl-D Experiment at Mont Terri

The objective of this modeling task is the predictive simulation of hydro-chemical-mechanical couplings occurring during the *in-situ* Cl-D experiment at Mont-Terri. In addition to providing understanding of the Cl-D field experiment and the coupled processes relevant to nuclear waste repository disposal, we will benchmark and improve our multi-dimensional software CrunchClay in the process.

CrunchClay represents an evolving branch of the code CrunchTope/CrunchFlow (Steefel et al, 2015) that considers electrostatic effects associated on transport (Tournassat and Steefel, 2019a, b; Tournassat et al, 2020; Steefel and Tournassat, 2021). The electrostatic effects on transport include those associated with the development of a diffusion potential as captured by the Nernst-Planck equation, and the formation of a diffuse layer bordering negatively charged clay particles within which partial anion exclusion occurs. The model is based on a dual continuum formulation that accounts for diffuse layer and bulk water pore space, providing a more flexible framework than is found in the classical mean electrostatic potential models. The diffuse layer model is obtained by volume averaging ion concentrations in the Poisson-Boltzmann equation, but includes the treatment of longitudinal transport within this continuum. The calculation of transport within the bulk and diffuse layer porosity is based on a new formulation for the Nernst-Planck equation that considers averaging of diffusion coefficients and accumulation factors at grid cell interfaces (Tournassat et al, 2020).

10.1 Model Changes

The CrunchClay simulator, which is able to model simultaneously the transport of anions, cations, and uncharged solutes in charged media, is now coupled to flow and reaction taking place in the bulk water (electrically neutral) porosity and has been demonstrated on a single discrete fracture-clay matrix problem in 2D (Tournassat and Steefel, 2019a,b; Tournassat et al., 2020; Steefel and Tournassat, 2021). However, it was necessary to add new capabilities to the code to fully take into account the complexity of the Cl-D simulation objectives. These developments are still on-going, and we present here a short summary of model changes.

10.1.1 Multi-porosity

The mechanical behavior of the clay rock is attributed to the swelling properties of clay mineral compounds. These properties are related to changes in pore water composition that in turn influence diffuse layer properties and water distribution in porosity domains exhibiting a range of dimensions: from less than 1 nm wide interlayer porosity to macroporosity in which bulk pore water can be found. The current version of the code can handle only two types of porosity: bulk water porosity and diffuse layer water porosity. To be able to model changes in the swelling properties required that the current implementation be extended to a multi-porosity treatment.

In this new implementation, we rely on the same working hypothesis as in the previous version of the code, i.e., a thermodynamic equilibrium between the various types of porosity:

$$\mu_{k_{sp},bulk} = \mu_{k_{sp},\mathrm{DL}_1} = \mu_{k_{sp},\mathrm{DL}_2} = \ldots = \mu_{k_{sp},\mathrm{Stern}_1} = \ldots \tag{10.1}$$

$$\mu_{k_{sp},bulk} = \mu^{o}_{k_{sp}} + \mathrm{R}T\ln\gamma_{k_{sp},bulk}c_{k_{sp},0} + z_{k_{sp}}\mathrm{F}\psi_{e,bulk} \tag{10.2}$$

with $c_{k_{sp},0}$ expressed in $\mathrm{mol}\cdot\mathrm{kg}^{-1}$.

$$\begin{aligned}\mu_{k_{sp},\mathrm{DL}_1} &= \mu^{\mathrm{o}}_{k_{sp}} + \mathrm{R}T\ln\gamma_{k_{sp},\mathrm{DL}}c_{k_{sp},\mathrm{DL}} + z_{k_{sp}}\mathrm{F}\psi_{e,\mathrm{DL}_1} \\ &= \mu^{\mathrm{o}}_{k_{sp}} + \mathrm{R}T\ln\gamma_{k_{sp},0}c_{k_{sp},bulk}e^{-\frac{z_{k_{sp}}\mathrm{F}\left(\psi_{e,\mathrm{DL}}-\psi_{e,\mathrm{bulk}}\right)}{\mathrm{R}T}} + z_i\mathrm{F}\psi_{e,\mathrm{DL}_1} \\ &= \mu^{\mathrm{o}}_{k_{sp}} + \mathrm{R}T\ln\gamma_{k_{sp},bulk}c_{k_{sp},bulk} + z_i\mathrm{F}\psi_{e,bulk}\end{aligned} \tag{10.3}$$

Under isothermal conditions, the diffusive flux is expressed as:

$$\begin{aligned}J_{k_{sp},\mathrm{diff},\mathrm{bulk}} &= -u_{k_{sp}}c_{k_{sp}}\frac{\partial\mu_{k_{sp},bulk}}{\partial x} \\ &= -\mathrm{R}Tu_{k_{sp},bulk}c_{k_{sp},bulk}\frac{\partial\ln\gamma_{k_{sp},bulk}c_{k_{sp},bulk}}{\partial x} - z_{k_{sp}}u_{k_{sp},bulk}c_{k_{sp},bulk}\frac{\partial\mathrm{F}\psi_{e,bulk}}{\partial x}\end{aligned} \tag{10.4}$$

The fact that $c_{k_{sp},0}$ is given in $\mathrm{mol}\cdot\mathrm{kg}^{-1}$ requires us to introduce a conversion in the $u_{k_{sp}}$ mobility term:

$$u_{k_{sp}} = \frac{\phi_0\tau_{k_{sp},bulk}D_{k_{sp},bulk}\rho_{bulk}}{\mathrm{R}T} \tag{10.5}$$

where ρ_{bulk} is expressed in $\mathrm{kg}\cdot\mathrm{m}^{-3}$.

$$\begin{aligned}J_{k_{sp},\mathrm{diff},\mathrm{bulk}} = &-\phi_0\tau_{k_{sp},bulk}D_{k_{sp},bulk}\rho_{bulk}c_{k_{sp},bulk}\frac{\partial\ln\gamma_{k_{sp},bulk}c_{k_{sp},bulk}}{\partial x} \\ &-z_{k_{sp}}\phi_0\tau_{k_{sp},bulk}D_{k_{sp},bulk}\rho_{bulk}c_{k_{sp},bulk}\frac{\mathrm{F}}{\mathrm{R}T}\frac{\partial\psi_{e,bulk}}{\partial x}\end{aligned} \tag{10.6}$$

For the diffuse layer porosity, DL_1:

$$\begin{aligned}J_{k_{sp},\mathrm{diff},\mathrm{DL}_1} = &-\phi_{DL_1}\tau_{k_{sp},DL_1}D_{k_{sp},DL_1}\rho_{DL_1}c_{k_{sp},DL_1}\frac{\partial\ln\gamma_{k_{sp},bulk}c_{k_{sp},bulk}}{\partial x} \\ &-z_{k_{sp}}\phi_{DL_1}\tau_{k_{sp},DL_1}D_{k_{sp},DL_1}\rho_{DL_1}c_{k_{sp},DL_1}\frac{\mathrm{F}}{\mathrm{R}T}\frac{\partial\psi_{e,bulk}}{\partial x}\end{aligned} \tag{10.7}$$

In the dual continuum treatment developed previously, we used different values of $\frac{\partial\psi_{e,bulk}}{\partial x}$ for the bulk and the DL water, which was somewhat not logical (it should be the same according to the formula above). This was because the two types of porosity had to maintain their electroneutrality independently. If the $\frac{\partial\psi_{e,bulk}}{\partial x}$ value had to remain the same whatever type of porosity was considered, then we need to consider the diffusive flux in the entire porosity at once to solve the equation for $\frac{\partial\psi_{e,bulk}}{\partial x}$, *i.e.*:

$$
\begin{aligned}
J_{k_{sp},\mathrm{diff},\mathrm{DL}_1} &= J_{k_{sp},\mathrm{diff},\mathrm{bulk}} + J_{k_{sp},\mathrm{diff},\mathrm{DL}_1} + J_{k_{sp},\mathrm{diff},\mathrm{DL}_2} + \ldots \\
&= -\left(\frac{\partial \ln \gamma_{k_{sp},bulk} c_{k_{sp},bulk}}{\partial x} + z_{k_{sp}} \frac{\mathrm{F}}{\mathrm{R}T} \frac{\partial \psi_{e,bulk}}{\partial x} \right) \\
&\times \left(\phi_0 \tau_{k_{sp},bulk} D_{k_{sp},bulk} \rho_{bulk} c_{k_{sp},bulk} + n_{\mathrm{DL,max}}^{n=1} \sum \phi_{DL_n} \tau_{k_{sp},DL_n} D_{k_{sp},DL_n} \rho_{DL_n} c_{k_{sp},DL_n} \right)
\end{aligned}
\tag{10.8}
$$

Considering now the accumulation terms $A_{\mathrm{DL,n}}$:

$$
\begin{aligned}
J_{k_{sp},\mathrm{diff},} = \; & -\left(\frac{\partial \ln \gamma_{k_{sp},bulk} c_{k_{sp},bulk}}{\partial x} + z_{k_{sp}} \frac{\mathrm{F}}{\mathrm{R}T} \frac{\partial \psi_{e,bulk}}{\partial x} \right) c_{k_{sp},bulk} \times \\
& \left(\phi_0 \tau_{k_{sp},bulk} D_{k_{sp},bulk} \rho_{bulk} + n_{\mathrm{DL,max}}^{n=1} \sum \phi_{DL_n} \tau_{k_{sp},DL_n} D_{k_{sp},DL_n} \rho_{DL_n} A_{k_{sp},DL_n} \right)
\end{aligned}
\tag{10.9}
$$

Equation (10.9) is the general multi-porosity equation being currently implemented in the code. Note that a new primary unknown is now added, which is $\psi_{e,bulk}$. Also, instead of one diffuse layer potential, it is now necessary to obtain the values of *n* diffuse layer potential, where *n* is the number of different diffusion layer domains considered in a simulation. These additions of new primary variables in the code resolution scheme made it necessary to change its structure.

10.1.2 Ionic strength and water activity

Ionic strength and water activity are important parameters to define osmotic properties and thus swelling properties. To date, the values of these parameters were evaluated either after every Newton iteration on the primary concentration variables, or at the end of the time step (and thus lagged effectively). In the current version, we have added these two parameters in the set of primary variables in order to be able to couple changes in ionic strength and water activity with changes in the swelling properties during the Newton iteration cycle.

10.1.3 Status of Model Changes

Currently, the modification of the speciation (batch) part of the code with the inclusion of the new variables has been accomplished. Speciation results are currently benchmarked with results obtained with the previous version of the code. Once this benchmarking is completed, the newly developed transport equations will be implemented.

10.1.4 Extension to 3D

In order to simulate the Cl-D experiment at Mont Terri, it will be necessary to have a full 3D treatment of the system, since there is no symmetry that can be made use of there. We are currently extending the loops and the geometry to 3D, working first with the legacy version of CrunchClay. Once completed, the changes will be migrated to the newer version of CrunchClay described above.

10.1.5 Future Work for Model Development

Future work will consist of completion of the tasks described above (Sections 10.1.1-10.1.4), all of which are presently in progress.

10.2 Preliminary 2D calculations

The objective of the work in this project is to develop a predictive understanding of the coupled processes determining the evolution of the Cl-D experiment at Mont Terri. The field campaign consisted of a number of boreholes, beginning with BCl-6 that placed cement within the Opalinus Clay. The key objective of the field experiment and associated modeling is to understand the long-term interaction of the cement with the Opalinus Clay. The latest borehole is angled from Gallery 98 and has the objective of overcoring the interaction zone between the cement (OPC) and the Opalinus Clay (OPA).

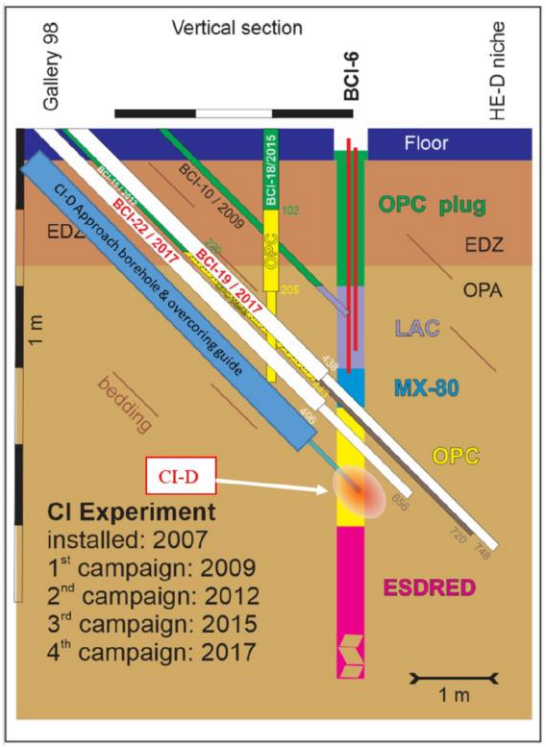

Figure 10-1. Schematic illustration of Cl-D field experiment at Mont Terri. The Cl-D overcoring borehole is approaching the zone of long-term interaction between concrete (OPC) and the Opalinus Clay (OPA).

Earlier boreholes were used to set a recirculation system into the borehole that could be used for injection of uncharged tracers (tritiated water, HTO) and the isotopologue of the anion chloride, ^{36}Cl. To make use of the data from the recirculation system, a 3D model is needed, and is in preparation as noted above.

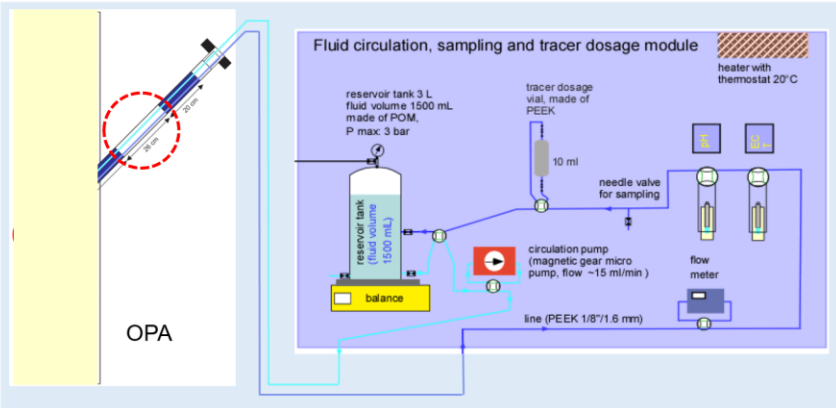

Tracers: ^{3}H, ^{36}Cl

Water tracer and anion (conservative, electrostatic effect)

Tracer	Activity conc.	LL	Activity (1.5 L)	LA (1.5 L)
^{3}H (HTO)	$2 \cdot 10^{5}$ Bq/kg	2	$3 \cdot 10^{5}$ Bq	0.001
^{36}Cl	$4 \cdot 10^{4}$ Bq/kg	40	$6 \cdot 10^{4}$ Bq	0.06

LL: clearance limit / Befreiungsgrenze; LA: licensing limit / Bewilligungsgrenze

Figure 10-2. Schematic illustration of fluid circulation, sampling, and tracer dosing system in the Cl-D experiment at Mont Terri. The data from this recirculation system will be used in 3D modeling when the 3D code is ready.

For the preliminary calculations presented here, we used the dual-continuum version of the code (Steefel and Tournassat, 2021). These simulations make use of ad hoc parameters, not definitive ones (see Table 10-3), with the purpose of viewing the approximate system behavior while at the same time demonstrating that the problem in 2D is tractable. 1,000 days of simulation time requires about 24 hours.

The system of interest was approximated with the geometry shown in Figure 10-3.-3. The total size of the system is 1.5 m × 0.8 m with mesh discretization down to 0.002 m (3000 cells in total). All boundary conditions are treated as no-flux, and only diffusive transport via the Nernst-Planck equation is considered. Initial conditions are given in Table 10-1. Self-diffusion coefficients for the aqueous species are given in Table 10-2. Tortuosity values used in the simulations for the various zones are given in Table 10-3. For the Opalinus Clay, we considered sorption on the clays with a specific surface area of 790 m^2/g and a volume fraction of 0.12%. The site density for surface hydroxyls on the clays of 4.59×10^{-6} mol/m^2 was used in the simulations.

Table 10-1. Initial conditions for three zones, including fracture (higher porosity zone), concrete (OPC), and Opalinus Clay (OPA).

Component	Fracture	Concrete	Opalinus Clay
pH	7.05	13.39	7.05
Na^+	0.0517	0.059	0.3
K^+	0.0005	0.32	0.0005
Ca^{2+}	0.0076	0.001	0.0076
Mg^{2+}	0.0051	0.0	0.0051
Cl^-	0.0509	0.0	0.3
$SiO_2(aq)$	0.00017	0.00007	0.00017
SO_4^{2-}	0.0112	0.0019	0.011
Tracer	0.001	0.0	0.0
Total Inorganic Carbon	0.00378	0.00017	0.038

Table 10-2. Self-diffusion coefficients for chemical species considered in simulations. Molecular diffusion is calculated using the Nernst-Planck equation (see Steefel et al, 2015).

Chemical Species	Diffusion Coefficient $\left(m^2 \cdot s^{-1}\right)$
H^+	9.31×10^{-9}
Na^+	1.30×10^{-9}
K^+	1.96×10^{-9}
Ca^{2+}	0.79×10^{-9}
Mg^{2+}	0.71×10^{-9}
Cl^-	2.10×10^{-9}
$SiO_2(aq)$	1.00×10^{-9}
SO_4^{2-}	1.07×10^{-9}
OH^-	5.27×10^{-9}
Tracer	2.15×10^{-9}

CO_3^{2-}	0.96×10^{-9}
HCO_3^-	1.18×10^{-9}

Table 10-3. Tortuosity values for various zones in simulation, including the high porosity fracture zone, the Opalinus Clay (OPA), and the concrete (OPC).

Zone	**Tortuosity**
Fracture	1.00
OPA	0.12
OPC	0.10

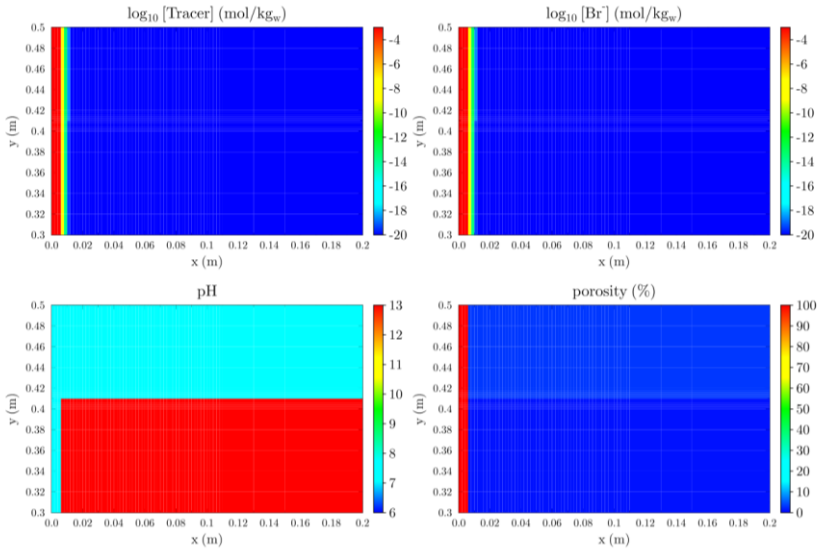

Figure 10-3. Initial conditions 2D simulation of system with a borehole or fracture on the left of the simulation domain, and a horizontal interface between OPA (Opalinus Clay) and concrete materials (OPC) on the right of the simulation domain. The concrete domain can be visualized with the high pH value resulting from the solubility of portlandite (pH = 13.39). OPA and concrete positions correspond to the low porosity domain. The system is discretized with 3000 cells with a dimension refinement down to 0.002 m at the interfaces between the three domains. The tracer is a neutral molecule (such as HTO). Br^- serves as an anionic tracer for the simulation, equivalent in behavior to $^{36}Cl^-$.

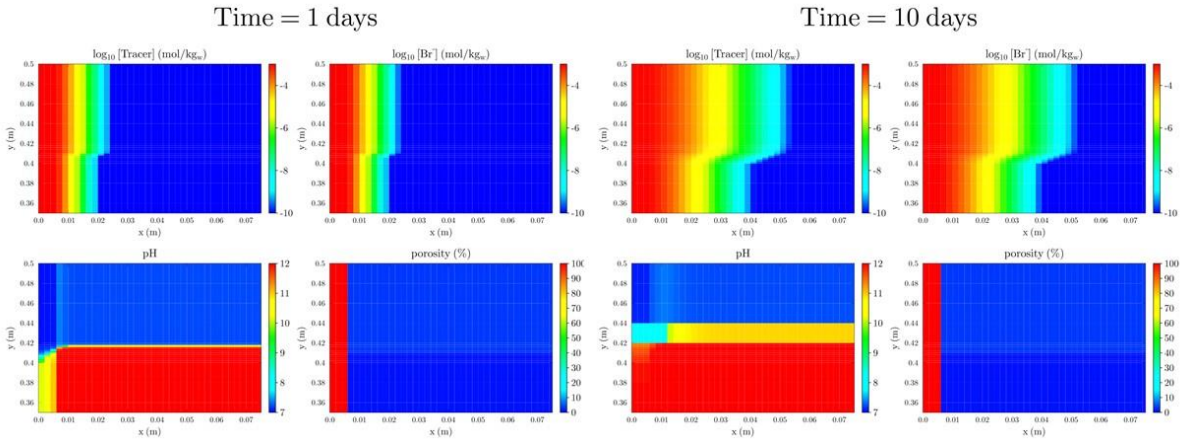

Figure 10-4. Early time behavior (1 day to 10 days). Note the retardation of the pH front relative to the tracer and the slight retardation of the anion front relative to the uncharged tracer. The relatively high ionic strength of the background electrolyte (0.3 M) minimizes to some extent the anion retardation compared to a more dilute case.

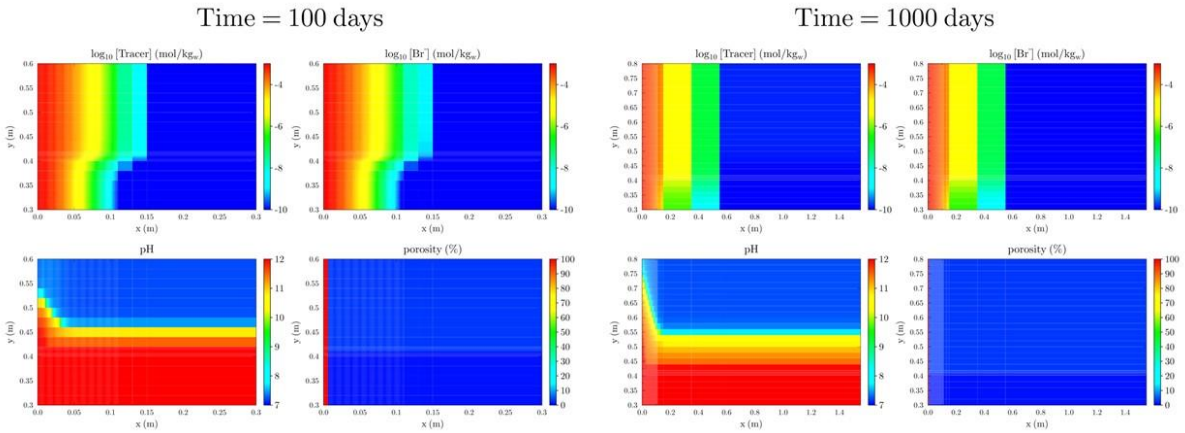

Figure 10-5. Diffusion-reaction simulation results from 100 to 1000 days. The high pH front propagates both within the micro-fracture zone on the left via diffusion and within the Opalinus Clay close to the concrete contact. Note the change in horizontal scales from Figure 10-4.

10.3 Discussion

Although preliminary, the 2D reactive transport simulations shown above display some of the expected behavior of a concrete-Opalinus Clay system within which a single higher porosity zone is developed within otherwise lower porosity clay rock. Only diffusive transport is considered and is treated with the dual porosity approach outlined above, with a Nernst-Planck rather than Fickian treatment of diffusion in all cases. The initial conditions for the simulation are shown in Figure 10-3.

The relatively high ionic strength of 0.3 M results in less difference between the anionic and uncharged tracer distributions than would be expected at lower ionic strength, but some difference can be seen if the results are examined closely. (Figure 10-4). Between 100 and 1,000 days (still a period of time less than the experiment), the high pH front propagates into the Opalinus Clay via diffusion, with greater advancement in the Y-direction within the high porosity zone on the left (Figure 10-5).

10.4 Future Work on Cl-D Experiment at Mont Terri

With the completion in particular of the 3D capability in CrunchClay, we will be able to consider the full geometry of the system under investigation in the Cl-D experiment at Mont Terri. As before, electrostatic effects on transport in the clay-rich Opalinus will be considered, and reaction-induced changes in porosity and permeability due to the reaction of the high pH cement and the OPA will be calculated. Results will be presented at a workshop that is likely to be held in the fall of 2021, with comparisons to those obtained by the other participating groups.

10.5 Summary

In this report, we provide a status update of progress on 1) development of a new model that includes a set of new master variables, including the electrical potential and the ionic strength, 2) conversion of the CrunchClay simulator to 3D, and 3) preliminary scoping calculations of a 2D system containing a single higher porosity zone in which diffusive transport is enhanced compared to typical Opalinus Clay (no flow is considered). The simulations, although preliminary, suggest the propagation of uncharged tracer, anion, and pH fronts over the time period of 100-1,000 years (Figure 10-5).

11. LINKING TO GEOLOGIC DISPOSAL SAFETY ASSESSMENT (GDSA)

A schematic of integration between the coupled THM processes models and a repository-scale model for GDSA and PA is shown in Figure 11-1. The GDSA and PA modeling is conducted with the PFLOTRAN code by Sandia National Laboratories. PFLOTRAN has the capability of modeling coupled TH processes and geochemistry, including radionuclide transport in a high-performance computing environment. The idea is to conduct the GDSA modeling of the entire repository, including all emplacement tunnels. In such a large-scale repository model, it will not be possible to model the detailed thermally driven coupled THM processes occurring in the EBS and near-field during the relatively early repository time period of elevated repository temperature.

An initial approach for linking a coupled processes model to the GDSA could be to use detailed coupled THM process models to simulate near field of emplacement tunnels in different parts of a repository, for different FEPs such as a nominal case or cases of extensive gas generation. The output from such modeling to the GDA and PA model would be the following: (1) changes in flow properties (e.g., permeability and porosity) in the near-field, including the buffer and EDZ, and (2) inform PA about local flow created by coupled processes.

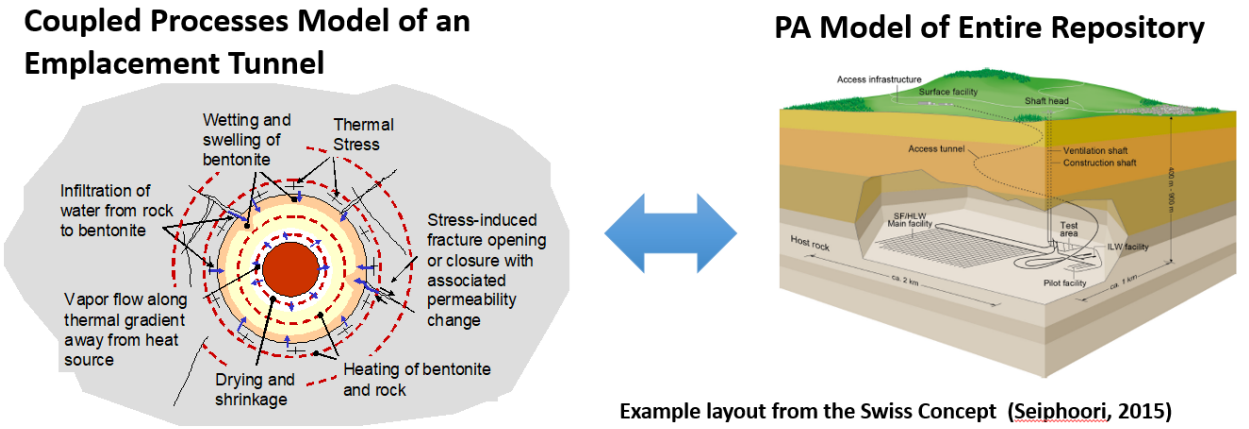

Figure 11-1. Schematic of links between near-field coupled THM processes modeling to repository-scale GDSA and PA models.

In FY20-FY21 we developed a new approach that could enable inclusion of coupled THM processes into the PFLOTRAN GDSA and PA modeling. This involves calculations of the EDZ permeability evolution as a function of temperature, pressure, and a buffer saturation. Thus, PFLOTRAN along with a number of analytical models can be used to consider THM effects on EDZ permeability. The approach was described in detail in a journal paper (Sasaki and Rutqvist, 2021) that have just been published. Future work on this topic may include application of alternative models for calculating EDZ permeability.

12. SUMMARY OF FY21 PROGRESS AND FUTURE WORK

In FY21, LBNL work on coupled processes in argillite rock has continued with a broad research portfolio, including model development, validations, and applications, along with fundamental studies of argillite and bentonite-based buffer materials. Summaries and future work have been provided in Sections 2 to 11 of this report. Below is a brief summary of performed and future work related to the current Argillite R&D work package:

- LBNL has begun initial work on investigating the effect of shale-creep on the long-term performance of an argillite repository. An appropriate shale-creep model has been identified based on experimental data of various shale host rock as reported in the literature. The model is being implemented and tested using TOUGH-FLAC, and will then be applied in modeling of the long-term repository THM performance. Future work will include modeling to investigate the potential impact of shale creep for different kinds of shale, including more ductile and more brittle shales.
- LBNL's scientists are participating in three DECOVALEX-2023 tasks that include coupled processes model validation against experiments and necessary model developments. These taskes are: DECOVALEX-2023 Task A on thermal and gas fracturing at MHM URL in France, Task B related to gas migration in clay, and Task C related to THM response

around the Mont Terri Full-Scale Emplacement Experiment. The 2nd and 3rd Workshops of DECOVALEX-2023 have been held in FY21, and included a comparison and discussion of modeling results obtained by international modeling teams. Future work will be conducted according to task descriptions including comparison to actual data obtained from the field experiments at Mont Terri and MHM URLs. For gas migration in bentonite, the model will be developed to include dual-structure behavior, i.e., micro- and macro-structure of bentonite clay.

- LBNL have launched new work related to modeling discrete fractures in argillite using machine learning for meshing of fracture morphology, and the development of networks from images of fractured rock. Moreover, in FY21 LBNL has conducted numerical modeling of complex fractured rock responses in argillite using the numerical manifold method that allows for more realistic representation of fracture geometry in the model. Future modeling will include sensitivity studies, taking into account creation of new fractures.
- LBNL scientists in collaboration with international scientists have achieved substantial progress in the study of fault activation and long-term sealing behavior in argillite at the Mont Terri URL. The study indicates that activation of faults in argillite may involve a small stress drop at rupture, limited number and magnitude of seismic events, largely aseismic movements and local fluid channeling, and a slow post activation sealing. For the rest of FY21 we will continue processing data from the new experiment in Mont Terri (FS-B) using the time-lapse p-waves tomographic images to explore the intricate relationships between aseismic flow paths and seismic volumes within a thick fault zone. We conducted numerical modeling to explore the effects of different fault zone complexity on induced seismicity and compared to measured seismic events and strains.
- LBNL has launched a new task on modeling of concrete-clay interfaces, involving model development and application using the Lattice Boltzmann Method as an alternative to continuum modeling for detailed modeling of interface alteration. The preliminary results showed that the current solver is capable for modeling flow and geochemical transport under multiphase flow conditions when the fluid density and viscosity ratios are in a certain range. Future work will include geochemical benchmarking of physical and chemical processes at concrete-clay interfaces.
- LBNL has launched another new task on concrete-clay interfaces that involves modeling the Cement–Opalinus Clay Interaction (CI-D) experiment at the Mont Terri URL, where the focus is on understanding the reaction-induced porosity, permeability, and diffusivity changes in both the cement and the Opalinus Clay as a result of their interaction. This effort builds on the new CrunchClay dual continuum code, which accounts for electrostatic effects on ion transport associated with the negatively charged clays that are present. The scope includes a number of code enhancements undertaken in collaboration with the Fundamental Geoscience program at Berkeley Lab, including extension to a 3D model and the introduction of the electrical potential as a master variable.
- Finally, as part of LBNL's Argillite R&D work package, LBNL, in collaboration with SNL, is developing new approaches for integrating coupled process models into the

Geological Disposal Safety Assessment (GDSA) and Performance Assessment (PA). In FY21, a journal paper (Sasaki and Rutqvist, 2021) was published. Future work will include collaboration with SNL for incorporating and testing of this approach in PFLOTRAN.

13. Acknowledgements

This work was supported by the Spent Fuel and Waste Science and Technology Campaign, Office of Nuclear Energy, of the U.S. Department of Energy under Contract Number DE-AC02-05CH11231 with Lawrence Berkeley National Laboratory.

14 References

Alonso, M.C., Calvo, J.L.G., Cuevas, J., Turrero, M.J., Fernandez, R., Torres, E., and Ruiz, A.I. (2017) Interaction processes at the concrete-bentonite interface after 13 years of FEBEX-Plug operation. Part I: Concrete alteration, Physics and Chemistry of the Earth, 99, 38-48.

Al-Yaarubi, A.H., Pain, C.C., Grattoni, C.A., and Zimmerman, R.W. (2005) Navier–Stokes simulations of fluid flow through a rough fracture. Dynamics of fluids and transport in fractured rock, geophysics monograph series 162: 55–64.

Amann, F., Wild, K.M., Loew, S., Yong, S., Thoeny, R., and Frank, E. (2018) Geomechanical behaviour of opalinus clay at multiple scales: results from Montterri rock laboratory (switzerland). In Mont Terri rock laboratory, 20 years (pp.153–173). Springer.

Asahina, D., Houseworth, J.E., Birkholzer, J.T., Rutqvist, J., and Bolander, J.E. (2014) Hydro-mechanical model for wetting/drying and fracture development in geomaterials, Computers & Geosciences, 65, 13–23.

Babhulgaonkar, S., Hu, M. , Luu, K., Derakhshandeh, Z. And Rutqvist, R. (2020) Machine learning of fracture morphology and growth in geological media: Preliminary study. 2nd International Conference on Coupled Processes in Fractured Geological Media: Observation, Modeling, and Application (CouFrac) Seoul, Korea.

Bartier, D., Techer, I., Dauzeres, A., Boulvais, P., Blanc-Valleron, M.M. and Cabrera, J. (2013), In situ investigations and reactive transport modelling of cement paste/argillite interactions in a saturated context and outside an excavated disturbed zone, Applied Geochemistry, 31, 94-108.

Bernard, E., Jenni, A., Fisch, M., Grolimund, D., and Mader, U. (2020) Micro -X-ray diffraction and chemical mapping of aged interfaces between cement pastes and Opalinus Clay, Applied Geochemistry, 115, 17.

Bertron, A., Jacquemet, N., Erable, B., Sablayrolles, C., Escadeillas, G., and Albrecht, A. (2014) Reactivity of nitrate and organic acids at the concrete-bitumen interface of a nuclear waste repository cell, Nuclear Engineering and Design, 268, 51-57.

Binder, G., Titov, A., Liu, Y., Simmons, J., Tura, A., Byerley, G., and Monk, D. (2020) Modeling the seismic response of individual hydraulic fracturing stages observed in a time-lapse distributed acoustic sensing vertical seismic profiling survey. Geophysics 85 (4), T225-T235.

Binder, G., Titov, A., Tamayo, D., Simmons, J., Tura, A., Byerley, G., and Monk, D. (2018) Time delays from stress-induced velocity changes around fractures in a time-lapse DAS VSP. SEG Technical Program Expanded Abstracts, Aug. 2018.

Biot, M.A., and Willis, D.G. (1957) The elastic coefficients of the theory of consolidation, Journal of Applied Mechanics, 24, 594–601.

Blaschke, T., Burnett, C., and Pekkarinen, A. (2004) Image segmentation methods for object-based analysis and classification. Remote sensing image analysis: Including the spatial domain. Springer: 211-236.

Bossart, P., Bernier, F., Birkholzer, J., Bruggeman, C., Connolly, P., Dewonck, S.,Wieczorek, K. (2017). Mont Terri rock laboratory 20 years of research: introduction, site characteristics and overview of experiments. In Mont Terri rock laboratory, 20 years (pp. 3–22). Springer International Publishing. doi:10.1007/978-3-319-70458-61.

Braun, P. (2019) Thermo-hydro-mechanical behavior of the Callovo-Oxfordian claystone: Effects of stress paths and temperature changes. Thesis, Université Paris-Est, 2019.

Chen, L., Kang, Q., Carey, B., and Tao, W.Q. (2014) Pore-scale study of diffusion–reaction processes involving dissolution and precipitation using the lattice Boltzmann method. International Journal of Heat and Mass Transfer, 75, 483-496.

Chiu, P.H., and Lin, Y.T. (2011) A conservative phase field method for solving incompressible two-phase flows. Journal of Computational Physics, 230(1), 185-204.

Corey, A.T. (1954) The Interrelation Between Gas and Oil Relative Permeabilities, Producers Monthly, 38-41.

Daley, T.M., Ajo-Franklin, J.B., and Doughty, C. (2011) Constraining the reservoir model of an injected CO2 plume with crosswell CASSM at the Frio-II brine pilot. Int J Greenhouse Gas Control. 2011; 5:1022–1030.

Daley, T.M., Myer, L.R., Peterson, J.E., Majer, E.L., and Hoversten, G.M., (2007) Time-lapse crosswell seismic and VSP monitoring of injected CO2 in a brine aquifer: Environmental Geology, http:dx.doi.org/ 10.10071500254-007-0943-2.

Deng, H., Tournassat, C., Molins, S., Claret, F., and Steefel, C.I. (2021) A Pore-Scale Investigation of Mineral Precipitation Driven Diffusivity Change at the Column-Scale, Water Resources Research, 57(5), e2020WR028483.

Dieterich, J. H. (1979) Modeling of rock friction experimental results and constitutive equations, J. Geophys. Res., 84, 2161–2168, doi:10.1029/JB084iB05p02161.

Dumont, V., Tribaldos, V.R., Ajo-Franklin, J., and. Wu, K. (2020) Deep learning for surface wave identification in distributed acoustic sensing data. arXiv:2010.10352v1.

Fakhari, A., and Bolster, D. (2017) Diffuse interface modeling of three-phase contact line dynamics on curved boundaries: A lattice Boltzmann model for large density and viscosity ratios. Journal of Computational Physics, 334, 620-638.

Fakhari, A., Bolster, D., and Luo, L.S. (2017) A weighted multiple-relaxation-time lattice Boltzmann method for multiphase flows and its application to partial coalescence cascades. Journal of Computational Physics, 341, 22-43.

Fakhari, A., Li, Y., Bolster, D., and Christensen, K. T. (2018) A phase-field lattice Boltzmann model for simulating multiphase flows in porous media: Application and comparison to experiments of CO2 sequestration at pore scale. Advances in water resources, 114, 119-134.

Fakhari, A., Mitchell, T., Leonardi, C., and Bolster, D. (2017) Improved locality of the phase-field lattice-Boltzmann model for immiscible fluids at high density ratios. Physical Review E, 96(5), 053301.

Fernandez, R., Gonzalez-Santamaria, D., Angulo, M., Torres, E., Ruiz, A.I., Turrero, M. J., and Cuevas, J. (2018) Geochemical conditions for the formation of Mg silicates phases in bentonite and implications for radioactive waste disposal, Applied Geochemistry, 93, 1-9.

Fernandez, R., Torres, E., Ruiz, A.I., Cuevas, J., Alonso, M.C., Calvo, J.L.G., Rodriguez, E., and Turrero, M.J. (2017) Interaction processes at the concrete-bentonite interface after 13 years of FEBEX-Plug operation. Part II: Bentonite contact, Physics and Chemistry of the Earth, 99, 49-63.

Freed, A.M. (2005) EARTHQUAKE TRIGGERING BY STATICDYNAMIC AND POSTSEISMIC STRESS TRANSFER. Annual Re view of Earth and Planetary Sciences, 33 (1), 335–367.

Fu, Y., Bai, L., Zhao, S., Zhang, X., Jin, Y., and Cheng, Y. (2018) Simulation of reactive mixing behaviors inside micro-droplets by a lattice Boltzmann method. Chemical Engineering Science, 181, 79-89.

Gaboreau, S., Rodriguez-Canas, E., Maeder, U., Jenni, A., Turrero, M.J., and Cuevas, J. (2020) Concrete perturbation in a 13-year *in situ* concrete/bentonite interaction from FEBEX experiments. New insight of 2:1 Mg phyllosilicate precipitation at the interface, Applied Geochemistry, 118, 14.

Gatys, L.A., Ecker, A.S., and Bethge, M. (2015) A neural algorithm of artistic style. arXiv:1508.06576v2.

Guglielmi, Y., Birkholzer, J., Rutqvist, J., Jeanne, P., and Nussbaum, C. (2017) Can Fault Leakage Occur Before or Without Reactivation? Results from an in Situ Fault Reactivation Experiment at Mont Terri. Energy Procedia, 114, 3167–3174. doi: 10.1016/j.egypro.2017.03.144.

Guglielmi, Y., Cappa, F., Avouac, J.-P., Henry, P., and Elsworth, D. (2015a) Seismicity triggered by fluid injections induced aseismic slip. Science, 348(6240), 1224–1226, doi:10.1126/science.aab047.

Guglielmi, Y., Cappa, F., Lancon, H., Janowczyk, J. B., Rutqvist, J., Tsang, C.F., and Wang, J.S.Y. (2013) ISRM Suggested Method for Step-Rate Injection Method for Fracture In-Situ Properties (SIMFIP): Using a 3-Components Borehole Deformation Sensor. In the ISRM suggested methods for rock characterization testing and monitoring: 2007-2014 (pp. 179–186). Springer International Publishing. doi: 10.1007/978-3-319-07713-0 14.

Guglielmi, Y., Elsworth, D., Cappa, F., Henry, P., Gout, C., Dick, P., and Durand, J. (2015b) In situ observations on the coupling between hydraulic diffusivity and displacements during fault reactivation in shales. J. Geophys. Res., 120, 7729–7748, doi:10.1002/2015JB01215.

Guglielmi, Y., Nussbaum C., Rutqvist, J., Cappa F., Jeanne, P., and Birkholzer, J. (2020b) Estimating perturbed stress from 3-D borehole displacements induced by fluid injection in fractured or faulted shales, Geophys. J. Int., 221, 1684-1695, doi: 10.1093/gji/ggaa103.

Guglielmi, Y., Nussbaum, C., Jeanne, P., Rutqvist, J., Cappa, F., and Birkholzer, J. (2020a) Complexity of fault rupture and fluid leakage in shale: Insights from a controlled fault activation experiment. Journal of Geophysical Research: Solid Earth, 125, e2019JB017781. https://doi.org/ 10.1029/2019JB017781.

Guglielmi, Y., Nussbaum, C., Jeanne, P., Rutqvist, J., Cappa, F., and Birkholzer, J. (2020). Complexity of Fault Rupture and Fluid Leakage in Shale: Insights from a Controlled Fault Activation Experiment. Journal of Geophysical Research: Solid Earth, 125 (2). doi: 10.1029/2019jb017781.

Handin, J. (1969) On the Coulomb-Mohr failure criterion. Journal of Geophysical Research, 74 (22), 5343–5348.

Harrington, J. (2016) Specification for DECOVALEX-2019: Task A: modElliNg Gas INjection ExpERiments (ENGINEER). Ref: BGS-DX-v3.

Harrington, J.F., and Horseman, S.T. (1999) Gas transport properties of clays and mudrocks. In: Muds And Mudstones: Physical And Fluid Flow Properties (eds A.C.Aplin, A.J. Fleet, and J.H.S. Macquaker). Geological Society of London, Special Publication No. 158, 107-124.

Hartog, A.H. (2017). An Introduction to Distributed Optical Fibre Sensors. CRC 760 Press. doi: 10 761 1201/9781315119014.

He, X., Chen, S., and Doolen, G.D. (1998) A novel thermal model for the lattice Boltzmann method in incompressible limit. Journal of computational physics, 146(1), 282-300.

Horiguchi, T., and Tateda, M. (1989) BOTDA-nondestructive measurement of 763 single-mode optical fiber attenuation characteristics using Brillouin interaction: 764 theory. Journal of Lightwave Technology, 7 (8), 1170–1176. doi: 10.1109/50.32378.

Horseman, S.T., Harrington, J.F., and Sellin, P. (1999) Gas migration in clay barriers. Engineering Geology, Vol. 54, 139-149.

Horseman, S.T., Harrington, J.F., and Sellin, P. (2004) Water and gas flow in Mx80 bentonite buffer clay. In: Symposium on the Scientific Basis for Nuclear Waste Management XXVII (Kalmar), Materials Research Society, Vol. 807. 715-720.

Hostettler, B., Reisdorf, A.G., Jaeggi, D., Deplazes, G., Bl¨asi, H., Morard, A., and Menkveld-Gfeller, U. (2017) Litho- and biostratigraphy of the 768 Opalinus Clay and bounding formations in the Mont Terri rock laboratory (Switzerland). Swiss Journal of Geosciences, 110 (1), 23–37. doi: 771 10.1007/s00015-016-0250-3.

Houseworth, J., Rutqvist, J., Asahina, D., Chen, F., Vilarrasa, V., Liu, H.H., and Birkholzer, J. (2013) Report on International Collaboration Involving the FE Heater and HG-A Tests at Mont Terri. Prepared for U.S. Department of Energy, Used Fuel Disposition Campaign, FCRD-UFD-2014-000002, Lawrence Berkeley National Laboratory.

Hu, M., Rutqvist, J., and Wang, Y. (2016) A Practical Model for Flow in Discrete-Fracture Porous Media by Using the Numerical Manifold Method. Advances in Water Resources 97: 38–51.

Hu, M., Rutqvist, J., and Steefel, C.I. (2021) Mesh Generation and Optimization from Digital Rock Fractures Based on Neural Style Transfer. Journal of Rock Mechanics and Geotechnical Engineering. https://doi.org/10.1016/j.jrmge.2021.02.002.

Hu, M., Rutqvist, J., and Wang, Y. (2017a) A numerical manifold method model for analyzing fully coupled hydro-mechanical processes in porous rock masses with discrete fractures. Advances in Water Resources 102: 111-126.

Hu, M., and Rutqvist, J. (2020a) Numerical manifold method modeling of coupled processes in fractured geological media at multiple scales. Journal of Rock Mechanics and Geotechnical Engineering 12(4): 66681. https://doi.org/10.1016/j.jrmge.2020.03.002.

Hu, M., and Rutqvist, J. (2020b) Microscale mechanical modeling of deformable geomaterials with dynamic contacts based on the numerical manifold method. Computational Geosciences 24: 1783–1797. https://doi.org/10.1007/s10596-020-09992-z.

Hu, M., and Rutqvist, J. (2020c) Finite volume modeling of coupled thermo-hydro-mechanical processes with application to brine migration in salt. Computational Geosciences 24: 1751–1765.

Hu, M., and Rutqvist, J. (2021) Multi-scale coupled processes modeling of fractures asporous, interfacial and granular systems from rock images with the numerical manifold method. Rock Mech. Rock Eng. https://doi.org/10.1007/s00603-021-02455-6.

Hu, M., Wang, Y., and Rutqvist, J. (2015a) Development of a Discontinuous Approach for Modeling Fluid Flow in Heterogeneous Media Using the Numerical Manifold Method. International Journal for Numerical and Analytical Methods in Geomechanics 39: 1932-1952.

Hu, M., Wang, Y., and Rutqvist, J. (2015b) An effective approach for modeling water flow in heterogeneous media using Numerical Manifold Method. International Journal for Numerical Methods in Fluids 77: 459–476.

Hu, M., Wang, Y., and Rutqvist, J. (2017b) Fully coupled hydro-mechanical numerical manifold modeling of porous rock with dominant fractures. Acta Geotechnica 12: 231-252.

Huertas, F.J., Hidalgo, A., Rozalen, M. L., Pelliciobe, S., Domingo, C., Garcia-Gonzalez, C.A., Andrade, C., and Alonso, C. (2009) Interaction of bentonite with supercritically carbonated concrete, Applied Clay Science, 42(3-4), 488-496.

Hyman, J.D., Karra, S. , Makedonska, N., Gable, C.W. , Painter, S.L., and Viswanathan, H.S. (2015) dfnWorks: A discrete fracture network framework for modeling subsurface flow and transport. Computers & Geosciences 84: 10–19.

International Formulation Committee (IFC) (1967) A Formulation of the Thermodynamic Properties of Ordinary Water Substance, IFC Secretariat, Düsseldorf, Germany.

Itasca, (2016) 3DEC, 3-Dimensional Distinct Element Code. Itasca Consulting Group, Minneapolis, MN.

Jaeger, J.C., and Cook, N.G.W. (1979) Fundamentals of Rock Mechanics, Chapman and Hall, London, U.K.

Jaeggi, D., Laurich, B., Nussbaum, C., Schuster, K., and Connolly, P. (2017) Tectonic structure of the "Main Fault" in the Opalinus Clay Mont Terri rock laboratory (Switzerland). Swiss Journal of Geosciences, 110 (1), 67– 780 84. doi: 781 10.1007/s00015-016-0243.

Jeanne, P., Guglielmi Y., Rutqvist J., Nussbaum C., and Birkholzer J. (2017) Field characterization of elastic properties across a fault zone reactivated by fluid injection, J. Geophys. Res., 122, doi:10.1002/2017JB014384.

Kang, Q., Lichtner, P.C., and Zhang, D. (2006) Lattice Boltzmann pore-scale model for multicomponent reactive transport in porous media. Journal of Geophysical Research: Solid Earth, 111(B5).

Kang, Q., Zhang, D., and Chen, S. (2003) Simulation of dissolution and precipitation in porous media. Journal of Geophysical Research: Solid Earth, 108(B10).

Kang, Q., Zhang, D., Chen, S., and He, X. (2002) Lattice Boltzmann simulation of chemical dissolution in porous media. Physical Review E, 65(3), 036318.

Karpatne, A., Ebert-Uphoff, I., Ravela, S., Babaie, H.A., and Kumar, V. (2018) Machine learning for the geosciences: challenges and opportunities. IEEE Transactions on Knowledge and Data Engineering 8: 1544-1554.

Kaufhold, S., Dohrmann, R., Ufer, K., and Kober, F. (2018) Interactions of bentonite with metal and concrete from the FEBEX experiment: mineralogical and geochemical investigations of selected sampling sites, Clay Minerals, 53(4), 745-763.

Kim, K., Rutqvist J. and Birkholzer J. (2020) Lattice modeling of excavation damage in argillaceous clay formations: Influence of deformation and strength anisotropy. Tunneling and Underground Space Technology, 98, 2020. https://doi.org/10.1016/j.tust.2019.103196.

Kim, K., Rutqvist, J., Harrington, J.F., Tamayo-Mas, E., and Birkholzer, J.T. (2021) Discrete dilatant pathway modeling of gas migration through compacted bentonite clay. International Journal of Rock Mechanics and Mining Sciences. 137, 104569 (2021). https://doi.org/10.1016/j.ijrmms.2020.104569.

Kim, K., Rutqvist, J., Nakagawa, S., and Birkholzer, J. (2017) TOUGH-RBSN simulator for hydraulic fracture propagation within fractured media: Model validations against laboratory experiments, Computers & Geosciences, 108, 72–85.

Kingma, D.P., and Ba, J. (2015) Adam: A Method for Stochastic Optimization. 3rd International Conference for Learning Representations, San Diego. arXiv:1412.6980v9.

Krietsch, H., Gischig, V., Jalali, M., Doetsch, J., Valley, B., Amann, F., et al. 790 (2018) A comparison of FBG-and Brillouin-strain sensing in the framework of a decameter-scale hydraulic stimulation experiment. In 52nd us rock 7mechanics/geomechanics symposium.

Krüger, T., Kusumaatmaja, H., Kuzmin, A., Shardt, O., Silva, G., and Viggen, E. M. (2017) The lattice Boltzmann method. Springer International Publishing, 10(978-3), 4-15.

Laurich, B., Urai, J.L., Vollmer, C., and Nussbaum, C. (2018) Deformation mechanisms and evolution of the microstructure of gouge in the main fault in opalinus clay in the Mont Terri rock laboratory (ch). Solid Earth, 9 (1), 1–24.

Lisjak, A., Tatone, B.S.A. Mahabadi, O.K., Grasselli, G., Marschall, P., Lanyon, G.W., de la Vaissiere, R., Shao, H. Leung, H., Nussbaum, C. (2016) Hybrid Finite-Discrete Element Simulation of the EDZ Formation and Mechanical Sealing Process Around a Microtunnel in Opalinus Clay. Rock Mech Rock Eng 49:1849–1873.

LLiu, J. F., Song, Y., Skoczylas, F., and Liu, J. (2016), Gas migration through water-saturated bentonite-sand mixtures, COx argillite, and their interfaces, Can. Geotech. J., 53(1), 60-71.

Mader, U., et al. (2017) 5-year chemico-physical evolution of concrete-claystone interfaces, Mont Terri rock laboratory (Switzerland), Swiss J. Geosci., 110(1), 307-327.

Madjdabadi, B., Valley, B., Dusseault, M. B., and Kaiser, P. K. (2016) Experimental evaluation of a distributed Brillouin sensing system for measuring extensional and shear deformation in rock. Measurement, 77, 54–66. doi: 806 10.1016/j.measurement.2015.08.040 807.

Madjdabadi, B., Valley, B., Dusseault, M., and Kaiser, P. (2014) Numerical study of grout–rock mass interaction effect on distributed optical fibre sensor measurements. In Proceedings of the seventh international conference on deep and high stress mining. Australian Centre for Geomechanics Perth. doi: 10.36487/acg rep/1410 31 madjdabadi.

Marchesini, P., Ajo-Franklin, J.B. and Daley, T. (2017) In situ measurement of velocity-stress sensitivity using crosswell continuous active-source seismic monitoring. Geophysics, Vol 82, N° 5 (September-October 2017), 319-326.

Marone, C. (1998) Laboratory-derived friction laws and their application to seismic faulting, Ann. Rev. Earth Planet. Sci., 26, 643–696.

Mital, U., Dwivedi, D., Brown, J.B., Faybishenko, B., Painter, S.L., and Steefel, C.I. (2020) Sequential Imputation of Missing Spatio-Temporal Precipitation Data Using Random Forests. Frontiers in Water. https://doi.org/10.3389/frwa.2020.00020.

Nussbaum, C., Bossart, P., Amann, F., and Aubourg, C. (2011) Analysis of tectonic structures and excavation induced fractures in the Opalinus Clay, Mont Terri underground rock laboratory (Switzerland), Swiss Journal of Geosciences, 104(2), 187–210. https://doi.org/10.1007/s00015- 011-0070-4.

Nussbaum, C., Kloppenburg, A., Caër, T., and Bossart, P., (2017) Tectonic evolution around the Mont Terri rock laboratory, northwestern Swiss Jura: constraints from kine-matic forward modelling. Swiss J. Geosci., 110, 39–66. https://doi.org/10.1007/s00015-016-0248-x.

Nutt, M. (2012) Used Fuel Disposition Campaign Disposal Research and Development Roadmap (FCRD-USED-2011-000065 REV1), U.S. DOE Used Fuel Disposition Campaign.

Orellana et al., (2018b) Do scaly clays control seismicity on faulted shale rocks? Earth Planet Sci Lett., 488, 59-67, doi:10.1016/j.epsl.2018.01.027.

Orellana, L. F., Giorgetti, C., and Violay, M., (2019) Contrasting mechanical and hydraulic properties of wet and dry fault zones in a proposed shale-hosted nuclear waste repository. Geophys Res Lett, 46, 1357–1366. doi :10.1029/2018GL080384.

Orellana, L. F., Scuderi, M. M., Collettini, C., and Violay, M., (2018a) Frictional properties of Opalinus Clay: Implications for nuclear waste storage, J. Geophys. Res, 123. https://doi.org/10.1002/ 2017JB014931.

Pignatelli, I., Bourdelle, F., Bartier, D., Mosser-Ruck, R., Truche, L., Mugnaioli, E., and Michau, N. (2014) Iron-clay interactions: Detailed study of the mineralogical transformation of claystone with emphasis on the formation of iron-rich T-O phyllosilicates in a step-by-step cooling experiment from 90 degrees C to 40 degrees C, Chemical Geology, 387, 1-11.

Pyrak-Nolte, L.J., Myer, L.R. and Cook, N.G.W. (1990a) Transmission of seismic-waves across single natural fractures. Journal of Geophysical Research-Solid Earth and Planets 95, 8617–8638.

Rabbani, A., Babaei, M., Shams, R., Wang, Y.D., and Chung, T. (2020) DeePore: A deep learning workflow for rapid and comprehensive characterization of porous materials. Advances in Water Resources 146: 103787. https://doi.org/10.1016/j.advwatres.2020.103787.

Rezatofighi, H., Tsoi, N., Gwak, J.Y., Sadeghian, A., Reid, I., and Savarese, S. (2019) Generalized intersection over union: A metric and a loss for bounding box regression. Proceedings of the IEEE Conference on Computer Vision and Pattern Recognition: 658-666.

Riaud, A., Zhao, S., Wang, K., Cheng, Y., and Luo, G. (2014) Lattice-Boltzmann method for the simulation of multiphase mass transfer and reaction of dilute species. Physical Review E, 89(5), 053308.

Rice, J.R. (1993) Spatio-temporal complexity of slip on a fault, J. Geophys. Res., 98, 9885–9907.

Riesinger, C., Bakhtiari, A., Schreiber, M., Neumann, P., and Bungartz, H. J. (2017) A holistic scalable implementation approach of the lattice Boltzmann method for CPU/GPU heterogeneous clusters. Computation, 5(4), 48.

Rinaldi A.P., Rutqvist J., Blanco-Martín L., Hu M., and Sentís M.L. (2018) Coupling TOUGH3 with FLAC3D for parallel computing of fluid-flow and geomechanics. Proceedings TOUGH Symposium 2018, Berkeley, California, October 8-10, 2018.

Rinaldi, A. P., Guglielmi, Y., Zappone, A., Soom, F., Robertson, M., Cook, P., Kakurina, M., Wenning, Q., Rebscher, D., and Nussbaum, C. (2020) Coupled processes in clay during tunnel excavation, EGU General Assembly Vienna, Austria, 4-8 May 2020, EGU2020-184, doi:10.5194/egusphere-egu2020-18041, 2020.

Ronneberger, O., Fischer, P., and Brox, T. (2015) U-Net: Convolutional networks for biomedical image segmentation. International Conference on Medical image computing and computer-assisted intervention. Springer: 234-241.

Rutqvist, J. and Rinaldi, A.P. (2019) Fault reactivation and seismicity associated with geologic carbon storage, shale-gas fracturing and geothermal stimulation– Observations from recent modeling studies. Proceedings of 14th Congress of the ISRM, Iguassu Falls, Brazil, Sept 13 - 18, 2019.

Rutqvist, J., Kim, K., Xu, H., Guglielmi, Y., and Birkholzer, J. (2018) Investigation of Coupled Processes in Argillite Rock: FY18 Progress. Prepared for U.S. Department of Energy, Spent Fuel and Waste Disposition, SFWD-SFWST-2018-000XXX, LBNL-2001168, Lawrence Berkeley National Laboratory.

Rutqvist, J. (2011) Status of the TOUGH-FLAC simulator and recent applications related to coupled fluid flow and crustal deformations. Computers & Geosciences, 37, 739–750.

Rutqvist, J. (2017) An overview of TOUGH-based geomechanics models. Computers & Geosciences, 108, 56–63.

Rutqvist, J. (2020) Thermal management associated with geologic disposal of large spent nuclear fuel canisters in tunnels with thermally engineered backfill. Tunnelling and Underground Space Technology 102: 103454.

Rutqvist, J., Bäckström, A., Chijimatsu, M., Feng, X.-T., Pan, P.-Z., Hudson, J., Jing, L., Kobayashi, A., Koyama, T., Lee, Huang, X.-H., Rinne, M., and Shen, B., (2009) Multiple-code simulation study of the long-term EDZ evolution of geological nuclear waste repositories. Environmental Geology 57: 1313–1324.

Rutqvist, J., and Tsang, C.-F. (2002) A study of caprock hydromechanical changes associated with CO2-injection into a brine formation, Environmental Geology, 42, 296–305.

Rutqvist, J., Börgesson, L., Chijimatsu, M., Hernelind, J., Jing, L., Kobayashi, A., and Nguyen, S. (2009) Modeling of damage, permeability changes and pressure responses during excavation of the TSX tunnel in granitic rock at URL, Canada. Environmental Geology, 57, 1263–1274.

Rutqvist, J., Börgesson, L., Chijimatsu, M., Kobayashi, A., Nguyen, T. S., Jing, L., Noorishad, J., and Tsang, C.-F. (2001) Thermohydromechanics of partially saturated geological media – Governing equations and formulation of four finite element models. International Journal of Rock Mechanics and Mining Sciences, 38, 105-127.

Rutqvist, J., Davis, J., Zheng, L., Vilarrasa, V., Houseworth, J., and Birkholzer, J. (2014a) Investigation of Coupled THMC Processes and Reactive Transport: FY14 Progress. Prepared for U.S. Department of Energy, Used Fuel Disposition, FCRD-UFD-2014-000497, Lawrence Berkeley National Laboratory, LBNL-6720E (2014a).

Rutqvist, J., Ijiri, Y, and Yamamoto, H. (2011) Implementation of the Barcelona Basic Model into TOUGH-FLAC for simulations of the geomechanical behavior of unsaturated soils. Computers & Geosciences, 37, 751–762.

Rutqvist, J., Wu, Y.-S., Tsang, C.-F., and Bodvarsson, G. (2002). A modeling approach for analysis of coupled multiphase fluid flow, heat transfer and deformation in fractured porous rock. International Journal of Rock Mechanics & Mining Sciences, 39, 429-442.

Rutqvist, J., Zheng, L., Chen, F., Liu, H.-H., and Birkholzer, J. (2014b) Modeling of Coupled Thermo-Hydro-Mechanical Processes with Links to Geochemistry Associated with Bentonite-Backfilled Repository Tunnels in Clay Formations. Rock Mechanics and Rock Engineering, 47, 167–186.

Senger R., Romero, E., Ferrari, A., and Marschall, P. (2014) Characterization of gas flow through low-permeability claystone: laboratory experiments and two-phase flow analyses. Norris, S., Bruno, J., Cathelineau, M., Delage, P., Fairhurst, C., Gaucher, E. C., Ho¨hn, E. H., Kalinichev, A., Lalieux, P. & Sellin, P. (eds) Clays in Natural and Engineered Barriers for Radioactive Wast Confinement. Geological Society, London, Special Publications, 400, http://dx.doi.org/10.1144/SP400.15.

Senger, R., and Marschall, P. (2008) Task Force on EBS / Gas Transport in Buffer Material, Nagra Arbeitsbericht NAB 08-24.

Shi, G. (1992) Manifold method of material analysis. Transaction of the 9th army conference on applied mathematics and computing. U.S. Army Research Office.

Shi, G. (1996) Simplex integration for manifold method, FEM and DDA. Discontinuous Deformation Analysis (DDA) and Simulations of Discontinuous Media. TSI press. 205-262.

Shipton, Z.K., and Cowie, P.A. (2003) A conceptual model for the origin of fault damage zone structures in high-porosity sandstone. Journal of Structural Geology, 25 (3), 333–344. 831.

Silver, P.G., Daley, T.M., Niu, F., and Majer, E.L. (2007) Active source monitoring of cross-well seismic traveltime for stress-induced changes: Bulletin of the Seismological Society of America, 97, 1B, 281–293; http://dx•.doi.org/10.1785/0120060120.

Simonyan, K., and Zisserman, A. (2015) Very deep convolutional networks for large-scale image recognition. arXiv:1409.1556v6.

Sirignano, J., and Spiliopoulos, K. (2018) DGM: A deep learning algorithm for solving partial differential equations. Journal of Computational Physics 375: 1339-1364.

Sone, H., and Zoback, M. D. (2014) Time-dependent deformation of shale gas reservoir rocks and its long-term effect on the *in situ* state of stress. International Journal of Rock Mechanics and Mining Sciences, 69, 120–132. https://doi.org/10.1016/j.ijrmms.2014.04.002.

Steefel, C.I. (2019) Reactive transport at the crossroads. Reviews in Mineralogy and Geochemistry 85: 1-26.

Steefel, C.I. and Tournassat, C., (2021) A model for discrete fracture-clay rock interaction incorporating electrostatic effects on transport. Computational Geosciences 25 (1): 395-410. DOI: 10.1007/s10596-020-10012-3.

Steefel, C.I., Appelo, C.A.J., Arora, B., Jacques, D., Kalbacher, T., Kolditz, O., Lagneau, V., Lichtner, P.C., Mayer, K.U., Meeussen, J.C.L. and Molins, S., (2015) Reactive transport codes for subsurface environmental simulation. Computational Geosciences, 19(3), pp.445-478.

Tamayo-Mas, E, Harrington, J.F., Brüning, T., Shao, H., Dagher, E.E., Lee, J., Kim, K., Rutqvist, J., Kolditz, O., Lai, S.H., Chittenden, N., Wang, Y., Damians, I. and Olivella, S. (2021) Modelling advective gas flow in compact bentonite: lessons learnt from different numerical approaches. International Journal of Rock Mechanics and Mining Sciences. 139, 104580. https://doi.org/10.1016/j.ijrmms.2020.104580.

Tournassat, C., Steefel, C., and Gimmi, T. (2020) Solving the Nernst-Planck equation in heterogeneous porous media with finite volume methods: Averaging approaches at interfaces. Water Resources Research https://DOI.org/10.1029/2019WR026832.

Tournassat, C.M., and Steefel, C.I. (2019a) Reactive transport modeling of coupled processes in nanoporous media. Reviews in Mineralogy and Geochemistry 85: 75-109.

Tournassat, C.M., and Steefel, C.I. (2019b) Modeling diffusion processes in the presence of a diffuse layer at charged mineral surfaces. A benchmark exercise. Computational Geosciences. 1-18. https://DOI.org/10.1007/s10596-019-09845-4.

Turrero and Cloet, (2017) FEBEX-DP Concrete ageing, concrete/bentonite and concrete/rock interaction analysis. Arbeitsbericht NAB 16-18.

Valley, B., Madjdabadi, B. M., Kaiser, P. K., Dusseault, M. B., et al. (2012) Monitoring mining-induced rock mass deformation using distributed strain monitoring based on fiber optics. In Isrm international symposium-eurock 2012. 843.

van Genuchten, M.T. (1980) A closed-form equation for predicting the hydraulic conductivity of unsaturated soils. Soil. Sci. Soc. Am. J., 44, 892-898.

Vilarrasa, V., Rutqvist, J., Blanco-Martin, L., and Birkholzer, J. (2016) Use of a dual structure constitutive model for predicting the long-term behavior of an expansive clay buffer in a nuclear waste repository.

Wang, Y., Hu, M., Zhou, Q., and Rutqvist, J. (2014) Energy-work-based numerical manifold seepage analysis with an efficient scheme to locate the phreatic surface. International Journal for Numerical and Analytical Methods in Geomechanics, 38, 1633–1650.

Wang, Y. (2011) Research & Development (R&D) Plan for Used Fuel Disposition Campaign (UFDC) Natural System Evaluation and Tool Development, U.S. DOE Used Fuel Disposition Campaign.

Wang, Y., Hu, M., Zhou, Q., and Rutqvist, J. (2016) A new Second-Order Numerical Manifold Method Model with an efficient scheme for analyzing free surface flow with inner drains. Applied Mathematical Modelling 40: 1427-1445.

Wenning, Q.C., Madonna, C., Zappone, A., Grab, M., Rinaldi, A.P., Plotze, M., and Wiemer, S. (2020) Shale fault zone structure and stress dependent anisotropic permeability and seismic velocity properties (opalinus clay, switzerland). Journal of Structural Geology, 104273.

Wu, X., Liang, L., Shi, Y., and Fomel, S.(2019) FaultSeg3D: Using synthetic data sets to train an end-to-end convolutional neural network for 3D seismic fault segmentation. Geophysics 84(3): IM35-IM45.

Wynants-Morel, N., Cappa, F., De Barros, L., and Ampuero, J.P. (2020). Stress Perturbation From Aseismic Slip Drives The Seismic Front During Fluid Injection In A Permeable Fault, J. Geophys. Res., doi:10.1029/2019JB019179.

Xu, H., Zheng, L., Rutqvist, J., and Birkholzer, J. (2021) Chemo-Mechanical behavior of bentonite in nuclear waste disposal based on the Barcelona expansive model. Computers and Geotechnics 132, 103968 (2021). https://doi.org/10.1016/j.compgeo.2020.103968.

Xu, H., Rutqvist, J., Plua, C., Armand, G., and Birkholzer, T. (2020) Modeling of thermal pressurization in tight claystone using sequential THM coupling: benchmarking and validation against in-situ heating experiments in COx claystone. Tunnelling and Underground Space Technology (accepted).

Ye, Y., Li, K., Wang, Y., and Deng, T. (2015) Parallel computation of Entropic Lattice Boltzmann method on hybrid CPU–GPU accelerated system. Computers & Fluids, 110, 114-12.

Zappone, A., Rinaldi, A.P., Grab, M., Wenning, Q., Roques, C., and Madonna, C., (2020) Fault sealing and caprock integrity for co2 storage: an in-situ injection experiment. Solid Earth Discussions, 1–51.

Zhao, S., Riaud, A., Luo, G., Jin, Y., and Cheng, Y. (2015) Simulation of liquid mixing inside micro-droplets by a lattice Boltzmann method. Chemical Engineering Science, 131, 118-128.

Zheng L., Kim K., Xu H., Rutqvist J., Voltolini M., and Xiaoyuan C. (2017) Investigation of Coupled Processes and Impact of High Temperature Limits in Argillite Rock: FY17 Progress. Prepared for U.S. Department of Energy, Spent Fuel and Waste Disposition. SFWD-SFWST-2017-000040, LBNL-2001014, Lawrence Berkeley National Laboratory.

Zheng, L., Rutqvist, J., Xu, H., and Birkholzer, J.T (2017) Coupled THMC models for bentonite in an argillite repository for nuclear waste: Illitization and its effect on swelling stress under high temperature, Engineering Geology, 230, 118-129.

Zheng, L., Kim, K., Xu, H., and Rutqvist, J. (2016) DR Argillite Disposal R&D at LBNL. FCRD-UFD-2016-000437, LBNL-1006013, Lawrence Berkeley National Laboratory.

Zheng, L., Rutqvist, J., Kim, K., and Houseworth, J. (2015) Investigation of Coupled Processes and Impact of High Temperature Limits in Argillite Rock. Prepared for U.S. Department of Energy, Used Fuel Disposition, FCRD-UFD-2015-000362. LBNL-187644, Lawrence Berkeley National Laboratory.

Zheng, L., Rutqvist, J., Steefel, C., Kim, K., Chen, F., Vilarrasa, V., Nakagawa, S., Houseworth, J., and Birkholzer J. (2014) Investigation of Coupled Processes and Impact of High Temperature Limits in Argillite Rock. Prepared for U.S. Department of Energy, Used Fuel Disposition, FCRD-UFD-2014-000493, Lawrence Berkeley National Laboratory, LBNL-6719E.

Zou, L., Jing, L., and Cvetkovic, V. (2015) Roughness decomposition and nonlinear fluid flow in a single rock fracture. International Journal of Rock Mechanics & Mining Scienc

Argillite R&D and International Collaborations – LANL (FY21) (Part III)

1. Introduction

1.1 Argillite Disposal R&D

The United States Department of Energy Spent Fuel and Waste Disposition program is investigating reference cases in multiple host rock types for the geologic disposal of spent nuclear fuel and waste. This report presents experimental results on engineered barrier system (EBS) interactions at elevated temperature and pressure in an argillite host rock formation. The generic disposal concept in argillite includes a horizontal waste package encapsulated in a bentonite clay barrier (pellets or compressed blocks) emplaced in a horizontal tunnel, likely lined with a form of concrete (e.g., shotcrete or pre-formed concrete blocks) (Figure 1). The bentonite barrier's function relies on the physical and chemical properties of swelling clay minerals (i.e. smectite), which are the main mineralogical components of bentonite (Pusch, 1979; Dohrmann et al., 2013; Sellin & Leupin, 2014). Smectite has unique swelling properties that 1) maintain in-drift pressure, 2) have the ability to seal cracks and fractures that may develop, and 3) retard the infiltration of fluid from the surrounding wall rock that may interact with the waste package. Further, clay minerals may act as a chemical barrier that attenuate actinide migration through sorption on clay mineral surfaces if a release occurs. However, there remain large uncertainties regarding the long-term stability of bentonite at potential repository conditions, particularly, under prolonged periods of high thermal loads in the presence of water and other repository materials such as cement and stainless steel.

U.S. DOE is interested in exploring repository concepts at higher temperatures than considered by foreign programs in order to vet disposal of large waste packages with a higher thermal load. For example, dual-purpose canisters (DPCs), designed for storage and transportation, may contain up to 37 spent-fuel assemblies (37 pressurized-water reactors (37-PWR)), whereas many of the European concepts are limited to four spent fuel assemblies (4-PWR) (Pusch, 2008; Hardin et al., 2015). The increased number of spent fuel assemblies within the U.S. DPCs have the potential to generate a greater amount of heat radiating into the EBS and host rock in a disposal scenario. For example, thermal modeling calculations show that the surface of a DPC containing 37-PWR (60 gigawatt-days per metric ton burnup) has the potential to reach 400ºC in a repository hosted in clay/shale rock (50-year decay storage and 100-year ventilation; 20 m package spacing; unsaturated bentonite thermal conductivity = 0.60 W/m-K, Hardin et al., 2015) (Figure 2). These calculations, based on a hypothetical repository layout, demonstrate the importance of thermal management and the potential for high temperatures in a clay/shale disposal environment. Thus, the thermal evolution of this potential repository design demonstrates the need for high temperature experimental work on the interaction of

wall rock, EBS backfill, cement liner, and canister materials that have not been explored previously by the foreign repository science programs.

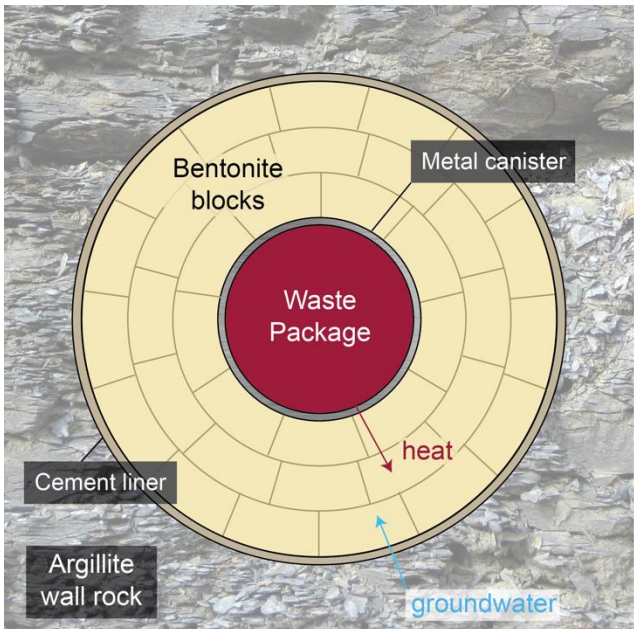

Figure 1. Schematic of a generic engineered barrier system concept in argillite host rock. Bentonite blocks surround a waste canister emplaced in a horizontal tunnel lined with cement.

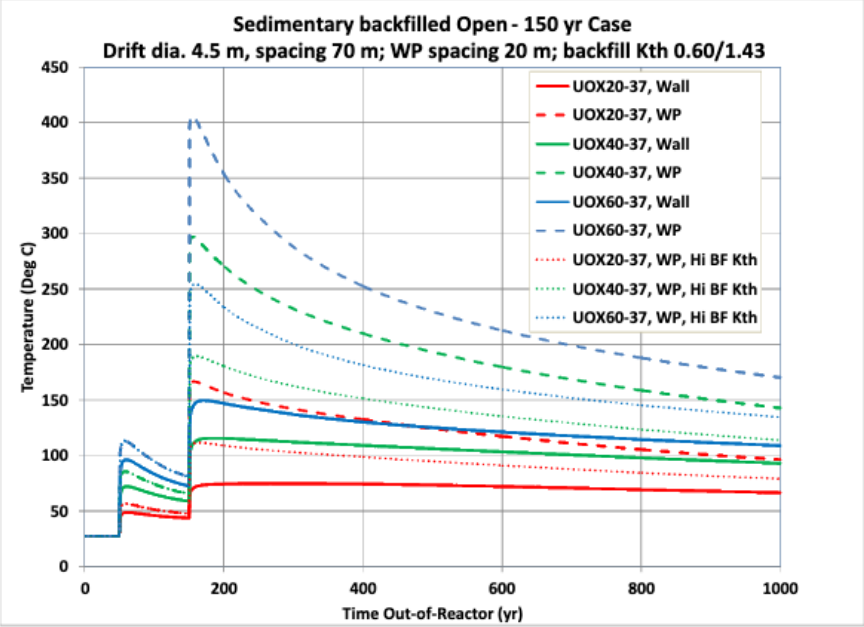

Figure 2. Calculated temperatures for various burnup levels (e.g., OUX20) of spent nuclear fuel 37-PWR at the repository drift wall (wall) and waste package surface (WP) in a backfilled sedimentary rock-hosted repository. The calculations include 50 years of decay storage and 100-year ventilation time. Waste package spacings and drift dimensions are listed on the figure. Thermal conductivity of the bentonite is either 0.60 W/m-K (unsaturated bentonite) or 1.43 W/m-K (fully hydrated bentonite). From Hardin et al. (2015).

Cementitious materials will likely make up a large component of the underground repository. Interaction between cement, bentonite, and steel will therefore likely occur at elevated temperature and pressure and in the presence of water. Experiments in FY21 included a comparison of the effects of uncured ordinary Portland cement (OPC) powder versus cured OPC chips on bentonite mineral and geochemical properties at temperatures of 200 to 300ºC.

The research scope of FY21 also included the investigation of "designer" EBS additives that may enhance the radionuclide retention capacity of the barrier system. Clay and zeolite minerals within bentonite have the potential to retain radionuclides in the case of a canister breach, through sorption on mineral surfaces or incorporation into the crystalline structure. For example, Redkin and Hemley (2020) studied the cesium (Cs) and strontium (Sr) sorption on analcime at 250 to 300ºC in rock buffered systems. They establish that there is a high sorption capacity for the albite-analcime assemblage at 250 to 300°C with respect to Cs and Sr. The interaction of Cs and Sr-bearing solution encouraged the mineralization of Cs-rich analcime, pollucite and Sr-analcime, especially in systems buffered at a higher pH. Phosphate minerals also have the potential for actinide element retention under ambient to hydrothermal conditions (e.g. Krejzker et al., 2003; Omel'yanenko et al., 2007; Rigali et al., 2016). It is unknown, however, how the presence of phosphate will affect bentonite mineral stability under repository temperature and pressures. One preliminary hydrothermal experiment was completed in FY20 with Wyoming bentonite and Durango apatite to assess bentonite-phosphate interaction and dissolution-reprecipitation of apatite, with the overall goal of understanding how phosphate additives may affect bentonite stability and/or enhance EBS function to retain radionuclides.

Overall, the hydrothermal experiments conducted at Los Alamos National Laboratory in FY21 aimed to develop concepts related to the function of EBS in the high-temperature isolation of spent fuel and waste in argillite host rock. Our work on bentonite interaction with Opalinus Clay in experimental hydrothermal systems was developed in the FY17, FY18, and FY19 reports and was published in Clays and Clay Minerals (Sauer et al., 2020). The FY21 report will focus on our current experimental focuses in argillite including: 1) the effects of cured and uncured Ordinary Portland cement on bentonite stability and Opalinus Clay mineralogy, 2) clay-steel interface mineralization and growth rates in systems with and without cement, and 3) the effects of phosphate additives to the EBS system. For details of the material presented in this part of the reports (e.g., SEM images, geochemical data) the reader is referred to the deliverable report M3SF-21LA010301011.

1.2 Background

1.2.1 Wyoming Bentonite in EBS Applications

Bentonite performance in the EBS relies on the physical and chemical properties of the mineral components, especially the clay mineral montmorillonite. Under dry conditions, the bentonite mineral assemblage may be stable to over 350°C (Wersin et al., 2007); however, moisture is likely to be present in the natural geologic environment. Under water saturated conditions and temperatures > 100°C, alteration of clay minerals may occur (e.g. Mosser-Ruck et al., 2010; Ferrage et al., 2011; Cheshire et al., 2014). The stability of bentonite at repository conditions has been documented in both laboratory and in situ (full-scale) experiments and are used to assess the long-term function of a nuclear waste disposal site.

Mineralogical changes within the bentonite EBS materials that affect the ability of smectite to expand are a primary concern for the long-term function of a nuclear waste repository. The reduction of swelling capacity of smectite, due to the formation of non-swelling clays, cementation of smectite lamellae caused by silica precipitation, and/or recrystallization to other mineral phases (e.g. zeolites), is believed to be one of the greatest risks to the repository stability and isolation capability compared to other mineral reactions (Pusch et al., 1998; Pusch & Kasbohm, 2002). Previous laboratory-scale investigations have investigated clay mineral transformations relevant to EBS systems over a wide range of repository temperatures (i.e. ~25 - 300°C), alone and in contact with metals that approximate potential canister materials (Madsen, 1998; Meunier et al., 1998; Guillaume et al., 2003; Hofmann et al., 2004; Wersin et al., 2007; Mosser-Ruck et al., 2010; Ferrage et al., 2011; Cheshire et al., 2014). The reduction of swelling capacity of montmorillonite may be due dominantly to the formation of non-swelling clays (e.g. illite, $K(Al,Mg,Fe)_2(Si,Al)_4O_{10}[(OH)_2]$) (Wersin et al., 2007). For example, in experimental systems where K^+ was reacted with bentonite, the formation of non-swelling K^+ rich, collapsed layer smectite and/or illite was observed (e.g. Mosser-Ruck et al. 1999; Kaufhold & Dohrmann, 2010; Cheshire et al. 2014). In the alteration of montmorillonite to illite, silica is liberated through the generalized reaction:

$$\text{Na-montmorillonite} + K^+ + H^+ \rightarrow \text{illite} + SiO_{2\,(aq)} + Na^+ + Mg^+ + H_2O \quad (1)$$

The low availability of K^+ and silica saturation in the system may limit illitization (Pusch & Madsen 1995; Cheshire et al. 2014; Savage et al. 2019). For example, in bentonite systems reacted with NaCl solutions, montmorillonite structural alteration is not observed (Kaufhold & Dohrmann, 2009; Cheshire et al., 2014) in comparison to experiments in a K^+ rich environment (Kaufhold & Dohrmann, 2010).

The influence of bulk chemistry on clay-mineral reactions is observed in full-scale experiments. In the full-scale Prospective Repository experiment at the Äspö Hard Rock Laboratory in Sweden, cation exchange was observed in the smectite, but no structural changes were observed in the bentonite blocks after a period of eight years at temperatures between 60 and 85°C (Dohrmann & Kaufhold, 2014). In the FEBEX experiment, smectite alteration was observed only close to the heater surface (100°C) and included recrystallization to saponite and chlorite and a decrease in cation exchange capacity and surface area (Fernandez et al., 2018).

Zeolite formation within bentonite EBS material has also been reported (e.g. Mosser-Ruck et al., 2010; Ferrage et al., 2011; Cheshire et al., 2013, 2014; Mosser-Ruck et al., 2016). Zeolites may form as a result of clinoptilolite dissolution under silica-saturated conditions (Cheshire et al., 2013; 2014) or clay-mineral reactions (Mosser-Ruck et al., 2010). Dissolution of clinoptilolite, which makes up roughly 13% of the Wyoming bentonite used in this study, and precipitation of analcime may result in a slight volume loss within the bentonite buffer (Cheshire et al., 2014).

1.2.2 Opalinus Clay

Opalinus Clay is considered to be a favorable medium for a repository based on its high clay content, low permeability, high sorption potential for radionuclides, and crack-sealing properties (Nagra, 2002; Bossart & Thury, 2008; Bossart & Milnes, 2017). Several experimental studies

have examined the mineralogical and chemical evolution of Opalinus Clay at temperatures below 200°C. The interaction of high pH fluids and Opalinus Clay had been evaluated at ambient (e.g. Adler et al., 1999; Taubald et al., 2000) and elevated (e.g. 90–200°C; Honty et al., 2012; Chermak, 1992) temperatures. The presence of cement and/or high-pH solutions at ambient temperatures (25°C) results in the dissolution of the precursor chlorite in the Opalinus Clay (Taubald et al., 2000) and the formation of Ca-zeolites and calcium aluminum silicate hydrate minerals (Alder et al., 1999). At higher temperature (150–200°C) and similar pH, the formation of analcime, vermiculite, and narectorite was observed within powdered Opalinus Clay (Chermak, 1992). In situ EBS experiments at the Mont Terri underground research laboratory in Opalinus Clay are in progress (HE-E, up to 140°C; Wieczorek et al., 2017; FE, up to 150°C; Müller et al., 2018).

1.2.3 Hydrothermal Interaction of Wyoming Bentonite and Opalinus Clay

The results and analysis of Opalinus Clay ± Wyoming bentonite experiments (EBS-14 through EBS-22) were published in Sauer et al. (2020) and summarized in Caporuscio et al. (2020).

1.2.4 Previous Research in Bentonite-Portland Cement Interaction

There have been many studies on the interaction of bentonite and cementitious materials in EBS systems as both materials are integral to most repository designs (e.g., Karnland, 1997; Cuevas et al., 2006; Watson et al., 2009; Fernandez et al., 2009a; Savage et al., 2010; Watson et al., 2018). Cementitious materials, such as shotcrete, cast-in-place, and/or preformed cement blocks, are necessary elements of repository infrastructure and provide ground support to maintain drift integrity and prevent collapse. However, the reaction of cement with water may have a significant chemical effect on the repository system through the dissolution of portlandite ($Ca(OH)_2$), alkali-rich phases, calcium silicate hydrate (CSH) minerals, and other reactive components of the cement (e.g., sulfates). Thus, cement reactions have the potential to release significant amounts of OH^- and Ca^{2+} into the groundwater migrating into the EBS system, leading to increase in pore water pH in the bentonite buffer, montmorillonite dissolution, and the formation of diverse secondary mineral phases (e.g., Ca-zeolites, CSH phases, feldspars). Cement-bentonite interaction is observed to be a non-linear system that involves multiple coupled processes that occur simultaneously and affect each other (e.g., Savage et al., 2010). These processes include the reaction of concrete to release Ca^{2+} and OH^-, transport of hydroxide and cations into bentonite, montmorillonite ion exchange and dissolution, precipitation of secondary phases, dissolution of accessory minerals, and porosity and swelling changes (Takasa, 2004; Savage et al., 2010).

The potential for significant and wide-ranging geochemical and mineralogical effects of bentonite-cement interaction has led repository programs to implement a pH limit for cement porewater (e.g., B, pH < 11). The pH limit is achievable using low pH cements that replace traditional cement components (e.g., limestone aggregate) with siliceous materials (e.g. fly ash and silica fume) resulting the reduced abundance of portlandite in the cured product and a lower Ca/Si ratio in the CSH minerals (Calvo et al., 2010; Lothenbach et al., 2011). Due to the potential for bentonite degradation in alkaline pore waters, low pH cement formulations are becoming increasingly standard for repository concepts. The experimental work reported here focuses on the effects of uncured Ordinary Portland cement (OPC) powder and cured chips containing 100% OPC. Future research will evolve to include low pH formulations. A summary

of previous modeling and experimental (laboratory and full-scale) studies is provided here to contextualize our experimental results.

1.2.4.1 Experimental Studies

Many experimental studies have been performed on the interaction of bentonite and cementitious materials and bentonite stability in highly alkaline environments (e.g, Balmer et al., 2017; Chen et al., 2019; Cuevas et al., 2006; de la Villa et al., 2001; Dolder et al., 2014; Fernandez et al., 2006; 2009a; 2016; Karnland et al., 2007; Karnland, 1997; Kaufhold et al., 2020). Experimental work at the laboratory scale and in full-scale demonstrations, especially at low temperature, may not fully capture the evolution of the cement-bentonite system due to kinetically slow reactions, but can provide insight into the potential for geochemical and mineralogical changes. Experiments below ~100ºC show that the reaction of bentonite in contact with cement and alkaline porewaters over relatively short timescales (~months to 1–2 years) result in changes to the physical property clay minerals (e.g., swelling) and the formation of secondary phases. For example, 16-month experiments with MX-80 Wyoming bentonite and solutions mimicking cement porewater (pH = 12.8–13.7) at 40ºC resulted in minor illite and chlorite formation, cristobalite dissolution and quartz precipitation, and CSH mineral and CSH gel formation (Karnland, 1997). At 60ºC over a period of 6 to 12 months, in column tests with FEBEX bentonite and alkaline solutions, alteration was concentrated in a 2.0 to 2.5 mm reaction front, which included brucite, chlorite, Mg-smectite, and minor zeolite formation and montmorillonite dissolution (Fernandez et al., 2009a). In a comparative study of 40 different bentonites in contact with Portland cement powder at 80ºC for 3 months showed that the presence of reactive silica in bentonite helped to stabilize clay minerals (Kaufhold et al., 2020). Comparative experiments over a range of temperatures between 25 and 200ºC demonstrated expansion of the alteration zone with increasing temperature and changes in alteration mineralogy (Cuevas et al., 2006). Overall, these cement-bentonite experiments demonstrate the potential for montmorillonite dissolution, zeolite, feldspar, and CSH mineral formation near the bentonite-cement contact, and the influence of bulk-system chemistry. Further, experiments demonstrated that alteration is concentrated in a thin alteration zone at the bentonite-cement interface, which expands with higher temperatures.

Observations from long-term, full-scale, in situ demonstrations at underground research facilities provide insight into cement-bentonite interactions in the natural environment, including potential effects on groundwater geochemistry, host-rock properties, and hydrologic processes. Several full-scale experimental studies at underground research laboratories have been conducted, including the PR (Prototype Repository) at the Äspö Hard Rock Laboratory in Sweden (Johannesson et al., 2007) and FEBEX at the Grimsel Test Site (Martin et al., 2006). Observations of cement-bentonite interaction after 13 years in the FEBEX demonstration are reported in Alonso et al. (2017) and Fernandez et al. (2017). The FEBEX experiment consisted of a heater that was held at 100ºC resulting in an observed maximum temperature of 28ºC in the concrete liner (Martinez et al., 2016). Therefore, the observed alteration was likely due only to water-rock interaction, and not temperature effects. Important observations, reported in Alonso et al. (2017) and Fernandez et al. (2017), include that both the shotcrete plug and bentonite experienced alteration due to groundwater interaction. In the concrete, portlandite dissolution occurred at the host rock-concrete interface and CSH phases in the concrete were altered due to the incorporation of aluminum, sulfur, and magnesium. At the bentonite-concrete interface, the main alteration mineral observed was ettringite ($Ca_6Al_2(SO_4)_3(OH)\cdot 26\ H_2O$), indicating that the

breakdown of sulfur-rich phases in the bentonite, concrete, and/or sulfur sourced from the groundwater resulted in mineral precipitation (Alonso et al., 2017). In the bentonite, alteration was mostly limited to the immediate interface zone, mostly in the form of precipitation Mg-rich phases and the change in exchangeable cations in the bentonite (Fernandez et al., 2017). These results highlight the potential for alteration at the cement-bentonite interface at ambient temperatures in a realistic repository scenario.

1.2.4.2 Modeling

Modelling efforts on cement-bentonite interaction are informed by experimental, thermodynamic, and natural analogue data. Models aim to predict the effect of cement degradation on bentonite physical properties (e.g., swelling capacity, cation exchange, and/or surface area) and clay-mineral stability over time in a repository environment. However, as mentioned above, the complex, non-linear processes involved in cement-interaction may complicate modelling efforts. In general, modeling studies show rapid development of porosity and pH changes in a zone ~1 m from the cement-bentonite interface within 100 years of repository operation (e.g., Steefel & Lichtner, 1994, 1998; Soler, 1998; Savage et al., 2002). For example, simulations at 25 and 70ºC over a 3.2 ka period predict that extensive bentonite dissolution occurs in a ~60 cm zone in the buffer adjacent to the cement boundary (Savage et al., 2002). The model results also show that bentonite dissolution results in CSH-mineral precipitation closest to the cement interface; sheet silicates and zeolites form farther away from the boundary. The precipitation of secondary minerals is the mechanism for the increase in porosity. The results from Savage et al. (2002) also show that the extent of bentonite alteration is highly dependent on the water-rock ratio and transport of high-pH pore fluid through the bentonite. In comparison, models that examine the effects of low-pH cement pore water (i.e., pH < 11) show that bentonite interaction with low pH cement water (at 25ºC) does not result in observable bentonite dissolution (Watson et al., 2007). This study highlights that increased amounts of aqueous silica and aluminum (sourced from the siliceous materials included in the low pH cement) may stabilize clay minerals. Models based on results from bentonite-cement column experiments predict the formation of secondary minerals such as zeolites, hydroxides, phyllosilicates, and CSH minerals in the bentonite in a ~cm-scale zone (Fernandez et al., 2009b). Overall, the modelling studies support experimental observations that cement alteration effects only affect the portion of the bentonite buffer in contact with cement materials. Further, modelling results highlight the importance of pore water pH and secondary mineral precipitation in understanding the long-term geochemical and mineralogical evolution of the cement-bentonite interface.

1.2.5 Steel Canister-Clay Interface Zone Alteration in an Argillite-Hosted Repository

The findings of our previous investigations on mineral precipitation at the steel-bentonite interface in EBS hydrothermal experiments have been described in Caporuscio et al. (2015; 2017; 2018; 2019) and Cheshire et al. (2018). These studies describe the layered alteration sequence observed on the surface of steel coupons included in Wyoming bentonite-only experiments. In general, an oxide layer forms directly at the surface of steel coupons mixed in with bentonite and wall rock components. The oxide layer is followed by newly crystallized Fe-saponite at the steel-clay interface with Fe being supplied by steel corrosion. Concurrent with Fe-saponite formation, sulfides precipitated from sulfide-bearing fluids, likely from pyrite

dissolution, near the steel interface. The thickness of the Fe-rich phyllosilicate minerals perpendicular to the SS surface ranges from 9 to 44 μm. There was no significant change in the precipitation thicknesses between the three different temperature profiles for 300°C (ramped, cooling and constant).

In general, the metal waste canister overpack (likely carbon steel) in a shale (argillite) hosted repository will be expected to corrode over time (e.g., Bryan et al., 2011). The steel will corrode at the bentonite buffer interface in the presence of oxygen according to one of the following reactions (aerobic corrosion) (Kursten at al., 2004):

$$4\ Fe^{o} + 3\ O_2 \rightarrow 2\ Fe_2O_3 \quad (2)$$

$$2\ Fe + 2\ H_2O + O_2 \rightarrow 2\ Fe(OH)_2 \quad (3)$$

The corrosive reaction (3) can be fairly fast for carbon steel, whereas corrosion can be slowed for stainless steels by an oxide film (i.e., Fe-oxide). In the presence of oxygen, the ferrous hydroxide in the second reaction can corrode further (Kursten et al., 2004):

$$4\ Fe(OH)_2 + 2\ H_2O + O_2 \rightarrow 4\ Fe(OH)_3 \quad (4)$$

$$4\ Fe^{o} + 6\ H_2O + 3\ O_2 \rightarrow 4\ Fe(OH)_3 \quad (5)$$

If magnetite is formed by the corrosion potential exceeding equilibrium (2), a resistant oxide film will precipitate on the metal surface. The oxide film will act as a protective coating against further corrosion in the effect called passivation. In an alkali solution where a porous $Fe(OH)_2$ develops, a passive layer may not form, but $Fe(OH)_2$ may still decrease the corrosion rate (5) (Kursten et al., 2004). Therefore, stainless steel and carbon steel are protected against corrosion by the presence of a thin “passive” layer in environments with cement that are highly alkaline conditions. The stainless steel is covered by a corrosion-resistant film of chromium oxy-hydroxide, whereas carbon steel forms a less resilient film composed of a mixture of Fe(II) and Fe(III) oxy-hydroxides (4 & 5) (Kursten et al., 2004).

Nevertheless, these oxide passive films can break down at lower pHs and/or by reactions with aggressive species, e.g., chlorides (Kursten et al., 2004). The passive film overlaying carbon steel can more easily be broken down by chloride corrosion than on stainless steel. Carbon steel, therefore, tends to suffer for general/uniform corrosion, whereas stainless steel tends to be highly localized (i.e. pitting corrosion, stress corrosion) (Smart, 2011).

Previous study by Smailos et al. (1997) and subsequently Kursten et al. (1996; 1997) examined the effect of the solid clay phase on the formation of the corrosion layers (16°C (baseline) increasing to 170°C, five years). The corrosion layer on the unheated carbon steel average about 10 to 20 μm thick. Both experiments had a precipitation thickness on average 30 to 50 μm thick in total. The experiment at 16°C had the multi-layered precipitation, but this layering was less obvious at 170°C. The precipitation could be subdivided into 3 sub-layers with the middle layer having a higher Fe/O ratio than the other two layers. A possible explanation for the middle layer having a higher Fe/O ratio was that the initial passive layer had cracked and further corrosion had occurred.

Other research by Schlegal et al. (2008) studied the interaction of ferrite iron and argillite (approximate mineralogy: 30 wt.% quartz, 30 wt.% calcite, 35 wt.% interstratified illite–smectite, traces of pyrite and feldspars) interface reacted in saturated condition at 90°C and 50

bars for 8 months. Their results show the presence of a corrosion layer (magnetite, Fe-phyllosilicate), an external sublayer enriched in sodium followed by a clay transformation layer (mainly Ca-rich siderite). The clay layer was depleted in Al and K, signifying the dissolution of rock-forming minerals. There was a transitional layer of irregular thickness (~100 μm) present between the new precipitation layer and unaltered argillite made up of small crystals containing argillite markers, such as quartz and clay minerals.

1.2.6 Steel Corrosion in a Cement Environment

The cement buffer in an EBS can provide a favorable geochemical environment (high pH), in which corrosion of the carbon steel overpack will be limited. In the high alkaline condition created by the cement, both stainless and carbon steel should also be protected against corrosion in the presence of a thin "passive" layer similar to as discussed above (Kursten et al., 2004; Smart, 2011). For low carbon steel with cement in anoxic solutions the corrosion rate increased with decreasing pH. The corrosion rates were about 5 to 15 times higher, at pH 7 and 4 respectively, than at a solution pH of 13 (Kursten et al., 2004). A common layer at the steel-cement interface is "laitance," a weak, easily-crumbled layer consisting of cement and fine aggregates. This laitance can act as a controlling factor for the rate of corrosion of steel in cement and has exhibited the ability to limit diffusion of chloride species (Smart et al., 1999). In cases where calcium hydroxides precipitation, they can reduce pitting corrosion by hindering the ability of chloride ions. The calcium hydroxides can provide hydroxides to counter local acidification caused by corrosion product hydrolysis (Smart et al., 1999).

1.2.7 Designer EBS Additives

The main function of the EBS is to enhance the radionuclide retention and geotechnical aspects of the repository system. As described above, bentonite has favorable properties for the overall safety function of the repository in terms of hydrologic transport processes and radionuclide sorption. Other materials have been proposed to enhance the overall radionuclide sorption capacity, including adding phosphates as a radionuclide "getter". Phosphate minerals are known to incorporate radionuclides into their crystal structure and can efficiently immobilize uranium and its mobile fission products through uptake from an aqueous solution by formation of U-rich phosphate minerals.

1.2.7.1 Apatite Stability

Apatite ($Ca_5(PO_4)_3(F,Cl,OH)$) is the tenth most abundant mineral on earth and is uncommonly versatile (Rigali et al., 2016). The ubiquitous nature of the apatite mineral group dictates an extremely large stability field, from accessory phases in garnet lherzolites (Konzett et al., 2012) at its upper P,T limit, to being an integral component of human teeth (Larsen & Jenson, 1989). In human dental enamel, apatite is stable from neutral to high pH. At low pH (<4) apatite converts to brushite (Larsen & Jenson, 1989). The durable nature of apatite is demonstrated by the observation of detrital apatite grains in Precambrian sandstones and gneisses.

In planned nuclear repositories, apatite could be used in permeable reactive barriers to isolate radionuclides in groundwater. The phosphorus produced from dissolving apatite could remove radionuclides, particularly cationic radionuclides including Sr, U, Pu, and Np, from solution by forming insoluble radionuclide-containing solids through incorporation into the apatite via substitution (Moore et al., 2002; Rigali et al., 2016). The surface of apatite may also exchange

anionic radionuclides for surface phosphates/hydroxyl groups (Moore et al., 2002). A radionuclide "getter" safety case study on the Yucca Mountain Project (YMP) in 2006 by Lukens et al. (2006) focused on the radioisotopes I-127, Tc-99 and Np-237, and U-238 primarily due to their high mobility in a Yucca Mountain scenario (oxidizing, unsaturated, depth to groundwater). Apatite was identified in this study as a material that could preferentially sorb I, Tc and Np. Further, Lukens et al. (2006) identified apatite's potential for high attraction of actinides, and recognized apatite as an inexpensive and readily available mineral. Apatite, however, was identified as slightly soluble, and likely not sufficiently durable if placed in the invert placed below the canister but could be utilized elsewhere in the design.

Radiation effects on apatite are also important to consider in EBS applications. Meldrum et al. (1997) irradiated single crystals of natural F-rich apatite and ion-beam amorphized apatite to determine phase transition/structural change. Irradiation of amorphized apatite using a high current density (16 A/cm^2) caused the precipitation of cubic CaO from the crystalline apatite matrix. The lower beam current (1.6 A/cm^2) resulted in nanometer-sized voids and CaO did not crystallize even after prolonged irradiation. The natural apatite underwent extensive void formation followed by the precipitation of cubic CaO under a 200 keV electron irradiation (Cameron et al. 1992).

Apatite has a strong tendency to crystallize under electron irradiation (Meldrum et al., 1997). The crystallization products depend on the dose rate and on the ambient temperature. These results suggest that beta-decay in natural or nuclear-waste loaded apatite has the potential to inhibit amorphization, contrary to the traditional understanding that beta decay may weakly enhance the damage-accumulation process.

Few previous experiments have been performed to evaluate the stability of apatites in hydrothermal conditions. Betkowski et al. (2016) performed experiments on fluoroapatites in Na- and Si-rich fluids to evaluate the mineral reactions. In the experiments performed at 300 and 400°C (100 MPa), the observed little reactivity or dissolution of the fluoroapatite. However, at 600°C, the fluorapatite was more reactive and partially altered into its pseudomorph, britholite.

The experimental results from the current study will be used to quantify apatite stability in the EBS, including possible phase transformations at high temperature repository conditions. The results would then help inform radionuclide-speciation in phosphate solution experiments in our partner radionuclide hydrothermal lab at LANL. For example, experiments would be conducted with apatite and relevant aqueous radionuclide species at 300ºC and 150 bar (i.e., maximum temperatures expected in the disposal of dual purpose canisters) in order to understand the potential for apatite to form radionuclide-bearing phases and/or how much sorption potential phosphate minerals may provide under relevant repository chemical, temperature, and pressure conditions. Experiments with apatite and U would address the formation of autunite (U-bearing phosphate) as an example of a phosphate mineral by-product that may enhance the radionuclide-retention potential of the EBS. Further, phosphate-based minerals may also incorporate other elements that are of particular concern for repository performance such as radiocesium, radiostrontium, and trivalent americium and curium (Krejzler et al., 2003).

2 Methods

Experiments EBS-23 through EBS-31, with the exception of EBS-29, were designed to explore the effect of ordinary Portland cement (OPC) on bentonite stability in the argillite system. The starting components and experiment parameters are reported in Table 1. The starting solid materials were mixed at 60 wt.% Wyoming bentonite (powder and granules), 20 wt.% Opalinus Clay (powder and fragments), and 20 wt.% uncured OPC powder or cured OPC chip. Experiment variations included: water:rock ratio (11 to 13 and 6.8 for the 6-month experiment), temperature (200 or 300ºC), duration (eight weeks or 6 months), and inclusion of different types of stainless steel (316SS, 304SS and LCS).

An experimental program on the effect of phosphate additives to the bentonite EBS was initiated in FY20. Experiment EBS-29 (250ºC, eight weeks) was completed in FY20 and characterized in FY21. EBS-29 included 80 wt.% Wyoming bentonite, 20 wt.% apatite from Durango, Mexico (referred to as Durango apatite), and Stripa V2.3 brine at a water-rock ratio of 7:1. Three sealed gold capsules that included only apatite crystals and brine at a water rock ratio of 11:1 were included at the bottom of the titanium vessel (Table 2).

In all experiments, fluid chemistry was monitored in aqueous samples extracted during and after the experiment. Solid phase reaction products were evaluated with X-ray diffraction (bulk and clay mineralogy), scanning electron and petrologic microscopy (mineralogy and textural observations), and electron microprobe and electron dispersive spectroscopy (mineral phase chemistry). Solid and aqueous phase characterization methods are reported in Appendix A.

Table 1. Initial components and reaction conditions for EBS experiments in the presence of Opalinus Clay. Experiments completed in FY21 are highlighted in green. Abbreviations: WB, Wyoming bentonite; OPC, ordinary Portland cement; OC, Opalinus Clay; SS, stainless steel; LCS, low carbon steel.

Exp.	Components	Temp (°C)	Run time	Synthetic GW (g)	Opalinus Clay (g)	WY bentonite (g)	Portland cement (g)	Durango apatite (g)	steel type	EBS metal (g)	Fe° (g)	Fe_3O_4 (g)	Deviations	Water:Rock
EBS-23	OC + WB + OPC Powder	200	8 weeks	150	2.0	5.9	2.1	-	-	-	0.57	0.48	-	13.6
EBS-24	OC + WB + OPC Powder + 316 SS	200	8 weeks	150	2.0	6.0	2.0	-	316 SS	4.52	0.52	0.51	-	13.6
EBS-25	OC + WB + OPC Powder + 304 SS	200	8 weeks	126	2.0	6.0	2.0	-	304 SS	3.27	0.55	0.51	-	11.4
EBS-26	OC + WB + OPC Powder + LCS	200	8 weeks	130	2.0	6.0	2.0	-	LCS	5.02	0.5	0.5	-	11.8
EBS-27	OC + WB + OPC Powder +316 SS	200	6 months	270	7.6	22.8	7.6	-	316 SS	5.06	0.95	0.95	-	6.8
EBS-28	OC + WB + OPC Powder + 316 SS	300	8 weeks	138	2.2	6.6	2.2	-	316 SS	5.06	0.50	0.50	-	11.7
EBS-29	WB + Durango apatite	250	8 weeks	156	-	17.8	-	4.5	-	-	0.63	0.63	Apatite + Stripa V2.3	7.0
EBS-30	OC + WB + Cured OPC chip + 316 SS	200	8 weeks	104	2.1	6.4	2.1	-	316 SS	5.1	0.5	0.5	-	11.7
EBS-31	OC + WB + Cured OPC chip + 316 SS	200	8 weeks	131	2.0	6.1	2.1	-	304 SS	4.7	0.5	0.5	-	11.6

Table 2. Initial components and reaction conditions for the capsules included in the EBS-29 with Durango apatite.

Capsule ID	Temp (°C)	Run Time	Stripa V2.3 Synthetic GW (g)	Durango apatite (g)	Fe° (g)	Fe_3O_4 (g)	Water:Rock
C1	250	8 weeks	1.10	0.104	0.003	0.003	11:1
C2	250	8 weeks	1.11	0.103	0.003	0.003	11:1
C3	250	8 weeks	1.11	0.100	0.003	0.003	11:1

3 Results

3.1 Starting Material Characteristics

Opalinus Clay. Opalinus Clay used in this study was sourced from the Mont Terri Underground Rock Laboratory in Canton Jura, northern Switzerland. The rock used was from the shaley facies of Opalinus Clay at Mont Terri (drill core BFE-A10) and was exposed to air (i.e. oxidizing conditions) before the experiment. Opalinus Clay is thinly laminated, dark grey shale with a dry density of 2.2 to 2.4 g/cm^3 and water content of 6.5 to 8.0% (Pearson et al., 2003). Opalinus Clay is dominantly composed of clay minerals, with lesser carbonates and silicates. The Opalinus Clay used in our experiments is composed of mixed illite, smectite, and illite-smectite (24%), kaolinite (17%), calcite (16%), chlorite (9%), mica (7%), K-feldspar (6%), and plagioclase (3%), with minor dolomite and pyrite, as determined by QXRD analyses. In the QXRD datasets, illite and smectite are typically reported together due to the difficulty of quantifying these mineral phases when they are mixed. Na^+ is the dominant exchangeable cation in the Opalinus Clay followed by Ca^{2+}, Mg^{2+}, K^+, and Sr^{2+}; however, the bulk composition is dominated with CaO (7.96 wt.%), K_2O (3.05 wt.%), MgO (2.38 wt.%), and Na_2O (0.48 wt.%) (Pearson et al., 2003). These exchangeable cations should be in equilibrium with the pore water described below (synthetic Opalinus Clay groundwater, Table 2). Other minerals present include calcite, ankerite, dolomite, quartz, and biotite. Well-preserved pyrite occurs primarily as < 2 μm octahedral crystals, filling fractures and/or along bedding planes. Calcite primarily occurs as pocket filling agglomerates showing layered structures with alternating calcite and clay layers (Figure 3).

Wyoming bentonite. The bentonite used in the present study is unprocessed and was provided by Bentonite Performance Minerals LLC from Colony, Wyoming, U.S.A. It is composed dominantly of Na-montmorillonite (general composition: $Na_{0.33}(Al,Mg)_2(Si_4O_{10})(OH)_2 \cdot nH_2O$), lesser clinoptilolite and feldspar, and minor biotite, pyrite, quartz, opal, and sulfide minerals.

Opalinus Clay synthetic groundwater. Synthetic groundwater was created to mimic the pore water found in the Mont Terri Opalinus Clay (Pearson et al., 2003). This solution has a pH of around 7.5 and is a Na-Cl type solution. The initial chemistry is reported in Table 3.

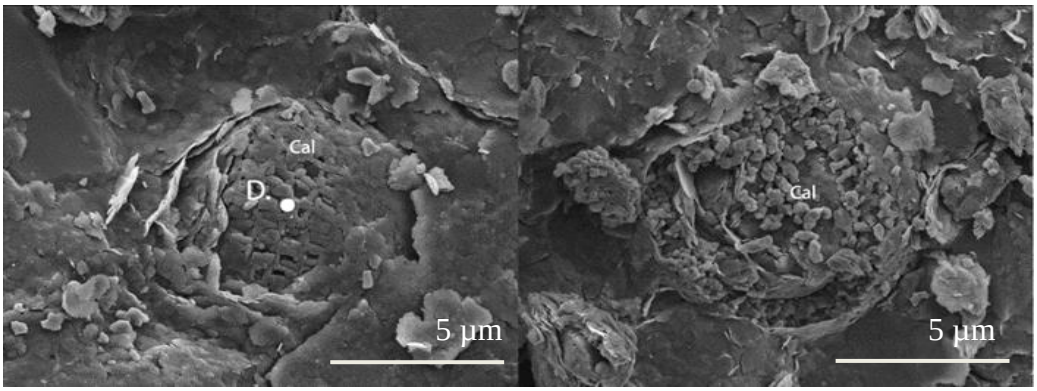

Figure 3. SEM images of unheated Opalinus Clay. [Left Panel] Biogenic calcite (Cal) filling a pocket with in the Opalinus Clay matrix. [Right Panel] Disturbed pocket-filling calcite showing layered structure with alternating calcite and clay layers.

Stripa V2.3 synthetic groundwater. The synthetic solution composition was chosen to represent that of a deep groundwater in granitic rock (Stripa sample V2) (Frape et al., 2003). This is a Na-Ca-Cl type solution of high pH (8–10). The initial chemistry is reported in Table 3.

Table 3: Brine compositions for synthetic Opalinus Clay solution modelled after data reported from the Mont Terri site (Pearson et al., 2002) used in the Opalinus Clay experiments and the composition of the Stripa synthetic solution used in the apatite experiment (after Frape et al., 2003). The Los Alamos Municipal tap water was used in the curing of the ordinary Portland cement. All values were measured at 25°C (n.m. = not measured).

	Opalinus Clay	**Stripa V2.3**	**Los Alamos Tap Water**
Species	mg/L	mg/L	mg/L
Ca^{2+}	426	670	9.62
Cl^{-}	6470	n.m.	24.7
CO_3^{2-}	n.m.	291	n.m.
K^{+}	225	163	2.04
Na^{+}	3846	1	12.8
Si	1	64	35.4
SO_4^{2-}	998	0.09	6.93
Sr^{2+}	0.16	7.1	0.0445
TDS	12153	46	n.m.
pH	7.50	6.70	6.61
Experiment Used	EBS-14 to -28, -30 to -31	EBS-29	Cured Cement in EBS-30 to -31

316SS. (NIST SRM 160b) is an iron alloy primarily with 18.37 wt.% Cr, 12.35 wt.% Ni, 2.26 wt.% Mo, 1.619 wt.% Mn, 0.5093 wt.% Si, and 0.175 wt.% Cu.

304SS. An ion alloy which differs from 316SS in Cr/Ni ratio. Along with Fe, it contains 18 wt.% Cr, 8 wt.% Ni, < 2 wt.% Mn, < 1 wt.% Si, < 0.045 wt.% P, and < 0.03 wt.% S, and < 0.08 wt.% C.

Low carbon steel (LCS). Composed of Fe along with ~0.2 wt.% C, 0.9 wt.% Mn, < 0.04 wt.% P, and < 0.05 wt.% S.

Ordinary Portland cement (OPC). Ordinary Portland cement (OPC) consists of ~77% of calcium silicates, (3 $CaO{\cdot}SiO_2$, and 2 $CaO{\cdot}SiO_2$), the remainder consisting of aluminum- and iron-containing silicate phases and other compounds. The ratio of CaO to SiO_2 is ~3.2. The magnesium oxide content (MgO) is ~2.6 wt.%. The mineralogy consisted of larnite, hatrurite, and brownmillerite. Uncured, powdered OPC was used in the experiments EBS-23 through EBS-28. Cured OPC cement chips were included in EBS-30 and -31 experiments. Cement curing began in November of 2018 using Los Alamos Municipal tap water (Table 3). Mineralogy of the cured OPC differed from the uncured powder with the formation of portlandite. The CaO to SiO_2 ratio increased to ~3.6 and the magnesium wt.% was unchanged.

Durango apatite. The apatite used in this study is from the Cerro de Mercado mine in Durango, Mexico, which is an open-pit iron mine known for the occurrence of abundant coarse-grained fluoroapatite ($Ca_5(PO_4)_3F$). The apatite crystals are readily available and have a consistent chemical composition; Durango apatite is commonly used as a standard material for isotope and trace element analyses (e.g., Chew et al., 2016).

3.2 Aqueous Geochemistry (EBS-23 to EBS-28)

pH. All experiments began with a near neutral pH at 25ºC of ~7.4. Of the 200ºC cement experiments, the pH of reaction fluids measured at 25ºC of EBS-23 and EBS-25 initially dropped to ~5 to 6, whereas EBS-24 and EBS-26 initially increased to ~11. The first measured pH value from EBS-27 was around 9, before stabilizing around 8.5 for the duration of the 6-month experiment. Although the 200ºC cement experiments diverged in pH initially, all experiments stabilized to pH values from ~8 to 9 around 3 weeks into the experiment duration and remained around the same values for the rest of the experiment (Figure 4). In comparison, pH values from EBS-28 (300ºC) initially rose from 7.5 to 9.5 in the first week of the experiment before stabilizing to values of around 6 for the duration of the 6-week experiment. In EBS-30 and EBS-31, which included a cured cement chip, pH values dropped to ~6 within the first two weeks of experiment time before gradually increasing to values between 6 and 7 by the end of the experiment.

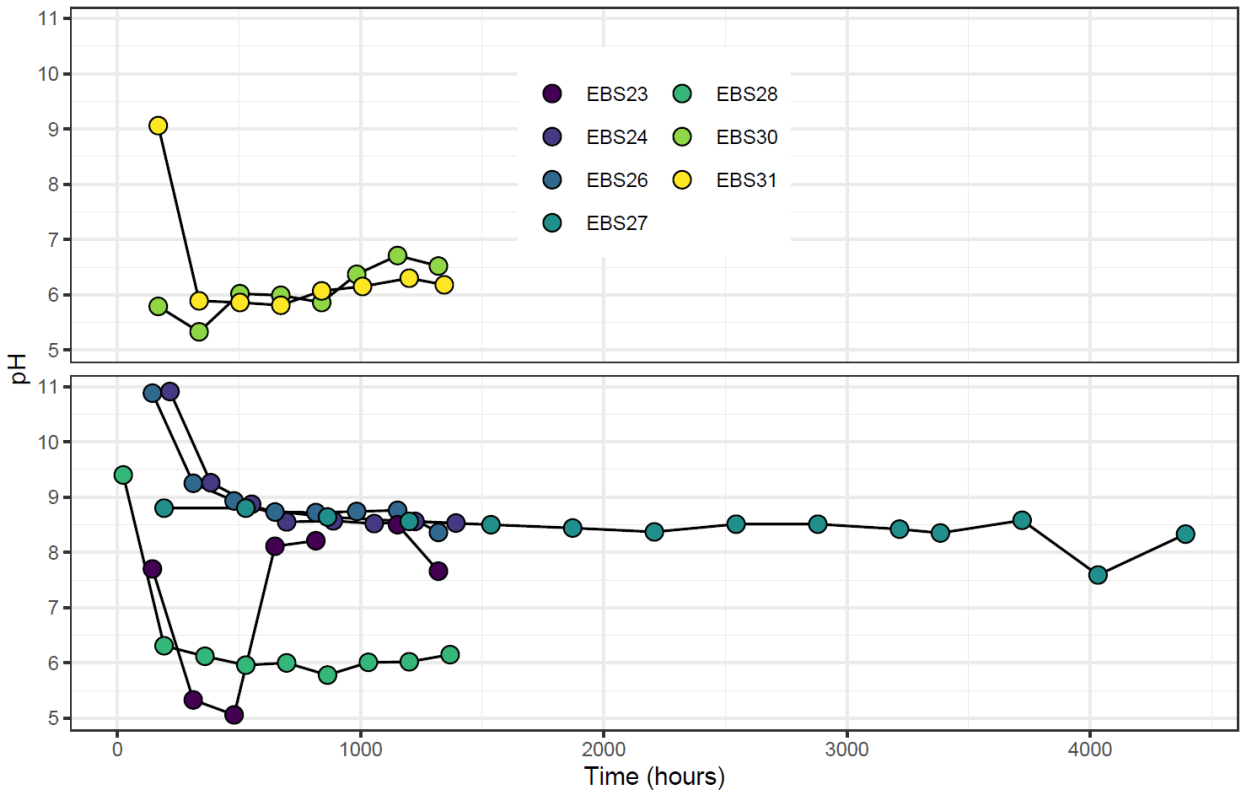

Figure 4. pH (measured at 25ºC) throughout each cement EBS experiment.

Silica. In all experiments, aqueous silica generally increases during each experiment (Figure 5). Aqueous silica increases rapidly until 1000 hours in EBS-25, and plateaus ~180 mg/L by 1200 hours into the experiment. The other three 200ºC/8 week experiments reach ~100 to 130 mg/L by 1200 hours. In comparison, EBS-27 (six months) shows significant variability in silica concentrations throughout the experiment duration; values vary between ~100 and 200 mg/L. In the 300ºC experiment, silica increases to 500 mg/L in the first 6 weeks, before slightly plateauing. In EBS-30 and EBS-31, silica reaches concentrations of ~300 mg/L by the end of the experiments.

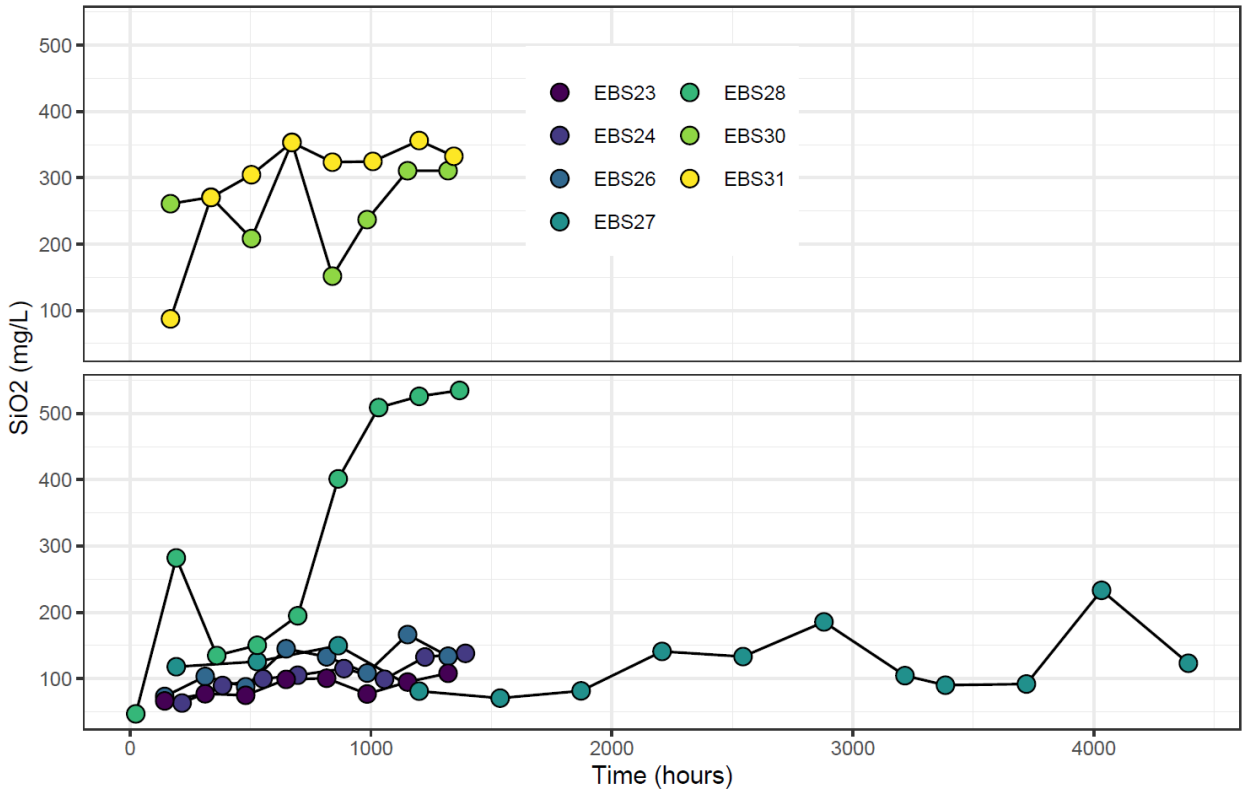

Figure 5. SiO2(aq) concentration (mg/L) throughout each cement EBS experiment.

Aluminum and Magnesium. Aqueous aluminum remains constant, near detection-limit values, or steadily decreases throughout each experiment. All values end below detection limits (< 0.032 mg/L). In experiments with cement powder, $Mg^{2+}{}_{(aq)}$ remains generally constant and below 0.15 mg/L throughout each experiment. In the experiments with the cured cement chip, Mg^{2+} values are initially elevated around 30 mg/L before reaching < 1 mg/L by the end of the experiments.

K^+, Na^+, Ca^{2+}. Sodium and potassium follow a decreasing trend throughout each 200ºC cement powder experiment (Figure 6). Calcium either remains constant (EBS-23 and EBS-24) or gradually increases (EBS-25 and EBS-26). [Ca^{2+}] continues to increase throughout the whole 6-month duration of EBS-27. The concentrations of these cations in aqueous solutions of EBS-23 and EBS-24 versus EBS-25 and EBS-26 differ by about 50% during the experiment. The starting solution for these four experiments had very similar concentrations of these cations; however, the water:rock ratio differed between these experiments. EBS-23 and EBS-24 had a higher water:rock ratio (~13.6) versus the ratio in EBS-25 and EBS-26 (~11.5). The 300ºC experiment (EBS-28) has a much higher [K^+] that initially rose during the first three weeks before beginning to decrease for the remainder of the experiment. Calcium concentrations are similar in magnitude to observations from the 200ºC experiments but follow a different trend: values increase initially and then drop in a similar manner to the potassium values. Sodium values in EBS-28 are initially elevated but sharply decrease during the experiment.

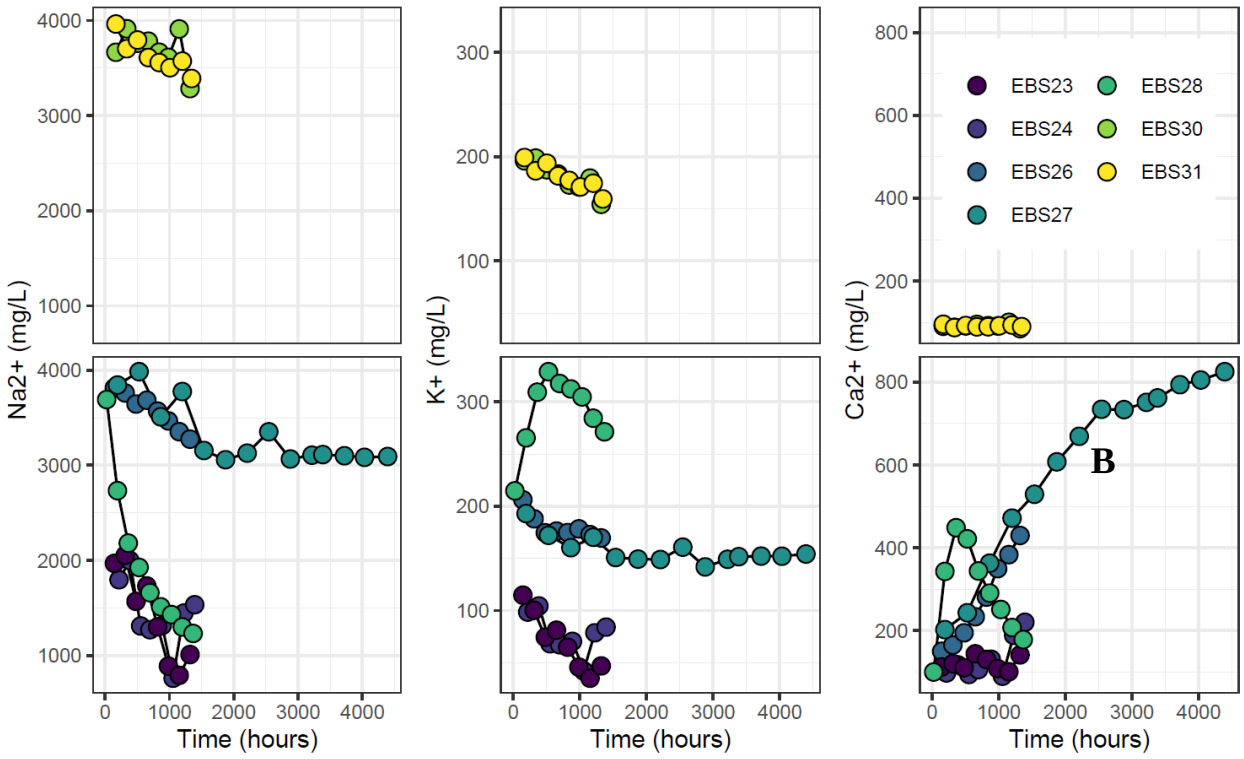

Figure 6. Sodium, potassium, and calcium concentrations in the cement EBS experiments.

In the cement chip experiments, EBS-30 and EBS-31, sodium and potassium concentrations follow a decreasing trend. Calcium concentrations are constant around 150 mg/L throughout both experiments.

Chloride. Chloride concentrations cover a wide range of values (2500 to 10000 mg/L) in the EBS cement powder experiments (Figure 7). [Cl^-] generally decreases gradually in 200ºC experiments and decreases more rapidly at 300ºC (EBS-28). In the experiments with the cement chip (EBS-30 and EBS-31), chloride values generally decrease and reach 5000 mg/L by the end of the experiment.

Sulfate. Sulfate generally decreases in all experiments, for at least the first 3000 hours of elapsed time (Figure 7). An increase from ~50 mg/L to ~125 mg/L is observed around 3000 hours in the 6-month experiments, followed by a return to decreasing concentrations. Sulfate concentrations are lower magnitude in the 300ºC experiment ([SO_4^{2-}] = ~10 mg/L at 1000 hours) compared to the 200ºC runs ([SO_4^{2-}] = ~50–80 mg/L at 1000 hours). In the cement chip experiments, sulfate generally remains around 250 mg/L.

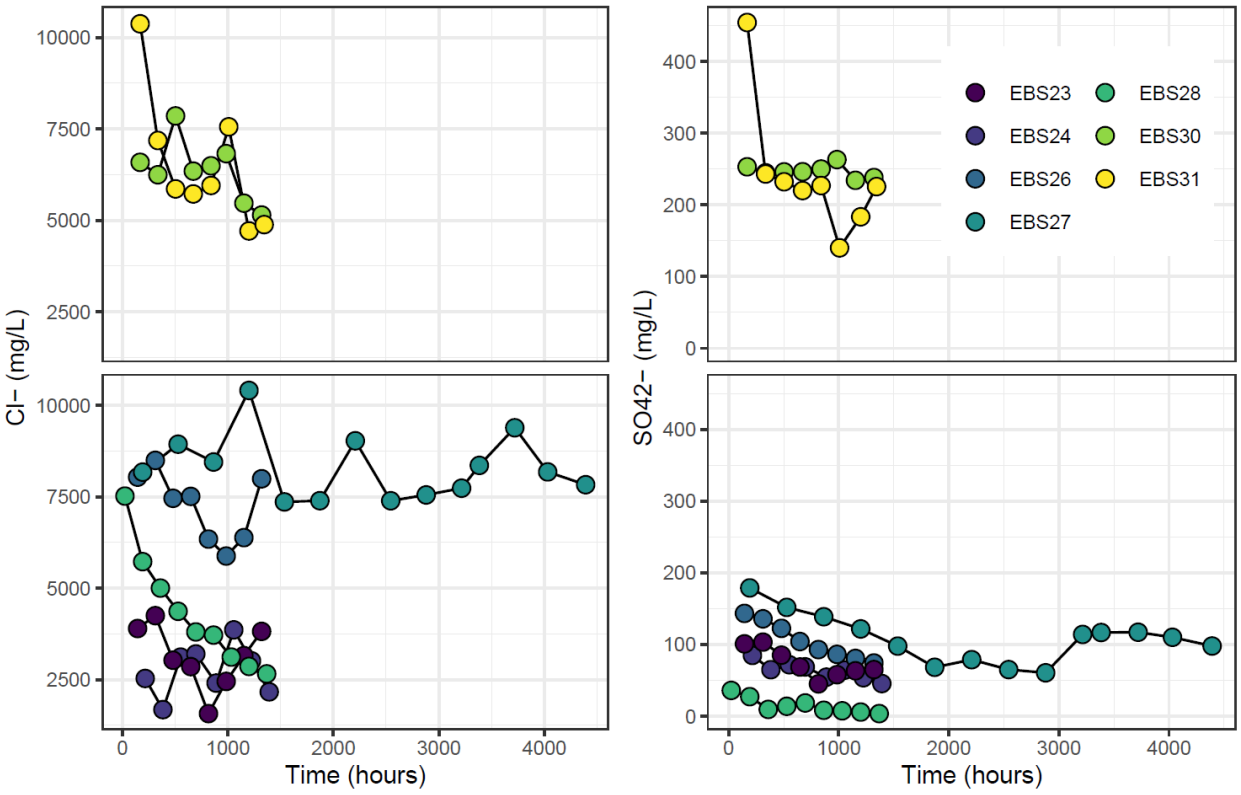

Figure 7. Concentrations of chloride and sulfate ions in solution in the cement EBS experiments.

3.3 XRF Results

XRF analyses for bulk rock oxide chemistry were performed on the unreacted starting material and the bulk reaction products. In the 200ºC experiments with uncured OPC powder, the bulk chemistry of the reaction products generally matched the composition of the starting mix. In the 6-month Wyoming bentonite + Opalinus Clay + powered OPC experiment (EBS-27), the solid reaction products were stratified at the end of the experiment. Samples were divided based on their depth in the reaction cell. EBS-27-1 was taken from the top layer inside the reaction cell contained a higher concentration of CaO and Fe_2O_3 (16.4 wt.% versus 11.6 wt.% and 8.4 wt.% versus 7.5 wt.%, respectively) in comparison to EBS-27-4, which was taken from near the bottom of the reaction cell. EBS-27-4 had increased wt% of SiO_2 and Al_2O_3 compared to EBS-27-1 (49.5 wt.% versus 41.5 wt.% and 15.4 wt.% versus 13.7 wt.%, respectively). In the 300ºC experiment with uncured OPC powder (EBS-28), Fe_2O_3 was elevated in the reaction products in comparison to the starting mix.

The Wyoming bentonite + Opalinus Clay + cured OPC chip experiments (EBS-30 and -31) only differed in the stainless steel type used and measured weight percent oxide values were consistent between the two experiments. There were only slight variations in Fe_2O_3 and loss on ignition (LOI). In comparison to the starting mixture chemistry, weight percent CaO decreased.

3.4 QXRD Results

QXRD results from the bulk reaction product mineralogy from the Wyoming bentonite + Opalinus Clay + OPC experiments and the bulk mineralogy of the starting materials, are shown in Figure 8. Results are presented from the 8-week 200ºC experiments (EBS-24, EBS-25, and EBS-26), the 6-month 200ºC experiment (EBS-27), the 300ºC experiment (EBS-28), and the 200ºC experiments with the cured cement chip (EBS-30 and EBS-31). In general, the addition of OPC powder to the starting experiment mixture resulted in significant changes to the bulk mineralogy of the reaction products at 200ºC. For example, in all reaction products from the cement experiments, precursor portlandite is not detected, indicating that it was consumed in mineral-forming reactions. Newly formed mineral phases include analcime, garronite, tobermorite, plagioclase feldspar, zeolites, calcite, illite-smectite mixed layers, illite, and amorphous material. The bulk abundance of smectite, illite-smectite, and illite is reduced. Increasing temperature to 300ºC resulted in different mineralogical changes, including a decrease in zeolites and formation of feldspars, chlorite-smectite mixed layers, and abundant Fe-saponite.

Swapping powder OPC for a cement chip resulted in less alteration to the bentonite at 200ºC (Figure 8). For example, combined smectite + illite + smectite-illite comprised 67 to 78 wt.% of the cement chip experiment versus 16 to 30 wt.% in the experiments containing cement powder. Further, the patterns preliminarily indicate that mixed layer phases are not abundant (i.e., the prominent peak at 6º 2 theta); detailed clay mineral XRD analyses are in progress. In addition, there was a reduction in zeolite and CSH mineral formation and amorphous material with the addition of the cement chip in comparison to cement powder.

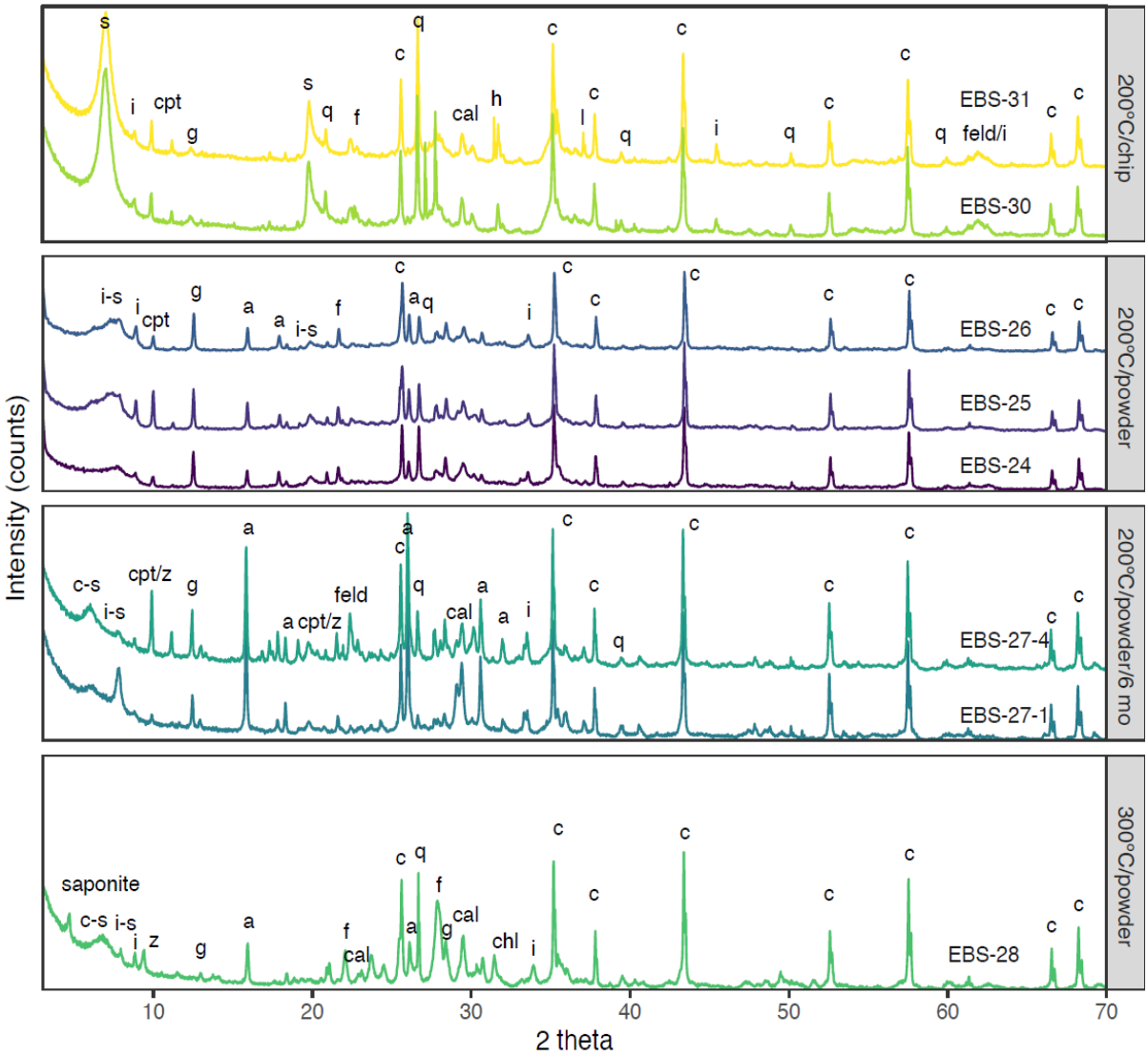

Figure 8. QXRD pattern of the bulk post-reaction products from the cement experiments. Peaks corresponding to corundum (c), smectite (s), illite (i), illite-smectite (I-S), clinoptolite (cpt), calcite (cal), quartz (q), zeolite (z), garronite (g), feldspar (f/feld), analcime (a), chlorite (chl) and chlorite-smectite (c-s).

3.5 Clay Mineral XRD

The addition of OPC to the experimental system affected the clay mineralogy in the reaction products, as observed in the reduction in illite, smectite, and illite-smectite mixed layers mineral abundance in the bulk system in the QXRD results from EBS-24, EBS-25, and EBS-26. XRD analyses of oriented clay fractions from both the Opalinus Clay fragments and the clay groundmass show significant shifts in mineral structure. Shifts of the glycolated smectite (GS) 002 and 003 peaks from the 2 µm fraction from the clay groundmass (mostly reacted bentonite with trace amounts of Opalinus Clay) correspond to ~10% reduction in expandability and ~10 to 20% increase in interlayered illite in the 8 week, 200ºC experiments (EBS-24, EBS-25, and EBS-26) (Table 4). The <2 µm clay fraction separated from EBS-28 (8 weeks, 300ºC) revealed a

similar reduction in expandability to the 200ºC experiments, but also included multiple other phases (e.g., chabazite, other unidentified peaks, Figure 9). The expandability of the remaining montmorillonite in experiment EBS-27 (6 months, 200ºC) was not able to be quantified. Amorphous material was present in the sample, resulting in a broad peak between 18 and 25º2θ, which obscured the position of the d003 glycolated smectite peak. Tobermorite is identified in all the clay fraction results, indicating potential CSH mineral interlayering in smectite.

In Opalinus Clay fragments extracted from the experiments EBS-24, EBS-25, and EBS-26, clay phases include I-S, illite, and chlorite (Figure 10). Tobermorite is detected in EBS-26. There was not enough sample of EBS-23 to analyze the Opalinus Clay fragments. The exact percentage of illite in illite-smectite mixed layers is difficult to quantify, but is likely < 40% illite based on the position of the 001 illite/002 GS-smectite peak (~8.9 Å). Analyses of the clay mineral structure for EBS-30 and EBS-31 are in progress.

Table 4. Glycolated smectite (GS) peak positions for the <2 µm clay fraction separated from the Opalinus Clay–Wyoming bentonite experiments (EBS-23 to -28). Expandability was calculated based on the position of the 002 and 003 GS peaks.

EG-smectite	**001**		**002**		**003**		**002/003**	**1**	**2**	**3**
Sample	**d (Å)**	**2θ**	**d (Å)**	**2θ**	**d (Å)**	**2θ**	**Δ 2θ**	**%Exp**	**%Exp**	**%Exp**
WY Bentonite	17.0	5.2	8.5	10.4	5.7	15.7	5.3	100	102	103
EBS-23	16.4	5.4	8.3	10.7	5.5	16.0	5.4	95	95	97
EBS-24	16.5	5.3	8.3	10.7	5.5	16.1	5.5	90	89	92
EBS-25	16.5	5.4	8.3	10.7	5.5	16.1	5.4	93	92	95
EBS-26	16.5	5.3	8.3	10.7	5.5	16.2	5.4	91	90	93
EBS-27	16.9	5.2	8.4	10.5	–	–	–	–	–	–
EBS-28	16.9	5.2	8.5	10.5	5.6	15.9	5.4	91	90	93

1: %Exp = 973.76 – 323.45Δ + 38.43Δ2 – 1.62Δ3 (Eberl et al., 1993)

2: %Exp = 1517.8 – 548.49Δ + 68.35Δ2 – 2.90Δ3 (Eberl et al., 1993)

3: %Exp = 766.01 – 194.10Δ + 12.924Δ2 (Moore and Reynolds, 1997)

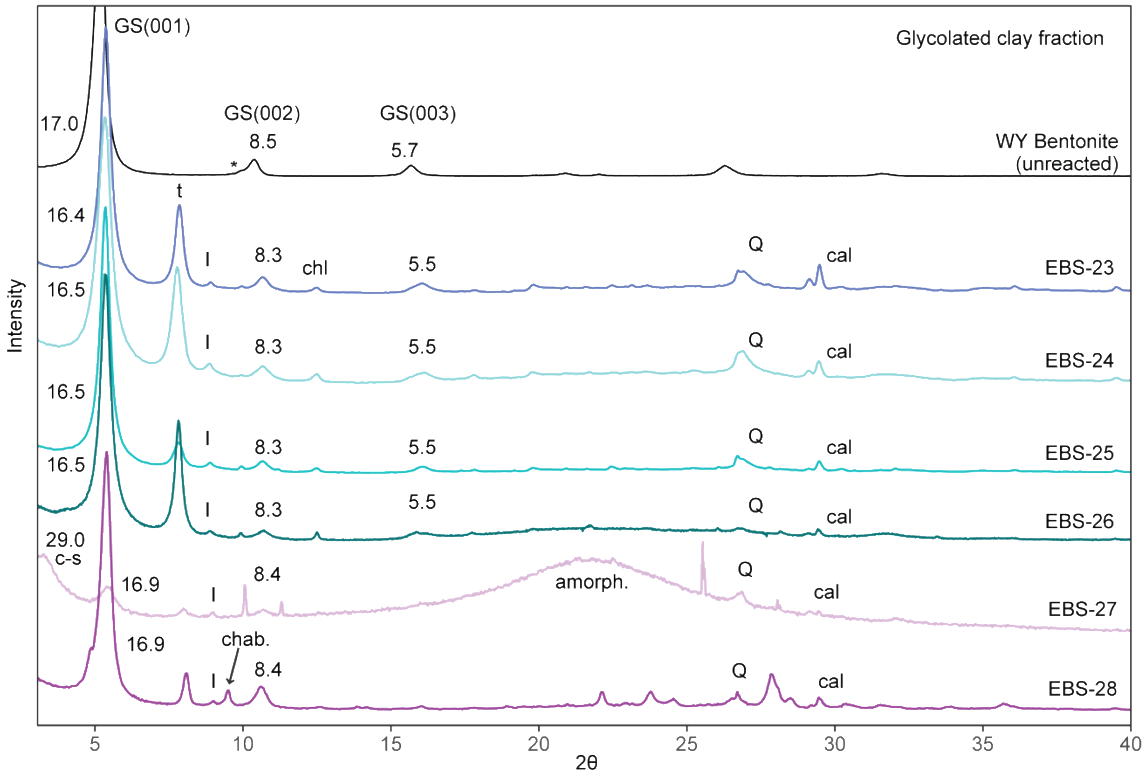

Figure 9. XRD patterns of the oriented and ethylene glycol saturated < 2 µm clay fraction from the clay groundmass of the cement experiments, compared to unheated Wyoming bentonite from the OPC experiments. Peaks correspond to amorphous material (amorph.), illite-smectite (I-S), chabazite (chab.), chlorite (chl), chlorite-smectite (c-s), illite (I), kaolinite (kao), quartz (Q), tobermorite.

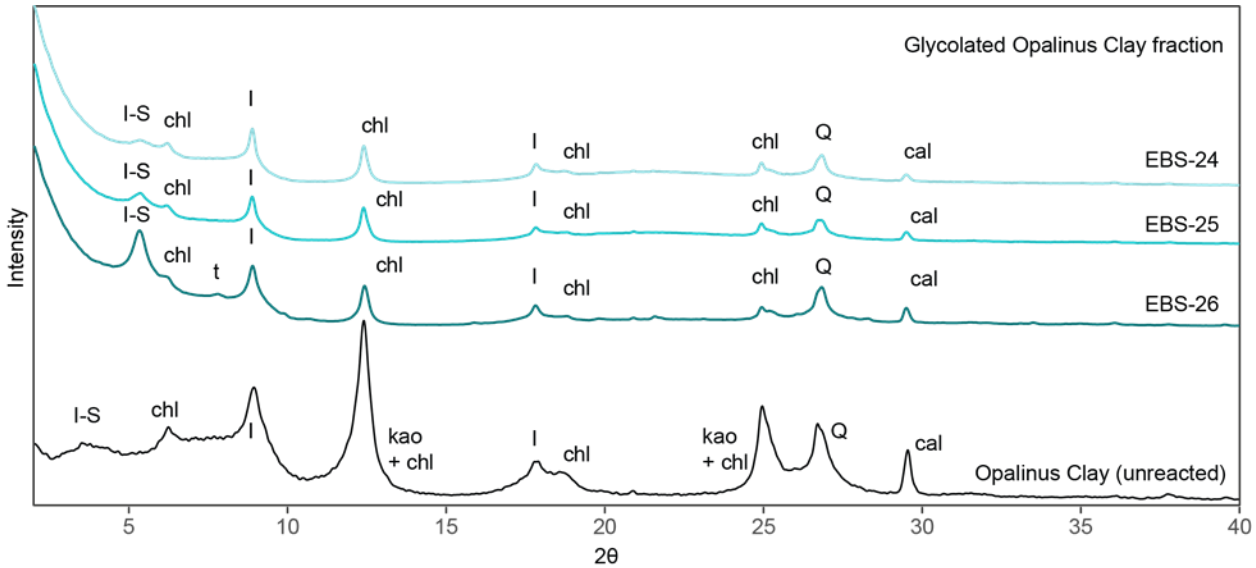

Figure 10. XRD results from the oriented and ethylene glycol saturated clay fraction of Opalinus Clay fragments extracted from each cement experiment and unreacted Opalinus Clay. Peaks correspond to illite-smectite (I-S), chlorite (chl), illite (I), kaolinite (kao), quartz (Q), tobermorite (t) and and calcite (cal) are labelled.

3.6 Cement Chip XRD Analyses

The surface of the unreacted cured cement chip and reacted cement chips from EBS-30 and EBS-31 was analyzed with XRD (Figure 11). The resulting patterns show that mineral reactions occurred at the chip surface. The unreacted chip is characterized by portlandite with calcite and larnite. The reacted chip pattern is dominated by calcite with smectite and CSH minerals.

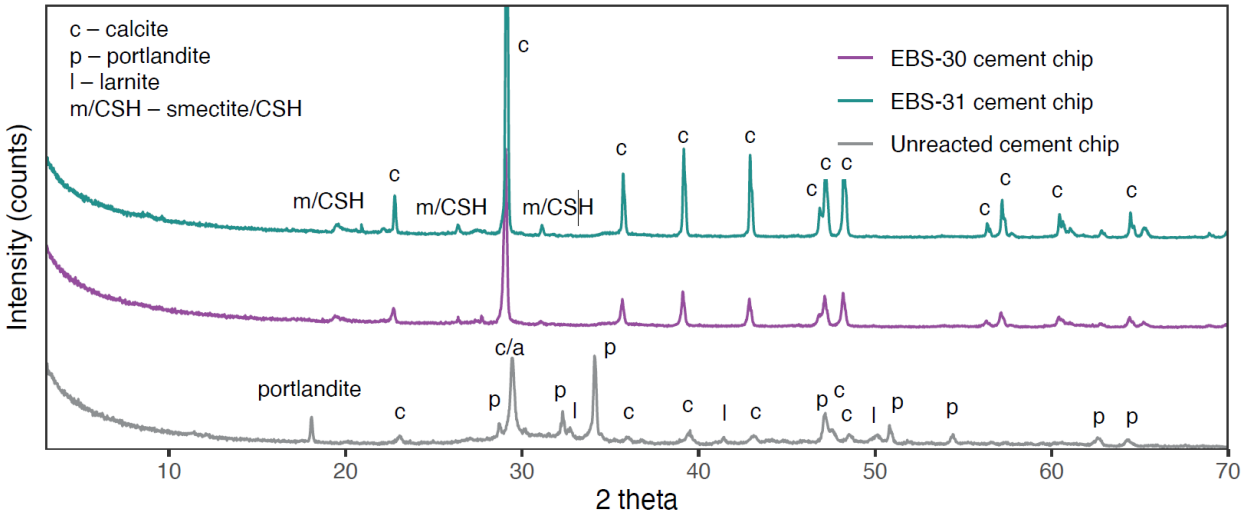

Figure 11. XRD pattern on the unreacted and reacted cement chip from EBS-30 and -31.

3.7 Electron Microprobe Analyses

In experiments that included OPC powder/chips (EBS-23 through EBS-28, EBS-30, EBS-31), abundant analcime and Ca-rich zeolite and aluminosilicate phases (feldspars, garronite, and chabazite) were formed (Figure 12). Major element compositions of these aluminosilicate phases were analyzed via electron microprobe for samples EBS-24, EBS-25, and EBS-26. Analyses for EBS-27, EBS-28, EBS-30, and EBS-31 were collected in July 2021; data reduction is in progress and will be reported in the next fiscal year. In general, garronite was typically found near the Opalinus Clay fragments (Figure 12). Analcime was observed in several contexts: (1) in the fine-grained clay (bentonite) groundmass, (2) rimming grains of Opalinus Clay, and (3) in the porous "cement" matrix (Figure 13), and (4) at the steel-clay/cement interface. The porous cement fraction of the samples is a different color (lighter), texture, and composition compared to the clay matrix. It contains silica, calcium, and likely water, with a similar composition to tobermorite. In experiments that contained steel coupons, analcime and garronite formed directly at the steel interface. The analyses of EBS-23 through EBS-26 reveal a wide range of Si/Al values and/or cation (Na^+, Ca^{2+}) compositions (Figure 14). SEM/EDS analyses of experiments EBS-29 through EBS-31 can be summarized as follows:

EBS-29. The bentonite SEM images from EBS-29 showed montmorillonite with "cornflake" texture with minor apatite, plagioclase, and pyroxene impurities throughout (Appendix B: Figure B-1 A-B). The apatite from the main reaction cell showed a planar texture with minor irregular and stepped texturing (Appendix B: Figure B-2 A-B). Apatite from the apatite-only capsules

showed the same planar and stepped textures with some pitting. Impurities from the Durango apatite were more apparent (Appendix B: Figure B-3 A-B).

EBS-30 SEM images of the clay-bentonite matrix show predominantly smectite with minor calcite and plagioclase phenocrysts (Appendix B: Figure B-5 A-B). The cured cement chip was coated with a CSH gel and calcite with minor smectite (Appendix B: Figure B-4 A-B).

EBS-31. The SEM of the post-reaction bentonite showed smectite and Fe-saponite with interbedded garronite (Appendix B: Figure B-8 A). A spherical mineral of either lime or CSH phase was observed sporadically throughout the sample (Appendix B: Figure B-8 B). Minor amounts of plagioclase phenocrysts are embedded within the smectite. The cement chip included in the experiment has a layer of calcite on the surface (Appendix B: Figure B-7 A-B).

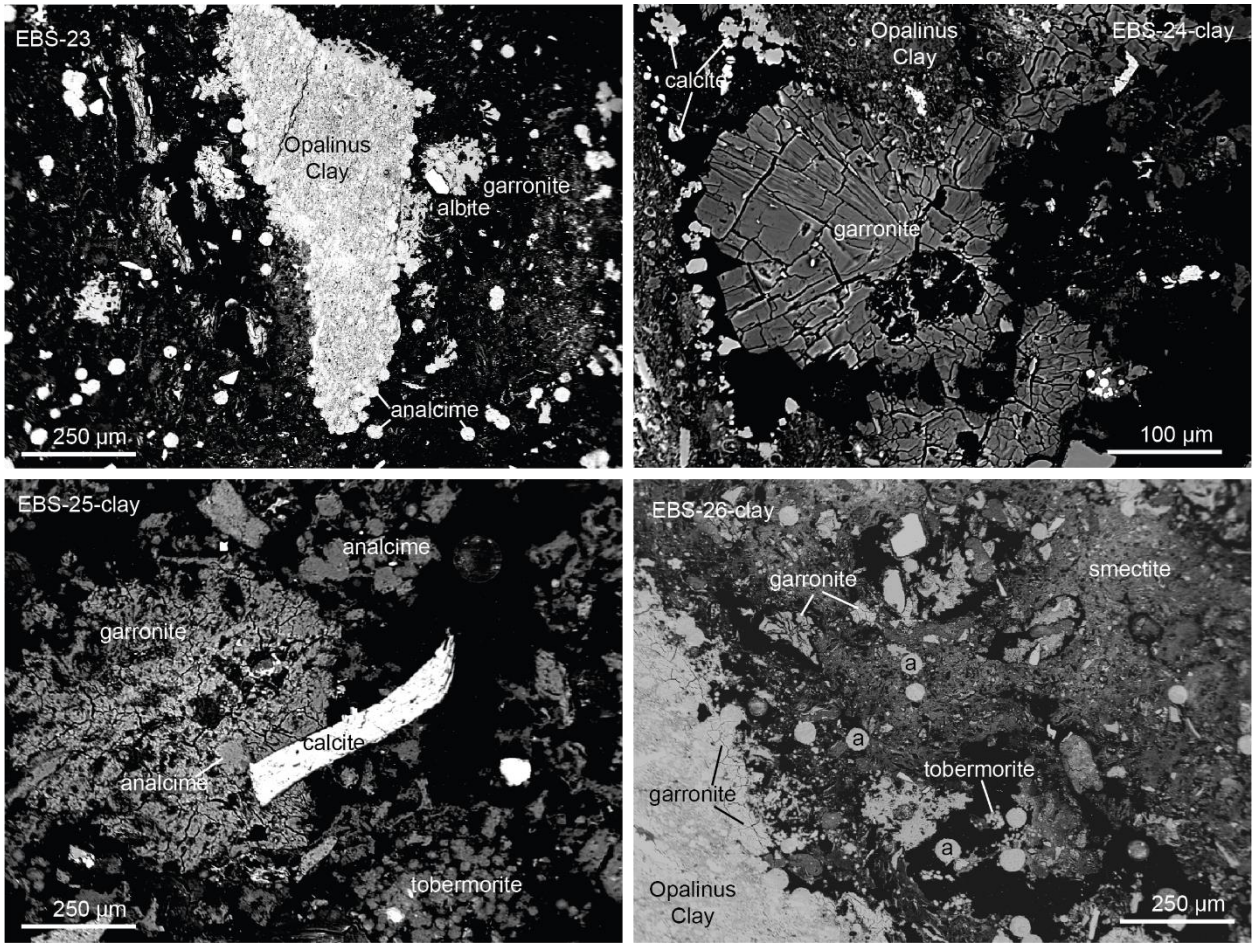

Figure 12. BSE images of thin sections from EBS-23, EBS-24, EBS-25, and EBS-26 showing the petrographic context of authigenic zeolite and CSH minerals (tobermorite). Analcime (a) and garronite crystals form at the interface of the Opalinus Clay fragments and the Wyoming bentonite.

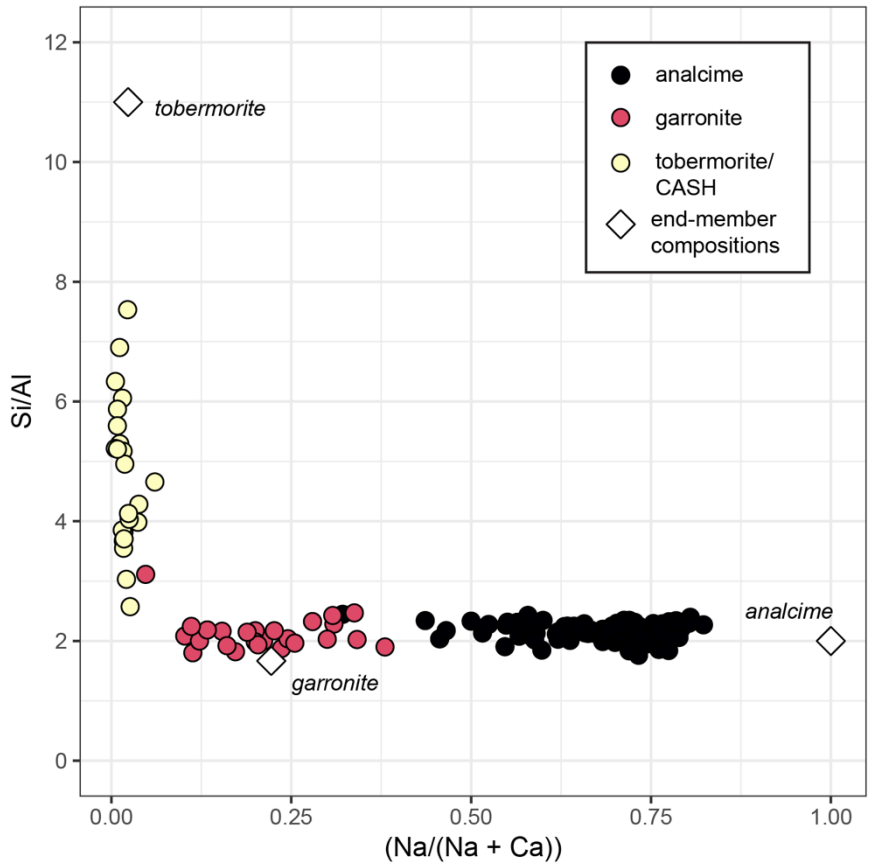

Figure 13. Electron microprobe analyses of zeolite and CSH minerals from EBS-23 through EBS-26. Each point represents a single analysis from the sample set.

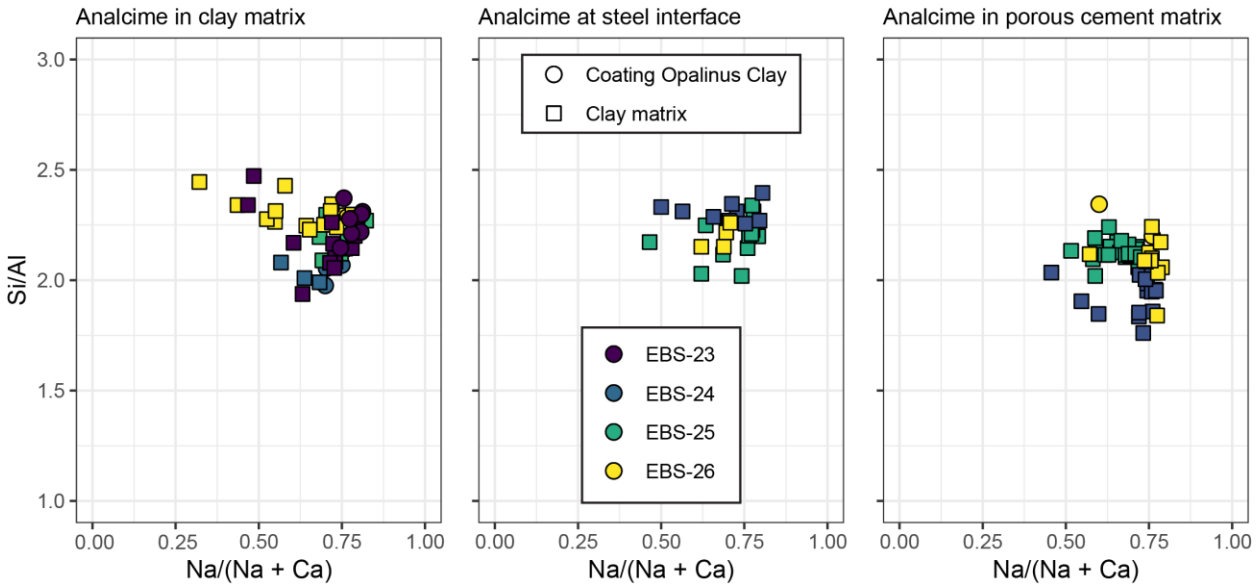

Figure 14. Analcime compositions divided by petrographic context within EBS-23 through EBS-26. Each point represents a single analysis as a wide range of compositions were observed in each sample.

3.8 Wyoming Bentonite + Durango Apatite: EBS-29

Characterization of EBS-29 and the effects on phosphate additives on bentonite stability were completed in FY21. Analyses include electron microprobe, SEM, aqueous geochemistry of major anions and cations, QXRD, and XRD of clay mineral structures and apatite crystals.

The pH of the EBS-29 experiment started around pH 7.4, the pH of the synthetic Opalinus Clay groundwater. The pH, measured at 25ºC (i.e., quench solution), dropped within the first week of the experiment to pH~6.5 and remained relatively stable between pH 6.5 and pH 7 for the duration of the experiment (Figure 15).

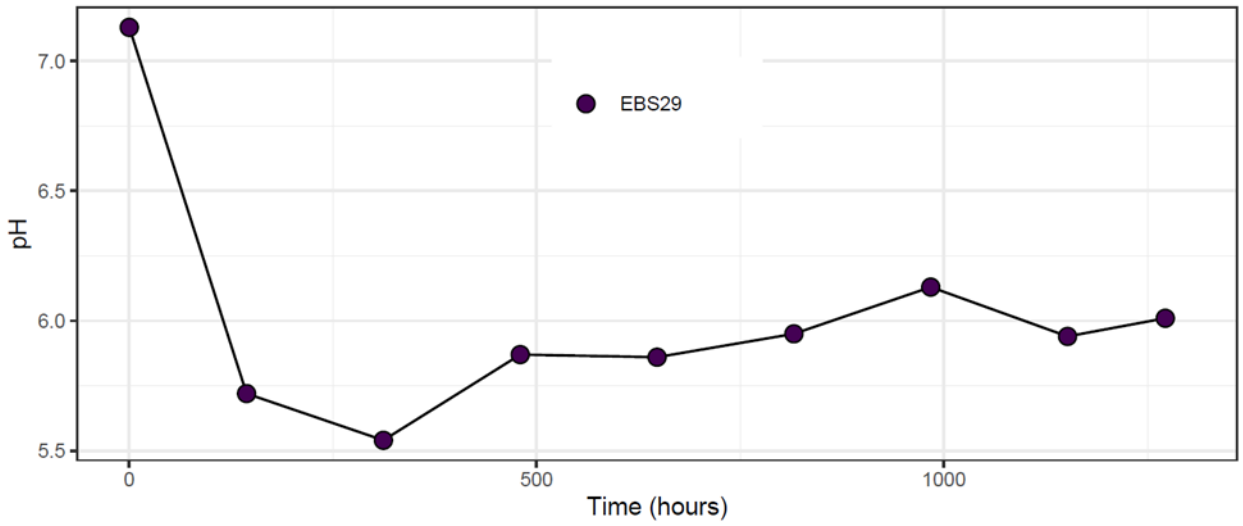

Figure 15. pH at 25ºC throughout the duration of experiment EBS-29 (see text).

Major cation concentrations (Na^+, K^+, Ca^{2+}) all showed decreasing trends throughout EBS-29 (Figure 16). At the first sampling, [Na^+] concentrations increased from the starting solution brine (162 mg/L) to 450 mg/L. Concentrations decreased to ~325 mg/L by the end of the experiment. For [K^+], concentrations sharply decreased from initial brine concentrations (290 mg/L) to 50 mg/L by the first sampling, reaching ~20 mg/L by the end of the experiment. Calcium concentrations were observed to decrease from 9 mg/L to 2 mg/L during the experiment from a starting brine concentration of 46 mg/L.

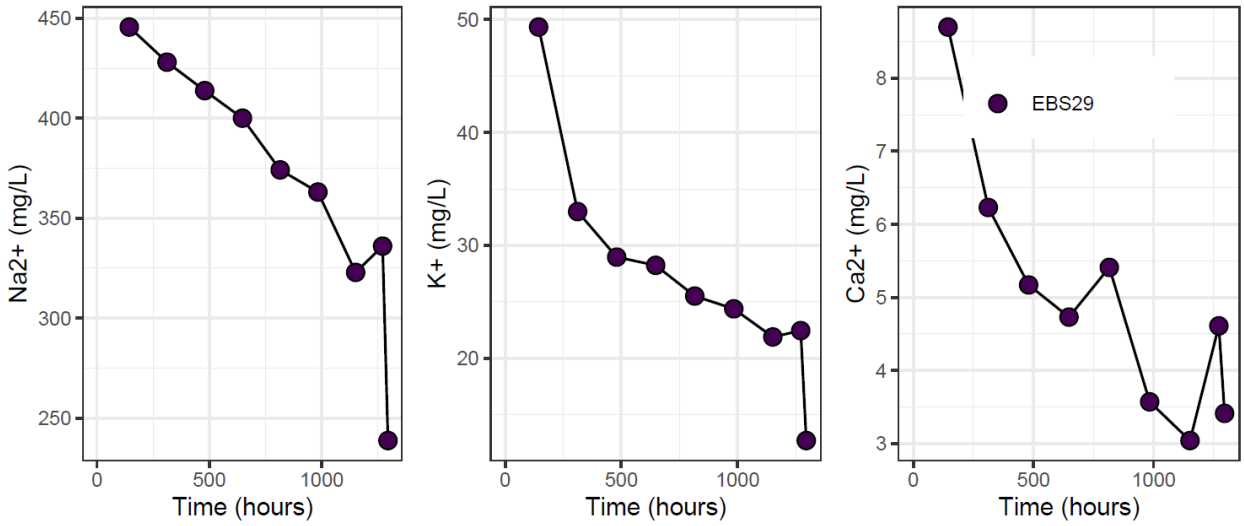

Figure 16. Cation concentrations throughout the duration of experiment EBS-29 (see text).

Phosphate concentrations remained ~0.2 mg/L throughout the experiment. However, upon experiment quenching, phosphate concentrations increased reaching ~0.75 mg/L (Figure 17). The initial chloride in the starting brine was around 670 mg/L but dropped to near the detection limit by the first sampling (Figure 18). Sulfate concentrations initially increased from 150 mg/L to 175 mg/L in the first week of the experiment and then steadily decreased to 125 mg/L by the end of the experiment (Figure 18).

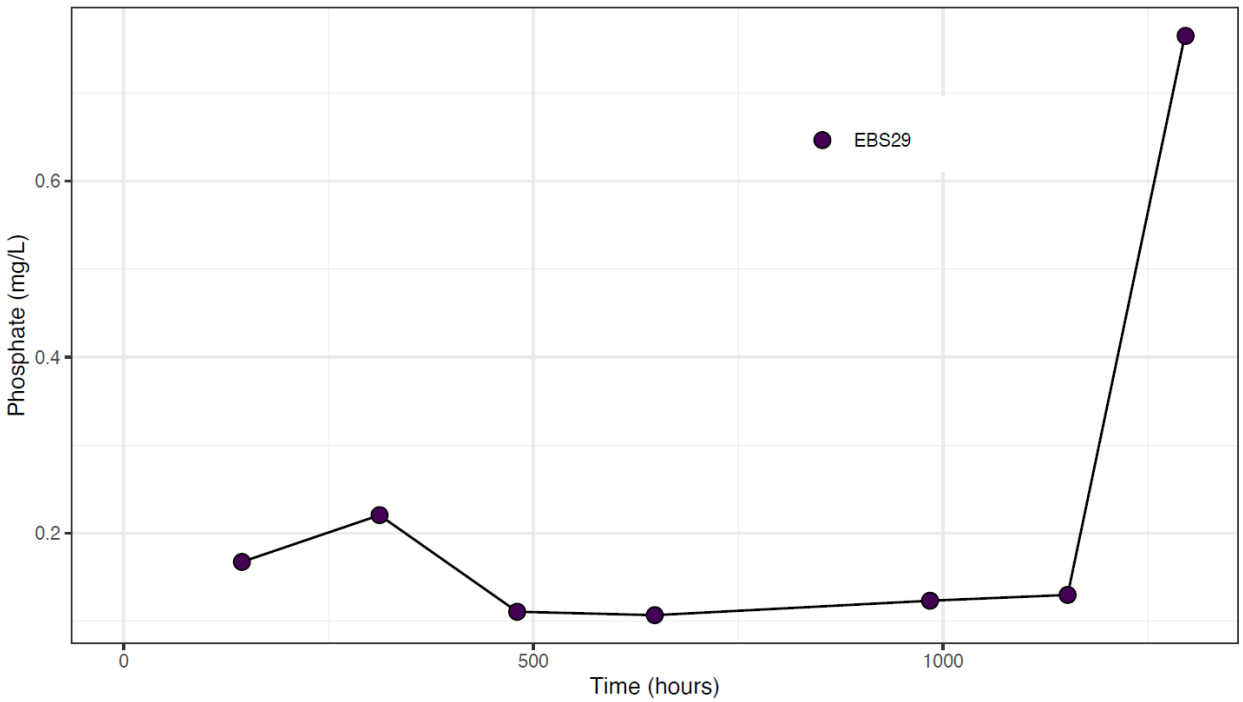

Figure 17. Phosphate concentrations throughout the duration of experiment EBS-29 (see text).

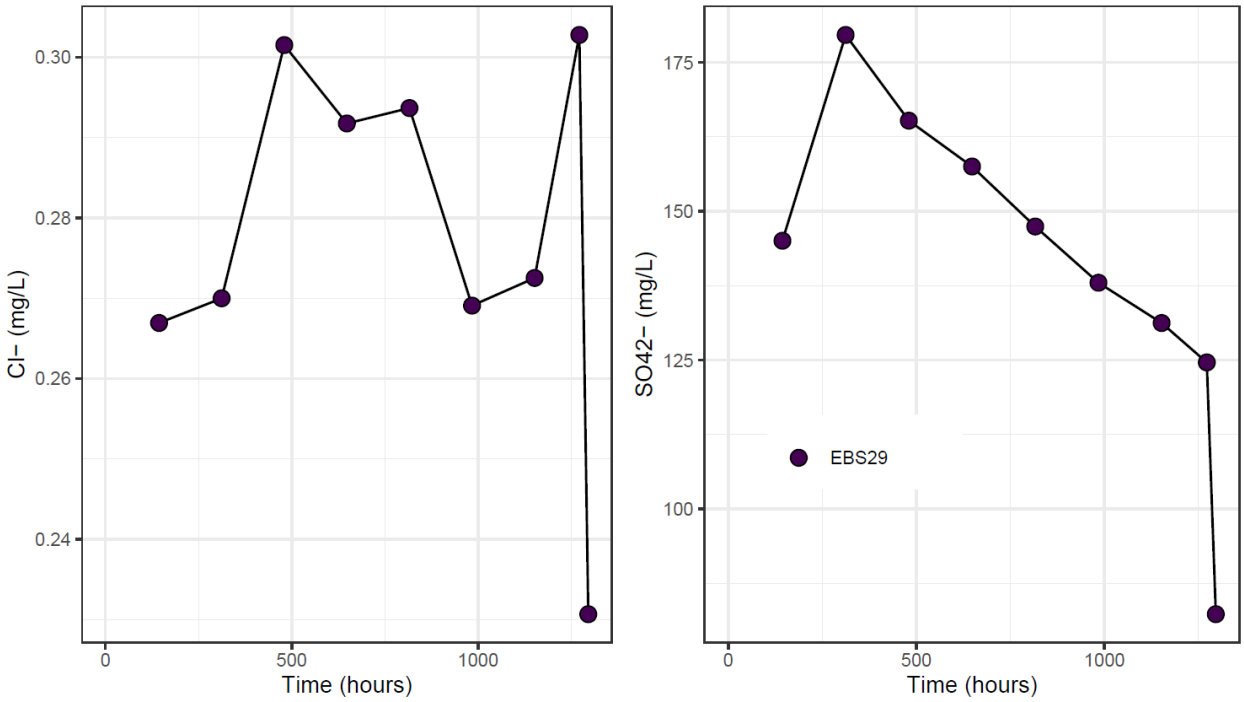

Figure 18. Anion concentrations throughout the duration of experiment EBS-29 (see text).

Silica concentrations remained constant around 700 mg/L throughout the experiment. Concentrations dropped to 500 mg/L upon experiment quenching (Figure 19).

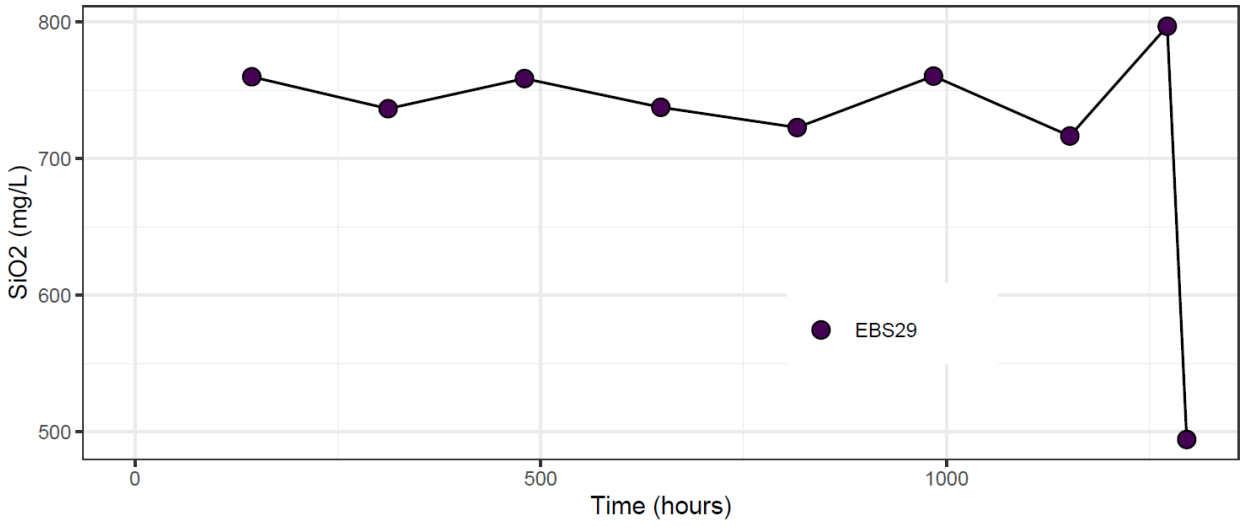

Figure 19. Silica concentrations throughout the duration of experiment EBS-29.

The XRD pattern of the < 2 μm clay fraction from the EBS-29 reaction products shows that the structure of montmorillonite was unchanged with respect to the characteristics of the starting bentonite (Figure 20). Peak positions show no significant shifts or loss of swelling (Table 5). QXRD analyses of the bulk reaction product and SEM images indicate that there was newly formed zeolite (analcime) and an amorphous phase, along with a reduction of combined smectite + illite + smectite-illite.

Table 5. Ethylene glycol saturated smectite (GS) peak positions for the clay fraction extracted from the Wyoming bentonite-Apatite experiment. Expandability was calculated based on the position of the 002 and 003 GS peaks.

EG-smectite	**001**		**002**		**003**		**002/003**	**1**	**2**	**3**
Sample	**d (Å)**	**2θ**	**d (Å)**	**2θ**	**d (Å)**	**2θ**	**Δ 2θ**	**%Exp**	**%Exp**	**%Exp**
WY Bentonite	17.0	5.2	8.5	10.4	5.7	15.7	5.3	100	102	103
EBS-29	17.1	5.2	8.6	10.3	5.7	15.6	5.3	100	102	103

1: %Exp = 973.76 – 323.45Δ + 38.43Δ2 – 1.62Δ3 (Eberl et al., 1993)

2: %Exp = 1517.8 – 548.49Δ + 68.35Δ2 – 2.90Δ3 (Eberl et al., 1993)

3: %Exp = 766.01 – 194.10Δ + 12.924Δ2 (Moore and Reynolds, 1997)

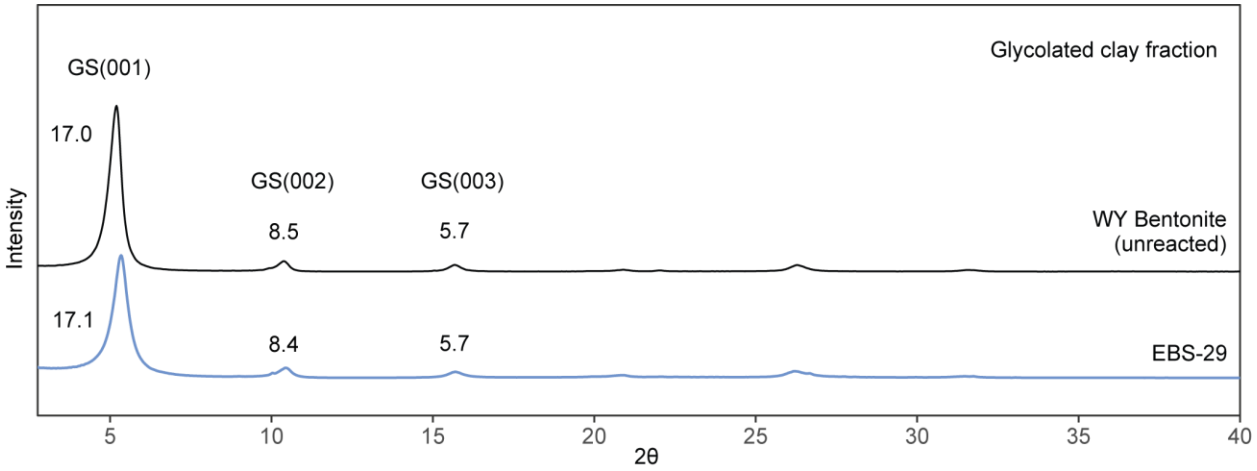

Figure 20. XRD results from the oriented clay fraction of heated bentonite from EBS-29 and unreacted Wyoming bentonite. Peaks corresponding to ethylene glycol saturated smectite are labelled.

Apatite crystals that reacted with synthetic Opalinus Clay groundwater in a sealed gold capsule at the bottom of the titanium experiment vessel were crushed and analyzed in a randomly oriented powder mount. The pattern of the reaction product did not show any significant shifts from the starting material pattern (Figure 21). The lack of peaks corresponding to secondary phases suggests that precipitation of other phosphate phases did not occur.

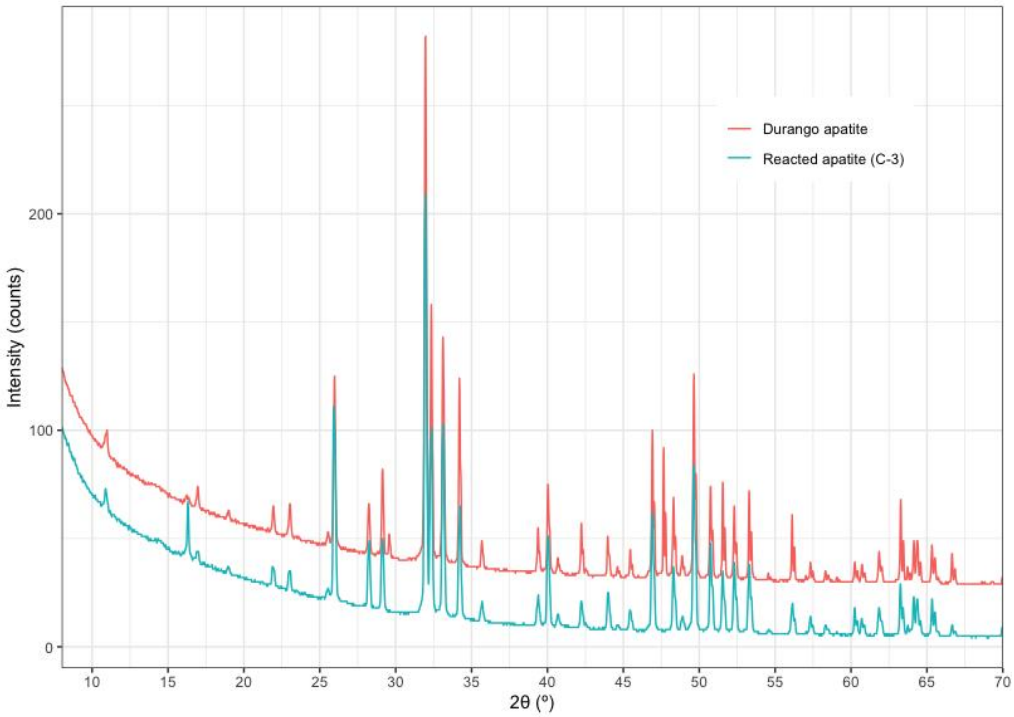

Figure 21. XRD of the apatite crystals that reacted with synthetic Opalinus Clay groundwater in a sealed gold capsule in EBS-29.

3.9 Steel-Bentonite Interface Mineralization

Steel coupons (316SS, 304SS, and LCS) were included in most Wyoming bentonite + Opalinus Clay ± OPC experiments (Table 1). Proportions of Wyoming bentonite:Opalinus Clay:OPC were either (in wt.% values) 80:20:0, 50:50:0, or 60:20:20. Experiments with Wyoming bentonite and Opalinus Clay were performed at either 200 or 300ºC and experiments containing Portland cement were run at 200ºC. Steel coupons were separated from the other solid reaction products. Interface mineralization was observed via secondary electron SEM imaging of the coupon surface and in cross-section view of a coupon mounted in epoxy and polished to show mineralization perpendicular to the coupon edge. The chemical composition of mineral phases on the surface of the steel coupons was analyzed via SEM-EDS and electron microprobe.

3.9.1 Experiment with Wyoming Bentonite and Opalinus Clay

In the set of experiments with Wyoming bentonite and Opalinus Clay, the following mineral phases were identified growing at the interface of the various steels: Fe-saponite, pentlandite, smectite, feldspars, and zeolites.

304SS: EBS-19. Post-reaction 304SS exhibited a layer of Fe-saponite with minor smectite and pentlandite crystals (Figure 22 C) covering the surface of the steel plate. Analcime- wairakite was embedded in the Fe-saponite. The Fe-saponite exhibited a honeycomb texture (Figure 22 A, B).

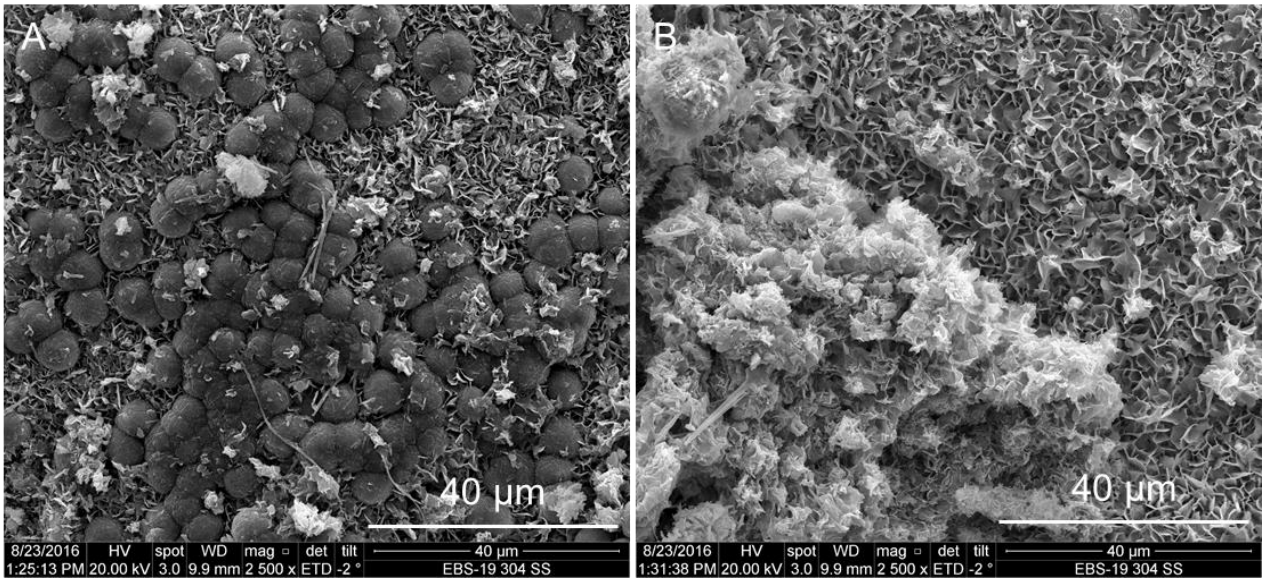

Figure 22. Secondary electron SEM images of the 304SS surface from EBS-19. [A] Fe-saponite with embedded zeolites (rounded) and [B] smectite overlying honeycomb-texture Fe-saponite from EBS-19.

LCS: EBS-18. Fe-saponite crystals grew perpendicular to the low carbon steel followed by secondary smectite rosettes. Minor analcime and millerite are embedded in the saponite mat (Figure 23). This experiment failed (i.e., developed a leak) before reaching the full experiment duration.

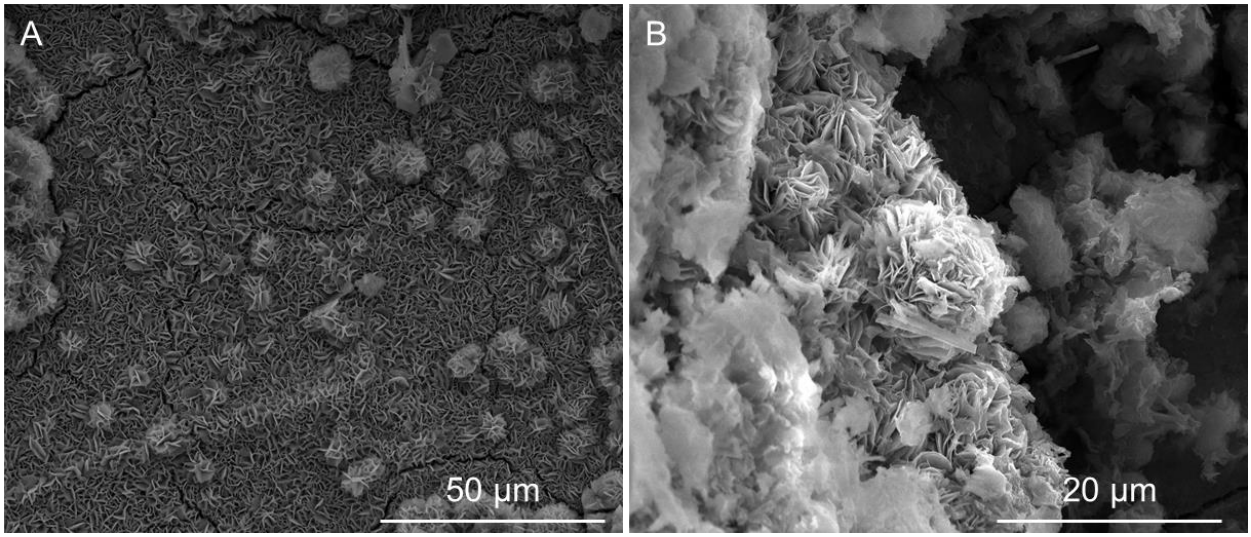

Figure 23. Secondary electron SEM images of the LCS surface from EBS-18. [A, B] Fe-saponite rosettes.

316SS: EBS-15 & -20. In the 6-week experiment, saponite formed in a honeycomb texture on the 316SS steel surface with lesser smectite (Figure 24 A-B). Minor minerals include millerite and analcime-wairakite on the saponite with feldspars embedded on the surface.

The 6-month experiment, EBS-20, was similar to the 6-week experiment with the presence of Fe-saponite with embedded analcime-wairakite, except the late-stage pentlandite were present in the Fe-saponite (Figure 24 C-D).

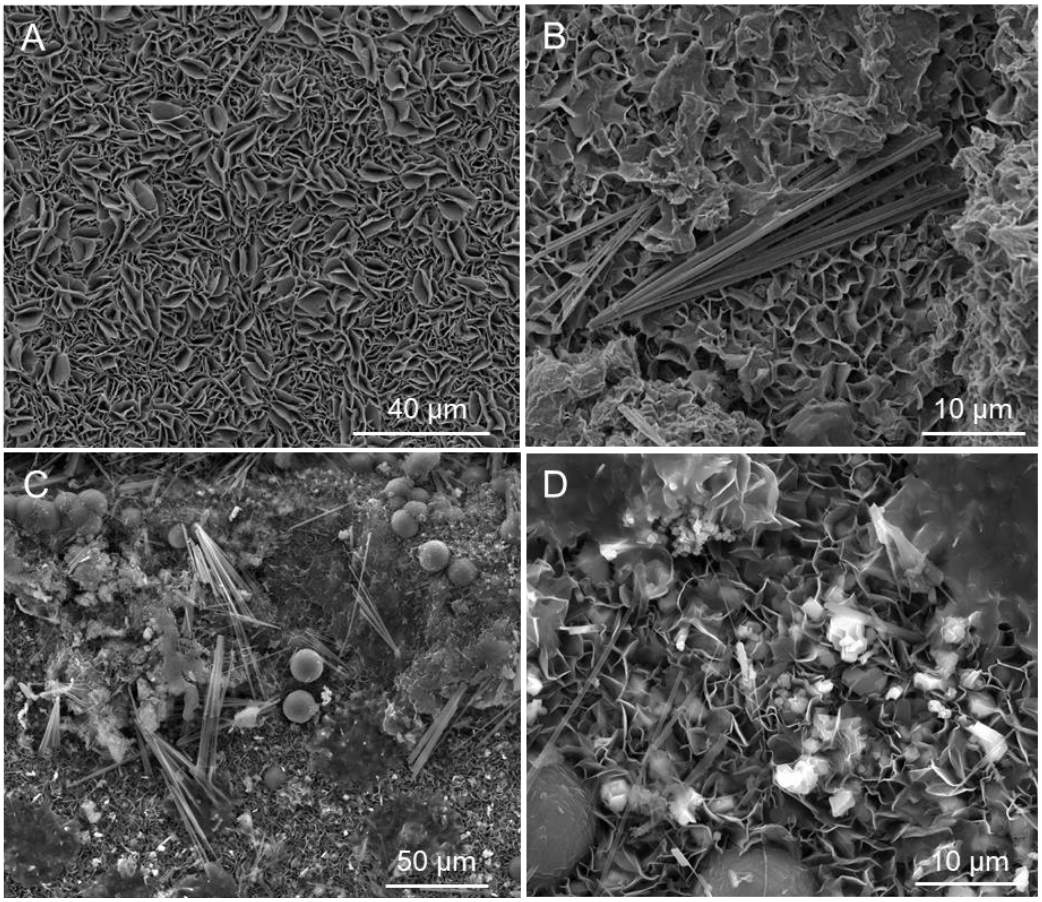

Figure 24. Secondary electron SEM images of the 316SS surface from EBS-15 and EBS-20. [A] Fe-saponite overlaying the 316SS in EBS-15 [B] Smectite, zeolites, and millerite from EBS-15 [C] Fe-saponite and smectite (around the edges) with millerite (bladed mineral) and zeolites and [C]. Pentlandite (blocky mineral) overtop smectite from EBS-20.

3.9.2 Experiments with Portland Cement

Fe-saponite growth on the surface of the steel coupons was not observed in the experiments containing OPC powder, unlike the coupons extracted from EBS experiments without OPC (described above) and experiments containing the cured cement chip. In experiments with OPC powder, mineral phases such as calcite, analcime, tobermorite (CSH minerals), Fe-oxides and Fe-Ni-Cr sulfides/oxides are observed at the steel coupon interface. In experiments containing the cured cement chip, observed newly formed mineral phases include Fe-saponite and gypsum.

316SS: EBS-24, -27, -28. The surface of the 316SS coupon was not characterized by a layer of Fe-rich clay (as observed in previous EBS experiments). The 316 stainless-steel surface is altered

to granular Fe-oxide with platy/bladed Fe-Ni-Cr oxide interbedded. Analcime and calcite are also observed on the layer of minerals attached to the steel surface.

Similarly to the other 200ºC experiments, the 6-month experiment did not have Fe-rich silicate reaction products on the steel surface. The steel surface is coated in Fe-oxides. CSH and smectite are attached to the steel surface as well as large (~100 µm diameter) analcime–wairakite crystals. Garronite is locally observed.

At 300 ºC, the post-reaction 316SS shows that the steel surface was covered in tobermorite and wairakite in a CSH-clay matrix. Gypsum and xonotlite were also present on the reacted coupon.

EBS-30. The reacted 31SS from the cured cement experiment was coated with smectite with large gypsum crystals (~100-300 µm in length) and corroded plagioclase embedded in the clay (Appendix B: Figure B-6 A). Fe-saponite is also observed on the steel coupon (Appendix B: Figure B-6 B).

304SS: EBS-25. Newly formed minerals attached to the stainless-steel surface outboard of the CSH layer include calcite splays, tobermorite rosettes, and analcime. Point EDS analyses on the EBS-25 bentonite-304SS interface show little to no alteration or oxidation. A thin fibrous mineral layer is observed attached to the 304SS and locally exhibits a honeycomb texture. EDS analyses indicate this thin layer was likely a CSH phase. Locally, Fe-Cr-Ni-sulfides are observed to separate the CSH layer from the steel surface. Similar to EBS-24, Fe-saponite is not observed on the surface of the coupon.

EBS-31: In the experiment with the cured cement chip, Fe-saponite formed a honeycomb texture on the 304SS steel surface with lesser smectite (Appendix B: Figure B-9 B). Calcite and garronite were present sporadically throughout the smectite and Fe-saponite (Appendix B: Figure B-9 A-B).

LCS: EBS-26. Analcime crystals formed mats along the surface. Gypsum and Fe-oxides were also observed. BSE images of the post-reaction coupon also show the formation of a zeolite layer adjacent to the surface. BSE images also show the formation of other newly formed secondary phases of garronite, analcime, and tobermorite, similar to the other EBS experiments with cement. No iron-rich clay was observed at the clay-steel interface.

3.9.3 Chemical Gradient across the Steel Surface

Chemical analyses were collected via SEM-EDS along a line perpendicular to the surface of the mounted steel coupon for EBS-15 (Wyoming bentonite + Opalinus Clay, 316SS, 300ºC, 6 weeks) and EBS-25 (Wyoming bentonite + Opalinus Clay + Portland cement, 304SS, 200ºC, 8 weeks). Analyses of the remaining stainless-steel coupon chemical gradients are in progress. The results from the steel coupons from two different experiment sets demonstrate the differences in steel surface mineralization with changes in bulk chemistry in the experimental system. The outermost surface of the 316SS coupon of EBS-15 is altered to Fe,Cr-oxide in which Cr is slightly enriched with respect to the steel (Figure 25). The portion of the surface of the 316SS

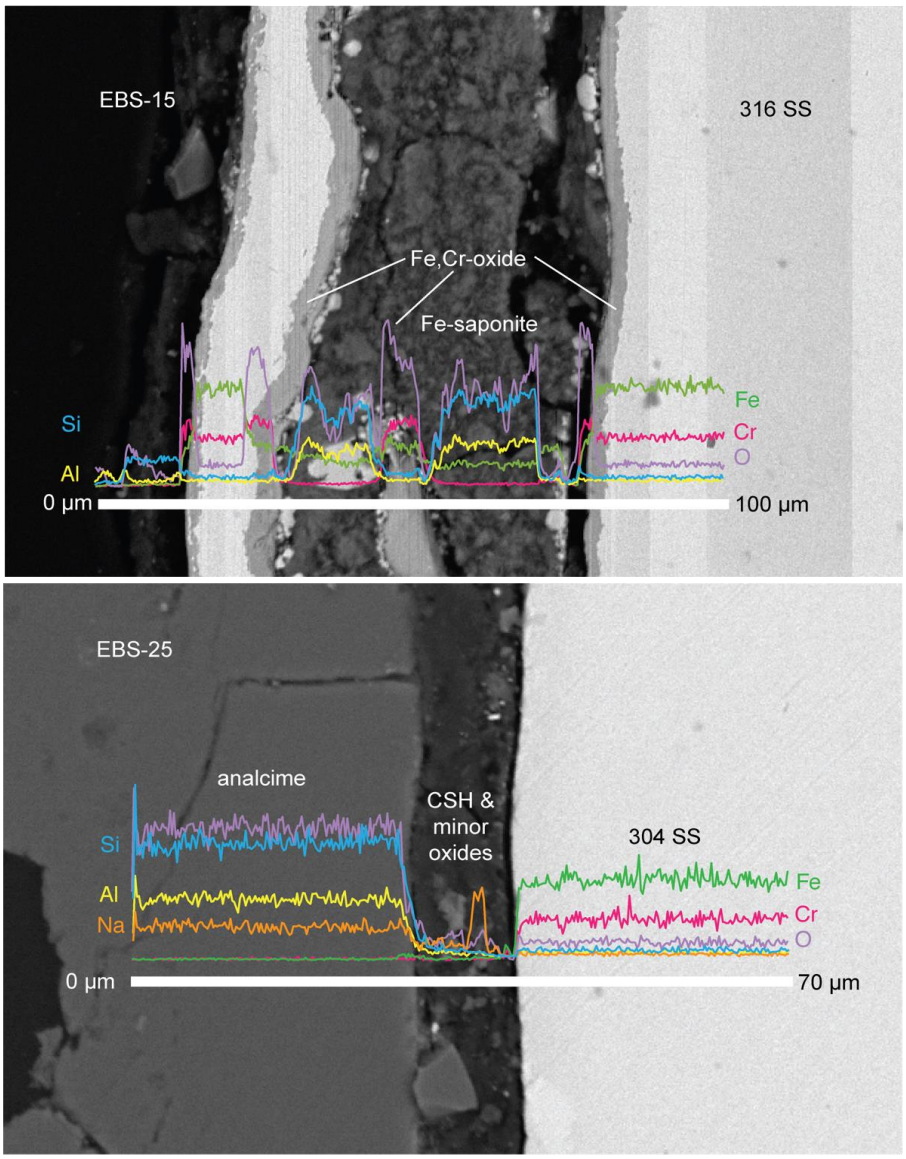

Figure 25. Energy dispersive X-ray spectroscopy (EDS) chemical results collected along a line (white) perpendicular to the steel surface in EBS-15 (top) and EBS-25 (bottom).

appears to have delaminated from the surface and Fe-saponite formed between the layers of steel (Figure 25). In comparison, zeolite minerals (analcime) formed at the surface of the coupon from the cement-bearing experiment (EBS-25). It does not appear that Fe or Cr were transferred to reaction products away from the coupon surface. Further, a distinct oxide rind is not observed at the coupon margin (Figure 18). There is a sharp chemical boundary of the steel and the attached reaction products in the EBS-25 sample, whereas a more diffuse, gradual boundary is observed in EBS-15 with respect to elements such as Fe and Cr.

Preliminary observations from experiments EBS-30 and EBS-31 indicate that the presence of the cement chip instead of OPC powder results in different reactions at the steel interface. Fe-saponite is observed, indicating that Fe is transferred from the coupon to the clay matrix. In progress analyses of the steel coupon surface will be compared with previous results.

3.9.4 Steel Precipitation Thickness of Alteration Phases

Estimates of the thickness of the zone of alteration products at the steel-bentonite interface were measured for experiments EBS-15 through EBS-26 that contained stainless-steel coupons. Precipitation thicknesses (Table 6) were determined from backscattered electron (BSE) images of a cross section of two steel coupons per experiment. Fifty measurements were taken from each long side at equal intervals with an additional eight measurements on each short side. Measurements were made in Adobe Photoshop using the measurement tool. Precipitation rates (Table 6) were determined by dividing the average precipitation thickness by the number of experimental run days. The stainless-steel sample for EBS-18 could not be located; subsequently, the thicknesses recorded are from an older measurement technique and were included for completeness. It is also important to note that EBS-18 did not run the full duration of the experimental time due to the gold bag failure.

The Fe-rich phyllosilicate mineral growth rates at the bentonite-steel interface were the highest in the 300ºC experiments that included Wyoming bentonite (80%) and Opalinus Clay (20%). In these 300ºC runs, LCS had the fastest average growth rate (3.56 μm/day, 6 weeks), followed by 316SS (0.67 μm/day, 6 weeks), 304SS (0.45 μm/day, 6 weeks) and 316SS (0.13 μm/day, 6 months). The 200ºC experiments, EBS-21 and -22, had lower precipitation rates than the higher temperature experiments (316SS, 0.14 μm/day and 0.38 μm/day over 8 weeks, respectively), likely due to experiment parameters such as lower temperature, longer run time, starting mixtures, and groundwater composition.

The thickness of zeolite and CSH phases that formed perpendicular to the stainless-steel surface in the 8-week experiments with OPC varied with steel type. Mineral formation on the LCS surface occurred at the fastest average growth rate (0.56 μm/day), followed by 304SS (0.40 μm/day) and 316SS (0.14 μm/day).

Table 6. Phyllosilicate (Fe-saponite/chlorite)/zeolite (analcime) thickness and growth rates. Rates are represented in µm per day. Three steel types were examined: 304SS, 316SS and LCS from EBS-15 through -26.

Sample	Steel	Matrix	Water: Rock	Temp	Time	Ave Precip (µm)	Prec./Day (µm/day)
EBS-19	304	Bent + Clay	6.0	300°C	6 weeks	12.58 (±11.67)	0.45
EBS-25		Bent + Clay + Cement	11.3	200°C	8 weeks	16.99 (±12.15)	0.40
					AVERAGE:	14.79	0.43
EBS-15	316	Bent + Clay	8.1	300°C	6 weeks	28.30 (±16.06)	0.67
EBS-20		Bent + Clay	7.1	300°C	6 months	24.10 (±19.59)	0.13
EBS-21		Bent + Clay (1 M NaCl)	9.1	200°C	8 weeks	7.37 (±8.89)	0.14
EBS-22		Bent + Clay (=)	8.4	200°C	8 weeks	21.10 (±24.75)	0.38
EBS-24		Bent + Clay + Cement	13.5	200°C	8 weeks	7.91 (±8.39)	0.14
					AVERAGE:	17.76	0.29
EBS-18*	LCS	*Bent + Clay*	*8.3*	*300°C*	*3 weeks*	*71.13*	*3.56*
EBS-26		Bent + Clay + Cement	11.7	200°C	8 weeks	31.63 (±16.11)	0.56

* Sample EBS-18 was analyzed with an older technique and did not run to completion. It was included for completeness.

4 Discussion

4.1 Portland Cement Effects

4.1.1 Aqueous Geochemistry

The solution chemistry changes observed in the extracted reaction fluids likely reflect mineral-brine reactions. The hydrothermal reaction of the solid reactants with the synthetic Opalinus Clay brine likely resulted in precursor phase dissolution/recrystallization and the precipitation of new mineral phases. As described above, the addition of OPC powder or cured chips to the reaction mixture resulted in changes in the observed newly formed mineral phases in comparison with the set of experiments without cement. In addition, temperature (200 or 300ºC) also affected the observed aqueous geochemistry changes. The main observations from the experiments with Opalinus Clay and Wyoming bentonite at 200ºC were silica undersaturation and difference in pH values. Increases in temperature resulted in different pH, silica, and cation concentrations in comparison to the 200ºC experiments. Swapping out OPC powder for a cured chip also resulted in different effects, described below.

4.1.2 Silica Saturation

Previous studies identified silica saturation as a major factor in the alteration of EBS materials (Smyth, 1982; Bish & Aronson, 1993; Neuhoff & Ruhl, 2006; Cheshire et al., 2014). The presence of Opalinus Clay wall rock and synthetic groundwater had significant effects on the aqueous chemistry of the system, in particular, on the silica saturation state throughout each experiment. Cheshire et al. (2014) observed saturation with respect to cristobalite throughout the

experiment duration of 300°C Wyoming bentonite only experiments. In comparison, measurements from the 300°C Opalinus Clay ± Wyoming bentonite experiments of this study showed similar silica concentrations throughout each experiment, regardless of the proportions of starting material (Sauer et al., 2020). Silica saturation calculations of the reaction fluids from the experiments with Portland cement are in progress.

4.1.3 pH

The pH (measured at 25ºC) of the reaction fluids extracted from the 300ºC experiment that contained cement (EBS-28) dropped to ~6 within two weeks of the experiment, indicating that OH^- derived from portlandite ($CaOH_2$) dissolution is quickly consumed at 300ºC (Figure 4). Mineral phases such as zeolites (e.g., analcime, garrnonite) and aluminosilicates (e.g., feldspar) likely buffered the pH, as has been observed in other experimental systems (e.g., Johnston & Miller, 1984; Heimann, 1993; Gailhanou et al., 2017; Sauer et al., 2020). Portlandite dissolution initially occurred as indicated by the pH of ~9.5 at the first sampling and the XRD pattern of the reacted mixture (Figure 4).

The pH values (measured at 25ºC) in the 200ºC experiments increased from the starting groundwater solution pH to values between 8 and 9. The elevated pH values are likely related to the OH^- contributed to the system from the OPC powder related to portlandite dissolution. In comparison to 300ºC, the OH^- was not immediately consumed in mineral-forming reactions. The increase of pH is likely related to the dissolution of portlandite and the presence of alkaline components (Na^+, K^+ and Ca^{2+}) in the cement powder entering into the solution (see the increase of Ca^{2+} in Figure 6). The pH of the pore water should gradually decrease during the evolution of cement degradation; however, this was not observed over the period of the 8-week 200ºC experiments. A slight decreasing trend in pH values was observed in the values recorded from the six-month experiment (EBS-27; Figure 3).

In experiments EBS-30 and EBS-31 that contained a cured cement chip at 200ºC, pH values were lower than were observed in the 200ºC powder experiments. A slight increasing trend is observed over time from pH = 6 to pH = 6.5 to 7. Portlandite dissolution is indicated by the XRD patterns of the chip surface. A thin section was made of a cross section of the cement chip; future work will include the assessment of the extent of the reaction into the center of the chip. Future work will also assess if calcite formation/recrystallization occurred.

The evolution of the pH pore water in a cementitious environment is modeled over time at 25ºC by Jacques et al. (2010). The reaction between an aqueous fluid and cement is a gradual change in composition, from a “young” concrete pore water (pH > 13) to more mature pore water with a lower pH (~10). Changes in solution pH are observed in stages, which can be related to mineral-brine reactions. The first stage of the pH evolution, when the pH is ~12.5, Na^+ and K^+ concentrations are elevated due to leaching of Na_2O and K_2O from the dissolution of portlandite from OPC. The pH will begin to decrease as all the portlandite is consumed from the cement and the pore water is then buffered by other cement phases, such as CSH minerals. When the pH drops below 10, the formation of calcite and aggregate minerals will likely be the phases responsible for buffering the pH (Jacques et al., 2010).

Significant solution chemistry differences are observed in the concentrations of aqueous species (e.g., SiO_2, K^+) and the pH between the reaction fluids from the 200 and 300ºC cement experiments. Reactions were likely kinetically faster at 300ºC, e.g., as demonstrated by the rapid changes observed within the first week of the 300ºC experiment duration (e.g., drop in pH

values, silica, cations) (Figure 4-6). The differences in the observed solution trends also reflect the formation of different mineral phases, potentially through different reaction pathways. In the experiments with cement powder, at 300ºC the formation of feldspar and analcime was favored versus at 200ºC where abundant zeolite phases (garronite, clinoptilolite/heulandite, analcime) were formed. Further, differences in the experiments with cured cement chips indicate that cured cement is less reactive and has less of an effect on the pH of the system than OPC powder.

4.2 Clay Alteration

The addition of uncured OPC powder affected the smectite mineral structure in the bentonite fraction, resulting in ~10% reduction in expandability from 8 weeks of hydrothermal treatment at 200ºC and 300ºC. In the 6-month experiment, the formation of mixed layer chlorite-smectite was also observed. A prominent tobermorite peak is present in the clay mineral fraction of all the cement-bentonite experiments (Figure 9). Previous investigations on the interaction of bentonite and cement materials have documented the formation of Al-tobermorite from the reaction of portlandite ($Ca(OH)_2$) with montmorillonite (Fernandez et al., 2014; 2016). Fernandez et al. (2016) similarly observed reduced expandability in smectite post hydrothermal reaction at 60 to 120ºC. Thus, montmorillonite in the Wyoming Bentonite used in our experiments likely reacted with Portland cement to create interlayered tobermorite in the clay mineral structure. Further, QXRD results indicate that combined illite, illite-smectite, and smectite in the bulk system was reduced by ~12 to 19 wt.%, whereas tobermorite comprises 2 to 4 wt.% of the reaction products and amorphous material comprises 9–26 wt.% in the reaction products from the 8 week, 200ºC experiments. Amorphous material that has an aluminosilicate composition (analyzed via SEM-EDS) indicates potential breakdown of clay minerals, as has previously been recognized in alkali-rich experimental systems (i.e., Khalifa et al., 2020).

In experiments with the cured OPC chip (EBS-30 and EBS-31), the clay mineral structure was less affected than in experiments with uncured OPC powder. Clay mineral separations are in progress for these experiments but XRD patterns from the bulk powder suggest that smectite remained stable during the experiment period and that mixed layer illite-smectite or chlorite-smectite phases were not formed.

4.3 Zeolite and CSH-Mineral Formation

The addition of uncured ordinary Portland cement powder to the Opalinus Clay + Wyoming bentonite system at 200ºC (EBS-23 through EBS-27) resulted in abundant zeolite and CSH mineral formation. Phases observed in previous EBS experiments (Wyoming bentonite only and Wyoming bentonite + Opalinus Clay) such as analcime likely formed through different reaction pathways involving different mineral phases. QXRD data from EBS-24, EBS-25, and EBS-26 correspond to 5 to 6 wt.% analcime, 6 to 9 wt.% garronite (a rare Ca-rich zeolite), 2 to 4 wt.% Al-tobermorite (CSH), and 9 to 26 wt.% amorphous material (CSH gel). In the 6-month experiment (EBS-27), more analcime–wairakite and other zeolites and less garronite, tobermorite, and amorphous material were observed. The minerals analcime, garronite, and tobermorite are commonly observed together (e.g., Figure 11). Garronite and tobermorite crystals from EBS-23 through EBS-26 are very sensitive to the microprobe electron beam and thus did not yield reliable compositional data (e.g., low silica and total oxide numbers). The compositions of analcime, garronite, and tobermorite/CSH phases obtained are plotted in Figure 12a. Feldspar, analcime, and garronite analyses have a wide range of Na/Na+Ca values between the end-member phase values. The observed compositional spread and textural association of

these phases in the 200ºC experiments and the reduction in garronite and CSH abundance after 6 months of reaction time indicates that garronite and CSH phases may be metastable precursors to more stable silicate phases, such as analcime–wairakite. Potential reactions related to this mineral sequence have been outlined by Bayliss and Levinson (1970) based on results from hydrothermal experiments involving quartz, kaolinite, and calcite/dolomite. Garronite and analcime are commonly found at the interface of the Opalinus Clay fragments, which contain calcite and kaolinite. Thus, the formation of garronite may be described by the reaction, generalized from Bayliss and Levinson (1970):

$$Na^{+} + \text{calcite} + \text{quartz} + \text{kaolinite} + H_2O \rightarrow \text{garronite} + CO_{2\,(gas)} \quad (6)$$

Analcime produced in the OPC powder-containing experiments has a distinct composition with respect to the analcime formed in previous EBS experiments (Figure 26). The Si/Al ratios of analcime from EBS-23 to EBS-26 have similar Si/Al ratio to analcime from EBS-14 (Opalinus Clay only). The Na/(Na+Ca) ratios are similar to analcime formed in experiments without Portland Cement (i.e., lower bulk Ca compositions). Future experiments with different parameters (length, temperature) could explore this difference. Petrographic evidence of intergrowth of analcime and garronite and mottled textures in analcime cores, along with the range of compositions, may suggest that the reaction from garronite to analcime was not complete. Therefore, intergrowth of garronite, or other Ca-rich phases (e.g., tobermorite), may be the reason for the wide range in Na and Ca contents observed in analcime in the electron microprobe analysis results. Electron microprobe analyses from EBS-27 through EBS-31 will be documented in FY22.

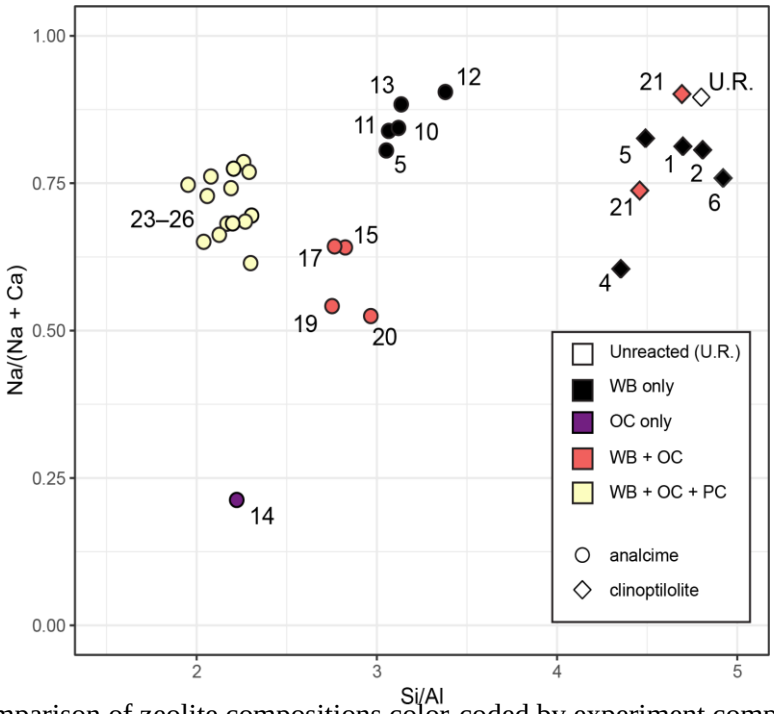

Figure 26. Comparison of zeolite compositions color-coded by experiment components. The numbers represent the EBS experiment identifier. The run conditions are as follows: 1–4, 6: 4–5 week bentonite only experiments with a ramped thermal profile (25/100/200/300/25 °C); 5, 10–13: 6 week bentonite only at 300 °C; 14: Opalinus Clay only for 6 weeks at 300 °C; 15–20: Opalinus Clay + bentonite 6–8 week experiments at 300 °C; 21: Opalinus Clay + bentonite 200 °C; and 23–26: Opalinus Clay + Wyoming bentonite + Portland cement for 8 weeks at 200 °C. Bentonite-only experiments generally have higher Na/Na+Ca and Si/Al values. Experiments with Opalinus Clay and/or Portland cement shift to lower Si/Al. Abbreviations: OC, Opalinus Clay; PC, Portland cement; WB, Wyoming bentonite.

4.4 Phosphate Effects

Phosphate minerals are a potential EBS additive that would function to enhance radionuclide-retention properties. Results from EBS-29, which included 80 wt.% Wyoming bentonite and 20 wt.% Durango apatite, showed that hydrothermal treatment at 250ºC and 150 bar for 8 weeks did not result in significant changes to the apatite but montmorillonite was decreased in abundance. Aqueous geochemical analyses of reaction fluids show a slight increase in phosphate, indicating minor apatite dissolution occurred. XRD/SEM analyses did not identify the formation of secondary phosphate mineral phases that may have formed. The amount of phosphate dissolved will inform hydrothermal experiments with relevant radionuclides at observed phosphate concentrations to understand the formation of radionuclide-bearing phosphate byproducts. Further, the sorption of radionuclides to phosphate mineral surfaces will also be explored at the relevant repository temperatures, pressures, and chemical conditions.

4.5 Steel Corrosion and Interface Mineral Precipitation

Results from these experiments show a dynamic environment in the experimental systems at the bentonite-metal interface. The bulk chemistry likely controls the alteration mineralogy, as demonstrated by the differences in mineral precipitation in the experiments with and without uncured/cured Portland cement (Figure 20). The new growth of surface-bound minerals is likely due to direct crystallization in the localized environments surrounding the metal with the steel

material acting as a substrate for mineral growth in response to corrosion. The following describes our finding from the (1) general argillite environment and (2) from the cement environment.

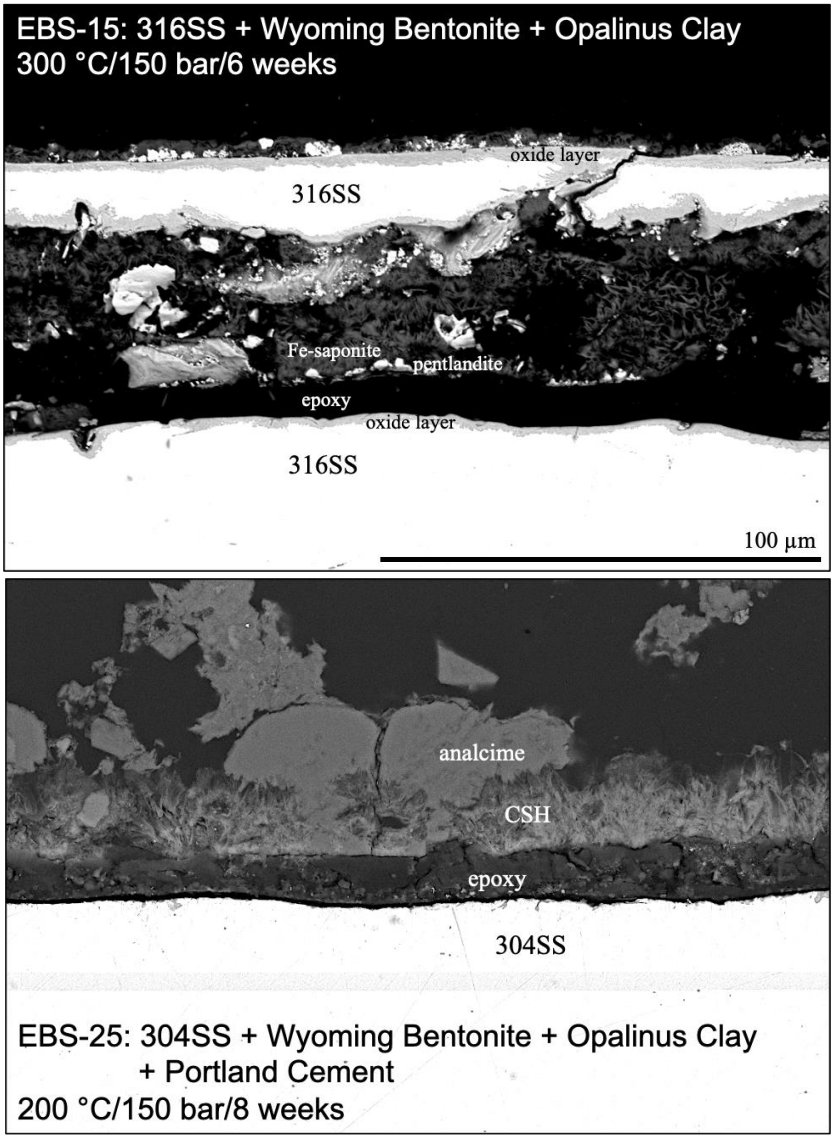

Figure 27. Backscattered electron SEM images showing layered mineral growth that the stainless-steel surface. [Top] The edge of a 316SS coupon from EBS-15. The edge of the steel is an Fe,Cr-oxide layer (medium gray), iron rich phases such as Fe-saponite and pentlandite are observed attached to the steel surface. [Bottom] The edge of the 304SS coupon from EBS-25. On the edge of the steel, a CSH layer formed followed by analcime.

4.5.1 Steel Corrosion in the Argillite Environment

In EBS-15 to 22 (Wyoming bentonite + Opalinus Clay experiments), iron corrosion products that formed on the steel coupon surface reacted with bentonite, resulting in the Fe/Cr/Ni-rich phases (Fe-saponite, chlorite, pentlandite, chromite). These reaction products are only observed in a thin (< ~50 µm) rind on the reacted coupons. Outboard of the Fe-rich phases, unaltered montmorillonite is observed.

In the Wyoming bentonite only experiment series described in Cheshire et al. (2018), a magnetite-like oxide layer developed at the outermost surface of the steel coupon. Further, an oxide layer on the steel coupon surface is observed in the Wyoming bentonite + Opalinus Clay experiments (reported above) that remained around circum-neutral pH values. Outboard of the oxide products, Fe-rich phyllosilicates (i.e., trioctahedral, Fe-rich saponite and chlorite) crystallized, forming a reactive zone with a high surface area in comparison to the original steel surfaces. The surface-bound Fe-rich minerals likely directly crystallized from solution in the local environments surrounding the metal plates as these phases are not observed elsewhere in the clay reaction products. Both steel surfaces for experiments with Wyoming bentonite only and experiments with Wyoming bentonite and Opalinus Clay (argillite environment) have Fe-rich minerals at the steel interface. The localized presence of the newly formed Fe-rich phases together with the lack of significant increase in aqueous Fe in the reaction fluids indicate that steel coupon reactions did not influence solution chemistry of the bulk system.

The general reaction between the steel and bentonite is depicted in Figure 28. The stainless-steel interaction with bentonite via congruent dissolution/oxidation can be detailed by the following reactions:

Stainless steel dissolution

$$Fe_{1.22}Cr_{0.37}Ni_{0.22} = 1.22\ Fe^{2+} + 0.37\ Cr^{+} + 0.22\ Ni^{2+} + 3.99e^{-} \quad (7)$$

Smectite evolution

$$Fe^{2+} + Ni^{2+} + Cr^{3+} + H_2S_{(aq)} + (Na,K,Ca)_{0.33}(Al_{1.67},Fe_3{+}0.20,Mg_{0.13})Si_4O_{10}(OH)_2 = \text{smectite}$$

$$(Fe,Ni,Cr)_9S_8 + (Na, K, Ca)_{0.33}Fe_3(Si_{3.67},Al_{0.33})O_{10}(OH)_2 \quad (8)$$

pentlandite Fe-saponite

Synthetic Fe-saponites have been crystallized in dilute solutions and gels of silica, Fe-, Al-chlorides at temperatures up to 850°C and pH of 8.5 to 9.5 (Kloprogge et al. 1999). In our experiments, the partial dissolution of the steel plates likely contributed ferrous iron into the fluid phase and, together with silica and aluminum from montmorillonite and other precursor aluminosilicate phases in the bentonite, resulted in Fe-saponite crystallization on the steel surface growth substrate. Further, Fe-saponite alteration into chlorite has been suggested (Mosser-Ruck et al., 2010) in the presence of ferrous iron at temperatures approaching 300°C and near-neutral pH. This was confirmed by Mosser-Ruck et al. (2016) through long duration experiments (up to 9 years). The authors were able to demonstrate that smectite is consumed by dissolution to produce chlorite (chamosite) by precipitation. Mosser-Ruck et al. (2016) depicts this reaction by:

$$3\ \text{smectite} + 3\ Fe + 4\ H_2O \rightarrow \text{chlorite} + 3\ \text{quartz} + 2\ \text{albite} + 3\ H_2 + \text{zeolite} \quad (9)$$

Electron microprobe analyses and SEM observations of our experimental reaction products show some instances of chlorite formation in contact with the steel, likely due to the relatively Si-deficient environment) Fe-saponite forms outboard of the chlorite layer, where Si is more abundant (Figure 28).

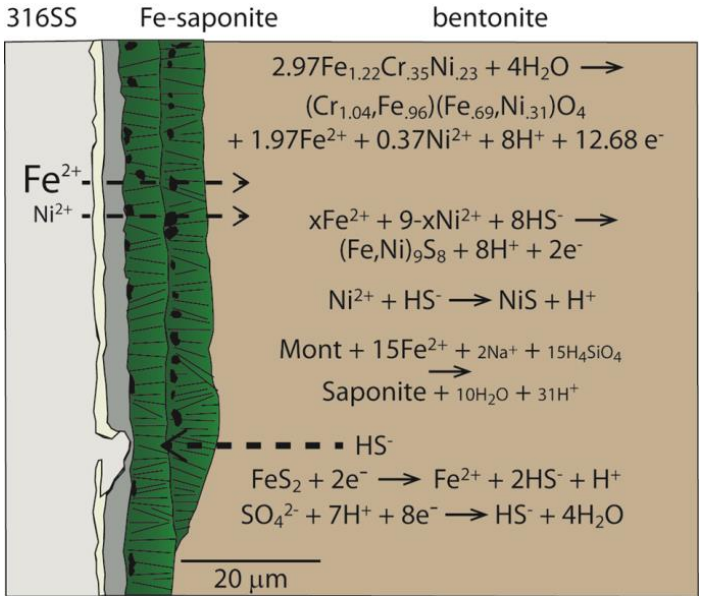

Figure 28. A stylized representation of phyllosilicate mineral growth at the steel interface. Of particular interest is the reaction: montmorillonite → Fe-saponite.

4.5.2 Corrosion in the Cement Environment

In experiments that included uncured OPC powder or cured OPC chips, at 200 and 300ºC, different mineral reactions occurred at the steel-bentonite interface. As described above, in the experiments without cement, an oxide layer formed on the outermost edge of the steel coupons. At 200ºC with uncured OPC powder (EBS-24 through EBS-27), an oxide layer was only locally observed and did not appear to be continuous along the steel surface (Figure 29). At 300ºC, Fe-saponite formation at the steel surface is observed. With the inclusion of a cured cement chip at 200ºC, an oxide layer and Fe-saponite is observed.

In general, pH can considerably influence the corrosion behavior of metals by forming or dissolving the protective oxide layers on the metal surface (Kursten et al., 2004). The corrosion rate of steel in an anoxic solution increases with decreasing pH. For example, observed steel corrosion rates were ~5 and 15 times higher at solution values pH of 7 and 4, respectively, than the corrosion rates in pH 13 solutions (Kursten et al., 2004). We interpret that the increased pH of the experiments with uncured ordinary Portland cement powder at 200ºC likely slowed oxide layer formation at the steel interface, leading to the lack of Fe-rich phyllosilicate minerals. Similarly, the surface of the steel coupon at 300ºC lacks iron rich clay phases. In comparison, pH values in the experiments with the cured cement chips (EBS-30 and EBS-31), observed values are much lower, between 6 and 7. When the pH of the experimental fluid is high, the corrosion of steel occurs at a much slower rate and is unable to provide iron into the system (e.g., Kursten et al., 2004). For the experiments without cement, pH values between 5 and 6 before the conclusion of the experiment are conducive for oxide precipitation for the corrosion of the steel

coupons. The experiments with Portland cement (EBS-24 to 27), the pH is higher, hovering between 8 and 9 before termination. Overall, the elevated pH observed in our experiments with uncured Portland cement powder slowed the corrosion of the steel coupons, and, therefore, the formation of an oxide layer and Fe-rich minerals.

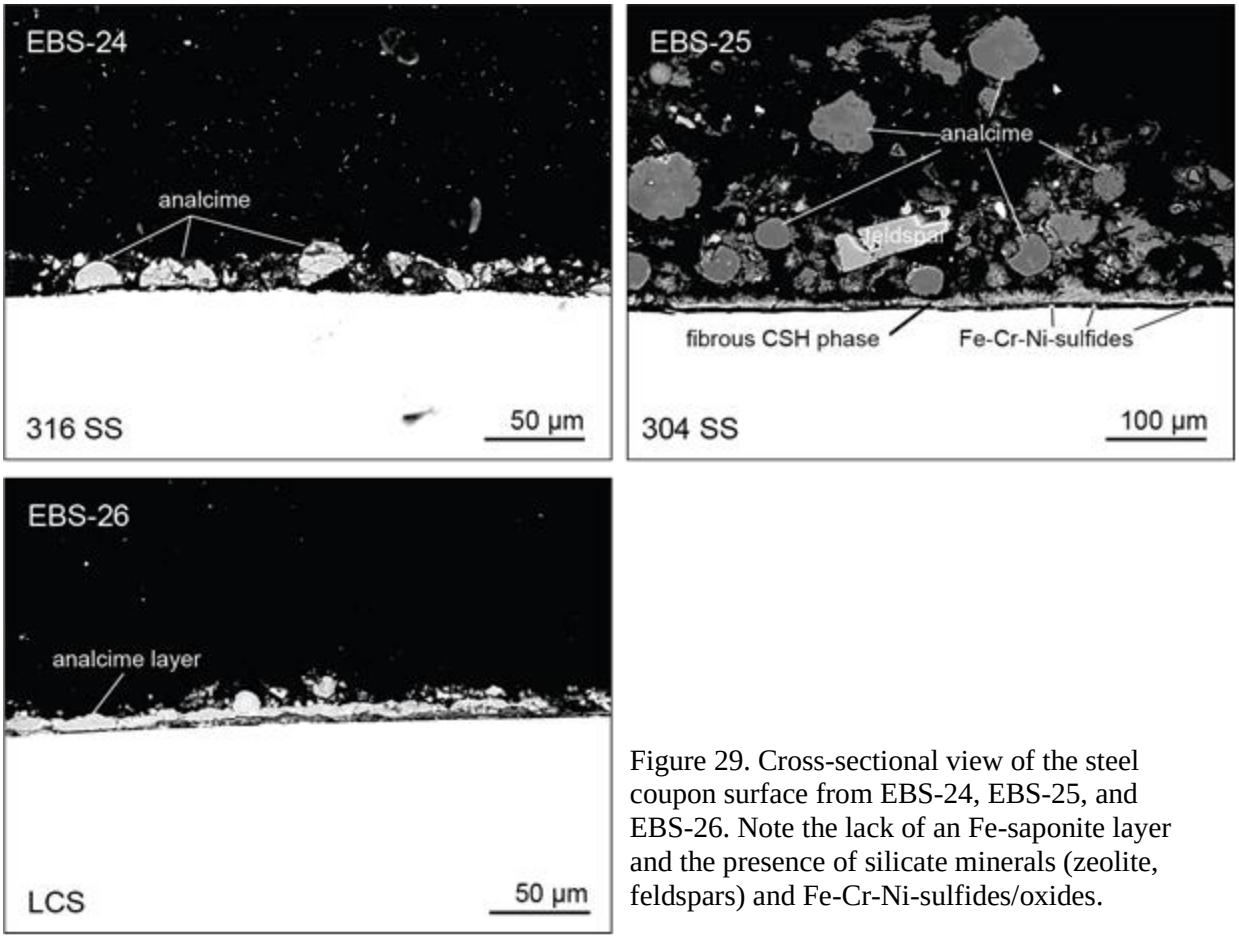

Figure 29. Cross-sectional view of the steel coupon surface from EBS-24, EBS-25, and EBS-26. Note the lack of an Fe-saponite layer and the presence of silicate minerals (zeolite, feldspars) and Fe-Cr-Ni-sulfides/oxides.

In experiments that included ordinary Portland cement powder, different mineral phases were observed at the steel coupon surface. In comparison, in the cement experiments, the steel surface provides a substrate for the formation of zeolite (analcime) and CSH phases. Instead, calcium-silicate-hydrate minerals (e.g., tobermorite), analcime, garronite (Ca-rich zeolite) and amorphous CSH minerals. The alkaline pH of the bulk system and difference in bulk chemistry in the system are reflected in the localized environment around the steel coupons, which ultimately inhibited steel corrosion and instead provided a substrate for the newly precipitated layers of CSH minerals and analcime at the steel interface.

In the cement experiments where circum-neutral pH values were observed (EBS-30 and EBS-31) the mineral phases attached to the steel coupon surface more closely matched the assemblage observed in the Wyoming bentonite + Opalinus Clay experiments (i.e., an oxide layer followed by a layer of Fe-saponite).

4.5.3 Steel Corrosion Summary

The results from the experiments discussed here indicate that the waste container will act as a substrate for mineral growth. At pH values between 4 and 7, we observe surface-bound minerals in response to steel corrosion that likely formed via direct crystallization from the solution in their specific localized environment surrounding the metal plates. The iron in the newly precipitated mineral layers at the steel interface is sourced as the steel corrodes; however, the steel coupons from this study have yet to be evaluated for general and localized corrosion. Future work is needed to address the extent these mineral precipitants influence the engineered barrier performance or the repository system as a whole, and to whether these minerals (e.g., Fe-saponite) will act as a passive protecting layer against further corrosion of the waste containers. In experiments where pH is elevated due to the influence of OPC powder, steel corrosion is inhibited and the surface of the coupons act as substrates for zeolite and CSH mineral crystallization.

4.6 Conclusions

The work in FY21 aimed to further develop concepts for a high-temperature, argillite-hosted repository with respect to: 1) bentonite-cement interaction, 2) bentonite-steel interaction, and 3) novel EBS additives. Characterization of a 6-month experiment and two 8-week experiments were completed during the FY (EBS-27, EBS-28, and EBS-29) and two 6-week experiments were completed (EBS-30 and EBS-31). This report presents new results and interpretations from our series of experiments with Opalinus Clay, Wyoming bentonite, and ordinary Portland cement (EBS-23 through EBS-28, EBS-30, EBS-31), new measurements of mineral (e.g., Fe-saponite, zeolite) growth rates on the surface of reacted steel coupons, and results from our first experiment investigating the use of apatite as a radionuclide isolating additive material.

Concepts developed include:

1. Bentonite stability in argillite:

- Montmorillonite is stable over the experimental time period (6 weeks to 6 months) at circum-neutral pH values and low bulk system [K^+]
- Zeolite formation is observed at 300ºC but not 200ºC
- Zeolite/aluminosilicate mineral reactions buffer the solution chemistry and pH
- Recrystallization of montmorillonite to illite is not observed, zeolite forming reactions are kinetically favored

2. Portland cement effects:

Uncured OPC powder

- The addition of uncured ordinary Portland cement powder results in precursor montmorillonite dissolution and the formation of abundant feldspar, zeolite, CSH, and amorphous phases
- Significant montmorillonite alteration occurs in the experiments with OPC powder, including recrystallization to illite and loss of swelling capacity
- The pH increase observed with the inclusion of OPC powder is temperature dependent: the pH of the cement-bearing experimental system at 200ºC stabilizes at pH (at 25ºC) values around 8 to 9, whereas at 300ºC, pH rapidly drops to ~6.

Cured OPC chip

- Inclusion of cured cement results in different geochemical and mineralogical effects in comparison to OPC powder
- Lower pH values are observed in the experiments with cured Portland cement
- Portlandite dissolution results in early elevated pH values, but pH values stabilize to 6–7 by the second week of experiment time.
- Montmorillonite is likely stable in the experiments with the cured chip.
- Zeolite formation is observed throughout the clay groundmass of the reaction products.

3. Steel-bentonite interface alteration:
   - Mineralization at the steel-bentonite interface varies with system bulk chemistry
   - Fe is transferred to the bentonite buffer in the form of Fe-rich phyllosilicate phases at circum-neutral pH
   - In a cementitious, high-pH environment, Fe-rich aluminosilicate phases are not observed; zeolite and CSH minerals are observed attached to the steel surface.

4. Apatite-bentonite interaction:
   - Preliminary results suggest that apatite was unreactive in the bentonite
   - Minor apatite dissolution may have occurred based on observed phosphate concentrations in reaction fluids

Future research will emphasize the following areas:

- Detailed geochemical modelling of the effects of cement on aqueous geochemistry of the experimental system.
- Incorporation of low-pH cement materials into the argillite experimental system.
- Clay mineral analyses of experiment products with cured cement.
- Conduct investigation into the physical properties of Fe-saponite and other mineral products observed at the steel-bentonite interface.
- Apatite stability in different geochemical EBS environments (i.e., cementitious).
- Incorporate results into generic modeling codes.

5 Argillite International Collaborations

5.1 Horonobe URL Research

5.1.1 Background

The geologic disposal of high-level radioactive waste at the Horonobe Underground Research Center is the focus of this research. Japan initiated a 20-year investigation on deep geologic disposal of high-level radioactive waste in 2000. The Japan Nuclear Cycle Development Institute (JNC) and later the Japanese Atomic Energy Agency (JAEA) have investigated disposal in both crystalline and argillite rock types. The first underground research laboratory (URL) was emplaced in a crystalline rock type, with fresh groundwater, and is located in Mizunami, Gifu. The second URL is located in an argillite rock type, with saline groundwater, and is centered at Horonobe (Hokkaido). Operational activities at the Horonobe URL, including detailed in-situ experiments, were detailed in Hama et al. (2007).

The most recent full scale experimental design was described at the DECOLOVEX 2023 meeting (JAEA, 2021) and is illustrated in Figure 1.

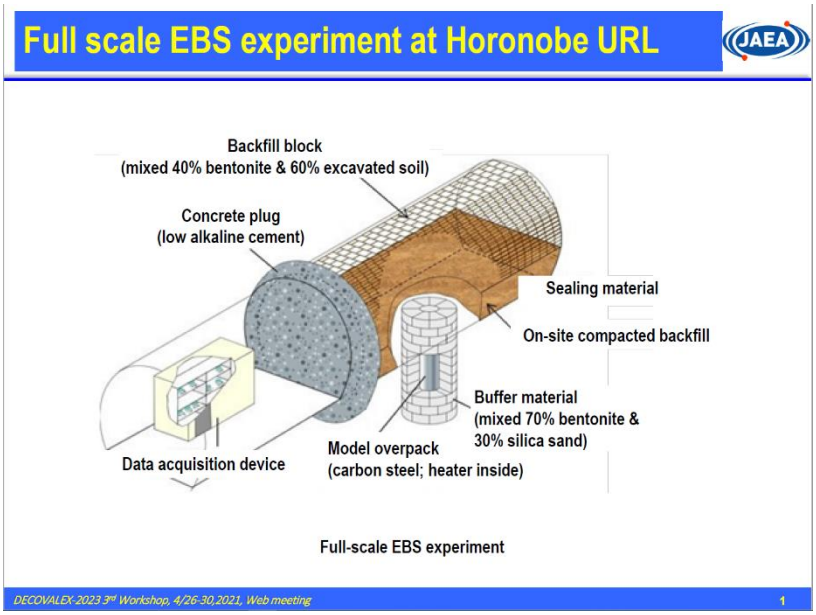

Figure 30. Simplified depiction on the full-scale EBS experiment at the Horonobe URL (JAEA, 2021).

5.1.2 Summary of FY20 Horonobe Report

We requested Kunigel bentonite and target Horonobe URL host rock (Wakkanai Formation) from the JAEA. This request was recommended to our Sandia project managers in November 2019. At present, we have not received an update from our JAEA counterparts as to when the material will be shipped.

In FY20, we performed a literature review and summarized the following: 1). Regional geology of the western coastal plain of Hokkaido, northern Japan. Major documents included geologic maps and stratigraphic columns of the region encompassing the URL (Wei & Seno, 1998; Ishii, 2012; Ishii et al., 2010). 2). Lithology of the Wakkanai and Koetoi Formations (the target URL repository horizon), which were well documented by Iijima and Tada, 1981; Tada and Iijima, 1982, Kemp et al., 2002; Barnes & Milodowski, 2004; Milodowski et al., 2004, Ishii et al., 2010. 3). Regional structural geology, such as faults and large-scale structures were addressed by Kunimari et al. (2010) and Milodowski et al. (2004), and 4). Finally, the water chemistry of the URL area was discussed by Hama et al. (2007). All of these summarized four sections are described in more detail in Caporuscio et al. (2020).

5.1.3 FY21 LANL Experiments

Our initial experimental plan for FY21 was to mimic the full-scale EBS test that is currently underway at the Honorobe URL. The full-scale test includes multiple phases of heating and groundwater injection (Figure 1). The experiments we proposed to run would contain combinations of the following components: Kunigel bentonite (EBS buffer material) + quartz, Wakkanai Formation wall rock, synthetic Wakkanai groundwater (formulated after Hama et al., 2007), and low carbon steel (waste canister material). The experiments will be conducted between 125 to 200°C and at hydrostatic pressure (~150 bar). The synthetic groundwater

composition was developed from water chemistry described by Hama et al. (2007) for the Horonobe area. The full data set was presented in Caporuscio et al. (2020). From the 14 analyses, we restricted the field to Wakkanai Formation waters greater than 300 meters in depth. The resulting seven analyses were then averaged to produce a "synthetic" Wakkanai groundwater (Table 7). This methodology is similar to the one used to develop the synthetic brines (example ERDA-9) used for Waste Isolation Pilot Plant (WIPP) experiments by DOE. Our experiments would provide insight into mineralogical and geochemical changes that may occur in the EBS region.

Table 7: Average synthetic groundwater composition developed to mimic Wakkanai Formation groundwater at depths greater than 300 meters. The composition is an average of seven different groundwater samples with an average depth of 431 m.

	pH	Na^+	K^+	Ca^{2+}	Mg^{2+}	Si	Fe_T	Cl^-	Br-	I^-	SO_4^{--}	HCO_3^-
Synthetic Wakkanai Groundwater	7.1	3577	81.0	100	66.0	26.0	1.0	4740	17.0	12.0	17.0	1745

Aqueous species concentrations in mg/L.

There were logistical problems obtaining the Kunigel bentonite and Wakkanai Formation wall rock from JAEA. After our Sandia National Laboratory contact informed us that samples may be held up for longer than this past year, we made contact with the mining company, Kunimine Kogyo Co., Ltd, in Japan that produces Kunigel V. Upon my request, within one week, one kilogram of Kunigel V1 arrived at Los Alamos National Laboratory on April 30, 2021 from Kunimine Kogyo Co., Ltd.

We plan to run a series of experiments using Kunigel bentonite in FY22 for the Argillite International Collaboration work package. The experiment will be at 200ºC and 150 bar with Kunigel bentonite/quartz sand (70:30 ratio) with or without low carbon steel coupons. The water rock ratio will be set at 11:1. Once the experiments are complete, the mineralogy and geochemistry of the reaction products will be evaluated by a variety of characterization methods (e.g. scanning electron microscopy, X-ray diffraction (XRD), scanning electron microprobe (SEM/EDS), aqueous geochemistry analyses, and modelling).

6 Steel corrosion experiments – FY21

6.1 Background

Steel corrosion with respect to waste canister integrity has been of significant concern to both the SFWST (Spent Fuel and Waste Science and Technology) program and international research programs for decades. The LANL experimental program in FY21 explored the effect of stainless steel welds and surface treatments (i.e., polishing) on corrosion in a high temperature and

pressure EBS environment. The following summarizes previous studies that provide context for the experimental work.

Hanson et al. (2012) performed a gap analysis to evaluate the type(s) of research needed to identify data and modeling needs to develop the technical bases to enable the extended storage of UNF (Used Nuclear Fuel). Additional research is needed for most structures, systems, and components important to safety in more modern fuels and dry storage cask systems. There is also limited data on the effects of high burnup and extended storage times. Research of canister corrosion under a variety of conditions (atmospheric, aqueous, of both welded and bolted casks) was ranked as high importance. Over the years, Sandia National Laboratories (SNL) have studied stainless steel (SS) corrosion at low temperatures and various redox conditions.

Enos et al. (2013) assessed localized corrosion on 304SS due to salt delinquency. Researchers used synthetic sea water as the salt source; however, although they did not control gas phases in the experiments, they recognized that in field conditions other salt components, ammonium, and nitrate are significant in atmospheric aerosols. As a reference point, they collected dust from Calvert Cliffs interim storage site, located near the Chesapeake Bay, where the majority of the dust particles were not salt, but rather terrestrial in nature. Furthermore, they investigated the cause of localized corrosion due to deliquescence of brines and the potential for stifling at elevated temperatures and times up to 100 days. Although localized (crevice) corrosion occurred, the effect of stifling was inconclusive.

Bryan and Enos (2014) produced an interim SNL report on the results of stainless steel corrosion. In summary, the report was a continuation of the Enos et al. (2013) research and centered on four pieces of research. First, they continued a collaboration with the Electric Power Research Institute (EPRI) to collect airborne particles at two other storage sites. The sites, Hope Creek NJ, and Diablo Canyon CA, were located near marine coastal waters. The dust particles collected at Hope Creek, NJ were primarily terrestrial in nature, while the Diablo Canyon particles were more marine salts in composition. Second, they designed and fabricated a full-diameter canister mockup. Third, experimental work was carried out to evaluate crevice corrosion of 304SS in the presence of limited reactants, hoping to prove limited salt loads would limit corrosion penetration over time. However, in experiments of up to 100 days, no stifling occurred. And finally, the fourth project was to design and implement a device to deposit sea salts onto metal surfaces in a controlled manner.

Bryan and Schundelholz (2017) calculated the chemical composition of the brines that form by deliquescence of sea-salt aerosols using thermodynamic methods. With this data, they estimated brine volumes and salt/brine volume ratios as a function of temperature and atmospheric relative humidity. The authors performed experiments of simple brine compositions where they mixed representative brines and measured the physical and electrochemical properties of those brines over a range of temperatures (up to 80ºC). The focus of these experiments was on carbonation of magnesium chloride brines, which are quite corrosive at higher temperatures.

A cooperative study between Ohio State University and SNL (Weirich et al., 2019) investigated the effect of relative humidity (RH) on the corrosion of 304SS exposed to sea salt. In their study, the total corrosion damage accumulation was higher at 40% RH than at 76% RH. These preliminary atmospheric exposure results showed that even though calculation that pit growth at 40% RH should have been slower, a lower anodic current caused by the oxidation allowed the pits to grow similar to the size of the metal exposed to the 76% RH. The researchers concluded

that this phenomenon coupled with a higher pit initiation leads to higher accumulation of steel damage at 40% RH than a RH of 78%.

Chatzidakis et al. (2021) employed neutron diffraction to investigate residual stress behavior in welds. The authors determined that significant tensile residual stresses would occur in welded samples. Following weld repairs, they observed a stress redistribution and introduction of beneficial compressive stresses. By using welding repair techniques, Chatzidakis et al. (2021) believes that through-thickness growth of cracks in the welds may be avoidable.

6.2 Methods

Welded stainless steel and polished stainless steel samples were obtained from SNL. Three experiments were designed to explore the effect of stainless steel welds and polished surfaces on steel corrosion in the argillite system. The starting components and experiment parameters are reported in Table 8. One experiment was completed in FY21 and two experiments are planned to be completed in FY22. The starting solid materials include Wyoming bentonite (powder and granules) and a steel coupon. All experiments have a set water:rock ratio of 11:1 and will be run at 300ºC, 150 bars for 6 weeks. The only variation in experiment parameters will be the types/treatment of stainless steel included.

In all experiments, fluid chemistry is monitored in aqueous samples extracted during and after the experiment. For the completed experiment, solid phase reaction product characterization is ongoing and will include X-ray diffraction, scanning electron and petrologic microscopy (mineralogy and textural observations), and electron microprobe and electron dispersive spectroscopy (mineral phase chemistry). Solid and aqueous phase characterization methods are reported in Appendix A.

Table 8: Initial components and reaction conditions for STL experiments. Initial components and reaction conditions for STL experiments. Abbreviations: SS, stainless steel; WB, Wyoming Bentonite; GW, groundwater.

Exp.	Components	Temp (ºC)	Pressure	Brine	Water:Rock	Run Time
STL-(W)-1	Welded 304SS + WB	300	150 bar	Opalinus GW	11:1	6 weeks
STL-(P)-2*	Polished 316SS + WB	300	150 bar	Opalinus GW	11:1	6 weeks
STL-(P)-3*	Polished 304SS + WB	300	150 bar	Opalinus GW	11:1	6 weeks

* Indicates future experiments

6.2.1 Starting Material

Welded 304SS: The welded sample was originally from the SNL canister mockup (Figure 2). The larger welded 304SS was cut into smaller coupons (Figure 3). Along with Fe, 304SS contains 18 wt.% Cr, 8 wt.% Ni, < 2 wt.% Mn, < 1 wt.% Si, < 0.045 wt. % P, and < 0.03 wt.% S, and < 0.08 wt.% C.

Polished Steel: The 316SS and 304SS polished samples were used in long-term (2-year) corrosion exposure tests in an RH chamber at SNL (Figure 3). The one side was reground with 600 grit sandpaper and pitted extensively (Figure 3). Both samples were cleaned with acetone

prior to use. The 304SS was similar to the welded steel sample, but the 316SS differs in the Cr/Ni ratio. The 316SS is 18.37 wt.% Cr, 12.35 wt.% Ni, 2.26 wt.% Mo, 1.619 wt.% Mn, 0.5093 wt.% Si, and 0.175 wt.% Cu.

Wyoming bentonite. The bentonite used in the present study is unprocessed and was provided by Bentonite Performance Minerals LLC from Colony, Wyoming, U.S.A. It is composed dominantly of Na-montmorillonite (general composition: $Na_{0.33}(Al,Mg)_2(Si_4O_{10})(OH)_2 \cdot nH_2O$), lesser clinoptilolite and feldspar, and minor biotite, pyrite, quartz, opal, and sulfide minerals.

Opalinus Clay synthetic groundwater. Synthetic groundwater was created to mimic the pore water found in the Mont Terri Opalinus Clay (Pearson et al., 2003). This solution has a pH of around 7.5 and is a Na-Cl type solution. The initial chemistry is reported in Table 3.

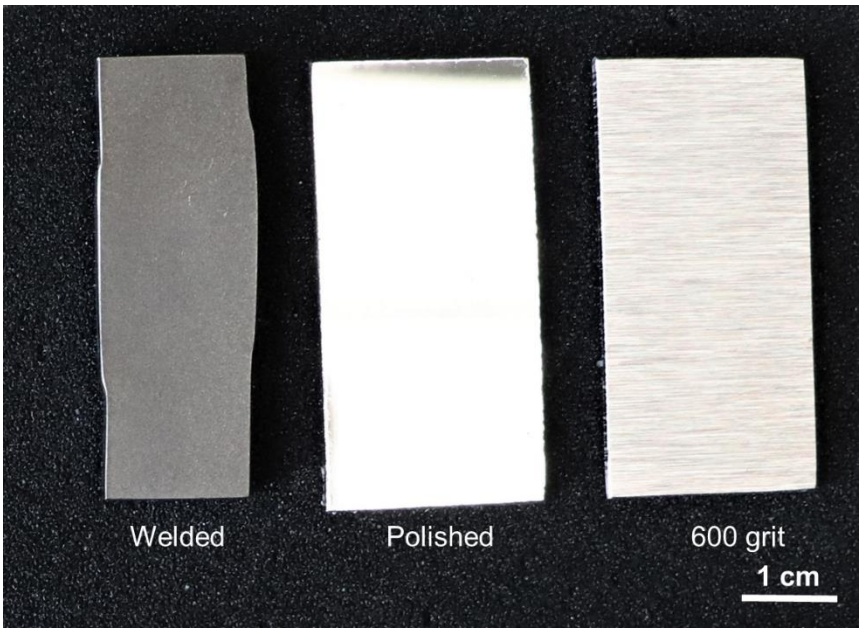

Figure 31. Examples of the welded, polished, and reground (600 grit) coupons used in the STL experiments.

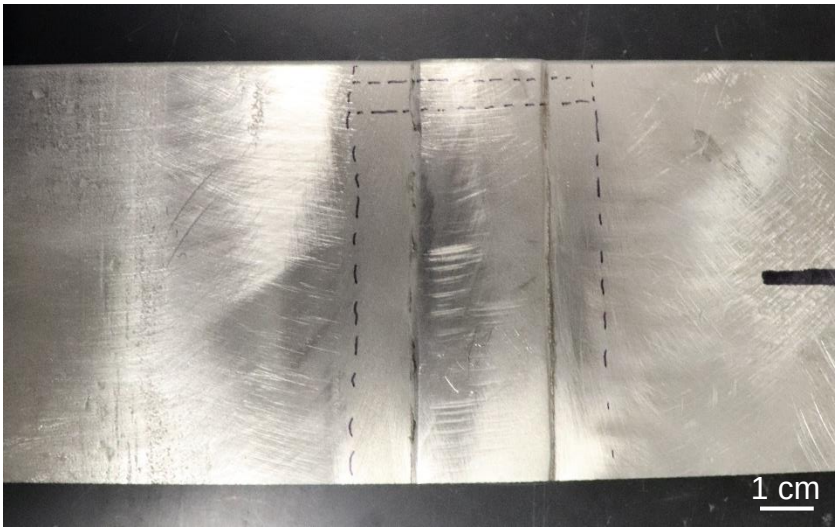

Figure 32. Original welded steel sample with cut lines. The left and right dashed lines indicate the cut to include the weld and unaltered 304SS. The smaller center dotted lines are cuts to isolate coupons across the weld that will be suitable for the experiment.

6.2.2 Current Status

The steel corrosion experiments are currently ongoing. STL-(W)-1 is the only completed experiment and is undergoing characterization. More data will be provided in FY22 report deliverables.

7 Acknowledgements

We would like to thank Oana Marina for water chemistry analyses and Rose Harris for the XRF analyses. Scanning electron microscopy facilities were provided by the Materials Science and Technology group at Los Alamos National Laboratory. Dr. Lindsey Hunt at the University of Oklahoma was instrumental in the obtaining of EMP analyses. Funding was through the Department of Energy's Spent Fuel and Waste Science and Technology.

8. References

Adler, M., Mäder, U. K., and Waber, H. N. (1999). High-pH alteration of argillaceous rocks: an experimental study. Schweizerische Mineralogische und Petrographische Mitteilungen, 79, 445–454.

Alonso, M. C., Calvo, J. L. G., Cuevas, J., Turrero, M. J., Fernández, R., Torres, E., and Ruiz, A. I. (2017). Interaction processes at the concrete-bentonite interface after 13 years of FEBEX-Plug operation. Part I: Concrete alteration. Physics and Chemistry of the Earth, Parts A/B/C, 99, 38-48.

Balmer, S., Kaufhold, S. and Dohrmann, R. (2017). Cement-bentonite-iron interactions on small scale tests for testing performance of bentonites as a barrier in high-level radioactive waste repository concepts. Applied Clay Science, 135, 427-436.

Barnes, R. P. and Milodowski, A. E. (2004): Characterisation of Fractures in Horonobe. Boreholes HDB-6, HDB-7 and HDB-8: Results of core examination, February 2004. BGS Report CR/04/043, BGS, Keyworth, UK.

Bayliss, P. and Levinson, A. A. (1970). Clay-mineralogy and boron determinations of the shales from the Reindeer well, Mackenzie River delta, NWT, Canada. Bulletin of Canadian Petroleum Geology, 18(1), 80-83.

Betkowski, W. B., Harlov, D. E., and Rakovan, J. F. (2016). Hydrothermal mineral replacement reactions for an apatite-monazite assemblage in alkali-rich fluids at 300–600°C and 100 MPa. American Mineralogist, 101, 2620-2637.

Bish, D. L. and Aronson, J. L. (1993). Paleogeothermal and paleohydrologic conditions in silicic tuff from Yucca Mountain, Nevada. Clays and Clay Minerals, 41(2), 148-161.

Bossart, P.J. and Thury, M. (2008). Mont Terri Rock Laboratory: Project, Programme 1996 to 2007 and Results, no. 3. Reports of the Swiss Geological Survey, Wabern.

Bossart, P. and Milnes, A. G. (2017). Mont Terri Rock Laboratory, 20 Years: Two Decades of Research and Experimentation on Claystones for Geological Disposal of Radioactive Waste (Vol. 5): Birkhäuser.

Bryan, C. R., Enos, D. G., Brown, N., Brush, L., Miller, A. and Norman, K. (2011). Engineered Materials Performance: Gap Analysis and Status of Existing Work. FCRD-USED-2011-000407. US Department of Energy.

Bryan, C., and Enos, D. (2014) Results of Stainless Steel Corrosion Studies and Environmental Sample Investigations. Sandia National Laboratory, DOE - Used Fuel Disposition Campaign, FCRD-UFD-2014-000055, SAND2014-20347 O

Bryan, C., and Schindelholz, E. (2017) Properties of Brines formed by Deliquescence of Sea-Salt Aerosols. Sandia National Laboratory, SAND2017-11231C.

Calvo, J. G., Hidalgo, A., Alonso, C. and Luco, L. F. (2010). Development of low-pH cementitious materials for HLRW repositories: Resistance against ground waters aggression. Cement and Concrete Research, 40(8), 1290-1297.

Cameron, M., Wang, L. M., Crowler, K. D. and Ewing, R. C. (1992). HRTEM observations on electron-irradiation damage in F-apatite. In G.W. Bailey, J. Bentley, and A. Small, Eds., Proceedings of the 50th Annual Meeting of the Electron Microscopy Society of America, p. 378. San Francisco Press, California.

Caporuscio, F. A., Cheshire, M. C., Rearick, M. S., and Jove Colón, C. (2014). LANL argillite EBS experimental program 2014. (FCRD-USED-2014-000491). Los Alamos National Lab. (LANL), Los Alamos, NM (United States).

Caporuscio, F. A., Cheshire, M. C., Palaich, S., Norskog, K. and Jove Colón, C. (2015). Argillite Disposal R&D-LANL 2015. Summary of baseline experiments for generic repository engineered barriers. (FY 2015). (FCRD-UFD-2015-000356, LA-UR-15-26110). Los Alamos National Lab. (LANL), Los Alamos, NM (United States).

Caporuscio, F.A., and Norskog, K. (2017). Disposal Overpack and Waste Package Options – LANL Petrographic descriptions of FEBEX Section 49 - Dismantlement Phase operation. (SFWD-SFWST-2017-000116, LA-UR -17-28576) Los Alamos National Lab. (LANL), Los Alamos, NM (United States).

Caporuscio, F. A., Sauer, K. B., Houser, L., Rock, M. (2018). Argillite R&D and International Collaborations – LANL. (SF-18LA01030102 Rev.2/SF-18LA01030106, LA-UR-18-27277) Los Alamos National Lab. (LANL), Los Alamos, NM (United States).

Caporuscio, F. A., Sauer, K. B., Rock, M. (2019). Argillite Disposal R&D – LANL (FY19). (SF-19LA01030801/SF-19LA01030805, LA-UR-19-24397). Los Alamos National Lab. (LANL), Los Alamos, NM (United States).

Caporuscio, F. A., Sauer, K. B., Rock, M. (2019). Argillite Disposal R&D – LANL (FY20). (SF-21LA01030101 Rev2/ SF-21LA01030102, LA-UR-20-24308). Los Alamos National Lab. (LANL), Los Alamos, NM (United States).

Caporuscio, F.A., Sauer, K.B., and Rock, M.J. (2020) Argillite Disposal R&D and Argillite International Collaborations – LANL. (SF-20LA01030102 / SF-20LA01030106, LA-UR-20-24308). Los Alamos National Lab. (LANL), Los Alamos, NM (United States).

Chatzidakis, S., Tang, W., Miller, R., Payzant, A., Bunn, J., Bryan, C., Scaglione, J., and Wang, J-A. (2021) Neutron diffraction illustrates residual stress behavior of welded alloys used as radioactive confinement boundary. Intl Jour of Press Vessels and Piping, 191, 104348

Chen, Y. G., Sun, Z., Cui, Y. J., Ye, W. M. and Liu, Q. H. (2019). Effect of cement solutions on the swelling pressure of compacted GMZ bentonite at different temperatures. Construction and Building Materials, 229, 116872.

Chermak, J.A. (1992). Low temperature experimental investigation of the effect of high pH NaOH solutions on the opalinus shale, Switzerland. Clays and Clay Minerals, 40, 650-658.

Cheshire, M. C., Caporuscio, F. A., Jove Colón, C. and McCarney, M. K. (2013). Alteration of clinoptilolite into high-silica analcime within a bentonite barrier system under used nuclear fuel repository conditions. Proceeding from the 14th International High-Level Radioactive Waste Management Conference, 410-415.

Cheshire, M. C., Caporuscio, F. A., Jove Colón, C. and McCarney, M. K. (2014). Bentonite Clay evolution at elevated pressures and temperatures: An experimental study for generic nuclear repositories. American Mineralogist, 99, 1662-1675.

Cheshire, M. C., Caporuscio, F. A., Jove Colón, C. and Norskog K. E. (2018). Fe-saponite growth on low-carbon and stainless steel in hydrothermal-bentonite experiments. Journal of Nuclear Materials, 2018. 511: p. 353-366.

Chew, D. M., Babechuk, M. G., Cogné, N., Mark, C., O'Sullivan, G. J., Henrichs, I. A., ... and McKenna, C. A. (2016). (LA, Q)-ICPMS trace-element analyses of Durango and McClure Mountain apatite and implications for making natural LA-ICPMS mineral standards. Chemical Geology, 435, 35-48.

Chipera, S. J. and Bish, D. L. (2002). FULLPAT: a full-pattern quantitative analysis program for X-ray powder diffraction using measured and calculated patterns. Journal of Applied Crystallography, 35, 744–749.

Chung, F. H. (1974). Quantitative interpretations of X-ray diffraction patterns of mixtures. I. Matrix flushing method for quantitative multicomponent analysis. Journal of Applied Crystallography, 7, 519-525.

Cuevas, J., De La Villa, R. V., Ramírez, S., Sánchez, L., Fernández, R. and Leguey, S. (2006). The alkaline reaction of FEBEX bentonite: a contribution to the study of the performance of bentonite/concrete engineered barrier systems. Journal of Iberian Geology, 32(2), 151-174.

De La Villa, R. V., Cuevas, J., Ramírez, S. and Leguey, S. (2001). Zeolite formation during the alkaline reaction of bentonite. European Journal of Mineralogy, 13(3), 635-644.

Dohrmann, R. and Kaufhold, S. (2014). Cation exchange and mineral reactions observed in MX 80 buffer samples of the Prototype repository in situ experiment in Äspö, Sweden. Clays and Clay Minerals. 62, 357–373. https://doi.org/10.1346CCMN.2014.0620501.

Dohrmann, R., Kaufhold, S. and Lundqvist, B. (2013). The role of clays for safe storage of nuclear waste. Pp. 677–710 in: Developments in Clay Science (Vol. 5). Elsevier. doi: https://doi.org/10.1016/B978-0-1201 08-098259-5.00024-X.

Dolder, F., Mäder, U. and Jenni, A. (2014). Stability of bentonite under high-pH conditions. https://www.researchgate.net/profile/Florian_Dolder/publication/274390805_Stability_of_bentonite_under_high-pH_conditions/links/551ed2860cf2f9c1304da570.pdf

Eberl, D. D. (1993). Three zones for illite formation during burial diagenesis and metamorphism. Clays and Clay Minerals, 41(1), 26-37.

Enos, D., Bryan, C., and Norman, K. (2013) Data Report on Corrosion Testing of Stainless Steel SNF Storage canisters. Sandia National Laboratory, DOE - Used Fuel Disposition Campaign, FCRD-UFD-2013-000324

Fernández, R., Cuevas, J., Sánchez, L., de la Villa, R. V. and Leguey, S. (2006). Reactivity of the cement–bentonite interface with alkaline solutions using transport cells. Applied Geochemistry, 21(6), 977-992.

Fernández, R., Cuevas, J., & Mäder, U. K. (2009a). Modelling concrete interaction with a bentonite barrier. European Journal of Mineralogy, 21(1), 177-191.

Fernández, R., Mäder, U. K., Rodríguez, M., De La Villa, R. V., & Cuevas, J. (2009b). Alteration of compacted bentonite by diffusion of highly alkaline solutions. European Journal of Mineralogy, 21(4), 725-735.

Fernández, R., González, L., Ruiz, A. I., and Cuevas, J. (2014). Nature of C-(A)-S-H Phases Formed in the Reaction Bentonite/Portlandite. Journal of Geochemistry, vol. 2014, Article ID 145425, 8 pages, 2014. https://doi.org/10.1155/2014/145425.

Fernandez, Raúl, Ruiz, A. I. and Cuevas, J. (2016). Formation of C-A-S-H phases from the interaction between concrete or cement and bentonite. Clay Minerals, 51(02), 223-235. doi:10.1180/claymin.2016.051.2.09

Fernández, R., Torres, E., Ruiz, A. I., Cuevas, J., Alonso, M. C., Calvo, J. L. G., ... and Turrero, M. J. (2017). Interaction processes at the concrete-bentonite interface after 13 years of FEBEX-Plug operation. Part II: Bentonite contact. Physics and Chemistry of the Earth, Parts A/B/C, 99, 49-63.

Fernandez, A. M., Kaufhold, S., Sánchez-Ledesma, D. M., Rey, J. J., Melón, A., Robredo, L. M., ... and Clavero, M. A. (2018). Evolution of the THC conditions in the FEBEX in situ test after 18 years of experiment: Smectite crystallochemical modifications after interactions of the bentonite with a C-steel heater at 100° C. Applied Geochemistry, 98, 152-171.

Ferrage, E., Vidal, O., Mosser-Ruck, R., Cathelineau, M. and Cuadros, J. (2011). A reinvestigation of smectite illitization in experimental hydrothermal conditions: Results from X-ray diffraction and transmission electron microscopy. American Mineralogist, 96, 207-223.

Frape, S. K., Blyth, A., Blomqvist, R., McNutt, R. H., Gascoyne, M. (2003). 5.17 - deep fluids in the continents: II. Crystalline rocks A2 - holland, heinrich D, in: K.vK. Turekian (Ed.), Treatise on Geochemistry, Pergamon, Oxford, 541-580.

Gailhanou, H., Lerouge, C., Debure,M., Gaboreau, S., Gaucher, E. C., Grangeon, S., Grenèche, J.M., Kars,M.,Madé, B.,Marty, N. C.M. and Warmont, F. (2017). Effects of a thermal perturbation on mineralogy and pore water composition in a clay-rock: an experimental and modeling study. Geochimica et Cosmochimica Acta, 197, 193–214. https://doi.org/10.1016/j.gca.2016.10.004.

Guillaume, D., Neaman, A., Cathelineau, M., Mosser-Ruck, R., Peiffert, C., Abdelmoula, M., Dubessy, J., Villieras, F., Baronnet, A. and Michau, N. (2003). Experimental synthesis of chlorite from smectite at 300°C in the presence of metallic Fe. Clay Minerals, 38, 281-302.

Hama, K., Kunimaru, T., Metcalfe, R., and Martin, A. J. (2007) The hydrochemistry of argillaceous rock formations at the Horonobe URL site, Japan. Phys. Chem. Earth, 32, 170-180.

Hanson, B., Alsaed, H., Stockman, C., Enos, D., Meyer., R, Sorenson, K. (2012) Gap Analysis to support extended storage of Used Nuclear Fuel Rev.0. Pacific Northwest National Laboratory, DOE - Used Fuel Disposition Campaign, PNNL -20509

Hardin, Ernest, Hadgu, Teklu, and Clayton, Daniel James. (2015). Cavern/Vault Disposal Concepts and Thermal Calculations for Direct Disposal of 37-PWR Size DPCs. United States: N. Web. doi:10.2172/1172177.

Heimann, R. B. (1993). Brønsted acidification observed during hydrothermal treatment of a calcium montmorillonite. Clays and Clay Minerals, 41, 718–725. https://doi.org/10.1346/CCMN.1993.0410610.

Hofmann, H., Bauer, A. and Warr, L. N. (2004). Behavior of smectite in strong salt brines under conditions relevant to the disposal of low-to medium-grade nuclear waste. Clays and Clay Minerals, 52, 14–24. https://doi.org/10.1346/CCMN.2004.0520102.

Honty, M., Wang, L., Osacký, M., Uhlík, P., Czímerová, A., & Madejová, J. (2012). Experimental interactions of the Opalinus Clay and Boom Clay with various repository relevant solutions at 90 C under closed conditions. Applied Clay Science, 59, 50–63. https://doi.org/10.1016/j.clay.2012.02.011.

Iijima, A. and Tada, R. (1981). Silica diagenesis of Neogene diatomaceous and volcaniclastic sediments in northern Japan. Sedimentology, 28, 185-200.

Ishii, E. (2012). Microstructure and origin of faults in siliceous mudstone at the Horonobe Underground Research Laboratory site, Japan. Jour. Struc. Geol., 34, 20-29.

Ishii, E., Funaki, H., Tokiwa, T., and Ota, K. (2010). Relationship between fault growth mechanism and permeability variations with depth of siliceous mudstones in northern Hokkaido, Japan. Jour. Struc. Geol., 32, 1792-1805.

Jacques, D., Wang, L., Martens, E. and Mallants, D. (2010). Modelling chemical degradation of concrete during leaching with rain and soil water types. Cement and Concrete Research, 40(8), 1306-1313.

JAEA (2021) Presentation at DECOVALEX-2023 3rd Workshop, April 23-30, 2021, Web meeting.

Johannesson, L. E., Börgesson, L., Goudarzi, R., Sandén, T., Gunnarsson, D. and Svemar, C. (2007). Prototype repository: A full scale experiment at Äspö HRL. Physics and Chemistry of the Earth, Parts A/B/C, 32, 58–76. https://doi.org/10.1016/j.pce.2006.04.027. 1252

Johnston, R.M. and Miller, H.G. (1984). The effect of pH on the stability of smectite (No. AECL–8366). Atomic Energy of Canada Ltd.

Karnland, O. (1997). Cement/bentonite interaction. Results from 16 month laboratory tests (No. SKB-TR--97-32). Swedish Nuclear Fuel and Waste Management Co.

Karnland, O., Olsson, S., Nilsson, U. and Sellin, P. (2007). Experimentally determined swelling pressures and geochemical interactions of compacted Wyoming bentonite with highly alkaline solutions. Physics and Chemistry of the Earth, Parts A/B/C, 32(1-7), 275-286.

Kaufhold, S. and Dohrmann, R. (2009). Stability of bentonites in salt solutions | sodium chloride. Applied Clay Science, 45, 171–177. https://doi.org/10.1016/j.clay.2009.04.011.

Kaufhold, S. and Dohrmann, R. (2010). Stability of bentonites in salt solutions: II. Potassium chloride solution—Initial step of illitization? Applied Clay Science, 49, 98–107. https://doi. org/10.1016/j.clay.2010.04.009.

Kaufhold, S., Dohrmann, R. and Ufer, K. (2020). Determining the extent of bentonite alteration at the bentonite/cement interface. Applied Clay Science, 186, 105446.

Kemp, S. J., Cave, M. R., Hodgkinson, E., Milodowski, A. E. and Kunimaru, T. (2002). Mineralogical Observations and Interpretation of Porewater Chemistry from the Horonobe Deep Boreholes HDB-1 and HDB-2, Hokkaido, Japan. BGS Report CR/02/303, BGS, Keyworth, UK.

Khalifa, A. Z., Cizer, Ö., Pontikes, Y., Heath, A., Patureau, P., Bernal, S. A., & Marsh, A. T. (2020). Advances in alkali-activation of clay minerals. Cement and Concrete Research, 132, 106050.

Kloprogge, J. T., Komarneni, S. and Amonette, J. E. (1999). Synthesis of Smectite Clay Minerals: A Critical Review. Clay and Clay Minerals, 47, 529–554.

Konzett, J., Rhede, D., and Frost, D. J. (2012) The high PT stability of apatite and Cl partitioning between apatite and hydrous potassic phases in peridotite: an experimental study to 19 GPa with implications for the transport of P, Cl and K in the upper mantle. Contributions to Mineralogy and Petrology volume 163, pages 277–296.

Krejzler, J., and Narbutt, J. (2003) Adsorption of strontium, europium, and americium(III) ions on a novel adsorbent Apatite II. Nukleonika, 48, 171–175.

Kunimaru, T., Ota, K., Alexander, W. R., and Yamamoto, H. (2010). Groundwater/Porewater Hydrochemistry at Horonobe URL: Data Freeze I - Preliminary Data Quality Evaluation for Boreholes HDB-9, 10 and 11 - Geological Isolation Research and Development Directorate, Japan Atomic Energy Agency, JAEA-Research 2010-035.

Kursten, B., Cornelis, B., Labat, S. and Van Iseghem, P. (1996). Geological Disposal of Conditioned High-Level and Long Lived Radioactive Waste. In situ experiments, Report R-3121, SCK•CEN (Mol, Belgium).

Kursten, B., Cornelis, B., Labat, S. and Van Iseghem, P. (1997). Completion of the Corrosion Programme in Boom Clay – in situ experiments, Report EUR-17105, SCK•CEN (Mol, Belgium).

Kursten, B., Smailos, E., Azkarate, I., Werme, L., Smart, N.R. and Santarini, G. (2004). COBECOMA. State of the art document on the Corrosion Behaviour of Container Materials.

Larsen M.J., Jensen, S.J. (1989) Stability and mutual conversion of enamel apatite and brushite at 20 °C as a function of pH of the aqueous phase. Archive Oral Biology, 34, 963-968.

Lothenbach, B., Scrivener, K. and Hooton, R. D. (2011). Supplementary cementitious materials. Cement and concrete research, 41(12), 1244-1256.

Lukens, W. W., Moore, R. C., and Holt, K.C. (2006) Workshop on Development of Radionuclide Getters for the Yucca Mountain Waste Repository: Proceedings. Sandia Report, SAND2006-0947. Sandia National Laboratory, Albuquerque, N.M. 68pp.

Madsen, F.T. (1998). Clay mineralogical investigations related to nuclear waste disposal. Clay Minerals, 33, 109-129.

Martin, P. L., Barcala, J. M. and Huertas, F. (2006). Large-scale and long-term coupled thermo-hydro-mechanic experiments with bentonite: the FEBEX mock-up test. Journal of Iberian Geology, 32, 259–282.

Martinez, V., Abós, H. and García-Siñeriz, J. L. (2016). FEBEXe: Final Sensor Data Report (FEBEX "in situ" Experiment) - Arbeitsbericht NAB 16-19, National Cooperative for the Disposal of Radioactive Waste (NAGRA), Wettingen, Switzerland.

Meldrum, A., Wang, L.M., and Ewing, R.C. (1997) Electron-irradiation-induced phase segregation in crystalline and amorphous apatite: A TEM study. American Mineralogist, (82), 858–869.

Meunier, A., Velde, B., and Griffault, L. (1998). The reactivity of bentonites: A Review. An application to clay barrier stability for nuclear waste storage. Clay Minerals, 33, 187-196.

Milodowski, A. E., Barnes, R. P., Kemp, S. J., Bouch, J. and Wagner, D. (2004). Characterisation of fractured rock and fracture mineralisation. Horonobe Boreholes HDB-6, HDB-7 and HDB-8: Final report. BGS Report CR/04/251, BGS, Keyworth, UK. 8.

Minoura, K, Susaki, T and Horiuchi, K. (1996). Lithification of biogenic siliceous sediments: Evidence from Neogene diatomaceous sequences of northeast Japan. Sedimentary Geology, 107, 45-59.

Moore, D. M. and Reynolds, R.C. (1989). X-ray Diffraction and the identification and analysis of clay minerals. Oxford University Press, New York, New York, 377.

Moore, R. C., Zhao, H., Sanchez, C. A., Holt, K. C., Salas, F., Hasan, A. A. M. and Lucero, D. A. (2002). In situ formation of apatite in soil and groundwater for containment of radionuclides and heavy metals (No. SAND2002-3642). Sandia National Labs., Albuquerque, NM (US); Sandia National Labs., Livermore, CA (US).

Mosser-Ruck, R., Cathelineau, M., Baronnet, A. and Trouiller, A. (1999). Hydrothermal reactivity of K-smectite at 300°C and 100 bar: dissolution-crystallization process and non-expandable dehydrated smectite formation. Clay Minerals, 34, 275–290.

Mosser-Ruck, R., Cathelineau, M., Guillaume, D., Charpentier, D., Rousset, D., Barres, O., and Michau, N. (2010). Effects of Temperature, pH, and Iron/Clay and Liquid/Clay Ratios on Experimental Conversion of Dioctahedral Smectite to Berthierine, Chlorite, Vermiculite, or Saponite. Clays and Clay Minerals, 58, 280-291.

Mosser Ruck, R., Pignatelli, I., Bourdelle, F., Abdelmoula, M., Odile Barres, O., Guillaume, D., Charpentier, D., Rousset, D., · Cathelineau, M., and Michau, N. (2016). Contribution of long term hydrothermal experiments for understanding the smectite to chlorite conversion in geological environments. Contributions to Mineralogy and Petrology, 171, 97-118.

Müller, H.R. et al. (2018) Implementation of the full-scale emplacement (FE) experiment at the Mont Terri rock laboratory. In: Mont Terri Rock Laboratory, 20 Years (P. Bossart and A.Milnes, editors). Swiss Journal of Geosciences Supplement, vol 5. Birkhäuser, Cham. https://doi.org/10.1007/978-3-319-70458-6_15

NAGRA (2002). Technischer Bericht 02-03, Projekt Opalinuston: Synthese der geowissenschaftlichen Untersuchungsergebnisse, December 2002.

Neuhoff, P. S., & Ruhl, L. S. (2006). Mechanisms and geochemical significance of Si–Al substitution in zeolite solid solutions. Chemical Geology, 225, 373–387.

Omel'yanenko, B. I., Livshits, T. S., Yudintsev, S. V. and Nikonov, B. S. (2007). Natural and artificial minerals as matrices for immobilization of actinides. Geology of Ore Deposits, 49(3), 173-193.

Pearson, F.J., Arcos, D., Bath, A., Boisson, J.-Y., Fernandez, A.M., Gabler, H.-E., Gaucher, E., Gautschi, A., Griffault, L., Hernan, P., and Waber, H.N. (2003). Mont Terri Project-geochemistry of water in the opalinus clay formation at the Mont Terri Rock Laboratory. Reports of the Federal Office for Water and Geology (FOWG), Geology Series No. 5.

Pouchou, J. L. and Pichoir, F. (1985). "PAP" φ(ρz) correction procedure for improved quantitative microanalysis. Microbeam Analysis, Ed. Armstrong, J.T., San Francisco Press, 104-106.

Pusch, R. (1979). Highly compacted sodium bentonite for isolating rock-deposited radioactive waste products. Nuclear Technology, 45, 153-157.

Pusch, R. (2008). Geological Storage of Radioactive Waste. Springer-Verlag, Berlin, Germany, 379.

Pusch, R. and Madsen, F. T. (1995). Aspects on the illitization of the Kinnekulle bentonites. Clays and Clay Minerals, 43(3), 261-270.

Pusch, R. and Kasbohm, J. (2002). Alteration of MX-80 by hydrothermal treatment under high salt content conditions. Svensk Kärnbränslehantering Technical Report, TR-02-06, 44.

Pusch, R. Takase, H., and Benbow, S. (1998) Chemical Processes causing cementation in heat-affected smectite- the Kinnekulle bentonite. Svensk Kärnbränslehantering Technical Report, TR-98-25, 62.

Redkin, A. F. and Hemley, J. J. (2000). Experimental Cs and Sr sorption on analcime in rock-buffered systems at 250–300 C and Psat and the thermodynamic evaluation of mineral solubilities and phase relations. European Journal of Mineralogy, 12(5), 999-1014.

Rigali, M.J., Brady, P.V., and Moore, R.C. (2016). Radionuclide removal by apatite. Am Min, 101, 2611–2619.

Sauer K., Caporuscio, F., Rock, M., Cheshire, M. and Jove Colon, C. (2020). Hydrothermal interactions of Wyoming bentonite and Opalinus clay. Clay and Clay Minerals, in press.

Savage, D., Noy, D., & Mihara, M. (2002). Modelling the interaction of bentonite with hyperalkaline fluids. Applied Geochemistry, 17(3), 207-223.

Savage, D., Watson, C., Benbow, S. and Wilson, J. (2010). Modelling iron-bentonite interactions. Applied Clay Science, 47(1-2), 91-98.

Savage, D., Wilson, J., Benbow, S., Sasamoto, H., Oda, C. and Walker, C. (2019). Natural systems evidence for the effects of temperature and the activity of aqueous silica upon montmorillonite stability in clay barriers for the disposal of radioactive wastes. Applied Clay Science, 179, 105146. https://doi.org/10.1016/j.clay.2019.105146.

Schlegel, M. L., Bataillon, C., Benhamida, K., Blanc, C., Menut, D. and Lacour, J. L. (2008). Metal corrosion and argillite transformation at the water-saturated, high-temperature iron–clay interface: a microscopic-scale study. Applied Geochemistry, 23(9), 2619-2633.

Sellin, P., & Leupin, O. (2014). The use of clay as an engineered barrier in radioactive waste management – a review. Clays and Clay Minerals, 61, 477–498. https://doi.org/10.13461361/CCMN.2013.0610601.

Seyfried, J.R., Janecky, D.R., and Berndt, M.E. (1987). Rocking autoclaves for hydrothermal experiments II. The flexible reaction-cell system. Hydrothermal Experimental Techniques, Eds. Ulmer, G.C. and Barnes, H.L. John Wiley & Sons, 216-239.

Smailos, E., Cuñado, M. A., Azkarate, I., Kursten, B. and Marx, G. (2002). Long-Term Performance of Candidate Materials for HLW/Spent Fuel Disposal Containers, Report FZKA 6706, FZK.INE (Karlsruhe, Germany).

Smart, N. R., Fennell, P. A. H., Rance, A. P., Winsley, R. J., Reddy, B. and Kursten, B. (2011). Experimental studies of the effect of irradiation on the anaerobic corrosion of carbon steel in relation to the Belgian supercontainer concept. In EPJ Web of Conferences (Vol. 12, p. 02003). EDP Sciences.

Smart N. R., Naish C. C. And Pritchard A. M. (1999). Corrosion Principles for the Assessment of Stainless Steel Radioactive Waste Containers, Report AEAT-1337, issue C, AEAT Technologye (Harwell, UK).

Smyth, J.R. (1982). Zeolite stability constraints on radioactive waste isolation in zeolite-bearing volcanic rocks. Journal of Geology, 90, 195-201.

Środoń, J. (1980). Precise identification of illite/smectite interstratifications by X-ray powder diffraction. Clays and Clay Minerals, 28, 401-411.

Soler, J.M. (1998). Reactive transport modelling of the interaction between a high pH plume and a fractured marl. V.M. Goldschmidt Abstracts, Toulouse. Min. Mag. 62A, 1427–1428.

Steefel, C. I. and Lichtner, P. C. (1994). Diffusion and reaction in rock matrix bordering a hyperalkaline fluid-filled fracture. Geochimica et Cosmochimica Acta, 58(17), 3595-3612.

Steefel, C. I. and Lichtner, P. C. (1998). Multicomponent reactive transport in discrete fractures: II: Infiltration of hyperalkaline groundwater at Maqarin, Jordan, a natural analogue site. Journal of Hydrology, 209(1-4), 200-224.

Tada, R. and Iijima, A. (1982). Petrology and diagenetic changes of Neogene siliceous rocks in northern Japan. Journal of Sedimentary Petrology, 53, 911–930.

Takase, H. (2004). Discussion on PA model development for bentonite barriers affected by chemical interaction with concrete: do we have enough evidence to support bentonite stability? International Workshop on Bentonite–Cement Interaction in Repository

Environments, Nuclear Waste Management Organisation of Japan (NUMO), NUMO Report TR-04-05 (2004), pp. 172-177

Taubald, H., Bauer, A., Schäfer, T., Geckeis, H., Satir, M. and Kim, J. I. (2000). Experimental investigation of the effect of high-pH solutions on the Opalinus Shale and the Hammerschmiede Smectite. Clay Minerals, 35(3), 515-524.

Watson, C., Benbow, S., & Savage, D. (2007). Modelling the interaction of low pH cements and bentonite. Issues affecting the geochemical evolution of repositories for radioactive waste (No. SKI-R--07-30). Swedish Nuclear Power Inspectorate.

Watson, C., Hane, K., Savage, D., Benbow, S., Cuevas, J. and Fernandez, R. (2009). Reaction and diffusion of cementitious water in bentonite: results of 'blind' modelling. Applied Clay Science, 45(1-2), 54-69.

Watson, C., Wilson, J., Savage, D. Norris, S. (2018). Coupled reactive transport modelling of the international Long-Term Cement Studies project experiment and implications for radioactive waste disposal. Applied Geochemistry, 97, 134-146.

Weirich, T.D., Srinivasan, J., Taylor, J.A., Melia, M., A., Noell, P., J., Bryan, C.,R., Frankel, G.,S., Locke, J.,S., and Schindelholz, E.J. (2019) Humidity Effects on Pitting of Ground Stainless Steel Exposed to Sea Salt Particles. Jour. Electrochem. Soc., 166, C3477-C3487.

Wersin, P., Johnson, L.H., and McKinley, I.G. (2007). Performance of the bentonite barrier at temperatures beyond 100°C: A critical review. Physics and Chemistry of the Earth, 32, 780-788.

Wieczorek, K., Gaus, I., Mayor, J. C., Schuster, K., García-Siñeriz, J.-L., & Sakaki, T. (2017). In-situ experiments on bentonite-based buffer and sealing materials at the Mont Terri rock laboratory (Switzerland). Swiss Journal of Geoscience., 110, 253–268. https://doi.org/10.1007/s00015-016-0247-y.

Development of the SUPCRTNE Thermodynamic Database Engine – LLNL (Part IV)

1. Introduction

This part of the report summarizes research conducted at Lawrence Livermore National Laboratory (LLNL) within the Disposal in Argillite media R&D activity. LLNL is leading efforts in the development of thermodynamic databases in support of the Spent Fuel and Waste Science Technology (SFWST) program. Thermodynamic models provide the basis for understanding the stability of solid phases and speciation of aqueous species and modeling the evolution of repository conditions. The LLNL effort is being performed in coordination with other US database development efforts. The effort includes a review of available thermochemical databases and a path forward for database integration. International coordination with the NEA-TDB is supported through crystalline international work package.

2. Background

The present effort follows the vision of H. C. Helgeson and students beginning in the 1970s to create an internally consistent thermodynamic database that would allow calculations of interactions of aqueous species and minerals over a wide range of geologically relevant temperatures and pressures. This was a major step forward as many early geochemistry-focused databases only addressed conditions of 25°C (298.15K) and atmospheric pressure, with little attention to internal consistency. Early efforts by the Helgeson school addressed the thermodynamic properties of water (Helgeson and Kirkham, 1974ab), aqueous species (Helgeson and Kirkham, 1976; Helgeson et al., 1981), and minerals (Helgeson et al., 1978).

This early work was associated with the development of a computer code called SUPCRT (see historical description by Johnson et al., 1992), which could be used to calculate thermodynamic properties of water, aqueous species, minerals, and chemical reactions over a wide range of temperature and pressure. The treatment of water was notable for the use of an equation of state (Keenan et al., 1969). The treatment of aqueous (solute) species was notable for the development of the "HKF equation of state," a model that allowed extrapolation of 25°C data to elevated temperature and pressures. The treatment of minerals was based on a groundbreaking analysis of published experimental studies of mineral equilibria at various temperatures and pressures. This work inspired a series of other, independent works (too numerous to list here) to develop "internally consistent" thermodynamic databases for minerals. The most recent of these is that of Holland and Powell (2011).

Subsequent development in the Helgeson school led to the creation of the computer code SUPCRT92 (Johnson et al., 1992), which incorporated various improvements over the earlier software. The water equation of state was replaced by that of Haar et al. (1984) and, near the critical point, that of Levelt Sengers et al. (1983), extending the range of application. SUPCRT92 was widely distributed and became a tool used by many members of the geochemistry community. Like the earlier SUPCRT, SUPCRT92 has its own thermodynamic database, consisting of 25°C data and other data necessary to extrapolate to high temperatures and pressures. A number of such databases were created, incorporating various improvements including data for additional chemical species. The most notable of which was slop98.dat, which was an important starting point for work by others.

In the early days of the Yucca Mountain Project at Lawrence Livermore, the functionality of SUPCRT92 was incorporated into software called GEMBOCHS (Johnson and Lundeen, 1994ab). GEMBOCHS used a relational database to contain thermodynamic data (of the sort

found in SUPCRT92 databases). This software could directly produce data files for geochemical modeling codes such as EQ3/6 (see for example Wolery, 1992), whereas SUPCRT92 output had to be integrated into such data files manually or by running scripts. A number of such data files were produced (see Johnson and Lundeen, 1994b). GEMBOCHS utilized costly proprietary relational database software. This had the effect of making the system inaccessible to other would-be users, which in turn made the system non-transparent. GEMBOCHS was also insufficiently documented. Today no copies of GEMBOCHS, or any pieces thereof, are known to exist. Also, the need for a relational database for this purpose now seems absurd owing to advances in computer technology.

In subsequent work on the Yucca Mountain Project (see Wolery and Jove-Colon, 2007, and references cited therein), the decision was made to use SUPCRT92 (with a partially updated form of slop98.dat representing basically the same set of chemical species) in combination with newly developed spreadsheet tools. Data for additional species were processed using the spreadsheet tools. This allowed multiple investigators to develop the data for new species that they required for their subsequent analyses. The output from SUPCRT92 and the spreadsheet tools were assembled by hand into a data file called data0.ymp, of which several versions were produced. Many NEA data (starting with Grenthe, 1992) were included. This later Yucca Mountain work was done under NQA-1 level quality assurance. The data0.ymp databases were used in analyses of interaction of aqueous solutions with both natural and engineering materials. Many of these analyses were included in the Yucca Mountain License Application.

3. Earlier Work Under the UFD and SFWST Campaigns

In 2011 the Used Fuel Disposition (UFD) Campaign was initiated to study disposal of spent fuel and other high level waste (U.S. Dept. of Energy, 2011). UFD was chartered to examine various possible disposal scenarios, including geologic disposal in a variety of geologic settings, under conditions different from those at Yucca Mountain. Work on thermodynamic database development began in 2015, reuniting two of the principal investigators (T. Wolery and C.F. Jove-Colon) who were involved in producing the Yucca Mountain thermodynamic database. In 2017, the UFD Campaign was replaced by the Spent Fuel and Waste Science and Technology (SFWST) Campaign (see Swift, 2017).

The first product under the UFD Campaign was an extensive and detailed examination of key thermodynamic data (Wolery and Jové Colón, 2017). Key data are data used to derive data for other species, using data for chemical reactions (as for solublities and phase equilibria). For example, considering quartz (SiO_2) as a key species, thermodynamic data for aqueous silica ($SiO_2(aq)$) can be obtained from quartz solubility data representing the reaction quartz (SiO_2) = $SiO_2(aq)$. Key data species include:

- Chemical elements in their standard reference forms
- Water and simple aqueous solute species such as Na^+ and Cl^-, as well as some more complex species such as HCO_3^- and $H_2PO_4^{2-}$
- Simple solids, such as quartz (SiO_2) and corundum (Al_2O_3)
- Simple gases such as O_2

A minimum of one key species is needed to represent a chemical element in each of its oxidation states. Apart from the chemical element reference forms (zero oxidation state), different choices

of key species are possible. Considering Al^{3+} and corundum (Al_2O_3), only one is required as the key species representing Al(III). However, as long as the relationship between two such species is strongly established, both can be used in practice (one primary key species and one or more secondary key species). It should be noted that other efforts are currently under way in the analysis of Mg^{2+} thermodynamic data updates and other Mg-bearing species in collaboration with the Storage and Transportation campaign. Such efforts will be described in the deliverable report M2SF-21SN010207056 "FY21 Status Report: SNF Interim Storage Canister Corrosion and Surface Environment Investigations" to be submitted later this year.

Wolery and Jové Colón (2017) reviewed decades' worth of thermodynamic data for commonly used key species and noted a number of trends and specific instances of errors. One purpose of this review was to serve as a guide to which key data should be used in developing a new internally consistent database (more or less in the form of a SUPCRT database). The other purpose was to provide a means of correcting data for non-key species to account for differences in key data. Thus, data from a significant body of historical sources (see Wolery and Jové Colón, 2017, covering all the major data efforts by U.S. and other programs over the years, including CODATA, NBS/NIST, the U.S. Geological Survey, NEA, and other organizations and entities) can be considered in the new database without introducing thermodynamic inconsistencies.

Although the intent of the Helgeson school was to produce accurate and internally consistent databases for SUPCRT and later SUPCRT92, cracks developed over the years. When the work began, the preferred source of key thermodynamic data was CODATA (Committee on Thermodynamic Data), an international organization. If needed key data were not available, they were taken from NBS (later NIST) reports. Unfortunately, when the Helgeson school was developing SUPCRT, both CODATA and NBS/NIST were periodically issuing updated values for key data (see Wolery and Jové Colón, 2017). Various data might require revision if key data values used to derive them were changed, for example by a revision in CODATA-recommended values. There seems to have been no dedicated, ongoing effort at such revision, other than replacing old values of key data by new ones in the database. Other affected (non-key) data would be left as-is, unless someone pointed that there was a problem. There were also accuracy concerns. In particular, Helgeson et al. (1978) made two notably unfortunate choices, one concerning the data for aqueous silica ($SiO_2(aq)$), the other for the data for kaolinite (see Wolery and Jové Colón, 2017, and pertinent references cited therein). The silica problem was recognized and corrected in the Yucca Mountain work described earlier, but the kaolinite problem was appreciated only later.

4. Updating SUPCRT92 in Support of the Spent Fuel and Waste Science and Technology Program

4.1. General Approach

GEMBOCHS (Johnson and Lundeen, 1994ab) is no longer supported. SUPCRT92 (Johnson et al., 1992) is still promising as a tool in continuing development, but only if the software is updated and otherwise improved, and if a new, updated and improved database is created for it. That is essentially our current approach. We note that the ability of SUPCRT92 to calculate thermodynamic data to high temperatures and pressures is critical to the application of geochemical and reactive transport modeling of the majority of actual and potential scenarios for the disposal of high-level nuclear waste. The Yucca Mountain thermodynamic database development was largely limited to relatively low temperatures and pressures.

Strong points of SUPCRT92 include representation of the body of work of the Helgeson school in the associated databases, open-source software (written in Fortran), the use of an equation of state to calculate the thermodynamic properties of water, the inclusion of the "HKF equation of state" model for aqueous solute species, the ability to specify reactions for which data are to be calculated, the ability to specify temperatures and pressures for which data are desired, long-term acceptance by the geochemical community (see for example Anderson, 2005; Walther, 2009)., and a quality assurance history from use on the Yucca Mountain Project. The only obvious open-source potential alternative is CHNOSZ (Dick, 2019), which was developed by one of Helgeson's later students (Jeffrey M. Dick). It has a strong focus on organics, is written in the R programming language, and at this point is more of a pure research code.

The weak points of SUPCRT92 include the use of a combination of obsolete equation of state models for water, the inclusion of obsolete "add-on" models for some additional water properties (discussed below), the use of obsolete coding practices that were concessions to the limitations of computers in the 1970s when SUPCRT was first created, a limitation of no more than 50 reactions on an input (.rxn) file, and output formats that are not optimal for building a thermodynamic data file intended directly support geochemical modeling and reactive transport codes. In addition, SUPCRT92 and its data files continue to use the obsolete calorie unit, instead of the modern accepted Joule. It is probably fair to say that the continued use of the calorie in geochemical studies is largely due to SUPCRT92. Another problem is that for solids and gases, SUPCRT92 and its databases use a three-term Maier-Kelley for the heat capacity of minerals and gases, while a four-term form is more appropriate (see for example Holland and Powell, 2011). This has been corrected in SUPCRTBL (Zimmer et al., 2016).

Our long-term plan is to revise the SUPCRT92 software to address the above deficiencies, to develop a series of internally consistent data files to support it, and to create a new suite of data files to directly support geochemical modeling and reactive transport codes, providing for various required formats for popular codes (e.g., EQ3/6, GWB, PHREEQC).

Our analysis of key thermodynamic data (Wolery and Jové Colón, 2017) represented a first step. After completion of that work, we began analysis and revision of SUPCRT92, dubbing the new product SUPCRTNE. This work is still ongoing. We have previously addressed the issues of conversion from calorie to Joule units, including writing a code to convert existing SUPCRT92 data files to Joule units. We also eliminated the "no more than 50 reactions at a time" limit. We then focused on replacing the part of the software dealing with the properties of water. This consists of a number of subroutines and functions contained in the "H2O92D" module, which comprises a large part of the SUPCRT92 source code.

The International Association for the Properties of Water and Steam (IAPWS, see iapws.org) is an international entity that sanctions models for the calculation of water properties. The equation of state model of Haar et al. (1984) used in SUPCRT92 is a second-generation IAPWS standard (IAPS-84). It does not extend to the critical point of water (647.096K and 22.064 MPa). Near the critical point, SUPCRT92 uses equation of state model of Levelt Sengers et al. (1983), which is unsanctioned. The present sanctioned model is that of Wagner and Pruss (2002), known as IAPWS-95. The model is valid across a wide range of temperature (273.16K-1273K) and pressure (0-1000 MPa), including at and near the critical point (647.9906K and 22.064 MPa). It is thus technically superior in addition to merely being the current sanctioned model.

Both IAPS-84 and IAPWS-95 are *general and scientific* models. They (and also the earlier model of Keenan et al. 1969) use temperature and density instead of temperature and pressure as the independent variables. Evaluating such models for specified temperature and pressure requires iteration to adjust the density to yield the desired pressure. A similar but more complex iteration is required to calculate results for a specified temperature on the liquid-vapor equilibrium curve (the saturation curve), or to calculate results for a specified pressure on that curve. Because in the past such iteration was considered overly onerous for engineering calculations, for each *general and scientific* model there is a corresponding *industrial formulation*, which is a model fit to the general and scientific model using temperature and pressure as the primary variables. Although that is advantageous in avoiding iteration for typical problems, it is not as accurate as the original models, and accuracy is critical for the thermochemical usage which is of interest here. There is additional complexity in the industrial formulation in the form of different equations for different regions of temperature-pressure space. The industrial formulation corresponding to IAPWS-95 is IAPWS-IF97 (Wagner et al., 2000).

4.2. H2OI95 v. 1.0: Software for Dealing with the IAPWS-95 Model (FY19)

Since the IAPWS-95 model has been around for some years, we first looked for an open source implementation (preferably in Fortran) that had no proprietary strings attached. None was located, so we began writing the requisite software from scratch. It was decided to first develop this as a stand-alone code, in order to facilitate testing. The code was dubbed H2OI95. H2OI95 was written in "simple" Fortran, with explicit variable typing, all passing of variables done through calling sequences, extensive commenting, straightforward flow in the coding, and no dependencies on external libraries.

In late 2018 we completed version 1.0 of H2OI95 (Wolery, 2018), which implements the IAPWS-95 model described by Wagner and Pruss (2002) and IAPWS (2016). H2OI95 includes calculation of thermochemical properties of water using the key thermodynamic data of CODATA (Cox et al., 1989). This is not a part of the IAPWS-95 model and is not a common feature of IAPWS-95 calculators.

The report, "H2OI95: A Stand-Alone Fortran Code for Evaluating the IAPWS-95 Equation-of-State Model for Water" (Wolery, 2018) was released by LLNL on December 12, 2018 as document LLNL-TR-761227. This document describes the implementation of the model, extensive convergence testing and numerical examination, and results of computer verification testing. Convergence testing was necessary to assure that starting values for density would converge rapidly to physically meaningful results. Neither Wagner and Pruss (2002) nor IAPWS (2016) speak to the issue of starting values. Testing of various schemes for defining starting estimates was required to find ones that would lead rapidly to physically valid results. It was found that, depending on starting values, convergence could lead to results that are non-physical, as shown by negative absolute entropy or some other non-physical condition. The report also describes results of computer verification tests specified by Wagner and Pruss (2002) and IAPWS (2016). These tests are high precision, at the level of eight or nine significant figures. The term "verification" here is that used by Wagner and Pruss (2002) and IAPWS (2016); it is equivalent in meaning to "validation" as used on the Yucca Mountain Project.

The H2OI95 software was released under an open source BSD-3 license and placed as a complete package (Windows executable, source code, report, associated text files, and a test case library of input and output files) in February 2019 on GitHub (https://github.com/llnl/h2oi95). Github is now the favored repository for LLNL open-source software. Our intent has been to also make the code available for download on the EQ3/6 website hosted at LLNL (https://www-gs.llnl.gov/energy-cyber-and-infrastructure/geochemistry) or on another LLNL institutional web site whose creation is presently under consideration. The reason for needing another web site is that GitHub is a product for software developers to use in the development process, not something intended as a repository for finished software products. It can be used that way, but the web pages cannot be set up in a way that is oriented toward geochemists.

4.3. H2OI95 v. 1.1: Calculation of Additional Water Properties (FY20)

After the release of H2OI95 version 1.0, we returned to SUPCRTNE to determine how best to link in the new EOS model for water properties. We had previously made other functional changes to SUPCRT92, including eliminating the inconvenient and obsolete direct access data file, and converting the code from obsolete calorie units to Joule units. We had also written a small code to convert SUPCRT92 data files from calorie units to Joule units.

Resuming work on SUPCRTNE, we found code in the H2O92D module for calculating additional properties that are not part of the IAPWS-95 model. These include the dynamic viscosity, thermal conductivity, surface tension, and dielectric constant, along with Born functions calculated from the dielectric constant. Examination of SUPCRT92 showed that coding used to calculate these properties is always executed when water properties are calculated. However, except for the four Born functions, these additional property values are not used in subsequent calculations, nor are they are written to any output. The Born functions are used in evaluating the HKF “equation of state” model (Helgeson and Kirkham, 1976; Helgeson et al., 1981) for calculating the thermodynamic properties of aqueous ions at elevated temperature and pressure.

The dielectric constant model can also be used to compute Debye-Hückel parameters (see Fernández et al., 1997), which we need to develop working data files to support geochemical modeling and reactive transport codes. These additional properties (especially the dielectric constant and derivative parameters) were a focus of attention in the early development of thermodynamic data and models for water and aqueous (solute) species by H. C. Helgeson and colleagues (see Helgeson and Kirkham, 1974a, 1974b, 1976; Helgeson et al., 1981). This makes current IAPWS-sanctioned models of additional water properties significant to ongoing and future thermodynamic database development (the models in SUPCRT92 being obsolete). The current IAPWS-sanctioned additional properties models are consistent with IAPWS-95. We decided to address additional properties in an extended version of H2OI95 (version 1.1). Full documentation of this work is given in Wolery (2020). The values of the new properties calculated by H2OI95 are output on a new comma-separated-variable (.csv) file called xtab.csv.

There are three “additional” thermodynamic properties of interest that can be obtained from the IAPWS-95 model itself but for which the requisite formulas were not given by Wagner and Pruss (2002) or IAPWS (2016). Consequently, most IAPWS-95 software does not provide them. These are the isothermal compressibility, the thermal expansivity, and the dimensionless isothermal compressibility. The requisite formulas were derived and coded into H2OI95, and values are reported on the xtab.csv output file. For details, see Wolery (2020).

IAWPS (2008) describes the IAPWS-sanctioned model for the dynamic viscosity of water. The model is developed in the corresponding paper by Huber et al. (2009). The model requires the isothermal compressibility function noted earlier, which is obtained from the IAPWS-95 model. During verification of the implementation of the dynamic viscosity model, a coding error was found involving the IAPWS-95 model's 55^{th} and 56^{th} terms, which are highly complex. This error notably affected "higher order" properties including the isothermal compressibility and the dimensionless isothermal compressibility in a small region close to the critical point. It also affected the calculated pressure and the pressure derivative with respect to density, but only slightly. Correction of the error was verified by comparison with results given by Huber et al. (2009).

In retrospect, the verification tests for IAPWS-95 implementation given by Wagner and Pruss (2002) and IAPWS (2016) appear to be insufficient. For example, the uncorrected code produced results that matched values in the steam tables (Table 13.2) of Wagner and Pruss (2002) to the precision used in those tables (four to five significant figures), except for very slight differences at a single pressure and temperature close to the critical point. See Wolery (2020) for more detailed discussion. Additional opportunities for verification close to the critical point are based on plots for "higher-order" water properties given by Wagner and Pruss (2002) and Kiselev and Friend (1999). Comparison of these plots with results for the corrected H2OI95 are only graphical, but still helpful.

IAPWS (2011a) describes the IAPWS-sanctioned model for the thermal conductivity of water. The model is developed in the corresponding paper by Huber et al. (2012). Like the above noted viscosity model, this model also has a dependency on the dimensionless isothermal compressibility.

The above described models for the viscosity (IAPWS, 2008) and thermal conductivity (IAPWS, 2011a) have temperature ranges of validity partially defined in terms of the melting temperature as a function of pressure. The model for the melting temperature is taken from IAPWS (2011b), which in turn is based on the paper of Wagner et al. (2011). This model describes the melting pressure as a function of temperature. To obtain the melting temperature as a function of pressure, it is necessary to invert the model. In H2OI95, the inversion is accomplished using secant method iteration. For further details, see Wolery (2020, Section 5.2.6).

IAPWS (2014) describes the IAPWS-sanctioned model for the surface tension of water. The model is based on the work of Vargaftik et al. (1983). The model describes to the surface tension between coexisting vapor and liquid as a function of temperature.

IAPWS (1997) describes the IAPWS-sanctioned model for the dielectric constant of water. The model is developed in the corresponding paper by Fernández et al. (1997). The dielectric constant is one of the most important properties of water, as it in turn is needed to calculate both Born functions (Helgeson and Kirkham, 1974ab) and Debye-Hückel parameters (Helgeson and Kirkham, 1974ab; Fernández et al., 1997).

IAPWS (2014) does not address partial derivatives (with respect to temperature and pressure) of the dielectric constant and various derivative properties, such as Debye-Hückel parameters and Born functions. However, the source paper by Fernández et al. (1997) addresses the first-order partial derivatives and the Debye-Hückel "A" (or limiting law) parameters. These partial derivatives are included on the xtab.csv output file.

IAPWS itself is silent on Debye-Hückel parameters. However, these parameters can be obtained from the dielectric constant model (IAPWS, 2014, Fernández et al., 1997). The discussion here is abbreviated. For a full discussion, see Wolery 2020, Section 5.2.5)

The Debye-Hückel parameters include the "A" or "limiting law" parameters and "B" or "extended" parameters. The primary A and B parameters (commonly given as A_γ and B_γ) are used in some form of the basic Debye-Hückel model for describing the activity coefficient of an aqueous electrolyte or ion in dilute solution, or as part of some more elaborate model for more concentrated solutions (such as Pitzer's 1973 equations). For an extended discussion of aqueous activity coefficient models, see Section 3 of Wolery, 1992 or any other pertinent review of the subject. Aqueous geochemistry texts such as Anderson (2005) and Walther (2009) include discussions of such models. Helgeson and Kirkham (1974b) provide a wide-ranging discussion of Debye-Hückel parameters and Born functions.

The Debye-Hückel "A" and "B" parameters are dependent on the dielectric constant, which depends on temperature and pressure. In addition to the constants noted above, there are others associated with related thermodynamic properties, for example A_V (with apparent molar volume), A_H (with apparent molar enthalpy), A_K (with apparent molar compressibility), and A_C (with apparent molar heat capacity). These are discussed by Fernández et al. (1997) and Helgeson and Kirkham (1974b). Helgeson and Kirkham also discuss the corresponding "B" parameters, which Fernández et al. (1977) does not.

The Born functions Z, Q, Y, and X used in SUPCRT92 were not included in H2OI95 v. 1.1 pending resolution of questions concerning their usage in SUPCRT92. They will be included in the next version (v. 1.2).

The report, "H2OI95: A Stand-Alone Fortran Code for Evaluating the IAPWS-95 Equation-of-State Model for Water (Rev. 1)" (Wolery, 2020) was released by LLNL on May 18, 2020 as document LLNL-TR-805304. This document (the report for H2OI95 v. 1.1) is an extended and revised version of the report for H2OI95 v. 1.0, documenting all the new material. The report documents the extensive testing and verification activities.

The H2OI95 v. 1.1 software was released on June 3, 2020 under an open source BSD-3 license. A complete package (Windows executable, source code, report, associated text files, and a test case library of input and output files) was completed on June 6, 2020. It was placed on GitHub on July 30, 2020, where the v. 1.0 package is also still available for download. We anticipate that v. 1.1 will also be made available on an LLNL institutional web site. The reason for needing an alternative web site is that GitHub is a product mainly intended for software developers to use in the development process. It can be is used utilized as a repository for finished software products. However, the GitHub web pages cannot be customized in a way that is oriented toward geochemists.

4.4 SUPCRTNE v 1.0 and H2OI95 v. 1.2 (FY21)

Work is presently focused on connecting SUPCRTNE (under development) with H2OI95. SUPCRT v. 1.0 will be the first working version of SUPCRTNE. It will use the "modularized" version of H2OI95 (v. 1.2). to in place of the existing H2O92d module from SUPCRT92 (Johnson et al., 1992). The existing H2O92d module uses the older IAPS-84 (Haar et al., 1984) equation-of-state model in conjunction with the Levelt Sengers et al. (1983) model near the critical point. Current intent is to retain this alongside the H2OI95 model for some time to allow

comparative studies of how much change the IAPWS-95 (IAPWS, 2016; Wagner and Pruss, 2002) model introduces to SUPCRTNE calculations.

H2OI95 v. 1.2 introduces two major changes from v. 1.1. The code is being "modularized" by breaking up the existing main program into a shorter main program that just reads the H2OI95 input file and a lead subroutine H2O95E that can be called by other programs, including SUPCRTNE. Also, the Born functions Z, Q, Y, and X are being added. These will be calculated using the Fernandez et al. (1997) model for the dielectric constant. Actually, X will not, because it requires the second partial derivative of the dielectric constant with respect to temperature. This is presently not available from the Fernandez et al. (1997) model.

The formula in the Fernandez et al. (1997) model for the first partial derivative is already quite complex, and Fernandez et al. have questioned whether the usefulness of the second partial derivative as obtained from their model. X appears to be needed in SUPCRT92 only to compute the heat capacity of aqueous ions, a result that is written on the main output file but appears otherwise unused. It does not appear to be needed for anything critical, for example computing Gibbs energies as a function of temperature and pressure.

Because of this and the importance of the other Born functions generally in computing the thermodynamic properties of aqueous species at elevated temperature and pressure, it was decided to "import" the Johnson and Norton (1991) model for the dielectric constant from SUPCRT92 and use it in parallel with the Fernandez et al. (1997) model. The Johnson and Norton model includes the formula for computing the second order partial derivative needed to compute the Born function X. Comparative studies will then be conducted.

At this writing, H2OI95 v. 1.2 is nearly complete. Testing of the modularized version with SUPCRTNE will be made to assess satisfactory completeness. SUPCRTNE will then contain the latest IAPWS-sanctioned models for water properties. The new version of H2OI95 (as both stand-alone code and as a module) will be placed on GitHub along with the previous versions.

6. Acknowledgements

This work was supported by the Spent Fuel and Waste Science and Technology campaign of the Department of Energy's Nuclear Energy Program. Prepared by LLNL under Contract DE-AC52-07NA27344.

7. References

Anderson G. (2005) Thermodynamics of Natural Systems, Second Edition. Cambridge University Press, New York. 648 pp. ISBN-13 978-0-521-84772-8.

Cox J. D., Wagman D. D., and Medvedev V. A., eds. (1989) *CODATA Key Values for Thermodynamics.* CODATA Series on Thermodynamic Values. Hemisphere Publishing Corp., New York. 271 pp. ISBN 0-89116-758-7.

Dick J. M. (2019) CHNOSZ: Thermodynamic calculations and diagrams for geochemistry. *Front. Earth Sci.* **7** (Article 180), 1-18.

Fernández D. P., Goodwin A. R. H., Lemmon, E. W., Levelt Sengers J. M. H., and Williams R. C. (1997) A formulation for the static permittivity of water and steam at temperatures from 238 k to 873 K at pressures up to 1200 MPa, including derivatives and Debye–Hückel coefficients. *J. Phys. Chem. Ref. Data* **26**, 1125-1166.

Grenthe I., Fuger J., Konings R. J. M., Lemire R. J., Muller A. B., Nguyen-Trung C., and Wanner, H. (1992) Chemical Thermodynamics of Uranium. Chemical Thermodynamics.

Volume 1. North Holland Elsevier Science Publishers B. V., Amsterdam, The Netherlands. 715 pp.

Haar L., Gallagher J. S., and Kell G. S. (1984) *NBS/NRC Steam Tables*. Hemisphere Publishing Corporation, Washington, DC. 320 pp. ISBN 0-89116-353-0.

Helgeson H. C. and Kirkham, D. H. (1974a) Theoretical prediction of the thermodynamic behavior of aqueous electrolytes at high pressures and temperatures: I. Summary of the thermodynamic/electrostatic properties of the solvent. Am. J. Sci. 274, 1089-1198.

Helgeson H. C. and Kirkham, D. H. (1974b) Theoretical prediction of the thermodynamic behavior of aqueous electrolytes at high pressures and temperatures: II. Debye-Hückel parameters for activity coefficients and relative partial molal properties. Am. Jour. Sci. 274, 1199-1261.

Helgeson H. C. and Kirkham, D. H. (1976) Theoretical prediction of the thermodynamic behavior of aqueous electrolytes at high pressures and temperatures: III. Equation of state for aqueous species at infinite dilution. Am. Jour. Sci. 276, 97-240.

Helgeson H. C., Kirkham D. H., and Flowers G. C. (1981) Theoretical prediction of the thermodynamic behavior of aqueous electrolytes at high pressures and temperatures: IV. Calculation of activity coefficients, osmotic coefficients, and apparent molal and standard and relative partial molal properties to 600°C and 5 kb. Am. Jour. Sci. 281, 1249-1546.

Holland T. J. B. and Powell R. (2011) An improved and extended consistent thermodynamic dataset for phases of petrological interest, involving a new equation of state for solids. J. Meta. Geol. 29, 333-383.

Huber M. L., Perkins R. A., Laesecke A., Friend D. G., Sengers J. V., Assael M. J., Metaxa I. N., Vogel N. E., Mareš R., and Miyagawa K. (2009) New international formulation for the viscosity of H2O. J. Phys. Chem. Ref. Data 38, 101-125.

Huber M. L., Perkins R. A., Friend D. G., Sengers J. V., Assael M.J., Metaxa I. N., Miyagawa K., Hellmann R., and Vogel E. (2012) New international formulation for the thermal conductivity of H2O. J. Phys. Chem. Ref. Data 41, 033102, 1-23.

International Association for the Properties of Water and Steam (1997) Release on the Static Dielectric Constant of Ordinary Water Substance for Temperatures from 238 K to 873 K and Pressures up to 1000 MPa. IAPWS R8-97, 9 pp.

International Association for the Properties of Water and Steam (2008) Release on the IAPWS Formulation 2008 for the Viscosity of Ordinary Water Substance. IAPWS R12-08, 9 pp.

International Association for the Properties of Water and Steam (2011a) Release on the IAPWS Formulation 2011 for the Thermal Conductivity of Ordinary Water Substance. IAPWS R15-11, 15 pp.

International Association for the Properties of Water and Steam (2011b) Revised Release on the Pressure along the Melting and Sublimation Curves of Ordinary Water Substance. IAPWS R14-08, 7 pp.

International Association for the Properties of Water and Steam (2014), Revised Release on Surface Tension of Ordinary Water Substance. IAPWS R1-76, 6 pp.

International Association for the Properties of Water and Steam (2016) Revised Release on the IAPWS Formulation 1995 for the Thermodynamic Properties of Ordinary Water Substance for General and Scientific Use. IAPWS R6-95, 19 pp.

Johnson J. W., Oelkers E. H., and Helgeson H. C. (1992) SUPCRT92: A software package for calculating the standard molal thermodynamic properties of minerals, gases, aqueous species, and reactions from 1 to 5000 bar and 0 to 1000°C. Comp. Geosci. 18, 899-947.

Johnson J. W. and Lundeen S. R. (1994a) Jewel: A graphical-user interface for generating custom GEMBOCHS thermodynamic datafiles for use with geochemical modeling software. LLNL-YMP Milestone report MOL63, 23 pp.

Johnson J. W. and Lundeen S. R. (1994b) GEMBOCHS thermodynamic datafiles for use with the EQ3/6 software package. LLNL-YMP Milestone report MOL72, 99 pp.

Johnson J. W. and Norton D. (1991) Critical phenomena in hydrothermal systems: state, thermodynamic, electrostatic, and transport properties of H_2O in the critical region. *Am. J. Sci*. **291**, 541-648.

Keenan J. H., Keyes F. G., Hill P. G., and Moore J. G. (1969) *Steam Tables*. John Wiley & Sons, New York. 162 pp. ISBN-10: 0471465011.

Levelt Sengers J. M. H., Kamgar-Parsi, B., Balfour F. W., and Sengers J. V. (1983) Thermodynamic properties of steam in the critical region. J. Phys. Chem. Ref. Data 12, 1-28.

Miron G. D., Wagner T., Kulik D. A. and Heinrich C. A. (2016) Internally consistent thermodynamic data for aqueous species in the system Na–K–Al–Si–O–H–Cl. *Geochim. Cosmochim. Acta* **187**, 41–78.

Miron G. D., Wagner T., Kulik D. A., and Lothenbach B. (2017) An internally consistent thermodynamic dataset for aqueous species in the system Ca-Mg-Na–K–Al–Si–O–C-H–Cl. *Am. J. Sci.* **317**, 754-805.

Swift P. (2017) Spent Fuel and Waste Science and Technology R&D Campaign Working Group Meeting. https://www.osti.gov/servlets/purl/1367219.

U.S. Dept. of Energy (2011) Used Fuel Disposition Campaign Disposal Research and Development Roadmap. FCR&D-USED-2011-000065 REV 0. https://www.energy.gov/sites/prod/files/UFD_Disposal_R%26D_Roadmap_Rev_0.1.pdf.

Vargaftik N. B., Volkov B. N., and Voljak L. D. (1983) International tables of the surface tension of water. *J. Phys. Chem. Ref. Data* **12**, 817-820.

Wagner W., Cooper J. R., Dittmann A., Kijima J., Kretzschmar H.-J., Kruse A., Mareš R., Oguchi K., Sato H., Stöcker I., Šifner O., Takaishi Y., Tanishita I., Trübenbach J., and Willkommen T. (2000) The IAPWS Industrial Formulation 1997 for the Thermodynamic Properties of Water and Steam. *J. Eng. Gas Turbines Power* **122**, 150-184.

Wagner W. and Pruss A. (2002) The IAPWS formulation 1995 for the thermodynamic properties of ordinary water substance for general and scientific use. J. Phys. Chem. Ref. Data 31, 387-535.

Wagner W, Riethmann T., Feistel R., and Harvey A. H. (2011) New Equations for the Sublimation Pressure and Melting Pressure of H_2O Ice Ih. *J. Phys. Chem. Ref. Data* **40**, 043103, 1-11.

Walther J. V. (2009) *Essentials of Geochemistry*, second edition. Jones and Bartlett Publishers, LLC, Boston. 797 pp. ISBN: 978-0-7637-5922-3.

Wolery T. J. and Jove-Colon C. F. (2007) Qualification of Thermodynamic Data for Geochemical Modeling of Mineral–Water Interactions in Dilute Systems. ANL-WIS-GS-000003 Rev. 1, Sandia National Laboratories, OCRWM Lead Laboratory for Repository Systems, Las Vegas, Nevada, 412 pp.

Wolery T. J. and Jové Colón C. F. (2017) Chemical thermodynamic data. 1. The concept of links to the chemical elements and the historical development of key thermodynamic data. *Geochim. Cosmochim Acta* **213**, 635-676.

Wolery, T. J. (2018) H2OI95: A Stand-Alone Fortran Code for Evaluating the IAPWS-95 Equation-of-State Model for Water. LLNL-TR-761227, Lawrence Livermore National Laboratory, Livermore, California, 43 pp.

Wolery, T. J. (2020) H2OI95: A Stand-Alone Fortran Code for Evaluating the IAPWS-95 Equation-of-State Model for Water (Rev. 1). LLNL-TR-805304, Lawrence Livermore National Laboratory, Livermore, California, 88 pp.

Zimmer K., Zhang Y., Lu P., Chen Y., Zhang G., Dalkilic M., and Zhu (2016) SUPCRTBL: A revised and extended thermodynamic dataset and software package of SUPCRT92. Comp. Geosci. 90 (Part A), 97-111.

Non-Electrostatic Surface Complexation Database for GDSA (LLNL) (Part V)

1. Introduction

This part of the report summarizes research progress conducted at Lawrence Livermore National Laboratory (LLNL). The activity is focused on our long-term commitment to engaging our partners in international nuclear waste repository research. The focus of this international activity is surface complexation model international collaborations. Specifically, we are developing a database framework for Spent Fuel and Waste and Science Technology (SFWST) that is aligned with the Helmholtz Zentrum Dresden Rossendorf (HZDR) sorption database development group in support of the database needs of the SFWST program. FY20 efforts focused primarily on building out an Access database of raw sorption data and developing a framework for surface complexation/ion exchange data fitting methods and surface complexation/ion exchange database development. Our effort was coordinated with international partners involved in similar database development efforts (e.g. HZDR RES^{3}T). In FY20, we captured ~24,000 data that include literature data as well as digitized data from our RES^{3}T partners. The focus was on radionuclide (Cs, Sr, U, Np, and Pu) sorption to clay minerals (with particular focus on bentonite/montmorillonite). However, large compilations of surface titration and other data were captured in the data mining process as well.

In FY21, a more complete methodology for development of a surface complexation/ion exchange constant database from the primary sorption data was pursued. A key component of that effort was the automation of commercially available fitting routines (e.g. PEST) that can be linked to surface complexation/ion exchange codes and produce optimized constants and associated parameter uncertainties. The scripts needed to perform this automation were originally implemented in Access and were translated into R and Python scripts that are much more flexible and adaptable. Of particular interest is the expansion of our data interrogation effort by applying modern data science methods (e.g. machine learning). The combination of machine learning approaches with more traditional PEST/PHREEQC data fitting approaches provide flexibility to GDSA efforts (e.g. use of mechanistic surface complexation/ion exchange models versus smart Kd lookup tables). The data analysis schemes were developed to facilitate links to thermodynamic database development efforts (e.g. SUPCRTNE, NEA-TDB) to allow for updates to our surface complexation/ion exchange databases as the thermodynamic databases are updated. This new workflow allows for testing of various surface complexation (Non electrostatic, diffuse layer, etc.) and ion exchange (Vanselow, Gapon, etc.) models and provides flexibility in testing surface complexation/ion exchange conceptual models and numerical constructs. A draft manuscript that describes this data driven approach was prepared for submission in late FY21. Initial efforts to simulate radionuclide surface complexation to iron oxide, calcite, and quartz minerals was also completed and is presented below.

This effort is coordinated with the thermodynamic database development efforts described in the Argillite and Crystalline International work package and in support of the SFWST program. Thermodynamic models, when combined with surface complexation/ion exchange provide the basis for understanding the stability of solid phases, speciation of aqueous species, partitioning between aqueous and solid surfaces, and modeling the evolution of repository conditions. The goal of this effort is the development of consistent models of radionuclide sorption to mineral surfaces that can be implemented in performance assessment models for the GDSA effort.

2. Digitized LLNL Surface Complexation Ion Exchange (SCIE) sorption database updates

To develop a comprehensive surface complexation database in support of the SFWST program, we continued to focus our effort on building a digital sorption data to support surface complexation database development. The LLNL Surface Complexation Ion Exchange (SCIE) digital sorption data was developed in Microsoft Access with a series of linked tables as reported in the FY19 and FY20 LLNL milestone reports. Thus, the structure of the database will not be reported here. However, some enhancements to the database were pursued in FY21 and are highlighted below.

In FY21, we removed all embedded digital files from the database and replaced them with hyperlinks. This better aligns our database with SQL database standards and will help with transitioning away from the Microsoft Access software in the future as the database expands. Embedded digital files included 1) original manuscript/report PDFs, 2) extracted image files from original figures from each manuscript, and 3) digitized datafiles associated with each figure. The change to a hyperlink format reduced the overall size of the Access database from 370 MB to 4 MB and will allow more rapid expansion of the digital database into the future.

Our LLNL SCIE digital sorption data continues to expand. **At present, the includes 215 references, 2011 datasets, and over 23,000 individual data points.** At the end of FY21, we expect the database to double in size by integrating a large fraction of the JAEA Kd database into the LLNL SCIE. A summary of that effort is described in the FY21 crystalline international work package milestone report.

3. A Data Mining/Data Driven Approach to Surface Complexation Model Database Development for Reactive Transport Modeling

The following is a description of our overall approach to surface complexation model database development for reactive transport. The information presented is an excerpt from a draft manuscript to be submitted for publication in late FY21.

Reactive transport models are an essential tool for the simulation of coupled physical, chemical, and biological processes in Earth systems and a resource for integrating fundamental research on biogeochemical processes to predict the spatial and temporal migration of nutrients, contaminants, etc. in the environment.(Steefel et al., 2005) Retardation processes play a central role in determining migration behavior. While a multitude of processes may impact retardation (solubility, diffusion, biological mineralization, etc.), reactions at the solid-water interface (i.e. sorption processes) often play a central role. Traditionally represented by an empirical linear distribution coefficient ($K_d = C_{solid}/C_{aqueous}$) in which C_{solid} represents the concentration associated with the solid phase (adsorbed or otherwise) while $C_{aqueous}$ represents the concentration associated with the mobile phase, the K_d approach is limited by the fact that surface site saturation and competitive effects are not accounted for but it is mathematically and computationally attractive as it can be very efficiently treated in numerical models through a simple correction to the local fluid velocity (i.e. a retardation factor). Unlike K_d models, surface complexation (SCMs) and ion exchange models provide a more robust mechanistic description of reactions at solid-liquid interfaces. These models are directly coupled to thermodynamic

models of aqueous speciation and solubility and can account for dynamic changes in solid and fluid composition, site saturation and competitive effects.

Over the past several decades, quantifying sorption phenomena has been the subject of intense research. A recent review of manuscripts published in the ACS journal Environmental Science & Technology reveals that sorption (the process that SCMs attempt to capture numerically) remains the most highly used word in the recent twenty year history of this journal (second only to the term "water")(Zhu et al., 2021). A cursory Web of Science search on the terms "sorption" and "adsorption" suggests that interest in sorption phenomena across all scientific disciplines continues to grow exponentially with nearly 100,000 manuscripts published in 2020. (Figure 1).

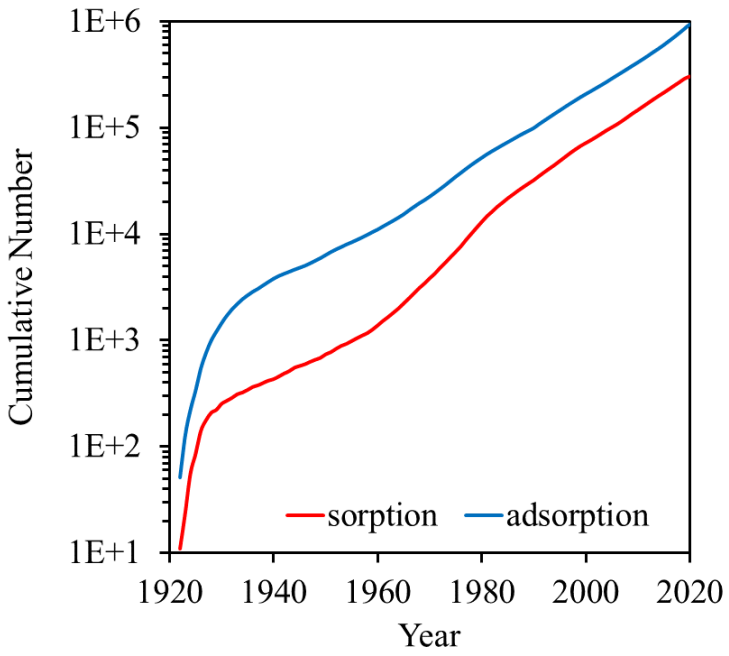

Figure 1. Cumulative number of publications referencing the topics of "sorption" and "adsorption" based on the compiled data available in the Web of Science.

A significant challenge to developing a universal approach to SCMs and associated reaction constants has been the absence of a universal framework to mine, compile, and analyze the massive numbers of sorption data available in the literature, and to test different SCMs across these common datasets. Analyzing these large sorption datasets has also been limited by the lack of access to digitized literature data and the lack of common standards and approaches to archiving these data types (i.e. findable, accessible, interoperable, reusable "FAIR" data (Wilkinson et al., 2016)). While these standards are in the process of development for new data collection activities (e.g. DOE SBR ESS-DIVE, https://ess-dive.lbl.gov/) (Damerow, 2021), data mining provides an opportunity to access an extensive collection of data and develop modeling consistency for a fundamental process that is critical to advancing reactive transport modeling in Earth science. The materials science community has been on the forefront of applying machine learning to the mining of scientific literature (Batra, 2021; Chen et al., 2021; Hiszpanski et al., 2020; Kim et al., 2020; Mukaddem et al., 2020; Olivetti et al., 2020; Swain and Cole, 2016). As

data mining approaches are applied to experimental geochemistry, data mining/data driven approaches will fundamentally change how predictive tools quantify uncertainty, impacts, and risks associated with the reactive transport of contaminant and nutrients in Earth systems.

Among the most notable (manual) data mining efforts for the development of SCM databases, Dzombak and Morel(Dzombak and Morel, 1990) developed a diffuse layer SCM database for the sorption of 22 elements to the mineral hydrous ferric oxide (HFO). A follow-on effort by Karamalidis and Dzombak (Karamalidis and Dzombak, 2010) developed a similar database for gibbsite. The HFO SCM database was developed by critically evaluating 169 literature references (109 references were rejected due to data quality issues). Manual digitization of the 60 high quality references yielded an estimated ~1910 batch sorption data which were fit to a two-site diffuse layer SCM. The HFO surface area, reactive site densities, and surface acidity constants were held constant and based on a critical review of HFO characterization data. On average, this modeling effort was comprised of 34 data per reference and 87 data per element-mineral pair. To this day, this database remains the most widely used SCM database for predicting metal interaction with HFO. Nevertheless, it is limited in that the database is static (no updates) and reactive transport models that use this database are constrained by the original choice of thermodynamic data and SCM employed by the authors (i.e. two-site diffuse layer surface complexation).

An alternative data mining approach that has been pursued for development of comprehensive SCM databases has been the mining of SCM reaction constants from the literature rather than the raw sorption data contained therein (i.e. the RES^{3}T database, https://www.hzdr.de/res3t).(Brendler et al., 2003) The compilation of reaction constants is the common approach taken in traditional thermodynamic database compilations (e.g. aqueous speciation, solubility, etc.) for which data treatment and reaction parameterization is relatively well established in the scientific community (Johnson and Lundeen, 1997; Ragoussi and Brassinnes, 2015; Ragoussi and Costa, 2019; Zimmer et al., 2016). However, SCMs have not yet reached that level of scientific consensus. Large number of SCMs persist in the literature (e.g. non-electrostatic, constant capacitance, diffuse layer, triple layer, MUSIC, multi-site vs one-site, etc.) and methodologies to convert parameters from one SCM to another have not been successful. Nevertheless, the RES^{3}T effort is mining the literature for SCM reaction constants and has developed an open-source database of reaction constants and associated meta-data (i.e. experimental conditions, DOI references, etc.). The focus of the RES^{3}T database effort is on chemical systems connected to radioactive waste management, to nuclear decommissioning and environmental remediation as well as NORM-related challenges. At present, this database contains information from 3172 literature references that include reactions between 147 minerals and 148 ligands and a total of 7062 reaction constants that span across all known SCMs.

The RES^{3}T database provides a comprehensive list of reaction constants reported in the literature for a very large number of metal-mineral reaction pairs. However, this database project does not provide recommended values. It also does not capture the primary (raw) sorption data or provide information on the aqueous speciation constants used in determining those SCM reaction constants. As a result, the RES^{3}T project provides a foundation for developing a self-consistent database of SCM reaction constants but does not go so far as to provide one. Three key issues prevent the direct application of the RES^{3}T database in reactive transport models. They are:

- An inability to integrate published SCM reaction constants and SCM constructs into single unified model and associated set of reaction constants

- An inability to produce self-consistent reaction constants based on a common set of aqueous speciation constants and surface properties.
- The absence of error propagation in the sorption data and/or database constants needed to assess model uncertainties.

To address the limitations of the RES^{3}T database, mining of the raw sorption data from publications contained in this database is necessary. These mined data could then be used to develop SCMs that are informed by the reported reaction constants in the RES^{3}T database but made self consistent by using a specified thermodynamic database, applying mineral-specific metadata (e.g. site density, acidity constants, etc.) uniformly, capturing uncertainties associated with the data fitting process, and incorporating the reactions and associated parameter uncertainties into a database for use in reactive transport models.

Based on the data density in the Dzomback and Morel database (34 data per reference), we can estimate that the data mining potential from the RES^{3}T database alone is on the order of 108,000 individual sorption data. Indeed, we hypothesize that the narrow scope of the RES^{3}T database effort suggests that historical sorption data in the literature is likely to be on the order of millions to tens of millions of data (Figure 1). Indeed, the application of ML and hybrid ML-SCM modeling of sorption data is not limited by the paucity of data, but, rather, the paucity of FAIR data.

3.1 Marerials and Methods

The need to develop SCMs, in concert with traditional thermodynamic models (for aqueous speciation and mineral solubility), for nuclear waste repository performance assessment was identified many years ago (Bradbury and Baeyens, 1993). This issue was expressly identified in NEA sorption project reports (Davis et al., 2005; Ochs et al., 2012). However, significant progress on this issue has been made only recently in various international nuclear waste repository programs (e.g. (Bradbury and Baeyens, 2009), (Dresden-Rossendorf, 2013), (Geckeis et al., 2013)). Hybrid approaches have also been attempted (Bradbury et al., 2010). The best path forward for developing such databases remains an open question (Geckeis et al., 2013), particularly in cases where generic repositories are being investigated resulting in a need to model radionuclide behavior over a very broad range of solution and mineralogic conditions. Our approach is based on principles of FAIR data that allows a SCM database to evolve with SCM constructs and reactive transport modeling codes. Figure 2 presents an overview of our data mining/data driven workflow for SCM database development.

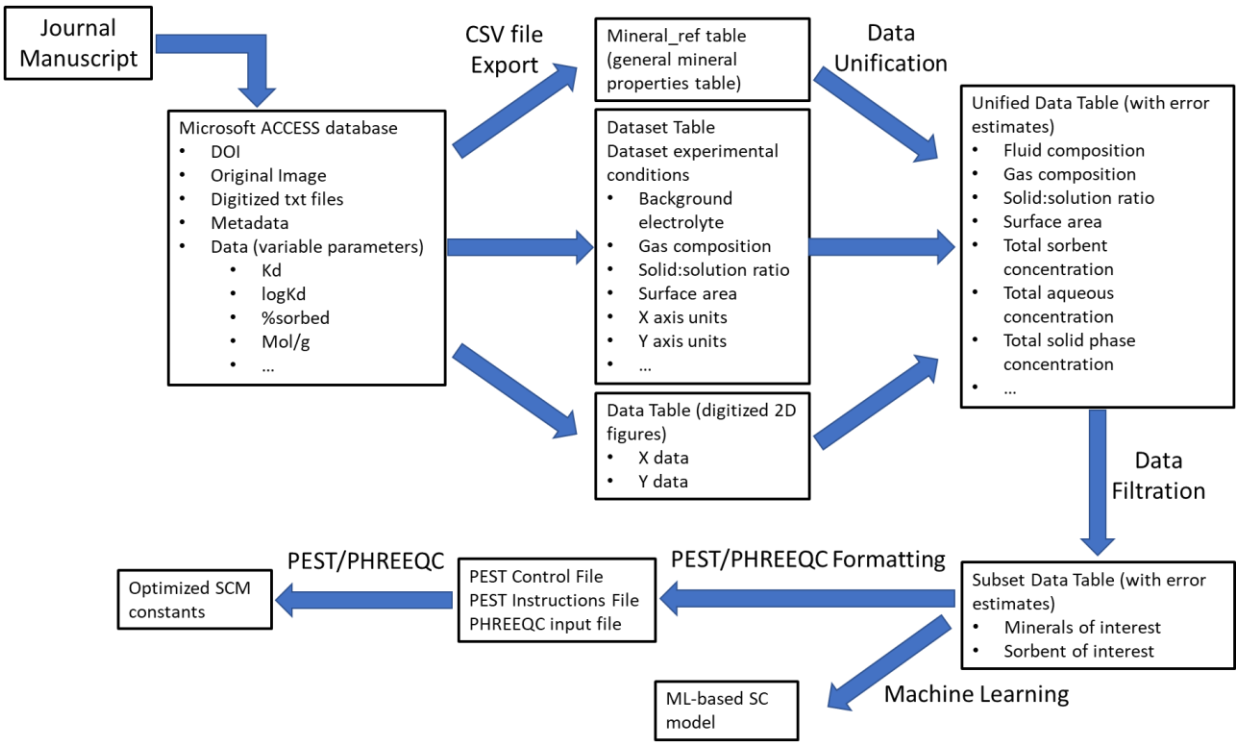

Figure 2. Workflow describing the process from literature data digitization, incorporation into the LLNL SCIE database, unit conversion and data unification, data filtration, data formatting, the SCM reaction constant fitting.

LLNL SCIE Database

In coordination with our RES^{3}T partners, we have focused on developing a data digitization pipeline that would merge the approach pioneered by Dzombak and Morel (i.e. data mining, digitization, and comprehensive fitting of raw data) with the SCM reaction constant mining efforts in RES^{3}T (i.e. reaction constant mining and metadata digitization) to develop a robust approach to database development that is amenable to both ML as well as traditional SCMs. The LLNL SCIE Database stores raw digitized sorption data from the literature, with a particular focus on references contained in RES^{3}T. At present, the LLNL SCIE database is stored as a Microsoft Access relational database with a series of linked tables. The tables include a Reference Table, Dataset Table, Atmospheric CO_2 Table, Mineral Site Density Table, and Data Table. Details regarding the structure of the database have been previously reported in milestone deliverables and FY21 updates to the structure are described in section 2.

Data mining process

The first step in mining raw sorption data is to identify target references for digitization. Target references are identified primarily through the RES^{3}T database which also provides metadata (e.g. mineral surface area) and reported surface complexation reaction constants. The metadata are primarily contained in the LLNL SCIE Dataset Table and are manually entered into the database. The raw data contained in the reference (typically in the form of X-Y figures) are digitized using the DataThief software which allows the user to capture data reported in digital plots, *including data uncertainties*. Most sorption data figures are reported as percent sorbed vs.

pH. However, some data are reported in terms of Kd (mL/g), Ka (m^2/g), or simply equilibrium aqueous concentration. Regardless of the units included in the plotted data, the DataThief software captures the raw information contained in the plot and the raw data are imported into the LLNL SCIE database *as-is*. To facilitate the data import process, a text import form is used to pull the digital data produced by the DataThief (including error bars) into the LLNL SCIE database automatically. From the standpoint of data uncertainty, data digitization is limited by the presence or absence of error bars on the figures. If error bars are included, the data uncertainties can be captured directly. If error bars are not included, an estimate of the data uncertainty is made.

Data Unification

Once raw data are imported into the LLNL SCIE database, a series of unit conversion and uncertainty estimates are necessary to make data amenable to SCM data fitting (or ML applications). Automating this process is essential. The data unification processes were scripted using the R environment. The goal is to convert raw data contained in the LLNL SCIE database into a unified CSV dataset with standard parameter units (mol/L is preferred unit) for all parameters contained in the original LLNL SCIE database. The most challenging aspect of this is the conversion of various types of X-Y plots into representative values of aqueous and sorbed concentrations. While unit conversion and error propagation is straightforward for some parameters, certain error propagations are challenging (e.g. conversion of reported log K_d uncertainties to sorbed concentration uncertainties). The plots digitized from the literature include as many as 38 different parameters and units that represent values associated with X-Y plots.

Upon completion of the unit conversion and uncertainty estimation for the parameters needed to perform SCM fitting, a unified database of raw sorption data is produced. The components in the unified database, parameters, and units are the following: Reference, Set, SetID(#), Mineral, Mineral_formula, Mineral_source, Temp (°C)*, ElectrolyteX(mol/L)*, pH*, Sorbing species, Species_total(mol/L)*, Aq_val(mol/L)*, Sorbed_val(mol/L)*, SurfCharge_val(microC/cm^2)*, Mineral_val(g/L)*, MineralSA(m^2/g)*, Mineralsites(sites/nm^2)*, CEC(meq/100g)*, GasX(bar)* (* Reported or Default standard deviations are included). The unified data can be used to plot all datasets in a uniform manner and automate formatting for use in the SCM data fitting process.

Data Fitting Process

The end goal of this effort is the development of a consistent database of surface complexation/ion exchange reaction constants for use in reactive transport modeling. As such, the digitization of raw data is simply the first step in the development of SCM reaction constants and an associated database. To achieve this end goal, data captured in the LLNL SCIE database must be fitted to SCMs to produce reaction constants. To this end, scripts were developed to extract and format the relevant data captured in the unified LLNL SCIE database as input into the PEST parameter estimation code (Doherty, 2003) that is linked to the SCM algorithms contained in the PHREEQC code(Parkhurst and Appelo, 1999). The details of the input files will not be described here. However, it should be noted that a robust approach that involves unit conversion, data manipulation, and input file formatting was developed in R to facilitate the data fitting workflow. These formatted outputs are passed over to PHREEQC/PEST data fitting routines (and ML applications not discussed here) that can then be visualized using scripts written in Python.

To perform the SCM parameter estimation, PHREEQC requires a thermodynamic database to simulate the aqueous speciation and precipitation of mineral phases at each solution condition for each sorption data point captured in the LLNL SCIE database. The PHREEQC package contains historical thermodynamic data based on LLNL's SUPCRT(Johnson and Lundeen, 1997) database that was supported by the US nuclear waste repository program at Yucca Mountain. More recently, the NEA-TDB effort(Ragoussi and Brassinnes, 2015; Ragoussi and Costa, 2019) is providing updates to thermodynamic data for radionuclides relevant to nuclear waste repository science. Our SCM database workflow can be integrated with thermodynamic database updates as they become available to provide a self-consistent set of reactions both from the standpoint of radionuclide speciation and solubility and reactions at the mineral-water interface. As new thermodynamic data become available, raw sorption data captured in the LLNL SCIE database can be routinely re-fit to provide a consistent representation of aqueous speciation, solubility, and mineral-water interface reaction constants (Figure 2).

PEST Minimization Routine

For the U(VI)-quartz test case describe herein, all PEST optimizations were performed by minimizing the difference between the measured and modeled aqueous U(VI) concentration in solution. Importantly, a weighting factor was assigned to each datapoint based on the reciprocal of the standard deviation of the aqueous concentration (e.g. 1/SD). The application of a weighting factor is essential to provide a balanced relevance to measured concentrations that range over many orders of magnitude. It is also essential to addressing uncertainties in measured values that arise from a combination of measurement error and data digitization error. Two parameters are examined from the standpoint of "goodness of fit". The first is the sum of squared weighted residuals (phi term) that is the objective function in PEST:

$$phi = \sum(c_i w_i - c_{0i} w_i)^2$$

where c_i and c_{0i} are the measured and simulated aqueous concentration for the i'th observation and w_i is the weight associated with i'th observation (1/SD here). When w_i is the uncertainty in the value c_i, the *phi* term is equivalent to weighted sum of squares (WSOS) parameter that is commonly reported in surface complexation data fitting.(Dzombak and Morel, 1990) Given the large number of data available in the SCIE database for U(VI) sorption to quartz, the number of degrees of freedom can be estimated by the total number of data (n) such that the commonly used "goodness of fit" parameter WSOS/DF is nearly equivalent to WSOS/n (n=526 in this example).

The second parameter that provides a general assessment of "goodness of fit" is the correlation coefficient (R):

$$R = \frac{\sum(c_i w_i - m)\,(c_{0i} w_i - m_0)}{(\sum(c_i w_i - m)^2 \sum(c_{0i} w_i - m_0)^2)^{1/2}}$$

where m and m_0 are the mean value of weighted aqueous concentration and mean value of weighted simulated aqueous concentration, respectively. The correlation coefficient is valuable in comparing various models as it is independent of the number of observations in the model run. The correlation coefficient R is equivalent to a *weighted* Pearson correlation coefficient that

accounts for the uncertainties associated with individual observations. A value of 0.9 is considered an acceptable fit to the data.(Doherty, 2003).

3.2 Results and Discussion

To evaluate the feasibility of using a raw sorption database (the LLNL SCIE) to build a self-consistent SCM database using the framework established in RES^{3}T, we describe a test-case for U(VI) sorption to quartz. The RES^{3}T database contains 12 publications(Arnold et al., 2000; Arnold et al., 2001; Coutelot et al., 2018; Davis and Kohler, 2001; Dong and Wan, 2014; Fox et al., 2006; Jung et al., 1999; Kohler et al., 1996; Kulik, 2002; Pabalan et al., 1998; Prikryl et al., 2001; Viani and Torretto, 1998) in total related to this binary system and reports 37 different surface complexation reactions constants based on three different SCMs (diffuse layer, non-electrostatic, and triple layer models). The reaction constants from a single reference may include multiple fitting exercises performed on all or a subset of data included in that reference. For example, for reference DK01, 11 reaction constants are reported. Upon detailed examination of this reference, the 11 reaction constants are associated with four separate data fitting exercises in which the authors chose particular subsets of data and reaction equations. The four separate fitting exercises and associated reactions constants are identified in Table 1.

Table 1. Fitting results using RES^{3}T surface complexation models.

SCM Type	Surface Area m^2/g	Site Density sites/nm^2	Orig pK_1	Orig pK_2	Species	Orig logK	SD[a]	Fit logK	Fit SD	Orig R	Fit R	Orig WSOS	Fit WSOS	Model Reference
DDL	0.2	4.81		5.62	>Si-O_2-UO_2	-5.72	0.03	-5.74	0.03	0.85	0.85	8485	8478	AZBN00a
DDL	0.2	4.81		5.62	>Si-O_2-UO_2	-5.51	0.03	-5.74	0.03	0.85	0.85	9239	8478	AZZBN01
DDL	0.2	2.3		7.2	(>SiOH)$_2$-UO_2^{2+} (>SiOH)$_2$-UO_2CO_3	5.12 16.943	0.09 0.07	3.65 16.52	0.11 0.05	0.70	0.84	19417	8591	CSB18
DDL	0.2	2.3		7.2	(>SiOH)$_2$-UO_2^{2+} (>SiOH)$_2$-UO_2CO_3	5.12 16.94	0.09 0.07	3.65 16.52	0.11 0.05	0.70	0.84	19395	8591	DW14
DDL	10	10	-1.6	7.6	>X-O-UO_2^+ >X-O-UO_2(OH) >X-O-$UO_2CO_3^-$	-1.978 -7.259 9.529	0.11 0.17 0.08	-1.32 -7.53 9.61	0.05 0.30 0.06	0.85	0.87	9037	**6893**	JHLCH99
DDL	0.31	2.3	-1.24	7.06	>Si-O-UO_2^+ >Si-O-$UO_2(OH)_3^{2-}$	-0.3 -18.7	0.04 0.10	-0.54 -17.30	0.03 0.08	0.77	0.85	11562	7590	PJTP01
DDL	0.03	2.3		7.2	>Si-O-UO_2^+ >Si-O-UO_2(OH) >Si-O-$(UO_2)_3(OH)_5$	0.3 -5.65 -16.75	0.06 0.10 0.45	-0.95 -5.54 -19.13	0.10 0.50 0.04	0.75	0.85	16105	7933	PTBP98
DDL	0.1	2.31		7.2	>Si-O-$UO_2(OH)_2^-$	-8.45	0.09	-10.18	0.04	0.79	0.85	23103	10449	VT98
NE	0.33	0.64w		7.2	>Si(w)-O-UO_2^+	-0.03	0.15	-2.18	8.05	0.80	0.84	10784	8815	DK01_3

		0.0078s		>Si(w)-O-$UO_2(OH)$	-4.95	0.07	-4.89	0.05					
				>Si(s)-O-UO_2^+	1.2	1.08	-0.76	5.73					
				>Si(s)-O-$UO_2(OH)$	-3.19	0.46	-2.51	0.21					
NE	0.33	0.64w 0.012s	7.2	>Si(w)-O-$UO_2(OH)$	-5.28	0.09	-5.55	0.08	0.88	0.89	6909	**6464**	DK01_4
				>Si(w)-O-$UO_2CO_3^-$	10.183	0.07	9.97	0.07					
				>Si(s)-O-$UO_2(OH)$	-2.56	0.08	-2.62	0.07					
NE	0.33	0.63w 0.0077s	7.2	>Si(w)-O-$UO_2(OH)$	-4.98	0.05	-4.88	0.05	0.84	0.84	9360	8792	DK01_c4
				>Si(s)-O-UO_2^+	1.06	0.56	-1.18	26.84					
				>Si(s)-O-$UO_2(OH)$	-3.28	0.35	-2.47	0.20					
NE	0.33	0.53	7.2	>Si(w)-O-$UO_2(OH)$	-4.64	0.03	-4.56	0.03	0.84	0.85	9018	8937	DK01_1
NE	0.33	0.53	7.2	>Si-O-$UO_2(OH)$	-4.73	0.03	-4.55	0.03	0.84	0.85	9283	8937	KCKD96_1
NE	0.33	0.64w 0.012s	7.2	>Si(w)-O-$UO_2(OH)$	-5.32	0.05	-4.90	0.05	0.83	0.84	9724	8830	KCKD96_2
				>Si(s)-O-$UO_2(OH)$	-2.65	0.09	-2.81	0.11					
NE	0.33	0.64w 0.012s	7.2	>Si(w)-$O_{(0.5)}$-$UO_2(OH)$	-5.28	0.07	-5.55	0.08	0.88	0.89	6924	**6472**	K02b_2
				>Si(w)-$O_{(0.5)}$-$UO_2CO_3^-$	10.17*	0.09	9.97	0.08					
				>Si(s)-$O_{(0.5)}$-$UO_2(OH)$	-2.56	0.08	-2.64	0.07					
NE	0.33	0.64w 0.012s	7.2	>Si(w)-$O_{(0.5)}$-$UO_2(OH)$	-6.56	0.39	-5.55	0.08	0.72	0.89	30052	**6472**	K02b_1
				>Si(w)-$O_{(0.5)}$-$UO_2CO_3^-$	8.89*	0.10	9.97	0.08					
				>Si(s)-$O_{(0.5)}$-$UO_2(OH)$	-5.57	1.93	-2.64	0.07					
TL	0.32	4.6051w 0.00184s	8.4	>Si(s)-O-UO_2^+	1.98	0.93	-	-	0.87 (0.89)	0.87	7606 (6131)	**6562**	FDZ06[b]
				>Si(s)-O-$UO_2(OH)$	-1.88	0.35	-1.97	0.26					
				>Si(w)-O-UO_2^+	-2.08	0.69	-1.00	0.09					
				>Si(w)-O-$UO_2(OH)$	-5.76	0.05	-6.37	0.10					
				>Si(w)-O-$UO_2(OH)CO_3^{2-}$	2.47	0.39	4.05	0.15					

* Reaction equation rewritten using CO_3^{--} rather than $CO_2(aq)$

[a] SD calculated in PEST based on original reaction constant.

[b] Surface species incorrectly identified in RES^{3}T database.

Importantly, it should be noted that the RES^{3}T database includes references in which no original data are presented (e.g., Kulik, 2002; Viani and Torretto, 1998) and does not include literature references with sorption data that did not include a surface complexation model. Thus, there are a number of publications for U(VI) sorption to quartz that are absent from the RES^{3}T database simply because a surface complexation reaction constant was not reported. Here, we supplemented the RES^{3}T references with additional sorption data from the literature (i.e., Allard et al., 2011; Arnold et al., 1998; Nair et al., 2014). The original figures contained in the 12 RES^{3}T publications (Figure 3), supplemented by several publications in our database that were

not capture in RES^{3}T, once digitized and unified, yield 526 individual data for the U(VI)-quartz system. These digitized and unified data (Figure 4) are captured in the LLNL SCIE database and subjected to the workflow described in Figure 2 for developing SCM reaction constants.

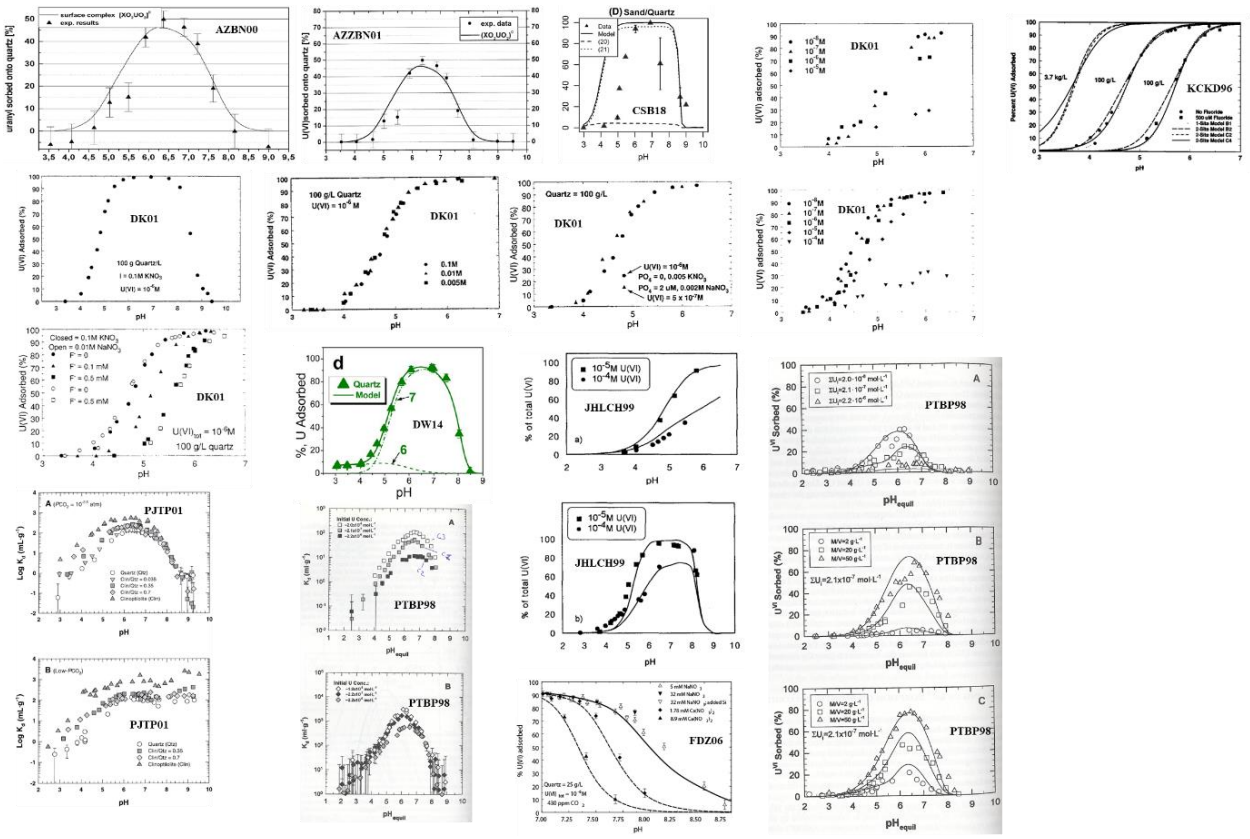

Figure 3. Sorption figures contained in the RES^{3}T references for U(VI) sorption to quartz.

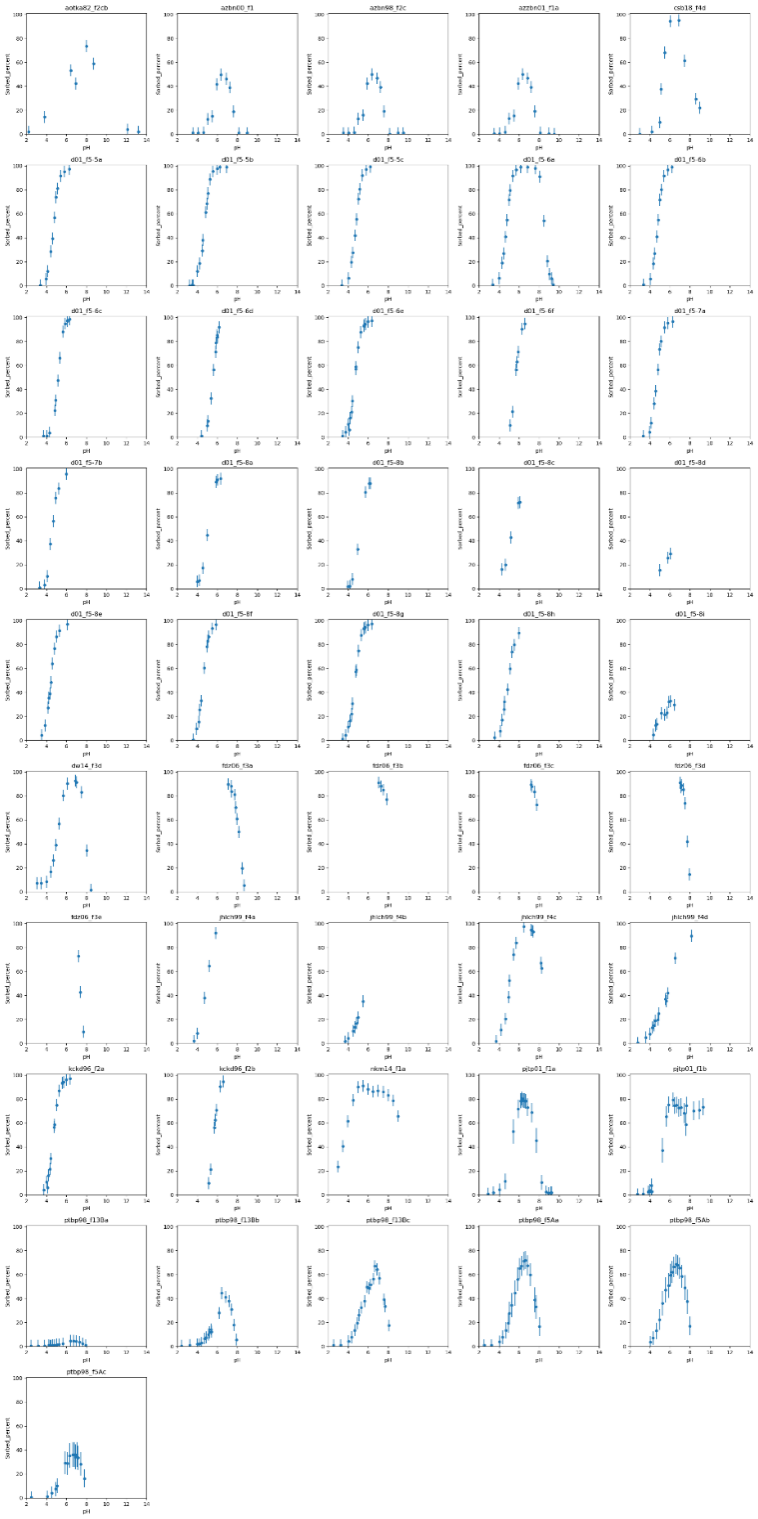

Figure 4. Complete set of sorption data for the U(VI)-quartz system in the LLNL SCIE database after passing through the data unification workflow.

Example of U(VI) sorption to quartz – comparison of RES^{3}T SCM reaction constants

In this example, the 17 sets of published reaction constants (Table 1) included in the RES^{3}T database were tested against the full U(VI)-quartz dataset available in the LLNL SCIE database. Model performance was tested both for the original constants and optimized values. The goodness of fit parameters using reaction constants in the RES^{3}T database are reported in Table 1. A second set of goodness of fit parameters are reported for each set of reaction constants after optimization using PEST.

Importantly, all sets of reaction constants reported in RES^{3}T provide an approximate fit to the global dataset (R = 0.7-0.88) (Figure 5). Once reaction constants are optimized, the fits can be further improved (R = 0.84-0.89). Non-uniqueness of the fitted reactions constants is a common challenge in implementing SCMs. Nevertheless, the large numbers of data (and wide range of solution conditions sampled by those data) in the LLNL SCIE database yield significant differences in data fits among the various proposed SCMs. For example, it is apparent that three surface species are needed, both for the NE and DDL models to achieve an adequate fit to the data (R $\rightarrow$0.9). The choice of bidentate or monodentate surface complexes does not appear to have a significant impact on the goodness of fits. However, the presence of a carbonate surface complex significantly improves the overall data fit (JHLCH99, DK01_4, K02b_2, and K02b_1 have WSOS<7000 and all contain a carbonate surface species). Comparison of similar models in the presence and absence of a carbonate surface species lead to the same conclusion (e.g. compare fit of KCKD96_2 and DK01_4 reactions in Figure 6). Surprisingly, the more realistic representation of the electrical double layer in the DDL model does not necessarily lead to a more robust fit to the sorption data. Indeed, it appears that a global modeling approach can be used to identify the preferred representation of mineral-water interface and the surface complexation reactions most representative of the observed sorption behavior. It must, nevertheless, be acknowledged that the fitting exercise does not yield a single preferred representation of reactions at the mineral-water interface. Various combinations of interface representations and surface species yield similar fit quality. While this result may be disappointing from the standpoint of identifying true surface complex stoichiometries on the quartz surface, the intention here is the development of reaction constants representative of the overall partitioning of U(VI) between the surface and the aqueous phases. From that perspective, the stoichiometry of the surface complex is less critical than the ability of the model to effectively capture the sorption of U(VI) for use in reactive transport models and the associated uncertainties. Indeed, further refinement of the surface complexation reaction stoichiometries may be warranted in the longterm and can be readily introduced with the inclusion of spectroscopic evidence from the literature. However, from a practical standpoint, this may not impact our reactive transport predictive ability unless system conditions deviate significantly from the range of solution conditions captured in the database.

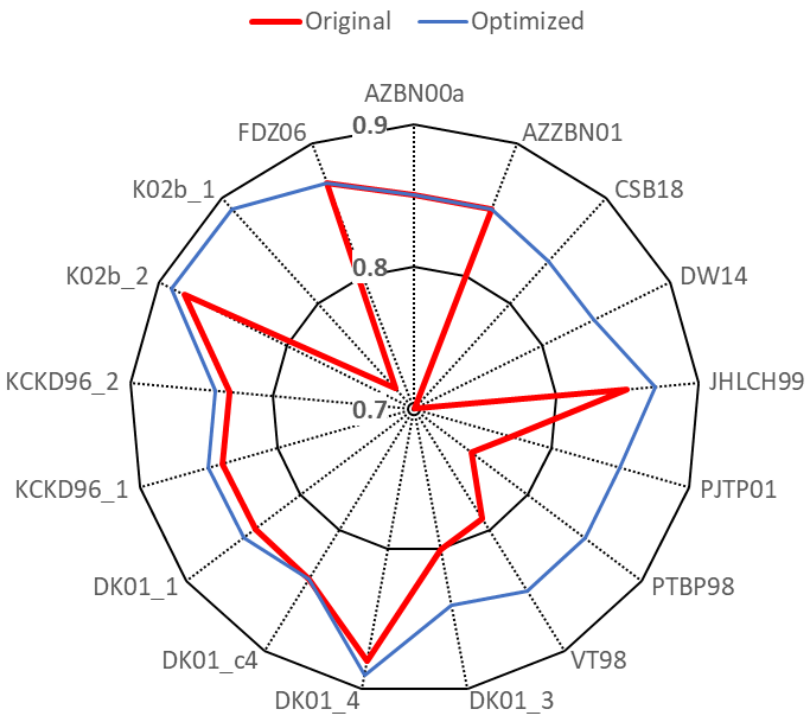

Figure 5. Comparison of R values for 17 sets of RES^{3}T reaction constants prior to and after global optimization using PEST/PHREEQC. R value range from 0.6 to 0.9.

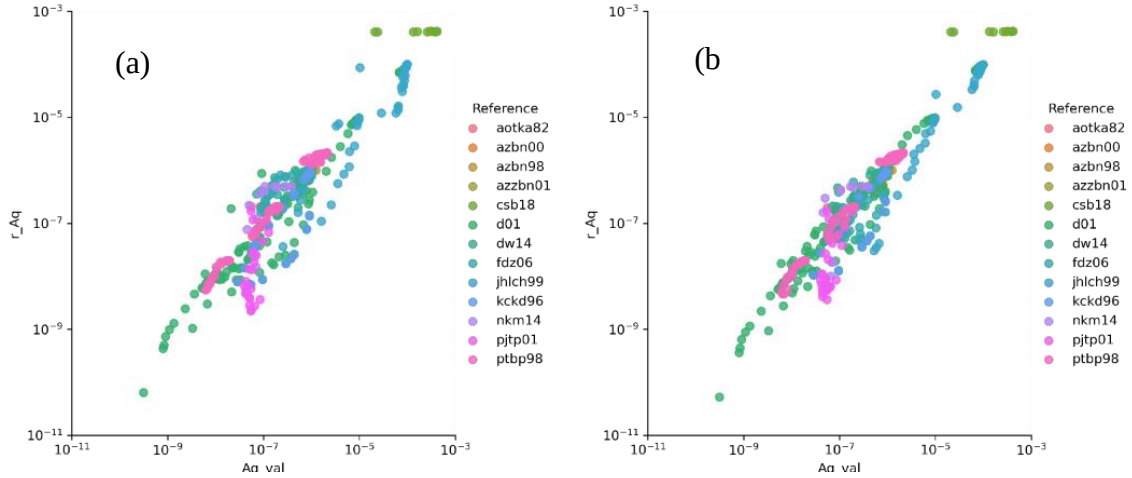

Figure 6. Comparison of U(VI)-quartz data fits of (a) Kckd96_2 (R=0.84) that includes >Si(w)-O-UO_2(OH) and >Si(s)-O-UO_2(OH) surface complexes to (b) Dk01_4 (R=0.89) that includes >Si(w)-O-UO_2(OH), >Si(s)-O-UO_2(OH), and >Si(w)-O-$UO_2CO_3^-$ surface complexes.

The application of large sets of FAIR sorption data to SC modeling does provide numerous advantages. First, the global data fitting approach includes uncertainty quantification that can be propagated through to reactive transport models and risk and performance assessment calculations (see Table 1). Second, regardless of the choice of surface reactions and SCM, the uncertainty associated with the choice of SCM can be propagated into reactive transport simulations. Finally, the availability of FAIR sorption data allows for reaction constants to be readily adjusted as new data, new spectroscopic information, and new SCM constructs become available.

Example of U(VI) sorption to quartz – systematic optimization of non-electrostatic and diffuse layer SCMs

The 17 sets of reaction constants reported in Table 1 were based on a variety of SCMs (non-electrostatic, diffuse layer, and triple layer models), varying estimated of reactive site density (0.00184 to 10 sites/nm^2), the inclusion of one or two site types, and surface acidity constants ranging from 5.62 to 8.4 and the absence or presence of a protonation constant ranging from -1.24 to -1.6. As such, the reported and fitted reaction constants are only valid when paired with the site density and surface acidity constants used during data fitting. This represents a fundamental impasse for building a coherent set of reaction constants for multiple sorbing elements on a single mineral. Such a self-consistent model requires all reaction constant to be fit using common metadata with regards to the surface properties of a particular mineral. For the case of mineral reactive site density, given that sorption data fitting is not sensitive to a unique site density, a pragmatic approach may be the most suitable for this parameter, particularly for the purpose of reactive transport modeling. For the case of surface acidity, the LLNL SCIE database contains a number of potentiometric titration data that can be used to independently fit surface acidity constants which can then be included in metal surface complexation data fitting. Finally, the choice of multisite vs single site models of metal sorption to mineral surfaces is dependent on the overall sorption behavior of the particular metal (U(VI) in our example) and the benefit of including multiple sorption sites when compared to the increased model complexity that a multisite model implies. In examining the results of Table 1, a two site non-electrostatic model yielded a better fit to the global dataset while a one site diffuse layer model yields a nearly equally good fit. Thus, the choice of single vs multisite sorption in the present example is somewhat ambiguous. However, it is important to consider that the U(VI) sorbent may not appear to exhibit behavior strongly indicative of a multisite sorption behavior on quartz but other sorbents may in fact exhibit the opposite behavior. The balance between model complexity and model uncertainty must be weighed by both the needs of the predictive model and the fit to the available data (i.e. the principle of parsimony).

For the purposes of comparing non-electrostatic versus diffuse layer models of the quartz surface, we chose the following pragmatic approach to fitting the available sorption data. A site density commonly used in SCMs is 2.31 sites/nm^2 and is chosen here (a “strong site” density equivalent to 1% of the total site density was used in the 2-site models). While potentiometric titration data could be used to optimize the surface acidity constants for the quartz surface, we apply a pKa that is most often reported in the RES^{3}T databased for this mineral (7.20) and assume that the protonation constant is sufficiently low to have little impact on the surface charge properties of quartz. Finally, all surface species are assumed to be mono-dentate inner-sphere reactions such that:

$$>SiOH + UO_2^{2+} + X\ H_2O \rightarrow SiOUO_2(OH)_X^{+1-X} + 1+X\ H^+$$

where X = 0-3. Similarly, for the carbonate species,

$$>SiOH + UO_2^{2+} + Y\ CO_3^{2-} \rightarrow SiOUO_2(CO_3)_Y^{+1-2Y} + -1\ H^+$$

where Y = 1-2. Based on our analysis of the RES^{3}T U(VI)-quartz reaction constants, it is apparent that the charge of the surface complex ranges from +1 to -2. Thus, the maximum number of surface species is 6 for a single site model and 12 for a two-site model. We systematically tested global fits to all data starting with a 6 or 12 surface reaction non-electrostatic and diffuse layer models. Surface reactions were removed from the simulation sequentially starting with the least sensitive reaction equations. The resulting plots of R-values are presented in Figure 7. It is apparent from this analysis that a 1-site model achieved a "best fit" with ≥3 reaction constants. Furthermore, a 2-site model is superior to a 1-site model even when the total number of reactions are the same. Finally, the diffuse layer model leads to a nominally better fit to the data in most cases. Most importantly, various combinations of SCMs and surface reactions can be used to achieve a good fit to the data. From the perspective of reactive transport modeling, one must weigh the quality of the data fit to the model complexity and parameter uncertainty to determine which sets of reaction constants are most appropriate for modeling purposes. With the exception of the 2-site non-electrostatic model, all models reach a plateau with the use of 3 reaction constant. Table 2 lists the results for the 3 surface reaction fits to the 4 SCMs examined here. As we concluded in the earlier RES^{3}T analysis, the presence of a carbonate surface species is nearly universal for all models. Even for the 2-Site NEM model that does not include a carbonate species in the 3 most sensitive surface species, the addition of a carbonate species improves the fit significantly as additional surface species are added to the model.

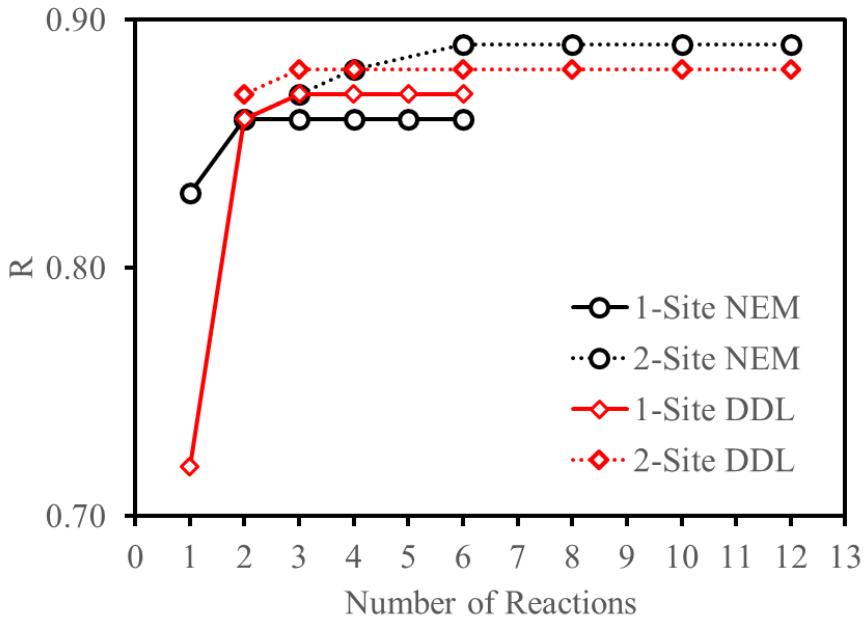

Figure 7. Comparison of quality of global fit as a function of surface complexation reactions included in 4 models of U(VI) sorption to quartz.

Table 2. Surface complexation reaction constants based on a 3-reaction fit using non-electrostatic and diffuse layer, 1-Site, and 2-Site models.

1-Site NEM		2-Site NEM	
$>SiOUO_2^+$	-1.05(0.11)	$>SiOwUO_2OH$	-6.07(0.08)
$>SiOUO_2OH$	-5.71(0.07)	$>SiOwUO_2(OH)_2^-$	-12.18(0.07)
$>SiOUO_2CO_3^-$	9.31(0.08)	$>SiOsUO_2^+$	1.49(0.05)
1-Site DDL		2-Site DDL	
$>SiOUO_2^+$	-0.60(0.04)	$>SiOwUO_2OH$	-6.26(0.09)
$>SiOUO_2(OH)_3^{2-}$	-20.19(0.60)	$>SiOwUO_2CO_3^-$	10.22(0.07)
$>SiOUO_2CO_3^-$	10.19(0.06)	$>SiOsUO_2^+$	1.47(0.05)

3.3 Implications

This work presents a comprehensive data analytics workflow for the mining of sorption data from the literature, evaluation of published SCMs using a global fitting approach, and comparing the performance metrics of different SCMs. This approach takes advantage on common scripting languages (python, R) combined with commonly used geochemical modeling software (PHREEQC) and parameter fitting code (PEST) to enabled us to compare global datasets through effective rapid model iteration and data visualization. In our U(VI)-quartz test case, for example, we establish the non-uniqueness of SCM constructs and associated reaction constants. Nevertheless, it is apparent that a uranyl carbonate species likely plays a role in uranium sorption to quartz. It also appears that multisite sorption models lead to significant improvements to global data fits. Finally, it is apparent that the choice of SCM and model complexity (e.g. multi-site vs one-site) implemented in reactive transport models may, in part, be based on a balance between acceptable model uncertainty and numerical complexity that is acceptable to a particular reactive transport problem. Nevertheless, our FAIR data approach, combined with automated workflows, provides a guide for developing SCM databases that are flexible and easily updated as SCM contructs, thermodynamic databases, and reactive transport modeling codes evolve.

As the LLNL SCIE raw sorption database grows, opportunities to explore application of ML and novel SCMs contructs are anticipated. Machine learning approaches and Random Forest (RF) learning algorithms should be considered as an alternative to traditional SCMs due to their robustness against overfitting and an ability to work well with limited sample sizes. Ultimately, the work presented here provides the necessary tools and advancements in data mining and data compilation to conduct novel sorption data analyses that are the ultimate goal of the FAIR data approach. The application of data-driven approaches to sorption and retardation processes could significantly reduce the computational costs in modeling Earth systems and help to bring consensus to the application of SCM in reactive transport modeling.

4. A Data-Driven Surface Complexation Database for Reactive Transport Modeling: Radionuclide Sorption to Iron Oxides, Carbonates, and Quartz

While section 3 summarizes a detailed analysis of the reaction constant fitting workflow, fitting of reaction constants to a larger set of radionuclide-mineral pairs contained in the database are summarized here. We are not providing detailed information regarding each fitting exercise. However, reaction constants are summarized in Table 3 for all the reactions fit to date. A more detailed analysis will be provided as part of our FY22 efforts.

A self-consistent set of surface complexation reaction constants requires that all reaction constants be fit using common metadata with regards to the surface properties of a particular mineral. For the purposes of testing the effectiveness of our workflow across a large set of data, we chose a non-electrostatic model. We also chose the following pragmatic approach to fitting the sorption data. A site density commonly used in SCMs is 2.31 sites/nm^2 and is chosen here for all iron oxide, quartz and calcite mineral data. While potentiometric titration data could be used to optimize the surface acidity constants, we apply pKa's that are most often reported in the RES^{3}T databased for iron oxides and quartz and do not account for protonation of the calcite surface. Finally, all surface species are assumed to be mono-dentate inner-sphere reactions similar to those formulated in the U(VI)-quartz example.

While a thorough evaluation of the reaction constants and data fits are still needed, this proof of principle fitting exercise indicates that our workflow is robust and capable of processing individual radionuclide-mineral sorption datasets efficiently. The results of this analysis will provide the foundation for development of a comprehensive set of reaction constants in FY22 and an analysis of multisite and electrostatic approaches to the surface complexation database development. Follow-on work will integrate these SC reaction constants with a fitting of ion exchange constants which are critical to simulating ion exchange processes in the bentonite backfill and extending to the far field of a nuclear waste repository.

Table 3. Summary of *preliminary* 1-site NEM reaction constants fit to date as part of the database development effort.

	logK	SD
>CaCO3AmCO3-	4.80	0.02
>FeOHAm+3	7.47	0.04
>FeOAmOH+	-5.49	0.07
>SiOAm+2	0.91	0.21
>SIOAm(OH)2	-14.01	0.17
>CaCO3EuCO3-	4.46	0.16
>FeOHEu+3	7.07	0.05
>FeOEu(OH)3	-20.35	0.53
>SIOEu(OH)2	-8.04	0.21
>CaCO3Ni	0.00	0.06
>FeOHNi+2	6.07	0.02
>FeONiOH	-13.18	1.34
>CaCO3NpO2-	3.46	0.49
>FeOHNpO2+	4.77	0.04
>FeONpO2(OH)-	-12.17	0.06
>CaCO3Pu(OH)3-	6.40	0.11
>FeOHPu(OH)2+	8.26	0.24
>FeOHPu(OH)4	-1.24	0.06
>CaCO3PuO2-	0.12	0.06
>FeOHPuO2+	5.69	0.10
>FeOPUO2(OH)-	-12.10	0.10
>CaCO3SmCO3-	4.66	0.12
>CaCO3Sr	-1.79	0.06
>FeOSr+	-2.38	0.06
>CaCO3UO2	6.95	0.04

>FeOHUO2+2	6.96	0.05
>FeOUO2OH	-1.89	0.02
>SiOUO2+	-1.10	0.13
>SiOUO2OH	-5.64	0.07
>SiOUO2(OH)2-	-12.46	0.09

5. Planned FY22 Efforts

The FY21 effort has focused primarily on building out the Access database of raw sorption data and developing a framework for surface complexation/ion exchange data fitting methods and surface complexation/ion exchange database development. Effort is coordinated with international partners involved in similar database development efforts (e.g. HZDR RES^{3}T). Here, we described a detailed analysis of U(VI) sorption to quartz and provided preliminary surface complexation reaction constants for a number of radionuclides and sorption to iron oxide, calcite, and quartz. Our focus in FY22 will be the buildout of a large set of surface complexation and ion exchange reactions constants for radionuclides and minerals of interest to nuclear waste repository performance assessment. A second effort will focus on the expansion of our data interrogation effort by applying modern data science methods (e.g. machine learning). The combination of machine learning approaches with more traditional PEST/PHREEQC data fitting approaches will provide flexibility to GDSA efforts (e.g. use of mechanistic surface complexation/ion exchange models versus “smart Kd” lookup tables). The effort will include testing of various surface complexation (Non-electrostatic, diffuse layer, etc.) and ion exchange (Vanselow, Gapon, etc.) models and will provide a path for incorporation of surface complexation/ion exchange reaction constants into repository performance assessment.

7. Acknowledgments

This work was supported by the Spent Fuel and Waste Science and Technology campaign of the Department of Energy's Nuclear Energy Program. Prepared by LLNL under Contract DE-AC52-07NA27344.

8. References

Allard, B., Olofsson, U., Torstenfelt, B., Kipatsi, H., and Andersson, K., 2011. Sorption of Actinides in Well-Defined Oxidation States on Geologic Media. *MRS Online Proceedings Library* **11**, 775.

Arnold, T., Zorn, T., Bernhard, G., and Nitsche, H., 1998. Sorption of uranium(VI) onto phyllite. *Chemical Geology* **151**, 129-141.

Arnold, T., Zorn, T., Bernhard, G., and Nitsche, H., 2000. Applying the DDLM to model the sorption of uranium onto quartz and muscovite*Annual report 1999*. Forschungszentrum Rossendorf e.V., Institute of Radiochemistry, Dresden (Germany).

Arnold, T., Zorn, T., Zänker, H., Bernhard, G., and Nitsche, H., 2001. Sorption behavior of U(VI) on phyllite: experiments and modeling. *Journal of Contaminant Hydrology* **47**, 219-231.

Batra, R., 2021. Accurate machine learning in materials science facilitated by using diverse data sources. *Nature* **589**, 524-525.

Bradbury, M. H. and Baeyens, B., 1993. A general application of surface complexation modeling radionuclide sorption in natural systems. *J. Colloid Interface Sci.* **158**, 364-371.

Bradbury, M. H. and Baeyens, B., 2009. Sorption modelling on illite. Part II: Actinide sorption and linear free energy relationships. *Geochim. Cosmochim. Acta* **73**, 1004-1013.

Bradbury, M. H., Baeyens, B., and Thoenen, T., 2010. Sorption Data Bases for Generic Swiss Argillaceous Rock Systems. Nagra, Wettingen, Switzerland.

Brendler, V., Vahle, A., Arnold, T., Bernhard, G., and Fanghänel, T., 2003. RES3T-Rossendorf expert system for surface and sorption thermodynamics. *J Contam Hydrol* **61**, 281-91.

Chen, C., Zuo, Y., Ye, W., Li, X., and Ong, S. P., 2021. Learning properties of ordered and disordered materials from multi-fidelity data. *Nature Computational Science* **1**, 46-53.

Coutelot, F. M., Seaman, J. C., and Baker, M., 2018. Uranium(VI) adsorption and surface complexation modeling onto vadose sediments from the Savannah River Site. *Environmental Earth Sciences* **77**, 148.

Damerow, J. E., Varadharajan, C., Boye, K., Brodie, E.L., Burrus, M., Chadwick, K.D., Crystal-Ornelas, R., Elbashandy, H., Alves, R.J.E., Ely, K.S., Goldman, A.E., Haberman, T., Hendrix, V., Kakalia, Z., Kemner, K.M., Kersting, A.B., Merino, N., O'Brien, F., Perzan, Z., Robles, E., Sorensen, P., Stegen, J.C., Walls, R.L., Weisenhorn, P., Zavarin, M. and Agarwal, D., , 2021. Sample Identifiers and Metadata to Support Data Management and Reuse in Multidisciplinary Ecosystem Sciences. *Data Science Journal* **20**, 11

Davis, J. and Kohler, M., 2001. Surface complexation modeling of uranium(VI) adsorption on quartz.*Surface Complexation Modeling of Uranium (VI) Adsorption on Natural Mineral Assemblages*. Office of Nuclear Regulatory Research, U.S. Nuclear Regulatory Commission, Washington, DC.

Davis, J., Ochs, M., Olin, M., Payne, T., and Tweed, C., 2005. Interpretation and prediction of radionuclide sorption onto substrates relevant for radioactive waste disposal using thermodynamic sorption models. OECD/Nuclear Energy Agency, Paris.

Doherty, J., 2003. PEST: Model-Independent Parameter Estimation. Watermark Numerical Computing.

Dong, W. and Wan, J., 2014. Additive Surface Complexation Modeling of Uranium(VI) Adsorption onto Quartz-Sand Dominated Sediments. *Environmental Science & Technology* **48**, 6569-6577.

Dresden-Rossendorf, H.-Z., 2013. RES³T - Rossendorf Expert System for Surface and Sorption Thermodynamics. RES³T - Rossendorf Expert System for Surface and Sorption Thermodynamics, Dresden, Germany.

Dzombak, D. A. and Morel, F. M. M., 1990. *Surface complexation modeling : hydrous ferric oxide*. Wiley, New York.

Fox, P. M., Davis, J. A., and Zachara, J. M., 2006. The effect of calcium on aqueous uranium(VI) speciation and adsorption to ferrihydrite and quartz. *Geochimica et Cosmochimica Acta* **70**, 1379-1387.

Geckeis, H., Lützenkirchen, J., Polly, R., Rabung, T., and Schmidt, M., 2013. Mineral–Water Interface Reactions of Actinides. *Chemical Reviews* **113**, 1016-1062.

Hiszpanski, A. M., Gallagher, B., Chellappan, K., Li, P., Liu, S., Kim, H., Han, J., Kailkhura, B., Buttler, D. J., and Han, T. Y.-J., 2020. Nanomaterial Synthesis Insights from Machine Learning of Scientific Articles by Extracting, Structuring, and Visualizing Knowledge. *Journal of Chemical Information and Modeling* **60**, 2876-2887.

Johnson, J. W. and Lundeen, S. R., 1997. GEMBOCHS thermodynamic datafiles for use with the EQ3/6 modeling package. Lawrence Livermore National Laboratory, Livermore.

Jung, J., Hyun, S. P., Lee, J. K., Cho, Y. H., and Hahn, P. S., 1999. Adsorption of UO22+ on natural composite materials. *Journal of Radioanalytical and Nuclear Chemistry* **242**, 405-412.

Karamalidis, A. K. and Dzombak, D. A., 2010. *Surface Coplexation Modeling: Gibbsite*. Wiley and Sons, New Jersey.

Kim, H., Han, J., and Han, T. Y.-J., 2020. Machine vision-driven automatic recognition of particle size and morphology in SEM images. *Nanoscale* **12**, 19461-19469.

Kohler, M., Curtis, G. P., Kent, D. B., and Davis, J. A., 1996. Experimental Investigation and Modeling of Uranium (VI) Transport Under Variable Chemical Conditions. *Water Resources Research* **32**, 3539-3551.

Kulik, D. A., 2002. Sorption modelling by Gibbs energy minimisation: Towards a uniform thermodynamic database for surface complexes of radionuclides. *Radiochimica Acta* **90**, 815-832.

Mukaddem, K. T., Beard, E. J., Yildirim, B., and Cole, J. M., 2020. ImageDataExtractor: A Tool To Extract and Quantify Data from Microscopy Images. *Journal of Chemical Information and Modeling* **60**, 2492-2509.

Nair, S., Karimzadeh, L., and Merkel, B. J., 2014. Sorption of uranyl and arsenate on SiO2, Al2O3, TiO2 and FeOOH. *Environmental Earth Sciences* **72**, 3507-3512.

Ochs, M., Payne, T. E., and Brendler, V., 2012. Thermodynamic sorption modeling in support of radioactive waste disposal safety cases. A guideline document. OECD/NEA, Paris.

Olivetti, E. A., Cole, J. M., Kim, E., Kononova, O., C., G., H., T.Y., and Hiszpanski, A. M., 2020. Data-driven materials research enabled by natural language processing and information extraction. *Appl. Phys. Rev.* 7:041317.

Pabalan, R. T., Turner, D. R., Paul Bertetti, F., and Prikryl, J. D., 1998. Chapter 3 - UraniumVI Sorption onto Selected Mineral Surfaces: Key Geochemical Parameters. In: Jenne, E. A. (Ed.), *Adsorption of Metals by Geomedia*. Academic Press, San Diego.

Parkhurst, D. L. and Appelo, C. A. J., 1999. User's guide to PHREEQC (Version 2)--a computer program for speciation, batch-reaction, one-dimensional transport, and inverse geochemical calculations*U.S. Geological Survey Water-Resources Investigations Report*.

Prikryl, J. D., Jain, A., Turner, D. R., and Pabalan, R. T., 2001. UraniumVI sorption behavior on silicate mineral mixtures. *Journal of Contaminant Hydrology* **47**, 241-253.

Ragoussi, M. E. and Brassinnes, S., 2015. The NEA Thermochemical Database Project: 30 years of accomplishments. *Radiochimica Acta* **103**, 679-685.

Ragoussi, M. E. and Costa, D., 2019. Fundamentals of the NEA Thermochemical Database and its influence over national nuclear programs on the performance assessment of deep geological repositories. *Journal of Environmental Radioactivity* **196**, 225-231.

Steefel, C. I., DePaolo, D. J., and Lichtner, P. C., 2005. Reactive transport modeling: An essential tool and a new research approach for the Earth sciences. *Earth and Planetary Science Letters* **240**, 539-558.

Swain, M. C. and Cole, J. M., 2016. ChemDataExtractor: A Toolkit for Automated Extraction of Chemical Information from the Scientific Literature. *Journal of Chemical Information and Modeling* **56**, 1894-1904.

Viani, B. E. and Torretto, P. C., 1998. Sorption and transport of uranium on hematite. Lawrence Livermore National Laboratory, Livermore.

Wilkinson, M. D., Dumontier, M., Aalbersberg, I. J., Appleton, G., Axton, M., Baak, A., Blomberg, N., Boiten, J.-W., da Silva Santos, L. B., Bourne, P. E., Bouwman, J., Brookes, A. J., Clark, T., Crosas, M., Dillo, I., Dumon, O., Edmunds, S., Evelo, C. T., Finkers, R., Gonzalez-Beltran, A., Gray, A. J. G., Groth, P., Goble, C., Grethe, J. S., Heringa, J., 't Hoen, P. A. C., Hooft, R., Kuhn, T., Kok, R., Kok, J., Lusher, S. J., Martone, M. E., Mons, A., Packer, A. L., Persson, B., Rocca-Serra, P., Roos, M., van Schaik, R., Sansone, S.-A., Schultes, E., Sengstag, T., Slater, T., Strawn, G., Swertz, M. A., Thompson, M., van der Lei, J., van Mulligen, E., Velterop, J., Waagmeester, A., Wittenburg, P., Wolstencroft, K., Zhao, J., and Mons, B., 2016. The FAIR Guiding Principles for scientific data management and stewardship. *Scientific Data* **3**, 160018.

Zhu, J.-J., Dressel, W., Pacion, K., and Ren, Z. J., 2021. ES&T in the 21st Century: A Data-Driven Analysis of Research Topics, Interconnections, And Trends in the Past 20 Years. *Environmental Science & Technology* **55**, 3453-3464.

Zimmer, K., Zhang, Y., Lu, P., Chen, Y., Zhang, G., Dalkilic, M., and Zhu, C., 2016. SUPCRTBL: A revised and extended thermodynamic dataset and software package of SUPCRT92. *Computers & Geosciences* **90**, 97-111.

Zavarin, M., Wolery, T.J., Atkins-Duffin, C. 2016. M4FT-16LL080302052-Update to Thermodynamic Database Development and Sorption Database Integration. LLNL-TR-701407, Lawrence Livermore National Laboratory.

Zavarin, M., Balboni, E., Booth, C.Wolery, T., Atkins-Duffin, C. 2018. M4SF-18LL010302082-Thermodynamic Database Development and Identification of Actinide Sequestration in Corrosion Products, LLNL-TR-756687, Lawrence Livermore National Laboratory.

Zavarin, M. 2019. M4SF-19LL010301082-SurfaceComplexation and Ion Exchange Database Development Phase 1: Clay Minerals, LLNL-TR-778004, Lawrence Livermore National Laboratory.

Appendices

Appendix A
Characterization Methods

Experimental Setup

The bentonite used in this experimental work was mined from a reducing horizon in Colony, Wyoming. The bentonite was pulverized and sieved to < 3 mm and used with a free moisture content of ~15.5 wt.%. The groundwater solution was prepared using reagent grade materials dissolved in double deionized water. NaOH and HCl were added to adjust the initial solution pH. This solution was then filtered through a 0.45 μm filter and sparged with He before each experiment. The synthetic brine solution was added at 9:1 water:bentonite ratio. Initial components for wall rock experiments have been summarized in Table 2 of text.

Experiments were performed to examine the bentonite system with host rock, waste canister, and cement inclusion. Host-rock experiments focused on Opalinus Clay from the Swiss Underground Research Laboratory located at Mont Terri. The core was collected from BFE-A10 drill core (interval from 11 to 12 m and interval from 33 to 34 m from the borehole head). A portion of the Opalinus Clay was crushed and sieved with 10 mesh (~2 mm). Opalinus Clay to be used in experiments was reconstituted at 80 wt.% -10 mesh and 20 wt.% +10 mesh. Synthetic groundwater was chosen to replicate the groundwater composition that represents Opalinus Clay pore water (Table 2 of text, Pearson et al., 2003). The salt solution was added at 9:1 water: rock ratio. The redox conditions for each system were buffered using a 1:1 mixture (by mass) of Fe3O4 and Fe° added at 0.07 wt.% of the bentonite mass. Approximately 7 wt.% (of total solids mass) 304 stainless steel (NIST SRM 101g), 316 stainless steel (NIST SRM 160b), and low-carbon steel (provided by Sandia National Laboratory) were added to the experiments to mimic the presence of a waste canister.

Reactants were loaded into a flexible gold bag and fixed into a 500 mL Gasket Confined Closure reactor (Seyfried et al., 1987). Experiments were pressurized to 150 to 160 bar and were heated isothermally to temperatures of either 200 or 300°C for 6–8 weeks or 6 months. Reaction liquids were extracted during the experiments and analyzed to investigate the aqueous geochemical evolution in relationship to mineralogical alterations. The sampled reaction liquids were split three-ways producing aliquots for unfiltered anion, unfiltered cation, and filtered (0.45 μm syringe filter) cation determination. All aliquots were stored in a refrigerator at 1°C until analysis.

Mineral Characterization

QXRD

Quantitative X-ray diffraction (XRD) analyses of experimental materials determined relative mineral abundances in the starting materials and reaction products. Each sample was ground with 20 wt. % corundum (Al_2O_3) for quantitative XRD analysis of the bulk rock (Chung, 1974). XRD measurements were conducted with a Siemens D500 diffractometer using Cu-Kα radiation. Data were collected from 2 to 70 º2θ with a 0.02 º2θ step-size and count times of 8 to 12 seconds per step. Quantitative phase analysis (QXRD) was performed using FULLPAT (Chipera and Bish, 2002) and Jade© 9.5 X-ray data evaluation software with the ICDD PDF-4 database.

Los Alamos National Laboratory Clay Mineral XRD

X-ray diffraction analyses at Los Alamos National Laboratory were conducted on a Bruker D8 Discover using Cu-Kα radiation. To better analyze the non-clay and clay fractions, the < 2 μm particles were separated via sedimentation in DI H2O. An aliquot of the < 2 μm suspension was dropped on a zero-background quartz plate and dried. This oriented mount was X-rayed from 2 to 40º2θ at 8 to 12 s per step. The oriented mount was then saturated with ethylene glycol in a 60ºC oven for 24 hours and XRD analysis was repeated. A portion of the > 2 μm particles was ground with a mortar/pestle, deposited on a zero-background quartz plate, and X-rayed under the same parameters as the bulk powder material. The remaining > 2 μm portion was used for electron microscopy. Mineral identification and unit-cell parameters analysis was performed using Jade© 9.5 X-ray data evaluation program with ICDD PDF-4 database. Illite-smectite composition of higher-ordered (R1-3) illite-smectites were modeled via ClayStrat+ (developed by Hongji Yuan and David Bish). Expandable component abundances for the disordered illite-smectites were calculated via the D°2Q method (Środoń, 1980; Eberl et al.,

1993; Moore and Reynolds, 1997). A regression from calculated data were used to calculate the % expandable (%Exp) component in each untreated and reacted bentonite. The equation is:

$$\%Exp = 973.76 - 323.45\Delta + 38.43\Delta 2 – 1.62\Delta 3$$

(Eberl et al., 1993, Eq. 3, R^2=0.99)

with Δ corresponding to D°2Q between the 002 and 003 peak positions for the oriented, ethylene glycol saturated samples.

Bulk X-ray Fluorescence (XRF) Spectroscopy analyses

Major elements were analyzed using the Rigaku Primus II wavelength-dispersive X-ray fluorescence (XRF) spectrometer. Samples were first crushed and homogenized in 5 to 10 g portions in a tungsten-carbide ballmill. Sample splits were heated at 110°C for 4 hrs, and then allowed to equilibrate at ambient laboratory conditions for 12 hrs to minimize weighing errors from atmospheric water gain. Fusion discs were prepared for analyses of the samples, by mixing 1.25 gram splits with 8.75 grams of lithium metaborate-tetraborate flux and heated in a muffle furnace for 45 minutes at 1050°C. Additional one-gram splits were heated at 1000°C to obtain the loss-on-ignition measurements used in the data reduction program.

SEM analyses

Analytical electron microscopy was performed using a FEI™ Inspect F scanning electron microscope (SEM) at Los Alamos National Laboratory. All samples were Au/Pd-coated prior to SEM analysis. Imaging with the SEM was performed using a 5.0 kV accelerating voltage and 1.5 spot size. Energy dispersive X-ray spectroscopy (EDS) was performed at 30 kV and a 3.0 spot size.

Appendix B
SEM Images (EBS-29 to EBS-31)

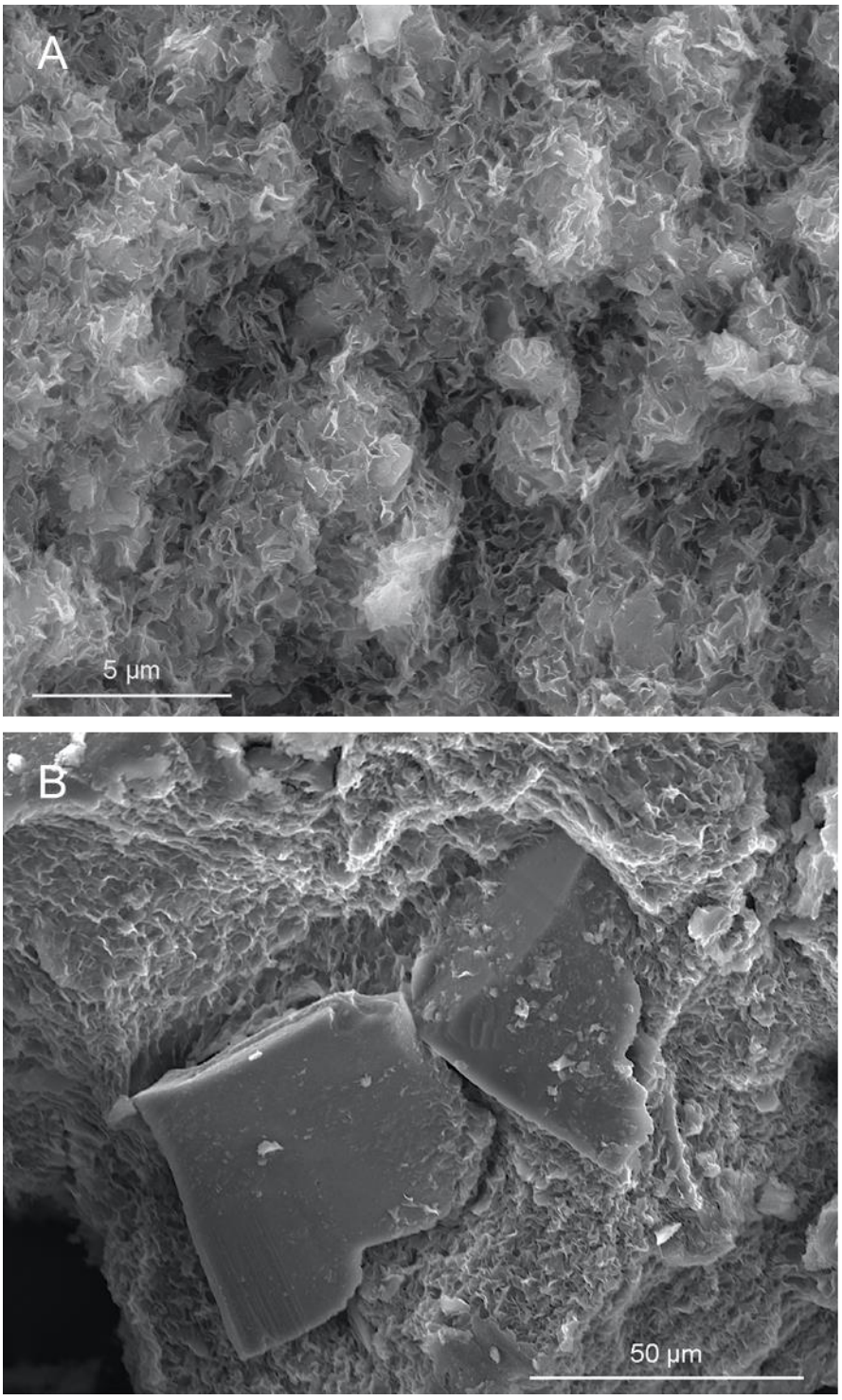

Figure B-1. EBS-29 SEM images of post-reaction products WY bentonite. [**A**] Fe-saponite [**B**] Plagioclase phenocryst in Fe-saponite

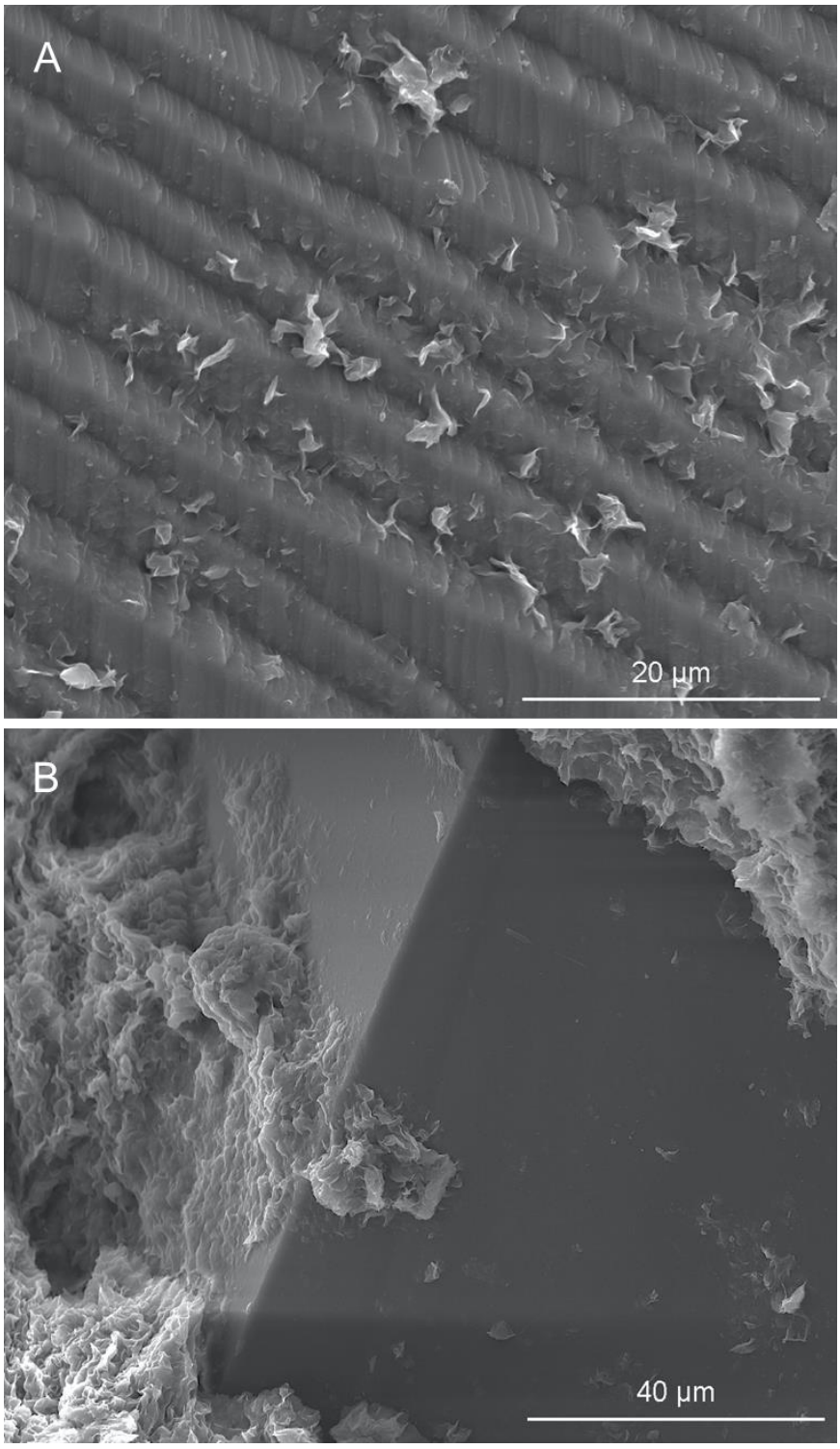

Figure B-2. EBS-29 SEM images of post-reaction products of apatite from WY bentonite. [**A**] Apatite surface with dissolution features [**B**] Apatite coated in smectite

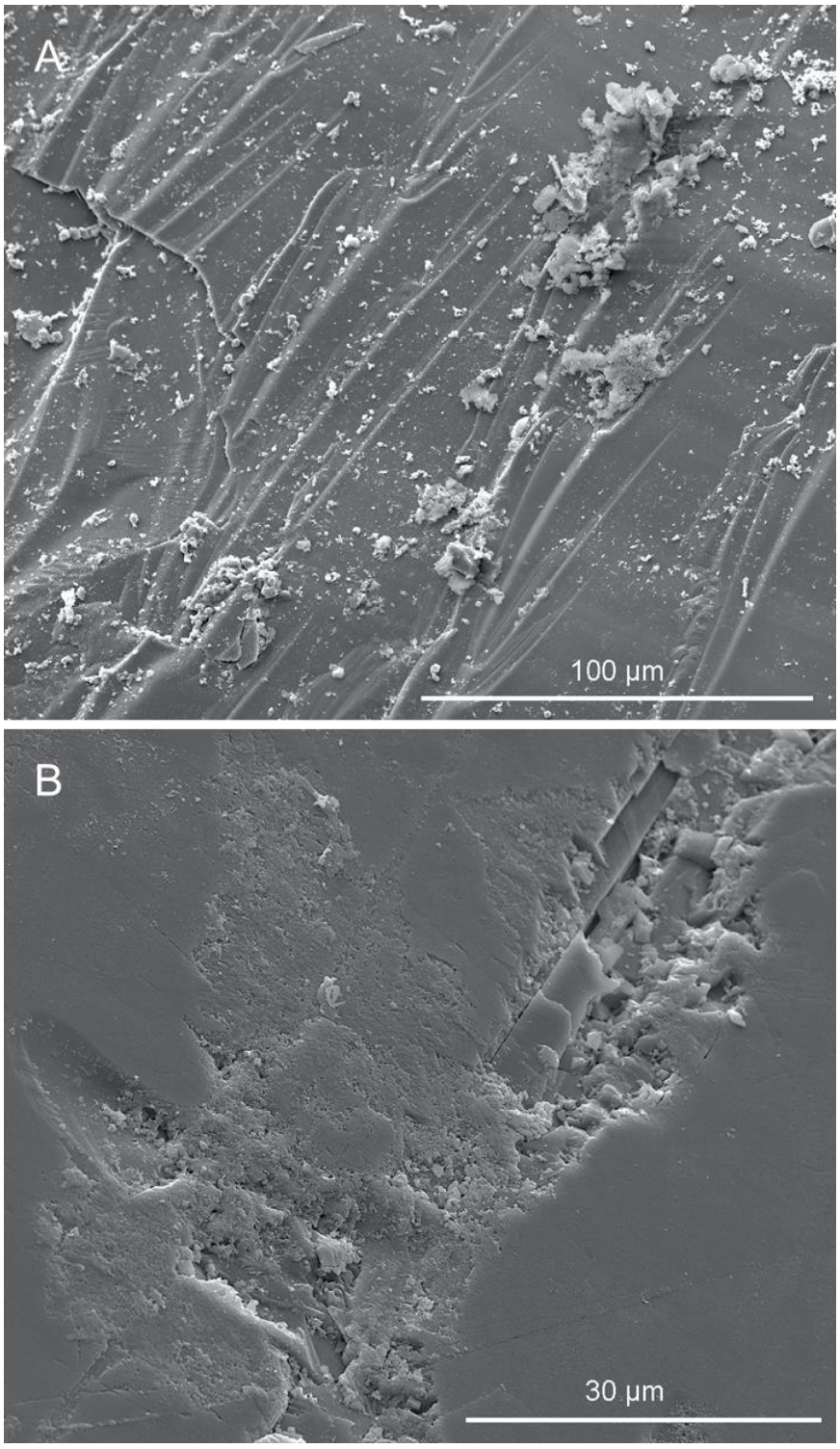

Figure B-3. EBS-29 SEM images of post-reaction products from apatite-only capsules. [**A**] Apatite with surface impurities [**B**] Pitting on apatite surface.

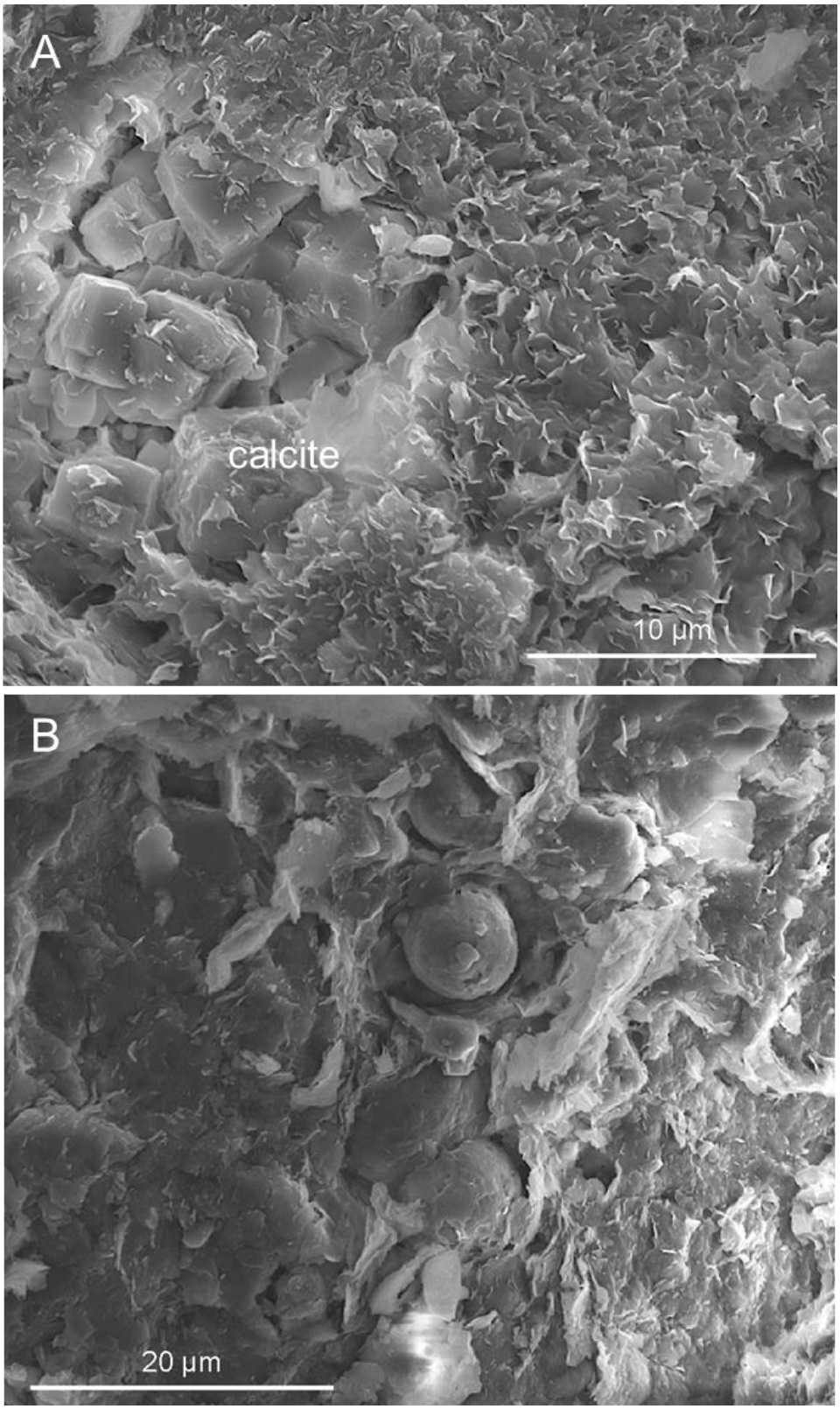

Figure B-4. EBS-30 SEM images of post-reaction products from OPC and WY bentonite. [**A**] Calcite embedded in smectite. [**B**] Calcite spheres, likely fossils from Opalinus Clay, imbedded in a clay matrix.

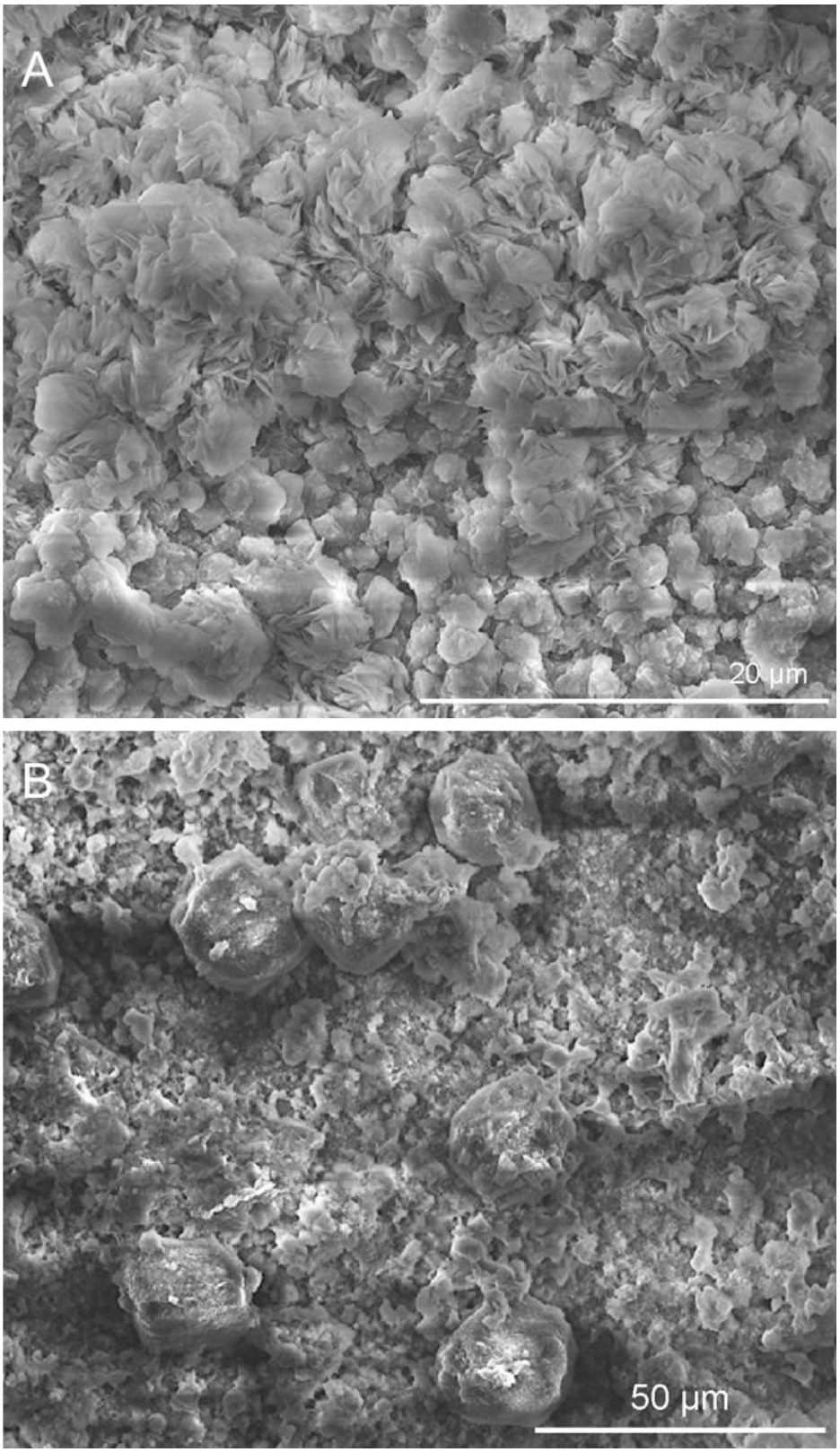

Figure B-5. EBS-30 SEM images of post-reaction cement chip surface. [**A**] CSH gel-smectite matrix [**B**] Calcite aggregates in the CSH/smectite matrix.

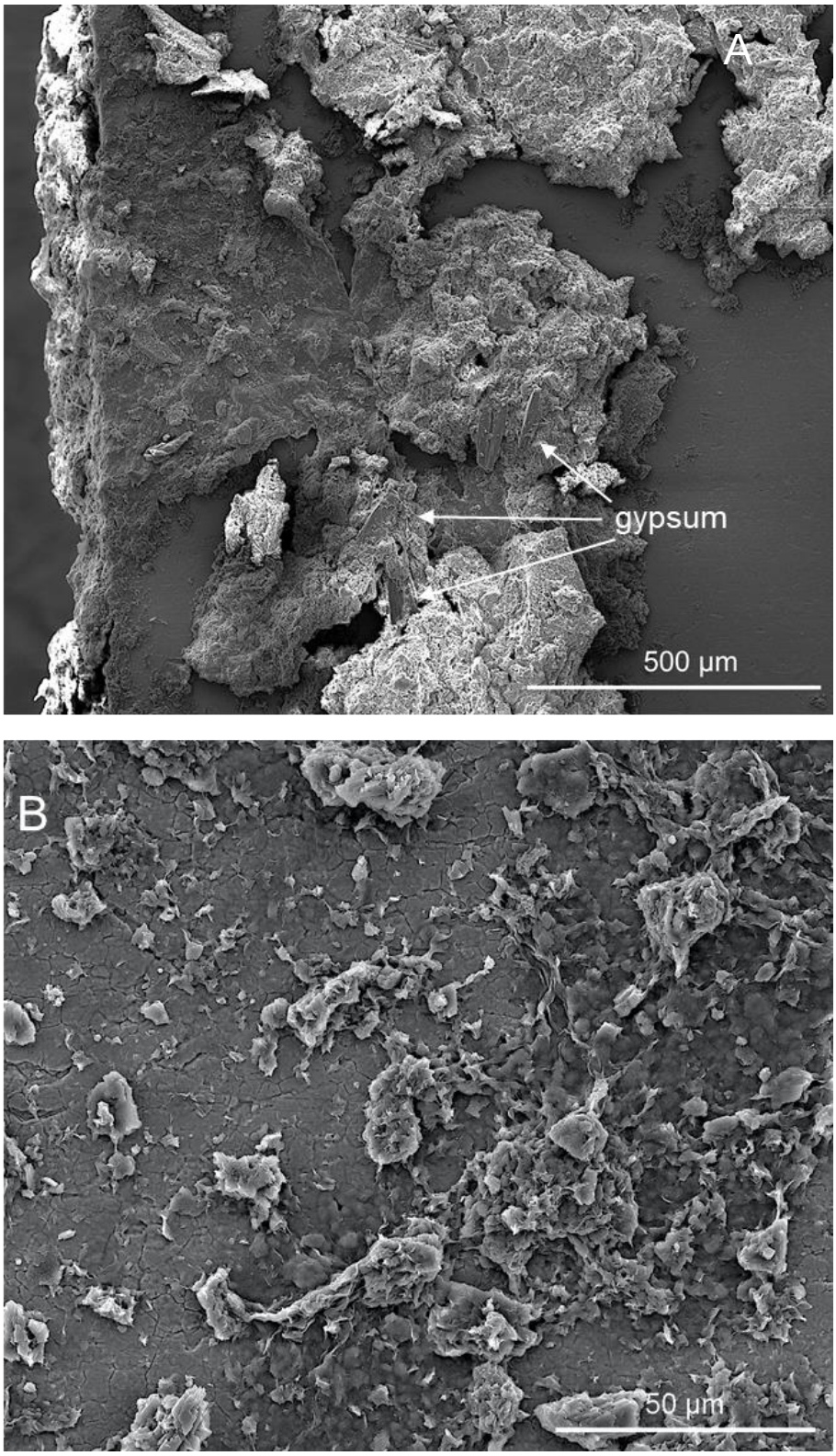

Figure B-6. EBS-30 SEM images of post-reaction products from the 316SS surface. [**A**] Large gypsum crystals in CSH-clay matrix [**B**] Smectite coating of the surface of the steel.

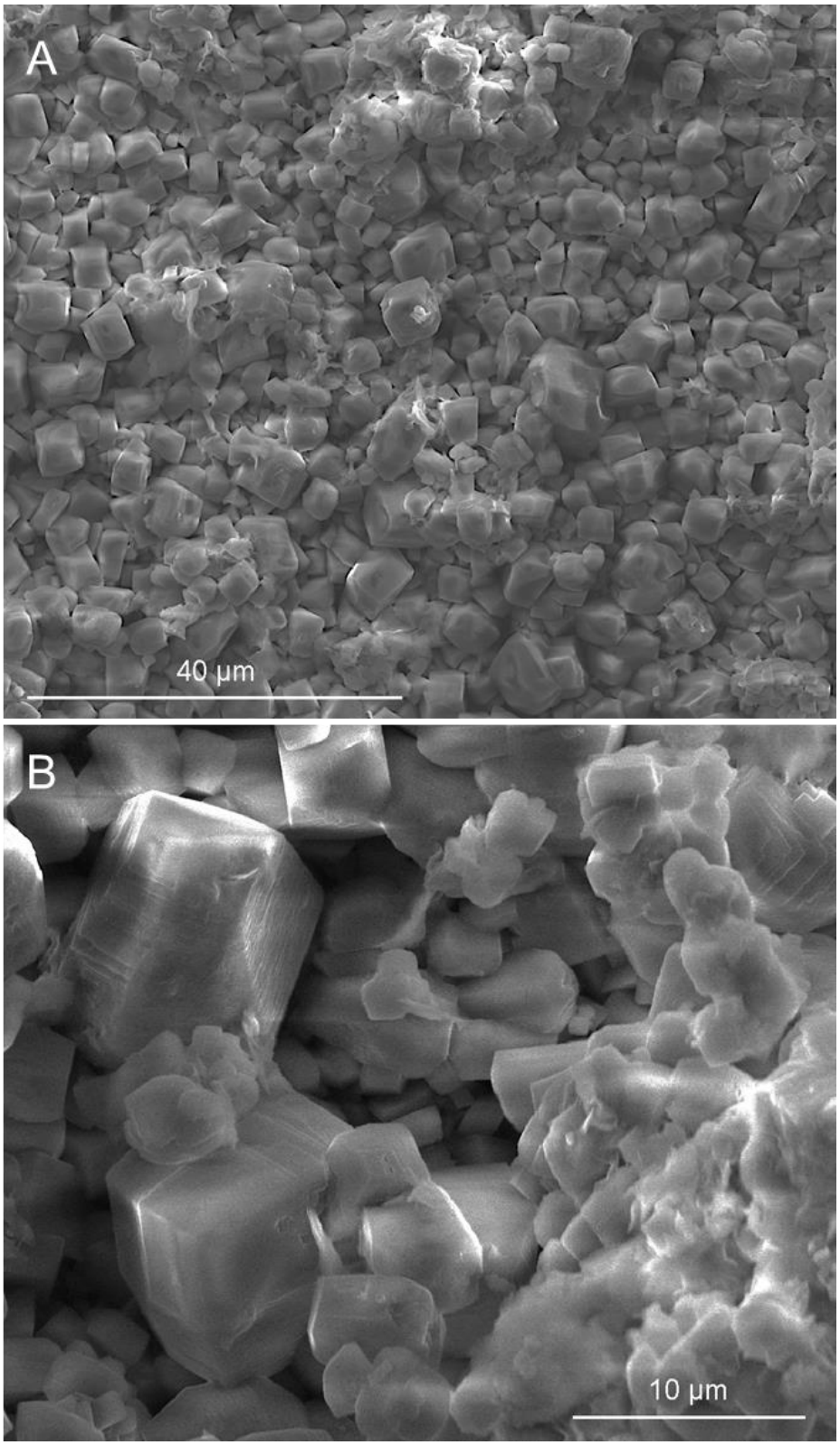

Figure B-7. EBS-31 SEM images of post-reaction cement surface. [**A**] Calcite covering the cement chip surface [**B**] Calcite with smectite.

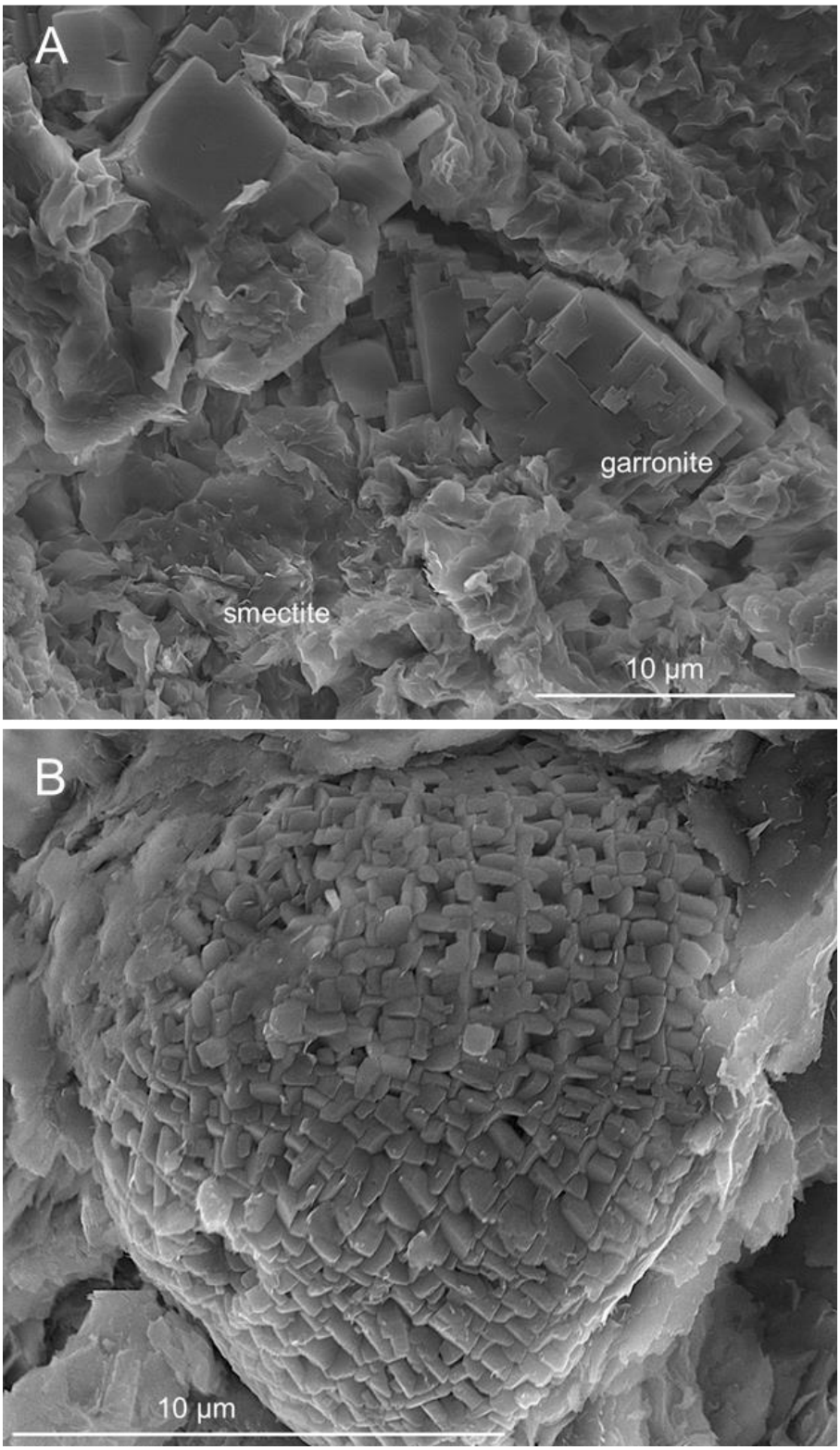

Figure B-8. EBS-31 SEM images of the WY bentonite and Opalinus Clay. [**A**] Garronite in a smectite matrix. [**B**] Lime or CSH sphere in smectite.

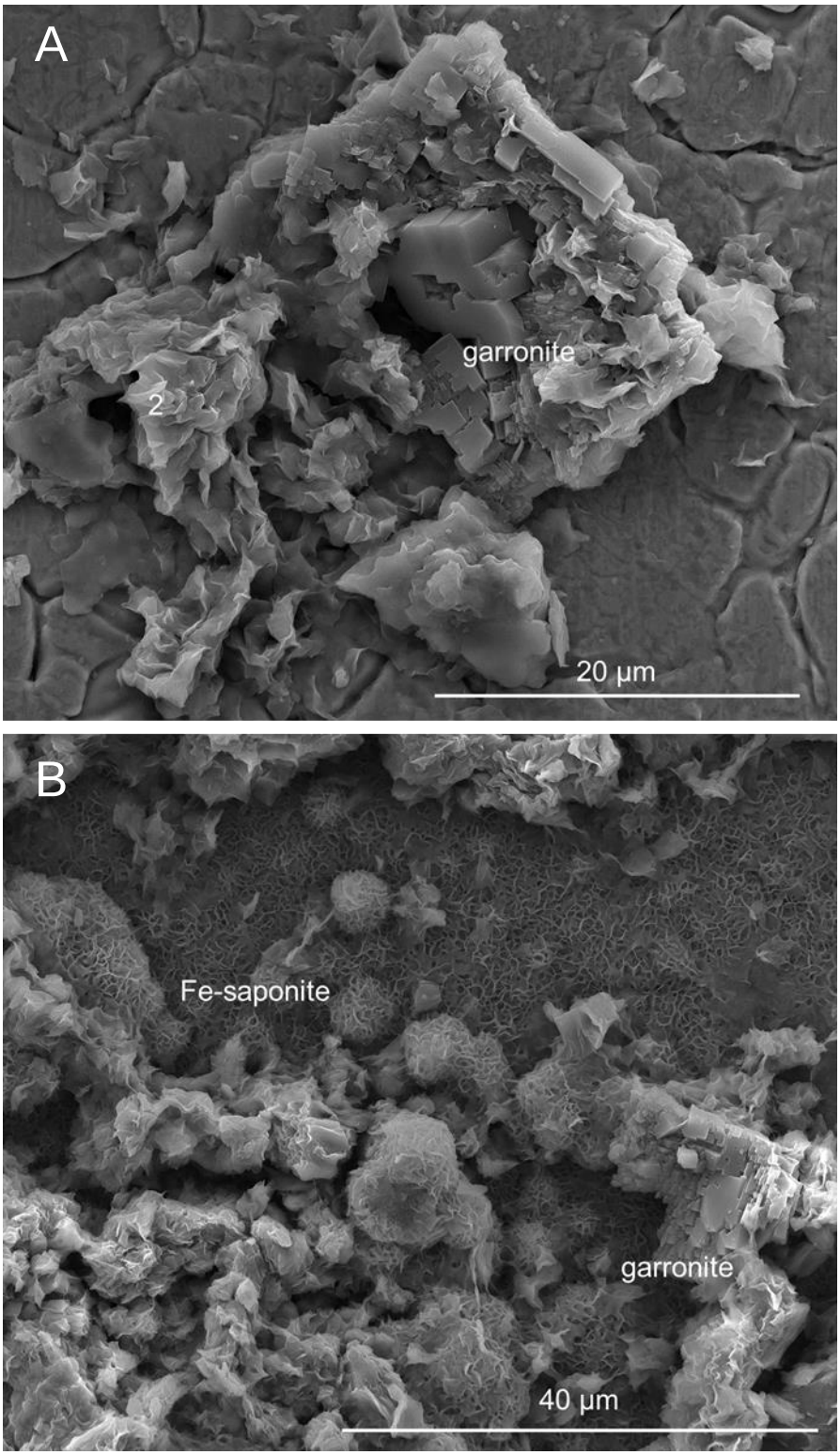

Figure B-9. EBS-31 SEM images of the post-reaction 304SS surface. [**A**] Garronite in a smectite matrix on the steel surface. [**B**] Fe-saponite honeycombs with minor garronite.